Core cross-linked polymeric micelles based on polypept(o)ides: from secondary structure formation of polypeptides to functional cross-linking strategies for polymeric micelles

Bauer, T.A.

Core Cross-Linked Polymeric Micelles Based on Polypept(o)ides

From Secondary Structure Formation of Polypeptides to Functional Core Cross-Linking Strategies for Polymeric Micelles

Core Cross-Linked Polymeric Micelles Based on Polypept(o)ides

From Secondary Structure Formation of Polypeptides to Functional Core Cross-Linking Strategies for Polymeric Micelles

Proefschrift

ter verkrijging van de graad van doctor aan de Universiteit Leiden,

op gezag van rector magnificus prof.dr.ir. H. Bijl,

volgens besluit van het college voor promoties

te verdedigen op 09.06.2022

klokke 16.15 uur

door

Tobias Alexander Bauer

geboren te Mainz, Duitsland

in 1989

Promotores: Prof. dr. Matthias Barz

                              Prof. dr. Alexander Kros

Promotiecommissie:

Prof. dr. H. Irth   LACDR (chair)

Prof. dr. J.A. Bouwstra   LACDR (secretary)

Prof. dr. J. Kuiper   LACDR

Prof. dr. T. Lammers   RWTH Aachen

Prof. dr. S.C. De Smedt   Ghent University

Table of Contents

1

General Introduction

Nanomedicine

Nanomedicine refers to the application of nanotechnology in medicine to improve diagnostic and therapeutic efficacy for patient compliance. In nanomedicine, nanoparticles serve as tools for drug delivery and disease diagnosis.[1–7] Following the guidelines of the International Organization for Standardization (ISO) and the Commission of the European Union, nanoparticles are objects of any shape with at least one external dimension in the range of 1-100 nm.[8–10] Nanoparticles offer the potential to modify the pharmacokinetic profile of active pharmaceutical ingredients (APIs) without editing the structural entities required for the mode of action.[11–13] Administration, distribution, metabolism, and excretion (ADME) can be altered and governed by the nanoparticle enhancing specificity and bioavailability of a given drug opening or extending the therapeutic window.[9,14,15] The nanocarrier design follows the structural demands of the API while referring to the intended application.[16–19] For nucleic acid delivery as required for BioNTech's and Moderna's Covid-19 vaccine, protection of the sensitive cargo to enable release of the intact mRNA into the cytosol of immune cells is of significance and featured by lipid nanoparticles.[20–23] Nanomedicine thus opened the therapeutic window for RNA-based therapies.[24–26] *Vice versa,* for small molecule APIs used in cancer therapy, nanomedicine aims to provide solubility and reduce the large volume distribution caused by the unspecific diffusion of the low molecular weight compounds.[6,27,28] Despite being highly potent in the mode of action, many small-molecule APIs are hydrophobic and require excipients and high dilutions for administration.[12,29–31] Approved for medical use in 1993 and 1996, the formulations of paclitaxel using ethanol and Cremophor EL (Taxol), and docetaxel with polysorbate 80 (Taxotere) are among the most successful drugs for adjuvant chemotherapy.[28,32,33] Nevertheless, anaphylactic hypersensitivity, hemolysis, and peripheral neuropathy are common side effects attributed to the excipients.[34,35] These restrict the maximum tolerated dose (MTD), while prolonged administration times limit patient compliance.[34,35] In this case, nanomedicine, therefore, aims to provide solubility and a selective distribution profile to APIs to reduce off-target toxicity and improve therapeutic success.[4,36,37]

Following the ambitions of nanomedicine shown in Figure 1, a large variety of nanoparticle therapeutics has been developed to improve the pharmacokinetic profiles of APIs. Initial investigations date back to 1954 when Horst Jatzkewitz reported on mescaline coupled to a copolymer of vinylpyrrolidone and acrylic acid *via* an enzymatically cleavable peptide linker.[19,38–41]
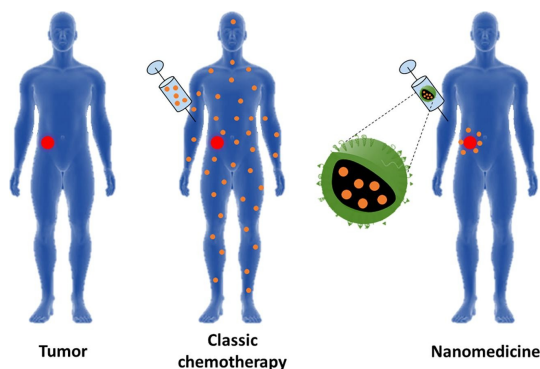
Figure 1. Idealized perspective on chemotherapy by nanomedicine. Figure reprinted from Gonzalez-Valdivieso *et al.* with permission from Elsevier (© 2021).[36]

In consecutive *in vivo* studies a sustained drug release was observed.[39] Mescaline could still be detected in urine after 17 days, compared to 16 h for the free drug, whereas no traces were found after direct conjugation without the cleavable section.[39] Jatzkewitz clearly derived the potential of polymer-drug conjugates to alter the pharmacokinetics of APIs.[38,39] The idea for polymer drug-conjugates was later refined and conceptualized by Helmut Ringsdorf considering solubility, drug conjugation, and targeting.[19,42] Beyond polymer-drug conjugates many different nanocarriers have been designed and evaluated in (pre-)clinical investigations.[5,12,13,41,43,44] A schematic overview is shown in Figure 2.[43,45] The encapsulated or conjugated small molecule APIs are typically in the range of 0.1 to 1.0 nm in hydrodynamic diameter and are displayed as red (hydrophobic drugs) and green (hydrophilic drugs) stars.[43]

The drug delivery systems can be generally divided into molecular and self-assembled structures and have been optimized for a broad variety of therapeutic cargos and diagnostic probes.[16,41,47] In particular self-assembled nanoparticles are characterized by their core-shell architecture and can be readily formed from amphiphilic lipids or polymers.[48–50] Lipophilic drugs can be encapsulated in the hydrophobic membrane or core compartment, while the hydrophilic corona provides steric shielding to reduce or prevent recognition by the immune system.[50–52] Likewise, hydrophilic polymers are used for shielding of molecular nanocarriers, e.g., to increase the blood circulation half-life and reduce the immunogenicity of proteins.[41,53,54] Polymersomes and liposomes further allow for encapsulation of hydrophilic drugs in the aqueous core pocket, while additional

stabilization is still essential for membrane-permeable drugs such as doxorubicin.[13,55–58]
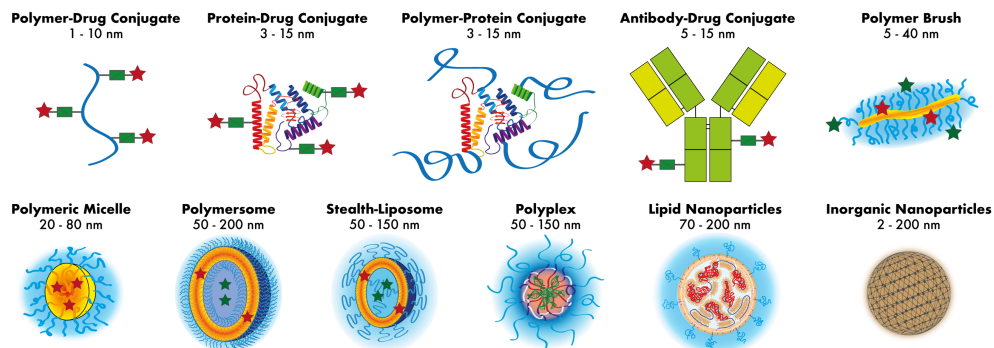
Figure 2. Schematic overview of the most common drug delivery systems in nanomedicine with approximate hydrodynamic diameters.[45,46] Small molecule drugs are represented by red (hydrophobic) and green (hydrophilic) stars, drug linkers by green rectangles.

In contrast, polyplexes and lipid nanoparticles comprise a cationic lipid or polymer block for complexation and have been designed as non-viral vectors for gene therapy to provide protection and stimuli-responsive release for RNA or DNA.[22,25,41,59,60] Besides lipid and polymer-based nanocarriers, inorganic nanoparticles, colloids, and metal-organic frameworks have been established for drug delivery and diagnosis.[45,61–64] As such, iron oxide nanoparticles have been thoroughly investigated for the treatment of iron deficiency anemia, in heat ablation therapy, as well as for their potential as contrast agent in magnetic resonance imaging.[65–70] Moreover, non-biodegradable electron-dense gold nanoparticles facilitate methodical *in vivo* studies using transmission electron microscopy (TEM) and enhance the sensitivity for surface-enhanced Raman scattering-based imaging.[3,71–75] For therapeutic inventions, polymeric micelles (PMs) are among the most promising carrier types for hydrophobic APIs.[52,76–78] Herein, the core compartment allows for high drug loading and can be designed and adjusted for the conjugation of (pro-)drugs featuring stimuli-responsive release.[79–84] Moreover, PMs can be prepared with hydrodynamic diameters below 100 nm, often between 30 - 50 nm, which facilitate long circulation time and penetration into tumorous or inflamed tissue.[76,85] As early as 1998, Torchilin and co-workers reported superior tumor accumulation of an ^{111}In-labelled protein in murine Lewis lung carcinoma xenograft models when PEG-DSPE micelles were selected over stealth liposomes as the carrier system.[86] In a detailed investigation,

Cabral *et al.* demonstrated the significance of particle size for deep tissue penetration.[85] As shown by intravital microscopy using PMs with distinct diameters of 30, 50, 70, and 100 nm, only the 30 nm particles were able to penetrate the poorly permeable pancreatic tumor leading to reduced tumor volumes by the release of the conjugated 1,2-diaminocyclohexane-platin(II) metallodrug.[85]

Physiological Barriers for Nanomedicine

On the journey to the target site, nanomaterials face several barriers and obstacles for successful drug delivery.[1,87,88] In general, the majority of nanocarriers are applied by parenteral administration routes.[89–91] Activation of the adaptive immune system typically follows intramuscular injection for addressing transport into the draining lymph node.[92–94] In contrast, for cancer therapy, nanomedicines are mainly administered by intravenous injection aiming to target metastasis as well as the primary tumor site.[95–97] Injection into the blood stream exposes the nanocarriers to the blood components, e.g., red blood cells, immune cells, and plasma proteins, as well as to dilution.[98–101] Stabilization and shielding strategies are thus required to prevent unspecific complement activation, opsonization, and recognition by the mononuclear phagocyte system (MPS).[1,51,101,102] The MPS consists of bone marrow progenitors, monocytes and tissue macrophages located in organs such as the liver and spleen.[102,103] Intended to remove foreign material from the blood stream, non-specific accumulation in these organs is a major obstacle for nanomedicines that impedes drug delivery to the diseased target site (Figure 3).[103,104]

Strategies to avoid rapid clearance comprise the decoration of nanocarriers with hydrophilic polymers, such as poly(ethylene glycol) (PEG) or polysarcosine (pSar), which follow the Whitesides' rules for protein resistant materials and reduce MPS recognition, phagocytosis, and clearance from the circulation.[106–110] Mechanistically, the enhanced repulsive forces among the hydrated polymer strands form an impermeable coating preventing van der Waals, electrostatic, and hydrophobic interaction with proteins.[51,111] Following PEG as the gold standard material, the term 'PEGylation' was coined for the surface modification of materials with PEG, attributing reduced recognition properties ('stealth'-effect).[53,112,113] Herein, the molecular weight of the hydrophilic polymer significantly influences the shielding efficiency.[111]
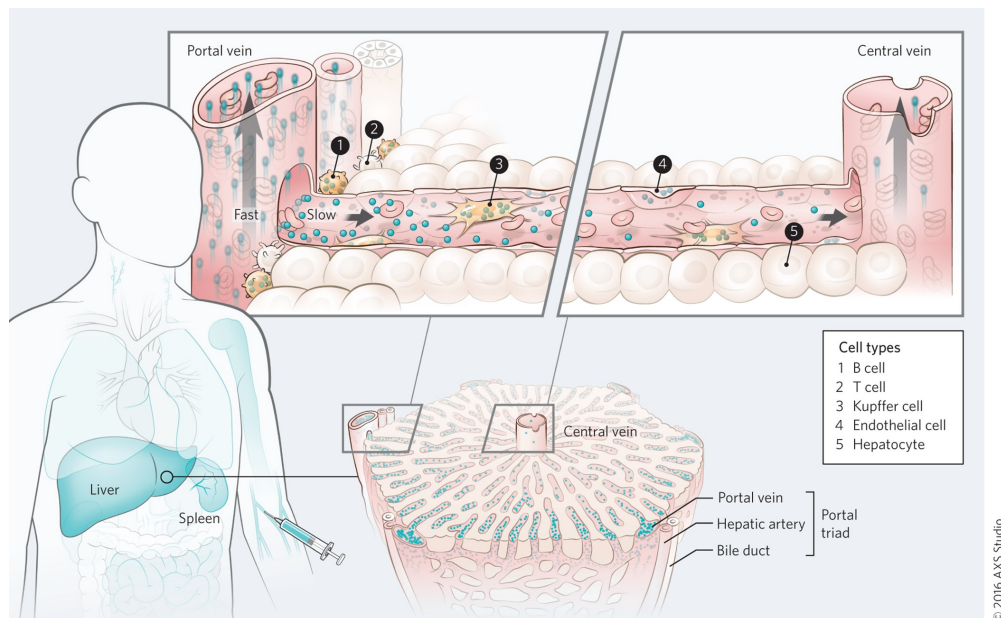
Figure 3. Intravenously administered nanoparticles encounter non-specific interaction with the MPS. The intensity of the turquoise color refers to the nanoparticle uptake within each organ.[105] The reduced flow rates in the liver sinusoid facilitates nanoparticle uptake by the residing immune cells, e.g., Kupffer cells. Figure reprinted from Tsoi *et al.* with permission from Springer Nature (© 2016).[103]

Consequently, the PEG chain length was carefully optimized for the development of Doxil (doxorubicin sulfate nanocrystals, encapsulated in stealth liposomes with a lipid bilayer of a high melting point (T_m = 53 °C)), and PEG_{2k}-lipid (lipid: 1,2-distearoyl-sn-glycero-3-phosphoethanolamine; DSPE) was selected considering circulation time and lipid metabolism.[13] For block copolymer micelles, Kwon *et al.* reported that PEG_{12k} significantly reduced the nanoparticle clearance compared to shielding by PEG_{5k}, resulting in a 5-fold increase of nanoparticles still in circulation after 4 h post-injection.[114,115]

Beyond the surface chemistry, the hydrodynamic diameter is an important parameter affecting the biodistribution of nanoparticles. Large particles with hydrodynamic diameters > 200 nm can be rapidly recognized and cleared *via* the MPS in the liver and spleen.[17,19,52] Contrariwise, glomerular filtration in the kidneys defines the lower size limit for nanoparticles that aim for long blood circulation.[1,116] Threshold values for rapid renal excretion were found as ≤ 5.5 nm for quantum dots, approx. 29 kDa for dextran, and around 30 kDa for linear

PEG.[117–119] Conversely, to avoid long-term side effects such as storage diseases the renal filtration sets an important limit for the maximum size of the individual nanocarrier components if the material is not biodegradable within relevant time frames.[38,113,120]

Tumor Targeting by the EPR Effect and Beyond

The discovery of the enhanced permeability and retention (EPR) effect supported the field of nanomedicine, giving a rationale for targeting nanoparticles to inflamed and tumorous tissue.[27,121,122] In 1984, Maeda *et al.* found an increased concentration of neocarzinostatin (NCS) in the tumor tissue of rabbits and mice when NCS was conjugated to a styrene-maleic acid copolymer (SMANCS).[123] After detailed elucidating studies in tumor-bearing mice using ^{51}Cr-labeled proteins of varying molecular weights in 1986, Matsumura and Maeda then accounted the unique vascular characteristics of the tumor tissue for the specific accumulation of macromolecules therein.[124] Due to extensive and rapid proliferation, the cancer vasculature shows a high tendency for deficient vessel structures leading to fenestrations with higher permeability for nanoparticles compared to normal tissue (Figure 4).[41,85,124] Moreover, insufficient lymphatic drainage reduces nanoparticle clearance from the tumor retaining the accumulated particles.[124] Consequently, if unspecific excretion and interaction with the MPS can be prevented, passive accumulation of the nanocarriers can be achieved.[30,41,125]
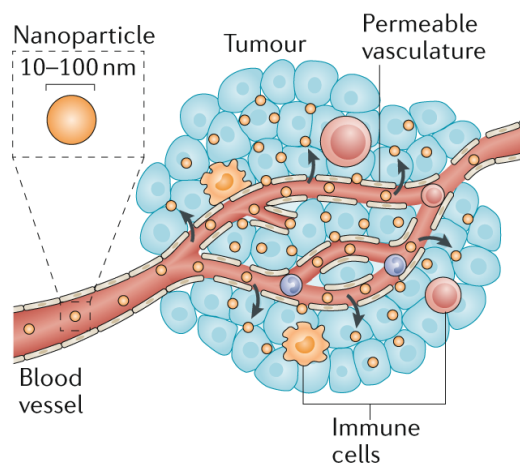

Figure 4. Schematic illustration of the nanoparticle accumulation in cancerous tissue due to the EPR effect. Figure reprinted from Irvine *et al.* with permission from Springer Nature (© 2020).[78]

Nevertheless, the EPR effect has been critically discussed, and cannot be applied as a general concept for all tumor types.[27,126–129] As such, the EPR effect was reported to be more prominent in murine (xenograft) tumor models compared to human patients.[130,131] Moreover, a large heterogeneity in EPR susceptibility was observed among cancer patients calling for personalized medicine and patient stratification before applying nanomedicines as a general treatment regimen.[132,133] Additionally, conjugation of targeting ligands ('active targeting') could improve tissue-selective distribution and enhance cell-specific uptake, while new types of drugs or drug combinations inaccessible for administration without nanomedicine are expected to contribute to therapeutic success.[31,129,134] The basic requirement for concepts adding specificity yet remains the absence of unspecific interaction since active targeting can only take place when receptor and ligand are already in close proximity.[135–138]

From the methodical viewpoint, more detailed investigations on the tissue level recently enlightened the actual targeting mechanism providing an deeper understanding and defining the basis for future therapeutic concepts.[88,139–141] Herein, Chan and co-workers employed PEGylated Gold nanoparticles to investigate the exact mechanism accounting for nanoparticle entry into tumor tissue.[72,73] Despite minor fractions of particle accumulation *via* passive diffusion, active transport mechanisms were described as the main driving force for nanoparticle entry into tumor tissue for a variety of tumor models.[72] Moreover, a specific type of endothelial cells, nanoparticle transport endothelial cells (N-TECs), was identified as a gatekeeper for the transport process.[73] On the other hand, Biancacci *et al.* combined optical whole-animal imaging by micro-computed tomography-fluorescence tomography (μCT-FLT) with immunohistochemistry for a detailed biodistribution analysis of dye-labeled core cross-linked polymeric micelles.[142] On the organ level, 18.6% ID/g of the injected dose (ID) were located within the tumor tissue, exceeding the doses found in the liver and spleen (9.1% and 8.9% ID/g). Interestingly, within the tumor microenvironment, 67% of the nanoparticles were found in macrophages and other immune cells, although cancer cells accounted for 71% of the overall cell population.[142] This underlines the potential of core cross-linked polymeric micelles for therapeutic approaches combining chemotherapy and immunomodulation.[140,142–145]

Polymeric Micelles in Nanomedicine

Considering their small size and the core-shell architecture PMs are ideal carrier systems for hydrophobic small-molecule drugs. PMs can be readily formed by self-assembly of amphiphilic copolymers above the critical micelle concentration (CMC) applying dialysis or microfluidic devices.[43,48,49,52,146] Self-assembly is an autonomous organization process leading to higher-ordered patterns or structures.[147] For self-assembly of linear block copolymers, spherical or worm-like micelles, lamellae and vesicles, as well as bicontinuous structures, can be obtained depending on the length and flexibility of the individual hydrophilic and hydrophobic segments.[49,148,149] Compared to surfactant-based micelles, PMs exhibit lower CMC values (typically 10^{-6} - 10^{-8} M vs. 10^{-3} - 10^{-4} M) which refer to the higher number of interaction points.[150,151] The CMC accounts for the free energy gain after reduction of free surface area by self-assembly and is the benchmark for the thermodynamic stability of a micelle.[49,101,149,150] At the same time, the CMC represents the concentration of free polymer, so-called unimer, that always remains present in solution (Figure 5).[43,101] Even after self-assembly, PMs are thus connected to the unimer concentration by a dynamic equilibrium, whereby the rate of exchange refers to the kinetic stability.[43,101,152] Considering the application of PMs as drug carriers, the equilibrium directly affects therapeutic success, as excretion or adsorption of unimer leads to micelle disassembly.[43,52,101] Upon injection into the bloodstream PMs are subjected to large dilutions and are exposed to plasma proteins, blood cells, hepatobiliary excretion, and renal filtration.[1,88,103,116] In combination, these factors can rapidly induce disintegration of the PMs, reducing the nanocarrier to a bare solubilizer incapable to provide target specificity.[27,37,43,153] In addition, the amphiphilic unimer may be susceptible to eliciting interaction with components of the immune system, e.g., the complement activation, promoting accelerated blood clearance (ABC) and affecting the safety profile of the medicinal product.[43,154–156]
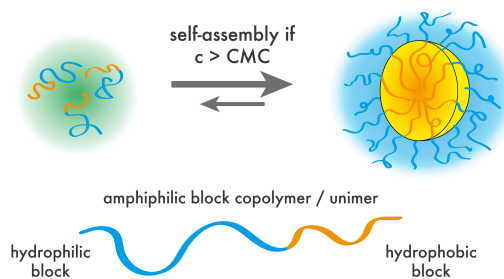
Figure 5. Polymeric micelles and the dynamic equilibrium of unimer and micelle.[43,101]

While multiple PMs containing hydrophobic small molecule drugs have already been investigated in clinical trials,[16,89,157–159] e.g., NK105,[160,161] NK012,[162] BIND-014,[163] the consequences of limited nanocarrier stability can be exemplified by studying Apealea and Abraxane. Both products have been developed and approved as Cremophor-free formulations of paclitaxel (PTX) to reduce the side effects associated with the excipient (as mentioned above).[9,32,34,88] In Abraxane, PTX is formulated with human serum albumin forming 130 nm particles in aqueous solutions and was approved by the Food and Drug Administration (FDA) for the treatment of advanced non-small cell lung cancer (NSCLC) in 2005.[12,164–166] However, upon infusion, the albumin-drug particles dissolve and albumin-PTX complexes are formed, whereby PTX can bind and unbind to readily available proteins within the bloodstream.[12,166] Compared to Taxol, higher response rates were found for Abraxane in NSCLC patients, while the overall survival (OS) was not significantly improved.[88,167] Similarly, response rate and progression-free survival (PFS) were higher for metastatic breast cancer patients, but OS was not significantly different.[88,168] In 2018, Apealea was approved by the European Medicines Agency (EMA) for the treatment of ovarian cancer in combination with carboplatin, and consists of micelles formed from *N*-(13-*cis*-retinoyl)-L-cysteic acid methyl ester sodium salt and *N*-(*all-trans*-retinoyl)-L-cysteic acid methyl ester sodium salt encapsulating PTX.[169,170] These micelles immediately release PTX into the blood plasma upon administration, yet offer shorter infusion times (1 h for Apealea vs. 3 h for Taxol), higher doses ($MTD_{Apealea}$ 250 mg m^{-2} vs. MTD_{Taxol} 175 mg m^{-2}) and no mandatory premedication.[169,170] Nevertheless, Apealea did not improve OS or PFS.[169,170] Although Apealea and Abraxane both successfully contribute to cancer therapy and patient compliance, passive targeting *via* the EPR effect is not substantiated by the rapidly disintegrating particles, which

exemplifies the need for stable nanocarriers with tumor-specific drug release to exploit the full potential of nanomedicine.[9,43,88,169]

Core Cross-Linked Polymeric Micelles

Based on the favorable structural properties of PMs, several modification strategies have been developed to suspend the equilibrium between unimer and polymeric micelle to achieve stable nanoparticles.[79] In general, non-covalent cross-linking strategies using π-π interactions, hydrogen bonds, or the chelation of metal ions, as well as different covalent cross-linking chemistries, have been investigated.[43,171–175] For the latter, dynamic covalent bonds offer the potential to precisely tailor carrier stability and stimuli-responsive drug release.[43,81,176] Beyond particle stabilization, only drug conjugation or specific interactions within the core assure to prevent drug leakage during transport and rapid transfer to the hydrophobic domains of surrounding proteins.[13,37,177]
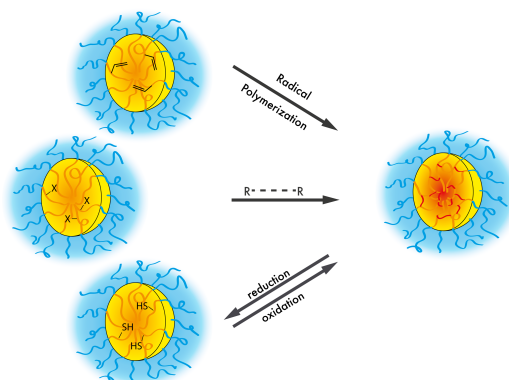
Figure 6. Core cross-linking strategies for polymeric micelles. Figure reproduced from Talelli *et al.* with permission from Elsevier (© 2015).[43]

Core cross-linked polymeric micelles (CCPMs) have attracted significant interest, and optimization of carrier stability and drug release is a key objective for the delivery of hydrophobic APIs.[30,43,79,178,179] As shown in Figure 6, the major strategies for core cross-linking include radical polymerization, reactions with bifunctional agents, and reversible oxidation of thiols.[43] Besides core cross-linking, shell cross-linking per-se offers a similar potential for stabilization of micelles.[180,181] Nevertheless, modifications in the nanoparticle shell may easily jeopardize the water-solubility and protein resistance required for effective steric shielding.[43,98] Early attempts to CCPMs for medicinal applications date back to

1992 when Rolland *et al.* used free radical polymerization for core cross-linking of PMs made from triblock copolymers of PEG-*block*-polyisoprene-*block*-PEG.[182,183] As a result, the CCPMs retained their structure even in organic solvents and showed a circulation half-life above 50 h after intravenous injection to mice.[182] More recently, Rijcken *et al.* from the Hennink lab developed CCPMs based on free radical cross-linking of thermosensitive PEG-*block*-poly(*N*-(2-hydroxypropyl) methacrylamidelactate) copolymers, culminating in the current evaluation of CPC634 in clinical phase II studies for the treatment of platinum-resistant ovarian cancer (NCT03742713).[184–188] For the production of CPC634, core cross-linking and drug stabilization are performed simultaneously by a docetaxel pro-drug, which is connected to a methacrylate by a pH-responsive linker gradually releasing the drug at pH 7.4.[184,186] Surprisingly, cumulative skin toxicity was found as the dose-limiting toxicity in phase I dose-escalation studies likely caused by micronucleation in the skin originating from slow drug release.[187,189] Nevertheless, for CPC634, in human patients, four-fold higher total docetaxel concentrations were found in the tumor tissue compared to conventional docetaxel.[188] These findings relate to promising preclinical results in which complete tumor regression was observed upon single-dose administration.[185] Besides free radical polymerization, disulfide bonds are frequently implemented as cross-links for PMs.[43,178,179] Disulfide bonds remain largely intact in extracellular fluids and can be cleaved by the elevated intracellular glutathione concentrations and are considered as the archetype of bio-reversible bonds for drug delivery.[190,191] Disulfides can either be introduced by the rather unselective oxidation of thiol-groups or by using bifunctional cross-linkers such as 3,3'-dithiodipropioic acid containing a pre-formed disulfide bond.[43,178,179,192] In addition, the Barz lab recently developed thiol-reactive protecting groups for chemoselective disulfide bond formation.[193–197] After self-assembly, amphiphilic copolymers containing the *S*-alkylsulfonyl-group can be addressed by thiol-based cross-linkers yielding either CCPMs or cross-linked nanohydrogels.[82] The combination of this approach with pro-drugs for therapeutic inventions will be elucidated in this thesis.

Among polymer-based nanomedicines, CCPMs have evolved from PMs and are expected to improve small-molecule-based drug delivery. The current challenges for CCPMs still comprise adjusting the intricate connection between carrier stability and stimuli-responsive yet rapid and complete drug release. Implementing multiple or even complex stimuli while accounting for robust and

scalable production thus requires innovative chemistry.[9,43,88,132,198,199] Focusing on therapeutic success, nanomedicine will always compete with other concepts of therapeutic care.[200–202] Expanding nanomedicine beyond its horizon implementing or assisting other technologies will thus lead to progress for treating devastating diseases and improving patients' lives.

Polypept(o)ides

Polypept(o)ides are hybrid materials combining the intrinsic functionality and stimuli-responsiveness of polypeptides with polypeptoids, e.g., polysarcosine for solubility and steric shielding.[108,203,204] Considering peptides and proteins are based on α-amino acids, Bartlett and co-workers defined peptoids as oligomers of *N*-substituted glycines that are connected by amide bonds in the main chain in 1992.[205,206] The term was later expanded by Zuckerman and co-workers, referring to polypeptoids for larger sequences, and polypeptoids can be considered as structural isomers of polypeptides.[204,207] Unlike polypeptides, polypeptoids generally lack the acidic hydrogen atom at the amide nitrogen atom and are thus exclusive hydrogen bond acceptors that do not form secondary structures unless specific substituents are introduced.[208–211] The highly water-soluble pSar, poly(*N*-methyl glycine), is among the most intensively studied polypeptoids.[212–214] The free amino acid sarcosine can be found in muscle tissue and as a component of creatine (*N*-amidino sarcosine) in tissues with high energy demand.[215–217] Sarcosine can be synthesized from glycine *via* the enzyme glycine-*N*-methyl transferase and degraded by sarcosine dehydrogenase.[218–220] Polypept(o)ides thus allow for synthetic polymers entirely based on endogenous amino acids.[108,203,204]

The term polypept(o)ides was coined by the Barz group in 2014 referring to the new class of polymeric materials combining polypeptides with polypeptoids (Figure 7).[108,203] Early examples of polypeptide/polypeptoid copolymers date back to the origins of *N*-carboxyanhydride (NCA) and *N*-substituted NCA (NNCA) polymerization when studying fundamental properties and reaction kinetics was the major focus of research.[221,222] Hanby, Waley, and Watson briefly described the first synthesis of pSar-*block*-poly(DL-phenylalanine) in 1950, yet, comprehensive study design and characterization of the copolymer was provided by Bamford and Ballard in 1956.[223,224] Besides block copolypept(o)ides, early on, also statistical copolypept(o)ides have been synthesized and studied, aiming to understand the structure and function of the synthetic polypeptides and their natural analogs.[225–227]
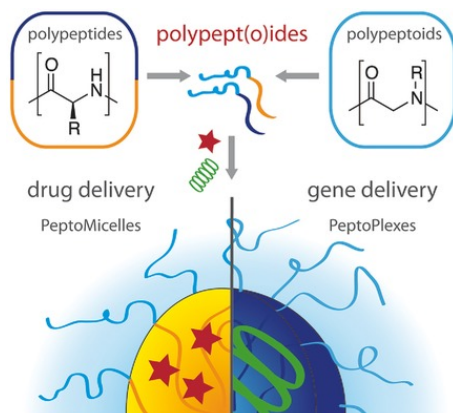
Figure 7. Polypept(o)ides combine the intrinsic functionality and stimuli-responsiveness of polypeptides with the shielding properties of the hydrophilic polypeptoid polysarcosine. Figure reprinted from Klinker *et al.* with permission form John Wiley and Sons (© 2015).[108]

Concerning medicinal applications, Kimura and co-workers investigated polypept(o)ides in the 1990s.[228–231] Among others, microcapsules were prepared from pSar-*b*-poly(ε-benzyloxycarbonyl-L-lysine) (pSar-*b*-pLys(Z)), pSar-*b*-poly(γ-methyl-L-glutamate) (pSar-*b*-pGlu(OMe)), and pSar-*b*-poly(L-alanine) (pSar-*b*-pAla), and the release of fluorescein isothiocyanate (FITC)-dextran was determined.[228] Nevertheless, for medical applications, polypept(o)ides have attracted increasing attention only recently since NCA polymerization provided easy access to functional materials with defined polymeric architecture and narrow molecular weight distribution.[108,204] The latest developments will thus be discussed in the paragraphs *Polysarcosine* and *Polypept(o)ides in Nanomedicine.*

NCA/NNCA Polymerization

Synthetic polypept(o)ides can be conveniently prepared by living amine-initiated ring-opening NCA/NNCA polymerization.[232–234] Depending on the desired application, polypept(o)ides can be designed with statistical or block-wise primary sequences, linear or branched architectures, and Poisson-like molecular weight distribution.[108,204] Despite early attempts by Bailey *et al.*,[235] NCA polymerization does not offer control on the primary amino acid sequence, making it a complementary tool distinct from solid-phase peptide synthesis (SPPS) or recombinant peptide expression techniques.[236–238] A general scheme for the amine-initiated polymerization of NCAs or NNCAs ($R^1 \neq H$) is given in Scheme 1.
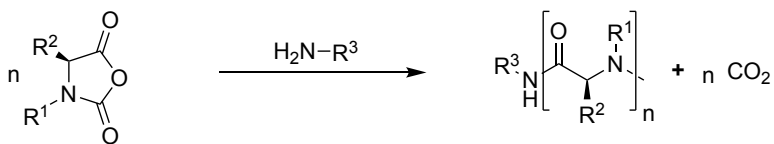
Scheme 1. Nucleophilic amine-initiated polymerization of NCAs and NNCAs.

The first NCA synthesis was discovered by Hermann Leuchs in 1906, and NCAs are thus also called Leuchs' anhydrides.[222,239] In the initial publication, Leuchs obtained glycine NCA upon heating of *N*-ethoxycarbonyl glycine chloride (Scheme 2).[239] Moreover, Leuchs carefully described the release of CO_2 after the reaction of the NCA with water at room temperature, whereby an insoluble product was formed, which was interpreted as a higher anhydride of glycine. Leuchs further applied the methodology to other amino acids, including phenylalanine, leucine, and *N*-phenyl glycine yielding comparable NCAs and reaction products.[240,241]
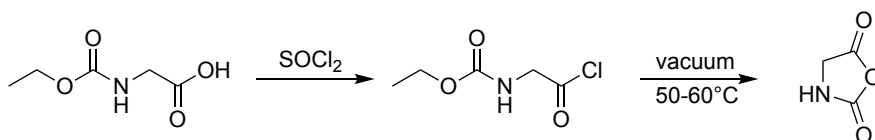
Scheme 2. Synthetic pathway to glycine NCA described by Hermann Leuchs.[239]

Despite the seminal publication from Hermann Staudinger in 1920, the general concept of polymerization and macromolecules was not completely established and still debated at that time.[222,242] Early reports on NCAs thus mainly focused on the analysis of the degradation products of NCAs, e.g., diketopiperazines and hydantoins, and referred to so-called higher condensed anhydrides for products with higher molecular weights.[243–245] Sigmund and Wessely described the first synthesis of sarcosine NCA in 1926.[246] Herein, the authors mention polypeptides as possible products of the reaction of sarcosine NCA with pyridine, yet still refuse to describe these as polymers rather referring to higher condensed anhydrides. In 1947, Woodward and Schramm thus claimed the first intended NCA polymerization using traces of water for the initiation of the reaction in benzene-solutions yielding polypeptides as synthetic analogs of proteins.[247] In the following, various polypeptides have been synthesized from this methodology and studied for their physicochemical properties.[214,221,226] The kinetics of the NCA polymerization was first examined by Waley and Watson, revealing a first-order reaction for the polymerization of sarcosine NCA in nitrobenzene.[248–250]
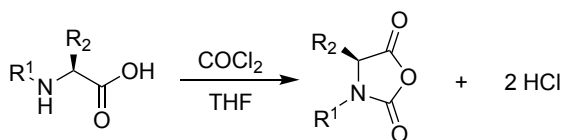
Scheme 3. NCA synthesis according to the Fuchs-Farthing method.[251,252]

To generate NCAs and NNCAs, Fuchs suggested the direct reaction amino acids with phosgene, which was refined and improved by Farthing (Scheme 3).[251,252] Addressing safety concerns and facilitating the application, gaseous phosgene can also be substituted by liquid diphosgene, or solid triphosgene, whereby phosgene is generated *in situ*.[253,254] The Fuchs-Farthing method is thus the preferred synthetic route to NCA monomers, allowing for high yields and sufficient monomer purity after sublimation and/or repetitive recrystallization.[255] Of note, the purity of all reagents, i.e., monomer, solvent, and initiator, is of significance for successful NCA polymerization. Beyond characterization by nuclear magnetic resonance (NMR) spectroscopy, Karl Fischer Titration to determine residual water content, and ion chromatography to detect inorganic contaminations, e.g., chloride ions, complement reagent analysis.[256,257] In addition, the melting point represents an indicator of monomer purity.[255]

The mechanistic pathways for the amine-initiated NCA polymerization are displayed in Scheme 4.[108,258] In general, two competing reaction pathways exist in parallel, namely, the activated monomer mechanism (AMM) and the normal amine mechanism (NAM). According to the NAM, the initiator solely acts as a nucleophile that attacks the NCA at C-5 leading to ring-opening and the formation of the carbamic acid. The carbamic acid then decarboxylates generating a primary amine readily available to attack the next NCA monomer. In case the decarboxylation is too slow, e.g., when the carbamic acid is deprotonated or the solvent is fully saturated with CO_2, a second NCA monomer can already be added at this stage ultimately leading to an urea derivative terminating the chain growth. Based on density functional theory (DFT) calculations, the nucleophilic attack at C-5 is the rate determining step of the NAM pathway using nucleophilic primary amines.[259]
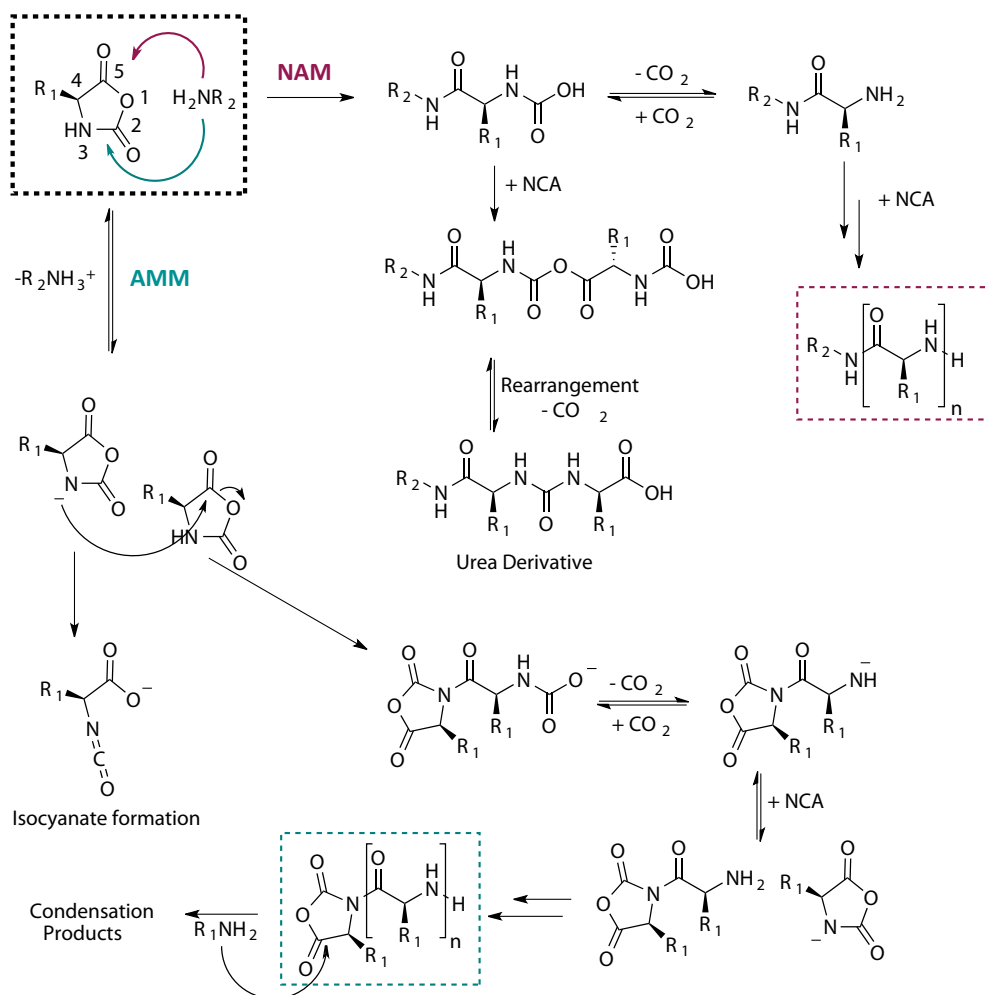
Scheme 4. Mechanistic pathways for the NCA polymerization. Reprinted from Klinker *et al.* with permission from John Wiley and Sons (© 2015).[108]

Contrarily, in the AMM, the initiator acts as a base and abstracts the acidic proton at N-3. In the following, the anionic activated monomer itself acts as the initiator of the reaction. The activated monomer can either undergo direct ring-opening leading to instable isocyanates easily subjected to further side reactions or attack a second NCA monomer at C-5. In the latter case, after decarboxylation, the AMM mechanism can continue in its pure form or in combinations with the NAM procedure. The AMM symptomatically leads to polymers with a reactive oxazolidin-2,5-dione as the end-group. Consequently, condensation products are

frequently observed, and polypeptides derived from AMM processes are characterized by a broad molecular weight distribution. Conversely, Poisson-like molecular weight distributions are obtained for living polymerizations following the NAM process, as the initiation is typically faster than the propagation.[108,258]

Since NNCAs do not contain an acidic proton at the nitrogen atom the AMM pathway is generally inhibited for polypeptoids. *Vice versa*, the polymerization of NCAs is easily affected by the nucleophilic or basic character of the initiator.[108,222,258] In addition and comparable to other living polymerization techniques, also NCA polymerization is highly sensitive to impurities since these may promote the AMM pathway, catalyze side reactions, and initiate or terminate the chain growth.[255,258,260] In 1997, Deming reported on the first living NCA polymerization by using zero-valent nickel amido-amidate complexes initiating and mediating the chain growth reaction.[261] Herein, homo- and block copolypeptides of pGlu(OBn) and pLys(Z) could be synthesized with high molecular weights and narrow dispersity ($Đ$ < 1.2). Deming further expanded the concept to cobalt and iron complexes, and synthesized library of functional polypeptides.[262,263] However, polymerization of NNCAs was not substantiated until recently since initiation required an acidic proton for β-hydride elimination. The Kramer group thus improved the Ni and Co initiators allowing for polymerization of proline NCA.[264] Nevertheless, elaborate synthesis and potentially remaining traces of toxic heavy metal ions hamper this technique.[108] In 2004, the groups of Schué and Hadjichristidis reported that reaction temperature, sufficient removal of CO_2, and the purity of the components, are the key parameters for the living amine-initiated polymerization of NCAs.[232,233] In the following, several groups contributed to expanding the living amine-initiated NCA polymerization leading to a well-established type of polymerization.[203,234,265–267]

Current investigations aim to accelerate the reaction rates of NCA polymerization and achieve chain lengths beyond 1000.[268] In particular organocatalysis techniques were therefore applied to NCA polymerization. In 2019, Zhao *et al.* combined 1,3-bis(2-hydroxyhexafluoroisopropyl)benzene (1,3-bis-HFAB) and *N*,*N*-dimethyl ethanol amine in dichloromethane to activate the NCA monomer by hydrogen bonds.[269] Moreover, Xia *et al.* demonstrated accelerated polymerization in DCM upon addition of crown ether as a catalyst.[270] In addition, emulsion techniques have been developed to enable facile synthesis of α-helical multi-block copolypeptides.[271] Regarding the biomedical applications, large

molecular weights are often not necessarily an advantage, since storage diseases are a realistic threats that also need to be considered for polypept(o)ides.[120] Nevertheless, fast and robust mechanisms facilitating large-scale production will aid translation of polypept(o)ides.

Polysarcosine

Polysarcosine is a non-ionic and highly water-soluble polymer that adopts random coil conformation in aqueous solution, which is attributed to the equal population of the *cis* and *trans* configuration of the amide bond.[212,272–274] Comparable to PEG, pSar solely acts as a weak hydrogen bond acceptor without any hydrogen bond donor properties, while being slightly less flexible referring to the respective Kuhn lengths of $l_{k,\,pSar}$ = 1.5 nm and $l_{k,\,PEG}$ = 1.1 nm.[212] PSar matches the requirements for protein resistant surfaces summarized by the Whitesides' rules in 2001.[106] Indeed, already Ostuni *et al.* described superior protein resistance of self-assembled monolayers (SAMs) functionalized with tri(sarcosine) since reduced levels of protein adsorption and cell adhesion were found.[106,275] These results were later confirmed by Messersmith and co-workers reporting excellent resistance of pSar-grafted TiO_2 surfaces toward non-specific adhesion of proteins or any attachment of mammalian or bacterial cells.[213] Moreover, Jordan/Luxenhofer and co-workers investigated the resistance of inorganic surfaces to biofouling after modification with polypeptoid brushes.[276,277] The experimental findings are further supported by molecular dynamics simulations, in which PEG and pSar showed an equally low affinity for interaction with human serum albumin.[278] Moreover, both pSar and PEG do not elicit activation of the complement cascade, but acetylation of the amine end-group remains significant.[109,212] Consequently, pSar can be classified as a 'stealth' material and has emerged as a potential substitute for PEG in medical applications when increased water solubility and reduced immunogenicity and MPS recognition are desired.[204,212] As an early example, in 1985, Moran and co-workers reported that covalent conjugation of pSar to grass pollen allergens decreased the immunoglobulin E (IgE) formation.[279,280] More recently, pSar attracted increasing attention as an alternative material to PEG and has been investigated for shielding of antibody-drug-conjugates,[281] proteins,[282–284] liposomes,[109,285] and lipid nanoparticles.[286] In 2020, Son *et al.* prepared PEG and pSar functionalized liposomes and compared the immune response after intravenous administration to rats.[285] As a result, significantly higher levels of IgM and IgG antibodies were found for the PEGylated liposomes. Hereafter, the second administration revealed the ABC

phenomenon for PEGylated liposomes, yet again identical circulation half-lives for the pSar functionalized liposomes. For LNPs, both, PEG-lipids and pSar-lipids yielded similar mRNA nanocarriers, whereby reduced cytokine secretion and lower immunogenicity were found for the pSar-containing LNPs.[286] In summary, pSar has emerged as a biocompatible polymeric material suitable for medicinal applications.

Polypept(o)ides in Nanomedicine

Since 2014, several polypept(o)ide-based polymer and nanoparticle architectures have been established and investigated for therapeutic applications. In these systems, the hydrophilic pSar provides solubility and prevents recognition of the structures by the MPS, while the polypeptide section can be selected and tuned for drug or gene delivery.[108] As polypept(o)ides are easily accessible by the mild chemical conditions of the NCA polymerization, a large variety of polymeric architectures has been synthesized, and functional side- or end groups were introduced and exploited for cross-linking, API incorporation, and addition of targeting motifs.[108,194,196,204,287,288]

In their seminal publication from 2014, Birke *et al.* reported that for pSar-*b*-poly(γ-benzyl-L-glutamate) (pSar-*b*-pGlu(OBn)) and pSar-*b*-pLys(Z), the succession of the block copolymerization is not relevant, and polymers with narrow dispersity (Đ < 1.2) can be obtained in all cases.[203] The amphiphilic copolymers were then applied for stabilization of organic colloids and for encapsulation of the small molecule adenylate cyclase (cAMP) inhibitor MDL-12.330A in polymeric micelles. Herein, MDL-12.330A is stabilized in the micelle core by π-π-interactions with the aromatic benzyl groups.[203,289] Just recently Johann *et al.* could demonstrate the potential of the cAMP inhibitor-loaded PMs when immune evasion of melanoma cells was successfully inhibited leading to reduced tumor growth after local administration.[289] In addition to the stabilization of organic colloids, polypept(o)ides have also been applied for the shielding of metal-organic frameworks (MOFs) and metal-oxide surfaces.[62,290,291] Besides polymeric micelles for hydrophobic APIs, polymersomes, so-called peptosomes, that allow for encapsulation of hydrophilic and/or hydrophilic cargo have been established by Tanisaka *et al.* using pSar-*b*-pGlu(OMe) and Weber *et al.* for pSar-*b*-pGlu(OBn).[292,293] Moreover, non-viral transfection agents for gene delivery have been developed based on polypept(o)ides.[59,60,294,295] For these systems, Heller *et al.* investigated the significance of the block ionomer

microstructure on the formation and transfection efficiency of plasmid DNA (pDNA) polyplexes.[59] Beyond self-assembled structures, also molecular nanocarriers have been prepared from polypept(o)ides. Compared to their self-assembled counterparts, molecular nanocarriers are chemically synthesized nanoparticles, whereby size and stability can be specified by the synthetic details. In particular, carrier systems with small hydrodynamic diameters, high stability or defined architecture can easily be prepared by these techniques.[47,108,296] In 2017, Holm *et al.* introduced peptostars with Poisson-like molecular weight distribution and small hydrodynamic diameters of 10 to 30 nm.[297–299] Interestingly, fluorescence correlation spectroscopy (FCS) in human blood plasma revealed the impact of branching on the shielding efficiency, since significant protein adsorption was observed for the 3-arm peptostars yet not for the 6-arm analog.[298] Referring to the defined architecture, Kappel *et al.* recently used cylindrical bottlebrush polymers (peptobrushes) with a dense pSar corona to demonstrate the significance of the number of antibodies for active targeting of nanoparticles to dendritic cells *in vivo*.[135,136,300] Therefore, fluorescently labeled peptobrushes based on a pLys backbone with grafted $pSar_{100}$ side chains were precisely engineered to bear on average either 2, 6, or 12 antibodies (anti-DEC205) per nanoparticle ($R_h \approx 23$ nm), and the circulation half-life and biodistribution were evaluated in mice. As a result, rapid uptake by liver sinusoidal endothelial cells and decreased circulation times were observed with increasing amounts of ligands per brush, which was attributed to the recognition by the Fc receptor. Conversely, low amounts of anti-DEC205 were efficient for targeting the cells of the lymphoid organs bypassing liver accumulation, making peptobrushes a suitable platform for systemic cancer vaccination strategies.[136] Aiming to improve nuclear imaging and radionucleotide therapy, Stéen *et al.* designed *trans*-cyclooctene (TCO) functionalized peptobrushes based on pGlu backbones as targeting agents for bio-orthogonal *in vivo* click chemistry.[301] For diagnosis, the TCO-peptobrush is administered first, whereby the small size ($\approx$ 10 nm) slightly above the value for renal filtration ensures optimal tumor tissue penetration.[116,302] After 22 to 72 h, when non-accumulated peptobrushes were excreted, a tetrazine-functionalized radiolabeled probe with a short circulation half-life was injected. Consequently, the radioactive probe is only retained at the location of the peptobrush after the successful ultra-fast click reaction between tetrazine and TCO.[303] The seminal pre-targeting approach thus decouples the tumor accumulation of the radiolabeled probe from the imaging step leading to enhanced contrast and reduced radiation exposure. Herein, the microstructure of

the TCO-modified graft copolymers encounters a specific function since the microphase separation of the TCO-modified amino acids improves TCO stability and leads to enhanced rate constants. Accordingly, the peptobrush-assisted TCO/tetrazine click reaction is among the fastest bio-orthogonal ligation techniques directing toward new drug release strategies (click-to-release) for tissue-selective drug release by functional nanomedicines.[303]
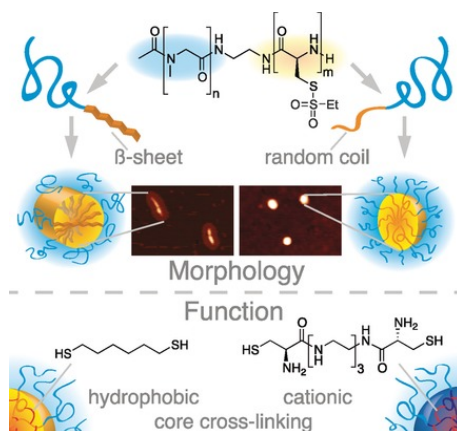
Figure 8. Synthesis of CCPMs and nanohydrogels from thiol-reactive polypept(o)ides using secondary structure formation as a guiding element for self-assembly. Reprinted from Klinker *et al.* with permission from John Wiley and Sons (© 2017).[82]

Core cross-linked polymeric micelles can be considered as hybrids of self-assembled and molecular nanocarriers. In fact, CCPMs are synthesized from PMs generated by self-assembly, yet the cross-linking reaction leads to a stabilized single-molecule entity.[46,183] Moreover, a large variety of hydrophobic cargos can be encapsulated and attached to the micellar core, while the release profile can be tuned by stimuli-responsive covalent bonds. To explore the full potential of disulfides as dynamic covalent bonds, Barz and co-workers previously developed reactive protecting groups for thiol-bearing amino acids, e.g., cysteine and homocysteine (Hcy).[193–195,304,305] As reported by Schäfer *et al.*, *S*-ethylsulfonyl-L-cysteine NCA could be successfully polymerized using nucleophilic amine initiators (hard nucleophiles), and the *S*-ethylsulfonyl group was separately addressed by soft nucleophiles, e.g., thiols yielding disulfides.[195,197,306] Following up on this, Klinker *et al.* synthesized block copolypept(o)ides of pSar-*block*-poly(*S*-ethylsulfonyl-L-cysteine) (pSar-*b*-pCys(SO$_2$Et).[82] The secondary structure formation of pCys(SO$_2$Et) was thereby used as a tool to govern the self-assembly

and morphology of PMs, whereby the core polarity could be tuned by hydrophilic or hydrophobic cross-linkers leading to CCPMs or cationic nanohydrogels as the extreme cases (Figure 8). Continuing the pioneering work, secondary structure formation will be further explored as a guiding element, and strategies for drug conjugation and robust production of CCPMs will be developed in this thesis. Furthermore, polymeric architectures that allow for stimuli-responsive cross-linking by pro-drugs based on platinum- or ruthenium-complexes will be designed and evaluated for their potential to overcome drug resistance mechanisms. Moreover, by combining iron oxide nanoparticles with disulfide cross-linked CCPMs, specific delivery of iron to macrophages will be facilitated and the implications for macrophage activation and immunomodulation will be investigated.

Thesis Outline

Envisioning to advance the next generation of nanomedicines this thesis aims to improve core cross-linked polymeric micelles as stimuli-responsive carrier systems for small molecule drugs and co-factors. The emerging potential of polypept(o)ides will be exploited and expanded to facilitate polymer synthesis, understand the relation of secondary structure formation on block copolymer self-assembly, implement disease-related and external stimuli for distinct release profiles, and ensure robust and scalable production of CCPMs. Functional core architectures will be designed by combining polymer science with organic and inorganic chemistry, connecting therapeutic cargo and fine-tuned carriers by dynamic covalent bonds. The discoveries of this thesis may contribute to establishing novel therapeutic approaches to improve patient compliance.

The rationale for nanomedicine and polypept(o)ides as a material class will be introduced in **chapter 1**. Herein, the basic requirements for drug delivery by nanomedicine and the characteristics of CCPMs will be reviewed. Moreover, NCA polymerization and the biomedical application of polypept(o)ides will be discussed.

In **chapter 2**, the synthesis and polymerization of racemic *S*-ethylsulfonyl-DL-cysteine NCA will be investigated to facilitate the production of thiol-reactive copolymers. The reduced tendency for anti-parallel ß-sheet formation grants access to higher chain lengths with narrow molecular weight distributions. Increased rate constants and full monomer conversion further enable the synthesis of triblock copolymers (pGlu(OBn)-*b*-p(DL)Cys(SO$_2$Et)-*b*-pSar) by sequential monomer addition inaccessible *via* the previously established enantiopure L-cysteine analog.

The influence of the secondary structure on the self-assembly of thiol-reactive polypept(o)ides will be discussed in **chapter 3**. Block copolymers of ß-sheet-forming enantiopure pSar-*b*-p(L)Cys(SO$_2$Et), racemic pSar-*b*-p(DL)Cys(SO$_2$Et), and α-helical pSar-*b*-p(L)Hcy(SO$_2$Et) will be prepared. The tendency for aggregation will be investigated by dynamic light scattering (DLS) during solvent switch considering various chain lengths of the hydrophobic segment. The significance of α-helix, anti-parallel ß-sheet, and racemic ß-sheet will be connected to the morphology of the CCPMs by applying TEM and atomic force microscopy (AFM).

For CCPMs based on pSar-*b*-p(L)Cys(SO$_2$Et), the influence of the core cross-linking on nanocarrier stability will be evaluated in **chapter 4**. Copolypept(o)ides with a short and a long cross-linkable p(L)Cys(SO$_2$Et) segment will be combined with mono-, bi-, or tri-functional thiol reagents leading to varied cross-linking densities. The cross-linked and non-cross-linked PMs will be subjected to detailed analysis by asymmetrical flow field-flow fractionation (AF4) and fluorescence correlation spectroscopy (FCS) in phosphate-buffered saline (PBS) or human blood plasma. Distinct structure-activity relationships will be examined and related to the circulation half-life and biodistribution of fluorescently labeled CCPMs after intravenous administration to mice.

Within **chapter 5**, the synthetic strategy for CCPMs based on pSar-*b*-p(L)Cys(SO$_2$Et) will be adjusted for scale-up by a continuous flow process. An optimized setup will be presented that allows for particle synthesis *via* micromixers and online purification by tangential flow filtration. Stimuli-responsive conjugation of paclitaxel (PTX) pro-drugs will be performed by a decoupled drug loading procedure. The prepared PTX-loaded CCPMs will be characterized and investigated for their therapeutic potential in cell culture and zebrafish larvae compared to state-of-the-art treatment by nanoparticle albumin-bound PTX.

Light as an external trigger for drug release of CCPMs will be discussed in **chapter 6**. Polypept(o)ides based on pSar-*b*-pGlu will be combined with polypyridyl ruthenium(II) complexes resembling cytotoxic cisplatin yet granting access to photoinduced ligand exchange reactions. The side chain of pGlu will be functionalized with aromatic nitrile moieties by post-polymerization modification reaction followed by core cross-linking with bifunctional ruthenium(II) complexes. The influence of the nitrile linker on nanoparticle morphology will be evaluated by AFM and TEM, and the practical application will be assessed in cell culture and by analysis in the *in ovo* model.

The significance of drug-resistance mechanisms will be covered in **chapter 7**, whereby polypept(o)ides are applied to overcome cisplatin resistance. Differential expression of the ion channel LRRC8A will be correlated to the survival of head and neck cancer patients under cisplatin therapy. Cisplatin-resistant head and neck cancer cells lacking LRRC8A mediating drug uptake will be generated and sequenced. Polypept(o)ides of pSar-*b*-pGlu(ONa) will be synthesized to reversibly conjugate cisplatin *via* the carboxyl group leading to small-sized polymeric micelles (NP$_{Cis}$) with narrow polydispersity. The colloidal particle stability and

the potential to bypass LRRC8A-induced drug resistance will be evaluated in zebrafish embryos and cell culture.

In **chapter 8**, the implications of the specific delivery of iron to macrophages will be investigated. Iron oxide nanoparticles (SPIONs) will be combined with CCPMs of pSar-b-p(L)Cys(SO$_2$Et) and connected by surface modification with lipoic acid, simultaneously cross-linking the micellar core (SPION-CCPMs). Applied to primary murine and human macrophages, the substantiated inflammatory responses are evaluated by flow cytometry and quantitative polymerase chain reaction (qPCR) analysis. Further, the results will be correlated to activation of alveolar or interstitial macrophages after intratracheal administration of SPION-CCPMs to mice, directing toward a new class of therapeutic agents for immunomodulation.

The results of this thesis will be briefly summarized and discussed in **chapter 9**, and the relevance and consequences for current and future research will be outlined.

References

(1)   Bertrand, N.; Leroux, J. C. The Journey of a Drug-Carrier in the Body: An Anatomo-Physiological Perspective. *J. Control. Release* **2012**, *161* (2), 152–163.

(2)   Duncan, R. Polymer Therapeutics: Top 10 Selling Pharmaceuticals - What Next? *J. Control. Release* **2014**, *190*, 371–380.

(3)   Kircher, M. F. How Can We Apply the Use of Surface-Enhanced Raman Scattering Nanoparticles in Tumor Imaging? *Nanomedicine* **2017**, *12* (3), 171–174.

(4)   Barz, M.; Luxenhofer, R.; Schillmeier, M. Quo Vadis Nanomedicine? *Nanomedicine* **2015**, *10* (20), 3089–3091.

(5)   Sindhwani, S.; Chan, W. C. W. Nanotechnology for Modern Medicine: Next Step towards Clinical Translation. *J. Intern. Med.* **2021**, *290* (3), 486–498.

(6)   Arranja, A. G.; Pathak, V.; Lammers, T.; Shi, Y. Tumor-Targeted Nanomedicines for Cancer Theranostics. *Pharmacol. Res.* **2017**, *115*, 87–95.

(7)   Duncan, R. Polymer Therapeutics as Nanomedicines: New Perspectives. *Curr. Opin. Biotechnol.* **2011**, *22* (4), 492–501.

(8)   Vert, M.; Doi, Y.; Hellwich, K.-H.; Hess, M.; Hodge, P.; Kubisa, P.; Rinaudo, M.; Schué, F. Terminology for Biorelated Polymers and Applications (IUPAC Recommendations 2012). *Pure Appl. Chem.* **2012**, *84* (2), 377–410.

(9)   Bisso, S.; Leroux, J. C. Nanopharmaceuticals: A Focus on Their Clinical Translatability. *Int. J. Pharm.* **2020**, *578*.

(10)   Soares, S.; Sousa, J.; Pais, A.; Vitorino, C. Nanomedicine: Principles, Properties, and Regulatory Issues. *Front. Chem.* **2018**, *6*, 1–15.

(11)   Lammers, T.; Ferrari, M. The Success of Nanomedicine. *Nano Today* **2020**, *31*, 0–1.

(12)   Ma, W. W.; Hidalgo, M. The Winning Formulation: The Development of Paclitaxel in Pancreatic Cancer. *Clin. Cancer Res.* **2013**, *19* (20), 5572–5579.

(13)   Barenholz, Y. Doxil® - The First FDA-Approved Nano-Drug: Lessons Learned. *J. Control. Release* **2012**, *160* (2), 117–134.

(14)   Markovsky, E.; Baabur-Cohen, H.; Eldar-Boock, A.; Omer, L.; Tiram, G.; Ferber, S.; Ofek, P.; Polyak, D.; Scomparin, A.; Satchi-Fainaro, R. Administration, Distribution, Metabolism and Elimination of Polymer Therapeutics. *J. Control. Release* **2012**, *161* (2), 446–460.

(15)   Hashida, M. Role of Pharmacokinetic Consideration for the Development of Drug Delivery Systems: A Historical Overview. *Adv. Drug Deliv. Rev.* **2020**, *157*, 71–82.

(16)   Mi, P.; Miyata, K.; Kataoka, K.; Cabral, H. Clinical Translation of Self-Assembled Cancer Nanomedicines. *Adv. Ther.* **2021**, *4* (1), 2000159.

(17)   Blanco, E.; Shen, H.; Ferrari, M. Principles of Nanoparticle Design for Overcoming Biological Barriers to Drug Delivery. *Nat. Biotechnol.* **2015**, *33* (9), 941–951.

(18)   Quader, S.; Kataoka, K. Nanomaterial-Enabled Cancer Therapy. *Mol. Ther.* **2017**, *25* (7), 1501–1513.

(19)   Petros, R. A.; DeSimone, J. M. Strategies in the Design of Nanoparticles for Therapeutic Applications. *Nat. Rev. Drug Discov.* **2010**, *9* (8), 615–627.

(20)   Polack, F. P.; Thomas, S. J.; Kitchin, N.; Absalon, J.; Gurtman, A.; Lockhart, S.; Perez, J. L.; Pérez Marc, G.; Moreira, E. D.; Zerbini, C.; Bailey, R.; Swanson, K. A.;

Roychoudhury, S.; Koury, K.; Li, P.; Kalina, W. V.; Cooper, D.; Frenck, R. W.; Hammitt, L. L.; Türeci, Ö.; Nell, H.; Schaefer, A.; Ünal, S.; Tresnan, D. B.; Mather, S.; Dormitzer, P. R.; Şahin, U.; Jansen, K. U.; Gruber, W. C. Safety and Efficacy of the BNT162b2 MRNA Covid-19 Vaccine. *N. Engl. J. Med.* **2020**, *383* (27), 2603–2615.

(21)   Schoenmaker, L.; Witzigmann, D.; Kulkarni, J. A.; Verbeke, R.; Kersten, G.; Jiskoot, W.; Crommelin, D. J. A. MRNA-Lipid Nanoparticle COVID-19 Vaccines: Structure and Stability. *Int. J. Pharm.* **2021**, *601* (April), 120586.

(22)   Delehedde, C.; Even, L.; Midoux, P.; Pichon, C.; Perche, F. Intracellular Routing and Recognition of Lipid-Based MRNA Nanoparticles. *Pharmaceutics* **2021**, *13* (7), 945.

(23)   Baden, L. R.; El Sahly, H. M.; Essink, B.; Kotloff, K.; Frey, S.; Novak, R.; Diemert, D.; Spector, S. A.; Rouphael, N.; Creech, C. B.; McGettigan, J.; Khetan, S.; Segall, N.; Solis, J.; Brosz, A.; Fierro, C.; Schwartz, H.; Neuzil, K.; Corey, L.; Gilbert, P.; Janes, H.; Follmann, D.; Marovich, M.; Mascola, J.; Polakowski, L.; Ledgerwood, J.; Graham, B. S.; Bennett, H.; Pajon, R.; Knightly, C.; Leav, B.; Deng, W.; Zhou, H.; Han, S.; Ivarsson, M.; Miller, J.; Zaks, T. Efficacy and Safety of the MRNA-1273 SARS-CoV-2 Vaccine. *N. Engl. J. Med.* **2021**, *384* (5), 403–416.

(24)   Cabral, H.; Uchida, S.; Perche, F.; Pichon, C. Nanomedicine-Based Approaches for MRNA Delivery. *Mol. Pharm.* **2020**, *17* (10), 3654–3684.

(25)   Gómez-Aguado, I.; Rodríguez-Castejón, J.; Vicente-Pascual, M.; Rodríguez-Gascón, A.; Solinís, M. Á.; Del Pozo-Rodríguez, A. Nanomedicines to Deliver MRNA: State of the Art and Future Perspectives. *Nanomaterials* **2020**, *10* (2).

(26)   Chaudhary, N.; Weissman, D.; Whitehead, K. A. MRNA Vaccines for Infectious Diseases: Principles, Delivery and Clinical Translation. *Nat. Rev. Drug Discov.* **2021**, *0123456789*.

(27)   Lammers, T.; Kiessling, F.; Hennink, W. E.; Storm, G. Drug Targeting to Tumors: Principles, Pitfalls and (Pre-) Clinical Progress. *J. Control. Release* **2012**, *161* (2), 175–187.

(28)   Van Eerden, R. A. G.; Mathijssen, R. H. J.; Koolen, S. L. W. Recent Clinical Developments of Nanomediated Drug Delivery Systems of Taxanes for the Treatment of Cancer. *Int. J. Nanomedicine* **2020**, *15*, 8151–8166.

(29)   Kataoka, K.; Harada, A.; Nagasaki, Y. Block Copolymer Micelles for Drug Delivery: Design, Characterization and Biological Significance. *Adv. Drug Deliv. Rev.* **2001**, *47* (1), 113–131.

(30)   Ho, K. S.; Shoichet, M. S. Design Considerations of Polymeric Nanoparticle Micelles for Chemotherapeutic Delivery. *Curr. Opin. Chem. Eng.* **2013**, *2* (1), 53–59.

(31)   Anchordoquy, T. J.; Barenholz, Y.; Boraschi, D.; Chorny, M.; Decuzzi, P.; Dobrovolskaia, M. A.; Farhangrazi, Z. S.; Farrell, D.; Gabizon, A.; Ghandehari, H.; Godin, B.; La-Beck, N. M.; Ljubimova, J.; Moghimi, S. M.; Pagliaro, L.; Park, J. H.; Peer, D.; Ruoslahti, E.; Serkova, N. J.; Simberg, D. Mechanisms and Barriers in Cancer Nanomedicine: Addressing Challenges, Looking for Solutions. *ACS Nano* **2017**, *11* (1), 12–18.

(32)   Ma, P.; Mumper, R. J. Paclitaxel Nano-Delivery Systems: A Comprehensive Review. *J. Nanomed. Nanotechnol.* **2013**, *4* (2), 1000164.

(33)   Montero, A.; Fossella, F.; Hortobagyi, G.; Valero, V. Docetaxel for Treatment of Solid

Tumours: A Systematic Review of Clinical Data. *Lancet Oncol.* **2005**, *6* (4), 229–239.

(34) Gelderblom, H.; Verweij, J.; Nooter, K.; Sparreboom, A. Cremophor EL. *Eur. J. Cancer* **2001**, *37* (13), 1590–1598.

(35) Sparreboom, A.; Van Teilingen, O.; Nooijen, W. J.; Beijnen, J. H. Nonlinear Pharmacokinetics of Paclitaxel in Mice Results from the Pharmaceutical Vehicle Cremophor EL. *Cancer Res.* **1996**, *56* (9), 2112–2115.

(36) Gonzalez-Valdivieso, J.; Girotti, A.; Schneider, J.; Arias, F. J. Advanced Nanomedicine and Cancer: Challenges and Opportunities in Clinical Translation. *Int. J. Pharm.* **2021**, *599* (March), 120438.

(37) Talelli, M.; Rijcken, C. J. F.; Hennink, W. E.; Lammers, T. Polymeric Micelles for Cancer Therapy: 3 C's to Enhance Efficacy. *Curr. Opin. Solid State Mater. Sci.* **2012**, *16* (6), 302–309.

(38) Luxenhofer, R. A Tutorial Translation of the Description of the Historically First Polymer Drug Conjugate and Its in Vivo Evaluation. *Zeitschrift fur Naturforsch. - Sect. C J. Biosci.* **2020**, *75* (910), 303–311.

(39) Jatzkewitz, H. An Ein Kolloidales Blutplasma-Ersatzmittel (Polyvinylpyrrolidon) Gebundenes Peptamin (Glycyl-L-Leucyl-Mezcalin) Als Neuartige Depotform Für Biologisch Aktive Primäre Amine (Mezcalin). *Zeitschrift fur Naturforsch. - Sect. B J. Chem. Sci.* **1955**, *10* (1), 27–31.

(40) Jatzkewitz, H. Uber Den Einbau Physiologisch Wirksamer Substanzen in Ein Kollodiales Blutplasma-Ersatzmittel. *Hoppe Seyler's Zeitschrift für Physiol. Chemie* **1954**, *297*, 149–156.

(41) Duncan, R. The Dawning Era of Polymer Therapeutics. *Nat. Rev. Drug Discov.* **2003**, *2* (5), 347–360.

(42) Ringsdorf, H. Structure and Properties of Pharmacologically Active Polymers. *J Polym Sci Polym Symp* **1975**, *153* (51), 135–153.

(43) Talelli, M.; Barz, M.; Rijcken, C. J. F. F.; Kiessling, F.; Hennink, W. E.; Lammers, T. Core-Crosslinked Polymeric Micelles: Principles, Preparation, Biomedical Applications and Clinical Translation. *Nano Today* **2015**, *10* (1), 93–117.

(44) Anselmo, A. C.; Mitragotri, S. Nanoparticles in the Clinic: An Update. *Bioeng. Transl. Med.* **2019**, *4* (3), 1–16.

(45) Mitchell, M. J.; Billingsley, M. M.; Haley, R. M.; Wechsler, M. E.; Peppas, N. A.; Langer, R. Engineering Precision Nanoparticles for Drug Delivery. *Nat. Rev. Drug Discov.* **2021**, *20* (2), 101–124.

(46) Talelli, M.; Barz, M.; Rijcken, C. J. F. F.; Kiessling, F.; Hennink, W. E.; Lammers, T. Core-Crosslinked Polymeric Micelles: Principles, Preparation, Biomedical Applications and Clinical Translation. *Nano Today* **2015**, *10* (1), 93–117.

(47) Müllner, M. Molecular Polymer Brushes in Nanomedicine. *Macromol. Chem. Phys.* **2016**, *217* (20), 2209–2222.

(48) Johnson, B. K.; Prud'homme, R. K. Mechanism for Rapid Self-Assembly of Block Copolymer Nanoparticles. *Phys. Rev. Lett.* **2003**, *91* (11), 1–4.

(49) Mai, Y.; Eisenberg, A. Self-Assembly of Block Copolymers. *Chem. Soc. Rev.* **2012**, *41* (18), 5969–5985.

(50) Allen, T. M.; Cullis, P. R. Liposomal Drug Delivery Systems: From Concept to

Clinical Applications. *Adv. Drug Deliv. Rev.* **2013**, *65* (1), 36–48.

(51)   Vonarbourg, A.; Passirani, C.; Saulnier, P.; Benoit, J. P. Parameters Influencing the Stealthiness of Colloidal Drug Delivery Systems. *Biomaterials* **2006**, *27* (24), 4356–4373.

(52)   Cabral, H.; Miyata, K.; Osada, K.; Kataoka, K. Block Copolymer Micelles in Nanomedicine Applications. *Chem. Rev.* **2018**, *118* (14), 6844–6892.

(53)   Davis, F. F. The Origin of Pegnology. *Adv. Drug Deliv. Rev.* **2002**, *54* (4), 457–458.

(54)   Graham, M. L. Pegaspargase: A Review of Clinical Studies. *Adv. Drug Deliv. Rev.* **2003**, *55* (10), 1293–1302.

(55)   Bangham, A. D.; Horne, R. W. Negative Staining of Phospholipids and Their Structural Modification by Surface-Active Agents as Observed in the Electron Microscope. *J. Mol. Biol.* **1964**, *8* (5), 660-IN10.

(56)   Discher, D. E.; Eisenberg, A. Polymer Vesicles. *Science* **2002**, *297* (5583), 967–973.

(57)   Discher, D. E.; Ahmed, F. Polymersomes. *Annu. Rev. Biomed. Eng.* **2006**, *8* (1), 323–341.

(58)   Bleul, R.; Thiermann, R.; Maskos, M. Techniques to Control Polymersome Size. *Macromolecules* **2015**, *48* (20), 7396–7409.

(59)   Heller, P.; Zhou, J.; Weber, B.; Hobernik, D.; Bros, M.; Schmid, F.; Barz, M. The Influence of Block Ionomer Microstructure on Polyplex Properties: Can Simulations Help to Understand Differences in Transfection Efficiency? *Small* **2017**, *13* (17), 1603694.

(60)   Heller, P.; Birke, A.; Huesmann, D.; Weber, B.; Fischer, K.; Reske-Kunz, A.; Bros, M.; Barz, M. Introducing PeptoPlexes: Polylysine-Block-Polysarcosine Based Polyplexes for Transfection of HEK 293T Cells. *Macromol. Biosci.* **2014**, *14* (10), 1380–1395.

(61)   Soenen, S. J.; Parak, W. J.; Rejman, J.; Manshian, B. (Intra)Cellular Stability of Inorganic Nanoparticles: Effects on Cytotoxicity, Particle Functionality, and Biomedical Applications. *Chem. Rev.* **2015**, *115* (5), 2109–2135.

(62)   Zimpel, A.; Al Danaf, N.; Steinborn, B.; Kuhn, J.; Höhn, M.; Bauer, T.; Hirschle, P.; Schrimpf, W.; Engelke, H.; Wagner, E.; Barz, M.; Lamb, D. C.; Lächelt, U.; Wuttke, S. Coordinative Binding of Polymers to Metal-Organic Framework Nanoparticles for Control of Interactions at the Biointerface. *ACS Nano* **2019**, *13* (4).

(63)   Cai, W.; Chu, C. C.; Liu, G.; Wáng, Y. X. J. Metal-Organic Framework-Based Nanomedicine Platforms for Drug Delivery and Molecular Imaging. *Small* **2015**, *11* (37), 4806–4822.

(64)   He, C.; Liu, D.; Lin, W. Nanomedicine Applications of Hybrid Nanomaterials Built from Metal-Ligand Coordination Bonds: Nanoscale Metal-Organic Frameworks and Nanoscale Coordination Polymers. *Chem. Rev.* **2015**, *115* (19), 11079–11108.

(65)   Dadfar, S. M.; Roemhild, K.; Drude, N. I.; von Stillfried, S.; Knüchel, R.; Kiessling, F.; Lammers, T. Iron Oxide Nanoparticles: Diagnostic, Therapeutic and Theranostic Applications. *Adv. Drug Deliv. Rev.* **2019**, *138*, 302–325.

(66)   Soetaert, F.; Korangath, P.; Serantes, D.; Fiering, S.; Ivkov, R. Cancer Therapy with Iron Oxide Nanoparticles: Agents of Thermal and Immune Therapies. *Adv. Drug Deliv. Rev.* **2020**, *163–164*, 65–83.

(67)   Kowalczyk, M.; Banach, M.; Rysz, J. Ferumoxytol: A New Era of Iron Deficiency Anemia Treatment for Patients with Chronic Kidney Disease. *J. Nephrol.* **2011**, *24* (6), 717–722.

(68)   Bhandari, S.; Pereira, D.; Chappell, H.; Drakesmith, H. Intravenous Irons: From Basic Science to Clinical Practice. *Pharmaceuticals* **2018**, *11* (3), 82.

(69)   Weissleder, R.; Stark, D.; Engelstad, B.; Bacon, B.; Compton, C.; White, D.; Jacobs, P.; Lewis, J. Superparamagnetic Iron Oxide: Pharmacokinetics and Toxicity. *Am. J. Roentgenol.* **1989**, *152* (1), 167–173.

(70)   Lee, N.; Yoo, D.; Ling, D.; Cho, M. H.; Hyeon, T.; Cheon, J. Iron Oxide Based Nanoparticles for Multimodal Imaging and Magnetoresponsive Therapy. *Chem. Rev.* **2015**, *115* (19), 10637–10689.

(71)   Ouyang, B.; Poon, W.; Zhang, Y. N.; Lin, Z. P.; Kingston, B. R.; Tavares, A. J.; Zhang, Y.; Chen, J.; Valic, M. S.; Syed, A. M.; MacMillan, P.; Couture-Senécal, J.; Zheng, G.; Chan, W. C. W. The Dose Threshold for Nanoparticle Tumour Delivery. *Nat. Mater.* **2020**, *19* (12), 1362–1371.

(72)   Sindhwani, S.; Syed, A. M.; Ngai, J.; Kingston, B. R.; Maiorino, L.; Rothschild, J.; MacMillan, P.; Zhang, Y.; Rajesh, N. U.; Hoang, T.; Wu, J. L. Y.; Wilhelm, S.; Zilman, A.; Gadde, S.; Sulaiman, A.; Ouyang, B.; Lin, Z.; Wang, L.; Egeblad, M.; Chan, W. C. W. The Entry of Nanoparticles into Solid Tumours. *Nat. Mater.* **2020**, *19* (5), 566–575.

(73)   Kingston, B. R.; Lin, Z. P.; Ouyang, B.; MacMillan, P.; Ngai, J.; Syed, A. M.; Sindhwani, S.; Chan, W. C. W. Specific Endothelial Cells Govern Nanoparticle Entry into Solid Tumors. *ACS Nano* **2021**, *15*, 14080-14094.

(74)   Harmsen, S.; Wall, M. A.; Huang, R.; Kircher, M. F. Cancer Imaging Using Surface-Enhanced Resonance Raman Scattering Nanoparticles. *Nat. Protoc.* **2017**, *12* (7), 1400–1414.

(75)   Wall, M. A.; Harmsen, S.; Pal, S.; Zhang, L.; Arianna, G.; Lombardi, J. R.; Drain, C. M.; Kircher, M. F. Surfactant-Free Shape Control of Gold Nanoparticles Enabled by Unified Theoretical Framework of Nanocrystal Synthesis. *Adv. Mater.* **2017**, *29* (21).

(76)   Varela-Moreira, A.; Shi, Y.; Fens, M. H. A. M.; Lammers, T.; Hennink, W. E.; Schiffelers, R. M. Clinical Application of Polymeric Micelles for the Treatment of Cancer. *Mater. Chem. Front.* **2017**, *1* (8), 1485–1501.

(77)   Cabral, H.; Kataoka, K. Progress of Drug-Loaded Polymeric Micelles into Clinical Studies. *J. Control. Release* **2014**, *190*, 465–476.

(78)   Irvine, D. J.; Dane, E. L. Enhancing Cancer Immunotherapy with Nanomedicine. *Nat. Rev. Immunol.* **2020**, *20* (5), 321–334.

(79)   McLaughlin, C. K.; Logie, J.; Shoichet, M. S. Core and Corona Modifications for the Design of Polymeric Micelle Drug-Delivery Systems. *Isr. J. Chem.* **2013**, *53* (9–10), 670–679.

(80)   Logie, J.; Ganesh, A. N.; Aman, A. M.; Al-awar, R. S.; Shoichet, M. S. Preclinical Evaluation of Taxane-Binding Peptide-Modified Polymeric Micelles Loaded with Docetaxel in an Orthotopic Breast Cancer Mouse Model. *Biomaterials* **2017**, *123*, 39–47.

(81)   Ulrich, S. Growing Prospects of Dynamic Covalent Chemistry in Delivery Applications. *Acc. Chem. Res.* **2019**, *52*, 510-519.

(82) Klinker, K.; Schäfer, O.; Huesmann, D.; Bauer, T.; Capelôa, L.; Braun, L.; Stergiou, N.; Schinnerer, M.; Dirisala, A.; Miyata, K.; Osada, K.; Cabral, H.; Kataoka, K.; Barz, M. Secondary-Structure-Driven Self-Assembly of Reactive Polypept(o)Ides: Controlling Size, Shape, and Function of Core Cross-Linked Nanostructures. *Angew. Chemie Int. Ed.* **2017**, *56* (32), 9608–9613.

(83) He, Z.; Wan, X.; Schulz, A.; Bludau, H.; Dobrovolskaia, M. A.; Stern, S. T.; Montgomery, S. A.; Yuan, H.; Li, Z.; Alakhova, D.; Sokolsky, M.; Darr, D. B.; Perou, C. M.; Jordan, R.; Luxenhofer, R.; Kabanov, A. V. A High Capacity Polymeric Micelle of Paclitaxel: Implication of High Dose Drug Therapy to Safety and in Vivo Anti-Cancer Activity. *Biomaterials* **2016**, *101*, 296–309.

(84) Grüne, M.; Luxenhofer, R.; Iuga, D.; Brown, S. P.; Pöppler, A. C. 14N-1H HMQC Solid-State NMR as a Powerful Tool to Study Amorphous Formulations-an Exemplary Study of Paclitaxel Loaded Polymer Micelles. *J. Mater. Chem. B* **2020**, *8* (31), 6827–6836.

(85) Cabral, H.; Matsumoto, Y.; Mizuno, K.; Chen, Q.; Murakami, M.; Kimura, M.; Terada, Y.; Kano, M. R.; Miyazono, K.; Uesaka, M.; Nishiyama, N.; Kataoka, K. Accumulation of Sub-100 Nm Polymeric Micelles in Poorly Permeable Tumours Depends on Size. *Nat. Nanotechnol.* **2011**, *6* (12), 815–823.

(86) Weissig, V.; Whiteman, K. R.; Torchilin, V. P. Accumulation of Protein-Loaded Long-Circulating Micelles and Liposomes in Subcutaneous Lewis Lung Carcinoma in Mice. *Pharmaceutical Research*. 1998, 1552–1556.

(87) Behzadi, S.; Serpooshan, V.; Tao, W.; Hamaly, M. A.; Alkawareek, M. Y.; Dreaden, E. C.; Brown, D.; Alkilany, A. M.; Farokhzad, O. C.; Mahmoudi, M. Cellular Uptake of Nanoparticles: Journey inside the Cell. *Chem. Soc. Rev.* **2017**, *46* (14), 4218–4244.

(88) de Lázaro, I.; Mooney, D. J. Obstacles and Opportunities in a Forward Vision for Cancer Nanomedicine. *Nat. Mater.* **2021**, *20*, 1469-1479.

(89) Anselmo, A. C.; Mitragotri, S. Nanoparticles in the Clinic. *Bioeng. Transl. Med.* **2016**, *1* (1), 10–29.

(90) Ragelle, H.; Danhier, F.; Préat, V.; Langer, R.; Anderson, D. G. Nanoparticle-Based Drug Delivery Systems: A Commercial and Regulatory Outlook as the Field Matures. *Expert Opin. Drug Deliv.* **2017**, *14* (7), 851–864.

(91) Duncan, R.; Gaspar, R. Nanomedicine(s) under the Microscope. *Mol. Pharm.* **2011**, *8* (6), 2101–2141.

(92) Park, J. H.; Lee, H. K. Delivery Routes for COVID-19 Vaccines. *Vaccines* **2021**, *9* (5).

(93) Ols, S.; Yang, L.; Thompson, E. A.; Pushparaj, P.; Tran, K.; Liang, F.; Lin, A.; Eriksson, B.; Karlsson Hedestam, G. B.; Wyatt, R. T.; Loré, K. Route of Vaccine Administration Alters Antigen Trafficking but Not Innate or Adaptive Immunity. *Cell Rep.* **2020**, *30* (12), 3964-3971.e7.

(94) Zhang, L.; Wang, W.; Wang, S. Effect of Vaccine Administration Modality on Immunogenicity and Efficacy. *Expert Rev. Vaccines* **2015**, *14* (11), 1509–1523.

(95) Youn, Y. S.; Bae, Y. H. Perspectives on the Past, Present, and Future of Cancer Nanomedicine. *Adv. Drug Deliv. Rev.* **2018**, *130*, 3–11.

(96) Zhang, P.; Zhai, Y.; Cai, Y.; Zhao, Y.; Li, Y. Nanomedicine-Based Immunotherapy for the Treatment of Cancer Metastasis. *Adv. Mater.* **2019**, *31* (49), 1–18.

(97)   Shi, J.; Kantoff, P. W.; Wooster, R.; Farokhzad, O. C. Cancer Nanomedicine: Progress, Challenges and Opportunities. *Nat. Rev. Cancer* **2017**, *17* (1), 20–37.

(98)   Richtering, W.; Alberg, I.; Zentel, R. Nanoparticles in the Biological Context: Surface Morphology and Protein Corona Formation. *Small* **2020**, *16* (39), 1–8.

(99)   Docter, D.; Distler, U.; Storck, W.; Kuharev, J.; Wünsch, D.; Hahlbrock, A.; Knauer, S. K.; Tenzer, S.; Stauber, R. H. Quantitative Profiling of the Protein Coronas That Form around Nanoparticles. *Nat. Protoc.* **2014**, *9* (9), 2030–2044.

(100)   Alberg, I.; Kramer, S.; Leps, C.; Tenzer, S.; Zentel, R. Effect of Core-Crosslinking on Protein Corona Formation on Polymeric Micelles. *Macromol. Biosci.* **2021**, *2000414*.

(101)   Owen, S. C.; Chan, D. P. Y.; Shoichet, M. S. Polymeric Micelle Stability. *Nano Today* **2012**, *7* (1), 53–65.

(102)   Hume, D. A. The Mononuclear Phagocyte System. *Curr. Opin. Immunol.* **2006**, *18* (1), 49–53.

(103)   Tsoi, K. M.; Macparland, S. A.; Ma, X. Z.; Spetzler, V. N.; Echeverri, J.; Ouyang, B.; Fadel, S. M.; Sykes, E. A.; Goldaracena, N.; Kaths, J. M.; Conneely, J. B.; Alman, B. A.; Selzner, M.; Ostrowski, M. A.; Adeyi, O. A.; Zilman, A.; McGilvray, I. D.; Chan, W. C. W. Mechanism of Hard-Nanomaterial Clearance by the Liver. *Nat. Mater.* **2016**, *15* (11), 1212–1221.

(104)   Chan, W. C. W. Nanomedicine 2.0. *Acc. Chem. Res.* **2017**, *50* (3), 627–632.

(105)   Fischer, H. C.; Liu, L.; Pang, K. S.; Chan, W. C. W. Pharmacokinetics of Nanoscale Quantum Dots: In Vivo Distribution, Sequestration, and Clearance in the Rat. *Adv. Funct. Mater.* **2006**, *16* (10), 1299–1305.

(106)   Ostuni, E.; Chapman, R. G.; Holmlin, R. E.; Takayama, S.; Whitesides, G. M. A Survey of Structure-Property Relationships of Surfaces That Resist the Adsorption of Protein. *Langmuir* **2001**, *17* (18), 5605–5620.

(107)   Klibanov, A. L.; Maruyama, K.; Torchilin, V. P.; Huang, L. Amphipathic Polyethyleneglycols Effectively Prolong the Circulation Time of Liposomes. *FEBS Lett.* **1990**, *268* (1), 235–237.

(108)   Klinker, K.; Barz, M. Polypept(o)Ides: Hybrid Systems Based on Polypeptides and Polypeptoids. *Macromol. Rapid Commun.* **2015**, *36* (22), 1943–1957.

(109)   Bleher, S.; Buck, J.; Muhl, C.; Sieber, S.; Barnert, S.; Witzigmann, D.; Huwyler, J.; Barz, M.; Süss, R. Poly(Sarcosine) Surface Modification Imparts Stealth-Like Properties to Liposomes. *Small* **2019**, *15* (50), 1–10.

(110)   Logie, J.; Owen, S. C.; McLaughlin, C. K.; Shoichet, M. S. PEG-Graft Density Controls Polymeric Nanoparticle Micelle Stability. *Chem. Mater.* **2014**, *26* (9), 2847–2855.

(111)   Carstens, Myrra G; Rijcken, C. J. F. *Multifunctional Pharmaceutical Nanocarriers*; Torchilin, V., Ed.; Fundamental Biomedical Technologies; Springer New York: New York, NY, 2008; Vol. 4.

(112)   Lasic, D. D.; Martin, F. J. *Stealth Liposomes*; Boca Raton : CRC Press, 1995.

(113)   Barz, M.; Luxenhofer, R.; Zentel, R.; Vicent, M. J. Overcoming the PEG-Addiction: Well-Defined Alternatives to PEG, from Structure–Property Relationships to Better Defined Therapeutics. *Polym. Chem.* **2011**, *2* (9), 1900–1918.

(114)   Kwon, G. S.; Yokoyama, M.; Okano, T.; Sakurai, Y.; Kataoka, K. Biodistribution of

Micelle-Forming Polymer-Drug Conjugates. *Pharm. Res.* **1993**, *10* (7), 970–974.

(115) Kwon, G.; Suwa, S.; Yokoyama, M.; Okano, T.; Sakurai, Y.; Kataoka, K. Enhanced Tumor Accumulation and Prolonged Circulation Times of Micelle-Forming Poly (Ethylene Oxide-Aspartate) Block Copolymer-Adriamycin Conjugates. *J. Control. Release* **1994**, *29* (1–2), 17–23.

(116) Du, B.; Yu, M.; Zheng, J. Transport and Interactions of Nanoparticles in the Kidneys. *Nat. Rev. Mater.* **2018**, *3* (10), 358–374.

(117) Soo Choi, H.; Liu, W.; Misra, P.; Tanaka, E.; Zimmer, J. P.; Itty Ipe, B.; Bawendi, M. G.; Frangioni, J. V. Renal Clearance of Quantum Dots. *Nat. Biotechnol.* **2007**, *25* (10), 1165–1170.

(118) Yamaoka, T.; Tabata, Y.; Ikada, Y. Body Distribution Profile of Polysaccharides after Intravenous Administration. *Drug Deliv.* **1993**, *1* (1), 75–82.

(119) Yamaoka, T.; Tabata, Y.; Ikada, Y. Distribution and Tissue Uptake of Poly(Ethylene Glycol) with Different Molecular Weights after Intravenous Administration to Mice. *J. Pharm. Sci.* **1994**, *83* (4), 601–606.

(120) Reske-Nielsen, E.; Bojsen-Møller, M.; Vetner, M.; Hansen, J. C. Polyvinylpyrrolidone-Storage Disease. *Acta Pathol. Microbiol. Scand. Sect. A Pathol.* **2009**, *84A* (5), 397–405.

(121) Maeda, H. The 35th Anniversary of the Discovery of EPR Effect: A New Wave of Nanomedicines for Tumor-Targeted Drug Delivery—Personal Remarks and Future Prospects. *J. Pers. Med.* **2021**, *11* (3), 229.

(122) Shi, Y.; van der Meel, R.; Chen, X.; Lammers, T. The EPR Effect and beyond: Strategies to Improve Tumor Targeting and Cancer Nanomedicine Treatment Efficacy. *Theranostics* **2020**, *10* (17), 7921–7924.

(123) Maeda, H.; Matsumoto, T.; Konno, T.; Iwai, K.; Ueda, M. Tailor-Making of Protein Drugs by Polymer Conjugation for Tumor Targeting: A Brief Review on Smancs. *J. Protein Chem.* **1984**, *3* (2), 181–193.

(124) Matsumura, Y.; Maeda, H. A New Concept for Macromolecular Therapeutics in Cancer Chemotherapy: Mechanism of Tumoritropic Accumulation of Proteins and the Antitumor Agent Smancs. *Cancer Res.* **1986**, *46* (8), 6387–6392.

(125) Mochida, Y.; Cabral, H.; Kataoka, K. Polymeric Micelles for Targeted Tumor Therapy of Platinum Anticancer Drugs. *Expert Opin. Drug Deliv.* **2017**, *14* (12), 1423–1438.

(126) Wilhelm, S.; Tavares, A. J.; Dai, Q.; Ohta, S.; Audet, J.; Dvorak, H. F.; Chan, W. C. W.; Chatterley, A.; Group, W. Analysis of Nanopar.Cle Delivery to Tumours. *Nat. Rev. Mater.* **2016**, *1* (1).

(127) van der Meel, R.; Lammers, T.; Hennink, W. E. Cancer Nanomedicines: Oversold or Underappreciated? *Expert Opin. Drug Deliv.* **2017**, *14* (1), 1–5.

(128) Lammers, T.; Kiessling, F.; Ashford, M.; Hennink, W.; Crommelin, D.; Strom, G. Cancer Nanomedicine: Is Targeting Our Target? *Nat. Rev. Mater.* **2016**, *1* (9), 1–2.

(129) Meel, R. Van Der; Sulheim, E.; Shi, Y.; Kiessling, F.; Mulder, W. J. M. Smart Cancer Nanomedicine. *Nat. Nanotechnol.* **2019**, *14* (November), 1007–1017.

(130) Nichols, J. W.; Bae, Y. H. EPR: Evidence and Fallacy. *J. Control. Release* **2014**, *190*, 451–464.

(131) Sun, D.; Zhou, S.; Gao, W. What Went Wrong with Anticancer Nanomedicine Design and How to Make It Right. *ACS Nano* **2020**, *14* (10), 12281–12290.

(132) Hare, J. I.; Lammers, T.; Ashford, M. B.; Puri, S.; Storm, G.; Barry, S. T. Challenges and Strategies in Anti-Cancer Nanomedicine Development: An Industry Perspective. *Adv. Drug Deliv. Rev.* **2017**, *108*, 25–38.

(133) Lee, H.; Shields, A. F.; Siegel, B. A.; Miller, K. D.; Krop, I.; Ma, C. X.; Lorusso, P. M.; Munster, P. N.; Campbell, K.; Gaddy, D. F.; Leonard, S. C.; Geretti, E.; Blocker, S. J.; Kirpotin, D. B.; Moyo, V.; Wickham, T. J.; Hendriks, B. S. 64Cu-MM-302 Positron Emission Tomography Quantifies Variability of Enhanced Permeability and Retention of Nanoparticles in Relation to Treatment Response in Patients with Metastatic Breast Cancer. *Clin. Cancer Res.* **2017**, *23* (15), 4190–4202.

(134) Li, J.; Kataoka, K. Chemo-Physical Strategies to Advance the in Vivo Functionality of Targeted Nanomedicine: The Next Generation. *J. Am. Chem. Soc.* **2021**, *143* (2), 538–559.

(135) Alkilany, A. M.; Zhu, L.; Weller, H.; Mews, A.; Parak, W. J.; Barz, M.; Feliu, N. Ligand Density on Nanoparticles: A Parameter with Critical Impact on Nanomedicine. *Adv. Drug Deliv. Rev.* **2019**, *143*, 22–36.

(136) Kappel, C.; Seidl, C.; Medina-Montano, C.; Schinnerer, M.; Alberg, I.; Leps, C.; Sohl, J.; Hartmann, A.-K.; Fichter, M.; Kuske, M.; Schunke, J.; Kuhn, G.; Tubbe, I.; Paßlick, D.; Hobernik, D.; Bent, R.; Haas, K.; Montermann, E.; Walzer, K.; Diken, M.; Schmidt, M.; Zentel, R.; Nuhn, L.; Schild, H.; Tenzer, S.; Mailänder, V.; Barz, M.; Bros, M.; Grabbe, S. Density of Conjugated Antibody Determines the Extent of Fc Receptor Dependent Capture of Nanoparticles by Liver Sinusoidal Endothelial Cells. *ACS Nano* **2021**.

(137) Darguzyte, M.; Holm, R.; Baier, J.; Drude, N.; Schultze, J.; Koynov, K.; Schwiertz, D.; Dadfar, S. M.; Lammers, T.; Barz, M.; Kiessling, F. Influence of Riboflavin Targeting on Tumor Accumulation and Internalization of Peptostar Based Drug Delivery Systems. *Bioconjug. Chem.* **2020**, *31* (12), 2691–2696.

(138) Kunjachan, S.; Pola, R.; Gremse, F.; Theek, B.; Ehling, J.; Moeckel, D.; Hermanns-Sachweh, B.; Pechar, M.; Ulbrich, K.; Hennink, W. E.; Storm, G.; Lederle, W.; Kiessling, F.; Lammers, T. Passive versus Active Tumor Targeting Using RGD- and NGR-Modified Polymeric Nanomedicines. *Nano Lett.* **2014**, *14* (2), 972–981.

(139) Poon, W.; Kingston, B. R.; Ouyang, B.; Ngo, W.; Chan, W. C. W. A Framework for Designing Delivery Systems. *Nat. Nanotechnol.* **2020**, *15* (10), 819–829.

(140) Sofias, A. M.; Combes, F.; Koschmieder, S.; Storm, G.; Lammers, T. A Paradigm Shift in Cancer Nanomedicine: From Traditional Tumor Targeting to Leveraging the Immune System. *Drug Discov. Today* **2021**, *00* (00).

(141) Matsumoto, Y.; Nichols, J. W.; Toh, K.; Nomoto, T.; Cabral, H.; Miura, Y.; Christie, R. J.; Yamada, N.; Ogura, T.; Kano, M. R.; Matsumura, Y.; Nishiyama, N.; Yamasoba, T.; Bae, Y. H.; Kataoka, K. Vascular Bursts Enhance Permeability of Tumour Blood Vessels and Improve Nanoparticle Delivery. *Nat. Nanotechnol.* **2016**, *11* (6), 533–538.

(142) Biancacci, I.; Sun, Q.; Möckel, D.; Gremse, F.; Rosenhain, S.; Kiessling, F.; Bartneck, M.; Hu, Q.; Thewissen, M.; Storm, G.; Hennink, W. E.; Shi, Y.; Rijcken, C. J. F.; Lammers, T.; Sofias, A. M. Optical Imaging of the Whole-Body to Cellular Biodistribution of Clinical-Stage PEG-b-PHPMA-Based Core-Crosslinked

Polymeric Micelles. *J. Control. Release* **2020**, *328*, 805–816.

(143) Cheng, Y.; Song, S.; Wu, P.; Lyu, B.; Qin, M.; Sun, Y.; Sun, A.; Mu, L.; Xu, F.; Zhang, L.; Wang, J.; Zhang, Q. Tumor Associated Macrophages and TAMs-Based Anti-Tumor Nanomedicines. *Adv. Healthc. Mater.* **2021**, *10* (18), 1–21.

(144) Mantovani, A.; Marchesi, F.; Malesci, A.; Laghi, L.; Allavena, P. Tumour-Associated Macrophages as Treatment Targets in Oncology. *Nat. Rev. Clin. Oncol.* **2017**, *14* (7), 399–416.

(145) Greco, F.; Vicent, M. J. Combination Therapy: Opportunities and Challenges for Polymer–Drug Conjugates as Anticancer Nanomedicines. *Adv. Drug Deliv. Rev.* **2009**, *61* (13), 1203–1213.

(146) Tyrrell, Z. L.; Shen, Y.; Radosz, M. Fabrication of Micellar Nanoparticles for Drug Delivery through the Self-Assembly of Block Copolymers. *Prog. Polym. Sci.* **2010**, *35* (9), 1128–1143.

(147) Whitesides, G. M.; Grzybowski, B. Self-Assembly at All Scales. *Science* **2002**, *295* (5564), 2418–2421.

(148) Bates, F. S. Polymer-Polymer Phase Behavior. *Science* **1991**, *251* (4996), 898–905.

(149) Israelachvili, J. N.; Mitchell, D. J.; Ninham, B. W. Theory of Self-Assembly of Hydrocarbon Amphiphiles into Micelles and Bilayers. *J. Chem. Soc. Faraday Trans. 2 Mol. Chem. Phys.* **1976**, *72*, 1525–1568.

(150) Adams, M. L.; Lavasanifar, A.; Kwon, G. S. Amphiphilic Block Copolymers for Drug Delivery. *J. Pharm. Sci.* **2003**, *92* (7), 1343–1355.

(151) Huesmann, D.; Sevenich, A.; Weber, B.; Barz, M. A Head-to-Head Comparison of Poly(Sarcosine) and Poly(Ethylene Glycol) in Peptidic, Amphiphilic Block Copolymers. *Polym. (United Kingdom)* **2015**, *67*, 240–248.

(152) Schaeffel, D.; Kreyes, A.; Zhao, Y.; Landfester, K.; Butt, H.-J.; Crespy, D.; Koynov, K. Molecular Exchange Kinetics of Diblock Copolymer Micelles Monitored by Fluorescence Correlation Spectroscopy. *ACS Macro Lett.* **2014**, *3* (5), 428–432.

(153) Lübtow, M. M.; Hahn, L.; Haider, M. S.; Luxenhofer, R. Drug Specificity, Synergy and Antagonism in Ultrahigh Capacity Poly(2-Oxazoline)/Poly(2-Oxazine) Based Formulations. *J. Am. Chem. Soc.* **2017**, *139* (32), 10980–10983.

(154) Hara, E.; Makino, A.; Kurihara, K.; Yamamoto, F.; Ozeki, E.; Kimura, S. Pharmacokinetic Change of Nanoparticulate Formulation Lactosome on Multiple Administrations. *Int. Immunopharmacol.* **2012**, *14* (3), 261–266.

(155) Sevast'ianov, V. I.; Tseytlina, E. A. The Activation of the Complement System by Polymer Materials and Their Blood Compatibility. *J. Biomed. Mater. Res.* **1984**, *18* (9), 969–978.

(156) Gabizon, A.; Szebeni, J. Complement Activation: A Potential Threat on the Safety of Poly(Ethylene Glycol)-Coated Nanomedicines. *ACS Nano* **2020**, *14* (7), 7682–7688.

(157) Zheng, X.; Xie, J.; Zhang, X.; Sun, W.; Zhao, H.; Li, Y.; Wang, C. An Overview of Polymeric Nanomicelles in Clinical Trials and on the Market. *Chinese Chem. Lett.* **2021**, *32* (1), 243–257.

(158) Hwang, D.; Ramsey, J. D.; Kabanov, A. V. Polymeric Micelles for the Delivery of Poorly Soluble Drugs: From Nanoformulation to Clinical Approval. *Adv. Drug Deliv. Rev.* **2020**, *156*, 80–118.

(159) Cabral, H.; Miyata, K.; Osada, K.; Kataoka, K. Block Copolymer Micelles in Nanomedicine Applications. *Chem. Rev.* **2018**, *118* (14), 6844–6892.

(160) Hamaguchi, T.; Matsumura, Y.; Suzuki, M.; Shimizu, K.; Goda, R.; Nakamura, I.; Nakatomi, I.; Yokoyama, M.; Kataoka, K.; Kakizoe, T. NK105, a Paclitaxel-Incorporating Micellar Nanoparticle Formulation, Can Extend in Vivo Antitumour Activity and Reduce the Neurotoxicity of Paclitaxel. *Br. J. Cancer* **2005**, *92* (7), 1240–1246.

(161) Fujiwara, Y.; Mukai, H.; Saeki, T.; Ro, J.; Lin, Y. C.; Nagai, S. E.; Lee, K. S.; Watanabe, J.; Ohtani, S.; Kim, S. B.; Kuroi, K.; Tsugawa, K.; Tokuda, Y.; Iwata, H.; Park, Y. H.; Yang, Y.; Nambu, Y. A Multi-National, Randomised, Open-Label, Parallel, Phase III Non-Inferiority Study Comparing NK105 and Paclitaxel in Metastatic or Recurrent Breast Cancer Patients. *Br. J. Cancer* **2019**, *120* (5), 475–480.

(162) Hamaguchi, T.; Tsuji, A.; Yamaguchi, K.; Takeda, K.; Uetake, H.; Esaki, T.; Amagai, K.; Sakai, D.; Baba, H.; Kimura, M.; Matsumura, Y.; Tsukamoto, T. A Phase II Study of NK012, a Polymeric Micelle Formulation of SN-38, in Unresectable, Metastatic or Recurrent Colorectal Cancer Patients. *Cancer Chemother. Pharmacol.* **2018**, *82* (6), 1021–1029.

(163) Von Hoff, D. D.; Mita, M. M.; Ramanathan, R. K.; Weiss, G. J.; Mita, A. C.; Lorusso, P. M.; Burris, H. A.; Hart, L. L.; Low, S. C.; Parsons, D. M.; Zale, S. E.; Summa, J. M.; Youssoufian, H.; Sachdev, J. C. Phase I Study of PSMA-Targeted Docetaxel-Containing Nanoparticle BIND-014 in Patients with Advanced Solid Tumors. *Clin. Cancer Res.* **2016**, *22* (13), 3157–3163.

(164) Miele, E.; Spinelli, G. P.; Miele, E.; Tomao, F.; Tomao, S. Albumin-Bound Formulation of Paclitaxel (Abraxane ABI-007) in the Treatment of Breast Cancer. *Int. J. Nanomedicine* **2009**, *4*, 99–105.

(165) Gradishar, W. J.; Tjulandin, S.; Davidson, N.; Shaw, H.; Desai, N.; Bhar, P.; Hawkins, M.; O'Shaughnessy, J. Phase III Trial of Nanoparticle Albumin-Bound Paclitaxel Compared with Polyethylated Castor Oil-Based Paclitaxel in Women with Breast Cancer. *J. Clin. Oncol.* **2005**, *23* (31), 7794–7803.

(166) Yardley, D. A. Nab-Paclitaxel Mechanisms of Action and Delivery. *J. Control. Release* **2013**, *170* (3), 365–372.

(167) Socinski, M. A.; Bondarenko, I.; Karaseva, N. A.; Makhson, A. M.; Vynnychenko, I.; Okamoto, I.; Hon, J. K.; Hirsh, V.; Bhar, P.; Zhang, H.; Iglesias, J. L.; Renschler, M. F. Weekly Nab-Paclitaxel in Combination with Carboplatin versus Solvent-Based Paclitaxel plus Carboplatin as First-Line Therapy in Patients with Advanced Non-Small-Cell Lung Cancer: Final Results of a Phase III Trial. *J. Clin. Oncol.* **2012**, *30* (17), 2055–2062.

(168) Lee, H.; Park, S.; Kang, J. E.; Lee, H. M.; Kim, S. A.; Rhie, S. J. Efficacy and Safety of Nanoparticle-Albumin-Bound Paclitaxel Compared with Solvent-Based Taxanes for Metastatic Breast Cancer: A Meta-Analysis. *Sci. Rep.* **2020**, *10* (1), 1–9.

(169) Vergote, I.; Bergfeldt, K.; Franquet, A.; Lisyanskaya, A. S.; Bjermo, H.; Heldring, N.; Buyse, M.; Brize, A. A Randomized Phase III Trial in Patients with Recurrent Platinum Sensitive Ovarian Cancer Comparing Efficacy and Safety of Paclitaxel Micellar and Cremophor EL-Paclitaxel. *Gynecol. Oncol.* **2020**, *156* (2), 293–300.

(170) Borgå, O.; Henriksson, R.; Bjermo, H.; Lilienberg, E.; Heldring, N.; Loman, N.

Maximum Tolerated Dose and Pharmacokinetics of Paclitaxel Micellar in Patients with Recurrent Malignant Solid Tumours: A Dose-Escalation Study. *Adv. Ther.* **2019**, *36* (5), 1150–1163.

(171) Sill, K. N.; Sullivan, B.; Carie, A.; Edward Semple, J. Synthesis and Characterization of Micelle-Forming PEG-Poly(Amino Acid) Copolymers with Iron-Hydroxamate Cross-Linkable Blocks for Encapsulation and Release of Hydrophobic Drugs. *Biomacromolecules* **2017**, *18* (6), 1874–1884.

(172) Shi, Y.; Van Steenbergen, M. J.; Teunissen, E. A.; Novo, L.; Gradmann, S.; Baldus, M.; Van Nostrum, C. F.; Hennink, W. E. Π-Π Stacking Increases the Stability and Loading Capacity of Thermosensitive Polymeric Micelles for Chemotherapeutic Drugs. *Biomacromolecules* **2013**, *14* (6), 1826–1837.

(173) Wu, G.; Li, C.; Liu, X.; Lv, J.; Ding, Y.; Liu, Y.; Liu, Y.; Huang, F.; Shi, L.; An, Y.; Ma, R. Glucose-Responsive Complex Micelles for Self-Regulated Delivery of Insulin with Effective Protection of Insulin and Enhanced Hypoglycemic Activity in Vivo. *Colloids Surfaces B Biointerfaces* **2019**, *180* (May), 376–383.

(174) Chen, J.; Yan, B.; Wang, X.; Huang, Q.; Thundat, T.; Zeng, H. Core Cross-Linked Double Hydrophilic Block Copolymer Micelles Based on Multiple Hydrogen-Bonding Interactions. *Polym. Chem.* **2017**, *8* (20), 3066–3073.

(175) Lin, M.; Dai, Y.; Xia, F.; Zhang, X. Advances in Non-Covalent Crosslinked Polymer Micelles for Biomedical Applications. *Mater. Sci. Eng. C* **2021**, *119*, 111626.

(176) Ke, X.; Ng, V. W. L.; Ono, R. J.; Chan, J. M. W.; Krishnamurthy, S.; Wang, Y.; Hedrick, J. L.; Yang, Y. Y. Role of Non-Covalent and Covalent Interactions in Cargo Loading Capacity and Stability of Polymeric Micelles. *J. Control. Release* **2014**, *193*, 9–26.

(177) Hofmann, D.; Messerschmidt, C.; Bannwarth, M. B.; Landfester, K.; Mailänder, V. Drug Delivery without Nanoparticle Uptake: Delivery by a Kiss-and-Run Mechanism on the Cell Membrane. *Chem. Commun.* **2014**, *50* (11), 1369–1371.

(178) Li, Y.; Xiao, K.; Zhu, W.; Deng, W.; Lam, K. S. Stimuli-Responsive Cross-Linked Micelles for on-Demand Drug Delivery against Cancers. *Adv. Drug Deliv. Rev.* **2014**, *66*, 58–73.

(179) Fan, W.; Zhang, L.; Li, Y.; Wu, H. Recent Progress of Crosslinking Strategies for Polymeric Micelles with Enhanced Drug Delivery in Cancer Therapy. *Curr. Med. Chem.* **2019**, *26* (13), 2356–2376.

(180) O'Reilly, R. K.; Hawker, C. J.; Wooley, K. L. Cross-Linked Block Copolymer Micelles: Functional Nanostructures of Great Potential and Versatility. *Chem. Soc. Rev.* **2006**, *35* (11), 1068–1083.

(181) Thurmond, K. B.; Huang, H.; Clark, C. G.; Kowalewski, T.; Wooley, K. L. Shell Cross-Linked Polymer Micelles: Stabilized Assemblies with Great Versatility and Potential. *Colloids Surfaces B Biointerfaces* **1999**, *16* (1–4), 45–54.

(182) Rolland, A.; O'Mullane, J.; Goddard, P.; Brookman, L.; Petrak, K. New Macromolecular Carriers for Drugs. I. Preparation and Characterization of Poly(Oxyethylene-b-isoprene-b-oxyethylene) Block Copolymer Aggregates. *J. Appl. Polym. Sci.* **1992**, *44* (7), 1195–1203.

(183) Van Nostrum, C. F. Covalently Cross-Linked Amphiphilic Block Copolymer Micelles. *Soft Matter* **2011**, *7* (7), 3246–3259.

(184) Rijcken, C. J.; Snel, C. J.; Schiffelers, R. M.; van Nostrum, C. F.; Hennink, W. E. Hydrolysable Core-Crosslinked Thermosensitive Polymeric Micelles: Synthesis, Characterisation and in Vivo Studies. *Biomaterials* **2007**, *28* (36), 5581–5593.

(185) Hu, Q.; Rijcken, C. J.; Bansal, R.; Hennink, W. E.; Storm, G.; Prakash, J. Complete Regression of Breast Tumour with a Single Dose of Docetaxel-Entrapped Core-Cross-Linked Polymeric Micelles. *Biomaterials* **2015**, *53*, 370–378.

(186) Hu, Q.; Rijcken, C. J. F.; van Gaal, E.; Brundel, P.; Kostkova, H.; Etrych, T.; Weber, B.; Barz, M.; Kiessling, F.; Prakash, J.; Storm, G.; Hennink, W. E.; Lammers, T. Tailoring the Physicochemical Properties of Core-Crosslinked Polymeric Micelles for Pharmaceutical Applications. *J. Control. Release* **2016**, *244*, 314–325.

(187) Atrafi, F.; Dumez, H.; Mathijssen, R. H. J.; Menke van der Houven van Oordt, C. W.; Rijcken, C. J. F.; Hanssen, R.; Eskens, F. A. L. M.; Schöffski, P. A Phase I Dose-Escalation and Pharmacokinetic Study of a Micellar Nanoparticle with Entrapped Docetaxel (CPC634) in Patients with Advanced Solid Tumours. *J. Control. Release* **2020**, *325* (March), 191–197.

(188) Atrafi, F.; van Eerden, R. A. G.; van Hylckama Vlieg, M. A. M.; Oomen-de Hoop, E.; de Bruijn, P.; Lolkema, M. P.; Moelker, A.; Rijcken, C. J.; Hanssen, R.; Sparreboom, A.; Eskens, F. A. L. M.; Mathijssen, R. H. J.; Koolen, S. L. W. Intratumoral Comparison of Nanoparticle Entrapped Docetaxel (CPC634) with Conventional Docetaxel in Patients with Solid Tumors. *Clin. Cancer Res.* **2020**, *26* (14), 3537–3545.

(189) Atrafi, F.; van Eerden, R. A. G.; Koolen, S. L. W.; de Bruijn, P.; Rijcken, C. J. F.; Hanssen, R.; Eskens, F. A. L. M.; Lolkema, M. P.; Oomen-de Hoop, E.; Damman, J.; Mathijssen, R. H. J. Docetaxel Skin Exposure and Micronucleation Contributes to Skin Toxicity Caused by CPC634. *Cancers (Basel).* **2021**, *13* (15), 3741.

(190) Sevier, C. S.; Kaiser, C. A. Formation and Transfer of Disulphide Bonds in Living Cells. *Nat. Rev. Mol. Cell Biol.* **2002**, *3* (11), 836–847.

(191) Poole, L. B. The Basics of Thiols and Cysteines in Redox Biology and Chemistry. *Free Radic. Biol. Med.* **2015**, *80*, 148–157.

(192) Li, L.; Li, D.; Zhang, M.; He, J.; Liu, J.; Ni, P. One-Pot Synthesis of PH/Redox Responsive Polymeric Prodrug and Fabrication of Shell Cross-Linked Prodrug Micelles for Antitumor Drug Transportation. *Bioconjug. Chem.* **2018**, *29* (8), 2806–2817.

(193) Huesmann, D.; Schäfer, O.; Braun, L.; Klinker, K.; Reuter, T.; Barz, M. Exploring New Activating Groups for Reactive Cysteine NCAs. *Tetrahedron Lett.* **2016**, *57* (10), 1138–1142.

(194) Schäfer, O.; Barz, M. Of Thiols and Disulfides: Methods for Chemoselective Formation of Asymmetric Disulfides in Synthetic Peptides and Polymers. *Chem. - A Eur. J.* **2018**, *24* (47), 12131–12142.

(195) Schäfer, O.; Huesmann, D.; Muhl, C.; Barz, M. Rethinking Cysteine Protective Groups: S -Alkylsulfonyl- l -Cysteines for Chemoselective Disulfide Formation. *Chem. - A Eur. J.* **2016**, *22* (50), 18085–18091.

(196) Huesmann, D.; Klinker, K.; Barz, M. Orthogonally Reactive Amino Acids and End Groups in NCA Polymerization. *Polym. Chem.* **2016**, *8* (6), 957–971.

(197) Schäfer, O.; Huesmann, D.; Barz, M. Poly(S -Ethylsulfonyl- l -Cysteines) for

Chemoselective Disulfide Formation. *Macromolecules* **2016**, *49* (21), 8146–8153.

(198) Barz, M. Complexity and Simplification in the Development of Nanomedicines. *Nanomedicine* **2015**, *10* (20), 3093–3097.

(199) Leroux, J. C. Drug Delivery: Too Much Complexity, Not Enough Reproducibility? *Angew. Chemie - Int. Ed.* **2017**, 2–4.

(200) Waldman, A. D.; Fritz, J. M.; Lenardo, M. J. A Guide to Cancer Immunotherapy: From T Cell Basic Science to Clinical Practice. *Nat. Rev. Immunol.* **2020**, *20* (11), 651–668.

(201) Bourgeois-Daigneault, M. C.; Roy, D. G.; Aitken, A. S.; El Sayes, N.; Martin, N. T.; Varette, O.; Falls, T.; St-Germain, L. E.; Pelin, A.; Lichty, B. D.; Stojdl, D. F.; Ungerechts, G.; Diallo, J. S.; Bell, J. C. Neoadjuvant Oncolytic Virotherapy before Surgery Sensitizes Triple-Negative Breast Cancer to Immune Checkpoint Therapy. *Sci. Transl. Med.* **2018**, *10* (422), 1–12.

(202) Ho, D. Artificial Intelligence in Cancer Therapy. *Science* **2020**, *367* (6481), 982–983.

(203) Birke, A.; Huesmann, D.; Kelsch, A.; Weilbächer, M.; Xie, J.; Bros, M.; Bopp, T.; Becker, C.; Landfester, K.; Barz, M. Polypeptoid- Block -Polypeptide Copolymers: Synthesis, Characterization, and Application of Amphiphilic Block Copolypept(o)Ides in Drug Formulations and Miniemulsion Techniques. *Biomacromolecules* **2014**, *15* (2), 548–557.

(204) Birke, A.; Ling, J.; Barz, M. Polysarcosine-Containing Copolymers: Synthesis, Characterization, Self-Assembly, and Applications. *Prog. Polym. Sci.* **2018**, *81*, 163–208.

(205) Simon, R. J.; Kania, R. S.; Zuckermann, R. N.; Huebner, V. D.; Jewell, D. A.; Banville, S.; Ng, S.; Wang, L.; Rosenberg, S.; Marlowe, C. K. Peptoids: A Modular Approach to Drug Discovery. *Proc. Natl. Acad. Sci.* **1992**, *89* (20), 9367–9371.

(206) Zuckermann, R. N.; Kerr, J. M.; Kent, S. B. H.; Moos, W. H. Efficient Method for the Preparation of Peptoids [Oligo(N-Substituted Glycines)] by Submonomer Solid-Phase Synthesis. *J. Am. Chem. Soc.* **1992**, *114* (26), 10646–10647.

(207) Kirshenbaum, K.; Barron, A. E.; Goldsmith, R. A.; Armand, P.; Bradley, E. K.; Truong, K. T. V.; Dill, K. A.; Cohen, F. E.; Zuckermann, R. N. Sequence-Specific Polypeptoids: A Diverse Family of Heteropolymers with Stable Secondary Structure. *Proc. Natl. Acad. Sci. U. S. A.* **1998**, *95* (8), 4303–4308.

(208) Secker, C.; Brosnan, S. M.; Luxenhofer, R.; Schlaad, H. Poly(α-Peptoid)s Revisited: Synthesis, Properties, and Use as Biomaterial. *Macromol. Biosci.* **2015**, *15* (7), 881–891.

(209) Gangloff, N.; Ulbricht, J.; Lorson, T.; Schlaad, H.; Luxenhofer, R. Peptoids and Polypeptoids at the Frontier of Supra- and Macromolecular Engineering. *Chem. Rev.* **2016**, *116* (4), 1753–1802.

(210) Sanborn, T. J.; Wu, C. W.; Zuckermann, R. N.; Barron, A. E. Extreme Stability of Helices Formed by Water-Soluble Poly-N-Substituted Glycines (Polypeptoids) with α-Chiral Side Chains. *Biopolymers* **2002**, *63* (1), 12–20.

(211) Mannige, R. V.; Haxton, T. K.; Proulx, C.; Robertson, E. J.; Battigelli, A.; Butterfoss, G. L.; Zuckermann, R. N.; Whitelam, S. Peptoid Nanosheets Exhibit a New Secondary-Structure Motif. *Nature* **2015**, *526* (7573), 415–420.

(212) Weber, B.; Birke, A.; Fischer, K.; Schmidt, M.; Barz, M. Solution Properties of

Polysarcosine: From Absolute and Relative Molar Mass Determinations to Complement Activation. *Macromolecules* **2018**, *51* (7), 2653–2661.

(213) Lau, K. H. A.; Ren, C.; Sileika, T. S.; Park, S. H.; Szleifer, I.; Messersmith, P. B. Surface-Grafted Polysarcosine as a Peptoid Antifouling Polymer Brush. *Langmuir* **2012**, *28* (46), 16099–16107.

(214) Astbury, W. T.; Dalgliesh, C. E.; Darmon, S. E.; Sutherland, G. B. B. M. Studies of the Structure of Synthetic Polypeptides. *Nature* **1948**, *162* (4120), 596–600.

(215) Brosnan, M. E.; Brosnan, J. T. The Role of Dietary Creatine. *Amino Acids* **2016**, *48* (8), 1785–1791.

(216) Snow, R. J.; Murphy, R. M. Creatine and the Creatine Transporter: A Review. *Mol. Cell. Biochem.* **2001**, *224* (1–2), 169–181.

(217) Horner, W. H.; Mackenzie, C. G. The Biological Formation of Sarcosine. *J. Biol. Chem.* **1950**, *187* (1), 15–22.

(218) Ogawa, H.; Gomi, T.; Takusagawa, F.; Fujioka, M. Structure, Function and Physiological Role of Glycine N- Methyltransferase. *Int. J. Biochem. Cell Biol.* **1998**, *30* (1), 13–26.

(219) Porter, D. H.; Cook, R. J.; Wagner, C. Enzymatic Properties of Dimethylglycine Dehydrogenase and Sarcosine Dehydrogenase from Rat Liver. *Arch. Biochem. Biophys.* **1985**, *243* (2), 396–407.

(220) Glorieux, F. H.; Scriver, C. R.; Delvin, E.; Mohyuddin, F. Transport and Metabolism of Sarcosine in Hypersarcosinemic and Normal Phenotypes. *J. Clin. Invest.* **1971**, *50* (11), 2313–2322.

(221) Katchalski, E. Poly-α-Amino Acids. In *Advances in Protein Chemistry*; **1951**; 123–185.

(222) Kricheldorf, H. R. Polypeptides and 100 Years of Chemistry of α-Amino Acid N-Carboxyanhydrides. *Angew. Chemie - Int. Ed.* **2006**, *45* (35), 5752–5784.

(223) Hanby, W. E.; Waley, S. G.; Watson, J. Synthetic Polypeptides. Part I. *J. Chem. Soc.* **1950**, 3009.

(224) Ballard, D. G. H.; Bamford, C. H. Studies in Polymerization. X. 'The Chain-Effect'. *Proc. R. Soc. London. Ser. A. Math. Phys. Sci.* **1956**, *236* (1206), 384–396.

(225) Kricheldorf, H. R.; Schilling, G. 13C NMR Sequence Analysis, 15. Copolymerization of Alanine-NCA with Other α-Amino Acid NCAs. *J. Macromol. Sci.-Chem.* **1978**, *179* (11), 1175–1191.

(226) Katchalski, E.; Sela, M. Synthesis and Chemical Properties of Poly-α-Amino Acids. *Adv. Protein Chem.* **1958**, *13* (C), 243–492.

(227) Katchalski, E.; Berger, A.; Bichowsky-Slomnicki, L.; Kurtz, J. Antibiotically Active Amino-Acid Copolymers Related to Gramicidin S. *Nature* **1955**, *176* (4472), 118–119.

(228) Kidchob, T.; Kimura, S.; Imanishi, Y. Preparation, Structure and Release Profile of Polypeptide Microcapsules. *J. Control. Release* **1996**, *40* (3), 285–291.

(229) Kidchob, T.; Kimura, S.; Imanishi, Y. PH-Responsive Release from Polypeptide Microcapsules. *J. Appl. Polym. Sci.* **1997**, *63* (4), 453–458.

(230) Kidchob, T. Thermoresponsive Release from Poly(Glu(OMe))-Block-Poly(Sar) Microcapsules with Surface-Grafting of Poly(N-Isopropylacrylamide). *J. Control.*

Release **1998**, *50* (1–3), 205–214.

(231) Kidchob, T.; Kimura, S.; Imanishi, Y. Amphiphilic Poly(Ala)-b-Poly(Sar) Microspheres Loaded with Hydrophobic Drag. *J. Control. Release* **1998**, *51* (2–3), 241–248.

(232) Vayaboury, W.; Giani, O.; Cottet, H.; Deratani, A.; Schué, F. Living Polymerization of α-Amino Acid N-Carboxyanhydrides (NCA) upon Decreasing the Reaction Temperature. *Macromol. Rapid Commun.* **2004**, *25* (13), 1221–1224.

(233) Aliferis, T.; Iatrou, H.; Hadjichristidis, N. Living Polypeptides. *Biomacromolecules* **2004**, *5* (5), 1653–1656.

(234) Gangloff, N.; Fetsch, C.; Luxenhofer, R. Polypeptoids by Living Ring-Opening Polymerization of N-Substituted N-Carboxyanhydrides from Solid Supports. *Macromol. Rapid Commun.* **2013**, *34* (12), 997–1001.

(235) Bailey, J. A New Peptide Synthesis. *Nature* **1949**, *164* (4177), 889–889.

(236) Merrifield, R. B. Solid Phase Peptide Synthesis. I. The Synthesis of a Tetrapeptide. *J. Am. Chem. Soc.* **1963**, *85* (14), 2149–2154.

(237) Li, Y. Recombinant Production of Antimicrobial Peptides in Escherichia Coli: A Review. *Protein Expr. Purif.* **2011**, *80* (2), 260–267.

(238) Kawakami, T.; Murakami, H.; Suga, H. Ribosomal Synthesis of Polypeptoids and Peptoid-Peptide Hybrids. *J. Am. Chem. Soc.* **2008**, *130* (50), 16861–16863.

(239) Leuchs, H. Ueber Die Glycin-Carbonsäure. *Berichte der Dtsch. Chem. Gesellschaft* **1906**, *39* (1), 857–861.

(240) Leuchs, H.; Manasse, W. Über Die Isomerie Der Carbäthoxyl-Glycyl Glycinester. *Berichte der Dtsch. Chem. Gesellschaft* **1907**, *40* (3), 3235–3249.

(241) Leuchs, H.; Geiger, W. Über Die Anhydride von α-Amino-N-Carbonsäuren Und Die von α-Aminosäuren. *Berichte der Dtsch. Chem. Gesellschaft* **1908**, *41* (2), 1721–1726.

(242) Staudinger, H. Über Polymerisation. *Berichte der Dtsch. Chem. Gesellschaft (A B Ser.* **1920**, *53* (6), 1073–1085.

(243) Wessely, F. Untersuchungen Über α-Amino-N-Carbonsäureanhydride. I. *Hoppe-Seyler´s Zeitschrift für Physiol. Chemie* **1925**, *146* (1–3), 72–90.

(244) Go, Y.; Tani, H. Über Die Hochkondensierten Produkte Aus Einigen Aminosäuren. *Bull. Chem. Soc. Jpn.* **1939**, *14* (11), 510–516.

(245) Sigmund., F.; Wessely, F. Untersuchungen Über α-Amino-N-Carbonsäureanhydride. II. *Hoppe-Seyler´s Zeitschrift für Physiol. Chemie* **1926**, *157* (1–3), 91–105.

(246) Wessely, F.; Sigmund, F. Untersuchungen Über α-Amino-N-Caxbonsäureanhydride. III. (Zur Kenntnis Höhermolekularer Verbindungen.). *Hoppe-Seyler´s Zeitschrift für Physiol. Chemie* **1926**, *159* (1–4), 102–119.

(247) Woodward, R. B.; Schramm, C. H. Synthesis of Protein Analogs. *J. Am. Chem. Soc.* **1947**, *69* (6), 1551–1552.

(248) Waley, S. G.; Watson, J. The Kinetics of the Polymerization of Sarcosine Carbonic Anhydride. *Proc. R. Soc. London. Ser. A. Math. Phys. Sci.* **1949**, *199* (1059), 499–517.

(249) Fessler, J. H.; Ogston, A. G. Studies of the Sedimentation, Diffusion and Viscosity of Some Sarcosine Polymers in Aqueous Solution. *Trans. Faraday Soc.* **1951**, *47*,

667.

(250) Ballard, D. G.; Bamford, C. H. Kinetics of the Formation of Polypeptides from N-Carboxy-α-Amino-Acid Anhydrides. *Nature* **1953**, *172* (4385), 907–908.

(251) Fuchs, F. Über N-Carbonsäure-Anhydride. *Chem. Ber.* **1922**, *55B*, 2943.

(252) Farthing, A. C.; Reynolds, R. J. W. Anhydro-N-Carboxy-DL-ß-Phenylalanine. *Nature* **1950**, *165* (4199), 647–647.

(253) Oya, M.; Katakai, R.; Nakai, H.; Iwakura, Y. A Novel Synthesis of N-Carboxy-α-Amino Acid Anhydride. *Chem. Lett.* **1973**, *2* (11), 1143–1144.

(254) Daly, W. H.; Poché, D. The Preparation of N-Carboxyanhydrides of α-Amino Acids Using Bis(Trichloromethyl)Carbonate. *Tetrahedron Lett.* **1988**, *29* (46), 5859–5862.

(255) Schäfer, O.; Schollmeyer, D.; Birke, A.; Holm, R.; Johann, K.; Muhl, C.; Seidl, C.; Weber, B.; Barz, M. Investigation of α-Amino Acid N-Carboxyanhydrides by X-Ray Diffraction for Controlled Ring-Opening Polymerization. *Tetrahedron Lett.* **2019**, *60* (3), 272–275.

(256) Fischer, K. Neues Verfahren Zur Maßanalytischen Bestimmung Des Wassergehaltes von Flüssigkeiten Und Festen Körpern. *Angew. Chemie* **1935**, *48* (26), 394–396.

(257) Semple, J. E.; Sullivan, B.; Sill, K. N. Large-Scale Synthesis of α-Amino Acid- *N* -Carboxyanhydrides. *Synth. Commun.* **2017**, *47* (1), 53–61.

(258) Hadjichristidis, N.; Iatrou, H.; Pitsikalis, M.; Sakellariou, G. Synthesis of Well-Defined Polypeptide-Based Materials via the Ring-Opening Polymerization of α-Amino Acid N-Carboxyanhydrides. *Chem. Rev.* **2009**, *109* (11), 5528–5578.

(259) Liu, J.; Ling, J. DFT Study on Amine-Mediated Ring-Opening Mechanism of α-Amino Acid N-Carboxyanhydride and N-Substituted Glycine N-Carboxyanhydride: Secondary Amine versus Primary Amine. *J. Phys. Chem. A* **2015**, *119* (27), 7070–7074.

(260) Webster, O. W. Living Polymerization Methods. *Science* **1991**, *251* (4996), 887–893.

(261) Deming, T. J. Facile Synthesis of Block Copolypeptides of Defined Architecture. *Nature* **1997**, *390* (6658), 386–389.

(262) Deming, T. J. Cobalt and Iron Initiators for the Controlled Polymerization of α-Amino Acid-N-Carboxyanhydrides. *Macromolecules* **1999**, *32* (13), 4500–4502.

(263) Deming, T. J. Synthesis of Side-Chain Modified Polypeptides. *Chem. Rev.* **2016**, *116* (3), 786–808.

(264) Detwiler, R. E.; Schlirf, A. E.; Kramer, J. R. Rethinking Transition Metal Catalyzed N-Carboxyanhydride Polymerization: Polymerization of Pro and AcOPro N-Carboxyanhydrides. *J. Am. Chem. Soc.* **2021**, *143* (30), 11482–11489.

(265) Conejos-Sánchez, I.; Duro-Castano, A.; Birke, A.; Barz, M.; Vicent, M. J. A Controlled and Versatile NCA Polymerization Method for the Synthesis of Polypeptides. *Polym. Chem.* **2013**, *4* (11), 3182.

(266) Dimitrov, I.; Schlaad, H. Synthesis of Nearly Monodisperse Polystyrene–Polypeptide Block Copolymers via Polymerisation of N-Carboxyanhydrides. *Chem. Commun.* **2003**, No. 23, 2944–2945.

(267) Habraken, G. J. M. M.; Peeters, M.; Dietz, C. H. J. T. J. T.; Koning, C. E.; Heise, A. How Controlled and Versatile Is N-Carboxy Anhydride (NCA) Polymerization at 0
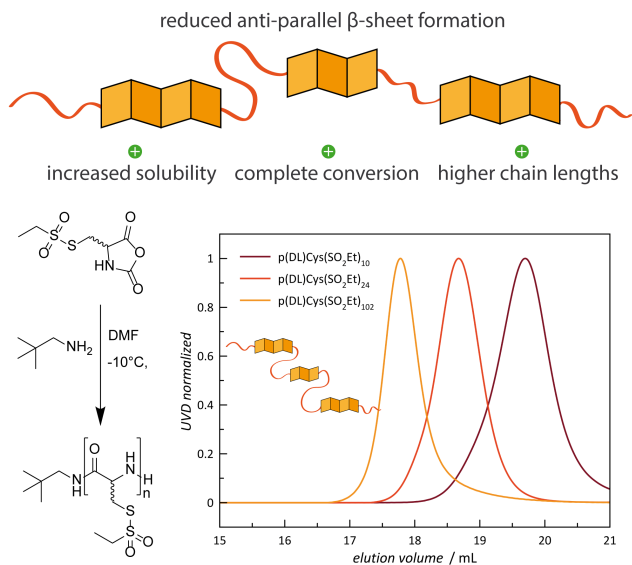
°C? Effect of Temperature on Homo-, Block- and Graft (Co)Polymerization. *Polym. Chem.* **2010**, *1* (4), 514–524.

(268) Rasines Mazo, A.; Allison-Logan, S.; Karimi, F.; Chan, N. J. A.; Qiu, W.; Duan, W.; O'Brien-Simpson, N. M.; Qiao, G. G. Ring Opening Polymerization of α-Amino Acids: Advances in Synthesis, Architecture and Applications of Polypeptides and Their Hybrids. *Chem. Soc. Rev.* **2020**, *49* (14), 4737–4834.

(269) Zhao, W.; Lv, Y.; Li, J.; Feng, Z.; Ni, Y.; Hadjichristidis, N. Fast and Selective Organocatalytic Ring-Opening Polymerization by Fluorinated Alcohol without a Cocatalyst. *Nat. Commun.* **2019**, *10* (1), 3590.

(270) Xia, Y.; Song, Z.; Tan, Z.; Xue, T.; Wei, S.; Zhu, L.; Yang, Y.; Fu, H.; Jiang, Y.; Lin, Y.; Lu, Y.; Ferguson, A. L.; Cheng, J. Accelerated Polymerization of N-Carboxyanhydrides Catalyzed by Crown Ether. *Nat. Commun.* **2021**, *12* (1).

(271) Wang, X.; Song, Z.; Tan, Z.; Zhu, L.; Xue, T.; Lv, S.; Fu, Z.; Zheng, X.; Ren, J.; Cheng, J. Facile Synthesis of Helical Multiblock Copolypeptides: Minimal Side Reactions with Accelerated Polymerization of N-Carboxyanhydrides. *ACS Macro Lett.* **2019**, 1517–1521.

(272) Heatley, F.; Bovey, F. A. Polymer Nuclear Magnetic Resonance Spectroscopy. XIV. The Nuclear Magnetic Resonance Spectrum of Poly (Isopropyl Acrylate). *Macromolecules* **1968**, *1* (4), 303–304.

(273) Edison, J. R.; Spencer, R. K.; Butterfoss, G. L.; Hudson, B. C.; Hochbaum, A. I.; Paravastu, A. K.; Zuckermann, R. N.; Whitelam, S. Conformations of Peptoids in Nanosheets Result from the Interplay of Backbone Energetics and Intermolecular Interactions. *Proc. Natl. Acad. Sci. U. S. A.* **2018**, *115* (22), 5647–5651.

(274) Sisido, M.; Imanishi, Y.; Higashimura, T. Monte Carlo Calculation on Trans/Cis-Polysarcosine. *Macromolecules* **1976**, *9* (3), 389–395.

(275) Ostuni, E.; Chapman, R. G.; Liang, M. N.; Meluleni, G.; Pier, G.; Ingber, D. E.; Whitesides, G. M. Self-Assembled Monolayers That Resist the Adsorption of Proteins and the Adhesion of Bacterial and Mammalian Cells. *Langmuir* **2001**, *17* (20), 6336–6343.

(276) Schneider, M.; Fetsch, C.; Amin, I.; Jordan, R.; Luxenhofer, R. Polypeptoid Brushes by Surface-Initiated Polymerization of N-Substituted Glycine N - Carboxyanhydrides. *Langmuir* **2013**, *29* (23), 6983–6988.

(277) Schneider, M.; Tang, Z.; Richter, M.; Marschelke, C.; Förster, P.; Wegener, E.; Amin, I.; Zimmermann, H.; Scharnweber, D.; Braun, H. G.; Luxenhofer, R.; Jordan, R. Patterned Polypeptoid Brushes. *Macromol. Biosci.* **2016**, *16* (1), 75–81.

(278) Settanni, G.; Schäfer, T.; Muhl, C.; Barz, M.; Schmid, F. Poly-Sarcosine and Poly(Ethylene-Glycol) Interactions with Proteins Investigated Using Molecular Dynamics Simulations. *Comput. Struct. Biotechnol. J.* **2018**, *16*, 543–550.

(279) Wheeler, A. W.; Henderson, D. C.; Garman, A. J.; Moran, D. M. Suppression of Murine IgE Responses with Amino Acid Polymer/Allergen Conjugates. *Int. Arch. Allergy Immunol.* **1985**, *76* (4), 361–368.

(280) Cook, R. M.; Henderson, D. C.; Wheeler, A. W.; Moran, D. M. Suppression of Murine IgE Responses with Amino Acid Polymer/Allergen Conjugates. *Int. Arch. Allergy Immunol.* **1986**, *80* (4), 355–360.

(281) Viricel, W.; Fournet, G.; Beaumel, S.; Perrial, E.; Papot, S.; Dumontet, C.; Joseph,

B. Monodisperse Polysarcosine-Based Highly-Loaded Antibody-Drug Conjugates. *Chem. Sci.* **2019**, *10* (14), 4048–4053.

(282) Hou, Y.; Lu, H. Protein PEPylation: A New Paradigm of Protein-Polymer Conjugation. *Bioconjug. Chem.* **2019**, *30* (6), 1604–1616.

(283) Wang, H.; Hou, Y.; Hu, Y.; Dou, J.; Shen, Y.; Wang, Y.; Lu, H. Enzyme-Activatable Interferon-Poly(α-Amino Acid) Conjugates for Tumor Microenvironment Potentiation. *Biomacromolecules* **2019**, *20* (8), 3000–3008.

(284) Hu, Y.; Hou, Y.; Wang, H.; Lu, H. Polysarcosine as an Alternative to PEG for Therapeutic Protein Conjugation. *Bioconjug. Chem.* **2018**, *29* (7), 2232–2238.

(285) Son, K.; Ueda, M.; Taguchi, K.; Maruyama, T.; Takeoka, S.; Ito, Y. Evasion of the Accelerated Blood Clearance Phenomenon by Polysarcosine Coating of Liposomes. *J. Control. Release* **2020**, *322* (March), 209–216.

(286) Nogueira, S. S.; Schlegel, A.; Maxeiner, K.; Weber, B.; Barz, M.; Schroer, M. A.; Blanchet, C. E.; Svergun, D. I.; Ramishetti, S.; Peer, D.; Langguth, P.; Sahin, U.; Haas, H. Polysarcosine-Functionalized Lipid Nanoparticles for Therapeutic MRNA Delivery. *ACS Appl. Nano Mater.* **2020**, *3* (11), 10634–10645.

(287) Klinker, K.; Holm, R.; Heller, P.; Barz, M. Evaluating Chemical Ligation Techniques for the Synthesis of Block Copolypeptides, Polypeptoids and Block Copolypept(o)Ides: A Comparative Study. *Polym. Chem.* **2015**, *6* (25), 4612–4623.

(288) Heller, P.; Mohr, N.; Birke, A.; Weber, B.; Reske-Kunz, A.; Bros, M.; Barz, M. Directed Interactions of Block Copolypept(o) Ides with Mannose-Binding Receptors: Peptomicelles Targeted to Cells of the Innate Immune System. *Macromol. Biosci.* **2015**, *15* (1), 63–73.

(289) Johann, K.; Bohn, T.; Shahneh, F.; Luther, N.; Birke, A.; Jaurich, H.; Helm, M.; Klein, M.; Raker, V. K.; Bopp, T.; Barz, M.; Becker, C. Therapeutic Melanoma Inhibition by Local Micelle-Mediated Cyclic Nucleotide Repression. *Nat. Commun.* **2021**, *12* (1), 5981.

(290) Steinborn, B.; Hirschle, P.; Höhn, M.; Bauer, T.; Barz, M.; Wuttke, S.; Wagner, E.; Lächelt, U. Core-Shell Functionalized Zirconium-Pemetrexed Coordination Nanoparticles as Carriers with a High Drug Content. *Adv. Ther.* **2019**, *2* (11), 1900120.

(291) Yoo, J.; Birke, A.; Kim, J.; Jang, Y.; Song, S. Y.; Ryu, S.; Kim, B.-S.; Kim, B.-G.; Barz, M.; Char, K. Cooperative Catechol-Functionalized Polypept(o)Ide Brushes and Ag Nanoparticles for Combination of Protein Resistance and Antimicrobial Activity on Metal Oxide Surfaces. *Biomacromolecules* **2018**, *19* (5), 1602–1613.

(292) Tanisaka, H.; Kizaka-Kondoh, S.; Makino, A.; Tanaka, S.; Hiraoka, M.; Kimura, S. Near-Infrared Fluorescent Labeled Peptosome for Application to Cancer Imaging. *Bioconjug. Chem.* **2008**, *19* (1), 109–117.

(293) Weber, B.; Kappel, C.; Scherer, M.; Helm, M.; Bros, M.; Grabbe, S.; Barz, M. PeptoSomes for Vaccination: Combining Antigen and Adjuvant in Polypept(o)Ide-Based Polymersomes. *Macromol. Biosci.* **2017**, *17* (10), 1–6.

(294) Heller, P.; Weber, B.; Birke, A.; Barz, M. Synthesis and Sequential Deprotection of Triblock Copolypept(o)Ides Using Orthogonal Protective Group Chemistry. *Macromol. Rapid Commun.* **2015**, *36* (1), 38–44.

(295) Heller, P.; Hobernik, D.; Lächelt, U.; Schinnerer, M.; Weber, B.; Schmidt, M.;

Wagner, E.; Bros, M.; Barz, M. Combining Reactive Triblock Copolymers with Functional Cross-Linkers: A Versatile Pathway to Disulfide Stabilized-Polyplex Libraries and Their Application as PDNA Vaccines. *J. Control. Release* **2017**, *258* (March), 146–160.

(296) Ren, J. M.; McKenzie, T. G.; Fu, Q.; Wong, E. H. H.; Xu, J.; An, Z.; Shanmugam, S.; Davis, T. P.; Boyer, C.; Qiao, G. G. Star Polymers. *Chem. Rev.* **2016**, *116* (12), 6743–6836.

(297) Holm, R.; Weber, B.; Heller, P.; Klinker, K.; Westmeier, D.; Docter, D.; Stauber, R. H.; Barz, M. Synthesis and Characterization of Stimuli-Responsive Star-Like Polypept(o)Ides: Introducing Biodegradable PeptoStars. *Macromol. Biosci.* **2017**, *17* (6), 1–14.

(298) Holm, R.; Douverne, M.; Weber, B.; Bauer, T.; Best, A.; Ahlers, P.; Koynov, K.; Besenius, P.; Barz, M. Impact of Branching on the Solution Behavior and Serum Stability of Starlike Block Copolymers. *Biomacromolecules* **2019**, *20* (1), 375–388.

(299) Holm, R.; Schwiertz, D.; Weber, B.; Schultze, J.; Kuhn, J.; Koynov, K.; Lächelt, U.; Barz, M. Multifunctional Cationic PeptoStars as SiRNA Carrier: Influence of Architecture and Histidine Modification on Knockdown Potential. *Macromol. Biosci.* **2020**, *20* (1), 1–17.

(300) Hörtz, C.; Birke, A.; Kaps, L.; Decker, S.; Wächtersbach, E.; Fischer, K.; Schuppan, D.; Barz, M.; Schmidt, M. Cylindrical Brush Polymers with Polysarcosine Side Chains: A Novel Biocompatible Carrier for Biomedical Applications. *Macromolecules* **2015**, *48* (7), 2074–2086.

(301) Stéen, E. J. L.; Jørgensen, J. T.; Johann, K.; Nørregaard, K.; Sohr, B.; Svatunek, D.; Birke, A.; Shalgunov, V.; Edem, P. E.; Rossin, R.; Seidl, C.; Schmid, F.; Robillard, M. S.; Kristensen, J. L.; Mikula, H.; Barz, M.; Kjær, A.; Herth, M. M. Trans-Cyclooctene-Functionalized PeptoBrushes with Improved Reaction Kinetics of the Tetrazine Ligation for Pretargeted Nuclear Imaging. *ACS Nano* **2020**, *14* (1), 568–584.

(302) Longmire, M.; Choyke, P. L.; Kobayashi, H. Clearance Properties of Nano-Sized Particles and Molecules as Imaging Agents: Considerations and Caveats. *Nanomedicine* **2008**, *3* (5), 703–717.

(303) Johann, K.; Svatunek, D.; Seidl, C.; Rizzelli, S.; Bauer, T. A.; Braun, L.; Koynov, K.; Mikula, H.; Barz, M. Tetrazine- and: Trans -Cyclooctene-Functionalised Polypept(o)Ides for Fast Bioorthogonal Tetrazine Ligation. *Polym. Chem.* **2020**, *11* (27).

(304) Barz, M.; Huesmann, D.; Schäfer, O.; Reuter, T.; Birke, A.; Heller, P. Thiol-Protected Amino Acid Derivatives and Uses Thereof, **2014**, EP2942348A1.

(305) Muhl, C.; Schäfer, O.; Bauer, T.; Räder, H.-J.; Barz, M. Poly(S -Ethylsulfonyl- l -Homocysteine): An α-Helical Polypeptide for Chemoselective Disulfide Formation. *Macromolecules* **2018**, *51* (20), 8188–8196.

(306) Schäfer, O.; Klinker, K.; Braun, L.; Huesmann, D.; Schultze, J.; Koynov, K.; Barz, M. Combining Orthogonal Reactive Groups in Block Copolymers for Functional Nanoparticle Synthesis in a Single Step. *ACS Macro Lett.* **2017**, *6* (10), 1140–1145.

2

Racemic S-(Ethylsulfonyl)-DL-N-carboxyanhydrides Improve Chain Lengths and Monomer Conversion for β-Sheet Controlled Ring-Opening Polymerization

reduced anti-parallel β-sheet formation

increased solubility   complete conversion   higher chain lengths

Racemic *S*-(Ethylsulfonyl)-DL-*N*-carboxyanhydrides Improve Chain Lengths and Monomer Conversion for β-Sheet Controlled Ring-Opening Polymerization

Tobias A. Bauer[a, b], Christian Muhl[b], Dieter Schollmeyer[b], Matthias Barz[a, b,*]

[a] Leiden Academic Centre for Drug Research (LACDR), Leiden University, Einsteinweg 55, 2333 CC Leiden, The Netherlands

[b] Department of Chemistry, Johannes Gutenberg University Mainz, Duesbergweg 10-14, 55128 Mainz, Germany

Abstract

The secondary structure formation of polypeptides not only governs folding and solution self-assembly but affects the nucleophilic ring-opening polymerization of α-amino acid-*N*-carboxyanhydrides (NCAs). Whereby helical structures are known to enhance polymerization rates, ß-sheet-like assemblies reduce the propagation rate or may even terminate chain growth by precipitation or gelation. To overcome these unfavorable properties, racemic mixtures of NCAs can be applied. In this work, racemic *S*-(ethylsulfonyl)-DL-cysteine NCA is investigated for the synthesis of polypeptides, diblock and triblock copolypept(o)ides. In contrast to the polymerization of stereoregular *S*-(ethylsulfonyl)-L-cysteine NCA, the reaction of *S*-(ethylsulfonyl)-DL-cysteine NCA proceeds with a rate constant of up to $k_p = 1.70 \times 10^{-3}$ L·mol^{-1}·s^{-1} and is slightly faster than the enatiopure polymerization. While the polymerization of *S*-(ethylsulfonyl)-L-cysteine NCA suffers from incomplete monomer conversion and DPs limited to 30 - 40, racemic mixtures yield polypeptides with DPs of up to 102 with high conversion rates and well-defined dispersities (1.2 - 1.3). The controlled living nature of the ring-opening polymerization of *S*-(ethylsulfonyl)-DL-cysteine NCA thus enables the synthesis of triblock copolymers by sequential monomer addition. This methodology allows for precise control over DPs of individual blocks and yields uniform triblock copolymers with symmetric molecular weight distributions at a reduced synthetic effort.

Keywords

polypept(o)ides · NCA polymerization · ring-opening polymerization · racemic amino acids · polypeptides

Introduction

Ring-opening polymerization (ROP) of *N*-carboxyanhydrides (NCAs) provides easy access to polypeptides, and their use as multi-functional polymeric material.[1–3] Besides properties derived from specific side- or end-groups, polypeptides feature the formation of higher ordered secondary structures, which can be mainly divided into either α-helices or ß-sheets, with exemptions for proline-type amino acids.[4] For controlled living NCA polymerization following the normal amine mechanism, secondary structure formation was shown to have a major impact on the polymerization itself, i.e., reaction kinetics and polypeptide solubility as well as polymer analytics.[1,5–8]

Polymerization of NCAs leading to homopolymers with a high degree of α-helical segments, e.g., *N*-ε-(carbobenzoxy-carbonyl)-L-lysine or γ-(benzyl)-L-glutamate (p(L)Glu(OBn)), starts upon initiation and a short induction period with relatively slow polymerization rate, which is displaced by fast and pseudo-first order kinetics for later stages of the reaction. Early investigations by Lundberg and Doty as well as recent detailed studies by the Cheng group, could explain the increased polymerization rate by an occurring transition from a rather ß-sheet-like structure to an α-helical growth supporting the addition of NCA monomers by directed hydrogen-bonds and an induced dipole.[9–11] In this context, for amino acids forming strong ß-sheets from homo-oligopeptides, NCA polymerization is slowed down and may even stop during the induction period as a result of precipitation or crystallization.[12–15] As such, poly(L-alanine) forms α-helical polypeptides at later stages, but strong ß-sheets of the L-alanine oligomers, which complicate NCA polymerization leading to broad and bimodal molecular weight distributions.[16] To mitigate this secondary structure-driven phenomenon, racemic alanine NCA mixtures were employed resulting in the successful synthesis of polyalanine with elevated molecular weights and narrow molecular weight distribution.[14]

In contrast to *per se* helix-forming amino acids, branching as well as the presence of a heteroatom (*O/S*) at the ß-carbon atom are both known to favour the formation of ß-sheets.[17] NCA polymerizations of isoleucine, valine, threonine, serine, and cysteine, thus, generally suffer from limited access to high molecular weights and narrow dispersities.[4,5,18] To overcome these limitations, again, racemic NCA mixtures have been employed for valine and isoleucine.[15,19–21] For polymerization of L-serine, L-threonine and L-cysteine NCAs, mostly, modifications were

introduced to the ß-heteroatom either weakening the ß-sheet structure or changing the preferred conformation to an α-helix supporting the chain growth.[20,22–25]

Among the 20 natural amino acids, cysteine takes a unique role due to its ability to stabilize proteins by (bio-) reversible disulfide bonds.[26,27] To transfer this feature to synthetic polymers for an application as "smart" or stimuli-responsive material, we previously reported on the *S*-alkylsulfonyl protecting group, which allows for nucleophilic amine-initiated polymerization of *S*-(ethylsulfonyl)-L-cysteine NCA and consecutive formation of asymmetric disulfide bonds with thiols (soft nucleophiles).[28,29] Moreover, block copolymers of poly(sarcosine)-*block*-poly(*S*-ethylsulfonyl-L-cysteine), so-called polypept(o)ides,[30,31] could be successfully employed to prepare disulfide cross-linked polymeric micelles and nanohydrogels.[32] Nevertheless, the polymerization of *S*-(ethylsufonly)-L-cysteine NCA was shown to be hampered by the formation of anti-parallel ß-sheets reducing the polymerization rate constants, lowering monomer conversion rates, and limiting accessible molecular weights.[29]

The aim of this work is now to investigate the nucleophilic ring-opening polymerization of racemic *S*-(ethylsulfonyl)-DL-cysteine *N*-carboxyanhydrides (NCA), to analyze the secondary structure of resulting homopolymers, and to incorporate these reactive amino acids into triblock copolymers.

Results and Discussion

To obtain *S*-(ethylsulfonyl)-DL-cysteine NCA (DL-Cys(SO$_2$Et) NCA), the corresponding amino acid, *S*-(ethylsulfonyl)-DL-cysteine, was synthesized from racemic cysteine hydrochloride by *S*-nitrosation (umpolung reaction) and *in situ* reaction with sodium ethylsulfinate, similar to previous reports on the L-enantiomer compound.[28,29] The NCA was prepared according to the Fuchs-Farthing method using diphosgene in tetrahydrofuran (THF) (Figure 1a).[33–35] Melting points of DL-Cys(SO$_2$Et) NCA (mp = 86 - 89°C) were significantly lower, compared to the L-enantiomer (mp = 113 - 115°C) compound.[36] From crystallization attempts of the racemic mixture, only crystals of the D-enantiomer could be isolated and analysed by X-ray crystallography (Figure S1 - S3), revealing NCA monomers arranged as an endless chain along the b-axis, mediated by N-H···O hydrogen bonds, which corresponds well with the previously published crystal structure of L-Cys(SO$_2$Et) NCA.[36]

ROP of DL-Cys(SO$_2$Et) NCA was performed at -10 °C in dry and purified *N,N*-dimethyl formamide (DMF) using neopentylamine as initiator (Figure 1a). These conditions have been reported optimal to ensure controlled living polymerization of L-Cys(SO$_2$Et) NCA, since the *S*-ethylsulfonyl protecting group remains intact during nucleophilic amine-initiated NCA polymerization, but can be used for consecutive disulfide bond formation with soft nucleophile thiols.[29,37]

For the synthesis of poly(*S*-ethylsulfonyl-DL-cysteine) (p(DL)Cys(SO$_2$Et)), racemic Cys(SO$_2$Et) NCA could be polymerized with high conversion rates of 89 - 100%, according to IR spectroscopy. As summarized in Table 1, the intended chain lengths are in well agreement with the results obtained from end-group analysis by NMR, and polypeptides with chain lengths from X_n = 8 to 102 with molecular weights up to 20.0 kDa could be successfully synthesized. Analysis by gel permeation chromatography (GPC) in hexafluoroisopropanol (HFIP) shows symmetric and monomodal molecular weight distributions for all polymers with well-defined dispersity (*Đ* = 1.19 to 1.33), relative to poly(methyl methacrylate) (PMMA) standards. A clear shift in the elution volume maximum can be detected by GPC, indicating controlled polymerization and valid chain lengths (Figure 1b and S4). The integrity of the polymer backbone as well as the reactive *S*-ethylsulfonyl protecting group was confirmed by the presence of only a single polymeric species in diffusion ordered spectroscopy (DOSY) NMR (Figure 1c) with all polymer signals being aligned. Furthermore, CD spectroscopy in HFIP verified the racemic nature of the isolated p(DL)Cys(SO$_2$Et) homopolymers, since no prevalent signal could be detected (Figure 1d).

In comparison to the results published on p(L)Cys(SO$_2$Et), indeed, longer chain lengths and higher conversion rates could be obtained from the racemic NCA.[29] For p(L)Cys(SO$_2$Et), the maximum chain length reported was X_n = 43, although, due to the formation of aggregates induced by strong anti-parallel β-sheets, multimodal molecular weight distributions were detected in HFIP GPC. While for p(L)Cys(SO$_2$Et) homopolymers with up to 20 repeating units narrow and symmetric molecular weight distributions were reported, chain lengths above X_n = 20 resulted in asymmetric distributions, which turned multimodal above X_n = 30.[29] In case of p(DL)Cys(SO$_2$Et), for chain lengths up to X_n = 102, symmetric molecular weight distributions and no aggregates were detected by HFIP GPC, thus facilitating polymer analysis and interpretation of the results (see Table 1 and Figure 1). For the synthesis of even higher molecular weights (M/I = 150), however, increased tailing was observed, as discussed further below.
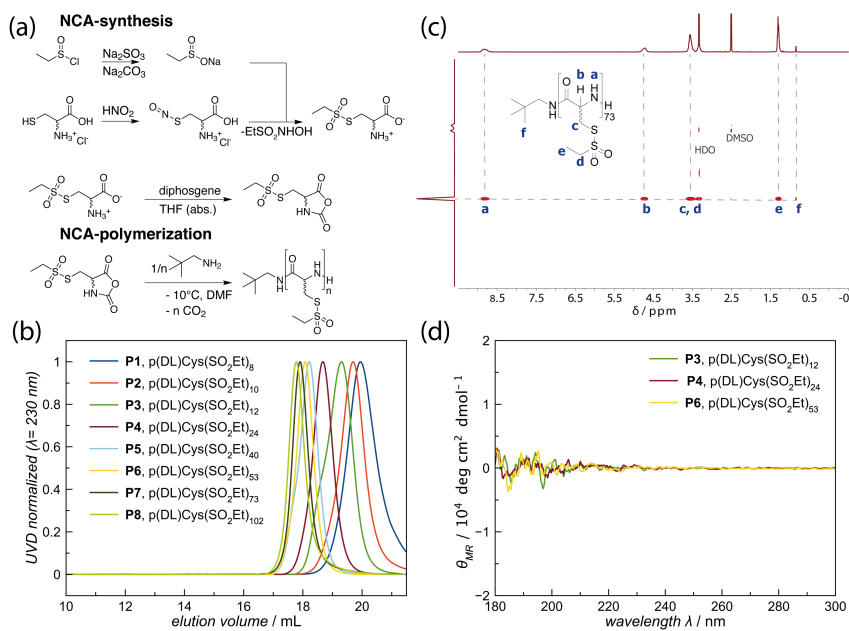
Figure 1. (**a**) Synthesis and ring-opening polymerization of *S*-ethylsulfonyl-DL-cysteine *N*-carboxyanhydride. (**b**) Analytical gel permeation chromatography in hexafluoro-isopropanol (HFIP GPC) of P1 to P8 indicates symmetric molecular weight distributions and a clear shift towards higher molecular weights with increasing monomer to initiator ratio. (**c**) DOSY NMR for p(DL)Cys(SO$_2$Et)$_{73}$ reveals the presence of only a single polymer species. (**d**) CD spectroscopy in HFIP does not give a prevalent signal irrespective of the polymer chain length, as expected for racemic compounds.

Table 1. Polymerization of *S*-(ethylsulfonyl)-DL-cysteine NCA.

No.	M/I	Conversion[a] / %	X_n[b]	M_n[b] / kDa	M_n[c] / kDa	$Đ$[c]
P1	4	100	8	1.65	2.92	1.31
P2	8	100	10	2.04	4.16	1.22
P3	15	100	12	2.43	6.20	1.21
P4	30	100	24	4.77	10.1	1.20
P5	40	100	40	7.90	18.0	1.24
P6	50	100	53	10.4	20.9	1.19
P7	75	89	73	14.3	23.8	1.27
P8	100	91	102	20.0	25.9	1.33

[a] based on IR spectroscopy, [b] end-group analysis by ^{1}H NMR, [c] HFIP GPC relative to PMMA standards.

To reveal the secondary structure of p(DL)Cys(SO$_2$Et), the racemic polypeptides were analysed by IR spectroscopy in solid state. As shown in Figure 2a, vibrational amide bands were detected at 1637 cm^{-1} (amide I), 1509 cm^{-1} (amide II), and 703 cm^{-1} (amide V), indicating ß-sheet secondary structure, while the weak shoulder at 1702 cm^{-1} suggests their anti-parallel orientation.[38,39] No chain length dependencies were detected for the general position of the amide bands, whereas the shoulder at 1702 cm^{-1} becomes more evident with increasing chain lengths. For comparison, p(L)Cys(SO$_2$Et), which is known to adopt an anti-parallel ß-sheet structure, shows similar wave numbers for the vibrational amide bands, but a distinct peak at 1702 cm^{-1} for p(L)Cys(SO$_2$Et)$_{13}$ (Figure 2a and S7, dashed green line).[29] In conclusion, p(DL)Cys(SO$_2$Et) seems to adopt ß-sheet secondary structure with weakly pronounced anti-parallel orientation.[40,41] In contrast, poly(*S*-ethylsulfonyl-L-homocysteine), bearing the same reactive protecting group, displays wavelength-dependent helix-formation (1652 cm^{-1}) in solid state, and a fraction of aggregated protein structure (1625 cm^{-1}) disappears with increasing chain lengths (see Figure S7).

Since IR spectroscopy does not allow for reliable analysis of the polypeptide tacticity, ^{1}H NMR spectra of racemic p(DL)Cys(SO$_2$Et) and enantiopure p(L)Cys(SO$_2$Et) in dimethyl sulfoxide were employed for comparison.[42,43] In absence of racemisation, enantiopure NCAs are known to form isotactic polypeptides, whereas the polymerization of racemic NCA mixtures can be considered a copolymerization, leading to an overall atactic polymer with only short isotactic sequences, unless stereoselective or guiding templates are involved.[42,44,45] In our case, polymerization is conducted in solution without any additional driving force. As such, the signals of the racemic homopolymers (Figure 2b, upper spectrum) appear to be much broader than those of purely isotactic p(L)Cys(SO$_2$Et) (Figure 2b, lower spectrum), which suggests the rather atactic nature of the prepared p(DL)Cys(SO$_2$Et) homopolymers. For a detailed understanding, however, further studies are required.

To gain deeper insight into the polymerization of DL-Cys(SO$_2$Et) NCA, the kinetic behaviour was investigated *via* IR spectroscopy. The carbonyl stretching bands at 1858 and 1788 cm^{-1} were monitored over the course of 5 days and the integrals analysed, which correspond to the monomer concentration.

The majority of NCAs investigated to date (e.g. *γ*-(benzyl)-L-glutamic acid NCA, *N*-ε-(carbobenzoxy)-L-lysine NCA) are known to adopt an α-helical conformation, after a short initiation period, resulting in pseudo first-order kinetics in polar

solvents (e.g. DMF).[1,5,20] In contrast, cysteine NCA-derivatives are known to form ß-sheets upon polymerization.[20] Exemptions were only reported when large polar (e.g. oligoethylene glycol) or bulky side-groups (e.g. menthyl) have been introduced *via* thioether bonds.[25,46] *Vice versa*, during the polymerization of *S*-(methyl)-L-cysteine NCA, Kawai *et al*. observed secondary structure-driven crystallization hampering polymerization progress.
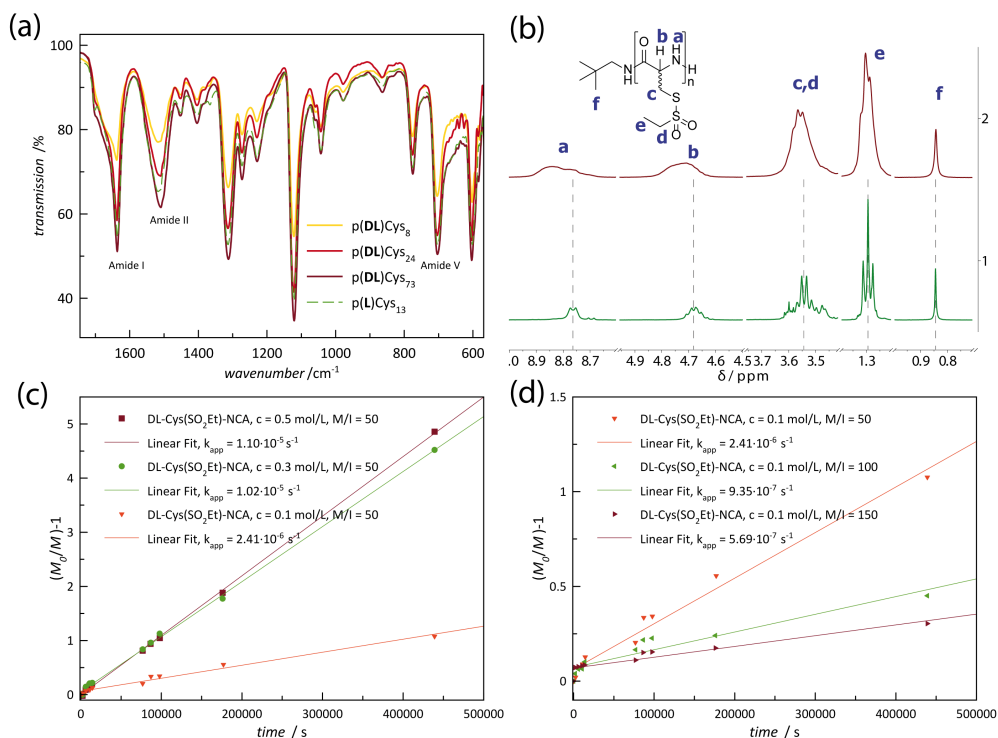

Figure 2. Secondary structure analysis and kinetic investigations. (**a**) Infrared spectroscopy (solid state) of racemic and enantiopure poly(*S*-ethylsulfonyl cysteine) with chain lengths of 8 to 73. (**b**) NMR spectroscopy of p(DL)Cys(SO$_2$Et)$_{22}$ (upper) and p(L)Cys(SO$_2$Et)$_{17}$ (lower) in DMSO-*d$_6$*. (**c**) Kinetic plot of p(DL)Cys(SO$_2$Et), M/I = 50 at varying monomer concentrations. (**d**) Kinetic plot of p(DL)Cys(SO$_2$Et), c_{NCA} = 0.1 mol·L^{-1} with varying monomer to initiator ratios.

Instead of first-order kinetics, the polymerization behaviour could be described by the Avrami-equation.[12] As suggested by Iguchi, the Avrami equation, originally developed for crystallization kinetics, can be applied to describe a polymerization system which starts as a homogenous mixture but turns heterogenous throughout

polymerization.[47] No transfer or chemical termination reactions occur, but the association of oligomers leads to soluble (nano-) crystallites ultimately leading to physical termination, as the growing chain-end loses its mobility. Further growth is only possible at the surface.[13,47] The adapted Avrami equation is given by[29,47]

$$\frac{\delta(x)}{\delta(t)} = k \, [I][M_0] \left(1 - \frac{x}{[M_0]}\right)^2 \tag{1}$$

with $[M_0]$ is the initial monomer concentration; $[I]$ is the initiator concentration; $x = [M_0] - [M_t]$ is the consumed monomer at time t; and k is the rate constant, and can also be written as:[29]

$$\frac{\delta(x)}{\delta(t)} = k \, [I] \frac{[M_t]^2}{[M_0]} \tag{2}$$

It can thus be derived as

$$\frac{[M_0]}{[M_t]} = k \, [I] \, t + 1 \tag{3}$$

By plotting $\frac{[M_0]}{[M_t]} - 1$ versus the reaction time (t), the apparent rate constant of the polymerization ($k_{app} = k_p \cdot [I]$) as well as the polymerization rate (k_p) can be calculated. As shown in Figure 2c and Figure 2d, the experimental values obtained from IR spectroscopy follow the derived linear dependency. At constant monomer to initiator ratio, apparent rate constants increase with increasing monomer concentration, and decrease with increasing monomer to initiator ratio, when the monomer concentration is kept constant. In a similar manner, the polymerization of L-Cys(SO₂Et) NCA was reported to follow the Avrami-model, and both polymerizations seem to be affected by the formation of insoluble crystallites which govern the general polymerization behaviour qualitatively.[29] In contrast, *S*-ethylsulfonyl-L-homocysteine (L-Hcy(SO₂Et)) NCA showed fast pseudo first-order kinetics typically observed for α-helical polymerization.[48] When comparing the (apparent) rate constants, as summarized in Table 2, racemic DL-Cys(SO₂Et) NCA polymerizes slightly faster than L-Cys(SO₂Et) NCA (40% on average). This observation also reflects on the weaker secondary structure indicated by IR spectroscopy (Figure 2a), the increased solubility (HFIP GPC, Figure 1b), the rather atactic polymer structure, as detected by NMR spectroscopy (Figure 2b), as well as the obtained higher molecular weights.

Table 2. Polymerization kinetics. Apparent rate constants (k_{app}) and rate constants (k_p) for the ring-opening polymerization of S-(ethylsulfonyl)-protected NCA monomers.

NCA monomer	c_{NCA} [mol·L^{-1}]	k_{app} [s^{-1}]	k_p [L·mol^{-1} s^{-1}]
	0.1	$2.41 \cdot 10^{-6}$	$1.21 \cdot 10^{-3}$
DL-Cys(SO$_2$Et)	0.3	$1.02 \cdot 10^{-5}$	$1.70 \cdot 10^{-3}$
	0.5	$1.10 \cdot 10^{-5}$	$1.10 \cdot 10^{-3}$
	0.17	$3.43 \cdot 10^{-6}$	$1.01 \cdot 10^{-3}$
L-Cys(SO$_2$Et)	0.43	$8.09 \cdot 10^{-6}$	$9.41 \cdot 10^{-4}$
	0.59	$1.13 \cdot 10^{-5}$	$9.58 \cdot 10^{-4}$
	0.1	$1.44 \cdot 10^{-5}$	$7.20 \cdot 10^{-3}$
L-Hcy(SO$_2$Et)	0.3	$4.33 \cdot 10^{-5}$	$7.22 \cdot 10^{-3}$
	0.5	$5.29 \cdot 10^{-5}$	$5.29 \cdot 10^{-3}$

[a] values taken/calculated from Schäfer *et al*.[29]; [b] values taken/calculated from Muhl *et al*.[48]

Nevertheless, for DL-Cys(SO$_2$Et) NCA, the discrepancy among the reaction performed at a monomer concentration of 0.3 mol·L^{-1} versus 0.5 mol·L^{-1} is not significant, and similar conversions were detected for each time point. In agreement with these findings, certain limitations were detected for the polymerization of DL-Cys(SO$_2$Et) NCA. As shown in Figure S5a, the monomer concentration has a major impact on the reaction. Polymerizations at high NCA concentration (β_{NCA} = 100 g·L^{-1}, c_{NCA} = 0.42 mol·L^{-1}) lead to gelation after 50% conversion, resulting in low molecular weight polymers and bimodal GPC elugrams (see also Figure S6). On the other hand, low NCA concentrations (β_{NCA} = 30 g·L^{-1}, c_{NCA} = 0.13 mol·L^{-1}) result in slow polymerization progress and only low molecular weight polymers, even though high NCA conversions were achieved after 6 weeks at -10 °C. Medium NCA concentrations (β_{NCA} = 60 g·L^{-1}, c_{NCA} = 0.25 mol·L^{-1}) finally granted polymer synthesis up to chain lengths of X_n = 102 with well-defined polydispersity index (PDI). However, increased tailing and no significant shift in the maximum elution volume was detected for M/I ratio of 150 (Figure S5b), even though polymerization was carried out at similar conditions in purified and dry DMF (<50 ppm water). Interestingly, for p(L)Cys(SO$_2$Et), gelation was not observed until monomer concentrations above 0.8 mol·L^{-1}.[29]

Since we generally found high conversion rates for the polymerization of DL-Cys(SO$_2$Et) NCA, we aimed to exploit the racemic NCA for the synthesis of block co-polypept(o)ides. As illustrated in Figure 3a, the triblock copolymer,

p(L)Glu(OBn)-*b*-p(DL)Cys(SO₂Et)-*b*-pSar, with poly(*S*-ethylsulfonyl-DL-cysteine) as the middle block, was prepared by sequential NCA addition, after full conversion of the predecessor monomer was ensured by IR spectroscopy. Of note, due to incomplete conversion, the displayed sequence would require an additional intermediate work-up step if the enantiopure (L)Cys(SO₂Et) NCA was used. The results of the triblock copolymer synthesis are given in Figure 3 and summarized in Table S1. As shown, the calculated block lengths are in well agreement with the results obtained from end-group analysis in NMR (Figure 3b). More importantly, symmetric and monomodal molecular weight distributions could be observed for each reaction step by HFIP GPC. The clear shift in the elution volume maximum without significant tailing underlines the controlled living nature of the polymerization. In addition, the final polymers displayed molecular weights of 19400 g·mol⁻¹ (diblock, p(L)Glu(OBn)-*b*-p(DL)Cys(SO₂Et)) and 33200 g·mol⁻¹ (triblock, p(L)Glu(OBn)-*b*-p(DL)Cys(SO₂Et)-*b*-pSar,) as well as well-defined polymer dispersities of 1.23 and 1.43, relative to PMMA standards (see Figure 3c and Table S1).

Since the individual GPC curves are not baseline-separated, due to the chosen block length values, which are ideal with respect to polypeptide solubility, we investigated the absence of homopolymers by DOSY NMR spectroscopy. As a result of the reduced size of homopolymers, compared to consecutive diblock and triblock copolymers, monomodal peaks at a distinct diffusion index would broaden, become multimodal or, in the case of homopolymers coexisting with triblock copolymers, even two distinct species appear. As displayed in Figure 3d and S18, we observed only one diffusing species with narrow diffusion index distribution for diblock as well as triblock copolymers. Therefore, DOSY NMR experiments confirm successful block copolymer synthesis by controlled living ROP, which specifies the applicability of the racemic DL-Cys(SO₂Et) NCA for the synthesis of thiol-reactive block copolymers.
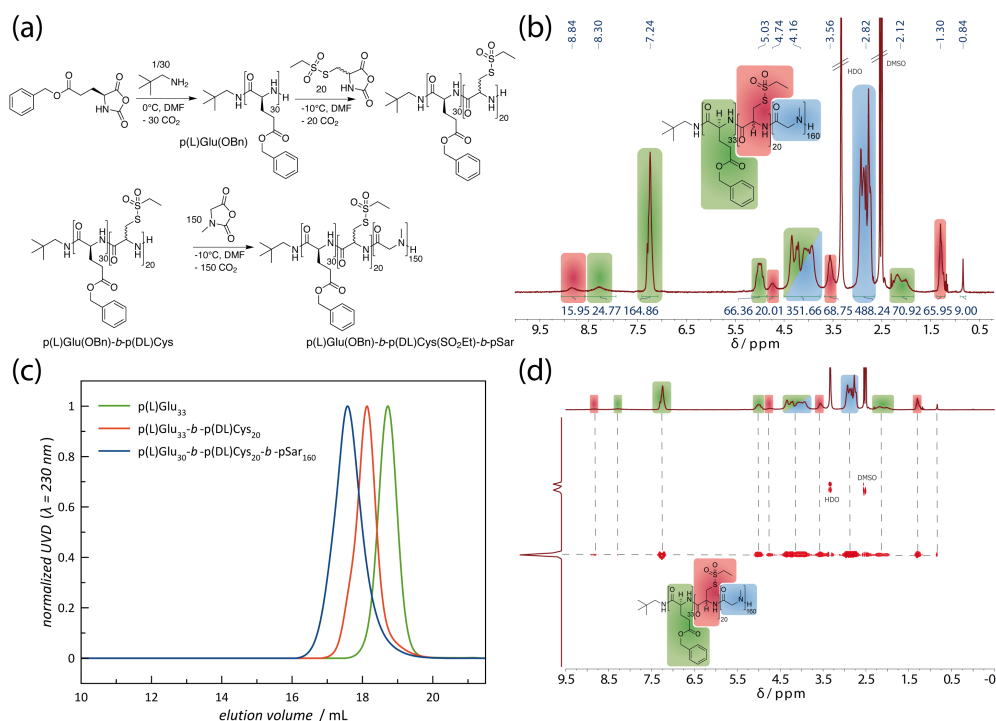
Figure 3. Triblock copolymer synthesis. (**a**) Synthesis of p(L)Glu(OBn)$_{30}$-b-p(DL)Cys(SO$_2$Et)$_{20}$-b-pSar$_{150}$ *via* sequential NCA polymerization. (**b**) End-group analysis by ^{1}H NMR spectroscopy. (**c**) Analytical HFIP GPC of the respective block sequences. For better visualization, p(L)Glu and p(DL)Cys were used as abbreviations for p(L)Glu(OBn) and p(DL)Cys(SO$_2$Et). (**d**) DOSY NMR indicates the presence of only a one diffusing polymer species.

Conclusion

We found that racemic DL-Cys(SO$_2$Et) NCAs can be successfully prepared and polymerized yielding well-defined homopolymers with symmetric molecular weight distributions for molecular weights up to 20.0 kDa, corresponding to an average degree of polymerization of 102 (determined by end-group analysis). To the best of our knowledge, for polypeptides forming β-sheets, this is the first comprehensive study on the use of racemic NCAs to improve their polymerization. The polymerization of DL-Cys(SO$_2$Et) NCA follows the Avrami-model for heterogenous polymerization, even though the formation of anti-parallel β-sheets was found to seem less pronounced than for purely isotactic p(L)Cys(SO$_2$Et),

resulting in slightly faster polymerization rates and full monomer conversion. As a consequence, the synthesis of triblock copolymers by sequential copolymerization can be achieved with excellent control over individual block lengths. Future research will thus address the question of how a reduced tendency for secondary structure formation affects the solution self-assembly of p(DL)Cys(SO₂Et)-containing block copolymers and the properties of nanoparticles thereof.

Experimental Section

Materials and Methods: Unless stated otherwise, reagents and solvents were purchased from Sigma Aldrich and used as received. THF was dried over Na and freshly distilled prior to use. DMF was bought from Acros (99.8%, extra dry over molecular sieve) and purified by repetitive freeze-pump thaw cycles to remove dimethylamine prior to use (water content < 50 ppm). Neopentylamine was purified by distillation over calcium hydride and stored over activated molecular sieves before further use. HFIP was purchased from Fluorochem. Deuterated solvents were obtained from Deutero GmbH and were used as received. ^{1}H NMR spectra were recorded on a Bruker Avance II 400 at room temperature at a frequency of 400 MHz. DOSY spectra were recorded on a Bruker Avance III HD 400 (400 MHz). Calibration of the spectra was achieved using the solvent signals. NMR spectra were analyzed with MestReNova version 12.0.4 from Mestrelab Research S.L. Degrees of polymerization (X_n) by ^{1}H NMR were calculated comparing the integral of the initiator peak and the integrals of the α-protons. Attenuated total reflectance Fourier transform infrared (ATR-FT-IR) spectroscopy was performed on a FT/IR-4100 (JASCO Corporation) with an ATR sampling accessory (MIRacle, Pike Technologies). IR spectra were analyzed using Spectra Manager 2.0 (JASCO Corporation). NCA polymerization was monitored by FT-IR spectroscopy. Polymerization was judged to be completed when NCA associated carbonyl peaks at 1858 and 1788 cm^{-1} had vanished. Analytical GPC was performed on a Jasco GPC setup at a flow rate of 0.8 ml·min^{-1} and a temperature of 40 °C. The eluent was HFIP equipped with 3 g·L^{-1} potassium trifluoroacetate. The column material was modified silica gel (PFG columns, particle size: 7 µm, porosity: 100 Å and 4000 Å), purchased from PSS Polymer Standards Service GmbH. For polymer detection, a UV detector (Jasco UV-2075+) at a wavelength of $\lambda = 230$ nm was employed. Molecular weights were determined by using a calibration with PMMA (PSS Polymer Standards Services GmbH) with

toluene as internal standard. The elution diagram was evaluated with PSS WinGPC (PSS Polymer Standard Service GmbH). Circular dichroism (CD) spectroscopy was performed on a Jasco J-815 spectrometer at room temperature and Spectra Manager 2.0 (Jasco) was used to analyze the spectra. A cell with a path length of 1 mm was used. Spectra were recorded at a concentration of 0.1 g·L^{-1} polymer in HFIP. Θ_{MR} was calculated using the equation with $M_{repeating\ unit}$ = 195.26 g·mol^{-1}, c_M = 0.1 g·L^{-1} and l = 0.1 cm for (Cys(SO$_2$Et)).

$$\theta_{MR} = \frac{\theta \ \cdot \ M_{repeating\ unit}}{10 \ \cdot \ l \ \cdot \ c_M} \ [\text{deg·cm}^2 \cdot \text{dmol}^{-1}]$$

Synthesis of Sodium Ethylsulfinate: The synthesis of sodium ethylsulfinate was adapted from literature.[28]

A solution of sodium sulfite (142.6 g, 1.38 mol, 3.5 eq.) in water (275 mL) was heated to 80 °C. Ethanesulfonyl chloride (37.6 mL, 50.84 g, 0.395 mol, 1.0 eq.) and sodium carbonate (84.09 g, 0.793 mol) were added simultaneously while significant quantities of CO_2 evolved. The reaction mixture was stirred for one hour at 80 °C. Next, the solvent was removed *in vacuo* at 40 °C. The resulting solid was suspended in methanol (approx. 300 mL) and filtered to remove sodium carbonate and side products. Evaporation of methanol yielded sodium ethylsulfinate (45.0 g, 0.388 mol, 98%) as a colorless solid.

^{1}H NMR (400 MHz, D$_2$O + TFA-d_1), δ [ppm] = 2.32 (q, ^3J = 7.6 Hz, 2H, -CH_2-), 1.06 (t, ^3J = 7.6 Hz, 3H, -CH_3).

Synthesis of *S*-(Ethylsulfonyl)-DL-Cysteine: An ice-cold solution of sodium nitrite (9.90 g, 144 mmol, 1.0 eq.) in degassed water (125 mL) was slowly added to a stirred solution of DL-cysteine hydrochloride (22.6 g, 144 mmol, 1.0 eq.) in previously degassed 2N HCl (150 mL) at a temperature of 0 °C. After 1 h, sodium ethylsulfinate (44.5 g, 388 mmol, 2.7 eq.) was added to the deep red solution in one portion. After 5 minutes, a colorless solid precipitated. The suspension was stirred for additional 5 h at 0 °C and was stirred at room temperature overnight. The precipitate was collected and washed with methanol to remove residual sulfinate. The product was dried *in vacuo* yielding *S*-(ethylsulfonyl)-DL-cysteine (13.5 g, 63.3 mmol, 44%) as a colorless powder.

^{1}H NMR (400 MHz, D$_2$O + TFA-d_1), δ [ppm] = 4.44 (dd, ^3J = 6.7 Hz, ^3J = 4.5 Hz, 1H, α-CH), 3.72 (dd, ^2J = 15.6 Hz, ^3J = 4.5 Hz, 1H, -CH_2-CH-), 3.58 (dd, ^2J = 15.6

Hz, ^3J = 6.7 Hz, 1H, -CH_2-CH-), 3.50 (dq, ^3J = 7.3 Hz, ^3J = 1.66 Hz, 2H, -CH_2-CH$_3$), 1.39 (t, ^3J = 7.3 Hz, 3H, -CH_3).

Synthesis of *S*-(Ethylsulfonyl)-DL-Cysteine *N*-Carboxyanhydride: *S*-(Ethylsulfonyl)-DL-cysteine (7.00 g, 32.82 mmol) was dried by azeotropic distillation with toluene. Next, the amino acid was suspended in absolute THF (100 mL) and diphosgene (3.60 mL, 5.84 g, 29.52 mmol) was added slowly. The suspension was stirred at room temperature until a clear solution was obtained (approx. 3 h). To remove excess diphosgene, a stream of dry nitrogen was led through the reaction mixture into gas washing bottles, equipped with an aqueous NaOH solution, for 2 h. The remaining solvent was removed *in vacuo* and the residue was dissolved in dry dioxane. Any insoluble compounds were removed by filtration avoiding contact with air, and the NCA solution was slowly precipitated into a mixture of absolute diethyl ether/*n*-hexane (1:2). The precipitation of the product was repeated two more times yielding *S*-(ethylsulfonyl)-DL-cysteine NCA (6.43 g, 26.87 mmol, 82%) as a colorless powder. Absence of chloride impurities was verified by silver nitrate chloride test. mp = 88.5 °C at a heating rate of 7 °C/min, 86.1 °C at 5 °C/min under decomposition.

^{1}H NMR (400 MHz, DMSO-d_6), δ [ppm] = 9.34 (bs, 1H, NH), 4.85 (ddd, ^3J = 5.7 Hz, ^3J = 5.2 Hz, ^3J = 1.3 Hz, 1H, α-CH), 3.62 (m, 4H, -CH_2-CH- & -CH_2-CH$_3$), 1.29 (t, ^3J = 7.2 Hz, 3H, -CH_3).

For crystallization, dry *n*-hexane was added very carefully on top of an NCA solution in dry ethyl acetate and kept at -20 °C until the formation of colorless NCA crystals was completed.

Synthesis of Poly(*S*-Ethylsulfonyl-DL-Cysteine): DL-Cys(SO$_2$Et) NCA (54.8 mg, 229 µmol, 75 eq.) was transferred into a dried Schlenk-flask, dissolved in 0.78 mL of anhydrous DMF (freshly purified by freeze-thaw cycles) and cooled to -10 °C. Neopentylamine initiator (0.266 mg, 3.05 µmol, 1.0 eq.) was added as a stock solution in DMF (133 µL, β_{NPA} = 2.0 g·L^{-1}) yielding the reaction mixture with a final NCA concentration of 60 g·L^{-1}. A steady flow of dry nitrogen was sustained during the polymerization. The progress of the polymerization was monitored *via* FT-IR spectroscopy and judged to be completed when the carbonyl stretching bands of the NCA at 1858 and 1788 cm^{-1} had vanished. Samples were taken using a nitrogen flushed syringe trough a septum. Upon completed monomer conversion, the polymer was precipitated in a mixture of cold diethyl ether and THF (1:1, v/v). The suspension was centrifuged (4500 rpm, 15 min, 4°C) and

decanted. This procedure was repeated twice concluding with pure diethyl ether. The product was dried *in vacuo* yielding poly(*S*-ethylsulfonyl-DL-cysteine) (45 mg, 100%) as a colorless to slightly yellow solid.

Polymerizations conducted at lower NCA concentrations (β_{NCA} = 30 g·L⁻¹) resulted in slow polymerization progress, whereas higher NCA concentrations (β_{NCA} = 100 g·L⁻¹) resulted in gelation, yielding low molecular weight polymers for both cases, and polymerization at (β_{NCA} = 60 g·L⁻¹) appears to be optimal.

¹H NMR (400 MHz, DMSO-d_6), δ [ppm] = 8.84 (b s, 1n H, *NH*), 4.71 (b s, 1n H, α-*H*), 3.57 (b s, 4n H, -*CH₂*-CH- & -*CH₂*-CH₃), 1.30 (b s, 3n H, -*CH₃*), 0.84 (b s, 9H, -(*CH₃*)₃).

Kinetic Investigations: Polymerizations were prepared as described above and analyzed over a period of 5 d. Samples were taken using a nitrogen flushed syringe trough a septum. The decreasing NCA carbonyl peaks at 1858 and 1788 cm⁻¹ were monitored and the integrals were correlated with the NCA concentration for kinetic evaluations.[49]

Synthesis of p(L)Glu(OBn)ₙ-*b*-p(DL)Cys(SO₂Et)ₘ-*b*-pSarₒ: Additional *N*-carboxyanhydride monomers, sarcosine NCA and *γ*-benzyl-L-glutamate NCA, were prepared according to previous publications.[31,36]

L-Glu(OBn) NCA (240 mg, 912 µmol, 30 eq.) was transferred into a pre-dried Schlenk-flask, dissolved in 2.0 mL of anhydrous DMF and cooled to 0 °C. Neopentylamine initiator (2.65 mg, 30.4 µmol, 1.0 eq.) was added as a stock solution in DMF (265 µL, β_{NPA} = 10.0 g·L⁻¹) and a steady flow of dry nitrogen was sustained during the polymerization. After 3 days, upon completed L-Glu(OBn) NCA conversion, as detected by FT-IR spectroscopy, the reaction mixture was cooled to -10 °C and DL-Cys(SO₂Et) NCA (145 mg, 608 µmol, 20 eq.) was added as a stock solution in anhydrous DMF (72.5 µL, β_{NCA} = 200 g·L⁻¹). Upon completed DL-Cys(SO₂Et) NCA conversion after additional 6 days, sarcosine NCA (525 mg, 4.56 mmol, 150 eq.) was added as a stock solution in DMF (1.75 mL, β_{NCA} = 300 g·L⁻¹) and the polymerization continued at -10 °C. The reaction was judged to be completed after polymerization for further 19 days, with a total duration of 28 days. Next, the polymer was precipitated into THF. The suspension was centrifuged (4500 rpm, 15 min, 4 °C) and decanted. This procedure was repeated twice concluding with pure diethyl ether. For further purification, the polymer was dialyzed against MilliQ water (MWCO 6-8 kDa) for one day and obtained as a colorless powder (385 mg, 58%) from lyophilization of the aqueous solution. For

polymer analytics, samples (each 150 µL) were taken by syringe through the septum, after completion of the respective blocks, and precipitated in THF and diethyl ether as described above.

^{1}H NMR p(L)Glu(OBn)$_n$ (400 MHz, DMSO-d_6), δ [ppm] = 8.30 (b s, 1n H, *NH*), 7.24 (b s, 5n H, Arom. *CH*), 5.03 (m, 2n H, O-*CH$_2$*), 3.92 (m, 1n H, α-*CH*), 2.29 - 1.85 (m, 4n H, *β-CH$_2$-* & *γ-CH$_2$-*), 0.84 (b s, 9H, -(*CH$_3$*)$_3$).

^{1}H NMR p(L)Glu(OBn)$_n$-*b*-p(DL)Cys(SO$_2$Et)$_m$ (400 MHz, DMSO-d_6), δ [ppm] = 8.84 (b s, 1m H, *NH*), 8.30 (b s, 1n H, *NH*), 7.24 (b s, 5n H, Arom. *CH*), 5.03 (m, 2n H, O-*CH$_2$*), 4.74 (b s, 1m H, α-*CH*), 3.92 (m, 1n H, α-*CH*), 3.57 (b s, 4m H, *β-CH$_2$* & -*CH$_2$*-CH$_3$), 2.29 - 1.85 (m, 4n H, *β-CH$_2$-* & *γ-CH$_2$-*), 1.30 (m, 3o H, -*CH$_3$*), 0.84 (b s, 9H, -(*CH$_3$*)$_3$).

^{1}H NMR p(L)Glu(OBn)$_n$-*b*-p(DL)Cys(SO$_2$Et)$_m$-*b*-pSar$_o$ (400 MHz, DMSO-d_6), δ [ppm] = 8.84 (b s, 1m H, *NH*), 8.30 (b s, 1n H, *NH*), 7.24 (b s, 5n H, Arom. *CH*), 5.03 (m, 2n H, O-*CH$_2$*), 4.74 (b s, 1m H, α-*CH*), 4.50 - 3 77 (m, 1n H+ 2p H, α-*CH* & *CH$_2$*), 3.57 (b s, 4m H, -*CH$_2$*-CH- & -*CH$_2$*-CH$_3$), 3.07 - 2.67 (m, 3o H, -*CH$_3$*), 2.29 - 1.85 (m, 4n H, *β-CH$_2$-* & *γ-CH$_2$-*), 1.30 (m, 3o H, -*CH$_3$*), 0.84 (b s, 9H, -(*CH$_3$*)$_3$).

Notes

CCDC 2002425 contains the supplementary crystallographic data for this paper. These data can be obtained free of charge from The Cambridge Crystallographic Data Centre via www.ccdc.cam.ac.uk/data_request/cif.

Acknowledgements

References

(1)   Kricheldorf, H. R. Polypeptides and 100 Years of Chemistry of α-Amino Acid N-Carboxyanhydrides. *Angew. Chemie - Int. Ed.* **2006**, *45* (35), 5752–5784.

(2)   Birke, A.; Ling, J.; Barz, M. Polysarcosine-Containing Copolymers: Synthesis, Characterization, Self-Assembly, and Applications. *Prog. Polym. Sci.* **2018**, *81*, 163–208.

(3)   Huang, J.; Heise, A. Stimuli Responsive Synthetic Polypeptides Derived from N-Carboxyanhydride (NCA) Polymerisation. *Chem. Soc. Rev.* **2013**, *42* (17), 7373–

7390.

(4)   Bonduelle, C. Secondary Structures of Synthetic Polypeptide Polymers. *Polym. Chem.* **2018**, *9* (13), 1517–1529.

(5)   Szwarc, M. The Kinetics and Mechanism of N-Carboxy-α-Amino-Acid Anhydride (NCA) Polymerisation to Poly-Amino Acids. In *Adv. Polym. Sci.*; 1965; Vol. 4, 1–65.

(6)   Cheng, J.; Deming, T. J. Synthesis of Polypeptides by Ring-Opening Polymerization of α-Amino Acid N-Carboxyanhydrides. In *Peptide-Based Materials*; **2011**; Vol. 310, 1–26.

(7)   Huesmann, D.; Birke, A.; Klinker, K.; Türk, S.; Räder, H. J.; Barz, M. Revisiting Secondary Structures in NCA Polymerization: Influences on the Analysis of Protected Polylysines. *Macromolecules* **2014**, *47* (3), 928–936.

(8)   Aliferis, T.; Iatrou, H.; Hadjichristidis, N. Living Polypeptides. *Biomacromolecules* **2004**, *5* (5), 1653–1656.

(9)   Lundberg, R. D.; Doty, P. Polypeptides. XVII. A Study of the Kinetics of the Primary Amine-Initiated Polymerization of N-Carboxy-Anhydrides with Special Reference to Configurational and Stereochemical Effects. *J. Am. Chem. Soc.* **1957**, *79* (15), 3961–3972.

(10)   Baumgartner, R.; Fu, H.; Song, Z.; Lin, Y.; Cheng, J. Cooperative Polymerization of α-Helices Induced by Macromolecular Architecture. *Nat. Chem.* **2017**, *9* (7), 614–622.

(11)   Chen, C.; Fu, H.; Baumgartner, R.; Song, Z.; Lin, Y.; Cheng, J. Proximity-Induced Cooperative Polymerization in "Hinged" Helical Polypeptides. *J. Am. Chem. Soc.* **2019**, *141* (22), 8680–8683.

(12)   Kawai, T.; Komoto, T. Crystallization of Polypeptides during Polymerization. *J. Cryst. Growth* **1980**, *48* (2), 259–282.

(13)   Komoto, T.; Oya, M.; Kawai, T. Crystallization of Polypeptides in the Course of Polymerization. *Macromol. Chem.* **1974**, *175* (1), 301–310.

(14)   Kricheldorf, H. R.; von Lossow, C.; Schwarz, G. Primary Amine-Initiated Polymerizations of Alanine-NCA and Sarcosine-NCA. *Macromol. Chem. Phys.* **2004**, *205* (7), 918–924.

(15)   Komoto, T.; Oya, M.; Kawai, T. Crystallization of Polypeptides in the Course of Polymerisation 5. *Macromol. Chem.* **1974**, *175*, 283–299.

(16)   Kricheldorf, H. R.; Mutter, M.; Maser, F.; Müller, D.; Förster, H. Secondary Structure of Peptides. 4:13C-Nmr CP/MAS Investigation of Solid Oligo- and Poly(L-Alanines). *Biopolymers* **1983**, *22* (5), 1357–1372.

(17)   Chou, P. Y.; Pasman, G. D. Conformational Parameters for Amino Acids in Helical, ß-Sheet, and Random Coil Regions Calculated from Proteins. *Biochemistry* **1974**, *13* (2), 211–222.

(18)   Kricheldorf, H. R. Polypeptide Und 100 Jahre Chemie Der α-Aminosäure-N-Carboxyanhydride. *Angew. Chemie* **2006**, *118* (35), 5884–5917.

(19)   Kricheldorf, H. R.; Von Lossow, C.; Schwarz, G. Cyclic Polypeptides by Solvent-Induced Polymerizations of α-Amino Acid n-Carboxyanhydrides. *Macromolecules* **2005**, *38* (13), 5513–5518.

(20)   Deming, T. J. Synthesis of Side-Chain Modified Polypeptides. *Chem. Rev.* **2016**, *116*

(3), 786–808.

(21) Akaike, T.; Aogaki, Y.; Inoue, S. Stereochemistry of the D and L Copolymerization of Valine N-carboxyanhydride. *Biopolymers* **1975**, *14* (12), 2577–2583.

(22) Huesmann, D.; Klinker, K.; Barz, M. Orthogonally Reactive Amino Acids and End Groups in NCA Polymerization. *Polym. Chem.* **2016**, *8* (6), 957–971.

(23) Hwang, J.; Deming, T. J. Methylated Mono- and Di(Ethylene Glycol)-Functionalized ß-Sheet Forming Polypeptides. *Biomacromolecules* **2001**, *2* (1), 17–21.

(24) Hayakawa, T.; Matsuyama, M.; Inouye, K. Poly(S-Alkyl-l-Cysteines) Containing Long Aliphatic Side Chains. *Polymer (Guildf).* **1977**, *18* (8), 854–855.

(25) Hayakawa, T.; Kondo, Y.; Matsuyama, M. Syntheses and Conformational Studies of Poly(S-Menthyloxycarbonylmethyl l- and d-Cysteines). *Polymer (Guildf).* **1976**, *17* (11), 1009–1012.

(26) Berger, A.; Noguchi, J.; Katchalski, E. Poly-L-Cysteine. *J. Am. Chem. Soc.* **1956**, *78* (17), 4483–4488.

(27) Poole, L. B. The Basics of Thiols and Cysteines in Redox Biology and Chemistry. *Free Radic. Biol. Med.* **2015**, *80*, 148–157.

(28) Schäfer, O.; Huesmann, D.; Muhl, C.; Barz, M. Rethinking Cysteine Protective Groups: S -Alkylsulfonyl- l -Cysteines for Chemoselective Disulfide Formation. *Chem. - A Eur. J.* **2016**, *22* (50), 18085–18091.

(29) Schäfer, O.; Huesmann, D.; Barz, M. Poly(S -Ethylsulfonyl- l -Cysteines) for Chemoselective Disulfide Formation. *Macromolecules* **2016**, *49* (21), 8146–8153.

(30) Klinker, K.; Barz, M. Polypept(o)Ides: Hybrid Systems Based on Polypeptides and Polypeptoids. *Macromol. Rapid Commun.* **2015**, *36* (22), 1943–1957.

(31) Birke, A.; Huesmann, D.; Kelsch, A.; Weilbächer, M.; Xie, J.; Bros, M.; Bopp, T.; Becker, C.; Landfester, K.; Barz, M. Polypeptoid- Block -Polypeptide Copolymers: Synthesis, Characterization, and Application of Amphiphilic Block Copolypept(o)Ides in Drug Formulations and Miniemulsion Techniques. *Biomacromolecules* **2014**, *15* (2), 548–557.

(32) Klinker, K.; Schäfer, O.; Huesmann, D.; Bauer, T.; Capelôa, L.; Braun, L.; Stergiou, N.; Schinnerer, M.; Dirisala, A.; Miyata, K.; Osada, K.; Cabral, H.; Kataoka, K.; Barz, M. Secondary-Structure-Driven Self-Assembly of Reactive Polypept(o)Ides: Controlling Size, Shape, and Function of Core Cross-Linked Nanostructures. *Angew. Chemie Int. Ed.* **2017**, *56* (32), 9608–9613.

(33) Farthing, A. C.; Reynolds, R. J. W. Anhydro-N-Carboxy-DL-ß-Phenylalanine. *Nature* **1950**, *165* (4199), 647–647.

(34) Fuchs, F. Über N-Carbonsäure-Anhydride. *Chem. Ber.* **1922**, *55B*, 2943.

(35) Fetsch, C.; Grossmann, A.; Holz, L.; Nawroth, J. F.; Luxenhofer, R. Polypeptoids from N -Substituted Glycine N -Carboxyanhydrides: Hydrophilic, Hydrophobic, and Amphiphilic Polymers with Poisson Distribution. *Macromolecules* **2011**, *44* (17), 6746–6758.

(36) Schäfer, O.; Schollmeyer, D.; Birke, A.; Holm, R.; Johann, K.; Muhl, C.; Seidl, C.; Weber, B.; Barz, M. Investigation of α-Amino Acid N-Carboxyanhydrides by X-Ray Diffraction for Controlled Ring-Opening Polymerization. *Tetrahedron Lett.* **2019**, *60* (3), 272–275.

(37) Barz, M.; Huesmann, D.; Schäfer, O.; Reuter, T.; Birke, A.; Heller, P. Thiol-Protected Amino Acid Derivatives and Uses Thereof, **2014**, EP2942348A1.

(38) Pelton, J. T.; McLean, L. R. Spectroscopic Methods for Analysis of Protein Secondary Structure. *Anal. Biochem.* **2000**, *277* (2), 167–176.

(39) Goormaghtigh, E.; Ruysschaert, J. M.; Raussens, V. Evaluation of the Information Content in Infrared Spectra for Protein Secondary Structure Determination. *Biophys. J.* **2006**, *90* (8), 2946–2957.

(40) Pauling, L.; Corey, R. B. Two Rippled-Sheet Configurations of Polypeptide Chains, and a Note about the Pleated Sheets. *Proc. Natl. Acad. Sci.* **1953**, *39* (4), 253–256.

(41) Nowick, J. S. Exploring β-Sheet Structure and Interactions with Chemical Model Systems. *Acc. Chem. Res.* **2008**, *41* (10), 1319–1330.

(42) Kricheldorf, H. R.; Müller, D. Secondary Structure of Peptides. *Polym. Bull.* **1983**, *10* (11–12), 513–520.

(43) Shapiro, Y. E. Analysis of Chain Microstructure by 1H and 13C NMR Spectroscopy. *Bull. Magn. Reson.* **1985**, *7*, 27–58.

(44) Rubinstein, I.; Eliash, R.; Bolbach, G.; Weissbuch, I.; Lahav, M. Racemic β Sheets in Biochirogenesis. *Angew. Chemie* **2007**, *119* (20), 3784–3787.

(45) Weissbuch, I.; Illos, R. A.; Bolbach, G.; Lahav, M. Racemic β-Sheets as Templates of Relevance to the Origin of Homochirality of Peptides: Lessons from Crystal Chemistry. *Acc. Chem. Res.* **2009**, *42* (8), 1128–1140.

(46) Fu, X.; Shen, Y.; Fu, W.; Li, Z. Thermoresponsive Oligo(Ethylene Glycol) Functionalized Poly- l -Cysteine. *Macromolecules* **2013**, *46* (10), 3753–3760.

(47) Iguchi, M. A Comment on the Kinetics in a Heterogeneous Polymerization System. *J. Polym. Sci. Part A-1 Polym. Chem.* **1970**, *8* (4), 1013–1021.

(48) Muhl, C.; Schäfer, O.; Bauer, T.; Räder, H.-J.; Barz, M. Poly(S -Ethylsulfonyl- l -Homocysteine): An α-Helical Polypeptide for Chemoselective Disulfide Formation. *Macromolecules* **2018**, *51* (20), 8188–8196.

(49) Idelson, M.; Blout, E. R. Polypeptides. XV. 1 Infrared Spectroscopy and the Kinetics of the Synthesis of Polypeptides: Primary Amine Initiated Reactions. *J. Am. Chem. Soc.* **1957**, *79* (15), 3948–3955.

Supporting Information

Results and Discussion

X-Ray Crystal Structure Analysis
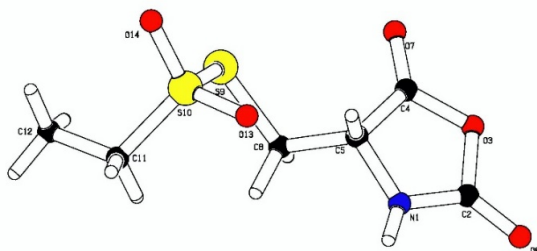
Figure S1. XRD-Analysis of *S*-(ethylsulfonyl)-D-cysteine *N*-carboxyanhydride as crystallized from the racemic mixture.
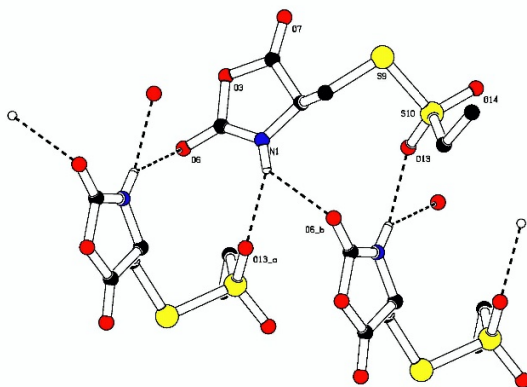
Figure S2. XRD-Analysis of *S*-(ethylsulfonyl)-D-cysteine *N*-carboxyanhydride. NCA monomers organize as linear chain *via* NH···O hydrogen bonds.
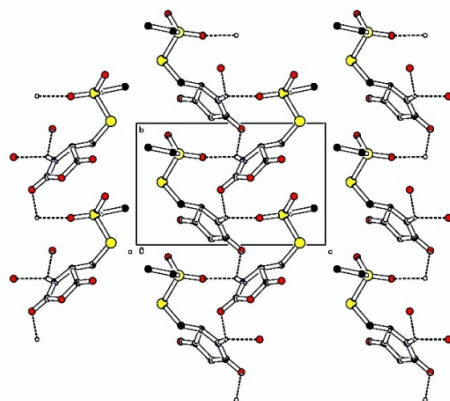
Figure S3. XRD-Analysis of *S*-(ethylsulfonyl)-D-cysteine *N*-carboxyanhydride. NCA monomers organize as linear chain along the b-axis *via* NH···O hydrogen bonds.

Crystal Data for S-Ethylsulfonyl-D-Cysteine N-Carboxyanhydride

formula	$C_6H_9O_5NS_2$
molecular weight	239.27 g·mol^{-1}
absorption	$\mu = 0.55$ mm^{-1}
transmission	$T_{min} = 0.9064$, $T_{max} = 0.9675$
crystal size	0.06 x 0.08 x 0.25 mm^3 colourless block
space group	P 2$_1$ (monoclinic)

lattice parameters
(calculated from
3231 reflections with
2.3° < θ < 28.3°)

a =	5.9154(5)Å	
b =	7.2438(5)Å	ß = 102.667(8)°
c =	11.5288(12)Å	
V =	481.99(7)Å^3	z = 2 F(000) = 248

temperature	120K
density	$d_{xray} = 1.649$ g·cm^{-3}

Data Collection

diffractometer	STOE IPDS 2T
radiation	Mo-K$_\alpha$ Graphitmonochromator

Scan – type   ω scans

Scan – width   1°

scan range $2° \leq \theta < 28°$; $-7 \leq h \leq 7$ $-9 \leq k \leq 9$ $-14 \leq l \leq 15$

number of reflections:

measured   3464

unique   2286 (R_{int} = 0.0369)

observed   1810 ($|F|/\sigma(F) > 4.0$)

Data Correction, Structure Solution and Refinement

corrections   Lorentz and polarisation correction.

structure solution   Program: SIR-2004 (Direct methods)

refinement   Program: SHELXL-2018 (full matrix). 159 refined parameters, weighting scheme: $w=1/[\sigma^2(F_o^2) + (0.0514*P)^2]$

with $(Max(F_o^2,0)+2*F_c^2)/3$. H-atoms localized and refined with isotropic thermal parameters, non H- atoms refined anisotropically.

R-values   wR2 = 0.0949 (R1 = 0.0433 for observed reflections, 0.0634 for all reflections)

goodness of fit   S = 0.993

Flack parameter   x=-0.1(1)

maximum deviation of parameters   0.001 * e.s.d

maximum peak height in diff. Fourier synthesis   0.4, -0.29 eÅ^{-3}

Gel Permeation Chromatography
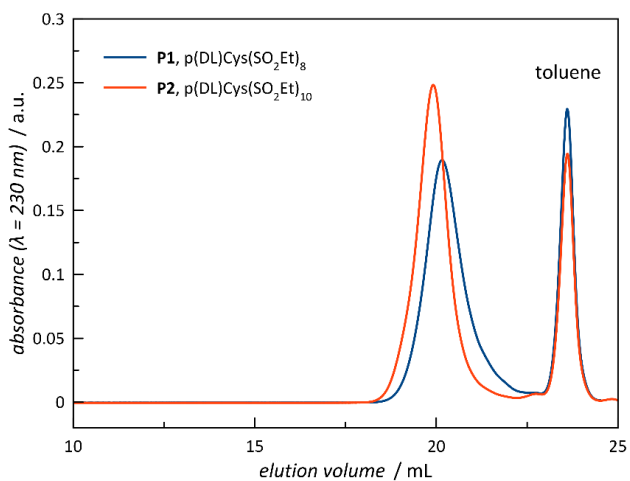
Figure S4. Analytical gel permeation chromatography in HFIP. UV-Detector signals (raw data) for poly(S-ethylsulfonyl-DL-cysteine) with short chain lengths (X_n = 8 to 10) show overlap with the internal standard (toluene).
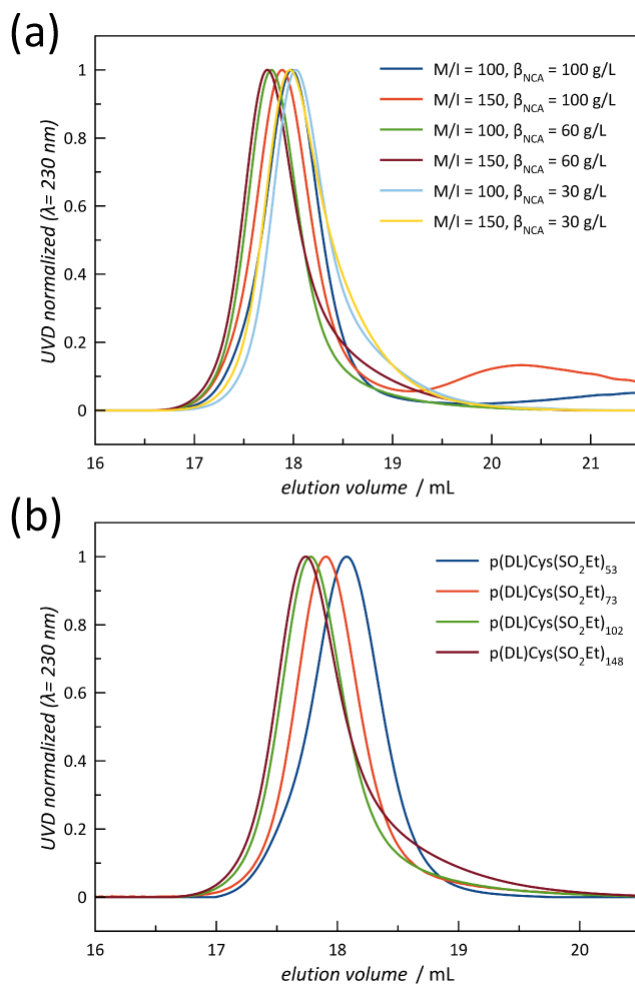
Figure S5. HFIP GPC indicates the limits of DL-Cys(SO₂Et) NCA polymerization. (**a**) Influence of the NCA concentration. (**b**) Influence of the monomer to initiator ratio.
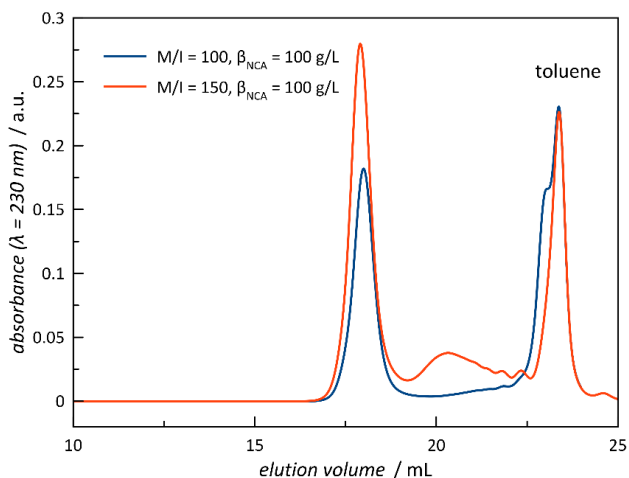
Figure S6. Analytical gel permeation chromatography in HFIP. UV-Detector signals (raw data) for the polymerization of *S*-ethylsulfonyl-DL-cysteine NCA at monomer to initiator ratios of 100 and 150 conducted at high NCA concentrations of $\beta_{NCA} = 100$ g·L^{-1} result in broad molecular weight distributions and overlap with the signal of the internal standard (toluene).

Table S1. Analytical results of the triblock copolymer synthesis.

polymer	M/I (calc.)[a]	X_n(Glu)[b]	X_m(Cys)[b]	X_o(Sar)[b]	M_n[c] / kDa	$Đ$[c]
p(L)Glu(OBn)$_n$	30	33	-	-	10.1	1.10
p(L)Glu(OBn)$_n$-*b*- p(DL)Cys(SO$_2$Et)$_m$	20	33	20	-	19.4	1.23
p(L)Glu(OBn)$_n$-*b*- p(DL)Cys(SO$_2$Et)$_m$-*b*-pSar$_o$	150	33	20	160	33.2	1.43

[a] monomer to (macro-)initiator ratio calculated for the respective NCAs; [b] end-group analysis by ^{1}H NMR; [c] HFIP GPC relative to PMMA standards.

FT-IR-Spectroscopy
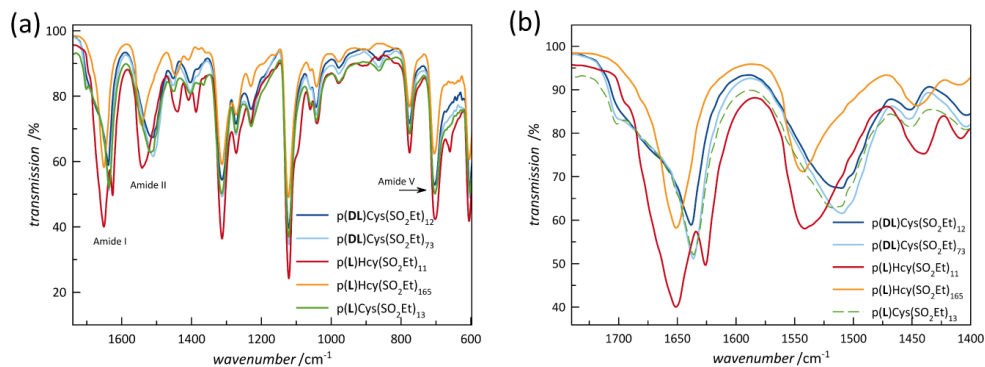
Figure S7. Infrared spectroscopy (solid state) of racemic and enantiopure poly(*S*-ethylsulfonyl-cysteine) and poly(*S*-ethylsulfonyl-L-homocysteine) (pHcy(SO$_2$Et)). pHcy(SO$_2$Et) shows wavelength-dependent helix formation.

NMR-Spectroscopy
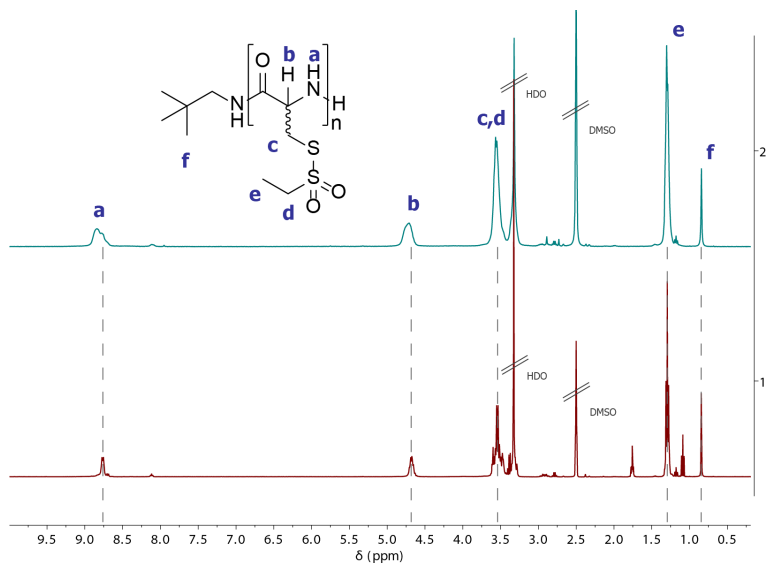
Figure S8. ^{1}H NMR of poly(*S*-ethylsulfonyl-DL-cysteine) (upper) shows broader signals compared to poly(*S*-ethylsulfonyl-L-cysteine) (lower) of similar chain length in DMSO-*d$_6$*, indicating atactic polymer structure.
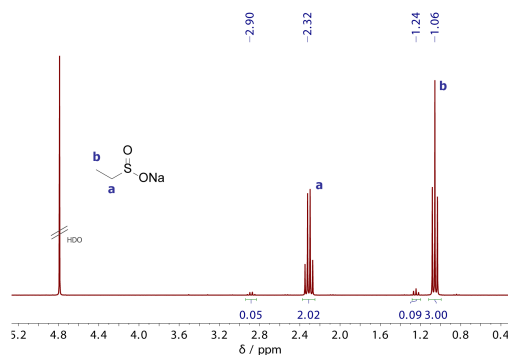
Figure S9. ^{1}H NMR spectrum of sodium ethylsulfinate in D$_2$O + TFA-d_1. Signals at 2.90 and 1.24 ppm indicate traces of oxidation product sodium ethanesulfonate (about 3%).
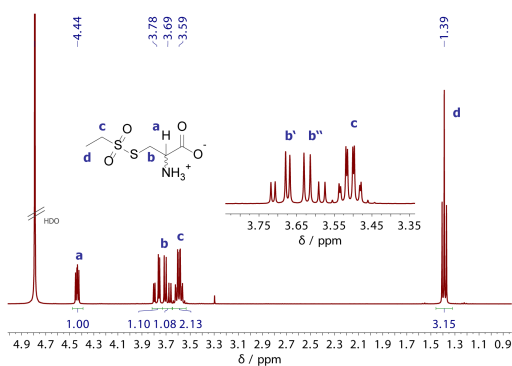
Figure S10. ^{1}H NMR spectrum of *S*-(ethylsulfonyl)-DL-cysteine in D$_2$O + TFA-d_1.
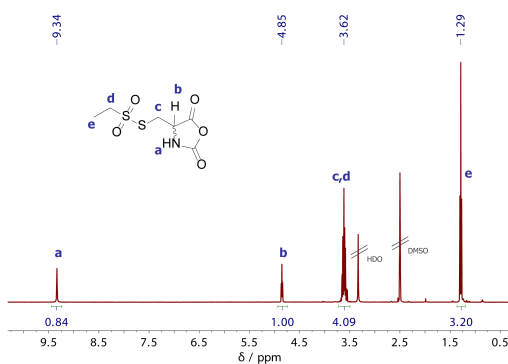
Figure S11. ^{1}H NMR spectrum of *S*-(ethylsulfonyl)-DL-cysteine *N*-carboxyanhydride in DMSO-d_6.
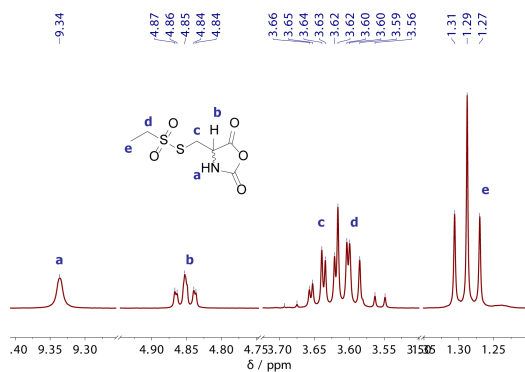
Figure S12. ^{1}H NMR spectrum of *S*-(ethylsulfonyl)-DL-cysteine *N*-carboxyanhydride in DMSO-*d₆*.
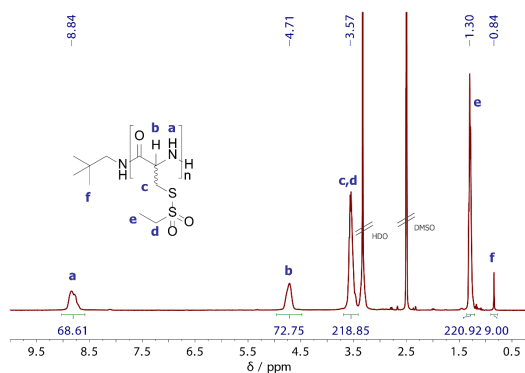
Figure S13. ^{1}H NMR spectrum of poly(*S*-(ethylsulfonyl)-DL-cysteine) in DMSO-*d₆*.
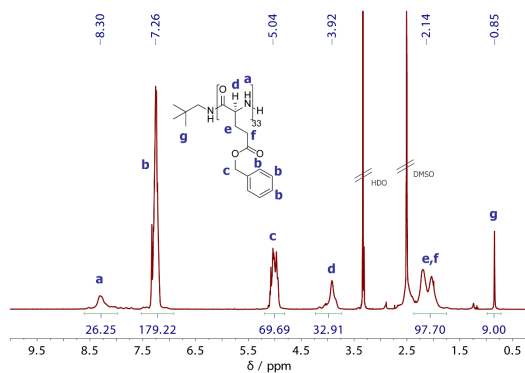
Figure S14. ^{1}H NMR spectrum of poly(ɣ-benzyl-L-glutamate) in DMSO-*d₆*.
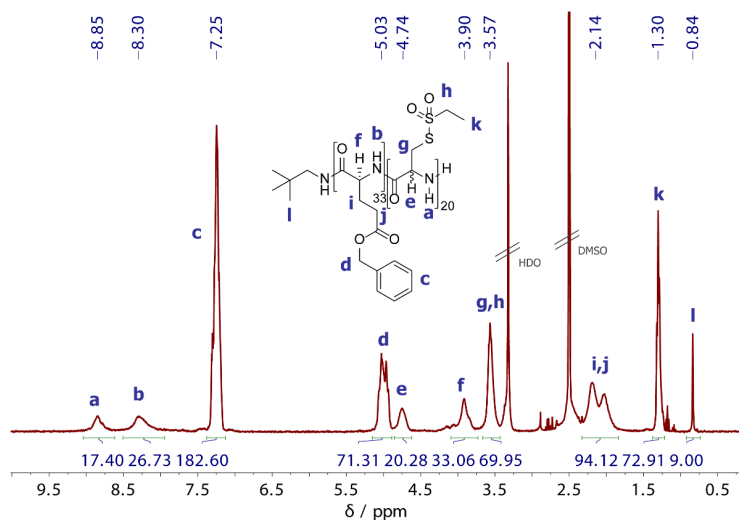
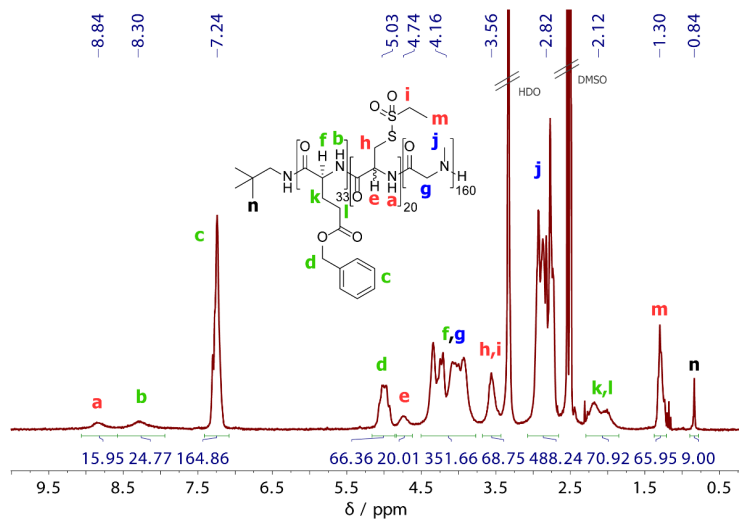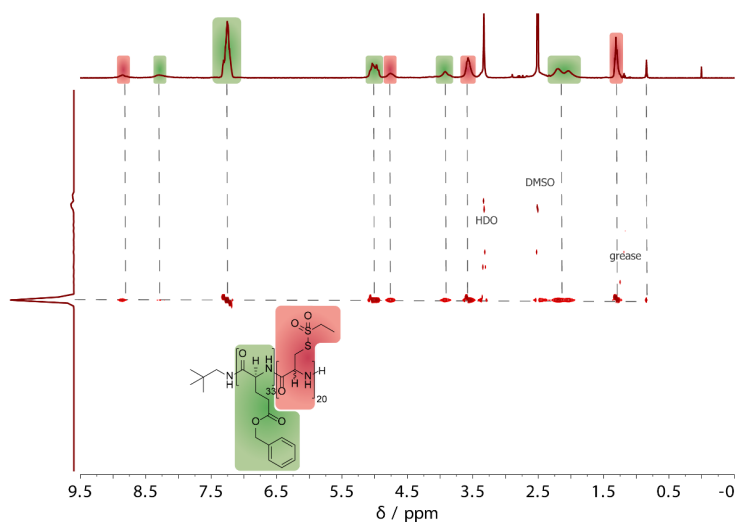**Figure S15.** ^{1}H NMR spectrum of poly(γ-benzyl-L-glutamate)-*block*-poly(S-(ethylsulfonyl)-DL-cysteine) in DMSO-d_6.

Figure S16. ^{1}H NMR spectrum of poly(γ-benzyl-L-glutamate)-*block*-poly(S-(ethylsulfonyl)-DL-cysteine)-*block*-poly(sarcosine) in DMSO-d_6.

Figure S17. DOSY NMR spectrum of poly(γ-benzyl-L-glutamate)-*block*-poly(*S*-(ethylsulfonyl)-DL-cysteine) in DMSO-*d₆*.
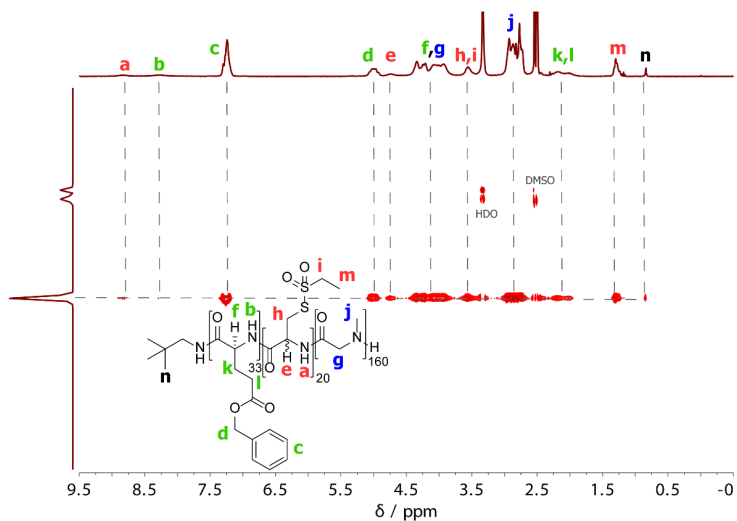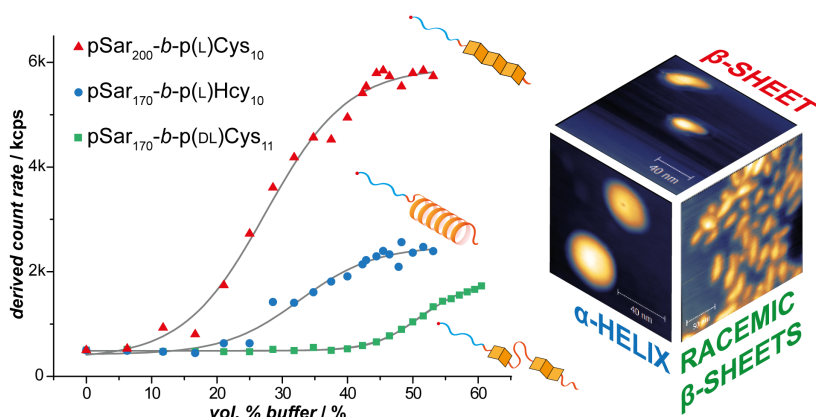

Figure S18. DOSY NMR spectrum of poly(γ-benzyl-L-glutamate)-*block*-poly(*S*-(ethylsulfonyl)-DL-cysteine)-*block*-poly(sarcosine) in DMSO-*d₆*.

3

Secondary Structure-Driven Self-Assembly of Thiol-Reactive Polypept(o)ides

Secondary Structure-Driven Self-Assembly of Thiol-Reactive Polypept(o)ides

Tobias A. Bauer[a, b], Jan Imschweiler[b], Christian Muhl[a, b], Benjamin Weber[b], Matthias Barz[a, b,*]

[a] Leiden Academic Centre for Drug Research (LACDR), Leiden University, Einsteinweg 55, 2333 CC Leiden, The Netherlands.

[b] Department of Chemistry, Johannes Gutenberg University Mainz, Duesbergweg 10-14, 55128 Mainz, Germany.

Abstract

Secondary structure formation differentiates polypeptides from most other synthetic polymers, and the transitions from random coil to rod-like α-helices or ß-sheets represent an additional parameter to direct self-assembly and the morphology of nanostructures. We investigated the influence of distinct secondary structures on the self-assembly of reactive amphiphilic polypept(o)ides. The individual morphologies can be preserved by core cross-linking *via* chemoselective disulfide bond formation. A series of thiol-responsive copolymers of racemic polysarcosine-*block*-poly(*S*-ethylsulfony-DL-cysteine) (pSar-*b*-p(DL)Cys), enantio-pure polysarcosine-*block*-poly(*S*-ethylsulfony-L-cysteine) (pSar-*b*-p(L)Cys), and polysarcosine-*block*-poly(*S*-ethylsulfony-L-homocysteine) (pSar-*b*-p(L)Hcy) was prepared by *N*-carboxyanhydride polymerization. The secondary structure of the peptide segment varies from α-helix (pSar-*b*-p(L)Hcy) to anti-parallel ß-sheet (pSar-*b*-p(L)Cys), and disrupted ß-sheet (pSar-*b*-p(DL)Cys). When subjected to nanoprecipitation, copolymers with anti-parallel ß-sheets display the strongest tendency to self-assemble, whereas disrupted ß-sheets hardly induce aggregation. This translates to worm-like micelles, solely spherical micelles or ellipsoidal structures, as analyzed by AFM and cryoTEM, which underlines the potential of secondary structure-driven self-assembly of synthetic polypeptides.

Keywords

secondary structure · polypept(o)ides · self-assembly · polymer · micelle · reactive polymer

Cover page
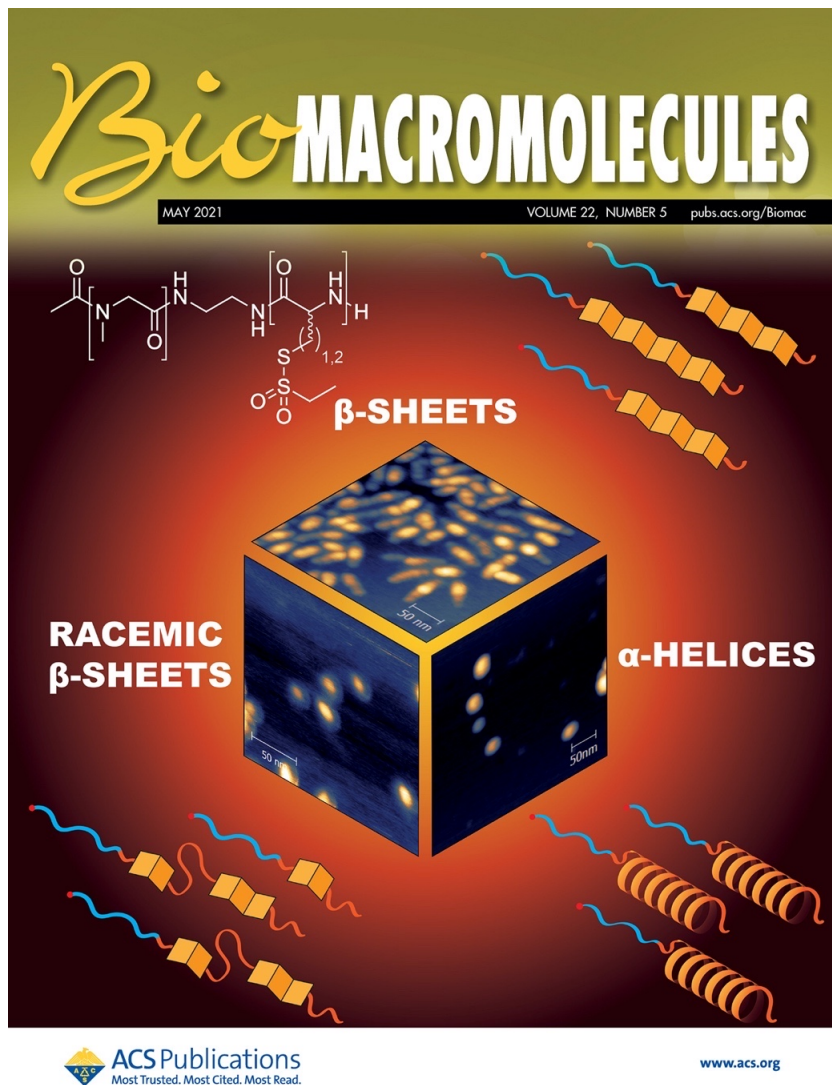
The secondary structure formation of reactive polypept(o)ides governs self-assembly, featuring control over the morphology of core cross-linked polymeric micelles.

Introduction

Secondary structure formation as a feature of polypeptides is the fundamental basis for the higher ordered structural diversity and specific function of proteins and other biomaterials.[1–3] As a prominent example, the polyalanine-domains of spider silk undergo a transition from α-helix in solution to highly ordered ß-sheets in the solid state, which, among other factors, accounts for feasible processing paired with exemptional elasticity and toughness.[4–7] Consequently, not only from a polymer chemistry perspective, secondary structure displays an additional parameter influencing the preparation and application of peptide materials.[8–11] For polypeptides derived from single amino acids, primarily α-helix or ß-sheet are obtained, with exceptions for proline-type amino acids.[1,12] Upon secondary structure formation, the induced coil-to-helix or coil-to-sheet transitions refer to a rigidification of the polymer segment (rod-like structures) and provide a driving-force for self-assembly.[1,13] In particular for synthetic polypeptides of polyglutamic acid and polylysine, the stimuli which induce α-helix formation, such as pH or temperature, have been the subject of multiple investigations.[14–20] Furthermore, Deming and co-workers intensively elucidated the thermo- and redox-responsiveness of α-helical polyhomocysteine derivatives.[21,22] On the other hand, for polyserine or polycysteine, research has been more dedicated to resolving the strong induction of ß-sheet formation, e.g., by side chain functionalization with oligo ethylene glycol moieties.[23–25]

In contrast to polypeptides, polypeptoids, with the branching on the nitrogen atom instead of the α-position do not show classical secondary structure formation as no hydrogen bond donor is present if no specific modification was introduced.[26–28] As such, polysarcosine (pSar, poly(N-methyl glycine)) adopts random coil conformation in aqueous solution, is highly water-soluble (A2 parameter of $3.50 \cdot 10^{-6} \cdot$ mol $\cdot$dm$^3 \cdot$g^{-2} for pSar$_{185}$ at 20 °C), and can be considered a stealth-like material.[29–33] For medical applications, polysarcosine is considered the most promising alternative to polyethylene glycol since substantial advantages like reduced proinflammatory cytokine secretion and reduced complement activation as well as evasion of the accelerated blood clearance (ABC) phenomenon have been reported.[30,33–35] The combination of polypeptides and polysarcosine in polypept(o)ides thus represent a promising class of bio-based or even endogenous materials.[26,36,37] While the concept of polypept(o)ides extents from linear block copolymers to cylindrical bottle-brush and star-shaped polymers including

miktoarm stars,[36,38–40] polysarcosine itself has further been successfully combined with various other classes of synthetic polymers.[37,41,42]

With its ability to form bio-reversible disulfide bonds, the non-essential amino acid cysteine plays a unique role within nature.[43,44] In living cells, catalyzing proteins and small molecules orchestrate disulfide bond formation among specific cysteines generating functional proteins.[45] To transfer chemoselective disulfide bond formation to functional polymers, our group reported on the reactive *S*-alkylsulfonyl protecting group for cysteine and homocysteine.[46,47] This reactive group differentiates hard and soft nucleophiles, and grants living amine-initiated ring-opening polymerization of *S*-alkylsulfonyl-protected *N*-carboxyanhydrides (NCAs). The *S*-alkylsulfonyl group can then be addressed by post polymerization modification reactions with soft nucleophiles, e.g., thiols, for disulfide bond formation. With respect to secondary structure, homopolypeptides of *S*-ethylsulfonyl-L-cysteine (p(L)Cys) were shown to adopt anti-parallel ß-sheets, while ß-sheets were even detected for the racemic mixture, poly(*S*-ethylsulfony-DL-cysteine) (p(DL)Cys), albeit to a much lesser extent.[47,48] In contrast, poly(*S*-ethylsulfonyl-L-homocysteine) (p(L)Hcy), which has only one additional methylene group in the side chain as compared to the parent cysteine, was shown to adopt an α-helical structure in solution and solid state.[49]

Since anti-parallel ß-sheets of enantiopure polysarcosine-*block*-poly(*S*-ethylsulfonyl-L-cysteine) (pSar-*b*-p(L)Cys) were shown to direct self-assembly to worm-like micelles previously,[50] we now contribute a comprehensive study on the influence of the secondary structure on the self-assembly of reactive block copolypept(o)ides. Therefore, *S*-ethylsulfonyl-protected reactive copolymers with varying secondary structure (α-helix, anti-parallel ß-sheet and a disrupted ß-sheet) have been synthesized by ring-opening NCA polymerization and their aggregation behavior was analyzed by DLS, AFM and cryoTEM.

Materials and Methods

Unless stated otherwise, reagents and solvents were purchased from Sigma-Aldrich and used as received. *N,N*-Dimethyl formamide (DMF) was bought from Acros (99.8%, extra dry over molecular sieve) and purified by repetitive freeze-pump thaw cycles prior to use (water content < 50 ppm). *N-tert*-butoxycarbonyl (Boc)-1,2-diaminoethane was obtained from Sigma-Aldrich (≥98%) and stored over activated molecular sieves before further use. MilliQ water was prepared using a MILLI-Q® Reference A+ System. Water was used at a resistivity of 18.2

MΩ·cm^{-1} and total organic carbon (TOC) of <5 ppm. Hexafluoro isopropanol (HFIP) and potassium trifluoro acetate was purchased from Fluorochem. Deuterated solvents were obtained from Deutero GmbH and were used as received.

^{1}H NMR spectra were recorded on a Bruker Avance II 400 at room temperature at a frequency of 400 MHz. DOSY spectra were recorded on a Bruker Avance III HD 400 (400 MHz). Calibration of the spectra was achieved using the solvent signals. NMR spectra were analyzed with MestReNova version 12.0.4 from Mestrelab Research S.L. Degrees of polymerization (X_n) by ^{1}H NMR were calculated comparing the integral of the initiator peak and the integrals of the α-protons. For block copolymers containing polysarcosine, the chain lengths of the second block were calculated from the integral of the α-protons and the signals of the polysarcosine backbone, as derived from HFIP-GPC relative to polysarcosine standards.

Attenuated total reflectance Fourier-transformed infrared (ATR-FT-IR) spectroscopy was performed on a FT/IR-4100 (JASCO Corporation) with an ATR sampling accessory (MIRacleTM, Pike Technologies). IR spectra were analyzed using Spectra Manager 2.0 (JASCO Corporation). NCA polymerization was monitored by FT-IR spectroscopy and the polymerization was judged to be completed if the carbonyl peaks at 1858 and 1788 cm^{-1} had vanished.

Analytical gel permeation chromatography (GPC) was performed on a Jasco GPC setup at a flow rate of 0.8 ml·min^{-1} and a temperature of 40 °C. The eluent was HFIP equipped with 3 g·L^{-1} potassium trifluoroacetate. The column material was modified silica gel (PFG columns, particle size: 7 µm, porosity: 100 Å and 4000 Å), purchased from PSS Polymer Standards Service GmbH. For polymer detection, a UV detector (Jasco UV-2075+) at a wavelength of λ = 230 nm was employed. Molecular weights were determined by using a calibration with PMMA (PSS Polymer Standards Services GmbH) with toluene as internal standard. The elution diagram was evaluated with PSS WinGPC (PSS Polymer Standard Service GmbH).

Single-angle dynamic light scattering (DLS) measurements were performed with a ZetaSizer Nano ZS (Malvern Instruments Ltd., Worcestershire, UK) equipped with a He-Ne laser (λ = 632.8 nm). All measurements were performed at 25 °C and a detection angle of 173°. Disposable polystyrene and organic solvent-resistant cuvettes (VWR, Darmstadt, Germany) were used for single-angle DLS

measurements. Cumulant size, polydispersity index (PDI), size distribution (intensity weighted) histograms, and the derived count rate were calculated based on the autocorrelation function of the samples, with automated position and attenuator adjustment at multiple scans.

Circular dichroism (CD) spectroscopy was performed on a Jasco J-815 spectrometer at a temperature of 20°C using Spectra Manager 1.53.04 (Jasco). The spectra were recorded in HFIP at a concentration of 0.1 g·L^{-1} using a quartz cell with a path length of 1 mm. θ_{MR} was calculated with the equation below with $c_M = 0.1$ g·L^{-1}, l = 0.1 cm, and $M_{Repeating\ Unit} = 195.26$ g·mol^{-1} for S-ethylsulfonyl-L-cysteine and S-ethylsulfonyl-DL-cysteine, $M_{Repeating\ Unit} = 209.26$ g·mol^{-1} for S-ethylsulfonyl-L-homocysteine and $M_{Repeating\ Unit} = 71.08$ g·mol^{-1} for sarcosine.

$$\theta_{MR} = \frac{\theta \cdot M_{Repeating\ Unit}}{10 \cdot c_M \cdot l} \ [deg \cdot cm^2 \cdot mol^{-1}]$$

Atomic force microscopy (AFM) was measured on mica using a CypherTM AFM (Asylum Research) using tapping mode at a scan rate of 1 Hz. Samples were prepared by drop-casting of a particle solution (V = 5 µL, ß = 50 mg·L^{-1} in MilliQ water) onto freshly cleaned mica. The sample was dried overnight at room temperature. Images were evaluated using Gwyddion 2.49.

For cryogenic transmission electron microscopy (CryoTEM), 5 µL of CCPM solution (50 mg·L^{-1}, in MilliQ water) were applied to freshly glow-discharged carbon grids with a copper 200 mesh (Quantfoil Micro Tools GmbH). Excess fluid was removed by direct blotting (2.5 s) and the grids were individually plunge-frozen in liquid ethane. Grids were cryotransferred in liquid nitrogen using a Gatan cryoholder (model 626 DH) to a Technai T12 transmission electron microscope equipped with a field emission electron source and operating at 120 kV accelerating voltage. Images were recorded using a TemCam-F416 (TVIPS, Gauting, Germany). Software imageJ 1.52h (National Institutes of Health, USA) was used for image evaluation.

Polymer Synthesis. Polymers were prepared by amine-initiated ring-opening N-carboxyanhydride (NCA) polymerization in dry DMF under Schlenk-conditions. The respective monomers, sarcosine-NCA, S-ethylsulfonyl-DL-cysteine-NCA, S-ethylsulfonyl-L-cysteine-NCA, and S-ethylsulfonyl-L-homocysteine-NCA were synthesized and characterized as reported previously.[46,48,49]

Polysarcosine (pSar$_n$) (P1, P2) Sarcosine-NCA (5.98 g, 52.0 mmol, 200 eq.) was transferred into a pre-dried Schlenk-tube, dissolved in 60 mL dry DMF and N-

(*tert*-butoxycarbonyl)-1,2-diaminoethane (41.6 mg, 0.26 mmol, 1.0 eq.) was added as a stock solution in dry DMF. The clear, colorless solution was stirred at 10 °C in the absence of light until the reaction was completed after six days, as monitored by IR spectroscopy. The sarcosine amino terminus was quenched by addition perfluorophenyl 4-azidobutanoate (153 mg, 0.52 mmol, 2.0 eq.) and *N,N*-diisopropylethylamine (221 µL, 1.30 mmol, 5.0 eq.). The reaction mixture was stirred overnight, followed by addition of acetic anhydride (248 µL, 2.60 mmol, 10 eq.) and *N,N*-diisopropylethylamine (884 µL, 5.20 mmol, 20 eq.) to react residual end groups. The slightly yellow solution was stirred for one additional day at room temperature before the polymer was precipitated in 600 mL diethyl ether, collected on a Buchner funnel, washed with acetone and diethyl ether and dried *in vacuo*. Next, the Boc-protecting group was removed. The polymer (3.4 g) was dissolved in 50 mL of water, cooled to 0 °C and 50 mL trifluoro acetic acid were added in one portion. After 4 h at 0 °C, the solution was transferred into dialysis bags (MWCO 3.5 kDa) and dialyzed against MilliQ water, saturated sodium hydrogen carbonate solution, and MilliQ water. The aqueous solution was lyophilized, and the polysarcosine (P1) was obtained as a colorless powder (3.08g, 82%). ^{1}H NMR (400 MHz, DMSO-d_6) δ (ppm) = 4.50-3.76 (m, 2nH, -CH_2-), 3.06-2.76 (m, 3nH, -CH_3). The chain length was determined by HFIP GPC relative to polysarcosine standards.[29]

Block copolymer syntheses. All block copolymers were prepared from pSar macroinitiators, following the procedure described below for pSar-*b*-p(DL)Cys using the respective NCAs.[50]

Polysarcosine$_n$-block-poly(S-ethylsulfonyl-DL-cysteine)$_m$ (pSar$_n$-b-p(DL)Cys$_m$) (P3-P6)
The polysarcosine macroinitiator (111.9 mg, 9.2 µmol, 1.0 eq.) was weighed into a pre-dried Schlenk-tube and dried by azeotropic distillation with toluene *in vacuo* twice. Next, the macroinitiator was dissolved in freshly degassed dry DMF (1.45 mL), cooled to -10 °C, and *S*-ethylsulfonyl-L-cysteine NCA (33.0 mg, 138 µmol, 15 eq.) was added as a stock solution in dry DMF. The polymerization was performed at an overall mass concentration of ß = 100 g·L^{-1} and monitored by IR spectroscopy. After 5 days, full conversion was observed, and the polymer was precipitated in THF. The suspension was centrifuged (4500 rpm, 15 min, 4°C) and decanted. This procedure was repeated twice concluding with pure diethyl ether. The product was dried *in vacuo* yielding pSar$_n$-*b*-p(DL)Cys$_m$ (P3) as a colorless solid (130 mg, 93%). ^{1}H NMR (400 MHz, DMSO-d_6) δ (ppm) = 9.04 - 8.59 (b s, 1mH, NHCO), 4.90 - 4.60 (m, 1m H, α-C$H_{(DL-Cys)}$), 4.49 - 3.78 (m, 2n H, -C$H_{2-(Sar)}$),

3.69 - 3.41 (m, 4m H, -CH_2S-, -SO$_2$CH_2-), 3.06 - 2.61 (m, 3n H, -C$H_{3(Sar)}$), 1.36 - 1.21 (t, 3m H, -C$H_{3(DL-Cys)}$).

Polysarcosine$_n$-block-poly(S-ethylsulfonyl-L-cysteine)$_p$ (pSar$_n$-b-p(L)Cys$_p$) (P7-P10) ^{1}H NMR (400 MHz, DMSO-*d$_6$*) δ (ppm) = 8.75 (b s, 1p H, NHCO), 4.69 (m, 1p H, α-C$H_{(L-Cys)}$), 4.49 - 3.78 (m, 2nH, -C$H_{2\text{-}(Sar)}$), 3.69 - 3.41 (m, 4p H, -CH_2S-, -SO$_2$CH_2-), 3.06 - 2.61 (m, 3p H, -C$H_{3(Sar)}$), 1.30 (t, 3p H, -C$H_{3(L-Cys)}$).

Polysarcosine$_n$-block-poly(S-ethylsulfonyl-L-homocysteine)$_q$ (pSar$_n$-b-p(L)Hcy$_p$) (P11-P14) ^{1}H NMR (400 MHz, DMSO-*d$_6$*) δ (ppm) = 8.34 (b s, 1q H, NHCO), 4.56 - 3.75 (m, 2n H + 1q H, -C$H_{2\text{-}(Sar)}$, α-C$H_{(L-Hcy)}$), 3.64 - 3.45 (m, 2q H, -SO$_2$CH_2-), 3.19 - 3.08 (m, 2q H, -CH_2S-), 3.06 - 2.61 (m, 3n H, -C$H_{3(Sar)}$), 2.18 - 1.85 (m, 2q H, -CH_2-CH_2S-), 1.30 (t, 3q H, -C$H_{3(L-Hcy)}$).

Cross-linker Synthesis. The synthesis of (*R*)-lipoic acid hydrazide (**3**) was performed in a two-step synthesis *via* (*R*)-methyl lipoate (**2**) starting from (*R*)-lipoic acid (**1**). The respective protocols were adapted and modified from Hassan and Maltman and Koufaki *et al.*[51,52]

(*R*)-Lipoic acid (2.0 g, 9.69 mmol, 1.0 eq.) was dissolved in 20 mL of methanol, and a catalytic amount of sulfuric acid (5.2 μL, 0.10 mmol, 0.01 eq.) was added. The reaction mixture was stirred at room temperature for 18h and protected from light. The solvent was removed under reduced pressure and the crude solid was re-dissolved in dichloromethane. The organic phase was washed with saturated NaHCO$_3$-solution and brine, dried over magnesium sulfate, filtered, and concentrated *in vacuo*. (*R*)-Methyl lipoate (**2**) was obtained as a yellow oil (1.90 g, 94%) and used without further purification. ^{1}H NMR (400 MHz, DMSO-*d$_6$*) δ (ppm) = 3.25 - 3.03 (s + m, 4H, -CH-, -OCH_3), 3.15 (m, 2H, -SCH_2-), 2.42 (m, 1H, -SCH_2CH_2-), 2.31 (t, ^3J = 7.3 Hz, 2H, -COCH_2-), 1.87 (m, 1H, -SCH_2CH_2-), 1.73 - 1.48 (m, 4H, -ß-CH_2, -δ-CH_2), 1.42 - 1.30 (m, 2H, -γ-CH_2-).

(*R*)-Methyl lipoate (**2**) (1.90 g, 8.6 mmol, 1.0 eq.) was dissolved in 10 mL of methanol and hydrazine hydrate (1.3 mL, 25.8 mmol, 3.0 eq.) was added in one portion. The reaction mixture was stirred at room temperature for 72 h in the absence of light. The solution was concentrated *in vacuo*, re-dissolved in chloroform, and the organic layer was washed with brine. The organic phase was dried over magnesium sulfate, filtered, and concentrated under reduced pressure. (*R*)-lipoic acid hydrazide (**3**) was obtained as a yellow oil (1.22 g, 64%) and used without further purification. ^{1}H NMR (400 MHz, DMSO-*d$_6$*) δ (ppm) = 8.92 (bs,

1H, NHCO), 4.14 (bs, 2H, -NH_2), 3.60 (m, 1H, -CH-), 3.14 (m, 2H, -SCH_2-), 2.40 (m, 1H, -SCH$_2$CH_2-), 2.00 (t, ^3J = 7.3 Hz, 2H, -COCH_2), 1.85 (m, 1H, -SCH$_2$CH_2- 1.70 - 1.43 (m, 4H, -ß-CH_2, -δ-CH_2), 1.38 - 1.27 (m, 2H, -γ-CH_2-). ESI-MS m/z = 243.20 [M+Na]$^+$, (M (calc.) 243.06 g·mol^{-1}).

Aggregation Curves. The respective polypept(o)ide (P3-P14) was dissolved in DMAc at a concentration of 7.5 g·L^{-1} and 300 µL were placed into a solvent-resistant plastic cuvette for DLS measurement. Aqueous sodium acetate buffer (1 mM, pH 4.75) was added in steps of 5 to 20 µL, and the derived count rate was obtained by DLS with automated positioning and attenuator adjustment at multiple scans. Data were analyzed using Origin 7.5 (OriginLab, USA) and a sigmoidal fit (Model: Dose Response).

Self-Assembly and Core Cross-Linking. The preparation of core cross-linked polymeric micelles was adapted and modified from Klinker *et al.*[50] Each polypept(o)ide was assembled at the respective turning point.

pSar$_{170}$-b-p(DL)Cys$_{11}$ (P3) was dissolved in DMAc at a concentration of 7.5 g·L^{-1} for 1 h. Next, 51 vol.% of 1 mM acetate buffer (pH 4.75) was added and the solution was left to equilibrate at room temperature for 3 h, followed by dialysis against 1 mM acetate buffer (pH 4.75). The solution was filtered (GHP 450) and concentrated to 7 g·L^{-1} by spin filtration (Amicon Ultra, MWCO 3 kDa), yielding the micelle solution. For cross-linking, in a separate flask, lipoic acid hydrazide was dissolved in ethanol at a concentration of ß = 20 g·L^{-1} and one equivalent of an aqueous solution of tris(2-carboxyethyl)phosphine hydrochloride (TCEP·HCl) (50 g·L^{-1}) was added per disulfide. After 18 h, the cross-linker solution was added to the micelle solution at equimolar amounts of thiols per cysteines. The reaction mixture was stirred at room temperature for 48 h. To remove residual cross-linker and free polymer, the solution was dialyzed against DMSO and MilliQ water (MWCO 6-8 kDa), followed by repetitive spin filtration (Amicon Ultra, MWCO 100 kDa). Both, micelles and core cross-linked micelles were analyzed by DLS. For CCPMs, the absence of free polymer was verified by gel permeation chromatography in hexafluoro isopropanol.

Results and Discussion

To investigate the influence of secondary structure on the self-assembly of thiol-reactive polypept(o)ides, amphiphilic block copolymers of racemic polysarcosine-*block*-poly(*S*-ethylsulfony-DL-cysteine) (pSar-*b*-p(DL)Cys, P3-P6), enantiopure polysarcosine-*block*-poly(*S*-ethylsulfony-L-cysteine) (pSar-*b*-p(L)Cys, P7-P10), and polysarcosine-*block*-poly(*S*-ethylsulfony-L-homocysteine) (pSar-*b*-p(L)Hcy, P11-P14) have been prepared.
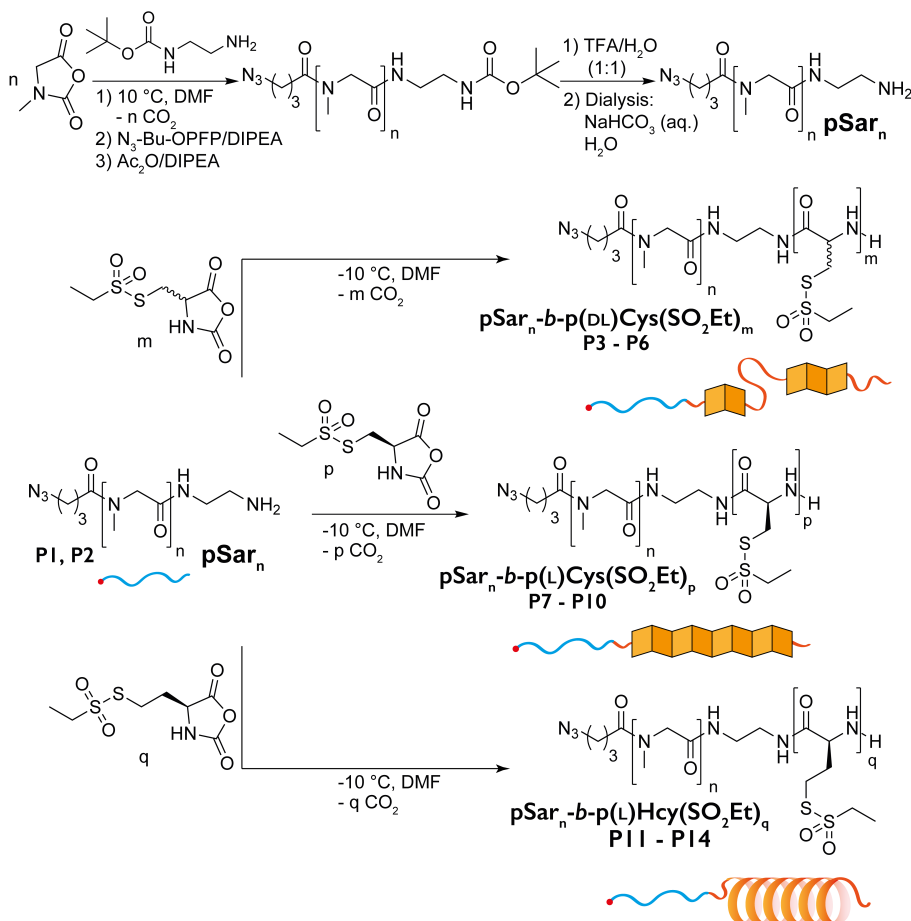
Scheme 1. Synthesis of block copolypept(o)ides with varying secondary structures.

As shown in Scheme 1, all polymers were synthesized by living ring-opening NCA polymerization. Respective secondary structures of the hydrophobic blocks, e.g.,

α-helix, ß-sheet, or disrupted ß-sheet, are illustrated as reported for the parent homopolymers.[47–49] The polymerization of sarcosine NCA was initiated by *N*-Boc-1,2-diaminoethane, and pSar (P1, P2) was end-capped with perfluorophenyl-4-azidobutanoate before the Boc-group was removed and block copolypept(o)ides were obtained from pSar macroinitiators. This strategy allows for trifold copolymer modification by [3+2] cycloaddition reactions with alkyne-modified dyes or targeting moieties, reactions with reactive esters at the amine end-group as well as reactions addressing the *S*-ethylsulfonyl group.[53]
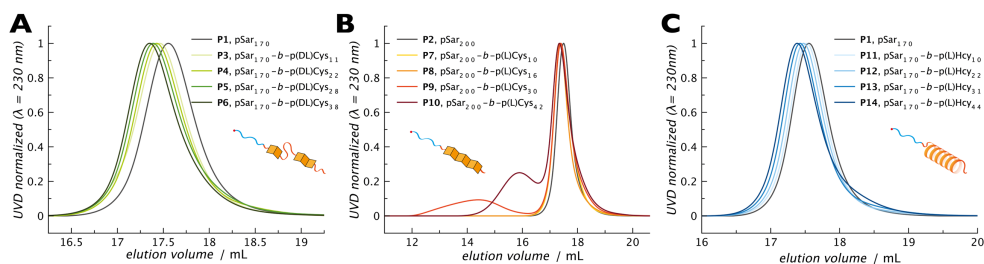

Figure 1. Analytical gel permeation chromatography in HFIP. (**A**) pSar-*b*-p(DL)Cys (P3-P6), (**B**) pSar-*b*-p(L)Cys (P7-P10), (**C**) pSar-*b*-p(L)Hcy (P11-P14), with the respective pSar macroinitiators (P1, P2).

For the preparation of block copolymers, when reacted at -10 °C in DMF, the reactive *S*-ethylsulfonyl protecting group remains intact,[46] and a shift compared to the pSar macroinitiator can be detected by GPC in hexafluoro isopropanol (HFIP) (Figure 1), which indicates successful chain extension. In detail, symmetric and monomodal molecular weight distributions with a distinct shift for increasing repetitive units were detected for $pSar_n$-*b*-$p(DL)Cys_m$ with X_m from 11 to 38 (P3-P6) and $pSar_n$-*b*-$p(L)Hcy_q$ X_q = 10 to 44 (P11-P14) (Figure 1A, 1C). Contrariwise, the strong anti-parallel ß-sheets of enantiopure $p(L)Cys_p$ could not be resolved by HFIP for higher chain lengths, accounting for the bimodal GPC in Figure 1B and the corresponding broad dispersity for block copolymers with $X_p > 16$. When analyzed by DOSY NMR in DMSO-d_6, however, only one diffusing species could be detected for all $pSar_n$-*b*-$p(L)Cys_n$ polymers (P7-P10) verifying successful polymer synthesis and the absence of homopolymer (see SI, Figure S26-S29).

Table 1. Analytical results of the polymer synthesis.

polymer	X_n (pSar)[a]	$X_{m, p, q}$ (react. block, calc.)	$X_{m, p, q}$ (react. block)[b]	M_n[c] / kDa	M_w[c] / kDa	$Đ$[c]	wt.% react. block
P1, pSar$_{170}$	170	-	-	37.7	45.7	1.21	-
P2, pSar$_{200}$	200	-	-	39.8	47.9	1.20	-
P3, pSar$_{170}$-b-p(DL)Cys$_{11}$	170	15	11	42.6	53.0	1.24	15
P4, pSar$_{170}$-b-p(DL)Cys$_{22}$	170	30	22	41.5	53.4	1.28	26
P5, pSar$_{170}$-b-p(DL)Cys$_{28}$	170	50	28	42.5	54.3	1.28	31
P6, pSar$_{170}$-b-p(DL)Cys$_{38}$	170	50	38	46.1	57.2	1.24	38
P7, pSar$_{200}$-b-p(L)Cys$_{10}$	200	20	10	42.3	53.4	1.26	12
P8, pSar$_{200}$-b-p(L)Cys$_{16}$	200	30	16	41.9	56.0	1.33	18
P9, pSar$_{200}$-b-p(L)Cys$_{30}$	200	50	30	47.7	215.5	4.52	29
P10, pSar$_{200}$-b-p(L)Cys$_{42}$	200	50	42	41.9	122.1	2.45	37
P11, pSar$_{170}$-b-p(L)Hcy$_{10}$	200	11	10	38.5	48.1	1.25	15
P12, pSar$_{170}$-b-p(L)Hcy$_{22}$	200	22	22	38.3	49.9	1.30	27
P13, pSar$_{170}$-b-p(L)Hcy$_{31}$	200	35	31	38.9	52.5	1.35	35
P14, pSar$_{170}$-b-p(L)Hcy$_{44}$	200	50	44	39.2	54.0	1.37	43

[a] determined by HFIP GPC relative to pSar standards[29], [b] determined by ^{1}H NMR, [c] determined by HFIP GPC relative to PMMA standards.

Since α-helices promote NCA polymerization at pseudo first-order kinetics,[1,12,20] full conversion was detected for the polymerization of L-Hcy(SO$_2$Et)-NCA, and thus, chain lengths determined for pSar-b-p(L)Hcy are in good agreement with the calculated chain lengths (Table 1). In contrast, the NCA polymerization of both, enantiopure and racemic L-Cys(SO$_2$Et)-NCA and DL-Cys(SO$_2$Et)-NCA, was governed by insoluble ß-sheets referring to an Avrami-type of chain growth.[47,48] Consequently, polymerizations were stopped when no further progress could be detected by FT-IR spectroscopy, accounting for the deviation between calculated and obtained chain lengths.[54] Of note, in our case, the addition of chaotropic thiourea, freshly purified by vacuum sublimation, did not help to overcome this limitation but solely resulted in homopolymer formation (Figure S1).[55] Nevertheless, as summarized in Table 1, three sets containing four reactive amphiphilic polypept(o)ides have been prepared successfully. These polymers are characterized by comparable chain lengths of 170 and 200 for hydrophilic pSar,

and 10 to 44 for the hydrophobic reactive *S*-ethylsulfonyl-protected blocks. The respective block ratios correspond to similar hydrophobic segments ranging from 12 to 43 weight%, well suitable for self-assembly to micellar structures.[56–58]

To verify the secondary structure, block copolypept(o)ides were analyzed by FT-IR spectroscopy in the solid state.[59,60] The characteristic signals for an α-helix can generally be found at 1650 cm^{-1} (Amide I) and 1546 cm^{-1} (Amide II), while for β-sheets these peaks can be observed at 1630 cm^{-1} (Amide I) and 1530 cm^{-1} (Amide II), as well as 1656 cm^{-1} (Amide I) and 1535 cm^{-1} (Amide II) for random coil structures.[1,59–61] As shown in Figure 2A, predominant signals of the amide bands at 1546 and 1317 cm^{-1} (amide II, amide III; blue arrows) can be assigned to the α-helical p(L)Hcy block despite the co-existence with the random coil of polysarcosine which overlaps for the amide I peak. Furthermore, CD-spectroscopy in HFIP showed an increasing concision of the characteristic signals (minima at 212 nm and 226 nm, maximum at 194 nm) for growing p(L)Hcy chain lengths confirming the α-helical structure (Figure S2).[62] For enantiopure pSar-*b*-p(L)Cys copolymers, the shoulder at 1703 cm^{-1} (red arrow) accounts for the anti-parallel orientation of the β-sheets, while no characteristic peaks can be distinguished for
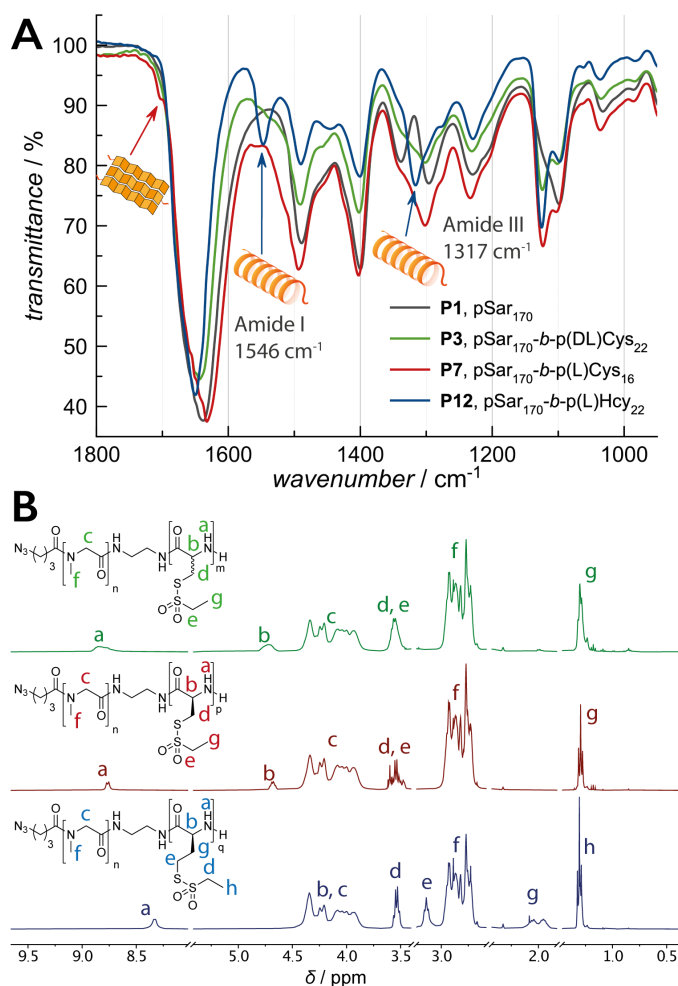
Figure 2. Secondary structure analysis of pSar-*b*-p(DL)Cys, pSar-*b*-p(L)Cys, and pSar-*b*-p(L)Hcy. (**A**) FT-IR spectroscopy, (**B**) ^{1}H NMR spectroscopy.

racemic pSar-*b*-p(DL)Cys copolymers. When analyzed by NMR spectroscopy (Figure 2B), block copolymers of pSar-*b*-p(DL)Cys show much broader peaks compared to enantiopure pSar-*b*-p(L)Cys, suggesting a rather atactic polymer structure similar to observations for the racemic p(DL)Cys homopolymers.[48] Taken together and referring to the secondary structures detected for the respective homopolypeptides in solution by circular dichroism spectroscopy,[47–49] GPC, IR and NMR spectroscopy confirm the successful preparation of reactive block

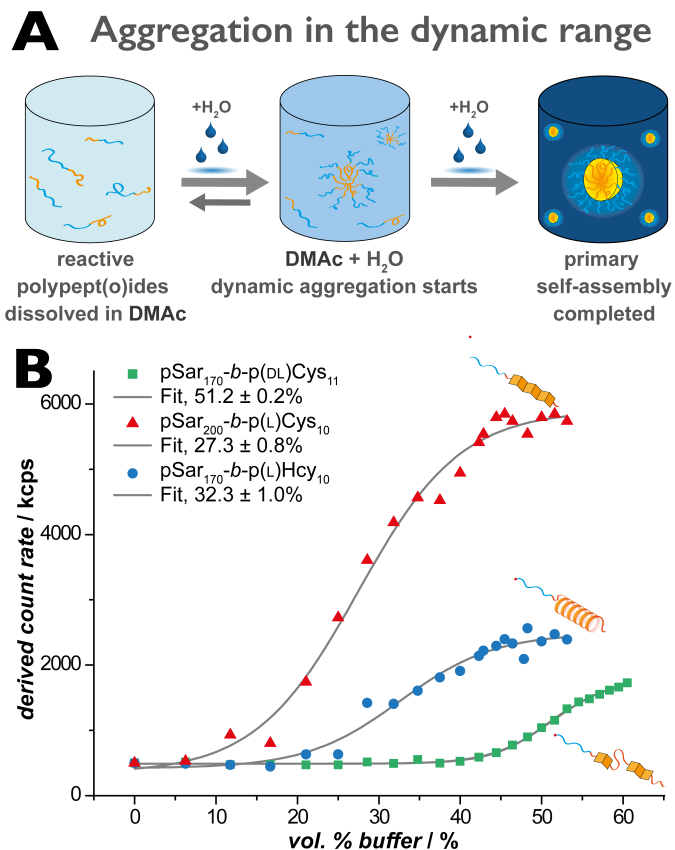copolypept(o)ides with secondary structures varying from α-helix to disrupted or anti-parallel ß-sheets.[63,64]

Figure 3. Influence of the secondary structure on the aggregation behavior. (**A**) Schematic illustration of the dynamic range. (**B**) Aggregation curve of polypept(o)ides (P3, P7, P11) with sigmoidal fit.

The influence of secondary structure on solution self-assembly was investigated by a titration- experiment. As illustrated in Figure 3A, the reactive polypept(o)ides were dissolved in a good solvent, N,N-dimethylacetamide (DMAc), and water, equipped with 1 mM sodium acetate (pH 4.75), was added stepwise. When a certain buffer concentration is reached, polymers start to assemble, and the scattering intensity increases, which correlates with the derived count rate detected by DLS. The count rate continues to increase as long as new micelles form or larger aggregates are growing ($I \sim r^6$).[65] Finally, a plateau gets reached when the concentration of the block-selective solvent exceeds a certain limit. Due to the low solubility of free polymer, micelles remain stable.[56,66,67] Besides additional parameters such as solvents and polymer concentration, the dynamic range of self-assembly is specific for each polymer. For head-to-head comparison, racemic pSar-b-p(DL)Cys, enantiopure pSar-b-p(L)Cys, and pSar-b-p(L)Hcy were dissolved in DMAc at equal concentrations, and the aqueous buffer was added at comparable time intervals. Interestingly, the three copolymers of comparable chain lengths showed significant variations in their aggregation behavior (Figure 3B). Sigmoidal shapes were obtained for all aggregation curves, however, the sigmoidal fit revealed a turning point at $27.3 \pm 0.8\%$ for the enantiopure $pSar_{200}$-b-p(L)Cys_{10}, while turning points of $51.2 \pm 0.2\%$ and $32.3 \pm 1.0\%$ were derived for racemic $pSar_{170}$-b-p(DL)Cys_{11} and $pSar_{170}$-b-p(L)Hcy_{10}, respectively. Moreover, the final plateau level of $pSar_{200}$-b-p(L)Cys_{10} was found ~3-fold higher compared to racemic $pSar_{170}$-b-p(DL)Cys_{11} and ~2-fold higher compared to $pSar_{170}$-b-p(L)Hcy_{10}. As the primary structure does not differ significantly among the selected copolymers, the observed effects can be attributed to the variation of the secondary structure, which testifies anti-parallel ß-sheets an assembly-promoting character stronger than α-helices, likely caused by attractive interactions between individual ß-sheets.
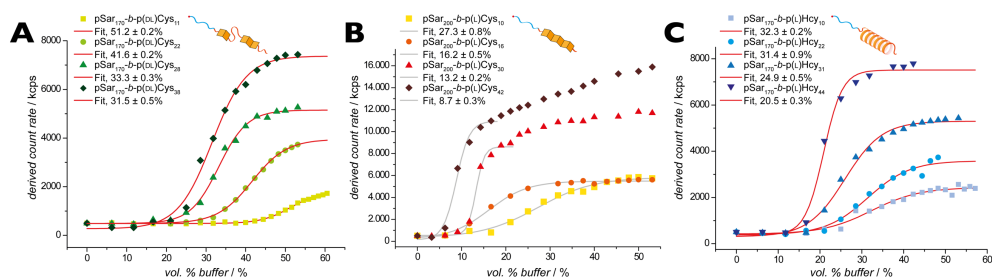
Figure 4. Aggregation curves for copolymers P3 - P14. (**A**) pSar-*b*-p(DL)Cys, (**B**) pSar-*b*-p(L)Cys, (**C**) pSar-*b*-p(L)Hcy.

When the chain lengths of the hydrophobic polypeptide blocks are increased, turning points generally shift to aggregation at lower buffer concentrations for all copolymers (Figure 4). In addition, the dynamic range, thus the area between the start of the aggregation and the primary plateau, becomes narrower by increasing the hydrophobic segment. As such, the dynamic range extents from 20 to 50 volume% buffer for $pSar_{170}$-*b*-p(L)Hcy$_{10}$, but from 15 to 30 vol.% buffer for $pSar_{170}$-*b*-p(L)Hcy$_{44}$. Furthermore, the trend of anti-parallel ß-sheets as being the strongest promotor of self-assembly can be confirmed by the shift of the turning point from 27.3 ± 0.8 vol.% for $pSar_{200}$-*b*-p(L)Cys$_{10}$ to concentrations as low as 8.7 ± 0.3 vol.% buffer for $pSar_{200}$-*b*-p(L)Cys$_{42}$. Interestingly, for $pSar_{200}$-*b*-p(L)Cys$_{30}$ and $pSar_{200}$-*b*-p(L)Cys$_{42}$, the primary aggregation seems accompanied by a secondary aggregation, as the sigmoidal fit cannot be applied over the entire range, indicating further re-arrangement of the initially formed micelles.[68,69]
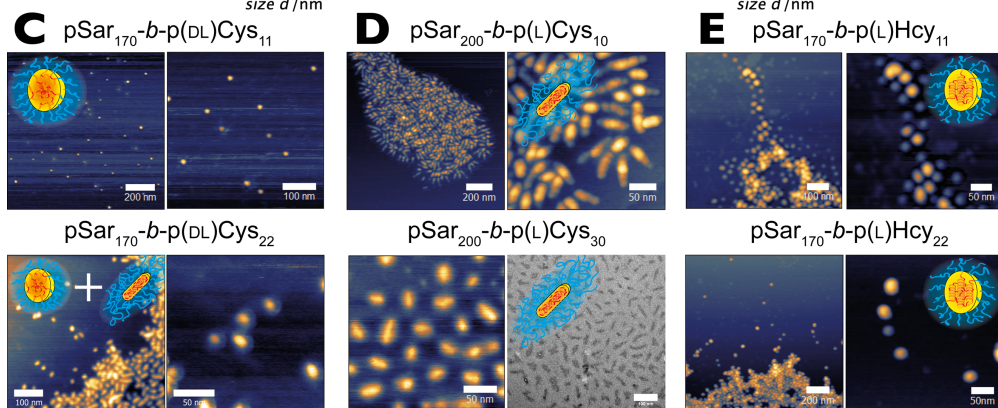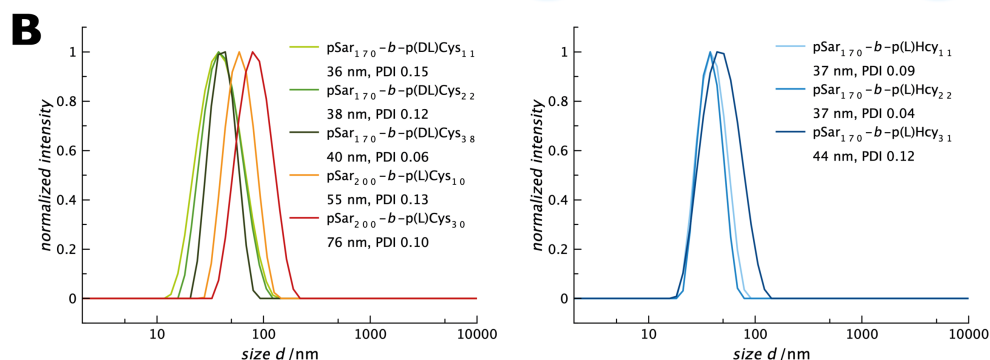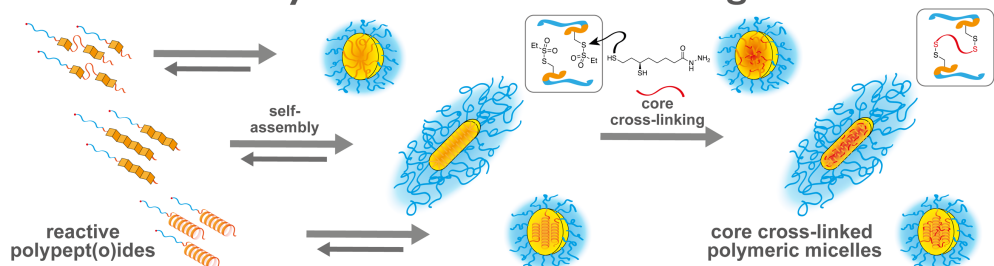
Figure 5. Self-assembly and core cross-linking. (**A**) Schematic illustration of secondary structure-driven self-assembly. (**B**) Single-angle DLS analysis of polymeric micelles (left: pSar-*b*-p(DL)Cys and pSar-*b*-p(L)Cys, right: pSar-*b*-p(L)Hcy). Morphological Analysis of core cross-linked polymeric micelles by AFM and cryoTEM: (**C**) pSar-*b*-p(DL)Cys, (**D**) pSar-*b*-p(L)Cys, (**E**) pSar-*b*-p(L)Hcy.

Finally, the findings on the aggregation behavior were transferred to the preparation of core cross-linked polymeric micelles (CCPMs) from the reactive polypept(o)ides, as illustrated in Figure 5A. The copolymers were dissolved in DMAc and equilibrated by addition of buffer at their respective turning points, before solvent exchange was completed by dialysis. When analyzed by DLS (Figure 5B), both, α-helical pSar-*b*-p(L)Hcy and racemic pSar-*b*-p(DL)Cys yielded small polymeric micelles of similar size (D_h 36-44 nm) and narrow PDI (0.04 - 0.15), despite increasing chain lengths of the respective hydrophobic blocks. In contrast, an increased size was detected for enantiopure pSar-*b*-p(L)Cys (D_h 55-76 nm) directing to larger structures for polymers with longer hydrophobic blocks. For further analysis, micelles were cross-linked by reaction of the *S*-ethylsulfonyl-group with dihydro lipoic acid hydrazide (3), and the morphology of the obtained disulfide cross-linked micelles was investigated by AFM (Figure 5C-E, Figure S5-S8). Of note, the cross-linking reaction did not influence the overall size distribution (Figure S4). Analysis by AFM revealed spherical structures with diameters well below 50 nm for CCPMs from racemic pSar-*b*-p(DL)Cys containing 15 wt.% p(DL)Cys, while spherical to slightly elongated particles could be observed for 26 wt.% p(DL)Cys (Figure 5C, Figure S5). As shown by AFM and cryoTEM (Figure 5D, Figure S6 - S7), solely worm-like micelles were obtained for pSar-*b*-p(L)Cys containing both, 12 or 29 wt.% of enantiopure p(L)Cys, which corresponds well with previous findings as well as with the larger sized determined by DLS.[50] Spherical CCPMs only were obtained from α-helical pSar-*b*-p(L)Hcy of 15 or 27 wt.% p(L)Hcy, as shown in Figure 5E and Figure S8.[70]

Taken together, secondary structure formation is a major parameter affecting the self-assembly of polypept(o)ides. In direct comparison, the reactive amphiphilic block copolymer with an α-helical segment, pSar-*b*-p(L)Hcy, only yielded spherical structures, whereas ß-sheets in enantiopure pSar-*b*-p(L)Cys strongly direct self-assembly to worm-like particles and even affect racemic pSar-*b*-p(DL)Cys with longer hydrophobic segments.

Conclusion

In conclusion, our head-to-head comparison underlines the influence of secondary structure formation on the aggregation and self-assembly of block copolypept(o)ides. Herein, we reported the successful synthesis of reactive, *S*-ethylsulfonyl-protected pSar-*b*-p(DL)Cys, pSar-*b*-p(L)Cys, and pSar-*b*-p(L)Hcy. Despite comparable primary structures, the secondary structure of these block

copolymers varies from disrupted ß-sheet to anti-parallel ß-sheet and α-helix, which impacts their tendency to self-assemble during the solvent switch. The anti-parallel ß-sheets of enantiopure pSar-*b*-p(L)Cys strongly induce early aggregation compared to the racemic pSar-*b*-p(DL)Cys counterpart and narrow the dynamic range. Moreover, the α-helix in pSar-*b*-p(L)Hcy, favors the formation of spherical structures, whereas ß-sheets direct self-assembly into worm-like micelles for enantiopure pSar-*b*-p(L)Cys and even influence the self-assembly of pSar-*b*-p(DL)Cys in which the anti-parallel orientation is disrupted by the racemic hydrophobic block. A detailed understanding of the secondary structure enables powerful control over the morphology of micellar assemblies and fine-tuning of particle properties beyond the hydrophilic-hydrophobic ratio. This implies a major significance for polypeptides as drug delivery systems and in materials science.

Author Contribution

Experiment design, polymer synthesis, nanoparticle preparation, AFM, and CD measurements were performed by T.A.B., J.I. contributed to polymer synthesis and nanoparticle formation, and C.M. contributed to polymer synthesis. B.W. performed cryoTEM analysis. The manuscript was written by T.A.B. and M.B. The project was supervised by M.B. All authors have given approval to the final version of the manuscript.

Notes

The authors declare the following competing financial interest(s): Matthias Barz holds the patent Thiol-protected amino acid derivatives and uses thereof WO2015169908A1.

Acknowledgement

Abbreviations

AFM, atomic force microscopy; Boc, *tert*-butyloxycarbonyl; CCPM, core cross-linked polymeric micelle; CD, circular dichroism; DLS, dynamic light scattering;

DMAc, *N*,*N*-dimethylacetamide; DMF, *N*,*N*-dimethylformamide; DMSO, dimethylsulfoxide; GPC, gel permeation chromatography; FT-IR spectroscopy, Fourier-transformed infrared spectroscopy; HFIP, 1,1,1,-3,3,3-hexafluoropropan-2-ol; MWCO, molecular weight cut-off; NCA, *N*-carboxyanhydride; pSar, polysarcosine; p(L)Cys, poly(*S*-ethylsulfonyl-L-cysteine); p(DL)Cys, poly(*S*-ethylsulfonyl-DL-cysteine); p(L)Hcy, poly(*S*-ethylsulfonyl-L-homocysteine); cryoTEM, cryogenic transmission electron microscopy.

References

(1)   Bonduelle, C. Secondary Structures of Synthetic Polypeptide Polymers. *Polym. Chem.* **2018**, *9* (13), 1517–1529.

(2)   Kricheldorf, H. R.; Müller, D. Secondary Structure of Peptides. *Polym. Bull.* **1983**, *10* (11–12), 513–520.

(3)   Deng, C.; Wu, J.; Cheng, R.; Meng, F.; Klok, H. A.; Zhong, Z. Functional Polypeptide and Hybrid Materials: Precision Synthesis via α-Amino Acid N-Carboxyanhydride Polymerization and Emerging Biomedical Applications. *Prog. Polym. Sci.* **2014**, *39* (2), 330–364.

(4)   van Beek, J. D.; Beaulieu, L.; Schäfer, H.; Demura, M.; Asakura, T.; Meier, B. H. Solid-State NMR Determination of the Secondary Structure of Samia Cynthia Ricini Silk. *Nature* **2000**, *405* (6790), 1077–1079.

(5)   Knight, D. P.; Vollrath, F. Liquid Crystalline Spinning of Spider Silk. *Nature* **2001**, *410* (6828), 541–548.

(6)   Wang, Z.; Cang, Y.; Kremer, F.; Thomas, E. L.; Fytas, G. Determination of the Complete Elasticity of Nephila Pilipes Spider Silk. *Biomacromolecules* **2020**, *21* (3), 1179–1185.

(7)   van Beek, J. D.; Hess, S.; Vollrath, F.; Meier, B. H. The Molecular Structure of Spider Dragline Silk: Folding and Orientation of the Protein Backbone. *Proc. Natl. Acad. Sci.* **2002**, *99* (16), 10266–10271.

(8)   Huesmann, D.; Birke, A.; Klinker, K.; Türk, S.; Räder, H. J.; Barz, M. Revisiting Secondary Structures in NCA Polymerization: Influences on the Analysis of Protected Polylysines. *Macromolecules* **2014**, *47* (3), 928–936.

(9)   Cheng, J.; Deming, T. J. Synthesis of Polypeptides by Ring-Opening Polymerization of α-Amino Acid N-Carboxyanhydrides. In *Peptide-Based Materials*; **2011**; Vol. 310, 1–26.

(10)   Huang, J.; Heise, A. Stimuli Responsive Synthetic Polypeptides Derived from N-Carboxyanhydride (NCA) Polymerisation. *Chem. Soc. Rev.* **2013**, *42* (17), 7373–7390.

(11)   Klok, H.-A.; Deming, T. J. Macromolecular Engineering of Polypeptides Using the Ring-Opening Polymerization of α-Amino Acid N-Carboxyanhydrides. In *Macromolecular Engineering*; Wiley-VCH Verlag GmbH & Co. KGaA: Weinheim, Germany, 2011; Vol. 1, pp 519–540.

(12)   Kricheldorf, H. R. Polypeptides and 100 Years of Chemistry of α-Amino Acid N-Carboxyanhydrides. *Angew. Chemie - Int. Ed.* **2006**, *45* (35), 5752–5784.

(13) Carlsen, A.; Lecommandoux, S. Self-Assembly of Polypeptide-Based Block Copolymer Amphiphiles. *Curr. Opin. Colloid Interface Sci.* **2009**, *14* (5), 329–339.

(14) Blout, E. R.; Idelson, M. Polypeptides. VI. Poly-α-L-Glutamic Acid: Preparation and Helix-Coil Conversions 1. *J. Am. Chem. Soc.* **1956**, *78* (2), 497–498.

(15) Lecommandoux, S.; Achard, M. F.; Langenwalter, J. F.; Klok, H. A. Self-Assembly of Rod-Coil Diblock Oligomers Based on α-Helical Peptides. *Macromolecules* **2001**, *34* (26), 9100–9111.

(16) Klok, H.-A.; Lecommandoux, S. Supramolecular Materials via Block Copolymer Self-Assembly. *Adv. Mater.* **2001**, *13* (16), 1217.

(17) Le Fer, G.; Wirotius, A.-L.; Brûlet, A.; Garanger, E.; Lecommandoux, S. Self-Assembly of Stimuli-Responsive Biohybrid Synthetic- b -Recombinant Block Copolypeptides. *Biomacromolecules* **2019**, *20* (1), 254–272.

(18) Yu, M.; Nowak, A. P.; Deming, T. J.; Pochan, D. J. Methylated Mono- and Diethyleneglycol Functionalized Polylysines: Nonionic, α-Helical, Water-Soluble Polypeptides. *J. Am. Chem. Soc.* **1999**, *121* (51), 12210–12211.

(19) Lu, H.; Wang, J.; Bai, Y.; Lang, J. W.; Liu, S.; Lin, Y.; Cheng, J. Ionic Polypeptides with Unusual Helical Stability. *Nat. Commun.* **2011**, *2* (1).

(20) Baumgartner, R.; Fu, H.; Song, Z.; Lin, Y.; Cheng, J. Cooperative Polymerization of α-Helices Induced by Macromolecular Architecture. *Nat. Chem.* **2017**, *9* (7), 614–622.

(21) Kramer, J. R.; Deming, T. J. Multimodal Switching of Conformation and Solubility in Homocysteine Derived Polypeptides. *J. Am. Chem. Soc.* **2014**, *136* (15), 5547–5550.

(22) Gharakhanian, E. G.; Deming, T. J. Chemoselective Synthesis of Functional Homocysteine Residues in Polypeptides and Peptides. *Chem. Commun.* **2016**, *52* (30), 5336–5339.

(23) Fu, X.; Shen, Y.; Fu, W.; Li, Z. Thermoresponsive Oligo(Ethylene Glycol) Functionalized Poly- l -Cysteine. *Macromolecules* **2013**, *46* (10), 3753–3760.

(24) Hwang, J.; Deming, T. J. Methylated Mono- and Di(Ethylene Glycol)-Functionalized ß-Sheet Forming Polypeptides. *Biomacromolecules* **2001**, *2* (1), 17–21.

(25) Deming, T. J. Synthesis of Side-Chain Modified Polypeptides. *Chem. Rev.* **2016**, *116* (3), 786–808.

(26) Klinker, K.; Barz, M. Polypept(o)Ides: Hybrid Systems Based on Polypeptides and Polypeptoids. *Macromol. Rapid Commun.* **2015**, *36* (22), 1943–1957.

(27) Sanborn, T. J.; Wu, C. W.; Zuckermann, R. N.; Barron, A. E. Extreme Stability of Helices Formed by Water-Soluble Poly-N-Substituted Glycines (Polypeptoids) with α-Chiral Side Chains. *Biopolymers* **2002**, *63* (1), 12–20.

(28) Mannige, R. V.; Haxton, T. K.; Proulx, C.; Robertson, E. J.; Battigelli, A.; Butterfoss, G. L.; Zuckermann, R. N.; Whitelam, S. Peptoid Nanosheets Exhibit a New Secondary-Structure Motif. *Nature* **2015**, *526* (7573), 415–420.

(29) Weber, B.; Birke, A.; Fischer, K.; Schmidt, M.; Barz, M. Solution Properties of Polysarcosine: From Absolute and Relative Molar Mass Determinations to Complement Activation. *Macromolecules* **2018**, *51* (7), 2653–2661.

(30) Barz, M.; Luxenhofer, R.; Zentel, R.; Vicent, M. J. Overcoming the PEG-Addiction:

Well-Defined Alternatives to PEG, from Structure–Property Relationships to Better Defined Therapeutics. *Polym. Chem.* **2011**, *2* (9), 1900–1918.

(31) Fetsch, C.; Grossmann, A.; Holz, L.; Nawroth, J. F.; Luxenhofer, R. Polypeptoids from N -Substituted Glycine N -Carboxyanhydrides: Hydrophilic, Hydrophobic, and Amphiphilic Polymers with Poisson Distribution. *Macromolecules* **2011**, *44* (17), 6746–6758.

(32) Lau, K. H. A.; Ren, C.; Sileika, T. S.; Park, S. H.; Szleifer, I.; Messersmith, P. B. Surface-Grafted Polysarcosine as a Peptoid Antifouling Polymer Brush. *Langmuir* **2012**, *28* (46), 16099–16107.

(33) Nogueira, S. S.; Schlegel, A.; Maxeiner, K.; Weber, B.; Barz, M.; Schroer, M. A.; Blanchet, C. E.; Svergun, D. I.; Ramishetti, S.; Peer, D.; Langguth, P.; Sahin, U.; Haas, H. Polysarcosine-Functionalized Lipid Nanoparticles for Therapeutic MRNA Delivery. *ACS Appl. Nano Mater.* **2020**, *3* (11), 10634–10645.

(34) Son, K.; Ueda, M.; Taguchi, K.; Maruyama, T.; Takeoka, S.; Ito, Y. Evasion of the Accelerated Blood Clearance Phenomenon by Polysarcosine Coating of Liposomes. *J. Control. Release* **2020**, *322* (March), 209–216.

(35) Melnyk, T.; Đorđević, S.; Conejos-Sánchez, I.; Vicent, M. J. Therapeutic Potential of Polypeptide-Based Conjugates: Rational Design and Analytical Tools That Can Boost Clinical Translation. *Adv. Drug Deliv. Rev.* **2020**, *160*, 136–169.

(36) Birke, A.; Huesmann, D.; Kelsch, A.; Weilbächer, M.; Xie, J.; Bros, M.; Bopp, T.; Becker, C.; Landfester, K.; Barz, M. Polypeptoid- Block -Polypeptide Copolymers: Synthesis, Characterization, and Application of Amphiphilic Block Copolypept(o)Ides in Drug Formulations and Miniemulsion Techniques. *Biomacromolecules* **2014**, *15* (2), 548–557.

(37) Birke, A.; Ling, J.; Barz, M. Polysarcosine-Containing Copolymers: Synthesis, Characterization, Self-Assembly, and Applications. *Prog. Polym. Sci.* **2018**, *81*, 163–208.

(38) Hörtz, C.; Birke, A.; Kaps, L.; Decker, S.; Wächtersbach, E.; Fischer, K.; Schuppan, D.; Barz, M.; Schmidt, M. Cylindrical Brush Polymers with Polysarcosine Side Chains: A Novel Biocompatible Carrier for Biomedical Applications. *Macromolecules* **2015**, *48* (7), 2074–2086.

(39) Skoulas, D.; Stuettgen, V.; Gaul, R.; Cryan, S. A.; Brayden, D. J.; Heise, A. Amphiphilic Star Polypept(o)Ides as Nanomeric Vectors in Mucosal Drug Delivery. *Biomacromolecules* **2020**, *21* (6), 2455–2462.

(40) Schwiertz, D.; Holm, R.; Barz, M. Facile Synthesis of Amphiphilic AB3 and A3B Miktoarm PeptoMiktoStars. *Polym. J.* **2020**, *52* (1), 119–132.

(41) England, R. M.; Moss, J. I.; Gunnarsson, A.; Parker, J. S.; Ashford, M. B. Synthesis and Characterization of Dendrimer-Based Polysarcosine Star Polymers: Well-Defined, Versatile Platforms Designed for Drug-Delivery Applications. *Biomacromolecules* **2020**, *21* (8), 3332–3341.

(42) Varlas, S.; Georgiou, P. G.; Bilalis, P.; Jones, J. R.; Hadjichristidis, N.; O'Reilly, R. K. Poly(Sarcosine)-Based Nano-Objects with Multi-Protease Resistance by Aqueous Photoinitiated Polymerization-Induced Self-Assembly (Photo-PISA). *Biomacromolecules* **2018**, *19* (11), 4453–4462.

(43) Combs, J. A.; DeNicola, G. M. The Non-Essential Amino Acid Cysteine Becomes

Essential for Tumor Proliferation and Survival. *Cancers (Basel).* **2019**, *11* (5), 678.

(44)   Yin, J.; Ren, W.; Yang, G.; Duan, J.; Huang, X.; Fang, R.; Li, C.; Li, T.; Yin, Y.; Hou, Y.; Kim, S. W.; Wu, G. L-Cysteine Metabolism and Its Nutritional Implications. *Mol. Nutr. Food Res.* **2016**, *60* (1), 134–146.

(45)   Sevier, C. S.; Kaiser, C. A. Formation and Transfer of Disulphide Bonds in Living Cells. *Nat. Rev. Mol. Cell Biol.* **2002**, *3* (11), 836–847.

(46)   Schäfer, O.; Huesmann, D.; Muhl, C.; Barz, M. Rethinking Cysteine Protective Groups: S -Alkylsulfonyl- l -Cysteines for Chemoselective Disulfide Formation. *Chem. - A Eur. J.* **2016**, *22* (50), 18085–18091.

(47)   Schäfer, O.; Huesmann, D.; Barz, M. Poly(S -Ethylsulfonyl- l -Cysteines) for Chemoselective Disulfide Formation. *Macromolecules* **2016**, *49* (21), 8146–8153.

(48)   Bauer, T. A.; Muhl, C.; Schollmeyer, D.; Barz, M. Racemic S -(Ethylsulfonyl)- Dl -cysteine N -Carboxyanhydrides Improve Chain Lengths and Monomer Conversion for B-Sheet-Controlled Ring-Opening Polymerization. *Macromol. Rapid Commun.* **2021**, *42* (8), 2000470.

(49)   Muhl, C.; Schäfer, O.; Bauer, T.; Räder, H.-J.; Barz, M. Poly(S -Ethylsulfonyl- l -Homocysteine): An α-Helical Polypeptide for Chemoselective Disulfide Formation. *Macromolecules* **2018**, *51* (20), 8188–8196.

(50)   Klinker, K.; Schäfer, O.; Huesmann, D.; Bauer, T.; Capelôa, L.; Braun, L.; Stergiou, N.; Schinnerer, M.; Dirisala, A.; Miyata, K.; Osada, K.; Cabral, H.; Kataoka, K.; Barz, M. Secondary-Structure-Driven Self-Assembly of Reactive Polypept(o)Ides: Controlling Size, Shape, and Function of Core Cross-Linked Nanostructures. *Angew. Chemie Int. Ed.* **2017**, *56* (32), 9608–9613.

(51)   Hassan, H. M. A.; Maltman, B. A. Mixed SAMs and MALDI-ToF MS: Preparation of N-Glycosylamine Derivative and Thioctic Acid Methyl Ester Bearing 1,2-Dithiolane Groups and Detection of Enzymatic Reaction on Au. *Bioorg. Chem.* **2012**, *40* (1), 6–9.

(52)   Koufaki, M.; Kiziridi, C.; Alexi, X.; Alexis, M. N. Design and Synthesis of Novel Neuroprotective 1,2-Dithiolane/Chroman Hybrids. *Bioorg. Med. Chem.* **2009**, *17* (17), 6432–6441.

(53)   Schäfer, O.; Klinker, K.; Braun, L.; Huesmann, D.; Schultze, J.; Koynov, K.; Barz, M. Combining Orthogonal Reactive Groups in Block Copolymers for Functional Nanoparticle Synthesis in a Single Step. *ACS Macro Lett.* **2017**, *6* (10), 1140–1145.

(54)   Idelson, M.; Blout, E. R. Polypeptides. XV. 1 Infrared Spectroscopy and the Kinetics of the Synthesis of Polypeptides: Primary Amine Initiated Reactions. *J. Am. Chem. Soc.* **1957**, *79* (15), 3948–3955.

(55)   Ulkoski, D.; Scholz, C. Synthesis and Application of Aurophilic Poly(Cysteine) and Poly(Cysteine)-Containing Copolymers. *Polymers (Basel).* **2017**, *9* (12), 500.

(56)   Mai, Y.; Eisenberg, A. Self-Assembly of Block Copolymers. *Chem. Soc. Rev.* **2012**, *41* (18), 5969–5985.

(57)   Zhang, L.; Eisenberg, A. Multiple Morphologies and Characteristics of "Crew-Cut" Micelle-like Aggregates of Polystyrene- b -Poly(Acrylic Acid) Diblock Copolymers in Aqueous Solutions. *J. Am. Chem. Soc.* **1996**, *118* (13), 3168–3181.

(58)   Lund, R.; Willner, L.; Monkenbusch, M.; Panine, P.; Narayanan, T.; Colmenero, J.; Richter, D. Structural Observation and Kinetic Pathway in the Formation of

Polymeric Micelles. *Phys. Rev. Lett.* **2009**, *102* (18), 1–4.

(59)   Pelton, J. T.; McLean, L. R. Spectroscopic Methods for Analysis of Protein Secondary Structure. *Anal. Biochem.* **2000**, *277* (2), 167–176.

(60)   Hu, X.; Kaplan, D.; Cebe, P. Determining Beta-Sheet Crystallinity in Fibrous Proteins by Thermal Analysis and Infrared Spectroscopy. *Macromolecules* **2006**, *39* (18), 6161–6170.

(61)   Goormaghtigh, E.; Ruysschaert, J. M.; Raussens, V. Evaluation of the Information Content in Infrared Spectra for Protein Secondary Structure Determination. *Biophys. J.* **2006**, *90* (8), 2946–2957.

(62)   Greenfield, N. J. Using Circular Dichroism Spectra to Estimate Protein Secondary Structure. *Nat. Protoc.* **2007**, *1* (6), 2876–2890.

(63)   Liu, G.; Dong, C. Photoresponsive Poly(S -(o -Nitrobenzyl)- l -Cysteine)- b -PEO from a l -Cysteine N -Carboxyanhydride Monomer: Synthesis, Self-Assembly, and Phototriggered Drug Release. *Biomacromolecules* **2012**, *13* (5), 1573–1583.

(64)   Jacobs, J.; Pavlović, D.; Prydderch, H.; Moradi, M. A.; Ibarboure, E.; Heuts, J. P. A.; Lecommandoux, S.; Heise, A. Polypeptide Nanoparticles Obtained from Emulsion Polymerization of Amino Acid N-Carboxyanhydrides. *J. Am. Chem. Soc.* **2019**, *141* (32), 12522–12526.

(65)   Fischer, K.; Schmidt, M. Pitfalls and Novel Applications of Particle Sizing by Dynamic Light Scattering. *Biomaterials* **2016**, *98*, 79–91.

(66)   Zhang, L.; Eisenberg, A. Thermodynamic vs Kinetic Aspects in the Formation and Morphological Transitions of Crew-Cut Aggregates Produced by Self-Assembly of Polystyrene- b -Poly(Acrylic Acid) Block Copolymers in Dilute Solution. *Macromolecules* **1999**, *32* (7), 2239–2249.

(67)   Zhang, L.; Shen, H.; Eisenberg, A. Phase Separation Behavior and Crew-Cut Micelle Formation of Polystyrene- b -Poly(Acrylic Acid) Copolymers in Solutions. *Macromolecules* **1997**, *30* (4), 1001–1011.

(68)   Gilroy, J. B.; Gädt, T.; Whittell, G. R.; Chabanne, L.; Mitchels, J. M.; Richardson, R. M.; Winnik, M. A.; Manners, I. Monodisperse Cylindrical Micelles by Crystallization-Driven Living Self-Assembly. *Nat. Chem.* **2010**, *2* (7), 566–570.

(69)   Kelley, E. G.; Murphy, R. P.; Seppala, J. E.; Smart, T. P.; Hann, S. D.; Sullivan, M. O.; Epps, T. H. Size Evolution of Highly Amphiphilic Macromolecular Solution Assemblies via a Distinct Bimodal Pathway. *Nat. Commun.* **2014**, *5* (1), 3599.

(70)   Mochida, Y.; Cabral, H.; Miura, Y.; Albertini, F.; Fukushima, S.; Osada, K.; Nishiyama, N.; Kataoka, K. Bundled Assembly of Helical Nanostructures in Polymeric Micelles Loaded with Platinum Drugs Enhancing Therapeutic Efficiency against Pancreatic Tumor. *ACS Nano* **2014**, *8* (7), 6724–6738.

Supporting Information

Results and Discussion

NCA-Polymerization with thiourea
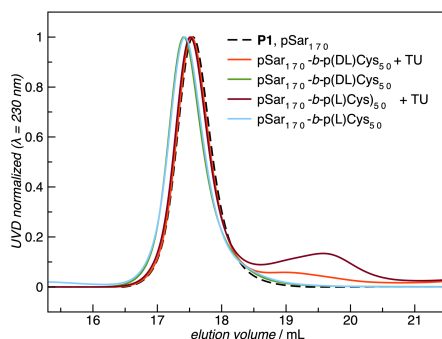
Figure S1. HFIP-GPC analysis of NCA polymerizations in the presence or absence of 1M thiourea in DMF. All polymerizations were performed with 50 eq. of DL-Cys(SO$_2$Et)- or L-Cys(SO$_2$Et)-NCA. No significant shift but only homopolymer formation was detected for polymerizations performed in the presence of 1M thiourea.
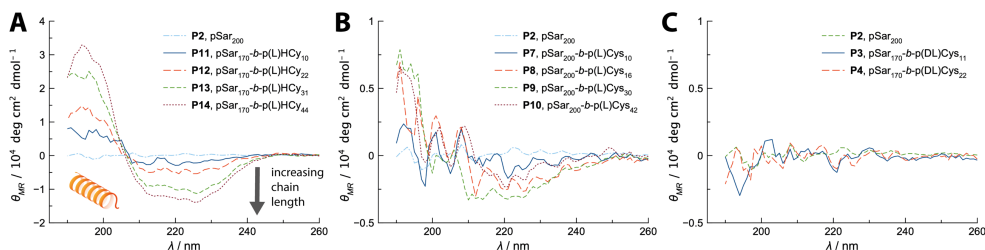
Figure S2. CD spectroscopy of polypept(o)ides P2 - P14. (**A**) pSar-*b*-p(L)Hcy. The α-helical secondary structure becomes more pronounced for growing chain lengths of p(L)Hcy. (**B**) pSar-*b*-p(L)Cys. No significant secondary structure detectable. (**C**) pSar-*b*-p(DL)Cys. No significant secondary structure detectable. Note that pSar significantly contributes to the overall absorbance limiting the resolution of this method.

Core Cross-Linked Polymeric Micelles
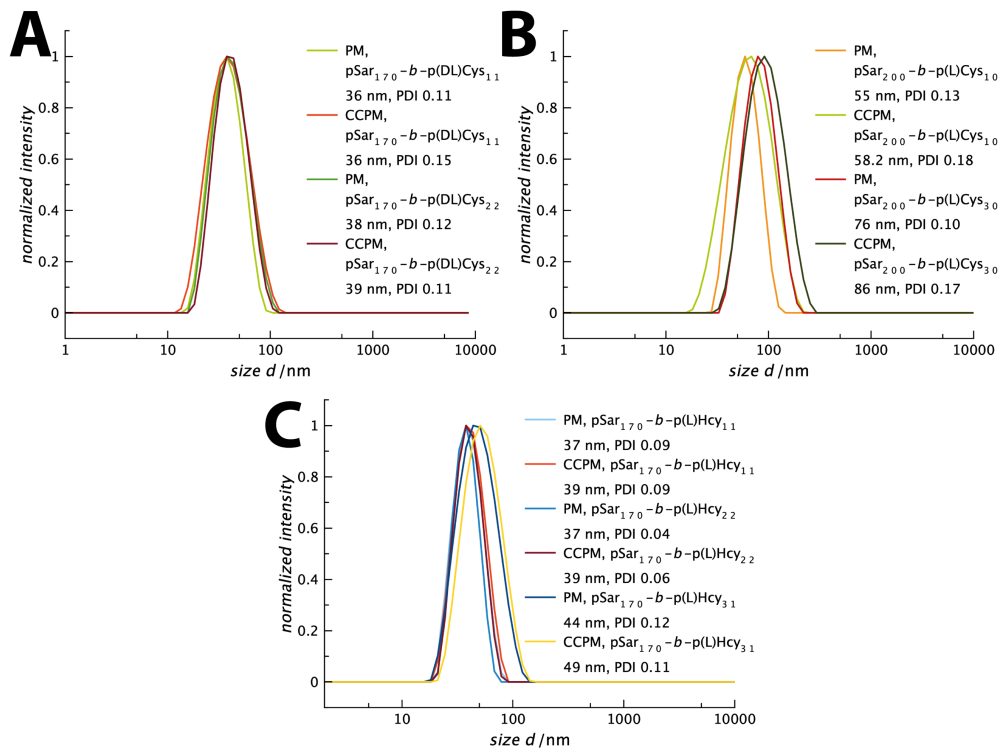
Figure S3. Single-Angle DLS analysis of polymeric micelles before (PM) and after cross-linking (CCPM). Nanoparticles were formed from (**A**) pSar-*b*-p(DL)Cys, (**B**) pSar-*b*-p(L)Cys, (**C**) pSar-*b*-p(L)Hcy.
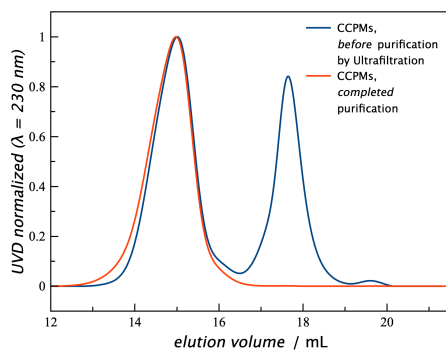
Figure S4. HFIP GPC analysis of CCPMs before and after purification by ultrafiltration (Amicon Ultra, MWCO 100kDa).
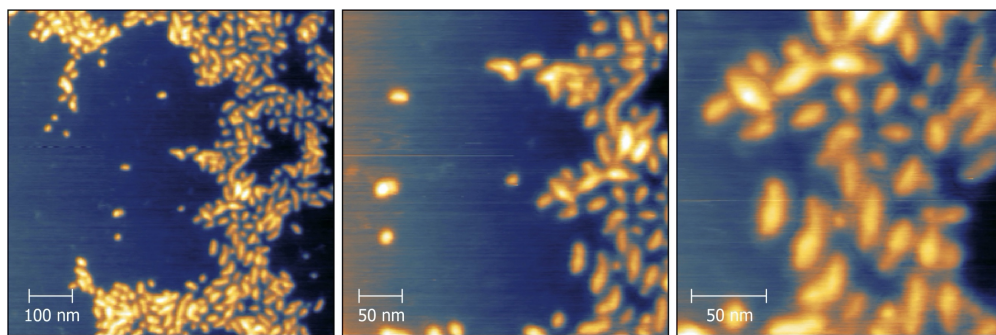
Figure S5. Additional AFM images of pSar$_{170}$-b-p(DL)Cys$_{22}$ (P4).
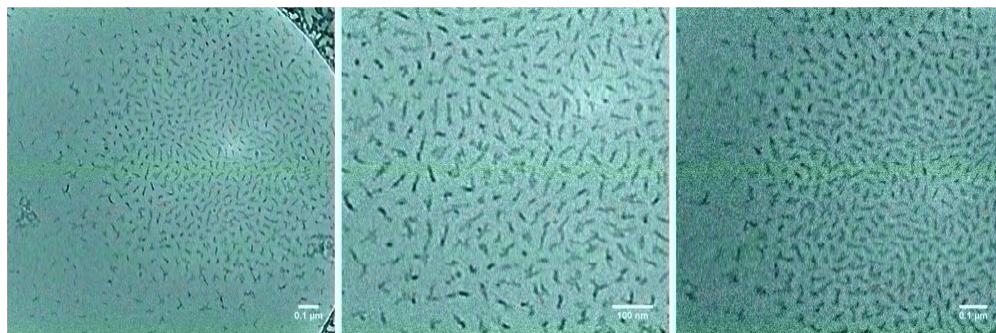
Figure S6. Additional CryoTEM images of pSar$_{200}$-b-p(L)Cys$_{30}$ (P9).
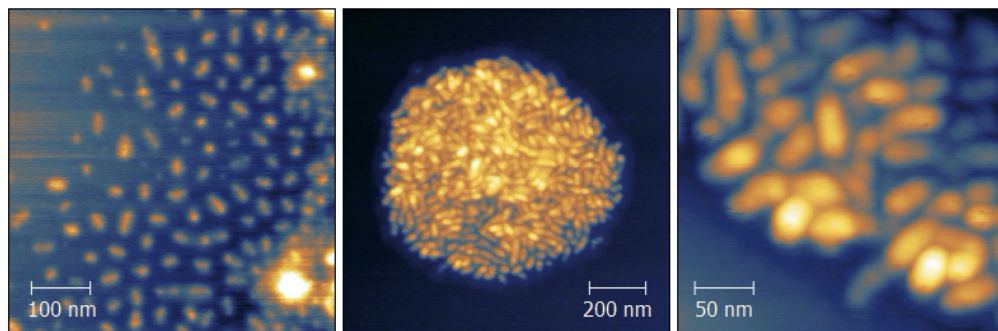
Figure S7. Additional AFM images of pSar$_{200}$-*b*-p(L)Cys$_{30}$ (P9).
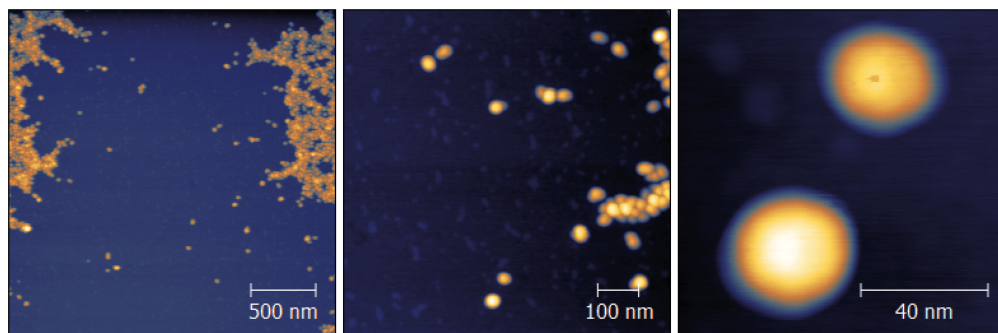
Figure S8. Additional AFM images of pSar$_{170}$-*b*-p(L)Hcy$_{22}$ (P12).

NMR-Data
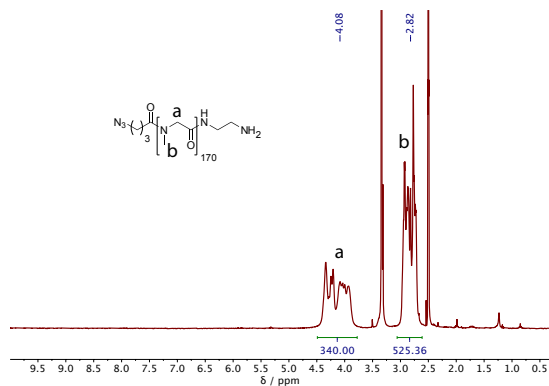
Figure S9. ^{1}H NMR analysis of **P1**, pSar$_{170}$, in DMSO-d_6.
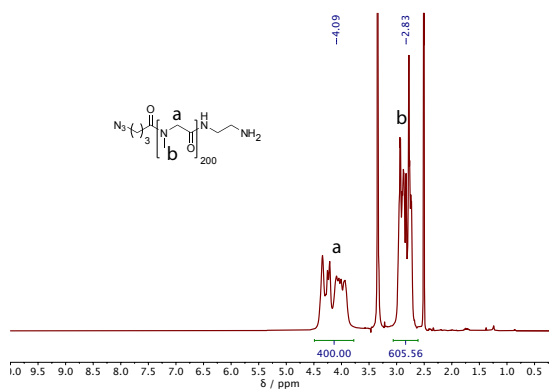
Figure S10. ^{1}H NMR analysis of **P2**, pSar$_{200}$, in DMSO-d_6.
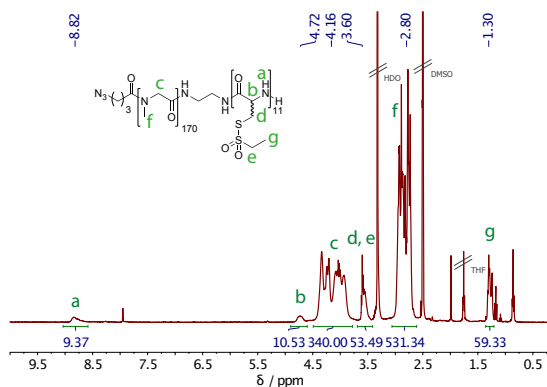
Figure S11. ^{1}H NMR analysis of **P3**, pSar$_{170}$-b-p(DL)Cys$_{11}$, in DMSO-d_6.
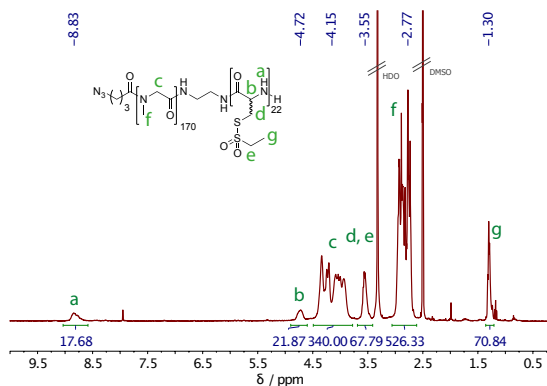
Figure S12. ^{1}H NMR analysis of **P4**, pSar$_{170}$-b-p(DL)Cys$_{22}$, in DMSO-d_6.
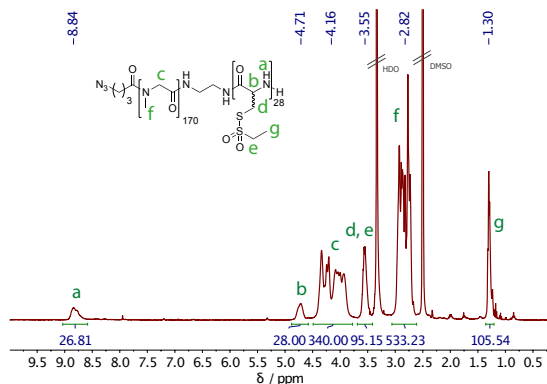
Figure S13. ^{1}H NMR Analysis of **P5**, pSar$_{170}$-b-p(DL)Cys$_{28}$, in DMSO-d_6.
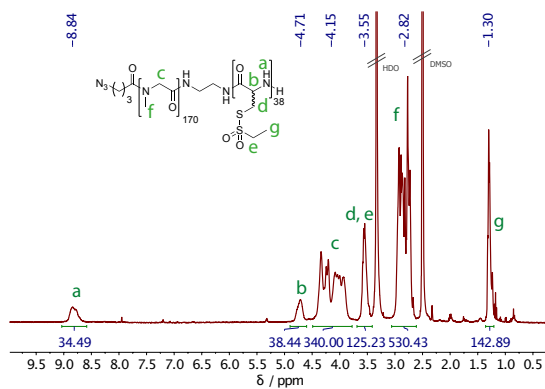
Figure S14. ^{1}H NMR analysis of **P6**, pSar$_{170}$-b-p(DL)Cys$_{38}$, in DMSO-d_6.
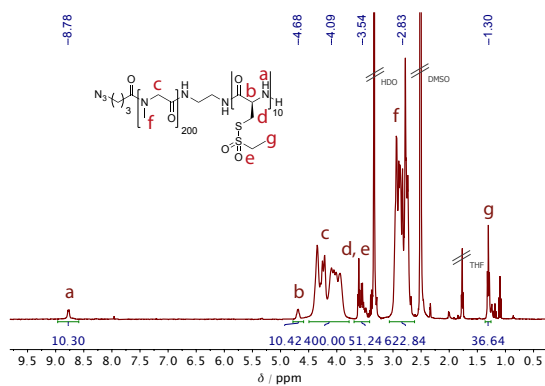
Figure S15. ^{1}H NMR analysis of **P7**, pSar$_{200}$-b-p(L)Cys$_{10}$, in DMSO-d_6.
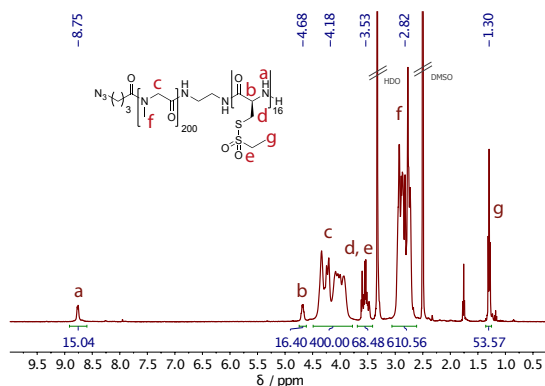
Figure S16. ^{1}H NMR Analysis of **P8**, pSar$_{200}$-b-p(L)Cys$_{16}$, in DMSO-d_6.
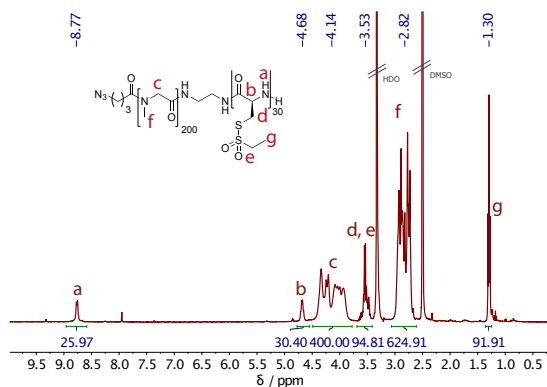
Figure S17. ^{1}H NMR analysis of **P9**, pSar$_{200}$-b-p(L)Cys$_{30}$, in DMSO-d_6.
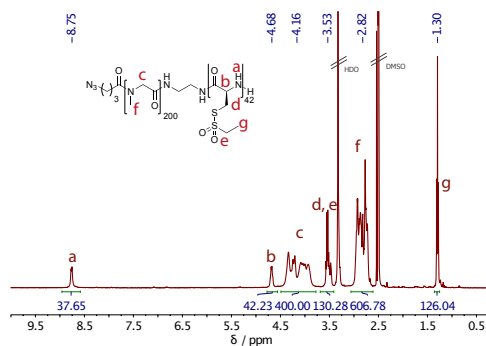
Figure S18. ^{1}H NMR analysis of **P10**, pSar$_{200}$-b-p(L)Cys$_{42}$, in DMSO-d_6.
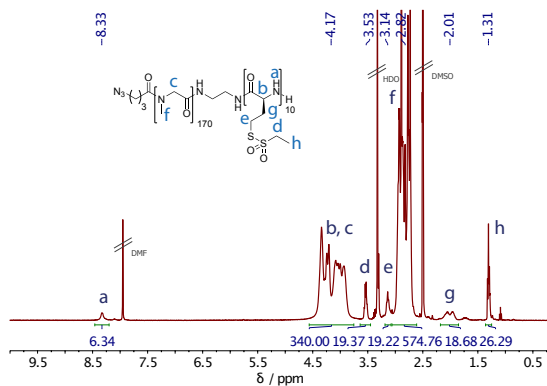
Figure S19. ^{1}H NMR analysis of **P11**, pSar$_{170}$-b-p(L)Hcy$_{10}$, in DMSO-d_6.
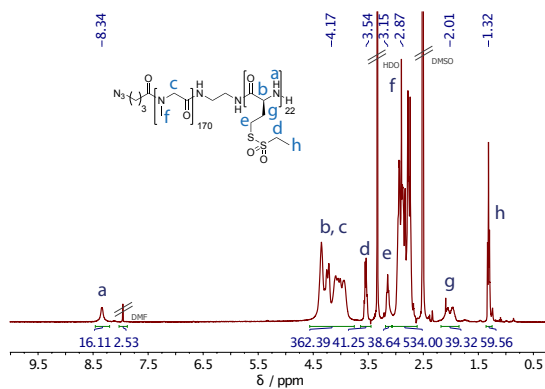
Figure S20. ^{1}H NMR analysis of **P12**, pSar$_{170}$-b-p(L)Hcy$_{22}$, in DMSO-d_6.
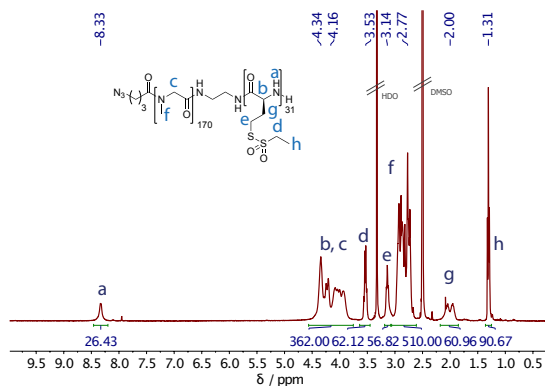
Figure S21. ^{1}H NMR Analysis of **P13**, pSar$_{170}$-b-p(L)Hcy$_{31}$, in DMSO-d_6.
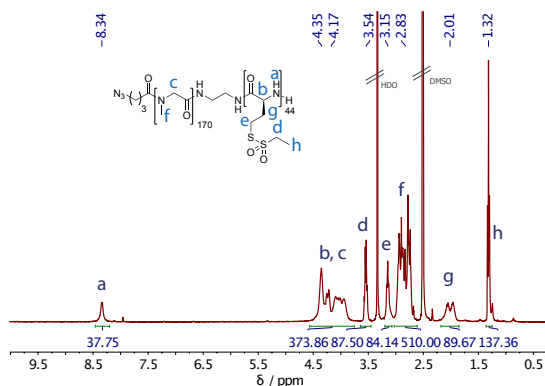
Figure S22. ^{1}H NMR analysis of **P14**, pSar$_{170}$-b-p(L)Hcy$_{42}$, in DMSO-d_6.
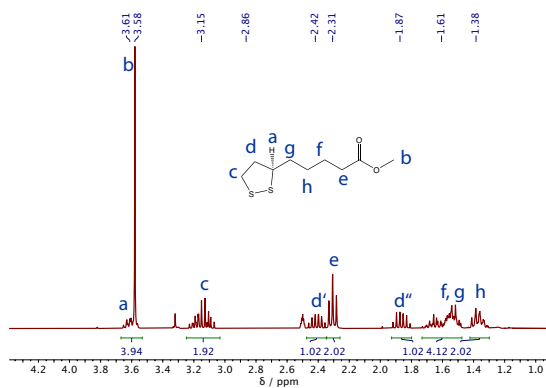
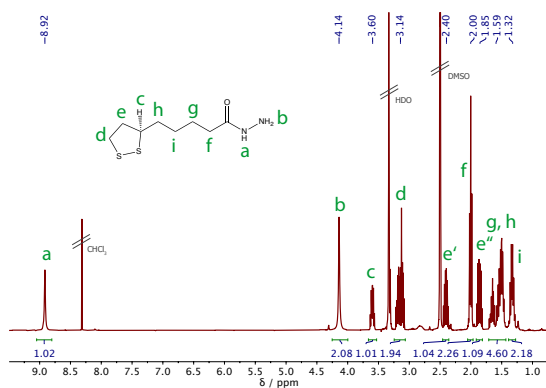**Figure S23.** ¹H NMR analysis of *R*-methyl lipoate (**2**) in DMSO-*d₆*.

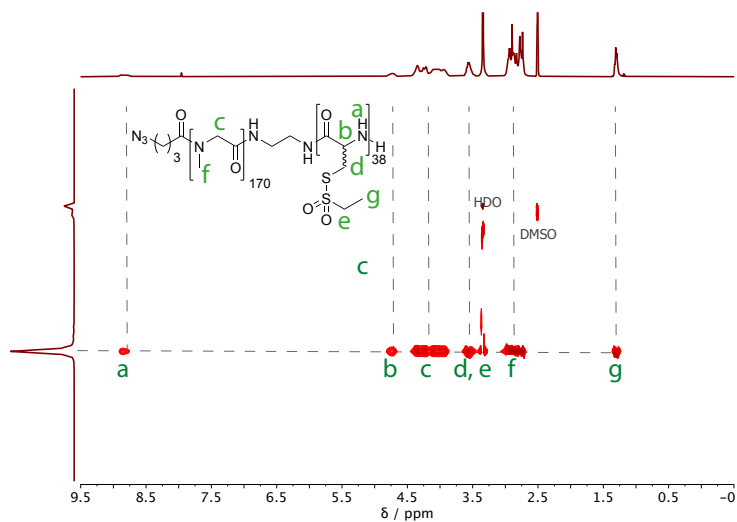**Figure S24.** ¹H NMR Analysis of *R*-lipoic acid hydrazide (**3**) in DMSO-*d₆*.

DOSY-NMRs

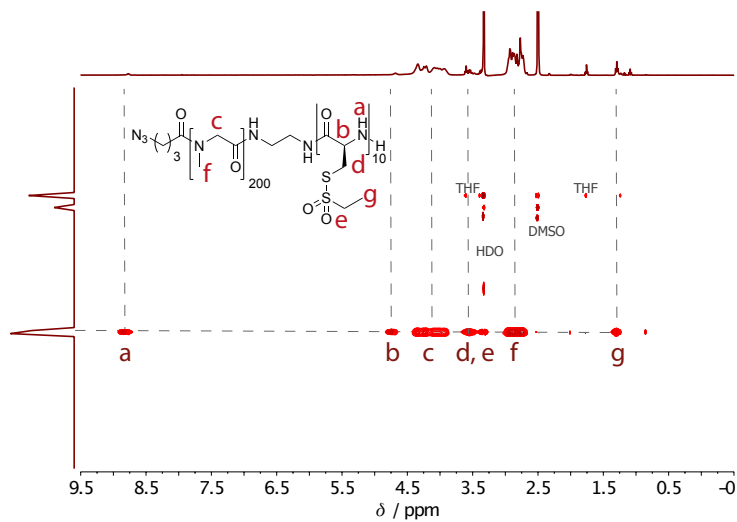**Figure S25.** DOSY NMR analysis of **P6**, pSar$_{170}$-b-p(DL)Cys$_{38}$, in DMSO-d_6.

Figure S26. DOSY NMR analysis of **P7**, pSar$_{200}$-b-p(L)Cys$_{10}$, in DMSO-d_6.
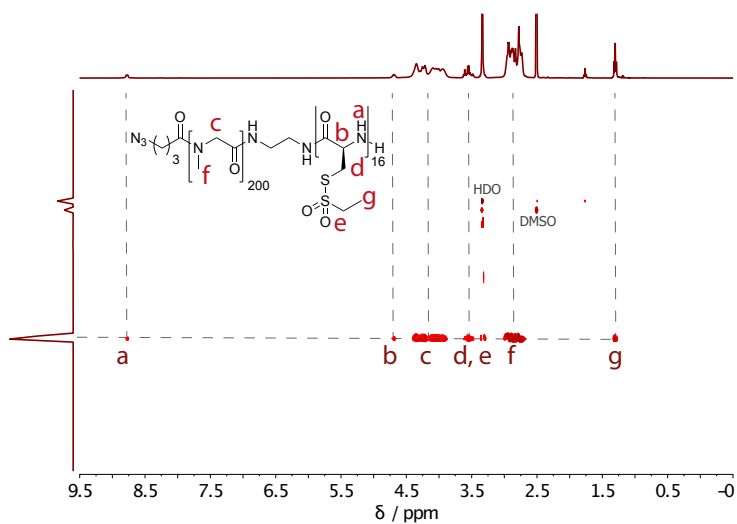
Figure S27. DOSY NMR analysis of **P8**, pSar$_{200}$-*b*-p(L)Cys$_{16}$, in DMSO-*d$_6$*.
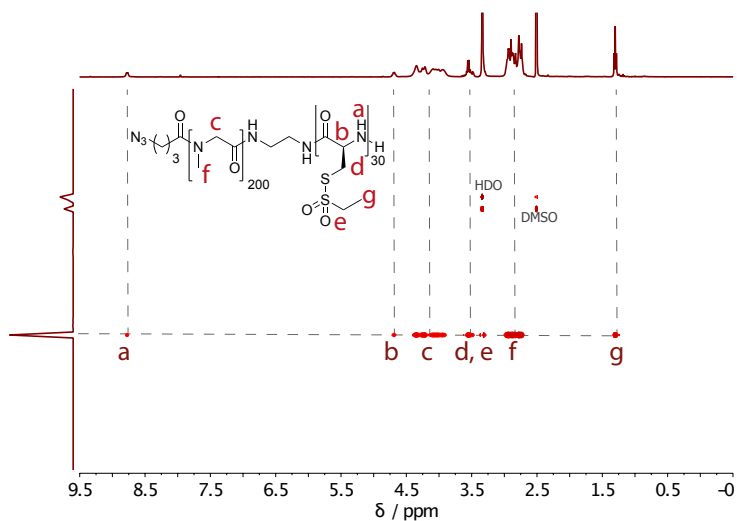
Figure S28. DOSY NMR analysis of **P9**, pSar$_{200}$-*b*-p(L)Cys$_{30}$, in DMSO-*d$_6$*.
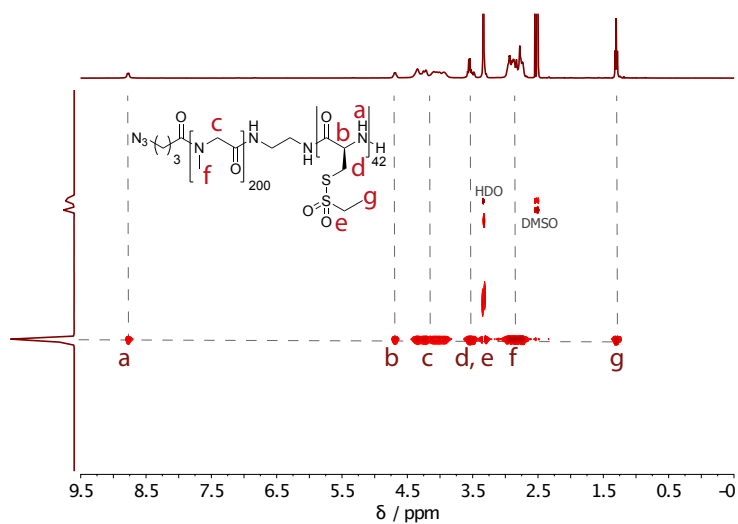
Figure S29. DOSY NMR analysis of **P10**, pSar$_{200}$-b-p(L)Cys$_{42}$, in DMSO-d_6.
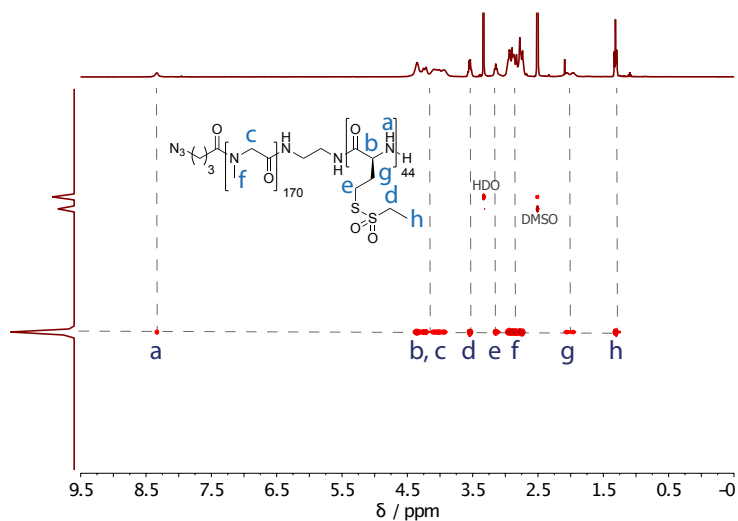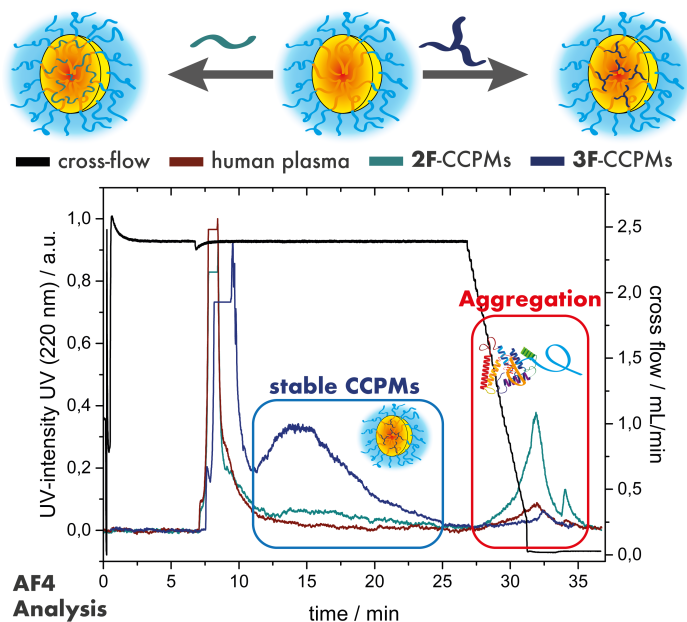

Figure S30. DOSY NMR analysis of **P14**, pSar$_{170}$-b-p(L)Hcy$_{44}$, in DMSO-d_6.

4

Tuning the Cross-Linking Density of Polymeric Micelles and its Implications on Particle Stability in Human Blood Plasma

to be submitted to Biomacromolecules.

Tuning the Cross-Linking Density of Polymeric Micelles and its Implications on Particle Stability in Human Blood Plasma

Tobias A. Bauer[a, b], Irina Alberg[b], Lydia A. Zengerling[b], Heyang Zhang[a], Pol Besenius[b], Kaloian Koynov[c], Bram Slütter[a], Rudolf Zentel[b], Matthias Barz[a, b,*]

[a] Leiden Academic Centre for Drug Research (LACDR), Leiden University, Einsteinweg 55, 2333 CC Leiden, The Netherlands

[b] Department of Chemistry, Johannes Gutenberg University Mainz, Duesbergweg 10-14, 55128 Mainz, Germany

[c] Max Planck Institute for Polymer Research, Ackermannweg 10, 55128 Mainz, Germany

Abstract

Core cross-linked polymeric micelles (CCPMs) are designed to improve the biodistribution of hydrophobic drugs aiming for an improved therapeutic profile. Compared to non-stabilized structures, cross-linking reduces the protein corona formation and prolongs the circulation half-life of the carrier. In this study, we provide details on how to tune the particle stability by using bi- or trifunctional cross-linkers and varying the length of the cross-linkable polymer block. For disulfide bond cross-linked polymeric micelles, amphiphilic thiol-reactive polypept(o)ides of polysarcosine-*block*-poly(*S*-ethylsulfonyl-L-cysteine) (pSar-*b*-pCys(SO_2Et)) are employed as the building block with pCys(SO_2Et) chain lengths of X_n = 17 or 30. For cross-linking, derivatives of dihydrolipoic acid and a sarcosine/cysteine pentapeptide are employed. Analysis by asymmetrical flow field-flow fraction (AF4) after incubation with human blood plasma clearly shows aggregate formation for non-cross-linked nanoparticles, yet surprisingly for CCPMs cross-linked with dihydrolipoic acid at X_n = 17. Increasing the cross-linking density leads to more stable nanoparticles in AF4, whereby a structure-activity relationship can be detected. Conversely, no differences are detectable by fluorescence correlation spectroscopy in human blood plasma or *in vivo* after intravenous administration to male C57BL/6 mice. In conclusion, our study provides a first insight on how to adjust CCPM stability for *in vivo* application as drug delivery systems.

Keywords

polymeric micelles · polypept(o)ides · AF4 ·cross-linking · nanomedicine

Introduction

Nanomedicine offers the potential to alter the biodistribution of active pharmaceutical ingredients (API) and may provide additional selectivity to the potent substances. For hydrophobic drugs, polymeric micelles are the preferred carrier system.[1,2] Within the core-shell architecture, the drug mainly resides in the inner hydrophobic core, and the hydrophilic corona provides solubility and shielding.[2,3] Following Nanomedicine 2.0 for drug targeting beyond replacing solubilizers, carrier and cargo need to be stabilized to prevent premature carrier disintegration and drug release immediately after administration.[4–6] The primary connection between amphiphilic copolymer and self-assembled polymeric micelle thus needs to be disrupted, by either non-covalent kinetic trapping (e.g., by π-π interactions, hydrogen bonding) or dynamic covalent bonds, i.e., by cross-linking.[6–9] Depending on the cargo, polymeric micelles can be cross-linked by individual strategies. For transition metal-complexes such as platin or ruthenium-based APIs, the drug itself can act as a cross-linker allowing for drug release upon ligand exchange.[10–13] Furthermore, click chemistry, amide bond formation, and free radical cross-linking are frequently employed to provide stability to polymeric micelles and allow, among others, for the conjugation of taxane and anthracycline (pro-) drugs.[14–17] Despite the early developed Genexol-PM and Nanoxel, non-cross-linked polymeric micelles (e.g., Bind-014, NK105) could not further demonstrate their superiority in clinical testing.[18,19] As a result, core cross-linked polymeric micelles (CCPMs) are considered the second generation of polymeric micelles and evolved to advanced stages of clinical testing. Currently, CPC634 containing conjugated docetaxel is examined for the treatment of ovarian cancer in clinical phase II, and NC-6004 comprising cisplatin is assessed in phase III for pancreatic cancer therapy.[19,20]

Due to the inherent potential for stable cross-linking yet reversible drug release after cellular uptake, disulfide bonds have attracted significant interest.[17,21] While disulfide cross-linked micelles can be readily formed from thiol-containing copolymers by oxidation with oxygen in a rather unspecific manner, the reactive *S*-alkylsulfonyl protecting group introduced by Schäfer *et al.* offers chemoselective disulfide bond formation.[22–25] Applied to cysteine or homocysteine the reactive group tolerates nucleophilic amine-initiated *N*-carboxyanhydride (NCA) polymerization and grants access to thiol-reactive polypeptides.[26–28] The combination of polypeptides with polysarcosine (pSar) in so-called polypept(o)ides is a straightforward approach leading to copolymers entirely based on endogenous

amino acids.[29,30] Polysarcosine, poly(*N*-methyl glycine), is an exclusive hydrogen bond acceptor characterized by random coil structure in aqueous solution matching all requirements stated by the Whitesides rules.[31,32] The hydrophilic pSar is thus considered the most promising alternative to poly(ethylene glycol) (PEG) for biomedical applications showing an improved safety profile such as a reduced induction of cytokine release.[33–37]

Beyond the intended chemical design of a nanoparticle, protein corona formation has been reported to determine the fate of many nanocarriers upon administration into the bloodstream.[38–41] Unambiguous signs of the protein corona were detected for nanoparticles with sharp and hydrophobic surfaces (e.g., polystyrene, silica nanoparticles) affecting the biological profile.[39,42–44] For nanoparticles with a smoothly decreasing radial density profile, such as CCPMs shielded with a dense corona of either PEG, pSar, or poly(*N*-(2-hydroxypropyl)methacrylamide), conversely, the absence of protein corona formation was observed.[40] Hereby, analysis by asymmetrical flow field-flow fractionation (AF4) was used to separate nanoparticles and nanoparticle/protein complexes after incubation with human blood plasma followed by high-resolution mass spectrometry.[40] Separation by AF4 relies solely on the diffusion of the analyte in the separation channel, whereby a parabolic flow profile is combined with an orthogonal cross-flow toward a semipermeable membrane.[45,46] Depending on Brownian motion, smaller structures elute earlier than larger assemblies or aggregates, while interactions with the static phase are minimized.[45,46] The interaction of blood plasma proteins with amphiphilic copolymers originating from insufficiently stabilized nanocarriers can thus be detected by AF4.[16,45,46] Non-cross-linked micelles are in constant equilibrium between unimers and micelles. Therefore, the situation is quite complex as the interaction of plasma proteins with amphiphilic polymers leads to defects in the hydrophilic shell. The defect sites are then prone to unspecific interaction, and the released free polymer may assemble to polymer/protein aggregates.[16,44,47]

The outlined strategies for core cross-linking could already demonstrate the potential to improve the carrier stability and control drug release *in vivo*.[48] Nevertheless, up to now, little attention was paid to the influence of the cross-linking itself, namely, how do cross-linker functionality and the length of the cross-linkable block contribute on the overall particle stability and in vivo performance. We now investigate the effect of the core size and length, and the valency of the cross-linker on the stability of polymeric micelles prepared from

thiol-reactive polysarcosine-*block*-poly(*S*-ethylsulfonyl-L-cysteine) using AF4 and fluorescence correlation spectroscopy (FCS) in human blood plasma for evaluation. We further correlate these results to the circulation half-life and biodistribution analysis after intravenous administration of CCPMs to C57BL/6 mice with the view toward defining parameters for CCPM stability.

Results and Discussion

Polymeric micelles are frequently applied as carrier systems for hydrophobic drugs, whereby cross-linking has already been demonstrated to improve the circulation time of the nanocarrier.[2,6,48] The aim of this study was to investigate whether the cross-linker or the length of the cross-linkable block has a relevant influence on the particle stability in human blood plasma. Therefore, functional cross-linkers were synthesized, and core cross-linked polymeric micelles prepared from polypept(o)ides building up on our previous reports.[49–51] As shown in Scheme 1, the polymeric micelles (PMs) were formed by self-assembly of thiol-reactive amphiphilic block copolymers of pSar-*b*-pCys(SO$_2$Et). In a second step, the *S*-ethylsulfonyl group was converted by chemoselective disulfide bond formation with the thiol-reagents. Thereby, the length of the cross-linkable pCys(SO$_2$Et) block was varied from X_n = 17 to 30 (PM$_{17/30}$), whereas the length of the pSar block was kept constant at X_n = 200 to provide sufficient steric shielding.

Since cross-linking itself is not sufficient to prevent premature drug release,[52] hydrazide-modified cross-linkers that grant stimuli-responsive drug conjugation were designed.[53] Even after the CCPM synthesis, these groups allow for coupling of ketone-bearing (pro-) drugs such as doxorubicine, epirubicine, or conjugates of taxanes with levulinic acid.[54] In detail, CCPMs were prepared from bifunctional dihydrolipoic acid hydrazide (2F-CL$_{17/30}$) and the trifunctional cysteine-sarcosine pentapeptide (3F-CL$_{17/30}$). The trifunctional pentapeptide was synthesized by solid-phase peptide synthesis, and the hydrazide linker was introduced *via* coupling with *N-tert*-butyloxycarbonyl-succinic acid monohydrazide in a consecutive step (Scheme S3). The alternating structure of sarcosine and cysteine was selected to provide solubility since pure polycysteine forms insoluble anti-parallel β-sheets that complicate the application.[55] As a control, non-cross-linked micelles were prepared by quenching the *S*-ethylsulfonyl group with monofunctional methyl 3-mercaptopropionate (NCL$_{17/30}$). The reagent was selected based on similar molecular weight and hydrophobicity compared to the
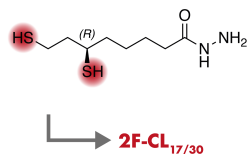
S-ethylsulfonyl group, while considering the odor nuisance and toxicity of small molecule thiol compounds such as ethanethiol.

Core Cross-Linked Polymeric Micelles
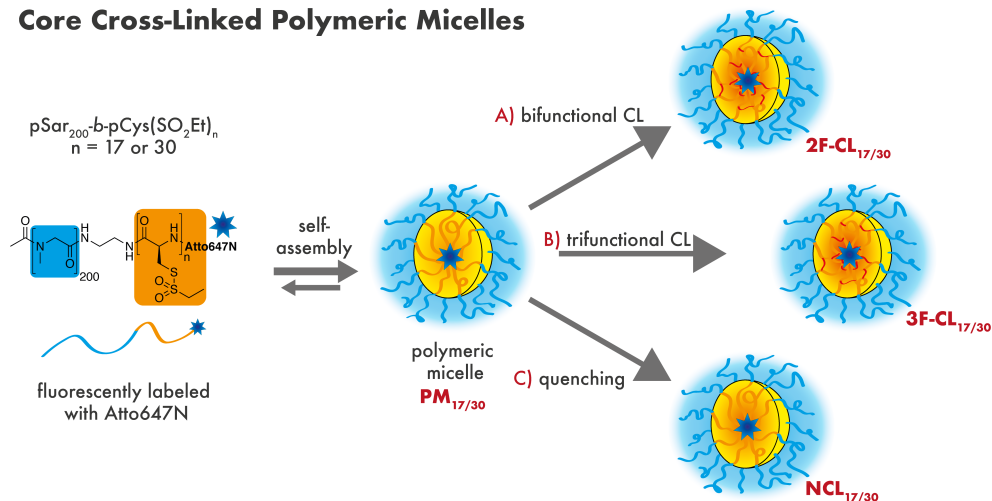
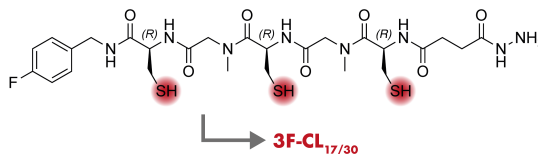

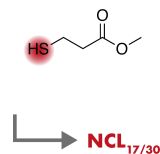**Scheme 1.** Preparation of core cross-linked polymeric micelles from pSar-*b*-pCys(SO$_2$Et)$_n$ with n = 17 or 30 and thiol-reagents of varying functionality.
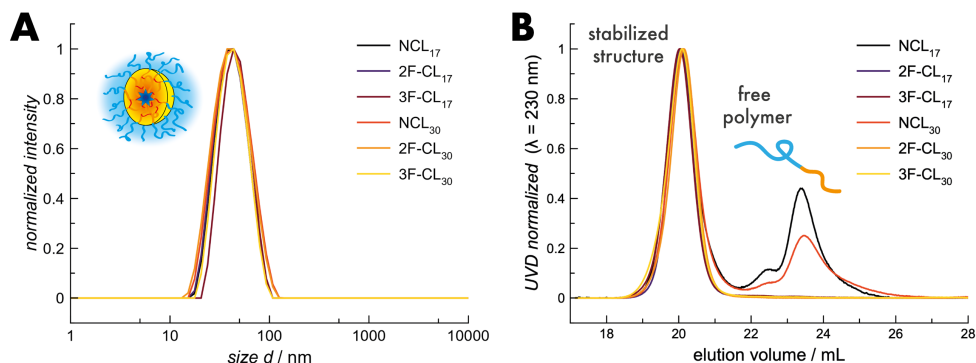

Figure 1. Nanoparticle characterization by DLS (**A**) and HFIP-GPC (**B**).

When analyzed by dynamic light scattering (DLS), all particles showed similar hydrodynamic diameters around 40 nm with narrow dispersities of 0.06 to 0.1 (Figure 1). The cross-linking or quenching reaction did thus not affect the overall size distribution.[50] Furthermore, for the cross-linked particles (2F-CL and 3F-CL) only stabilized structures but no unimers could be detected by HFIP-GPC after purification. Vice versa, significant amounts of free polymer could be detected for non-cross-linked particles. Despite the strong anti-parallel ß-sheet formation of pCys which accounts for the stabilized structures correlating with the chain length (free polymer content: NCL_{30} < NCL_{17}), a certain degree of cross-linking originating from disulfide-exchange reactions cannot be excluded.[56] Nevertheless, successful conversion of the *S*-ethylsulfonyl group could be verified by ^{1}H NMR, referring to the assigned methoxy group (Figure S2).

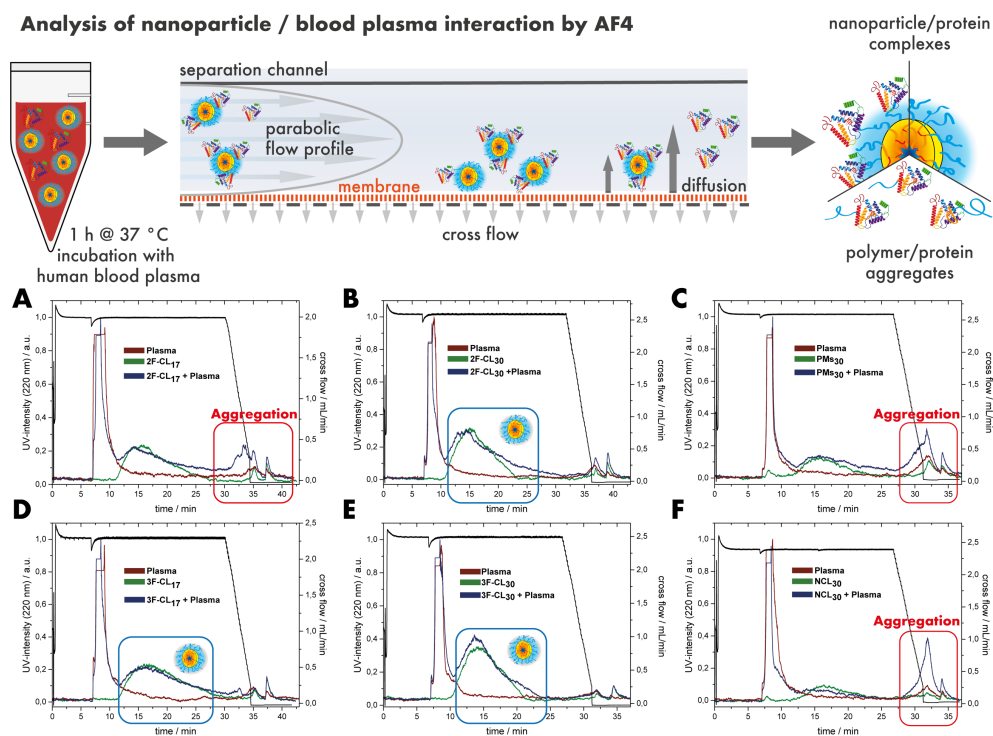**Figure 2.** Analysis of CCPMs by AF4 after incubation with human blood plasma. The results of the AF4 analysis as detected by UV absorbance (λ = 220 nm): CCPMs after incubation in PBS (green) or human blood plasma (blue), and plasma controls (red). The following particles have been used: 2F-CL$_{17}$ (**A**), 2F-CL$_{30}$ (**B**), PMs$_{30}$ (**C**), 3F-CL$_{17}$ (**D**), 3F-CL$_{30}$ (**E**), NCL$_{30}$ (**F**).

In the following, the polypept(o)ide-based nanoparticles were analyzed by AF4 and FCS in human blood plasma. The procedure of the AF4 analysis is shown in Figure 2. As illustrated, the samples were incubated in either PBS or human blood plasma for 1 h at 37 °C. Hereby, a regenerated cellulose membrane (pore size 10 kDa) and a cross flow of up to 2.5 mL/min was applied. The isolated nanoparticle-protein complexes or polymer/protein aggregates were then detected based on UV-absorbance and light scattering (LS) intensity. For well stabilized structures, identical elution profiles are expected regardless of the incubation in human plasma.[16,40]

For all samples incubated in PBS (green color), a distinct particle peak could be identified by the UV-detector at elution times of 10-20 min (Figure 2A-F). After incubation in human blood plasma, however, aggregate formation was detected when the cross flow was again reduced to 0 mL/min and a rinse-peak at 30-40 min became visible, as in the case of $2F\text{-}CL_{17}$ (Figure 2A). Since these nanoparticles were considered stable previously, showing no free polymer in HFIP-GPC, no aggregation when analyzed by multi-angle DLS after incubation in human blood plasma as well as decent circulation time in zebrafish embryos and mice,[49,57] this set the motivation for the detailed study. In fact, when the cross-linking density was enhanced by increasing the number of available net-points, the rinse peak could be reduced significantly following the sequence $2F\text{-}CL_{17} < 2F\text{-}CL_{30} < 3F\text{-}CL_{17} < 3F\text{-}CL_{30}$. Changing the cross-linker functionality from 2 to 3 appears slightly more effective for stabilization than (almost) doubling the cross-linkable polymer block, which reflects the gel-point theory for polymerization of multifunctional monomers (Carothers equation). In addition, for the CL_{30} species, the particle peak became slightly broader after incubation with blood plasma, which could indicate an increased protein corona formation.[40] On the other hand, for PM_{30} and NCL_{30} the particle peak almost entirely vanished after incubation in blood plasma leading to a strongly elevated rinse peak (Figure 2C and 2F). Beyond detection by UV-absorbance, light scattering is even more sensitive to large structures providing extra resolution to AF4. As shown in Figure 3, the insufficiently stabilized samples $2F\text{-}CL_{17}$, PM_{30}, and NCL_{30} show almost no particle peak but only a large fraction of aggregates after incubation with human blood plasma. Furthermore, the rinse peak practically disappeared for $3F\text{-}CL_{30}$ with intermediate intensities for $2F\text{-}CL_{30} > 3F\text{-}CL_{17}$ supporting the findings from the UV-detection.
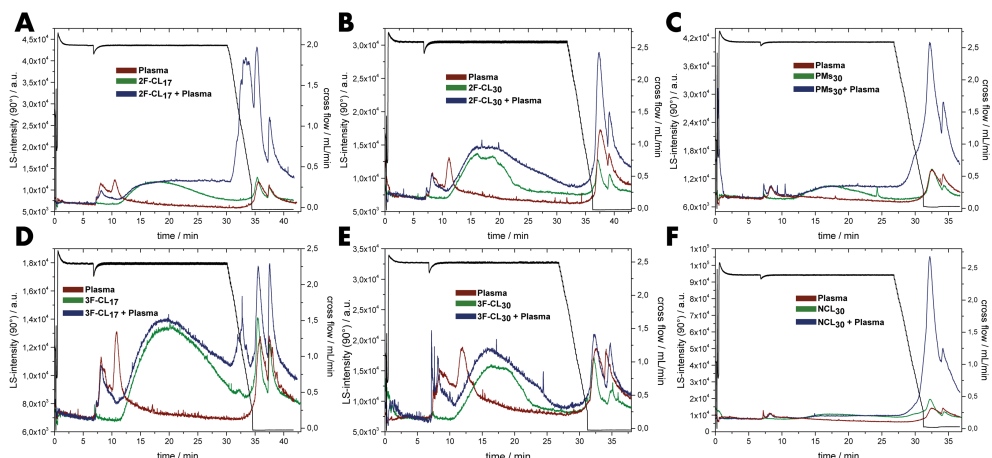
Figure 3. Results of the AF4 analysis as detected by light scattering (scattering angle: 90°): CCPMs after incubation in PBS (green) or human blood plasma (blue), and plasma controls (red). The following particles have been used: 2F-CL$_{17}$ (**A**), 2F-CL$_{30}$ (**B**), PMs$_{30}$ (**C**), 3F-CL$_{17}$ (**D**), 3F-CL$_{30}$ (**E**), NCL$_{30}$ (**F**).

Opposing on the trend of the particle stability revealed by AF4, analysis by FCS in human blood plasma did not detect any differences among the samples (Figure 4). In aqueous solution, hydrodynamic radii from 19 to 21 nm were detected for all particles, which is in good agreement with the results from DLS. In addition, no remaining free dye (Atto647N) could be detected. However, the exact same radii were calculated after incubation with human blood plasma regardless of cross-linking (2F-CL$_{17/30}$ and 3F-CL$_{17/30}$) or quenching (NCL$_{17/30}$). FCS is a precise method to determine the size of colloids, nanoparticles or proteins.[58] Moreover, following the procedure established by Negwer *et al.*, FCS can even be applied directly in human blood.[59] FCS relies on the diffusion of the fluorescent probe through the small confocal observation volume. The diffusion coefficient can be derived from the autocorrelation function translating to the hydrodynamic radius *via* the Stokes-Einstein relation. Alterations in the radius or the quality of the fit indicate interaction, aggregation, or protein corona formation with high sensitivity.[59,60] The unchanged radii of 19 to 21 nm thus indicate stable particles in both conditions.
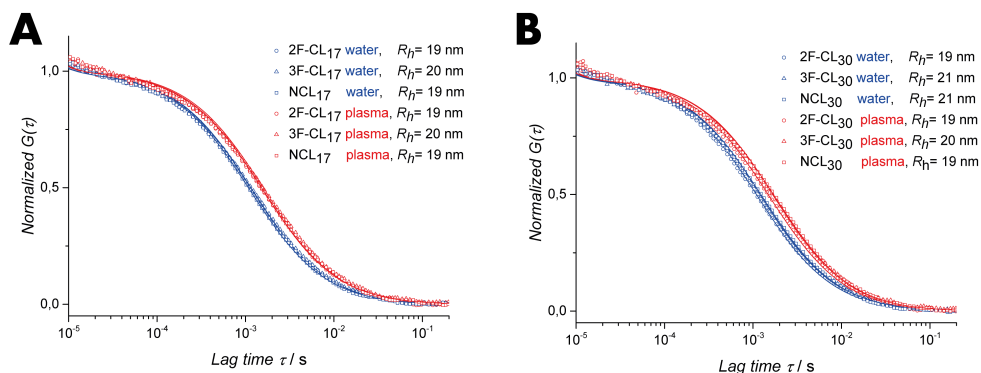
Figure 4. Results of the FCS analysis in water (blue) and plasma (red): The normalized autocorrelation functions $G(\tau)$ are given for nanoparticles prepared from pSar-*b*-pCys(SO$_2$Et)$_{17}$ (**A**) or pSar-*b*-pCys(SO$_2$Et)$_{30}$ (**B**) and monofunctional, bifunctional or trifunctional cross-linkers. The hydrodynamic radii were derived *via* the Stokes-Einstein relation.

To relate the contradictory results of the two screening techniques to the *in vivo* situation, the cross-linked (2F-CL$_{30}$ and 3F-CL$_{30}$) and not-cross-linked (NCL$_{30}$) nanoparticles were investigated for their circulation time and biodistribution. As displayed in Figure 5A, the nanoparticles were administered to C57BL/6 mice by intravenous injection, and blood samples were taken at the indicated time intervals and analyzed for nanoparticle-associated fluorescence. In addition, the tissue exposure was measured by *ex vivo* organ imaging after 72 h post injection. The results of the *in vivo* study are displayed in Figure 5, and all screening data are summarized in Table 1.
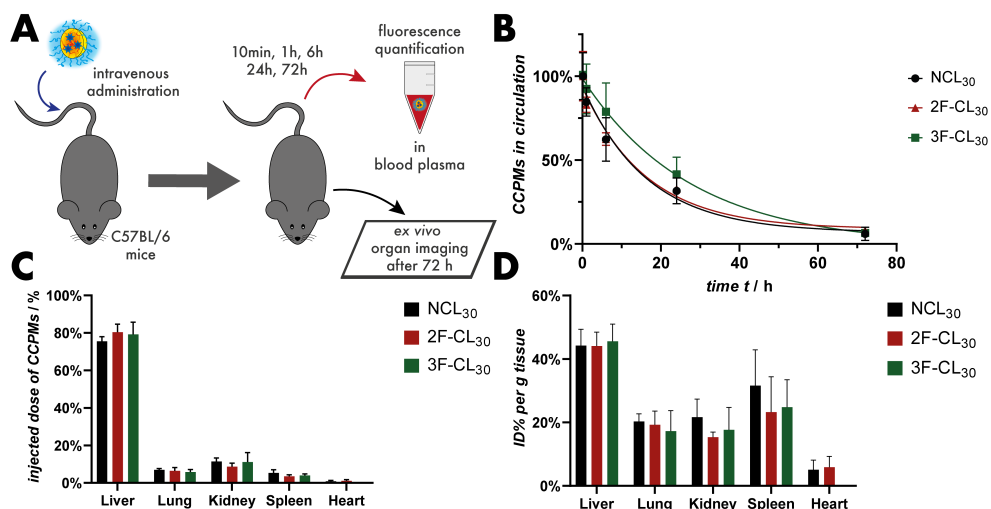
Figure 5. Evaluation of cross-linked and non-cross-linked polymeric micelles in C57BL/6 mice. Schematic illustration of the *in vivo* experiment (**A**). Nanoparticle circulation time analysis calculated from the nanoparticle fluorescence in blood plasma samples. Normalization to 10 min time point, fit model: mono-exponential decay (**B**). Nanoparticle biodistribution in liver, lungs, kidneys, spleen, and heart after 72 h post injection based on the total fluorescence intensity in *ex vivo* organ imaging (**C**). Nanoparticle biodistribution in liver, lungs, kidneys, spleen, and heart after 72 h post injection based on the fluorescence intensity relative to the organ weight in *ex vivo* organ imaging (**D**).

For all particle groups, circulation half-lives of 11.3 h - 19.1 h were detected. Interestingly, no clear trend could be derived among the treatment groups. Within the error of the mean ($N \geq 4$) and the calculated 95% confidence intervals (CI), no significances could be detected for any distinct time point or the circulation half-life. Nevertheless, compared to NCL_{30} and $2F\text{-}CL_{30}$, $3F\text{-}CL_{30}$ showed a slightly decreased clearance as higher particle contents could be detected at 6 h ($p \leq 0.265$) and 24 h ($p \leq 0.261$) post-administration. For the accumulation of the nanoparticles in the liver, lung, kidney, spleen, and heart no significant differences could be detected among the treatment groups. In absolute numbers, approx. 80% of the total fluorescence intensity were detected in the liver. Relative to the tissue weight, approx. 40% and 30% can be detected in liver and spleen. Since the liver is the major organ for nanoparticle clearance, the predominant accumulation could aid to improve the toxicologic profile of drugs with high toxicity to the heart (doxorubicine) or the kidneys (cisplatin), while the long circulation time sets the basis for passive tumor targeting via the EPR effect.[19,61,62]

Table 1. Summary of the nanoparticle characterization and evaluation.

particle	D_h / nm[a]	PDI[a]	R_h / nm[b]	R_h / nm[c]	AF4-score[d]	$t_{1/2}$ / h[e]	CI ($t_{1/2}$) / h[e]
NCL$_{17}$	39	0.06	19	19	-	-	-
2F-CL$_{17}$	39	0.09	19	19	3	-	-
3F-CL$_{17}$	43	0.08	20	20	2	-	-
NCL$_{30}$	40	0.09	21	19	4	11.4	6.8 - 18.7
2F-CL$_{30}$	38	0.10	19	19	2	11.3	7.4 - 17.1
3F-CL$_{30}$	40	0.07	21	20	1	19.1	12.3 - 34.8

[a] DLS in PBS; [b] FCS in PBS; [c] FCS with human plasma; [d] AF4 with human plasma, qualitative score: 1: no interaction detectable, 2: slight rinse peak detectable, 3: large rinse peak detectable, 4: large rinse peak detectable and particle peak vanished; [e] intravenous administration in C57BL/6 mice, fluorescence detection from plasma samples, fit model: mono-exponential decay.

Taken together, we applied AF4 and FCS to determine the stability of disulfide cross-linked polymeric micelles in human blood plasma with the aim to derive structure-activity relationships predicting the *in vivo* fate. AF4 analysis revealed a very detailed image of the nanoparticle properties, clearly linking the number of cross-linkable groups to the tendency to form polymer/protein aggregates. Conversely, FCS analysis in human plasma did not indicate any aggregation or undesired interaction of nanoparticles and blood plasma components. In a similar manner, upon intravenous administration, no differences could be detected for the circulation half-life or biodistribution of cross-linked or non-cross-linked particles based on pSar-*b*-pCys(SO$_2$Et). However, the error bars of the circulation time analysis are relatively large, preventing narrow confidence intervals. Furthermore, the 10 min time point, which was used for normalization, may have been selected too late, since initial drop values are typically observed for structures without additional stabilization.[63,64] Of note, even for the NCL particles additional stabilization by antiparallel ß-sheets needs to be taken into account, as well as possible cross-linking by disulfide shuffling, as mentioned above.[51,55,56] Despite the clear improvement of the particle stability as recognized by AF4 upon increasing the cross-linker functionality and the length of the cross-linkable section, it remains challenging to derive the quantitative means. In particular, light scattering is very sensitive to large structures ($I \sim r^6$), potentially overrating a small fraction of the sample. On the other hand, both, FCS and the *in vivo* experiment only refer to the particle fluorescence, and thus a number weighted

result, in which a small species may simply be overlooked. Considering the careful development of a medicinal product, all signs of aggregation or interaction of the product with blood plasma components need to be taken very seriously, as they may affect the patient compliance and the patient's life. Our findings thus provide a valuable insight on nanoparticle stability in human plasma and detection thereof.

Conclusion

We have investigated core cross-linked polymeric micelles for their stability in human blood plasma by AF4 and FCS and correlated the results to the biodistribution and circulation half-life after intravenous administration in C57BL/6 mice. Based on thiol-reactive polypept(o)ides of $pSar_{200}$-b-$pCys(SO_2Et)$, the length of the cross-linkable $pCys(SO_2Et)$ block was chosen 17 or 30. The polymeric micelles were cross-linked by linkers with varied functionality. Bifunctional dihydrolipoic acid hydrazide and a trifunctional Cys/Sar pentapeptide were used to generate core cross-linked particles. Monofunctional methyl 3-mercapto propionate was applied to convert the reactive S-ethylsulfonyl group into a disulfide bond without intending any cross-linking. After incubation in human blood plasma, AF4 analysis revealed a clear connection between the nanoparticle stability and the number of net points or the cross-linker functionality. Clear signs of aggregation could be detected for non-cross-linked structures. Opposing on these results, FCS analysis in human blood plasma did not detect any signs of aggregation or protein corona formation for any sample. Moreover, a similar biodistribution and comparable circulation half-times of 11.3 - 19.1 h were found for all nanoparticles, indicating no significant differences. The observed variances may be attributed to the sensitivity and detection modes of the analytical techniques. For the optimal design of nanomedicines, our findings demonstrate how the stability of CCPMs can be adjusted most efficiently.

Experimental Section

Materials and Methods: All solvents and reagents were used as received as purchased from Sigma-Aldrich, unless stated otherwise. Fmoc-L-cysteine(Trt)-OH, Fmoc-sarcosine, and 2-chlorotrityl chloride-resin were obtained from Iris Biotech GmbH, HFIP and trifluoroethanol (TFE) were purchased from Fluorochem, 1-[Bis(dimethylamino)methylene]-1H-1,2,3-triazolo[4,5-b]-pyridinium 3-oxide hexafluorophosphate (HATU) was obtained from Carbolution,

deuterated solvents were obtained from Deutero GmbH, and (*R*)-lipoic and was bought from TCI Europe. Atto647N *N*-hydroxysuccinimide (NHS) was obtain from Atto Tec GmbH. Tetrahydrofuran (THF) was dried over Na and was freshly distilled before use. *N,N*-Diisopropylethylamine (DIPEA) and *N,N*-triethylamine (NEt$_3$) were dried over sodium hydroxide, distilled, and stored at -20 °C until further use. *N,N*-Dimethylformamide (DMF) (99.8 %, extra dry over molecular sieve) was bought from Acros Organics and purified by freeze-pump-thaw cycles to remove dimethyl amine. MilliQ water was prepared by using a MILLI-Q Reference A+ System and used at a resistivity of 18.2 MΩ cm^{-1} and total organic carbon (TOC) content of ≤ 5 ppm.

Column chromatography: Qualitative thin layer chromatography (TLC) was performed on silica coated aluminum sheets (60 Å, F$_{254}$) with a fluorescence indicator from *Merck*. The detection of the analytes was performed with UV light (λ = 254 nm). Purification *via* size-exclusion chromatography (SEC) was performed using a Sephadex® LH-20 column with methanol or chloroform/methanol (1:1).

Gel Permeation Chromatography: For gel permeation chromatography (GPC), a Jasco GPC setup was used operating on a flow rate of 1.0 mL min^{-1} at 40°C. HFIP equipped with 3 g L^{-1} of potassium trifluoroacetate was used as eluent and toluene as the internal standard. Three PFG columns (particle size 7 µm, porosity 100 Å, 300 Å, and 4000 Å) were used for separation (PSS Polymer Standards Service GmbH, Germany), and poly(methyl methacrylate) standards (PSS Polymer Standards Service GmbH, Germany) and pSar standards were used for calibration.[31] A UV detector (UV-4070, λ = 230 nm) was used for polymer detection and data were analyzed using PSS WinGPC.

Infrared Spectroscopy: Attenuated total reflectance Fourier transform infrared (ATR-FT-IR) spectroscopy was performed on a FT/IR-4600 spectrometer (Jasco Corporation) equipped with a Jasco ATR Pro ONE unit using Jasco spectra manager 2.15.18 for data evaluation

Nuclear Magnetic Resonance: The NMR spectra were recorded at room temperature on Avance II 400, Avance III 400, Avance I 500, or Avance III 600 spectrometers (Bruker). DOSY NMR spectra were recorded on the Bruker Avance I 500 using a bipolar pulse program (stebpgp1s) with d20 = 0.2 and p30 = 2750 µs for gradient amplitudes from 5 to 95%. Spectra were calibrated

using the solvent signals and the data were analyzed using MestReNova 14.1.2 (Mestrelab Research S.L.).

Single-Angle Dynamic Light Scattering: DLS measurements were performed on a Zetasizer Ultra (Malvern Panalytical Ltd.) equipped with a He-Ne laser (λ = 632.8 nm). The measurements were performed at 25 °C and at a detection angle of 173° using disposable half-micro polystyrene cuvettes (Carl Roth GmbH & Co. KG, Germany). The cumulant size, polydispersity index (PDI), and size distribution histograms (intensity weighted) were derived from the autocorrelation function using automated position seeking and attenuator selection at multiple scans, with fluorescence filter.

Polymer Synthesis: The polymers were prepared by ring-opening NCA polymerization in anhydrous DMF using flame-dried glassware and Schlenk conditions. Sarcosine-NCA and *S*-ethylsulfonyl-L-cysteine-NCA were synthesized as published previously.[22,30]

Polysarcosine: The pSar macroinitiator was synthesized according to our previous reports.[50,51]

Briefly, sarcosine-NCA (9.18 g; 79.8 mmol; 220 eq.) was transferred to a flame-dried Schlenk tube and dissolved in degassed absolute DMF (50 mL). Next, *N*-(*tert*-butoxycarbonyl)-1,2-diaminoethane (58.1 mg; 363 µmol; 1.0 eq.) was added as a stock solution in dry DMF (β = 20 g·L^{-1}). The polymerization was stirred at 10 °C shielded from light until the monomer peaks had vanished in IR spectroscopy (9 days). Subsequently, the amine end-group was reacted with perfluorophenyl-4-azidobutanoate (215 mg; 725 µmol; 2.0 eq.) and DIPEA (308 µL; 1.81 mmol; 5.0 eq.). The reaction was stirred overnight. Next, acetic anhydride (346 µL; 3.63 mmol; 10 eq.) and DIPEA (1.23 mL; 7.25 mmol; 20 eq.) were added and the reaction was stirred for one day at room temperature. The polymer was precipitated in diethyl ether (500 mL), centrifuged (4500 rpm; 3 min; 4°C), and the pellet collected and was dried *in vacuo*. In the following, the Boc-group was cleaved. The crude polymer was transferred to a single-neck round-bottom flask and dissolved in water (25 mL). The solution was cooled to 0 °C and trifluoro acetic acid (25 mL) was added in one portion. The reaction mixture was stirred at 0 °C for 4 h. The solution was transferred into 3 dialysis bags (MWCO, 3.5 kDa) and dialyzed against water (2 medium changes), sodium hydrogen carbonate solution (8 medium changes), and water (8 medium changes). The polymer solution was filtered and lyophilized. Polysarcosine (P1) was obtained as

a colorless solid (4.04 g, 71%). Complete deprotection was verified by ^{1}H NMR (absence of the Boc-group signal at 1.37 ppm). The degree of polymerization was determined by HFIP GPC relative to pSar standards (DP = 200). ^{1}H NMR (500 MHz, DMSO-d_6): δ (ppm) 4.49 - 3.80 (m, 2nH, -CH$_2$), 3.03 - 2.66 (m, 3nH, -CH$_3$).

Polysarcosine-block-Poly(S-Ethylsulfonyl-L-Cysteine): The block copolypept(o)ides were synthesized following our previous reports.[50,51] The pSar macroinitiator (P1) (523 mg; 36.6 µmol; 1.0 eq.) was weighed into a flame dried Schlenk tube and the solid was dried by azeotropic distillation with toluene (2x). Next, pSar was dissolved in freshly degassed dry DMF (5.75 mL) and cooled to -10 °C. Then, *S*-ethylsulfonyl-L-cysteine NCA (438 mg; 1.83 mmol; 50 eq.) was added from a stock solution in dry DMF (ß = 200 g·L^{-1}). The reaction was performed at an overall NCA concentration of ß = 55 g·L^{-1}. The reaction progress was monitored by IR spectroscopy, and the reaction was stopped after 20 h, when a conversion of 38% was detected (correlating to DP 19). The polymer was precipitated in THF, and the suspension was centrifuged (4500 rpm; 5 min; 4 °C) and decanted. The procedure was repeated once with THF followed by diethyl ether for two times. The polymer was dried *in vacuo* yielding pSar$_{200}$-*b*-pCys(SO$_2$Et)$_{17}$ (P2) as a colorless solid (600 mg, 68%). For P3, pSar$_{200}$-*b*-pCys(SO$_2$Et)$_{30}$, the polymerization was performed at an overall NCA concentration of ß = 100 g·L^{-1} and the reaction was stopped at 60% conversion. For dye labeling, the copolymer (P2, 142 mg; 8.1 µmol; 1.0 eq.) was dissolved in DMSO, Atto647N-*N*-hydroxysuccinimide (2.59 mg; 3.08 µmol; 0.3 eq.) was added, and the solution was stirred at room temperature for 24 h. Subsequently, unconjugated dye was removed by repetitive precipitation in THF (4500 rpm, 3 min, 4°C), as verified by HFIP-GPC. ^{1}H NMR (500 MHz, DMSO-d_6): δ (ppm) 8.77 (b s, 1mH, CON*H*), 4.72 (m, 1mH, α-C*H*$_{(L-Cys)}$), 4.50 - 3.79 (m, 2nH, -C*H*$_{2(Sar)}$), 3.54 (m, 4mH, -S-C*H*$_2$, -SO$_2$-C*H*$_2$), 3.06 - 2.61 (m, 3nH, -CH$_{3(Sar)}$), 1.29 (t, J = 7.3 Hz, 3mH, -CH$_{3(L-Cys)}$).

Cross-Linker Syntheses: The bifunctional cross-linker (*R*)-lipoic acid hydrazide (3) was synthesized in a two-step procedure following our previous report (Scheme S1).[51]

(R)-Methyl Lipoate: (*R*)-Methyl lipoate (2) was prepared according to our previous report and the synthesis was adapted and modified from Hassan and Maltman.[51,65] (*R*)-Lipoic acid (1) (4.00 g; 19.4 mmol; 1.0 eq.) was dissolved in dry methanol (12 mL), and sulfuric acid (10.3 µL; 194 µmol; 0.01 eq.) was added. The reaction mixture was stirred at room temperature for 18 h and protected from

light. A yellow solid precipitated after 30 minutes. The yellow suspension was concentrated *in vacuo*, and the crude was dissolved in dichloromethane. The organic phase was washed with NaHCO$_3$ solution (3x) and brine (3x), dried over MgSO$_4$, filtered, and concentrated *in vacuo*. (*R*)-Methyl lipoate (**2**) was obtained as a yellow oil (3.84 g; 17.4 mmol; 90%) and used without further purification. ^{1}H NMR (400 MHz, DMSO-*d$_6$*): δ (ppm) 3.62 (m, 1H, -S-C*H*), 3.58 (s, 3H, -OC*H$_3$*), 3.15 (m, 2H, -S-C*H$_2$*), 2.40 (m, 1H, -S-CH$_2$-C*H$_2$*), 2.33 (t, *J* = 7.5 Hz, 2H, α-C*H$_2$*), 1.87 (m, 1H, -S-CH$_2$-C*H$_2$*), 1.73–1.61 (m, 4H, ß-C*H$_2$*, δ-C*H$_2$*), 1.39 (m, 2H, γ-C*H$_2$*).

(R)-Lipoic Acid Hydrazide: (*R*)-Lipoic acid hydrazide (**3**) was synthesized following our previous report, and the synthesis was adapted and modified from Koufaki *et al.*[51,66] (*R*)-Methyl lipoate (**2**) (2.00 g; 9.04 mmol; 1.0 eq.) was dissolved methanol (10 mL), and hydrazine hydrate (1.33 mL; 27.1 mmol; 3.0 equiv) was added to the yellow solution. The reaction mixture was stirred at room temperature for 96 h in the absence of light. The solution was concentrated *in vacuo* and dissolved in chloroform. The organic layer was washed with brine (3x), dried with MgSO$_4$, filtered, and concentrated *in vacuo*. (*R*)-Lipoic acid hydrazide (**3**) was obtained as a yellow oil (1.50 g; 6.78 mmol; 75%) and used without further purification. ^{1}H NMR (400 MHz, DMSO-*d$_6$*): δ (ppm) 8.91 (b s, 1H, -CON*H*), 4.14 (b s, 2H, -NH-N*H$_2$*), 3.60 (m, 1H, -S-C*H*), 3.11 (m, 2H, -SC*H$_2$*), 2.40 (m, 1H, -S-CH$_2$C*H$_2$*), 2.00 (t, *J* = 7.3 Hz, 2H, α-C*H$_2$*), 1.87 (m, 1H, -S-CH$_2$C*H$_2$*), 1.60-1.43 (m, 4H, -ß-C*H$_2$*, δ-C*H$_2$*), 1.40-1.27 (m, 2H, γ-C*H$_2$*).

Solid Phase Peptide Synthesis

Resin loading: Fmoc-L-cysteine(Trt)-OH (2.0 eq. relative to the resin loading capacity) was dissolved in DCM (10 mL·g^{-1} resin), and a small amount of DMF was added to aid solvation. The vessel (Merryfield Apparatus) was charged with 2-chlorotrityl chloride resin and the dissolved Fmoc-L-cysteine(Trt)-OH and DIPEA (each 2.0 eq. relative to resin loading capacity) were added. The mixture was shaken for 5 min before additional DIPEA (3.0 eq.) was added and, the reaction mixture was shaken for 1 h at room temperature. Subsequently, MeOH (1 mL·g^{-1} resin) was added, and the reaction mixture was shaken for 15 min. Next, the vessel was drained and washed with 10 mL of DCM (3 x), DMF (3 x), DCM (3 x), and MeOH (3 x). The loaded resin was dried under high vacuum overnight.

Peptide Synthesis: The following steps were performed on a CS136XT peptide synthesizer (CSBio Ltd.). The loaded resin was placed in a reaction vessel and DCM was added to induce swelling. To cleave the Fmoc-group, the DCM was

removed, and a piperidine solution (20% in DMF) was added, and the vessel was shaken for 20 min. The reaction mixture was drained, and the beads were washed with DMF (4x) and DCM (2x). In the next step, a solution of a Fmoc-protected amino acid (4.0 eq. relative to the resin loading capacity) in DMF, HATU (4.0 eq.), and DIPEA (6.0 eq.) were added to the reaction vessel. The reaction mixture was shaken for 4 h. After the completed reaction the resin was washed with DMF (2x) and DCM (1x), followed by the deprotection procedure. The Fmoc-deprotection step and the coupling reactions were repeated with respect to the targeted amino acid sequence (NH-Cys-Sar-Cys-Sar-Cys).

Cleavage of the Peptide from the Resin: The resin-bound peptide was transferred from the reaction vessel of the peptide synthesizer to a Merryfield Apparatus. A mixture of trifluoroethanol and DCM (2:8; 30 mL) was added, and the beads were shaken for 1 h. The vessel was drained, washed with DCM, and the procedure was repeated two times. The obtained solutions were combined and concentrated *in vacuo*. The peptide was precipitated into cold cyclohexane/diethyl ether (2:1), centrifuged, and lyophilized.

Peptide Modification

N-tert-Butyloxycarbonyl-Succinic Acid Monohydrazide (Boc-Hydrazine): Succinic anhydride (6) (3.3 g; 33.0 mmol; 1.0 eq.) and Boc-hydrazine (5) (4.36 g; 33.0 mmol; 1.0 eq) were placed in a flask and suspended in H_2O (60 mL). After 30 min, the solution turned clear. The solution was lyophilized, and *N-tert*-butyloxycarbonyl-succinic acid monohydrazide (7) (7.63 g; 33.0 mmol; quant.) was obtained as a colorless solid. The product was used without any further purification. ^{1}H NMR (400 MHz, DMSO-d_6): δ (ppm) 11.85 (bs, 1H, -COO*H*), 9.53 (s, 1H, -N*H*COCH2), 8.68 (s, 1H, -OCON*H*), 2.44-2.37 (m, 2H, -C*H*2), 2.33-2.29 (m, 2H, -C*H*2), 1.38 (s, 9H, -C*H*3). ^{13}C NMR (101 MHz, DMSO-d_6): *δ* (ppm) 173.6 (-*C*OOH), 170.8 (-NH*C*OCH3), 155.3 (-O*C*ONH), 83.6 (-*C*(CH3)3), 28.7 (-*C*H2), 28.1 (-*C*H3). ESI-HRMS (MeOH) (*m/z*): calculated for $[C_9H_{16}N_2O_5+H]^+$: 233.1132, found: 233.1136, calculated for $[C_9H_{16}N_2O_5+Na]^+$: 255.0951, found: 255.0958 .

Boc-Hydrazine-Cys(Trt)-Sar-Cys(Trt)-Sar-Cys(Trt)-OH: The peptide was synthesized according to the general procedures on SPPS with 1.72 g (1.6 mmol ·g⁻¹; 2.75 mmol) resin. The crude product was purified through FC on silica gel (DCM:EtOAc = 1:1 to DCM:EtOAc:MeOH = 5:3:2). After freeze drying, the product (8) was obtained as a colorless solid. ^{1}H NMR (400 MHz, DMSO-d_6): δ (ppm) 12.81 (s, 1H, -COO*H*), 9.52 (s, 1H, -N*H*COCH2), 8.68 (s, 1H, -OCON*H*), 8.60-8.55 (m, 1H, α-CHN*H*), 8.36-

8.20 (m, 2H, α-CHN*H*), 7.38-7.19 (m, 45H, -C*H*$_{arom.}$), 4.70-4.56 (m, 2H, α-C*H*), 4.26-3.60 (m, 5H, α-C*H*, α$_{Sar}$-C*H*$_2$), 2.72-2.62 (m, 6H, -NC*H*$_3$), 2.48 - 2.28 (m, 10H, -C*H*$_2$C*H*$_2$, -C*H*$_2$S), 1.39 (s, 9H, -(C*H*$_3$)$_3$). ESI-HRMS (MeOH) (*m/z*): calculated for [C$_{81}$H$_{83}$N$_7$O$_{10}$S$_3$+Na]$^+$: 1432.5256, found 1432.5254.

Boc-Hydrazine-Cys(Trt)-Sar-Cys(Trt)-Sar-Cys(Trt)-4-Fluorobenzylamine: Compound (8) (2.46 g; 1.74 mmol; 1.0 eq.) was dissolved in DMF (50 mL) and 4-fluorobenzylamine (654 mg; 5.22 mmol; 3.0 eq.), PyBOP (1.36 g; 2.61 mmol; 1.5 eq.), HOAt (237 mg; 1.74 mmol; 1.0 eq.) as well DIPEA (546 µL; 2.09 mmol; 1.2 eq.) were added. The reaction mixture was stirred overnight at RT. Further PyBOP (453 mg; 871 µmol; 0.5 eq.) and DIPEA (227 µl; 871 µmol; 0.5 eq.) were added and stirred for another two hours. The solvent was removed *in vacuo*, the crude was purified by SEC (CHCl$_3$:MeOH = 1:1) and the product (9) was obtained as a colorless solid (1.91 g; 1.74 mmol; 72%). ^{1}H NMR (400 MHz, DMSO-*d$_6$*): δ (ppm) = 9.52 (s, 1H, -N*H*COCH$_2$), 8.67 (s, 1H, -OCON*H*), 8.62-8.46 (m, 2H, αCH-N*H*), 8.35-8.17 (m, 2H, -N*H*CH$_2$), 7.33-7.19 (m, 47H, -C*H*$_{arom-Trityl}$, -CH$_2$CC*H*$_{arom}$), 7.09-6.96 (m, 2H, -C*H*$_{arom}$CF), 4.69-4.55 (m, 2H, α-C*H*), 4.39-4.24 (m, 3H, α-C*H*, -NHC*H*$_2$), 4.06-3.62 (m, 4H, α$_{Sar}$-C*H*$_2$), 2.68-2.60 (m, 6H, -NC*H*$_3$), 2.43-2.17 (m, 10H, -C*H*$_2$C*H*$_2$, -C*H*$_2$S), 1.38 (s, 9H, -(C*H*$_3$)$_3$). ^{19}F NMR (376 MHz, DMSO-*d$_6$*): δ (ppm) = -117.4 (CH$_{arom}$C*F*). ESI-HRMS (MeOH) (*m/z*): calculated for [C$_{88}$H$_{89}$FN$_8$O$_9$S$_3$+H]$^+$: 1517.5971 found: 1517.5969; calculated for [C$_{88}$H$_{89}$FN$_8$O$_9$S$_3$+Na]$^+$: 1539.5791, found: 1539.5796.

Hydrazine-Cys-Sar-Cys-Sar-Cys-4-Fluorobenzylamine: The protecting groups of compound (9) (1.01 g; 663 µmol; 1.0 eq.) were cleaved from the peptide with a mixture of TFA:TIPS:H$_2$O:Ethanedithiol (94 : 1 : 2.5 : 2.5 = 5 ml). The reaction mixture was stirred for 90 min and in the meantime the solution turned yellow. Then the solution was precipitated in a cold mixture of diethyl ether and pentane (1:1), centrifuged, the pellet dried in high vacuum and freeze dried. Not all the cleaved protecting groups could be removed through precipitation, therefore the peptide was solved in water (10 mL) and extracted with diethyl ether (3 x 15 mL). The aqueous layer was lyophilized, and the protecting group-free product (10) was obtained as a colorless solid (392 mg, 488 µmol, 74%). ^{1}H NMR (600 MHz, DMSO-*d$_6$*): δ (ppm) 10.63 (s, 1H, -N*H*COCH$_2$), 8.66-8.64 (m, 0.5H, α-CHN*H*), 8.58-8.55 (m, 1H, α-CHN*H*), 8.49-8.46 (m, 0.5H, α-CHN*H*), 8.39-8.36 (m, 1H, α-CHN*H*), 8.29-8.19 (m, 1H, α-CHN*H*), 7.30-7.28 (m, 2H, -CH$_2$CC*H*$_{arom}$), 7.15-7.11 (m, 2H, -C*H*$_{arom}$CF), 4.90-4.78 (m, 1H, α-C*H*), 4.72-4.54 (m, 1H, α-C*H*), 4.44-4.34 (m, 2H, α-C*H*), 4.30-4.27 (m, 2H, -NHC*H*$_2$), 4.24-3.82 (m, 4H, α$_{Sar}$-C*H*$_2$), 3.08-3.02 (m, 4H,

n), 2.86-2.69 (m, 6H, -NCH_3), 2.62-2.52 (m, 4H, -CH_2CH_2), 2.47-2.24 (m, 6H, -CH_2S). ^{19}F NMR (376 MHz, DMSO-d_6): δ (ppm) -74.7 (CF$_3$), -117.4 (CH$_{arom}$CF). ESI-HRMS (MeOH) (m/z): calculated for [C$_{26}$H$_{40}$FN$_8$O$_7$S$_3$+H]$^+$: 691.2161 found: 691.2146; calculated for [C$_{88}$H$_{89}$FN$_8$O$_9$S$_3$+Na]$^+$: 713.198, found: 713.197.

Polymeric Micelles: The preparation of core cross-linked polymeric micelles (CCPMs) was adapted and modified from our previous reports.[50,51] Briefly, Atto 647N labeled pSar$_{200}$-b-p(L)Cys(SO$_2$Et)$_{17/30}$, was dissolved in DMSO (β = 7.5 g·L^{-1}) equipped with 1 M thiourea. After 1 h, 20 vol.% 1 mM acetate buffer (pH 4.75) containing 10 mM thiourea was added, and the solution was left to equilibrate at room temperature for 4 h. The solution was placed into a dialysis bag and dialyzed with 1 mm acetate buffer (pH 4.75, 10 mM thiourea), and the solvent was changed 4 times. The solution was filtered by syringe filter (PVDF; 450 nm) and concentrated to 7 g·L^{-1} by spin filtration (Amicon Ultra; MWCO, 3 kDa), yielding the polymeric micelles (PMs). In a following step, the PMs were treated with (A) (R)-dihydrolipoic acid hydrazide (4) for 2F-CL$_{17/30}$, (B) the cys/sar pentapeptide (10) for 3F-CL$_{17/30}$, or (C) with methyl 3-mercaptopropionate for NCL$_{17/30}$ at equimolar amounts of thiols per S-ethylsulfonyl-L-cysteine.

For cross-linking with bifunctional (R)-dihydrolipoic acid hydrazide (4), (R)-lipoic acid hydrazide (3) was dissolved in ethanol at a concentration of β = 20 g·L^{-1}, and 0.5 equivalents of tris(2-carboxyethyl)phosphine hydrochloride (TCEP·HCl) (β = 50 g·L^{-1} in water) were added. After reaction for 18 h, the cross-linker solution (4) was added to the PMs. For cross-linking with trifunctional Cys/Sar pentapeptide (10), the cross-linker was dissolved in ethanol at a concentration of β = 20 g·L^{-1} and added to the PMs. After 48 h of reaction, the CCPM solutions were dialyzed against DMSO/water mixtures (1/1; MWCO, 6-8 kDa) and water, followed by repetitive spin filtration (Amicon Ultra; MWCO, 100 kDa) to remove residual cross-linker and free polymer, as verified by HFIP-GPC.

For quenching with monofunctional methyl 3-mercaptopropionate, the thiol-reagent was dissolved in ethanol at a concentration of β = 20 g·L^{-1} and added to the PMs. After 48 h of reaction, the NCL particles were dialyzed against ethanol/water mixtures (1/2; MWCO, 3 kDa) and water, followed by concentration via spin filtration (Amicon Ultra; MWCO, 3 kDa). The final particle concentrations were determined from lyophilization of aliquots.

AF4-Analysis: A 20-fold stock solution of the used phosphate buffered saline (PBS) was prepared out of sodium chloride, potassium chloride, disodium phosphate and

potassium phosphate with a final salt concentration of 151.7 mmol·L⁻¹, further containing 0.2 mmol·L⁻¹ sodium azide. The stock solution was filtered (Millipore GHP 0.22 µm) before using it in the AF4 system. Human blood plasma was provided from the transfusion center of the Medical Department of the Johannes Gutenberg-University Mainz. It was pooled of six healthy donors and stabilized with EDTA.

The nanoparticles (30 g·L⁻¹) were incubated with EDTA-stabilized, pure and undiluted plasma 1:1 (v:v) at 37 °C for 1 h. For a sufficient separation the AF4 is limited to a maximal plasma concentration of 5 vol%. Therefore, after incubation time, the samples were diluted with PBS to a particle concentration of 1.5 g·L⁻¹ corresponding to a 5 vol% solution of plasma in PBS. Samples were measured by AF4 immediately after preparation.

The AF4 measurements were performed using an installation from the ConSenxuS GmbH using a constaMETRICR 3200 main pump, a Spectra Series UV150 detector (Thermos Separation), a Dark V3 LS Detector (ConSenxuS GmbH), a Pharmacia P-3500 injection pump, a LV-F flow controller (HORIBA ATEC), and an In-Line Degasser-AF (Waters). A separation channel with a 190 µm spacer and a regenerated cellulose membrane with a molecular weight cut-off of 10 kDa suitable for protein separation was used.[67] The UV absorption was detected at 220 nm. For all measurements PBS (151.7 mM) containing 0.2 mmol·L⁻¹ sodium azide was used as the solvent. The main flow was 1 mL·min⁻¹ higher than the crossflow for every measurement. The crossflow is illustrated in the respective AF4 elugrams. Every nanoparticle was analyzed by at least three independent measurements performed *via* plasma independent incubation experiments.

FCS-Analysis: The FCS experiments was performed on a LSM 880 (Carl Zeiss, Jena, Germany) setup.[68] The excitation laser (He-Ne laser at 633 nm) was focused on the samples using a Zeiss C-Apochromat 40×/1.2 W water immersion objective. The fluorescence emission was collected with the same objective and directed to a spectral detection unit (Quasar, Carl Zeiss) after passing through a confocal pinhole. The fluorescence emission was spectrally separated by a grating element on a 32-channel array of GaAsP detectors operating in single photon counting mode. A detection range of 642–696 nm was used. An eight-well polystyrene-chambered cover glass (Nunc Lab-Tek, Thermo Fisher Scientific, Waltham, MA) was used as the sample cell. For each sample, a series of 15 measurements, 10 s

each, was performed at room temperature (23 °C). For experiments with human blood plasma, the samples were incubated with human blood plasma for 1 h at 37°C prior to the measurement. The obtained experimental autocorrelation curves were fitted with the following analytical model function:

$$G(\tau) = 1 + \frac{1}{N} \sum_{i=1}^{m} \frac{f_i}{\left(1 + \frac{\tau}{\tau_{D,i}}\right) \cdot \sqrt{1 + \frac{\tau}{S^2 \cdot \tau_{D,i}}}}$$

whereby N is the average number of diffusing fluorescencent species in the observation volume, $\tau_{D i}$ is the lateral diffusion time of the i-th species, f_i is the fraction of the component i ($1 \leq i \leq m$), and S is the structure parameter, $S = z_0/r_0$, where z_0 and r_0 represent the axial and radial dimensions of the observation volume. The diffusion coefficients of the species D_i are related to the respective diffusion times $\tau_{D i}$ and the radial dimension r_0 of V_{obs} by $D_i = r_0^2/(4\tau_{D i})$. By inserting D_i into the Stokes-Einstein equation, $R_h = \frac{k_B \cdot T}{6 \cdot \pi \cdot \eta \cdot D}$, we can calculate the hydrodynamic radius of the respective fluorescent species. Here, k_B is the Boltzmann constant, T is the temperature, and η is the viscosity of the solvent. As the value of r_0 depends on the optical setup, a calibration was performed using Alexa Fluor 647 ($D = 330$ µm^2 s^{-1} at 25 °C) as reference standard with known diffusion coefficient.

Biologic Evaluation: All animal work was performed at the Leiden University animal facility and was approved by the Leiden University Animal Ethics Committee. The animal experiments were performed according to the guidelines from Dutch government guidelines and the Directive 2010/63/EU of the European Parliament on the protection of animals used for scientific purposes under the permit number AVD1060020187085.

Male C57Bl/6 mice, aged 13-17 weeks, were housed in individually ventilated cages under a constant 12 h light-dark cycle and maintained on a standard mouse diet. Prior to the experiment, mice were weighed and randomly allocated to the different groups using the randomization tool RandoMice with the weight as blocking factor for randomization. After 1 week of acclimatization, the mice received a single intravenous injection (200 µL) of Atto647N-labeled CCPMs in PBS (5 µg/µL) or PBS (control) through the tail vein. Blood samples of 50 µL were collected from the tail vein at the following time points after systemic administration: 10 min, 1 h, 6 h, 24 h, 72 h. EDTA-treated Eppendorf tubes were applied to prevent blood clotting and kept at 4 °C. For fluorescence quantification,

blood cells were separated by centrifugation (Mikro 200R, Andreas Hettich GmbH & Co KG) (1000 rpm, 10 min, 4°C) and 25 µL of the supernatant were transferred into a transparent 96-well plate (Greiner Bio-one, The Netherlands) and diluted with 75 µL of PBS. The particle fluorescence was quantified by Tecan Spark plate reader (Tecan Group Ltd.) at an emission wavelength of 640 nm and detection wavelength of 670 nm at a fixed gain of 200 and a bandwidth of 5 nm. The fraction of particles in circulation for each time point was calculated as:

$$CCPMs\ in\ circulation = \frac{(fluorescence_{CCPM}(t = x) - fluorescence_{PBS})}{(fluorescence_{CCPM}(t = 0) - fluorescence_{PBS})}$$

The values obtained at t = 10 min were considered as 100% value.

At post-administration 72 h, mice were euthanized, and after perfusion the organs were collected and analyzed by ex vivo fluorescence analysis. Lungs, liver, spleen, kidneys, heart, and small intestine were collected, and kept in a 6-well plate under PBS stored on ice. The fluorescence per organ was measured on an IVIS Spectrum (Perkin Elmer, Massachusetts, USA) using the IS0709N4132 camera (Spectral Instruments TE) at an excitation wavelength of 605 nm and a detection wavelength of 680 nm. Image acquisition and analysis was performed with Living Image (version 4.7.2; Perkin Elmer). For normalization, the total fluorescence intensity was divided by the fluorescent area or the respective organ weight.

Author Contribution

Experimental design, polymer synthesis, nanoparticle preparation, DLS measurements, NP-fluorescence quantification in blood samples, and statistical analysis were performed by T.A.B., I.A. executed AF4 analyses, L.A.Z. synthesized the trifunctional peptide cross-linker. H.Z. supervised IVIS imaging, K.K. contributed FCS analysis, and B.S. performed the *in vivo* experiments. The manuscript was written by T.A.B. and M.B. The project was supervised by R.Z. and M.B.

Notes

The authors declare the following competing financial interest(s): Matthias Barz holds the patent Thiol-protected amino acid derivatives and uses thereof WO2015169908A1.

Acknowledgement

References

(1)   Zhang, C.; Yan, L.; Wang, X.; Zhu, S.; Chen, C.; Gu, Z.; Zhao, Y. Progress, Challenges, and Future of Nanomedicine. *Nano Today* **2020**, *35*.

(2)   Cabral, H.; Miyata, K.; Osada, K.; Kataoka, K. Block Copolymer Micelles in Nanomedicine Applications. *Chem. Rev.* **2018**, *118* (14), 6844–6892.

(3)   Duncan, R. The Dawning Era of Polymer Therapeutics. *Nat. Rev. Drug Discov.* **2003**, *2* (5), 347–360.

(4)   Chan, W. C. W. Nanomedicine 2.0. *Acc. Chem. Res.* **2017**, *50* (3), 627–632.

(5)   Bertrand, N.; Leroux, J. C. The Journey of a Drug-Carrier in the Body: An Anatomo-Physiological Perspective. *J. Control. Release* **2012**, *161* (2), 152–163.

(6)   Talelli, M.; Barz, M.; Rijcken, C. J. F.; Kiessling, F.; Hennink, W. E.; Lammers, T. Core-Crosslinked Polymeric Micelles: Principles, Preparation, Biomedical Applications and Clinical Translation. *Nano Today* **2015**, *10* (1), 93–117.

(7)   Shi, Y.; Van Steenbergen, M. J.; Teunissen, E. A.; Novo, L.; Gradmann, S.; Baldus, M.; Van Nostrum, C. F.; Hennink, W. E. Π-Π Stacking Increases the Stability and Loading Capacity of Thermosensitive Polymeric Micelles for Chemotherapeutic Drugs. *Biomacromolecules* **2013**, *14* (6), 1826–1837.

(8)   Talelli, M.; Rijcken, C. J. F.; Hennink, W. E.; Lammers, T. Polymeric Micelles for Cancer Therapy: 3 C's to Enhance Efficacy. *Curr. Opin. Solid State Mater. Sci.* **2012**, *16* (6), 302–309.

(9)   Lu, J.; Owen, S. C.; Shoichet, M. S. Stability of Self-Assembled Polymeric Micelles in Serum. *Macromolecules* **2011**, *44* (15), 6002–6008.

(10)   Muhammad, N.; Guo, Z. Metal-Based Anticancer Chemotherapeutic Agents. *Curr. Opin. Chem. Biol.* **2014**, *19* (1), 144–153.

(11)   Nishiyama, N.; Kato, Y.; Sugiyama, Y.; Kataoka, K. Cisplatin-Loaded Polymer-Metal Complex Micelle with Time-Modulated Decaying Property as a Novel Drug Delivery System. *Pharm. Res.* **2001**, *18* (7), 1035–1041.

(12)   Bauer, T. A.; Eckrich, J.; Wiesmann, N.; Kuczelinis, F.; Sun, W.; Zeng, X.; Weber, B.; Wu, S.; Bings, N. H.; Strieth, S.; Barz, M. Photocleavable Core Cross-Linked Polymeric Micelles of Polypept(o)ides and Ruthenium(II) Complexes. *J. Mater. Chem. B* **2021**, 9, 8211-8223.

(13)   Endo, K.; Ueno, T.; Kondo, S.; Wakisaka, N.; Murono, S.; Ito, M.; Kataoka, K.; Kato, Y.; Yoshizaki, T. Tumor-Targeted Chemotherapy with the Nanopolymer-Based Drug NC-6004 for Oral Squamous Cell Carcinoma. *Cancer Sci.* **2013**, *104* (3), 369–

374.

(14) Hu, Q.; Rijcken, C. J.; Bansal, R.; Hennink, W. E.; Storm, G.; Prakash, J. Complete Regression of Breast Tumour with a Single Dose of Docetaxel-Entrapped Core-Cross-Linked Polymeric Micelles. *Biomaterials* **2015**, *53*, 370–378.

(15) Van Driessche, A.; Kocere, A.; Everaert, H.; Nuhn, L.; Van Herck, S.; Griffiths, G.; Fenaroli, F.; De Geest, B. G. PH-Sensitive Hydrazone-Linked Doxorubicin Nanogels via Polymeric-Activated Ester Scaffolds: Synthesis, Assembly, and in Vitro and in Vivo Evaluation in Tumor-Bearing Zebrafish. *Chem. Mater.* **2018**, *30* (23), 8587–8596.

(16) Alberg, I.; Kramer, S.; Leps, C.; Tenzer, S.; Zentel, R. Effect of Core-Crosslinking on Protein Corona Formation on Polymeric Micelles. *Macromol. Biosci.* **2021**, *2000414*.

(17) Talelli, M.; Barz, M.; Rijcken, C. J. F. F.; Kiessling, F.; Hennink, W. E.; Lammers, T. Core-Crosslinked Polymeric Micelles: Principles, Preparation, Biomedical Applications and Clinical Translation. *Nano Today* **2015**, *10* (1), 93–117.

(18) Cabral, H.; Kataoka, K. Progress of Drug-Loaded Polymeric Micelles into Clinical Studies. *J. Control. Release* **2014**, *190*, 465–476.

(19) Mi, P.; Miyata, K.; Kataoka, K.; Cabral, H. Clinical Translation of Self-Assembled Cancer Nanomedicines. *Adv. Ther.* **2021**, *4* (1), 2000159.

(20) Atrafi, F.; Dumez, H.; Mathijssen, R. H. J.; Menke van der Houven van Oordt, C. W.; Rijcken, C. J. F.; Hanssen, R.; Eskens, F. A. L. M.; Schöffski, P. A Phase I Dose-Escalation and Pharmacokinetic Study of a Micellar Nanoparticle with Entrapped Docetaxel (CPC634) in Patients with Advanced Solid Tumours. *J. Control. Release* **2020**, *325* (March), 191–197.

(21) Sevier, C. S.; Kaiser, C. A. Formation and Transfer of Disulphide Bonds in Living Cells. *Nat. Rev. Mol. Cell Biol.* **2002**, *3* (11), 836–847.

(22) Schäfer, O.; Huesmann, D.; Muhl, C.; Barz, M. Rethinking Cysteine Protective Groups: S -Alkylsulfonyl- l -Cysteines for Chemoselective Disulfide Formation. *Chem. - A Eur. J.* **2016**, *22* (50), 18085–18091.

(23) Huesmann, D.; Schäfer, O.; Braun, L.; Klinker, K.; Reuter, T.; Barz, M. Exploring New Activating Groups for Reactive Cysteine NCAs. *Tetrahedron Lett.* **2016**, *57* (10), 1138–1142.

(24) Li, Y.; Xiao, K.; Luo, J.; Xiao, W.; Lee, J. S.; Gonik, A. M.; Kato, J.; Dong, T. A.; Lam, K. S. Well-Defined, Reversible Disulfide Cross-Linked Micelles for on-Demand Paclitaxel Delivery. *Biomaterials* **2011**, *32* (27), 6633–6645.

(25) Schäfer, O.; Barz, M. Of Thiols and Disulfides: Methods for Chemoselective Formation of Asymmetric Disulfides in Synthetic Peptides and Polymers. *Chem. - A Eur. J.* **2018**, *24* (47), 12131–12142.

(26) Bauer, T. A.; Muhl, C.; Schollmeyer, D.; Barz, M. Racemic S -(Ethylsulfonyl)- Dl -cysteine N -Carboxyanhydrides Improve Chain Lengths and Monomer Conversion for Β-Sheet-Controlled Ring-Opening Polymerization. *Macromol. Rapid Commun.* **2021**, *42* (8), 2000470.

(27) Muhl, C.; Schäfer, O.; Bauer, T.; Räder, H.-J.; Barz, M. Poly(S -Ethylsulfonyl- l -Homocysteine): An α-Helical Polypeptide for Chemoselective Disulfide Formation. *Macromolecules* **2018**, *51* (20), 8188–8196.

(28) Schäfer, O.; Huesmann, D.; Barz, M. Poly(S -Ethylsulfonyl- l -Cysteines) for

Chemoselective Disulfide Formation. *Macromolecules* **2016**, *49* (21), 8146–8153.

(29) Klinker, K.; Barz, M. Polypept(o)ides: Hybrid Systems Based on Polypeptides and Polypeptoids. *Macromol. Rapid Commun.* **2015**, *36* (22), 1943–1957.

(30) Birke, A.; Huesmann, D.; Kelsch, A.; Weilbächer, M.; Xie, J.; Bros, M.; Bopp, T.; Becker, C.; Landfester, K.; Barz, M. Polypeptoid- Block -Polypeptide Copolymers: Synthesis, Characterization, and Application of Amphiphilic Block Copolypept(o)Ides in Drug Formulations and Miniemulsion Techniques. *Biomacromolecules* **2014**, *15* (2), 548–557.

(31) Weber, B.; Birke, A.; Fischer, K.; Schmidt, M.; Barz, M. Solution Properties of Polysarcosine: From Absolute and Relative Molar Mass Determinations to Complement Activation. *Macromolecules* **2018**, *51* (7), 2653–2661.

(32) Ostuni, E.; Chapman, R. G.; Holmlin, R. E.; Takayama, S.; Whitesides, G. M. A Survey of Structure-Property Relationships of Surfaces That Resist the Adsorption of Protein. *Langmuir* **2001**, *17* (18), 5605–5620.

(33) Son, K.; Ueda, M.; Taguchi, K.; Maruyama, T.; Takeoka, S.; Ito, Y. Evasion of the Accelerated Blood Clearance Phenomenon by Polysarcosine Coating of Liposomes. *J. Control. Release* **2020**, *322* (March), 209–216.

(34) Nogueira, S. S.; Schlegel, A.; Maxeiner, K.; Weber, B.; Barz, M.; Schroer, M. A.; Blanchet, C. E.; Svergun, D. I.; Ramishetti, S.; Peer, D.; Langguth, P.; Sahin, U.; Haas, H. Polysarcosine-Functionalized Lipid Nanoparticles for Therapeutic MRNA Delivery. *ACS Appl. Nano Mater.* **2020**, *3* (11), 10634–10645.

(35) Ishida, T.; Ichihara, M.; Wang, X.; Yamamoto, K.; Kimura, J.; Majima, E.; Kiwada, H. Injection of PEGylated Liposomes in Rats Elicits PEG-Specific IgM, Which Is Responsible for Rapid Elimination of a Second Dose of PEGylated Liposomes. *J. Control. Release* **2006**, *112* (1), 15–25.

(36) Huesmann, D.; Sevenich, A.; Weber, B.; Barz, M. A Head-to-Head Comparison of Poly(Sarcosine) and Poly(Ethylene Glycol) in Peptidic, Amphiphilic Block Copolymers. *Polym. (United Kingdom)* **2015**, *67*, 240–248.

(37) Bleher, S.; Buck, J.; Muhl, C.; Sieber, S.; Barnert, S.; Witzigmann, D.; Huwyler, J.; Barz, M.; Süss, R. Poly(Sarcosine) Surface Modification Imparts Stealth-Like Properties to Liposomes. *Small* **2019**, *15* (50), 1–10.

(38) Mahmoudi, M.; Bertrand, N.; Zope, H.; Farokhzad, O. C. Emerging Understanding of the Protein Corona at the Nano-Bio Interfaces. *Nano Today* **2016**, *11* (6), 817–832.

(39) Schöttler, S.; Landfester, K.; Mailänder, V. Controlling the Stealth Effect of Nanocarriers through Understanding the Protein Corona. *Angew. Chemie - Int. Ed.* **2016**, *55* (31), 8806–8815.

(40) Alberg, I.; Kramer, S.; Schinnerer, M.; Hu, Q.; Seidl, C.; Leps, C.; Drude, N.; Möckel, D.; Rijcken, C.; Lammers, T.; Diken, M.; Maskos, M.; Morsbach, S.; Landfester, K.; Tenzer, S.; Barz, M.; Zentel, R. Polymeric Nanoparticles with Neglectable Protein Corona. *Small* **2020**, *16* (18), 1907574.

(41) Kappel, C.; Seidl, C.; Medina-Montano, C.; Schinnerer, M.; Alberg, I.; Leps, C.; Sohl, J.; Hartmann, A.-K.; Fichter, M.; Kuske, M.; Schunke, J.; Kuhn, G.; Tubbe, I.; Paßlick, D.; Hobernik, D.; Bent, R.; Haas, K.; Montermann, E.; Walzer, K.; Diken, M.; Schmidt, M.; Zentel, R.; Nuhn, L.; Schild, H.; Tenzer, S.; Mailänder, V.; Barz,

M.; Bros, M.; Grabbe, S. Density of Conjugated Antibody Determines the Extent of Fc Receptor Dependent Capture of Nanoparticles by Liver Sinusoidal Endothelial Cells. *ACS Nano* **2021**, *15*, 15191-15209.

(42) Kokkinopoulou, M.; Simon, J.; Landfester, K.; Mailänder, V.; Lieberwirth, I. Visualization of the Protein Corona: Towards a Biomolecular Understanding of Nanoparticle-Cell-Interactions. *Nanoscale* **2017**, *9* (25), 8858–8870.

(43) Docter, D.; Distler, U.; Storck, W.; Kuharev, J.; Wünsch, D.; Hahlbrock, A.; Knauer, S. K.; Tenzer, S.; Stauber, R. H. Quantitative Profiling of the Protein Coronas That Form around Nanoparticles. *Nat. Protoc.* **2014**, *9* (9), 2030–2044.

(44) Richtering, W.; Alberg, I.; Zentel, R. Nanoparticles in the Biological Context: Surface Morphology and Protein Corona Formation. *Small* **2020**, *16* (39), 1–8.

(45) Giddings, J. C. A New Separation Concept Based on a Coupling of Concentration and Flow Nonuniformities. *Sep. Sci.* **1966**, *1* (1), 123–125.

(46) Giddings, J. C. Field-Flow Fractionation: Analysis of Macromolecular, Colloidal, and Particulate Materials. *Science* **1993**, *260* (5113), 1456–1465.

(47) Bresseleers, J.; Bagheri, M.; Lebleu, C.; Lecommandoux, S.; Sandre, O.; Pijpers, I. A. B.; Mason, A. F.; Meeuwissen, S.; van Nostrum, C. F.; Hennink, W. E.; van Hest, J. C. M. Tuning Size and Morphology of Mpeg-b-p(Hpma-Bz) Copolymer Self-Assemblies Using Microfluidics. *Polymers (Basel).* **2020**, *12* (11), 1–18.

(48) Rijcken, C. J.; Snel, C. J.; Schiffelers, R. M.; van Nostrum, C. F.; Hennink, W. E. Hydrolysable Core-Crosslinked Thermosensitive Polymeric Micelles: Synthesis, Characterisation and in Vivo Studies. *Biomaterials* **2007**, *28* (36), 5581–5593.

(49) Dal, N. K.; Kocere, A.; Wohlmann, J.; Van Herck, S.; Bauer, T. A.; Resseguier, J.; Bagherifam, S.; Hyldmo, H.; Barz, M.; De Geest, B. G.; Fenaroli, F. Zebrafish Embryos Allow Prediction of Nanoparticle Circulation Times in Mice and Facilitate Quantification of Nanoparticle–Cell Interactions. *Small* **2020**, *16* (5), 1906719.

(50) Klinker, K.; Schäfer, O.; Huesmann, D.; Bauer, T.; Capelôa, L.; Braun, L.; Stergiou, N.; Schinnerer, M.; Dirisala, A.; Miyata, K.; Osada, K.; Cabral, H.; Kataoka, K.; Barz, M. Secondary-Structure-Driven Self-Assembly of Reactive Polypept(o)Ides: Controlling Size, Shape, and Function of Core Cross-Linked Nanostructures. *Angew. Chemie Int. Ed.* **2017**, *56* (32), 9608–9613.

(51) Bauer, T. A.; Imschweiler, J.; Muhl, C.; Weber, B.; Barz, M. Secondary Structure-Driven Self-Assembly of Thiol-Reactive Polypept(o)Ides. *Biomacromolecules* **2021**, *22* (5), 2171–2180.

(52) Hofmann, D.; Messerschmidt, C.; Bannwarth, M. B.; Landfester, K.; Mailänder, V. Drug Delivery without Nanoparticle Uptake: Delivery by a Kiss-and-Run Mechanism on the Cell Membrane. *Chem. Commun.* **2014**, *50* (11), 1369–1371.

(53) Quader, S.; Liu, X.; Toh, K.; Su, Y. L.; Maity, A. R.; Tao, A.; Paraiso, W. K. D.; Mochida, Y.; Kinoh, H.; Cabral, H.; Kataoka, K. Supramolecularly Enabled PH-Triggered Drug Action at Tumor Microenvironment Potentiates Nanomedicine Efficacy against Glioblastoma. *Biomaterials* **2021**, *267*, 120463.

(54) Talelli, M.; Iman, M.; Varkouhi, A. K.; Rijcken, C. J. F.; Schiffelers, R. M.; Etrych, T.; Ulbrich, K.; van Nostrum, C. F.; Lammers, T.; Storm, G.; Hennink, W. E. Core-Crosslinked Polymeric Micelles with Controlled Release of Covalently Entrapped Doxorubicin. *Biomaterials* **2010**, *31* (30), 7797–7804.

(55)   Berger, A.; Noguchi, J.; Katchalski, E. Poly-L-Cysteine. *J. Am. Chem. Soc.* **1956**, *78* (17), 4483–4488.

(56)   Zhang, X.; Waymouth, R. M. 1,2-Dithiolane-Derived Dynamic, Covalent Materials: Cooperative Self-Assembly and Reversible Cross-Linking. *J. Am. Chem. Soc.* **2017**, *139* (10), 3822–3833.

(57)   Bauer, T. A.; Horvat, N. K.; Marques, O.; Chocarro, S.; Mertens, C.; Colucci, S.; Schmitt, S.; Carrella, L. M.; Morsbach, S.; Koynov, K.; Fenaroli, F.; Blümler, P.; Jung, M.; Sotillo, R.; Hentze, M. W.; Muckenthaler, M. U.; Barz, M. Core Cross-Linked Polymeric Micelles for Specific Iron Delivery: Inducing Sterile Inflammation in Macrophages. *Adv. Healthc. Mater.* **2021**, *2100385* (19), 2100385.

(58)   Koynov, K.; Butt, H. J. Fluorescence Correlation Spectroscopy in Colloid and Interface Science. *Curr. Opin. Colloid Interface Sci.* **2012**, *17* (6), 377–387.

(59)   Negwer, I.; Best, A.; Schinnerer, M.; Schäfer, O.; Capeloa, L.; Wagner, M.; Schmidt, M.; Mailänder, V.; Helm, M.; Barz, M.; Butt, H. J.; Koynov, K. Monitoring Drug Nanocarriers in Human Blood by Near-Infrared Fluorescence Correlation Spectroscopy. *Nat. Commun.* **2018**, *9* (1).

(60)   Holm, R.; Douverne, M.; Weber, B.; Bauer, T.; Best, A.; Ahlers, P.; Koynov, K.; Besenius, P.; Barz, M. Impact of Branching on the Solution Behavior and Serum Stability of Starlike Block Copolymers. *Biomacromolecules* **2019**, *20* (1), 375–388.

(61)   Maeda, H. Macromolecular Therapeutics in Cancer Treatment: The EPR Effect and Beyond. *J. Control. Release* **2012**, *164* (2), 138–144.

(62)   Barenholz, Y. Doxil® - The First FDA-Approved Nano-Drug: Lessons Learned. *J. Control. Release* **2012**, *160* (2), 117–134.

(63)   Shi, Y.; Lammers, T.; Storm, G.; Hennink, W. E. Physico-Chemical Strategies to Enhance Stability and Drug Retention of Polymeric Micelles for Tumor-Targeted Drug Delivery. *Macromol. Biosci.* **2016**, 1–11.

(64)   Talelli, M.; Barz, M.; Rijcken, C. J. F. F.; Kiessling, F.; Hennink, W. E.; Lammers, T. Core-Crosslinked Polymeric Micelles: Principles, Preparation, Biomedical Applications and Clinical Translation. *Nano Today* **2015**, *10* (1), 93–117.

(65)   Hassan, H. M. A.; Maltman, B. A. Mixed SAMs and MALDI-ToF MS: Preparation of N-Glycosylamine Derivative and Thioctic Acid Methyl Ester Bearing 1,2-Dithiolane Groups and Detection of Enzymatic Reaction on Au. *Bioorg. Chem.* **2012**, *40* (1), 6–9.

(66)   Koufaki, M.; Kiziridi, C.; Alexi, X.; Alexis, M. N. Design and Synthesis of Novel Neuroprotective 1,2-Dithiolane/Chroman Hybrids. *Bioorg. Med. Chem.* **2009**, *17* (17), 6432–6441.

(67)   Marioli, M.; Kok, W. T. Recovery, Overloading, and Protein Interactions in Asymmetrical Flow Field-Flow Fractionation. *Anal. Bioanal. Chem.* **2019**, *411* (11), 2327–2338.

(68)   Rigler, R.; Wennmalm, S.; Edman, L. *FCS in Single Molecule Analysis*; Springer-Verlag: Berlin, 2001.

Supporting Information
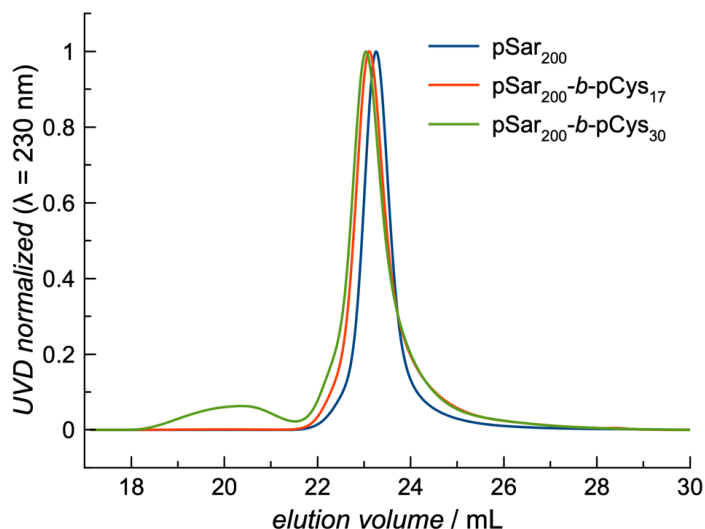
Results and Discussion

Polymer Synthesis

Figure S1. Analytical HFIP GPC of polypept(o)ides. Of note, secondary structure formation (anti-parallel ß-sheet) is not suppressed in HFIP accounting for the broad PDI of copolymers with increasing chain length of p(L)Cys(SO$_2$Et).

Table S1. Characterization of core cross-linked polymeric micelles with and without embedded iron oxide nanoparticles.

polymer	X_n pSar[a]	X_n pCys(SO$_2$Et)[b]	M_n[c]	$Đ$[c]
P1, pSar$_{200}$	200	-	40.9 kg·mol^{-1}	1.17
P2, pSar$_{200}$-b-pCys(SO$_2$Et)$_{17}$	200	17	40.9 kg·mol^{-1}	1.19
P3, pSar$_{200}$-b-pCys(SO$_2$Et)$_{17}$	200	30	40.9 kg·mol^{-1}	2.52

[a] HFIP-GPC relative to pSar standards. [b] determined by ^{1}H NMR. [c] HFIP-GPC releative to PMMA standards; secondary structure formation of p(L)Cys(SO2Et) is not suppressed accounting for broad dispersities.
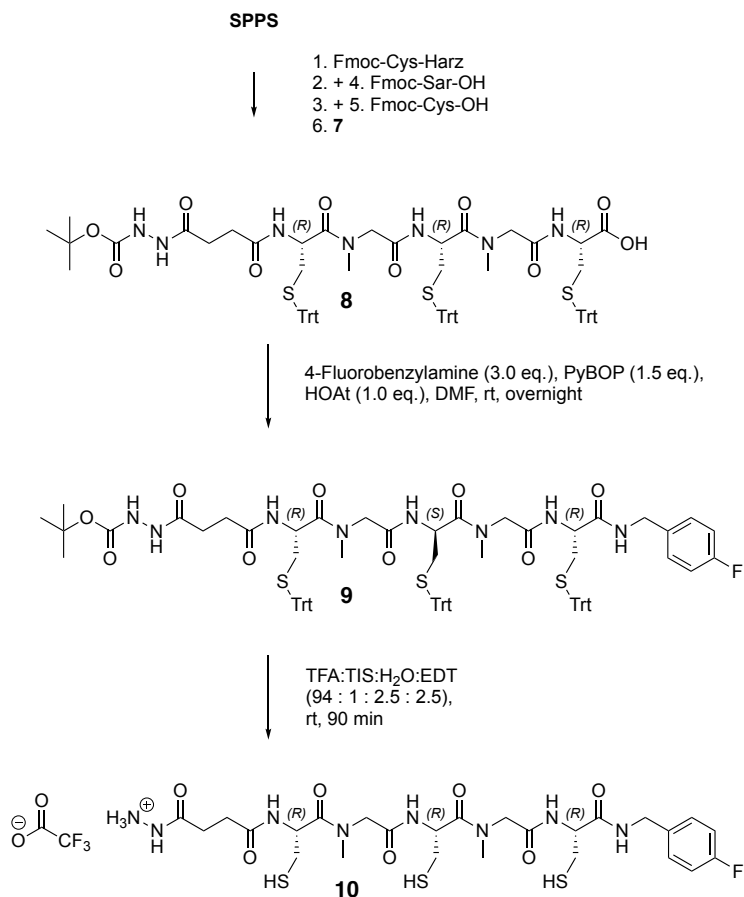
Cross-Linker Synthesis
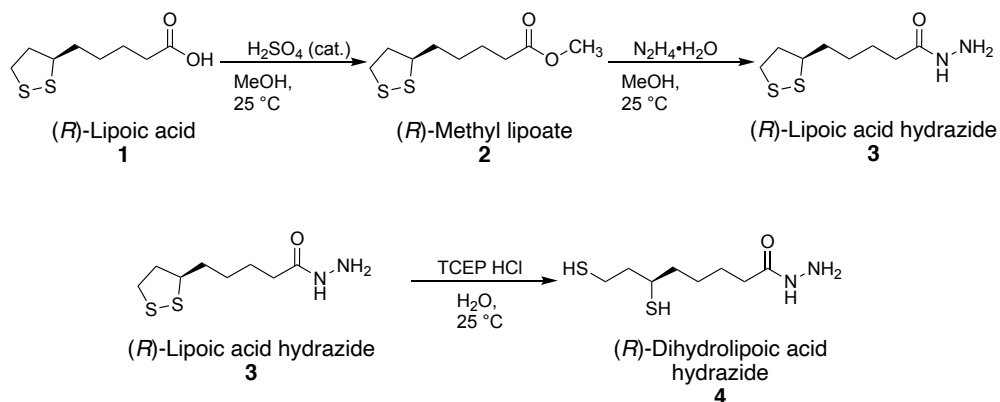
Scheme S1. Synthetic pathway to the bifunctional lipoic acid hydrazide (**4**) cross-linker.
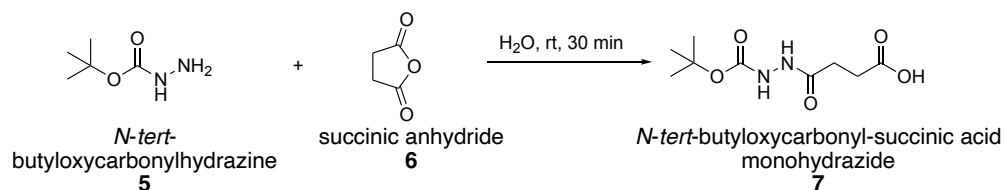
Scheme S2. Synthetic pathway to the N-tert-butyloxycarbonyl-succinic acid monohydrazide (**7**).

SPPS

1. Fmoc-Cys-Harz
2. + 4. Fmoc-Sar-OH
3. + 5. Fmoc-Cys-OH
6. **7**

4-Fluorobenzylamine (3.0 eq.), PyBOP (1.5 eq.),
HOAt (1.0 eq.), DMF, rt, overnight

TFA:TIS:H₂O:EDT
(94 : 1 : 2.5 : 2.5),
rt, 90 min

Scheme S3. Synthetic pathway to the trifunctional pentapeptide cross-linker **10** via solid-phase peptide synthesis.
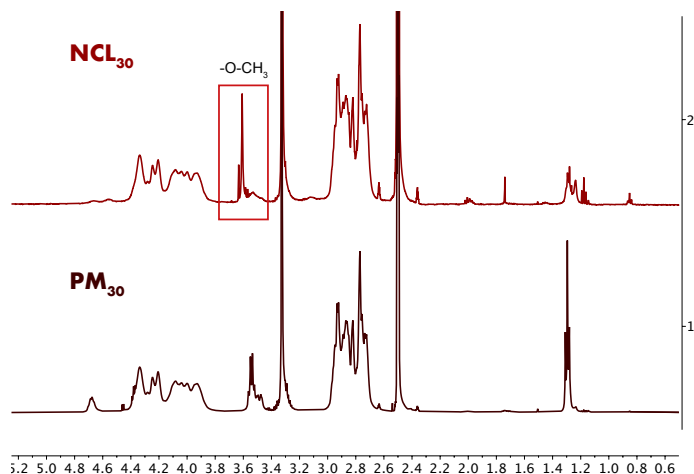
Particle Synthesis

Figure S2. NMR analysis of the polymeric micelles before (PM_{30}) and after quenching of the *S*-ethylsulfonyl group with methyl 3-mercaptopropionate (NCL_{30}). For NCL_{30}, no signals of the *S*-ethylsulfonyl group but only signals of the methoxy group can be detected indicating complete removal of the reactive group.
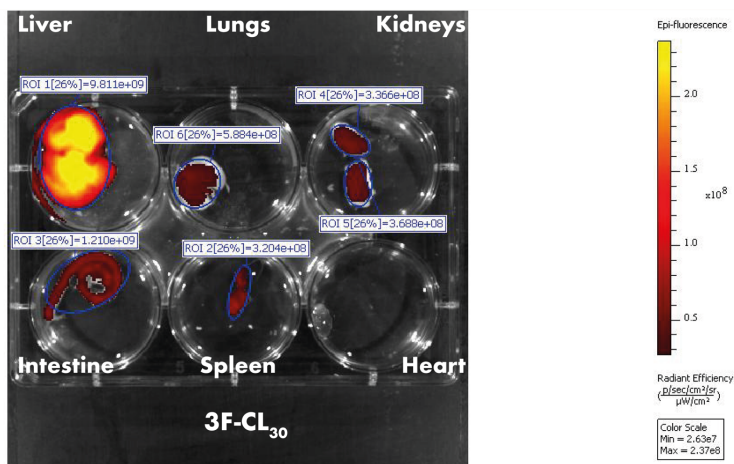
Ex vivo Imaging

Figure S3. Ex vivo organ imaging by IVIS Spectrum (Perkin Elmer, Massachusetts, USA) shown for a representative mouse treated with $3F\text{-}CL_{30}$. Fluorescence associated to the intestine originates from the diet.

NMR-Data

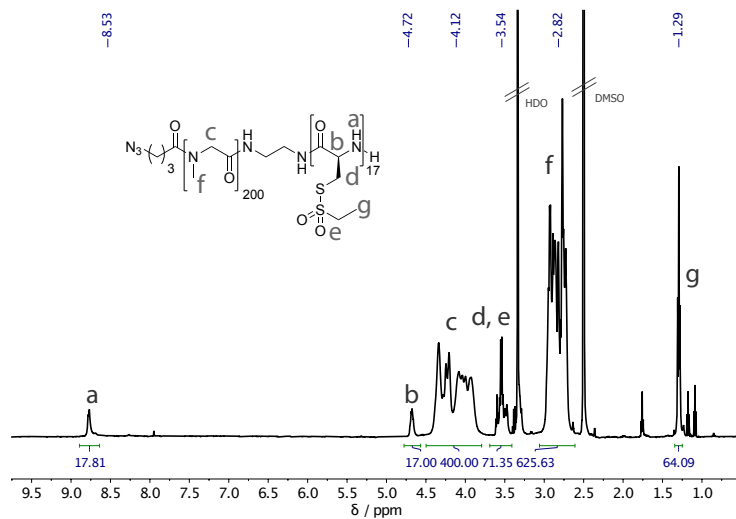### Polypept(o)ides

Figure S4. ^{1}H NMR of pSar$_{200}$-b-p(L)Cys(SO$_2$Et)$_{17}$ in DMSO-d_6.
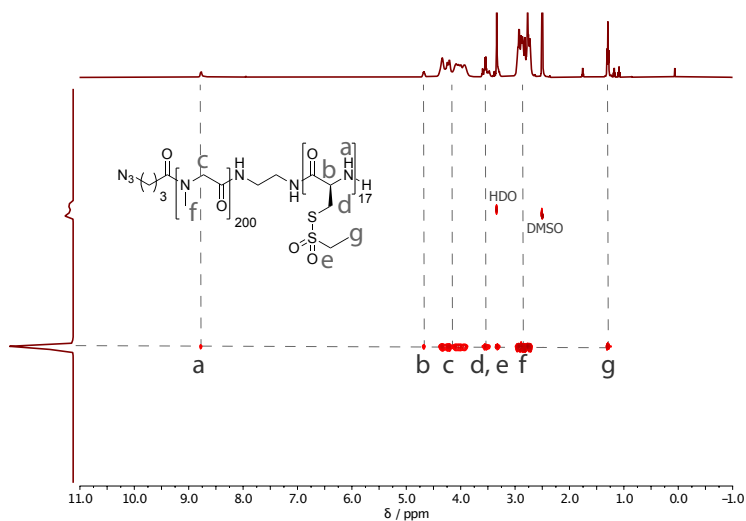
Figure S5. DOSY NMR analysis of pSar$_{200}$-b-p(L)Cys(SO$_2$Et)$_{17}$ in DMSO-d_6.

Figure S6. ^{1}H NMR of pSar$_{200}$-b-p(L)Cys(SO$_2$Et)$_{27}$ in DMSO-d_6.

Figure S7. DOSY NMR analysis of pSar$_{200}$-b-p(L)Cys(SO$_2$Et)$_{27}$ in DMSO-d_6.
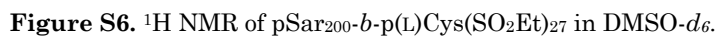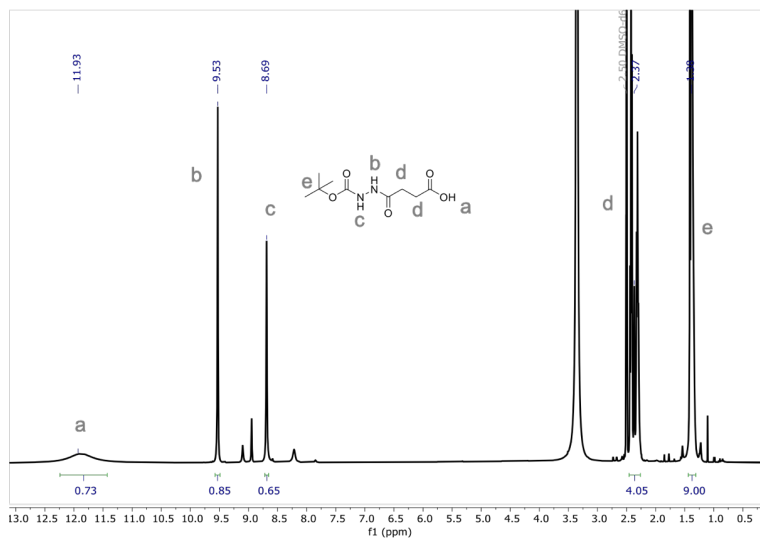
Peptide Cross-Linker

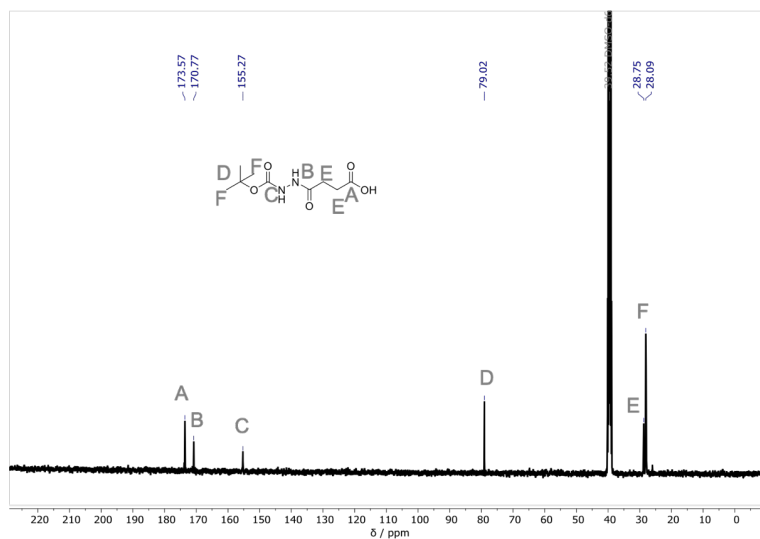**Figure S8.** ¹H NMR of *N-tert*-butyloxycarbonyl-succinic acid monohydrazide (**7**) in DMSO-*d₆*.

Figure S9. ¹³C NMR of *N-tert*-butyloxycarbonyl-succinic acid monohydrazide (7) in DMSO-*d₆*.

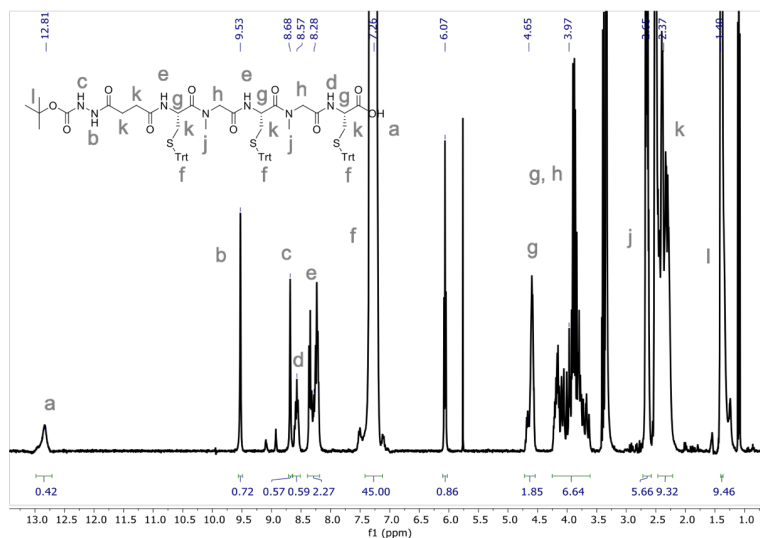**Figure S10.** ^{1}H NMR of Boc-hydrazine-Cys(Trt)-Sar-Cys(Trt)-Sar-Cys(Trt)-OH (8) in DMSO-d_6.
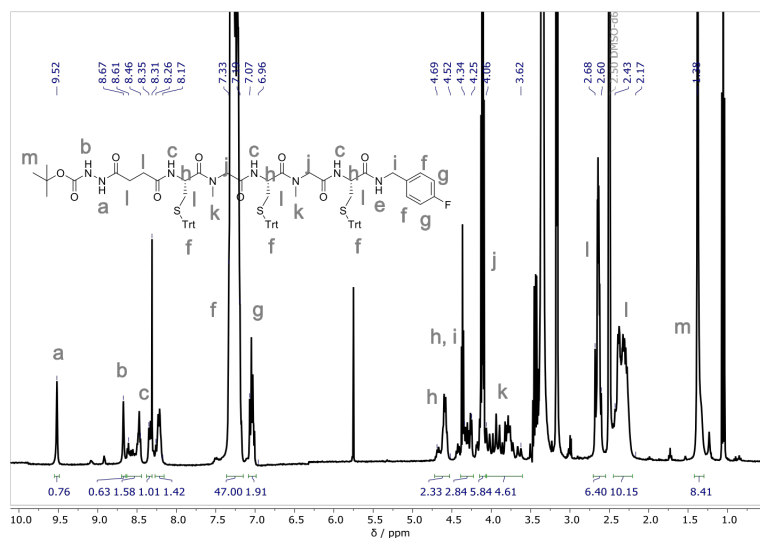
Figure S11. ^{1}H NMR of Boc-hydrazine-Cys(Trt)-Sar-Cys(Trt)-Sar-Cys(Trt)-(4-fluorobenzylamine) (9) in DMSO-d_6.
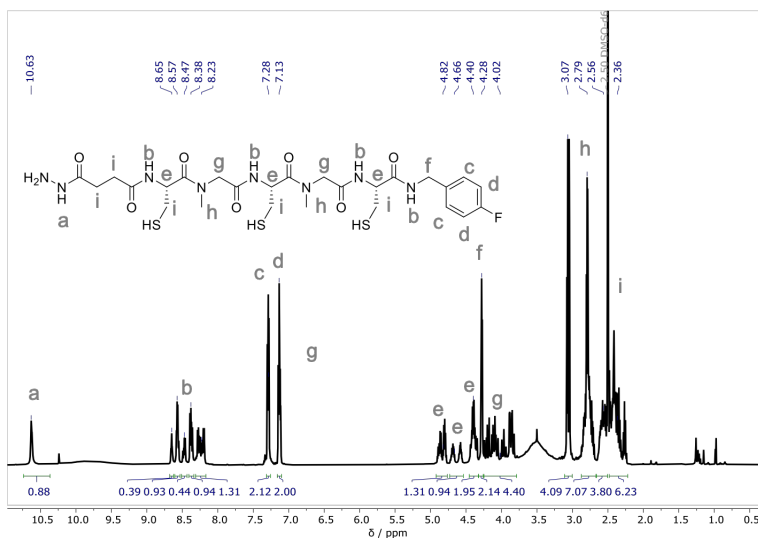
Figure S12. ^{1}H NMR of hydrazine-Cys-Sar-Cys-Sar-Cys-(4-fluorobenzylamine) (10) in DMSO-d_6.

Figure S13. ^{19}F NMR of hydrazine-Cys-Sar-Cys-Sar-Cys-4-fluorobenzylamine (10) in DMSO-d_6.

5

Complex Structures Made Simple - Continuous Flow Production of Core Cross-Linked Polymeric Micelles for Paclitaxel Pro-Drug-Delivery

Continuous Flow Production and Purification of CCPMs

to be submitted to *Advanced Materials*.

Complex Structures Made Simple -

Continuous Flow Production of Core Cross-Linked

Polymeric Micelles for Paclitaxel Pro-Drug-Delivery

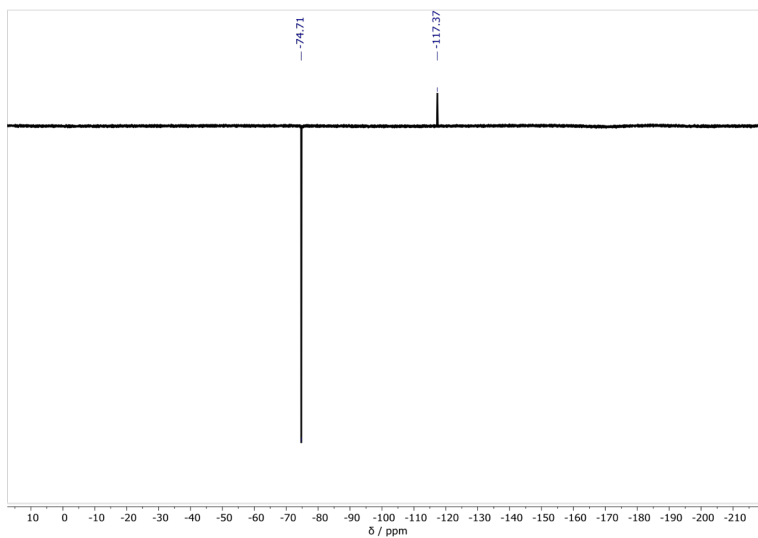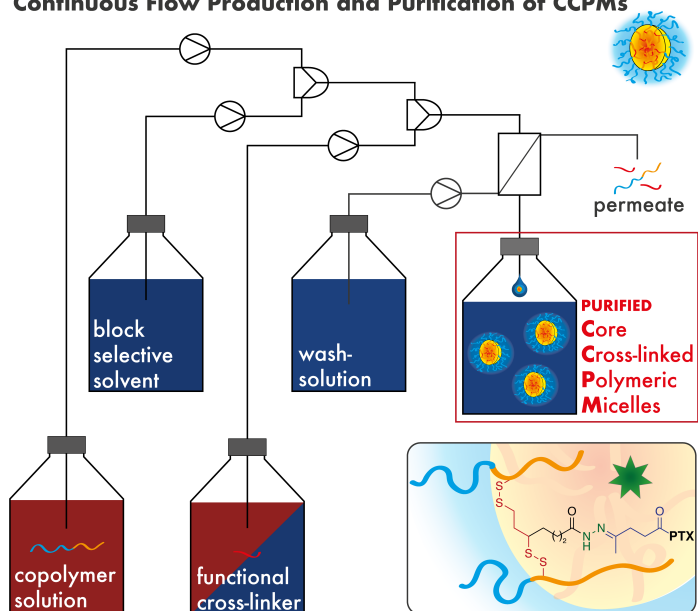Tobias A. Bauer[a, b], Jonas Schramm[c], Federico Fenaroli[d], Svenja Siemer[e], Christine I. Seidl[a, b], Svenja Morsbach[f], Regina Bleul[c], Roland Stauber[e], Michael Maskos[c], Matthias Barz[a, b,*]

[a] Leiden Academic Centre for Drug Research (LACDR), Leiden University, Einsteinweg 55, 2333 CC Leiden, The Netherlands

[b] Department of Chemistry, Johannes Gutenberg University Mainz, Duesbergweg 10-14, 55128 Mainz, Germany

[c] Fraunhofer Institute for Microengineering and Microsystems, Carl-Zeiss-Str. 18-20, 55129, Mainz, Germany

[d] Department for Biosciences, University of Oslo, Blindernveien 31, 0371 Oslo, Norway

[e] Molecular and Cellular Oncology/Nanobiomedicine, ENT Department, University Medical Center Mainz, Langenbeckstraße 1, Mainz, Germany

[f] Max Planck Institute for Polymer Research, Ackermannweg 10, 55128 Mainz, Germany

Abstract

Translating innovative nanomaterials to products requires efficient manufacturing techniques that ease large-scale and high-throughput synthesis with high reproducibility. Drug carriers in medicine embrace a complex subset of tasks calling for functionality yet robust concepts. Here, we report the synthesis of core cross-linked polymeric micelles (CCPMs) in a continuous flow process, which combines the commonly separated steps of micelle formation, core cross-linking, and purification into a single device. Redox-responsive CCPMs are formed from thiol-reactive polypept(o)ides of polysarcosine-*block*-poly(*S*-ethylsulfonyl-L-cysteine) and functional cross-linkers based on dihydrolipoic acid hydrazide for pH-dependent release of paclitaxel. The precisely controlled microfluidic self-assembly process allows the production of spherical micelles (D_h = 35 nm) while avoiding organic solvents and additives with unfavorable toxicity profiles. Self-assembly and functional cross-linking *via* slit interdigital micromixers produce 350-700 mg of CCPMs/h per single system, while purification by online tangential flow filtration successfully removes impurities (unimer $\leq 0.5\%$). The formed paclitaxel-loaded CCPMs (PTX@CCPMs) possess the desired pH-responsive drug release profile, display stable drug encapsulation, an improved toxicity profile compared to Abraxane, as well as therapeutic efficiency in the B16F1-xenotransplanted zebrafish larvae model. Therefore, the combination of reactive polymers, functional cross-linkers, and microfluidics enables the continuous-flow synthesis of therapeutically active CCPMs.

Keywords

polymeric micelles · polypept(o)ides · micromixer ·continuous flow · cross-linking · stimuli-responsive

Introduction

Envisioning Paul Ehrlich's idea of the magic bullet, nanocarriers were designed to provide specificity, stability, and solubility to active pharmaceutical ingredients (APIs).[1–3] Due to their small size and high drug loading capacity, polymeric micelles have been thoroughly investigated for the delivery of small-molecule drugs such as anthracyclines and taxanes.[4–8] When non-specific interactions are absent and a long half-life in the bloodstream permits slow accumulation in diseased tissue, the selective biodistribution of the encapsulated API can be achieved enabling higher maximum tolerated doses and improved therapeutic efficiency.[3,9–11] To prevent premature drug release and carrier disintegration immediately after the administration into the bloodstream, additional stabilization strategies are required.[12–14] Core cross-linked polymeric micelles (CCPMs) have thus evolved as the second generation of polymeric micelles.[14] Moreover, (bio-) reversible drug conjugation strategies have been described that allow for external or disease-related drug release from CCPMs.[15–18] As the most promising example, CCPMs containing pH-cleavable docetaxel (CPC634) are currently under clinical evaluation for the treatment of platinum-resistant ovarian cancer in phase II (NCT03742713).[11,19,20]

The production of CCPMs typically involves the self-assembly of reactive block copolymers, cross-linking, and purification but requires facile, robust, and scalable manufacturing.[21] By combining the shielding properties of polysarcosine (pSar) with the inherent functionality and reactivity of polypeptides, the hybrid systems thereof, so-called polypept(o)ides, have attracted increasing attention.[22–24] Polypept(o)ides can be prepared by living amine-initiated ring-opening N-carboxyanhydride (NCA) polymerization leading to well-defined polymers with narrow dispersity.[25–27] Polysarcosine, poly(N-methyl glycine), is hydrophilic, non-charged, and exclusively a weak hydrogen bond acceptor that adopts a random coil structure in aqueous solutions, meeting the characteristics for protein resistant materials.[28–30] Besides similar solution properties compared to poly(ethylene glycol) (PEG), pSar showed an improved safety profile, characterized by a reduced induction of cytokine release and evasion from accelerated blood clearance phenomenon.[28,31–33] In combination with pSar as the shell material, poly(S-ethylsulfonyl-L-cysteine) (pCysSO$_2$Et) provides multi-functionality to CCPMs.[34,35] The thiol-reactive S-alkylsulfonyl group allows for NCA polymerization and can be addressed for chemoselective disulfide bond

formation, leading to CCPMs with tunable morphology and core functionality.[35–38]

While microfluidics have evolved to the state-of-the-art technique for the production of lipid nanoparticles (LNP) and colloidal nanoparticles, polymeric micelles and in particular CCPMs are synthesized in batch-mode using either film rehydration, solvent exchange, temperature-induced aggregation or precipitation techniques, which grant access to well-defined particles at optimized conditions.[39–41] Beyond such methods, micromixers enable continuous-flow processes and offer automated manufacturing increasing production rates and reproducibility, whereby the closed setup facilitates sterile particle preparation.[42,43] In the micrometer-sized compartments self-assembly can be tuned *via* solvents and concentrations, while diffusive mixing of the fluid streams governs the transfer of solvents or reagents, and can be adjusted for optimal particle size and PDI.[44–46] Mixing by simple T- or Y-junctions mainly leads to single and thick fluid lamellae resulting in high mixing times.[47] To reduce the mixing time and gain precise spatial and temporal control, interdigital micromixers have been developed. In the slit-interdigital micromixer (SIMM), multi-lamination and geometric flow focusing lead to thin fluid lamellae and high flow velocities.[47,48] The short mixing times in interdigital micromixers could thus be used to control self-assembly kinetically, giving access to non-equilibrium structures as reported for polymersomes from non-vesicle forming polymers by Thiermann *et al.*[42,45,49] Although micromixers are the preferred technique for LNPs in nucleic acid delivery,[41,42,50–55] a complete setup for the continuous flow production of CCPMs including online purification has not been reported to the best of our knowledge. The combination of self-assembly, core cross-linking and purification by this methodology is highly desirable feature to enable larger-scale production and provide access to CCPM libraries for screening of drugs and combination therapies by nanomedicine.[56]

We now propose the two-step synthesis and purification of CCPMs in a continuous flow process with online tangential flow filtration, whereby functional cross-linkers permit the decoupled and bio-reversible conjugation of a paclitaxel pro-drug yielding drug-loaded CCPMs (PTX@CCPMs) for tumor therapy. Nanoparticle performance is evaluated in cell culture and xenotransplanted tumor-bearing zebrafish larvae and compared to Abraxane. Xenotransplant tumor-bearing zebrafish larvae have evolved as a complementary *in vivo* model

to reduce animal test in rodents, enabling high throughput screening in combination with pharmacokinetic and pharmacodynamic studies.[57–60]

Results and Discussion

The concept for the synthesis of stimuli-responsive CCPMs via the continuous flow process is based on the cross-linking of thiol-reactive polypept(o)ides with functional cross-linkers. As illustrated in Figure 1A, block copolymers of polysarcosine-*block*-poly(*S*-ethylsulfonyl-L-cysteine) (pSar-*b*-pCys(SO$_2$Et)) were assembled to polymeric micelles by solvent switch methods. In a second step, the *S*-ethylsulfonyl-groups were addressed by chemoselective disulfide bond formation with thiols.[34,35] The designed cross-linker based on lipoic acid grants access to functional groups for bio-reversible drug conjugation *via* pH-responsive hydrazone bonds. While high reaction rates have been reported for the chemoselective disulfide bond formation,[61] the bottlenecks for a potential large-scale production of CCPMs were identified as the considerable amounts of solvent required by dialysis-based processes and the purification of the product CCPMs from residual polymer and cross-linker *via* the laborious and time-consuming spin filtration procedure. Moreover, to obtain spherical morphologies from batch processes, chaotropic additives such as thiourea are required to disrupt secondary structure formation of the thiol-reactive pCys(SO$_2$Et) block to direct self-assembly.[35]

In this study, we report on a continuous flow process for the production of therapeutically active CCPMs to address the identified shortcomings. As shown by the process chart in Figure 1C, self-assembly and core cross-linking were conducted in two consecutive micromixers connected to the online purification by tangential flow filtration. In the first step, the solution of the copolymer in the organic solvent is mixed with water as the block selective solvent. In the second micromixer, the cross-linker dissolved in ethanol/water mixtures is added to the micelle solution from micromixer #1. Since ethanol does not dissolve pCys(SO$_2$Et) the mixing step does not impair micelle integrity. For purification by tangential flow filtration regenerated cellulose membranes (molecular weight cut-off (MWCO), 30 kDa) and water were employed yielding CCPMs in the retentate. The permeate (or waste) contains residual polymer, cross-linker, organic solvents, and tris(2-carboxyethyl)phosphine oxide, which was used to generate dihydrolipoic acid hydrazide from the parent disulfide (3).
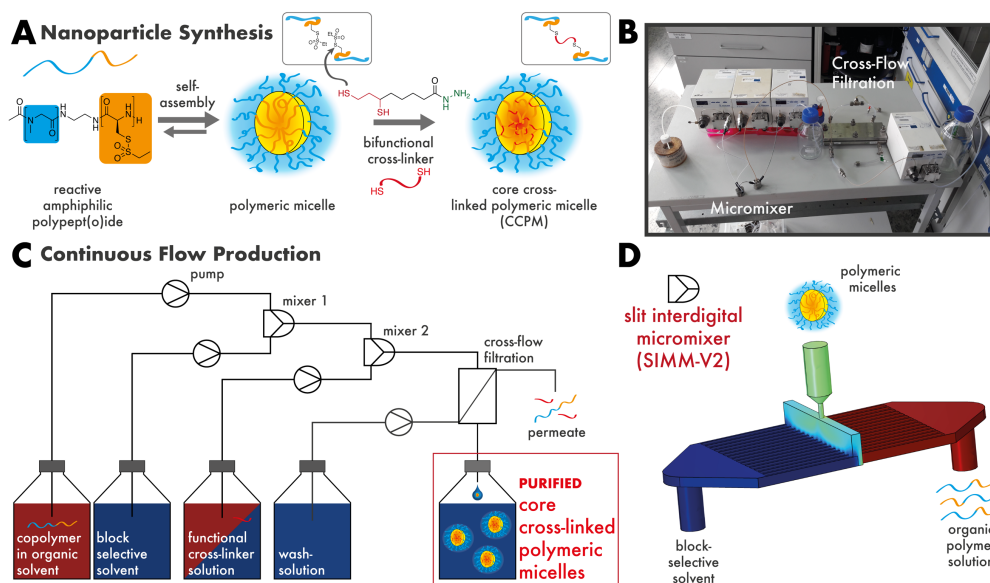
Figure 1. Synthesis of core cross-linked polymeric micelles in a continuous flow process. (**A**) Amphiphilic thiol-reactive pSar-*b*-pCys(SO$_2$Et) polypept(o)ides are assembled to polymeric micelles *via* solvent switch followed by cross-linking by chemoselective disulfide bond formation with dihydrolipoic acid hydrazide. (**B**) Photo of the continuous flow setup (**C**) Chart of the continuous flow process. Reagent mixing by slit interdigital micromixers operated by HPLC pumps, and online particle purification by tangential flow filtration (MWCO, 30 kDa; regenerated cellulose membrane). (**D**) Schematic illustration of the slit interdigital micromixer used for self-assembly and cross-linking (SIMM-V2).

The complete setup of the continuous flow process and the online tangential flow filtration is displayed in Figure 1B. The micromixer for self-assembly was directly connected to the reactor for the cross-linking step, and both were operated by HPLC pumps. After cross-linking, the particles entered the tangential flow filtration, where a four-fold dilution was performed, and the 10-fold concentrated particle solution could be collected (β_{CCPM} = 14 g·L^{-1}). All mixing processes were performed in a slit-interdigital micromixer V2 (SIMM; Fraunhofer IMM), which allows for asymmetric flow ratios (e.g., 1-9) and shows a low tendency for aggregate formation (Figure S2). The SIMM splits the two fluid streams into eight lamellae fusing in an interdigital fashion (Figure 1D). The optimal overall flow rate was 10-12 mL·min^{-1} at which the microstructures (inner volume 8 µL) direct laminar flow at the beginning and rather turbulent flow near the outlet capillary after geometric flow focusing (outlet diameter 60 µm; Reynolds number ~ 4500;

total mixing time 40 ms). To dissolve pSar-*b*-pCys(SO$_2$Et) dimethyl sulfoxide (DMSO) was selected over *N,N*-dimethylacetamide (DMAc) used previously since the higher polymer solubility supports the formation of well-defined micelles (Figure S3).[35,62,63] According to the guidelines of the International Council for Harmonization (ICH), DMSO and ethanol are classified as substances with a low toxic potential (class 3 solvent), allowing for a process without potentially hazardous solvents. In addition, potentially carcinogenic thiourea (TU) was rendered unnecessary for the synthesis of spherical particles from pSar-*b*-pCys(SO$_2$Et) using the continuous flow process.
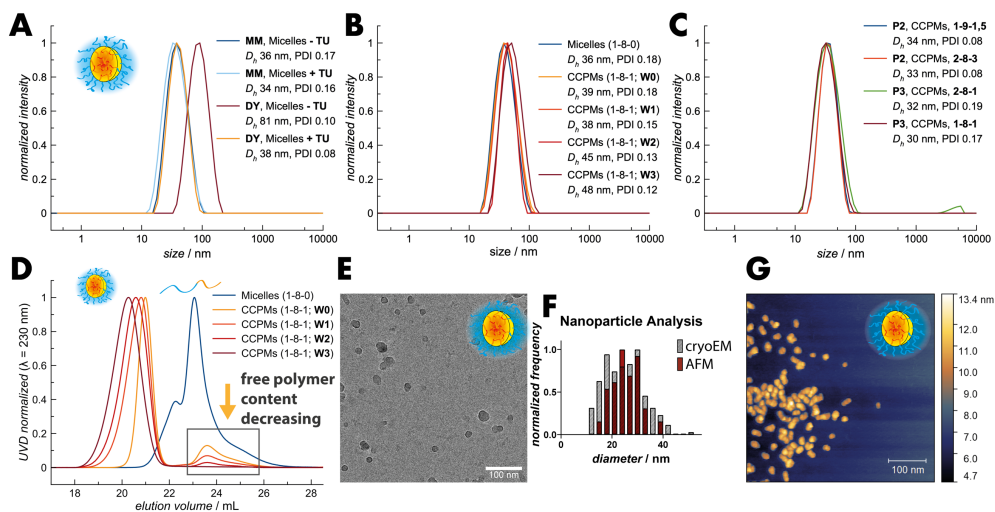

Figure 2. Analysis of micelles and CCPMs produced by continuous flow process. (**A**) DLS analysis of micelles and CCPMs by self-assembly or micromixer process. (**B**) DLS analysis of micelles and CCPMs before (W0) and after purification by tangential filtration cycles (W1-W3). (**C**) DLS analysis of CCPMs formed by varied relative flow rate ratios (**D**) HFIP-GPC analysis of micelles and CCPMs before and after purification by tangential-flow filtration cycles (W0 - W3). (**E**) Cryo-EM image of micromixer-CCPMs. (**F**) Diameter of micromixer-CCPMs determined by AFM and cryo-EM image analysis. (**G**) AFM image of micromixer-CCPMs.

As shown in Figure 2, the micromixer process (MM) yielded polymeric micelles with small diameters (D_h = 34-36 nm) and narrow PDIs ≤0.17, irrespective of chaotropic additives (+/- TU). Conversely, larger structures were obtained when the dialysis procedure (DY) was applied without TU, resulting in worm-like micelles referring to secondary structure-driven self-assembly of the pCys(SO$_2$Et)

block.[35,62] Within the micromixer, the fast and precisely controlled solvent exchange thus overruled the secondary structure formation as the guiding element.[46,64] Consequently, small spherical nanoparticles were obtained from pSar-*b*-pCys(SO$_2$Et) in the micromixer that were identical to the CCPMs from the dialysis procedure with TU, in which anti-parallel β-sheets were disrupted by saturation of the hydrogen bonds *via* the chaotropic agent.[35] Cross-linking with dihydrolipoic acid hydrazide in SIMM #2 did not affect the particle size or PDI, as shown in Figure 2B (CCPM, W0). Moreover, the continuous flow process was robust to alterations in the polymer block lengths and in the relative flow rate ratios (Figure 2C, Figure S4). For each device 350-700 mg of CCPMs could be obtained per hour, whereby channel fouling was not observed. Since the microstructures are crucial for the performance of micromixers, scale-up can best be performed by parallelization, i.e., numbering up.[48] Purification of the CCPMs by tangential flow filtration slightly increased the particle diameter during the process (39 nm to 48 nm) yet slight decreasing the PDI to 0.1. The tangential flow filtration ultimately lead to CCPMs with free polymer contents below the limit of detection in HFIP-GPC analysis (≤ 0.5%) (Figure 2D, Figure S5), which further underlines the stability of the CCPMs. Beyond small molecule contamination, purification from unconjugated polymer is of significance for most biomedical applications of CCPMs as free amphiphilic unimers cause unspecific interaction with plasma proteins.[65] Analysis of the CCPMs by cryogenic transmission electron microscopy (cryo-EM) and atomic force microscopy (AFM) confirmed the spherical morphology of the purified nanoparticles. The diameters of 24.8 ± 7.6 nm (cryo-EM) and 25.7 ± 5.3 nm (AFM) were in good agreement with (multi-angle) DLS analysis, where no angle dependency was observed (Figure 2B, Figure 2E-G, and Figure S6-S9).

The presented continuous flow process successfully yielded CCPMs from pSar-*b*-pCys(SO$_2$Et) at varied chain lengths and flow rate ratios when the functional cross-linker dihydrolipoic acid hydrazide was used. In fact, the selection of the cross-linker was an important parameter for the process. If larger and more hydrophobic cross-linkers were used, aggregate formation and channel fouling were readily observed in the micromixer (Figure S10-S11). As a solution, functional cross-linkers allowed decoupling of carrier synthesis and drug conjugation. Each process could thus be optimized separately with the potential to achieve higher yields at reduced synthetic effort and cost. This relies on stable nanocarriers that do not aggregate during drug loading and purification, a task

well suitable for core cross-linked particles.[66] As illustrated in Figure 3, the functional cross-linker lipoic acid hydrazide was designed to conjugate ketone-modified PTX-LEV to CCPMs by hydrazone bond formation. Hydrazone bonds remain intact at physiological pH and enable stimuli-responsive drug release by cleavage at endo-lysosomal pH values.[17] In combination with the disulfide cross-links, PTX-loaded CCPMs (PTX@CCPMs) featured dual stimuli-responsive drug release accounting for optimal API delivery.[67] The contemporaneous availability of PTX and cysteine was not expected to interfere with the drug's mechanism of action but may be relevant for delivery of APIs such as cisplatin.[68,69]

Two techniques were evaluated for PTX conjugation to CCPMs: film-hydration and reaction in DMSO. For the latter, DMSO was employed to solubilize the drug and induce swelling of the micellar core. To provide an additional driving force for drug loading into the core, the film-hydration technique was adapted and modified from vesicle and micelle preparation methods. In both cases, excess PTX-LEV was removed by centrifugation and filtration, and the final drug-loaded nanoparticles were obtained in aqueous solution after reconstitution with sterile water from lyophilization. The conjugation of PTX-LEV to lipoic acid hydrazide-functionalized CCPMs was verified by NMR analysis, whereby characteristic signals of the hydrazone-bond formation could be detected (Figure S12). Further, both loading techniques lead to PTX@CCPMs with narrow PDIs below 0.1 (Figure 3A). In addition, the particle sizes were not significantly affected by the drug loading *via* film-hydration (PTX@CCPMs-F) or reaction in DMSO (PTX@CCPMs-D). Since vast swelling is inhibited by the high cross-linking density within the micellar core, the comparable sizes account for absence of aggregation.
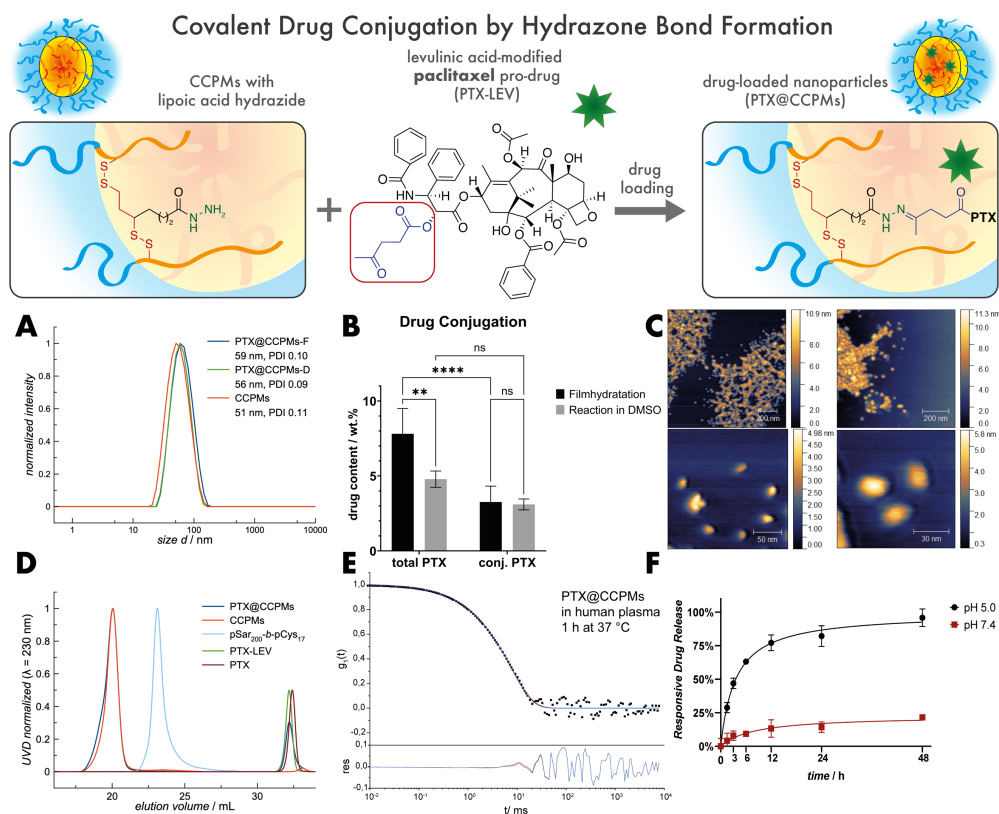
Figure 3. PTX pro-drug conjugation to functional CCPMs by hydrazone bond formation (PTX@CCPMs). (**A**) DLS analysis showed narrow PDIs for CCPMs before and after drug loading, purification, lyophilization and reconstitution in water. No significant differences were observed when film-hydration (PTX@CCPMs-F) or reaction in DMSO (PTX@CCPMs-D) were applied for drug conjugation. (**B**) Quantification of total and conjugated amount of PTX (in wt.%) by RP-HPLC. Data reported as N ± standard error of the mean for at least 4 independent experiments. Two-way ANOVA (*): *p < 0.05, **p < 0.01, ***p < 0.001, ****p < 0.0001. (**C**) AFM images of PTX@CCPMs confirmed spherical particle morphology. (**D**) HFIP-GPC analysis confirmed particle integrity after drug-loading. (**E**) Multi angle DLS of PTX@CCPMs in undiluted human plasma: autocorrelation function $g_1(t)$ given for a representative measurement angle of 30°. The fits with (blue line) and without (red line) aggregation term (upper graph), and the derived residuals for the fit w/o aggregate and correlation function (lower graph) indicated no significant aggregation. (**F**) Stimuli-responsive drug release at 37 °C in biologically relevant osmolar conditions (pH = 5.0 or 7.4), evaluated by RP-HPLC (N = 3).

As shown in Figure 3B, total paclitaxel contents of 7.81 ± 1.51 wt.% and 4.79 ± 0.47 wt.% were determined for PTX@CCPMs-F and PTX@CCPM-D by RP-HPLC, while similar amounts of approx. 3 wt.% were conjugated covalently. Film-hydration thus leads to significantly higher total drug loading ($p < 0.0001$) compared to the reaction in DMSO. The comparable amounts of conjugated drug point toward a densely packed micellar core hampering the reaction of the cross-linker with the relatively large drug molecule.[44,70] In fact, loading polymeric micelles with taxanes frequently leads to low drug contents below 3 wt.% unless specific drug-polymer interactions are employed.[71–73] When the conjugation reactions were performed in DMF or $CHCl_3$ which also solubilize the copolymer, no drug loading could be identified. In addition, reactions in DMSO in the presence of buffer containing aniline, which has been reported to catalyze the hydrazone bond formation for small molecules in solution, did not improve but decrease drug loading.[74,75] Since higher drug-loading was achieved by film-hydration, only these particles were further investigated. When analyzed by AFM, spherical structures with sizes well below 50 nm were revealed for PTX@CCPMs (Figure 3C). Drug loading by film-hydration did thus not affect the morphology of the nanoparticles. In addition, the GPC confirmed the integrity of the cross-linked nanomedicine, as no significant traces of homopolymer could be detected after incubation in HFIP for 1 h (Figure 3D). For passive targeting of diseased tissue *via* the enhanced permeability and retention (EPR) effect or related phenomena, stable circulation in the blood stream without premature carrier disintegration and drug release is a basic requirement, which stimulated the development of CCPMs.[76] Unspecific interaction of the carrier with components of the blood plasma shall thus be prevented.[77] Consequently, PTX@CCPMs were analyzed by multi-angle DLS in human blood plasma following the procedure established by Rausch *et al*.[78] Here, no significant aggregation could be detected after incubation at 37°C for 1 h (Figure 3E and Figure S13). To study the stimuli-responsive drug release, PTX@CCPMs were incubated at physiological or endo-lysosomal pH and analyzed by RP-HPLC. As shown in Figure 3F, PTX-LEV was quickly released from the nanoparticle providing $46.9 \pm 3.2\%$ after 3 h, and up to $95.8 \pm 5.4\%$ cumulative drug release after incubation at pH 5 for 48 h. Vice versa, a slower release profile was observed in PBS (pH 7.4), whereby only $7.9 \pm 2.8\%$ and $21.5 \pm 1.1\%$ could be detected after incubation for 3h and 48 h. This underlines the stimuli-responsive release mediated by the pH-sensitive hydrazone bone.[17,79,80]

For biologic evaluation PTX@CCPMs were tested in cell culture and in zebrafish embryos, and the performance was compared to Abraxane as internal therapeutic reference (Figure 4). Abraxane is considered as the first FDA-approved nanomedicine, whereby PTX is formulated with human serum albumin replacing castor oil and ethanol used in Taxol.[81,82] As shown in Figure 4A, the time-dependent toxicity varied among the three formulations (Figure 4B and Figure S15B). At equal drug concentration, free PTX in DMSO induced severe toxicity immediately. In contrast, Abraxane and PTX@CCPMs showed reduced or modest toxicity at the early 2 h time point. After 48 h, no differences could be observed for the cell viability among all groups. In addition, PTX@CCPMs and Abraxane showed similar IC_{50} values of 20.6 and 14.9 nm in HeLa cells (Figure 4A), both comparable with the free drug dissolved in DMSO (11.9 nm) (Figure S14). Referring to the release profile of PTX@CCPMs (Figure 3F), the slower kinetics matched the expectation, as the nanomedicine requires cleavage of the pro-drug before inducing toxicity.[14] The identical cellular toxicity after 48 h, thus underlined the successful PTX release.
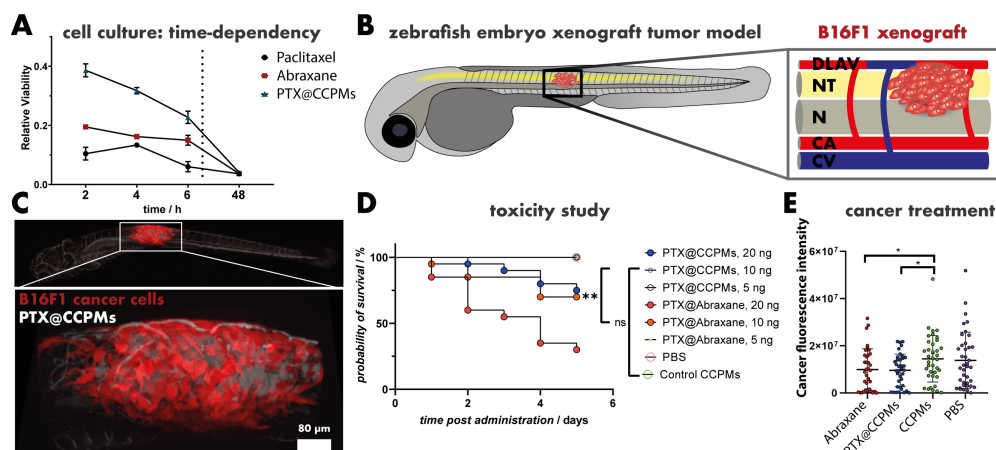

Figure 4. Biologic evaluation of PTX@CCPMs. (**A**) Time-dependent toxicity of paclitaxel formulations in HeLa cells. (**B**) Schematic illustration of the B16F1 mouse melanoma cell xenograft tumor model in zebrafish embryos. Cancer cells were injected in the trunk central region indicated by the black rectangle. The magnification shows neural tube (NT), noto-chord (N), dorsal longitudinal anastomotic vessel (DLAV), caudal artery (CA), and caudal vein (CV) with tumor formation after xenotransplantation in the neural tube.[83] (**C**) Fluorescence microscopy image of the PTX@CCPM (white) accumulation in the tumor-region of RFP expressing B16F1 mouse melanoma cell (red) xenotransplanted zebrafish embryos, 8 h post nanoparticle injection. (**D**) Toxicity study for paclitaxel formulations in

zebrafish embryos (without tumor). (**E**) Cancer treatment study for paclitaxel formulations in B16F1 bearing zebrafish embryos. The schematic illustration in (B) was adapted and modified from Kocere *et al*.[83]

For the consequent *in vivo* study, we chose the zebrafish larvae model. Zebrafish larvae are an emerging preclinical model allowing for rapid drug screening for novel therapeutic approaches against bacterial infections and cancer, substantially contributing to reducing animal testing in rodents.[58–60,83] In zebrafish larvae xenotransplanted with red fluorescent protein (RFP) expressing B16F1 mouse melanoma cells, PTX@CCPMs significantly accumulate in the tumor region within 8 h post injection according to fluorescence-based image analysis (Figure 4D and Figure S16).[57,84] At this time point, more than 40% of the injected dose were still in circulation and could be detected in the vasculature (Figure S17, Figure 4D, upper image, PTX@CCPM in white). The drug loading did not impair the circulation behavior of the carrier but slightly reduced nanoparticle clearance from the blood stream (Figure S17). The maximum tolerated dose of PTX@CCPMs and Abraxane was tested using healthy zebrafish embryos (Figure 4E). For PTX@CCPMs, up to 10 ng of PTX per fish could be administered without detectable toxicity at day 5 post injection. In comparison, application of PTX *via* Abraxane was less tolerated allowing for only 5 ng of PTX without inducing toxicity. The same trend for the survival rate was found for doses of 20 ng PTX administered by PTX@CCPMs and 10 ng of PTX *via* Abraxane. The more stable encapsulation of PTX in PTX@CCPMs thus reduced off-target toxicity of the API. These findings are in line with earlier reports on the reduced toxicity of doxorubicine encapsulated in polymersomes compared to the free drug tested in zebrafish embryos.[57] Ultimately, the nanomedicines were investigated in B16F1 tumor-bearing zebrafish embryos. Cancer cells were injected 24 h before the treatment, and the therapeutic efficacy was evaluated by fluorescence-based image analysis after 6 days. Tumor therapy was performed at equal toxicity using 10 and 5 ng PTX per fish administered by PTX@CCPMs or Abraxane compared to empty CCPMs or PBS. As shown in Figure 4F, both PTX treatments showed a reduction in cancer growth, whereby no statistical significances could be evaluated among PTX@CCPMs or Abraxane. In this preclinical study, Abraxane and PTX@CCPMs showed comparable performance, whereby the improved toxicity profile of PTX@CCPMs is a first indication for a beneficial patient compliance.

Taken together, the presented design concept for decoupling CCPM synthesis and drug loading enables continuous flow production of nanoparticles and stimuli-responsive encapsulation and conjugation of small molecule (pro-) drugs. Future research will be directed to explore this platform beyond the model drug PTX and for encapsulation of synergistic APIs realizing combination therapy.

Conclusion

We have established a continuous flow process for the synthesis of core cross-linked polymeric micelles aiming for precise control over the molecular properties of the next generation of nanomedicines. The core-shell architectures were produced by self-assembly and cross-linking in two consecutive slit interdigital micromixers using chemoselective disulfide bond formation of thiol-reactive polypept(o)ides (pSar-b-pCys(SO$_2$Et)) with functional cross-linkers. Online purification by tangential flow filtration was used for particle purification and could successfully reduce the amount of unconjugated polymer to below the limit of detection ($\leq 0.5\%$). Without any numbering up by parallelization, the process leads to 350-700 mg CCPMs/h. Due to the well-defined self-assembly kinetics, spherical micelles (D_h = 35 nm, PDI = 0.17) were obtained. Consequently, the continuous flow process could be performed in solvents with a low toxicity profile (DMSO, ethanol). After CCPM synthesis and purification, paclitaxel-levulinic acid was conjugated to the CCPMs *via* hydrazone bond formation with the lipoic acid cross-linker (PTX@CCPMs). The drug-loading did not affect the nanoparticle size and morphology while featuring pH-responsive drug release. In cell culture (HeLa, B16F1) and the zebrafish embryo xenograft model (B16F1), PTX@CCPMs showed similar performance compared to Abraxane, while the stable encapsulation in PTX@CCPMs reduced the toxicity of the paclitaxel *in vivo*. Committing to the strategy of decoupled CCPM synthesis and drug conjugation, future research will focus on tuning the release kinetics of APIs to establish combination therapies. The presented continuous flow process for the production and purification will ease the translation of CCPMs by enabling the straightforward synthesis of particle libraries under precisely controlled conditions.

Author Contribution

Conceptual design, polymer synthesis, cross-linker synthesis, drug conjugation, single-angle DLS measurements, AFM measurements, GPC measurements, and HPLC studies were performed by T.A.B. J.S. designed the continuous flow setup and executed CCPM synthesis and purification therein. F.F. performed *in vivo* experiments, S.S. and R.S. provided the in vitro experiments. C.I.S. and S.M. contributed multi-angle DLS measurements. R.B. and M.M. supervised the microfluidic experiments. The manuscript was written by T.A.B. and M.B. The project was supervised M.B.

Notes

The authors declare the following competing financial interest(s): Matthias Barz holds the patent Thiol-protected amino acid derivatives and uses thereof WO2015169908A1.

Acknowledgement

References

(1)   Bertrand, N.; Leroux, J. C. The Journey of a Drug-Carrier in the Body: An Anatomo-Physiological Perspective. *J. Control. Release* **2012**, *161* (2), 152–163.

(2)   Lammers, T. SMART Drug Delivery Systems: Back to the Future vs. Clinical Reality. *Int. J. Pharm.* **2013**, *454* (1), 527–529.

(3)   Lammers, T.; Kiessling, F.; Hennink, W. E.; Storm, G. Drug Targeting to Tumors: Principles, Pitfalls and (Pre-) Clinical Progress. *J. Control. Release* **2012**, *161* (2), 175–187.

(4)   Cabral, H.; Miyata, K.; Osada, K.; Kataoka, K. Block Copolymer Micelles in Nanomedicine Applications. *Chem. Rev.* **2018**, *118* (14), 6844–6892.

(5)   Murakami, M.; Cabral, H.; Matsumoto, Y.; Wu, S.; Kano, M. R.; Yamori, T.; Nishiyama, N.; Kataoka, K. Improving Drug Potency and Efficacy by Nanocarrier-Mediated Subcellular Targeting. *Sci. Transl. Med.* **2011**, *3* (64).

(6)   Talelli, M.; Iman, M.; Varkouhi, A. K.; Rijcken, C. J. F.; Schiffelers, R. M.; Etrych,

T.; Ulbrich, K.; van Nostrum, C. F.; Lammers, T.; Storm, G.; Hennink, W. E. Core-Crosslinked Polymeric Micelles with Controlled Release of Covalently Entrapped Doxorubicin. *Biomaterials* **2010**, *31* (30), 7797–7804.

(7)   Von Hoff, D. D.; Mita, M. M.; Ramanathan, R. K.; Weiss, G. J.; Mita, A. C.; Lorusso, P. M.; Burris, H. A.; Hart, L. L.; Low, S. C.; Parsons, D. M.; Zale, S. E.; Summa, J. M.; Youssoufian, H.; Sachdev, J. C. Phase I Study of PSMA-Targeted Docetaxel-Containing Nanoparticle BIND-014 in Patients with Advanced Solid Tumors. *Clin. Cancer Res.* **2016**, *22* (13), 3157–3163.

(8)   Mukai, H.; Kato, K.; Esaki, T.; Ohsumi, S.; Hozomi, Y.; Matsubara, N.; Hamaguchi, T.; Matsumura, Y.; Goda, R.; Hirai, T.; Nambu, Y. Phase I Study of NK105, a Nanomicellar Paclitaxel Formulation, Administered on a Weekly Schedule in Patients with Solid Tumors. *Invest. New Drugs* **2016**, *34* (6), 750–759.

(9)   Matsumura, Y.; Maeda, H. A New Concept for Macromolecular Therapeutics in Cancer Chemotherapy: Mechanism of Tumoritropic Accumulation of Proteins and the Antitumor Agent Smancs. *Cancer Res.* **1986**, *46* (8), 6387–6392.

(10)   Maeda, H. Macromolecular Therapeutics in Cancer Treatment: The EPR Effect and Beyond. *J. Control. Release* **2012**, *164* (2), 138–144.

(11)   Atrafi, F.; van Eerden, R. A. G.; van Hylckama Vlieg, M. A. M.; Oomen-de Hoop, E.; de Bruijn, P.; Lolkema, M. P.; Moelker, A.; Rijcken, C. J.; Hanssen, R.; Sparreboom, A.; Eskens, F. A. L. M.; Mathijssen, R. H. J.; Koolen, S. L. W. Intratumoral Comparison of Nanoparticle Entrapped Docetaxel (CPC634) with Conventional Docetaxel in Patients with Solid Tumors. *Clin. Cancer Res.* **2020**, *26* (14), 3537–3545.

(12)   Lu, J.; Owen, S. C.; Shoichet, M. S. Stability of Self-Assembled Polymeric Micelles in Serum. *Macromolecules* **2011**, *44* (15), 6002–6008.

(13)   Richtering, W.; Alberg, I.; Zentel, R. Nanoparticles in the Biological Context: Surface Morphology and Protein Corona Formation. *Small* **2020**, *16* (39), 1–8.

(14)   Talelli, M.; Barz, M.; Rijcken, C. J. F. F.; Kiessling, F.; Hennink, W. E.; Lammers, T. Core-Crosslinked Polymeric Micelles: Principles, Preparation, Biomedical Applications and Clinical Translation. *Nano Today* **2015**, *10* (1), 93–117.

(15)   Su, Z.; Liang, Y.; Yao, Y.; Wang, T.; Zhang, N. Polymeric Complex Micelles Based on the Double-Hydrazone Linkage and Dual Drug-Loading Strategy for PH-Sensitive Docetaxel Delivery. *J. Mater. Chem. B* **2016**, *4* (6), 1122–1133.

(16)   Rijcken, C. J.; Snel, C. J.; Schiffelers, R. M.; van Nostrum, C. F.; Hennink, W. E. Hydrolysable Core-Crosslinked Thermosensitive Polymeric Micelles: Synthesis, Characterisation and in Vivo Studies. *Biomaterials* **2007**, *28* (36), 5581–5593.

(17)   Sonawane, S. J.; Kalhapure, R. S.; Govender, T. Hydrazone Linkages in PH Responsive Drug Delivery Systems. *Eur. J. Pharm. Sci.* **2017**, *99*, 45–65.

(18)   Bauer, T. A.; Eckrich, J.; Wiesmann, N.; Kuczelinis, F.; Sun, W.; Zeng, X.; Weber, B.; Wu, S.; Bings, N. H.; Strieth, S.; Barz, M. Photocleavable Core Cross-Linked Polymeric Micelles of Polypept(o)Ides and Ruthenium(II) Complexes. *J. Mater. Chem. B* **2021**, *9* (39), 8211–8223.

(19)   Hu, Q.; Rijcken, C. J.; Bansal, R.; Hennink, W. E.; Storm, G.; Prakash, J. Complete Regression of Breast Tumour with a Single Dose of Docetaxel-Entrapped Core-Cross-Linked Polymeric Micelles. *Biomaterials* **2015**, *53*, 370–378.

(20)   Biancacci, I.; Sun, Q.; Möckel, D.; Gremse, F.; Rosenhain, S.; Kiessling, F.; Bartneck, M.; Hu, Q.; Thewissen, M.; Storm, G.; Hennink, W. E.; Shi, Y.; Rijcken, C. J. F.; Lammers, T.; Sofias, A. M. Optical Imaging of the Whole-Body to Cellular Biodistribution of Clinical-Stage PEG-b-PHPMA-Based Core-Crosslinked Polymeric Micelles. *J. Control. Release* **2020**, *328*, 805–816.

(21)   Barz, M. Complexity and Simplification in the Development of Nanomedicines. *Nanomedicine* **2015**, *10* (20), 3093–3097.

(22)   Birke, A.; Huesmann, D.; Kelsch, A.; Weilbächer, M.; Xie, J.; Bros, M.; Bopp, T.; Becker, C.; Landfester, K.; Barz, M. Polypeptoid- Block -Polypeptide Copolymers: Synthesis, Characterization, and Application of Amphiphilic Block Copolypept(o)Ides in Drug Formulations and Miniemulsion Techniques. *Biomacromolecules* **2014**, *15* (2), 548–557.

(23)   Birke, A.; Ling, J.; Barz, M. Polysarcosine-Containing Copolymers: Synthesis, Characterization, Self-Assembly, and Applications. *Prog. Polym. Sci.* **2018**, *81*, 163–208.

(24)   Klinker, K.; Barz, M. Polypept(o)Ides: Hybrid Systems Based on Polypeptides and Polypeptoids. *Macromol. Rapid Commun.* **2015**, *36* (22), 1943–1957.

(25)   Aliferis, T.; Iatrou, H.; Hadjichristidis, N. Living Polypeptides. *Biomacromolecules* **2004**, *5* (5), 1653–1656.

(26)   Vayaboury, W.; Giani, O.; Cottet, H.; Deratani, A.; Schué, F. Living Polymerization of α-Amino Acid N-Carboxyanhydrides (NCA) upon Decreasing the Reaction Temperature. *Macromol. Rapid Commun.* **2004**, *25* (13), 1221–1224.

(27)   Fetsch, C.; Grossmann, A.; Holz, L.; Nawroth, J. F.; Luxenhofer, R. Polypeptoids from N -Substituted Glycine N -Carboxyanhydrides: Hydrophilic, Hydrophobic, and Amphiphilic Polymers with Poisson Distribution. *Macromolecules* **2011**, *44* (17), 6746–6758.

(28)   Weber, B.; Birke, A.; Fischer, K.; Schmidt, M.; Barz, M. Solution Properties of Polysarcosine: From Absolute and Relative Molar Mass Determinations to Complement Activation. *Macromolecules* **2018**, *51* (7), 2653–2661.

(29)   Ostuni, E.; Chapman, R. G.; Holmlin, R. E.; Takayama, S.; Whitesides, G. M. A Survey of Structure-Property Relationships of Surfaces That Resist the Adsorption of Protein. *Langmuir* **2001**, *17* (18), 5605–5620.

(30)   Lau, K. H. A.; Ren, C.; Sileika, T. S.; Park, S. H.; Szleifer, I.; Messersmith, P. B. Surface-Grafted Polysarcosine as a Peptoid Antifouling Polymer Brush. *Langmuir* **2012**, *28* (46), 16099–16107.

(31)   Weber, B.; Seidl, C.; Schwiertz, D.; Scherer, M.; Bleher, S.; Süss, R.; Barz, M. Polysarcosine-Based Lipids: From Lipopolypeptoid Micelles to Stealth-like Lipids in Langmuir Blodgett Monolayers. *Polymers (Basel).* **2016**, *8* (12).

(32)   Nogueira, S. S.; Schlegel, A.; Maxeiner, K.; Weber, B.; Barz, M.; Schroer, M. A.; Blanchet, C. E.; Svergun, D. I.; Ramishetti, S.; Peer, D.; Langguth, P.; Sahin, U.; Haas, H. Polysarcosine-Functionalized Lipid Nanoparticles for Therapeutic MRNA Delivery. *ACS Appl. Nano Mater.* **2020**, *3* (11), 10634–10645.

(33)   Son, K.; Ueda, M.; Taguchi, K.; Maruyama, T.; Takeoka, S.; Ito, Y. Evasion of the Accelerated Blood Clearance Phenomenon by Polysarcosine Coating of Liposomes. *J. Control. Release* **2020**, *322* (March), 209–216.

(34) Schäfer, O.; Klinker, K.; Braun, L.; Huesmann, D.; Schultze, J.; Koynov, K.; Barz, M. Combining Orthogonal Reactive Groups in Block Copolymers for Functional Nanoparticle Synthesis in a Single Step. *ACS Macro Lett.* **2017**, *6* (10), 1140–1145.

(35) Klinker, K.; Schäfer, O.; Huesmann, D.; Bauer, T.; Capelôa, L.; Braun, L.; Stergiou, N.; Schinnerer, M.; Dirisala, A.; Miyata, K.; Osada, K.; Cabral, H.; Kataoka, K.; Barz, M. Secondary-Structure-Driven Self-Assembly of Reactive Polypept(o)Ides: Controlling Size, Shape, and Function of Core Cross-Linked Nanostructures. *Angew. Chemie Int. Ed.* **2017**, *56* (32), 9608–9613.

(36) Schäfer, O.; Huesmann, D.; Barz, M. Poly(S -Ethylsulfonyl- l -Cysteines) for Chemoselective Disulfide Formation. *Macromolecules* **2016**, *49* (21), 8146–8153.

(37) Muhl, C.; Schäfer, O.; Bauer, T.; Räder, H.-J.; Barz, M. Poly(S -Ethylsulfonyl- l - Homocysteine): An α-Helical Polypeptide for Chemoselective Disulfide Formation. *Macromolecules* **2018**, *51* (20), 8188–8196.

(38) Schäfer, O.; Klinker, K.; Barz, M.; Braun, L.; Huesmann, D.; Schultze, J. Combining Orthogonal Reactive Groups in Blockcopolymers for Functional Nanoparticle Synthesis in a Single Step. *ACS Macro Lett.* **2017**, *6*, 1140-1145.

(39) Marre, S.; Jensen, K. F. Synthesis of Micro and Nanostructures in Microfluidic Systems. *Chem. Soc. Rev.* **2010**, *39* (3), 1183–1202.

(40) Mai, Y.; Eisenberg, A. Self-Assembly of Block Copolymers. *Chem. Soc. Rev.* **2012**, *41* (18), 5969–5985.

(41) Zhang, H.; Zhu, Y.; Shen, Y. Microfluidics for Cancer Nanomedicine: From Fabrication to Evaluation. *Small* **2018**, *14* (28), 1–25.

(42) Johnson, B. K.; Prud'homme, R. K. Mechanism for Rapid Self-Assembly of Block Copolymer Nanoparticles. *Phys. Rev. Lett.* **2003**, *91* (11), 1–4.

(43) Dou, Y.; Wang, B.; Jin, M.; Yu, Y.; Zhou, G.; Shui, L. A Review on Self-Assembly in Microfluidic Devices. *J. Micromechanics Microengineering* **2017**, *27* (11).

(44) Tyrrell, Z. L.; Shen, Y.; Radosz, M. Fabrication of Micellar Nanoparticles for Drug Delivery through the Self-Assembly of Block Copolymers. *Prog. Polym. Sci.* **2010**, *35* (9), 1128–1143.

(45) Bleul, R.; Thiermann, R.; Maskos, M. Techniques to Control Polymersome Size. *Macromolecules* **2015**, *48* (20), 7396–7409.

(46) Keßler, S.; Drese, K.; Schmid, F. Simulating Copolymeric Nanoparticle Assembly in the Co-Solvent Method: How Mixing Rates Control Final Particle Sizes and Morphologies. *Polymer (Guildf).* **2017**, *126*, 9–18.

(47) Ziegenbalg, D.; Kompter, C.; Schönfeld, F.; Kralisch, D. Evaluation of Different Micromixers by CFD Simulations for the Anionic Polymerisation of Styrene. *Green Process. Synth.* **2012**, *1* (2), 211–224.

(48) Tonhauser, C.; Natalello, A.; Löwe, H.; Frey, H. Microflow Technology in Polymer Synthesis. *Macromolecules* **2012**, *45* (24), 9551–9570.

(49) Thiermann, R.; Bleul, R.; Maskos, M. Kinetic Control of Block Copolymer Self-Assembly in a Micromixing Device – Mechanistical Insight into Vesicle Formation Process. *Macromol. Chem. Phys.* **2017**, *218* (2), 1–9.

(50) Schoenmaker, L.; Witzigmann, D.; Kulkarni, J. A.; Verbeke, R.; Kersten, G.; Jiskoot, W.; Crommelin, D. J. A. MRNA-Lipid Nanoparticle COVID-19 Vaccines: Structure and Stability. *Int. J. Pharm.* **2021**, *601* (April), 120586.

(51) Chen, D.; Love, K. T.; Chen, Y.; Eltoukhy, A. A.; Kastrup, C.; Sahay, G.; Jeon, A.; Dong, Y.; Whitehead, K. A.; Anderson, D. G. Rapid Discovery of Potent SiRNA-Containing Lipid Nanoparticles Enabled by Controlled Microfluidic Formulation. *J. Am. Chem. Soc.* **2012**, *134* (16), 6948–6951.

(52) Rhee, M.; Valencia, P. M.; Rodriguez, M. I.; Langer, R.; Farokhzad, O. C.; Karnik, R. Synthesis of Size-Tunable Polymeric Nanoparticles Enabled by 3D Hydrodynamic Flow Focusing in Single-Layer Microchannels. *Adv. Mater.* **2011**, *23* (12), 79–83.

(53) Capretto, L.; Carugo, D.; Cheng, W.; Hill, M.; Zhang, X. Continuous-Flow Production of Polymeric Micelles in Microreactors: Experimental and Computational Analysis. *J. Colloid Interface Sci.* **2011**, *357* (1), 243–251.

(54) Belliveau, N. M.; Huft, J.; Lin, P. J.; Chen, S.; Leung, A. K.; Leaver, T. J.; Wild, A. W.; Lee, J. B.; Taylor, R. J.; Tam, Y. K.; Hansen, C. L.; Cullis, P. R. Microfluidic Synthesis of Highly Potent Limit-Size Lipid Nanoparticles for in Vivo Delivery of SiRNA. *Mol. Ther. - Nucleic Acids* **2012**, *1* (8), e37.

(55) von Bomhard, S.; Schramm, J.; Bleul, R.; Thiermann, R.; Höbel, P.; Krtschil, U.; Löb, P.; Maskos, M. Modular Manufacturing Platform for Continuous Synthesis and Analysis of Versatile Nanomaterials. *Chem. Eng. Technol.* **2019**, *42* (10), 2085–2094.

(56) Greco, F.; Vicent, M. J. Combination Therapy: Opportunities and Challenges for Polymer–Drug Conjugates as Anticancer Nanomedicines. *Adv. Drug Deliv. Rev.* **2009**, *61* (13), 1203–1213.

(57) Kocere, A.; Resseguier, J.; Wohlmann, J.; Skjeldal, F. M.; Khan, S.; Speth, M.; Dal, N. J. K.; Ng, M. Y. W.; Alonso-Rodriguez, N.; Scarpa, E.; Rizzello, L.; Battaglia, G.; Griffiths, G.; Fenaroli, F. Real-Time Imaging of Polymersome Nanoparticles in Zebrafish Embryos Engrafted with Melanoma Cancer Cells: Localization, Toxicity and Treatment Analysis. *EBioMedicine* **2020**, *58*, 102902.

(58) Dal, N.-J. K.; Kocere, A.; Wohlmann, J.; Van Herck, S.; Bauer, T. A.; Resseguier, J.; Bagherifam, S.; Hyldmo, H.; Barz, M.; De Geest, B. G.; Fenaroli, F. Zebrafish Embryos Allow Prediction of Nanoparticle Circulation Times in Mice and Facilitate Quantification of Nanoparticle–Cell Interactions. *Small* **2020**, *16* (5). 1906719.

(59) Fenaroli, F.; Repnik, U.; Xu, Y.; Johann, K.; Van Herck, S.; Dey, P.; Skjeldal, F. M.; Frei, D. M.; Bagherifam, S.; Kocere, A.; Haag, R.; De Geest, B. G.; Barz, M.; Russell, D. G.; Griffiths, G. Enhanced Permeability and Retention-like Extravasation of Nanoparticles from the Vasculature into Tuberculosis Granulomas in Zebrafish and Mouse Models. *ACS Nano* **2018**, *12* (8), 8646–8661.

(60) Sieber, S.; Grossen, P.; Detampel, P.; Siegfried, S.; Witzigmann, D.; Huwyler, J. Zebrafish as an Early Stage Screening Tool to Study the Systemic Circulation of Nanoparticulate Drug Delivery Systems in Vivo. *J. Control. Release* **2017**, *264* (August), 180–191.

(61) Schäfer, O.; Huesmann, D.; Muhl, C.; Barz, M. Rethinking Cysteine Protective Groups: S -Alkylsulfonyl- l -Cysteines for Chemoselective Disulfide Formation. *Chem. - A Eur. J.* **2016**, *22* (50), 18085–18091.

(62) Bauer, T. A.; Imschweiler, J.; Muhl, C.; Weber, B.; Barz, M. Secondary Structure-Driven Self-Assembly of Thiol-Reactive Polypept(o)Ides. *Biomacromolecules* **2021**, *22* (5), 2171–2180.

(63) Clay, N. E.; Whittenberg, J. J.; Leong, J.; Kumar, V.; Chen, J.; Choi, I.; Liamas, E.;

Schieferstein, J. M.; Jeong, J. H.; Kim, D. H.; Zhang, Z. J.; Kenis, P. J. A.; Kim, I. W.; Kong, H. Chemical and Mechanical Modulation of Polymeric Micelle Assembly. *Nanoscale* **2017**, *9* (16), 5194–5204.

(64) Thiermann, R.; Bleul, R.; Maskos, M. Kinetic Control of Block Copolymer Self-Assembly in a Micromixing Device – Mechanistical Insight into Vesicle Formation Process. *Macromol. Chem. Phys.* **2017**, *218* (2), 1–9.

(65) Alberg, I.; Kramer, S.; Leps, C.; Tenzer, S.; Zentel, R. Effect of Core-Crosslinking on Protein Corona Formation on Polymeric Micelles. *Macromol. Biosci.* **2021**, *2000414*.

(66) Ojha, T.; Hu, Q.; Colombo, C.; Wit, J.; Geijn, M.; Steenbergen, M. J.; Bagheri, M.; Königs-Werner, H.; Buhl, E. M.; Bansal, R.; Shi, Y.; Hennink, W. E.; Storm, G.; Rijcken, C. J. F.; Lammers, T. Lyophilization Stabilizes Clinical-stage Core-crosslinked Polymeric Micelles to Overcome Cold Chain Supply Challenges. *Biotechnol. J.* **2021**, *16* (6), 2000212.

(67) Van Eerden, R. A. G.; Mathijssen, R. H. J.; Koolen, S. L. W. Recent Clinical Developments of Nanomediated Drug Delivery Systems of Taxanes for the Treatment of Cancer. *Int. J. Nanomedicine* **2020**, *15*, 8151–8166.

(68) Lee, Y. K.; Han, S. Y.; Chin, Y. W.; Choi, Y. H. Effects of Cysteine on the Pharmacokinetics of Paclitaxel in Rats. *Arch. Pharm. Res.* **2012**, *35* (3), 509–516.

(69) Galluzzi, L.; Senovilla, L.; Vitale, I.; Michels, J.; Martins, I.; Kepp, O.; Castedo, M.; Kroemer, G. Molecular Mechanisms of Cisplatin Resistance. *Oncogene* **2012**, *31* (15), 1869–1883.

(70) Gou, J.; Feng, S.; Xu, H.; Fang, G.; Chao, Y.; Zhang, Y.; Xu, H.; Tang, X. Decreased Core Crystallinity Facilitated Drug Loading in Polymeric Micelles without Affecting Their Biological Performances. *Biomacromolecules* **2015**, *16* (9), 2920–2929.

(71) Tyrrell, Z. L.; Shen, Y.; Radosz, M. Near-Critical Fluid Micellization for High and Efficient Drug Loading: Encapsulation of Paclitaxel into PEG-b-PCL Micelles. *J. Phys. Chem. C* **2011**, *115* (24), 11951–11956.

(72) Logie, J.; Ganesh, A. N.; Aman, A. M.; Al-awar, R. S.; Shoichet, M. S. Preclinical Evaluation of Taxane-Binding Peptide-Modified Polymeric Micelles Loaded with Docetaxel in an Orthotopic Breast Cancer Mouse Model. *Biomaterials* **2017**, *123*, 39–47.

(73) Huh, K. M.; Lee, S. C.; Cho, Y. W.; Lee, J.; Jeong, J. H.; Park, K. Hydrotropic Polymer Micelle System for Delivery of Paclitaxel. *J. Control. Release* **2005**, *101* (1-3 SPEC. ISS.), 59–68.

(74) Larsen, D.; Kietrys, A. M.; Clark, S. A.; Park, H. S.; Ekebergh, A.; Kool, E. T. Exceptionally Rapid Oxime and Hydrazone Formation Promoted by Catalytic Amine Buffers with Low Toxicity. *Chem. Sci.* **2018**, *9* (23), 5252–5259.

(75) Morales, S.; Aceña, J. L.; García Ruano, J. L.; Cid, M. B. Sustainable Synthesis of Oximes, Hydrazones, and Thiosemicarbazones under Mild Organocatalyzed Reaction Conditions. *J. Org. Chem.* **2016**, *81* (20), 10016–10022.

(76) Meel, R. Van Der; Sulheim, E.; Shi, Y.; Kiessling, F.; Mulder, W. J. M. Smart Cancer Nanomedicine. *Nat. Nanotechnol.* **2019**, *14* (November), 1007–1017.

(77) Alberg, I.; Kramer, S.; Schinnerer, M.; Hu, Q.; Seidl, C.; Leps, C.; Drude, N.; Möckel, D.; Rijcken, C.; Lammers, T.; Diken, M.; Maskos, M.; Morsbach, S.; Landfester, K.; Tenzer, S.; Barz, M.; Zentel, R. Polymeric Nanoparticles with Neglectable Protein

Corona. *Small* **2020**, *16* (18), 1907574.

(78)   Rausch, K.; Reuter, A.; Fischer, K.; Schmidt, M. Evaluation of Nanoparticle Aggregation in Human Blood Serum. *Biomacromolecules* **2010**, *11* (11), 2836–2839.

(79)   Shi, Y.; Van Nostrum, C. F.; Hennink, W. E. Interfacially Hydrazone Cross-Linked Thermosensitive Polymeric Micelles for Acid-Triggered Release of Paclitaxel. *ACS Biomater. Sci. Eng.* **2015**, *1* (6), 393–404.

(80)   Bae, Y.; Nishiyama, N.; Fukushima, S.; Koyama, H.; Yasuhiro, M.; Kataoka, K. Preparation and Biological Characterization of Polymeric Micelle Drug Carriers with Intracellular PH-Triggered Drug Release Property: Tumor Permeability, Controlled Subcellular Drug Distribution, and Enhanced in Vivo Antitumor Efficacy. *Bioconjug. Chem.* **2005**, *16* (1), 122–130.

(81)   Yardley, D. A. Nab-Paclitaxel Mechanisms of Action and Delivery. *J. Control. Release* **2013**, *170* (3), 365–372.

(82)   Miele, E.; Spinelli, G. P.; Miele, E.; Tomao, F.; Tomao, S. Albumin-Bound Formulation of Paclitaxel (Abraxane ABI-007) in the Treatment of Breast Cancer. *Int. J. Nanomedicine* **2009**, *4*, 99–105.

(83)   Kocere, A.; Resseguier, J.; Wohlmann, J.; Skjeldal, F. M.; Khan, S.; Speth, M.; Dal, N. K.; Ng, M. Y. W.; Alonso-Rodriguez, N.; Scarpa, E.; Rizzello, L.; Battaglia, G.; Griffiths, G.; Fenaroli, F. Real-Time Imaging of Polymersome Nanoparticles in Zebrafish Embryos Engrafted with Melanoma Cancer Cells: Localization, Toxicity and Treatment Analysis. *EBioMedicine* **2020**, *58*, 102902.

(84)   Dal, N. K.; Kocere, A.; Wohlmann, J.; Van Herck, S.; Bauer, T. A.; Resseguier, J.; Bagherifam, S.; Hyldmo, H.; Barz, M.; De Geest, B. G.; Fenaroli, F. Zebrafish Embryos Allow Prediction of Nanoparticle Circulation Times in Mice and Facilitate Quantification of Nanoparticle–Cell Interactions. *Small* **2020**, *16* (5), 1906719.

Supporting Information

Experimental Section

Materials and Methods: Unless stated otherwise, solvents and reagents were used as received and purchased from Sigma-Aldrich. HFIP was purchased from Fluorochem, deuterated solvents were obtained from Deutero GmbH, (*R*)-lipoic and was bought from TCI Europe. PTX-LEV was obtained from Mercachem, Atto647N *N*-hydroxysuccinimide (NHS) was obtain from Atto Tec GmbH. Tetrahydrofuran (THF) was dried over Na, chloroform ($CHCl_3$) was dried over CaH_2 and were freshly distilled before use. *N*,*N*-Diisopropylethylamine (DIPEA) and *N*,*N*-triethylamine (NEt_3) were dried over sodium hydroxide, distilled, and stored at -20 °C until further use. *N*,*N*-Dimethylformamide (DMF) (99.8 %, extra dry over molecular sieve) was bought from Acros and freshly freeze-pumped prior to use to remove residual dimethyl amine. MilliQ water was prepared by using a MILLI-Q Reference A+ System and used at a resistivity of 18.2 $M\Omega \cdot cm^{-1}$ and total organic carbon content below 5 ppm. Human blood plasma for DLS measurements was obtained from the Transfusion Center of the University Clinic of Mainz (Germany) from ten healthy donors after physical examination and after obtaining informed consent in accordance with the Declaration of Helsinki. The study was approved by the local ethics committee "Landesärztekammer Rheinland-Pfalz" (837.439.12 (8540-F)). All plasma batches were pooled and stored at -20 °C.

Atomic Force Microscopy: AFM was measured on Cypher (Asylum Research) or Dimension Icon (Bruker) AFMs in non-contact mode at a scan rate of 1 Hz. Samples were prepared by drop-casting of a particle solution (β = 50 mg·L^{-1} in water) onto freshly cleaned mica. The sample was dried overnight at room temperature. The AFM images were evaluated using Gwyddion 2.49.

Cryogenic Transmission Electron Microscopy: Cryo-EM images were recorded on a Talos L120C transmission electron microscope (Thermo Fisher Scientific) operating at 120 kV. The images were recorded at 13'500, 36'000, and 57'000-fold magnification. CCPMs (3.5 µL, β = 150 mg·L^{-1}) were applied to freshly glow discharged Quantifoil® holey carbon films (R2/1 Cu 200, Quantifoil Micro Tools GmbH) and the grids were blotted for 2.5 s in a Vitrobot plunge-freezer (100% humidity, FEI Vitrobot Mark III, Thermo Fisher Scientific).

Single-Angle Dynamic Light Scattering: DLS measurements were performed on ZetaSizer Nano ZS or a Zetasizer Ultra (Malvern Panalytical Ltd.) equipped with a He-Ne laser (λ = 632.8 nm). All measurements were performed at 25 °C and a detection angle of 173° using disposable polystyrene cuvettes (VWR, Germany). Disposable folded capillary cells (Malvern Instruments Ltd.) were employed for ξ-potential measurements (3 mM sodium chloride). Cumulant size, polydispersity index (PDI), and size distribution histograms (intensity weighted) were calculated based on the autocorrelation function of the samples, with automated position and attenuator adjustments at multiple scans, and optional fluorescence filter.

Gel Permeation Chromatography: Gel permeation chromatography (GPC) was performed on a Jasco GPC setup at a flow rate of 1.0 mL·min^{-1} at 40°C using HFIP equipped with 3 g·L^{-1} of potassium trifluoroacetate as eluent and toluene as internal standard. GPC columns were purchased from PSS Polymer Standards Service GmbH (PFG-columns, particle size 7 µm, porosity 100 Å, 300 Å, and 4000 Å). Poly(methyl methacrylate) standards (PSS Polymer Standards Service GmbH) and pSar standards were used for calibration.[1] A UV detector (UV-4070, λ = 230 nm,) was used for polymer detection. Analysis was performed using PSS WinGPC (PSS Polymer Standards Service GmbH).

High Performance Liquid Chromatography: HPLC measurements were performed on a Beckman Coulter System Gold HPLC (Beckman Coulter, Inc), with a 508 autosampler, a 126 solvent module, a 168 detector, and a column oven equipped with a Luna C18(2) column (5µm, 100 Å, 250 × 4.6 mm) (Phenomenex LTD, Germany), controlled by the 32 Karat software (version 5.0, Beckman Coulter, Inc).

Infrared Spectroscopy: Attenuated total reflectance Fourier transform infrared (ATR-FT-IR) spectroscopy was performed on a FT/IR-4100 spectrometer (Jasco Corporation) with an ATR sampling accessory (MIRacle, Pike Technologies).

Multi-Angle Dynamic Light Scattering: For multi-angle DLS, cylindrical quartz cuvettes (Hellma, Mühlheim, Germany) were cleaned by dust-free distilled acetone and transferred to a dust free flow box. Light scattering measurements were performed on ALV spectrometers (ALV-5004 multiple-τ full digital correlator with He-Ne laser (632.8 nm) or ALV-CGS-3). The correlation functions of the particles were fitted using the sum of two exponentials. The z-average diffusion coefficient D_z was calculated by extrapolating D_{app} for q = 0. By formal application of Stokes law, the inverse z-average hydrodynamic radius is R_h=

$\langle R_h^{-1}\rangle_z^{-1}$ was determined. To investigate the aggregation behavior of the particles in human plasma, undiluted citrate plasma was filtered through a Millex GS 0.2 µm filter. The particle solutions were filtered through 0.2 µm pore size Millex GS filters. The following mixtures were prepared from initial particle solutions in 0.9% NaCl (β = 30 g·L^{-1}): NaCl/particle solution 40:1 (β = 0.75 g·L^{-1}), and plasma/particle solution 40:1 (β = 0.75 g·L^{-1}). The cuvettes were incubated for 60 min at 37 °C before measurement at T = 20 °C. Data analysis was performed according to a procedure reported by Rausch *et al.*[2] The correlation functions of plasma were fitted with a triexponential decay function, and the particles were fitted using a sum of two exponentials. Mixtures were fitted using a sum of both exponential decay functions with or without additional aggregate term.

Nuclear Magnetic Resonance: All NMR spectra were recorded at room temperature on Avance II 400, Avance III 400, or Avance III 600 spectrometers (Bruker). Calibration of the spectra was achieved using the solvent signals and the spectra were analyzed with MestReNova 14.1.2 from Mestrelab Research S.L.

Polymer Synthesis: All polymers were synthesized by amine-initiated ring-opening NCA polymerization in dry DMF under a stream of dry N$_2$. The NCA monomers, sarcosine-NCA and *S*-ethylsulfonyl-L-cysteine-NCA were prepared as reported previously.[3,4]

Polysarcosine: The pSar macroinitiators were prepared following our procedure published previously.[5,6] Sarcosine-NCA (10.0 g; 86.9 mmol; 250 eq.) was weighed into a pre-dried Schlenk tube and dissolved in dry DMF (50 mL). Next, *N*-(*tert*-butoxycarbonyl)-1,2-diaminoethane (55.7 mg; 348 µmol; 1.0 eq.) was added as a stock solution in dry DMF. The reaction mixture was stirred at 10 °C in the absence of light until the reaction was completed, as monitored by FT-IR. The amine end-group was reacted with perfluorophenyl-4-azidobutanoate (205 mg; 695 µmol; 2.0 eq.) and DIPEA (296 µL; 1.74 mmol; 5.0 eq.). The reaction mixture was stirred overnight followed by addition of acetic anhydride (331 µL; 3.48 mmol; 10 eq.) and DIPEA (1.18 mL; 6.95 mmol; 20 eq.) to react with residual end-groups. The solution was stirred for one day at room temperature before the polymer was precipitated in acetone (800 mL), collected on a Buchner funnel, washed with acetone and diethyl ether, and dried *in vacuo*. Next, the Boc-group was removed. The polymer (5.50 g) was transferred to a round-bottom flask, dissolved in water (75 mL) and cooled to 0 °C. Trifluoro acetic acid (TFA) (75 mL) was added, and the solution was stirred at 0 °C for 5 h. Next, the solution was transferred into

dialysis bags (MWCO, 3.5 kDa) and dialyzed with water, sodium hydrogen carbonate solution, and water. The solution was lyophilized, and pSar (**P1**) was obtained as a colorless powder (4.20 g, 68%). Complete deprotection was confirmed by ^{1}H NMR, when the singlet of the Boc-group had vanished (1.37 ppm). The chain length was determined by HFIP-GPC relative to pSar standards (X_n = 200). For pSar with X_n > 250, the sarcosine NCA was added sequentially after monomer conversion was verified (120 eq. each).

^{1}H NMR (400 MHz, DMSO-d_6): δ (ppm) 4.49 - 3.77 (m, 2nH, -CH$_2$), 3.06−2.61 (m, 3nH, -CH$_3$).

Polysarcosine-block-Poly(S-ethylsulfonyl-L-cysteine): Block copolymers were prepared from pSar macroinitiators following the procedure published previously.[5,6] The pSar macroinitiator (**P1**) (2.08 g; 145 µmol; 1.0 eq.) was weighed into a Schlenk tube and dried by azeotropic distillation with toluene *in vacuo*. Next, pSar was dissolved in dry DMF (12 mL), cooled to -10 °C, and *S*-ethylsulfonyl-L-cysteine NCA (1.73 g; 7.25 mmol; 50 eq.) was added as a stock solution in dry DMF. The polymerization was performed at an NCA concentration of ß = 100 g·L^{-1} and monitored by FT-IR. After 5 days, no further reaction progress was observed (approx. 50%). The polymer was precipitated in THF, and the suspension was centrifuged (4500 rpm; 5 min; 4 °C) and decanted. The procedure was repeated twice, concluding with diethyl ether. The product was dried *in vacuo* yielding pSar$_{200}$-*b*-p(L)Cys(SO$_2$Et)$_{27}$ (**P3**) as a colorless solid (2.57 g, 74%). For dye labeling, the polymer (**P3**, 58 mg; 2.91 µmol; 1.0 eq.) was dissolved in 1.5 mL of DMSO and Atto647N-*N*-hydroxysuccinimide (3.69 mg; 4.37 µmol; 1.5 eq.) was added from a stock solution in DMSO (ß = 10 g·L^{-1}; 369µL), and the solution was stirred at room temperature for 48 h. The unconjugated dye was removed by repetitive precipitation in THF (4500 rpm, 3 min, 4°C) and the polymer was dried *in vacuo*. Absence of free dye was verified by HFIP-GPC. ^{1}H NMR (400 MHz, DMSO-d_6): δ (ppm) 8.77 (b s, 1mH, CON*H*), 4.68 (m, 1mH, α-C*H*$_{(L-Cys)}$), 4.49 - 3.78 (m, 2nH, -C*H*$_{2(Sar)}$), 3.55 (m, 4mH, -S-C*H*$_2$, -SO$_2$-C*H*$_2$), 3.06 - 2.61 (m, 3nH, -CH$_{3(Sar)}$), 1.29 (t, 3mH, -CH$_{3(L-Cys)}$).

Cross-Linker Synthesis:

(R)-Methyl Lipoate: (*R*)-Methyl lipoate (**2**) was synthesized according to our previous publication, following a modified procedure from Hassan and Maltman.[6,7] (*R*)-Lipoic acid (**1**) (1.00 g; 4.85 mmol; 1.0 eq.) was dissolved in dry methanol (10 mL), and a catalytic amount of sulfuric acid (2.58 µL; 48.5 µmol;

0.01 eq.) was added. The reaction mixture was stirred at room temperature for 18 h in the absence of light. Next, methanol was removed *in vacuo* and the crude was dissolved in dichloromethane (DCM). The organic phase was washed with saturated $NaHCO_3$ solution (3x) and brine (3x), dried over $MgSO_4$, filtered, and concentrated *in vacuo*. (*R*)-Methyl lipoate (**2**) was obtained as a yellow oil (0.90 g, 84%) and used without further purification. ^{1}H NMR (400 MHz, $CDCl_3$): δ (ppm) 3.67 (s, 3H, -OC*H*$_3$), 3.57 (m, 1H, -S-C*H*), 3.15 (m, 2H, -S-C*H*$_2$), 2.47 (m, 1H, -S-CH$_2$-C*H*$_2$), 2.33 (t, *J* = 7.5 Hz, 2H, α-C*H*$_2$), 1.91 (m, 1H, -S-CH$_2$-C*H*$_2$), 1.73–1.61 (m, 4H, ß-C*H*$_2$, δ-C*H*$_2$), 1.49 (m, 2H, γ-C*H*$_2$).
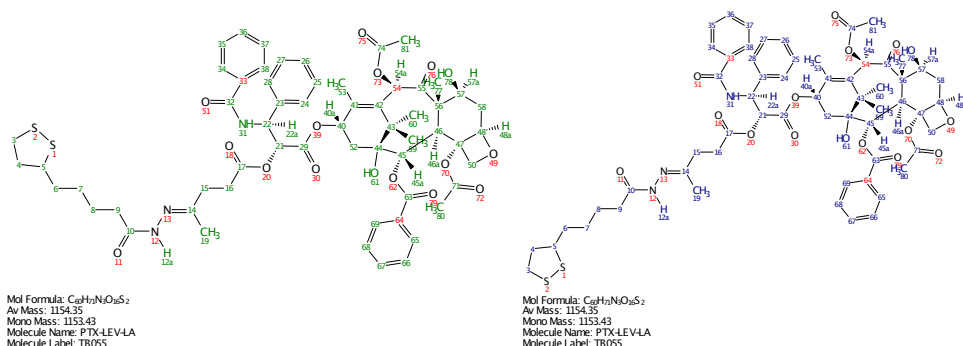
^{13}C NMR (101 MHz, $CDCl_3$): δ (ppm) 174.1, 56.5, 51.7, 40.4, 38.6, 34.8, 34.0, 28.9, 24.8.

(R)-Lipoic Acid Hydrazide: (*R*)-Lipoic acid hydrazide (**3**) was synthesized according to our previous publication, following a modified procedure from Koufaki *et al.*[6,8] (*R*)-Methyl lipoate (**2**) (895 mg; 4.04 mmol; 1.0 eq.) was dissolved methanol (8 mL), and hydrazine hydrate (1.19 mL; 24.3 mmol; 6.0 equiv) was added. The reaction mixture was stirred at room temperature for 72 h shielded from light. The solution was concentrated *in vacuo* and dissolved in ethyl ethanoate. The organic layer was washed with brine (5x), dried with $MgSO_4$, filtered, and concentrated *in vacuo*. (*R*)-Lipoic acid hydrazide (**3**) was obtained as a yellow oil (630 mg, 71%) and used without further purification. ^{1}H NMR (400 MHz, $CDCl_3$): δ (ppm) 6.71 (b s, 1H, -CON*H*), 3.56 (m, 1H, -S-C*H*), 3.15 (m, 2H, -SC*H*$_2$), 2.46 (m, 1H, -S-CH$_2$C*H*$_2$), 2.16 (t, *J* = 7.3 Hz, 2H, α-C*H*$_2$), 1.91 (m, 1H, -S-CH$_2$C*H*$_2$), 1.77-1.59 (m, 4H, -ß-C*H*$_2$, δ-C*H*$_2$), 1.55-1.39 (m, 2H, γ-C*H*$_2$). ^{13}C NMR (101 MHz, $CDCl_3$): δ (ppm) 173.7, 56,5, 40.4, 38.6, 34.7, 34.4, 29.0, 25.3. ESI-MS (*m/z* = 243.20): [M + Na]$^+$; [M+Na]$^+$ (calc.), 243.06 g·mol^{-1}.

Synthesis of PTX-LEV-LA: (*R*)-Lipoic acid hydrazide (**3**) (27.8 mg; 126 µmol; 3.0 eq.) was dissolved in a mixture of absolute MeOH (200 µL) and dry $CHCl_3$ (200 µL). Next, paclitaxel-levulinic acid (PTX-LEV) (40.0 mg; 42.0 µmol; 1.0 eq.) was added and the flask was equipped with three beads of activated molecular sieve 3A and the reaction mixture was stirred at room temperature. After full conversion of PTX-LEV (3 days), as monitored by TLC, the solvents were removed with a stream of dry nitrogen and the crude product was purified by column chromatography (dichloromethane + 5 vol.% EtOH) yielding PTX-LEV-LA (**4**) as a yellow solid (36.2 mg; 3.14 µmol; 75%).

ESI-MS (m/z = 1176.4187 [M+Na]$^+$; [M+Na]$^+$ (calc.) 1176.4168 g·mol^{-1}).

The structure was confirmed by NMR analysis, whereby coexisting rotamers were observed by NOESY.

Mol Formula: C₆₀H₇₂N₆O₁₆S₂
Av Mass: 1154.35
Mono Mass: 1153.43
Molecule Name: PTX-LEV-LA
Molecule Label: TB055

Mol Formula: C₆₀H₇₂N₆O₁₆S₂
Av Mass: 1154.35
Mono Mass: 1153.43
Molecule Name: PTX-LEV-LA
Molecule Label: TB055

cis-Rotamer (green numbering):

¹H NMR (600 MHz, DMSO-*d₆*): δ (ppm) = 9.98 (s, 1H, 12a), 9.19 (s, 1H, 31), 7.97 (m, 2H, 65, 69), 7.82 (m, 2H, 34, 38), 7.74 (m, 1H, 67), 7.67 (m, 2H, 66, 68), 7.48 (m, 7H, 24, 25, 27, 28, 35, 36, 37), 7.17 (m, 1H, 26), 6.27 (s, 1H, 54a), 5.79 (m, 1H, 40a), 5.45 (t, J_{HH} = 9.1 Hz, 1H, 22a), 5.40 (dd, J_{HH} = 12.8, 7.2 Hz, 1H, 45a), 5.27 (dd, J_{HH} =8.6, 2.6 Hz, 1H, 21), 4.91 (m, 2H, 48a, 78), 4.62 (s, 1H, 61), 4.09 (m, 1H, 57a), 4.00 (m, 2H, 50), 3.56 (m, 3H, 5, 46a), 3.12 (m, 2H, 3), 2.62 (m, 2H, 16), 2.55 (m, 2H, 15), 2.40 (m, 3H, 4', 9), 2.25 (s, 3H, 80), 2.10 (s, 3H, 81), 1.84 (m, 1H, 4"), 1.76 (s, 3H, 53), 1.72 (s, 3H, 19), 1.70 - 1.50 (m, 8H, 6, 8, 52, 58), 1.48 (s, 3H, 77), 1.40 - 1.30 (m, 2H, 7), 1.01 (d, J_{HH} = 4.5 Hz, 1H, 60), 0.99 (d, J_{HH} = 3.7 Hz, 1H, 61);

trans-Rotamer (blue numbering):

¹H NMR (600 MHz, DMSO-*d₆*): δ (ppm) = 10.29 (d, J_{HH} = 3.2 Hz, 1H, 12a), 9.30 (dd, J_{HH} = 8.3 Hz, 3.1 Hz, 1H, 31), 7.97 (m, 2H, 65, 69), 7.82 (m, 2H, 34, 38), 7.74 (m, 1H, 67), 7.67 (m, 2H, 66, 68), 7.48 (m, 7H, 24, 25, 27, 28, 35, 36, 37), 7.17 (m, 1H, 26), 6.27 (s, 1H, 54a), 5.79 (m, 1H, 40a), 5.56 (t, J_{HH} = 8.6 Hz, 1H, 22a), 5.40 (dd, J_{HH} = 12.8, 7.2 Hz, 1H, 45a), 5.23 (d, J_{HH} = 10.0, 1H, 21), 4.91 (m, 2H, 48a, 78), 4.62 (s, 1H, 61), 4.09 (m, 1H, 57a), 4.00 (m, 2H, 50), 3.56 (m, 3H, 5, 46a), 3.12 (m, 2H, 3), 2.62 (m, 2H, 16), 2.55 (m, 2H, 15), 2.40 (m, 1H, 4'), 2.30 (m, 2H, 9), 2.25 (s, 3H, 80), 2.10 (s, 3H, 81), 1.84 (m, 4H, 4", 19), 1.76 (s, 3H, 53), 1.70 - 1.50 (m, 8H, 6, 8, 52, 58), 1.48 (a, 3H, 77), 1.40 - 1.30 (m, 2H, 7), 1.01 (d, J_{HH} = 4.5 Hz, 1H, 60), 0.99 (d, J_{HH} = 3.7 Hz, 61).

Perfluorophenyl (R)-5-(1,2-dithiolan-3-yl)pentanoate: Perfluorophenyl (*R*)-5-(1,2-dithiolan-3-yl)pentanoate (**5**) was synthesized according to our previous publication.[5] (*R*)-Lipoic acid (**1**) (4.00 g; 19.4 mmol; 1.0 eq.) was weighed into a dry Schlenk flask and dissolved in dry THF (10.0 mL) at room temperature. Next, DIPEA (3.96 mL; 23.3 mmol; 1.2 eq.) and pentafluorophenyl trifluoroacetate (4.00 mL; 23.3 mmol; 1.2 eq.) were added with a counterflow of dry N_2 and the reaction mixture was stirred for 48 h at room temperature in the absence of light. The solvent was concentrated *in vacuo* and the crude product was purified by column chromatography (cyclohexane/ethyl ethanoate; 9/1 to 7/1) yielding perfluorophenyl (*R*)-5-(1,2-dithiolan-3-yl)pentanoate (**5**) as a yellow oil (6.73 g; 18.1 mmol; 93%). ^{1}H NMR (300 MHz, CDCl$_3$) δ (ppm) = 3.59 (m, 1H, -SC*H*), 3.16 (m, 2H, -S-C*H$_2$*), 2.69 (t, *J* = 7.3 Hz, 2H, α-C*H$_2$*), 2.47 (m, 1H, -S-CH$_2$-*CH$_2$*), 1.93 (m, 1H, -S-CH$_2$-*CH$_2$*), 1.87 - 1.69 (m, 4H, ß-C*H$_2$*, δ-C*H$_2$*), 1.69 - 1.47 (m, 2H, ɣ-C*H$_2$*). ^{19}F NMR (282 MHz, CDCl$_3$) δ (ppm) = -154.0 (m), -159.2 (t) , -163.5 (m). FD-MS (m/z = 372.2847 [M]$^+$; [M]$^+$ (calc.) 372.0272 g·mol^{-1}).

(R)-5-(1,2-Dithiolan-3-yl)-N-(naphthalen-1-ylmethyl)pentanamide: Perfluorophenyl (*R*)-5-(1,2-dithiolan-3-yl)pentanoate (**5**) (1.17 g; 3.14 mmol; 1.0 eq.) was weighed in a pre-dried Schlenk-flask, dissolved in absolute DCM (12 mL) and cooled to 0 °C. Next, NEt$_3$ (1.32 mL; 9.43 mmol; 3.0 eq.) and naphthalen-1-ylmethanamine (592 mg; 3.77 mmol; 1.2 eq.) were added, and the reaction mixture was allowed to reach room temperature. A colorless solid precipitated after 30 minutes. After 24 h, the solid was removed by filtration. The filtrate was diluted with DCM and washed with 10% NaHCO$_3$ solution (5x) and brine (3x). The organic phase was dried with MgSO$_4$, filtered, and concentrated *in vacuo*. To remove pentafluorophenol, the crude yellow oil was placed in a water bath (40 °C) and connected to high vacuum for 5 h. The crude product was purified by column chromatography (DCM + 2% MeOH) yielding (*R*)-5-(1,2-dithiolan-3-yl)-*N*-(naphthalen-1-ylmethyl)pentanamide (**6**) as a yellow solid (800 mg; 2.32 mmol; 74%). ^{1}H NMR (400 MHz, CDCl$_3$): δ (ppm) = 8.00 (m, 1H, -C$_{8, arom.}$-*H*), 7.85 (m, 2H, -C$_{5, arom.}$-*H*, -C$_{4, arom.}$-*H*), 7.54 (m, 2H, -C$_{6, arom.}$-*H*, C$_{7, arom.}$-*H*), 7.44 (m, 2H, -C$_{1, arom.}$-*H*, -C$_{2, arom.}$-*H*), 5.69 (m, 1H, -N*H*), 4.91 (d, *J* = 5.3 Hz, 2H, -NH-C*H$_2$*), 3.52 (m, 1H, -S-C*H*), 3.13 (m, 2H, -S-C*H$_2$*), 2.42 (m, 1H, -S-CH$_2$-C*H$_2$*), 2.20 (t, *J* = 7.3 Hz, 2H, α-C*H$_2$*), 1.86 (m, 1H, -S-CH$_2$-C*H$_2$*), 1.80 - 1.60 (m, 4H, ß-C*H$_2$*, δ- C*H$_2$*), 1.55 - 1.34 (m, 2H, ɣ-C*H$_2$*). ESI-MS (m/z = 346.1221 [M+H]$^+$; M$^+$ (calc.) 345.1294 g·mol^{-1}).

CCPMs by Self-Assembly: The preparation of core cross-linked polymeric micelles (CCPMs) was adapted from our previous publications and modified by the use of

DMSO.[5,6] The polypept(o)ide, $pSar_{200}$-b-p(L)Cys(SO_2Et)$_{17}$ (**P1**), was dissolved in DMSO equipped with 1 M thiourea at a concentration of 7.5 g·L^{-1}. After 1 h, 20 vol.% 1 mm acetate buffer (pH 4.75) equipped with 10 mm thiourea was added, and the solution was left to equilibrate at room temperature for 3 h, followed by dialysis against 1 mm acetate buffer (pH 4.75) containing 10 mM thiourea. The solution was filtered (PVDF 450) and concentrated to approx. 7 g·L^{-1} by spin filtration (Amicon Ultra; MWCO, 3 kDa), yielding the micelle solution. For cross-linking, (R)-lipoic acid hydrazide (**3**) was dissolved in ethanol at a concentration of ß = 20 g·L^{-1} in a separate flask, and one equivalent of tris(2-carboxyethyl)phosphine hydrochloride (TCEP·HCl) (ß = 50 g·L^{-1} in water) was added. After reaction overnight, the cross-linker solution was added to the micelle solution at equimolar amounts of thiols per cysteines. The reaction mixture was stirred at room temperature for at least 48 h. To remove thiourea, residual cross-linker and unconjugated polymer, the solution was dialyzed against DMSO and water mixtures (1/1 and 100% water) (MWCO, 6−8 kDa) followed by spin filtration (Amicon Ultra; MWCO, 100 kDa). The absence of the free polymer was verified by HFIP-GPC.

CCPMs by Continuous Flow Process: CCPMs were created in a three-step process, consisting of 1) the self-assembly of polymeric micelles, 2) the cross-linking of polymeric micelles and 3) the purification and concentration of the product solution. The first two steps were prepared by fluidic mixing over a SIMM V2 micromixer produced by Fraunhofer IMM. In preparation of the reaction, two reaction fluids were prepared. For the polymer solution, 450 mg of the polypept(o)ide, $pSar_{200}$-b-p(L)Cys(SO_2Et)$_{17}$ were dissolved in 60 mL of DMSO, leading to a clear solution after 30 min. To this solution, 18 mL of water were added, and the mixture was left to equilibrate for another 30 min. The total concentration of the polypept(o)ide was thus 5.7 g·L^{-1}. For the cross-linker solution, 49,5 mg of (R)-lipoic acid hydrazide was dissolved in 40 mL of ethanol and 20 mL water. To this solution, one equivalent of tris(2-carboxyethyl)phosphine hydrochloride (TCEP·HCl) in 18 mL water was added and left to react for 2 h, leading to a clear solution. The concentrations of polymer and cross-linker in their respective solutions were prepared to ensure full conversion of the polymer when applying an equal volume of cross-linker solution. For the micelle preparation, the polymer solution was combined with water over a micromixer. Generally, the delivery of the reagent solutions was done by HPLC pumps with subsequent backpressure valves. All pumps were under regular

inspection to ensure reproducible flowrates. The total flowrate was kept at 10 mL$\cdot$min^{-1}, the individual flowrates were adjusted to achieve a 1/10 or 1/5 dilution. The first 10 mL of the produced micelle solution were recovered before the process stream was switched into the second stage. Here, a volume stream of cross-linker solution equivalent to the polymer solution stream was added. No intermediate clean-up was performed. The product solution was then forwarded to a tangential flow filtration system for downstream processing.

Downstream processing via TFF: Before entering the membrane system, the product stream was diluted by an additional stream of 30 mL$\cdot$min^{-1} of deionized water. The combined stream was fed over a regenerated cellulose membrane with an average porosity of 30 kDa. With an outlet stream of 3 mL$\cdot$min^{-1} on retentate side and 37 mL$\cdot$min^{-1} on permeate side. After completing the reaction, the TFF membrane was flushed with 15 mL of deionized water with closed permeate line to recover the remaining particles between the membranes. In total the unreacted polymer as well as crosslinker and organic solvents in the product stream were reduced by >90 % and the concentration of CCPMs was increased 3-fold. For higher purification, a discontinuous procedure was added. In this approach, the product solution was diluted with an aliquot of water and then fed through the TFF system maintaining a permeate-to-retentate ratio of 3 to 1. The recovered retentate was re-fed to the original solution while the permeate was continuously removed until the total volume of raw product is reduced to one tenth of its original volume. After this step, the solution was diluted with additional water; the cycle was then repeated until HFIP-GPC didn't show any leftover unreacted polymer.

PTX Conjugation in DMSO: CCPMs (3.05 mg; 0.15 µmol copolymer; 2.23 µmol hydrazide-CL; 1.0 eq.) were weighed into an Eppendorf tube, dissolved in dry DMSO (500 µL), and PTX-LEV (0.64 mg; 0.67 µmol; 0.3 eq. per hydrazide-CL) was added from a stock solution in dry DMSO. The reaction mixture was placed on a benchtop shaker at 50°C for 7 days. The reaction mixture was transferred to a dialysis bag (3.5 kDa, MWCO) and dialyzed against water. The white precipitate was separated by centrifugation (4500 rpm, 5 min, 20 °C) and the supernatant was collected, filtered (PVDF; 220 nm), and lyophilized. The particles were weighed (2.68 mg; 73% yield) and reconstituted in sterile water at a concentration of 30 g$\cdot$L^{-1}.

PTX Conjugation by Film-Hydration: CCPMs (10.0 mg; 0.49 µmol copolymer; 7.30 µmol hydrazide-CL; 1.0 eq.) were placed into a 50 mL round bottom flask and PTX-LEV (2.0 mg; 2.19 µmol; 0.3 eq. per hydrazide-CL) was added from a stock solution in EtOH. The reaction mixture was placed in a water bath for 1 h (50 °C) before the solvent was removed *in vacuo*. The particles were re-suspended with water (3 mL) and ethanol (7 mL) and dried *in vacuo* once more. Subsequently, the particles were reconstituted in water at a concentration of 1 g·L^{-1}, the white precipitate was separated by centrifugation (4500 rpm, 5 min, 20 °C) and the supernatant was collected, filtered (PVDF; 220 nm), and lyophilized. The particles were weighed (9,35 mg; 78% yield) and reconstituted in sterile water at a concentration of 30 g·L^{-1}.

PTX Quantification and Release: The PTX content was determined by RP-HPLC using an external calibration (PTX-LEV; 8.450 min; UV-detector, λ = 230 nm) with gradient mixtures of water (+ 0.1 vol.% TFA) and acetonitrile (ACN) as mobile phase at a flow rate of 1 mL·min^{-1}: 60% ACN for 1 min, increase to 85% ACN over 8 minutes, hold at 85% for 5 min, decrease to 60% ACN in 1 min. PTX@CCPM solutions were analyzed in buffer (β_{CCPM} = 1 g·L^{-1}) containing 20 mm NH_4OAc, 134 mM NaCl, and 1.0 vol.% Tween 80 (pH 5.0). Samples (50 µL) were diluted with ACN (550 µL) and filtered (PTFE, 220 nm) before analysis. To determine the amount of non-conjugated drug, samples were taken immediately after mixing. For total drug content, the solution was additionally equipped with 10 mM TCEP, and the sample was taken after incubation for 24 h. For release studies, PTX@CCPMs were incubated in buffer at pH 5.0 (20 mM NH_4OAc, 134 mM NaCl, 1.0 vol.% Tween 80) or pH 7.4 (PBS, 1.0 vol.% Tween 80). Aliquots were taken at: 1 min, 0.5 h, 1.5 h, 3 h, 7 h, 17 h, 24 h, and 48 h. The PTX release was calculated based on the total PTX content, and data were taken from 3 independent experiments.

Cell Culture: HeLa cells (CCL-2) and B16F1 cells were cultured in their respective medium (DMEM/PenStrep/Glutamine) at 37 °C and 5 % CO_2 and were handled under sterile working conditions. They were subcultured every 3 days. To determine the viable cell count, cells were counted using a Casy TTC Cell (OLS). Cells were seeded in 96well plates at a density of 6,000 cells/well and treated for the indicated time spans 24 h post-seeding. For IC_{50} evaluations, cells were treated for 48 h. Viability was assayed 48 h after start of treatment using CellTiter-Glo® 2.0 Viability Assay according to the manufacturer's instructions. Luminescence readings were performed on a Tecan Spark® (Tecan) and signal

intensities normalized to untreated control samples incubated under the same conditions. Further analysis and plotting was performed on GraphPad PRISM.

In Vivo Experiments in Zebrafish Larvae:

Zebrafish Handling and Care: Zebrafish embryos were maintained in petri dishes containing zebrafish egg water supplemented with 0.003% phenythiourea (PTU). The petri dishes were kept in an incubator at a stable temperature of 28.5 °C. A maximum of 20 zebrafish embryos were placed in each dish which contained no less than 20 mL of egg water. All experiments were performed in accordance with the ethical standards and legislation for animal research in Norway (License FOTS-ID: 13563).

Circulation Time Analysis in Zebrafish: To evaluate the stability of CCPMs in the blood circulation of zebrafish the protocol described in Dal *et al.* was used.[9] Briefly, a pipette puller (P-97, Sutter Instrument) was used to produce borosilicate needles for injections. The needle was mounted on a micromanipulator (Narishige MN-153) connected to an Eppendorf FemtoJet express pump. Before injections, zebrafish were sedated in a tricaine bath (Finquel; 0.02% in zebrafish egg water) and placed on a plate containing hardened agarose gel (2% in water). Two-day old zebrafish embryos were injected in the posterior cardinal vein with 5 nL of CCPM solution. At defined times (5 min, 1 h, 4 h, and 24 h) an image of the whole zebrafish (30X magnification) and of the caudal region (120X magnification) was acquired using a Leica DFC365FX stereo microscope with a 1.0X plan apo lens.

The average fluorescence of the artery (AF, 30X), normalized by the average total fluorescence of the zebrafish (TF, 120X), was used to determine the nanoparticle circulation in the blood flow. The average artery fluorescence at 5 minutes (AF-5min) was considered as 100% meaning that all nanoparticles were considered in circulation at this time point. The values obtained were subtracted by the background fluorescence analyzed in zebrafish injected with PBS. The final analysis was therefore performed as follows:

$$\text{CCPM circulation, } \% = \frac{\frac{AF - \text{time x}}{TF - \text{time x}} - \text{background}}{\frac{AF - 5 \text{ min}}{TF - 5 \text{ min}} - \text{background}} * 100\%$$

CCPM Accumulation in Zebrafish: Mouse melanoma B16 cells expressing RFP (pGIPZ-RFP lentiviral vector) were used. The cells were grown at 37°C in RPMI-1640 medium (Lonza, Switzerland) with 10% FBS (Saveen & Werner, Norway)

puromycin (2 µg/mL, Sigma-Aldrich, USA). Cancer cells were detached using Versene (Life Technologies, USA) and centrifuged at 400 relative centrifugal force to obtain a cell pellet that was used to load borosilicate needles for subsequent zebrafish injections. Three-day old zebrafish embryos were xenotransplanted in the neural tube with approx. 200 B16F1 cells. After this, zebrafish embryos were kept in petri dishes in an incubator at 32 °C. After 5 days, treatment (PTX@CCPMs, ABX) or control (CCPMs, PBS) were injected in the posterior cardinal vein. To determine the nanoparticle accumulation in the tumor region, and an image of the zebrafish was taken after 8 hours at 30X using a Leica DFC365FX stereomicroscope with a 1.0X plan apo lens, and images were analyzed using the software Fiji.

Toxicity Analysis in Zebrafish: Zebrafish embryos were injected in the posterior cardinal vein at day 3 post fertilization with varying amounts of PTX@CCPMs or ABX. CCPMs and PBS were used as controls. The survival of zebrafish embryos in each treatment group was analyzed up to day 5 post injection.

Tumor Therapy in Zebrafish: Three-day old zebrafish embryos were injected in the neural tube with approx. 200 mouse melanoma B16F1 cells expressing RFP. After 24 h, the zebrafish embryos were divided into four groups each receiving one of the following treatments by injection in the posterior cardinal vein: 1. Abraxane, 5 ng of PTX; 2. PTX@CCPM, 10 ng of PTX; 3. CCPMs (control); 4. PBS (control). Six days later, images were recorded for each zebrafish (30X magnification) using a Leica DFC365FX stereomicroscope with a 1.0X plan apo lens, and images were analyzed using Fiji.

Data Management and Statistical Analysis: Data sets were managed using Microsoft Excel (Microsoft Corporation, USA), Graph Pad Prism (GraphPad Software, USA), and MagicPlot Student 2.9.3. For statistical analysis, differences between individual were evaluated by two-way ANOVA, and were considered significant for $p < 0.05$ (*$p < 0.05$, **$p < 0.01$, ***$p < 0.001$, ****$p < 0.0001$).

Results and Discussion
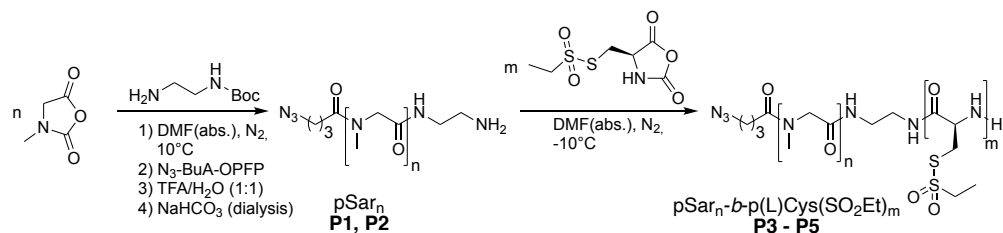
Polymer Synthesis

Scheme S1. Scheme of the polypept(o)ide synthesis by ring-opening NCA polymerization according to Klinker *et al.* and Bauer *et al.*[5,6]
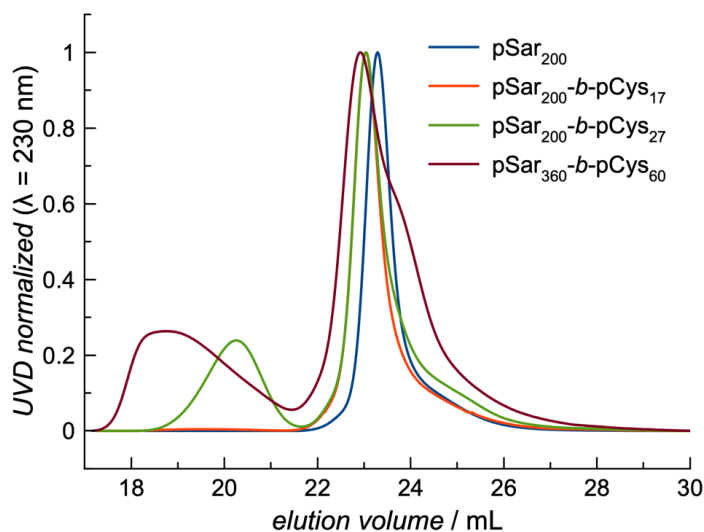

Figure S1. Analytical HFIP-GPC of polypept(o)ides. Note that secondary structure formation (anti-parallel ß-sheet) is not suppressed in HFIP accounting for the broad PDI of copolymers with increasing chain length of p(L)Cys(SO$_2$Et).[10,11]

Table S1. Characterization of core cross-linked polymeric micelles with and without embedded iron oxide nanoparticles.

polymer	X_n pSar[a]	X_n pCys(SO$_2$Et)[b]	M_n[c]	yield	Đ[c]
P1	200	-	36.6 kg·mol^{-1}	4.20 g	1.17
P2	360	-	38.3 kg·mol^{-1}	0.55 g	1.23

P3	200	17	40.6 kg·mol^{-1}	2.30 g	1.19
P4	200	27	40.3 kg·mol^{-1}	2.57 g	4.65
P5	360	60	45.1 kg·mol^{-1}	0.53 g	8.52

[a] HFIP-GPC relative to pSar standards. [b] determined by ^{1}H NMR. [c] HFIP-GPC relative to PMMA standards; note that secondary structure formation of p(L)Cys(SO2Et) is not suppressed, which induces aggregation accounting for multimodal GPC elugrams and broad dispersities.
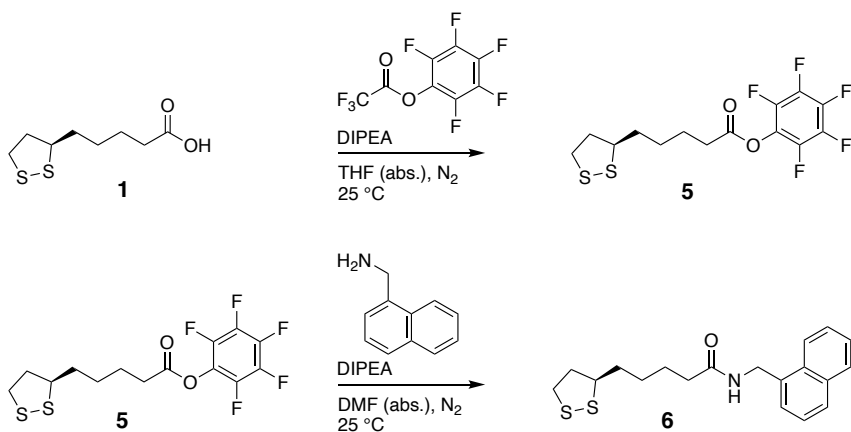
Cross-Linker Synthesis
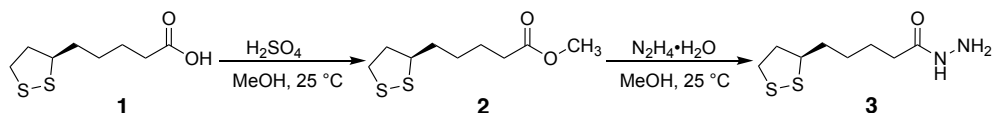
Scheme S2. Chemical reaction pathway to (R)-lipoic acid hydrazide (**3**) starting from (R)-lipoic acid (**1**), according to Bauer *et al.*[6]
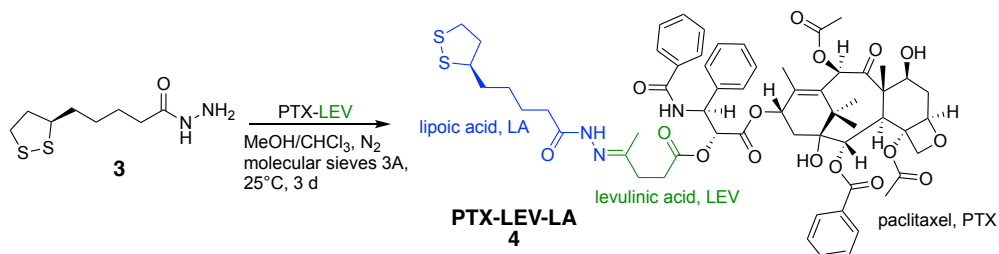
Scheme S3. Chemical reaction pathway to functional cross-linker PTX-LEV-LA (**4**).

Scheme S4. Chemical reaction pathway to (*R*)-5-(1,2-dithiolan-3-yl)-*N*-(naphthalen-1-ylmethyl)pentanamide (**6**) via perfluorophenyl (*R*)-5-(1,2-dithiolan-3-yl)pentanoate (**5**). The procedure was adapted and modified from Klinker *et al.*[5]

Core Cross-Linked Polymeric Micelles
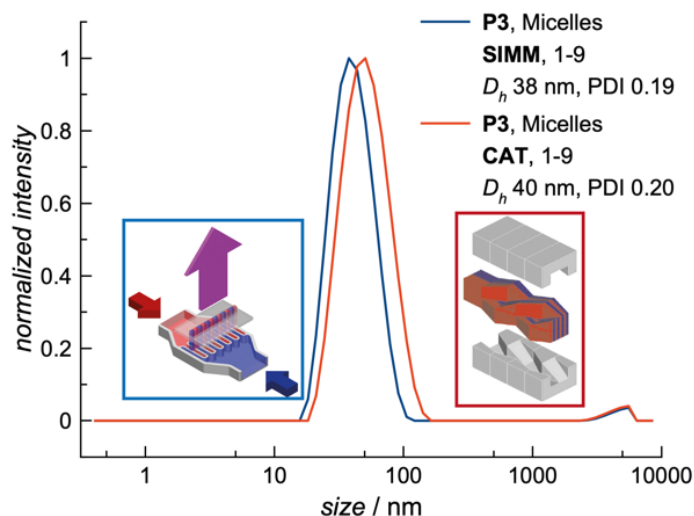
Particle Synthesis by Micromixer

Figure S2. DLS analysis of polymeric micelles by micromixer: influence of the micromixer. Polymeric micelles could be successfully generated from slit interdigital micromixers (SIMM) and caterpillar micromixers (CAT) at asymmetric flow rates of 1 to 9 and optimal overall flow rates of 10 mL·min^{-1}. Lower overall flow rates lead to polydisperse samples, and pulsation effects are observed beyond 20 mL·min^{-1}. Despite only minor differences were detected for CAT and SIMM at entirely optimized conditions in DLS, SIMM offered easier handling and reduced tendency to form aggregates. The SIMM was therefore chosen in the following for self-assembly and cross-linking.
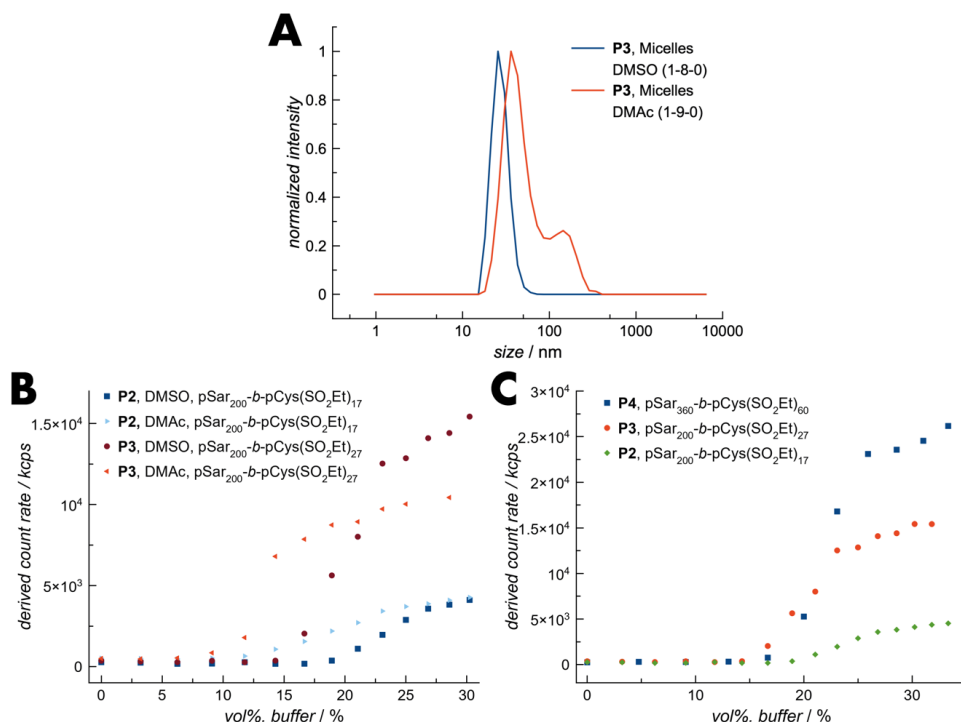
Figure S3. DLS analysis of polymeric micelles by micromixer: influence of the solvent. (**A**) Micelles formed via micromixer from **P3** using DMAc or DMSO. DMSO leads to more uniform particles due to the better solubility of the copolymer. (**B**) Aggregation curve of **P2** and **P3** in DMSO or DMAc. The aggregation in DMSO starts at higher buffer content, indicating better solubility of the copolymer. (**C**) Aggregation curve of **P2**, **P3** and **P4** in DMSO. Higher $pCys(SO_2Et)$ fractions lead to earlier aggregation.[6]
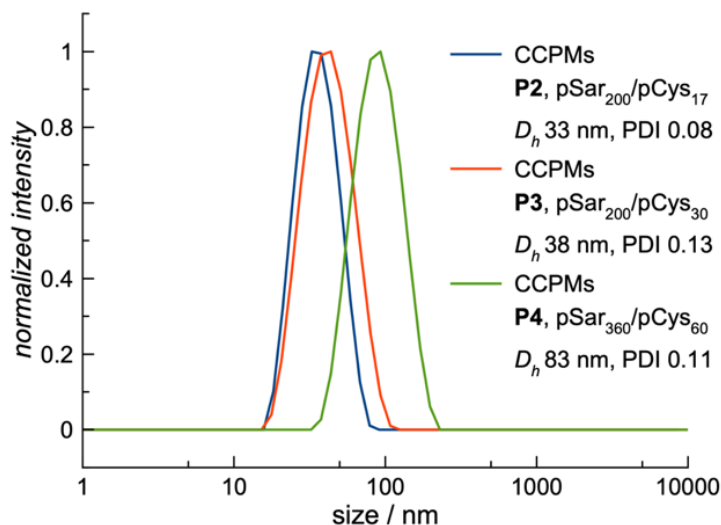
Figure S4. DLS analysis of CCPMs by micromixer: influence of the chain length. CCPM size increases for increasing block lengths of pSar$_n$-b-pCys(SO$_2$Et)$_m$ with n = 200 or 360 and m = 17, 30, and 60 (**P2**, **P3**, **P4**).
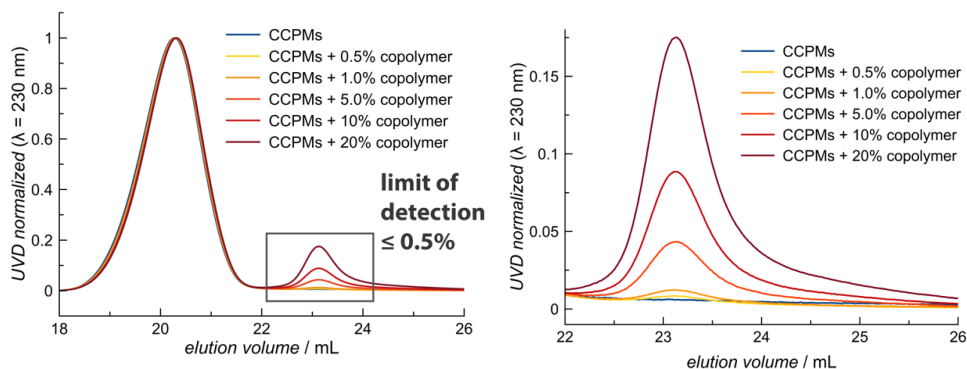

Figure S5. HFIP-GPC analysis: Determining the limit of detection. Contaminations as low as 0.5% copolymer can be detected.
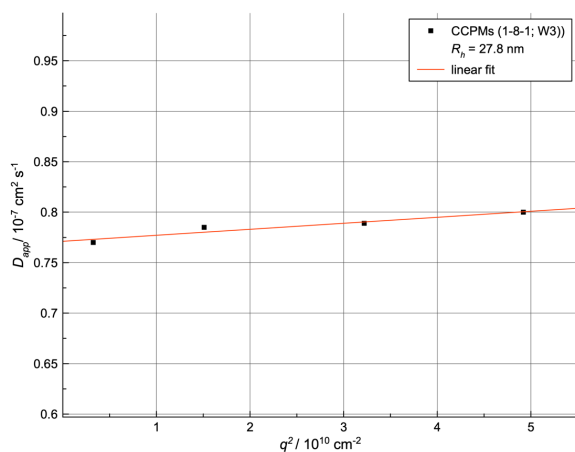
Figure S6. Multi-angle DLS analysis of micromixer CCPMs after purification by cross-flow filtration. A hydrodynamic diameter of 27.8 nm was derived from the bi-exponential fit of the autocorrelation curve, whereby only a slight angle-dependency could be detected for measurements at 26°, 58°, 90°, and 122°.
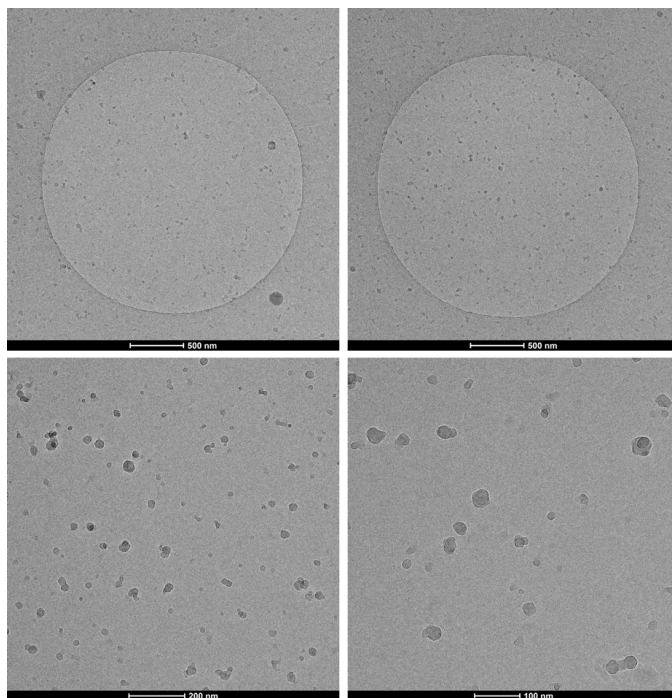

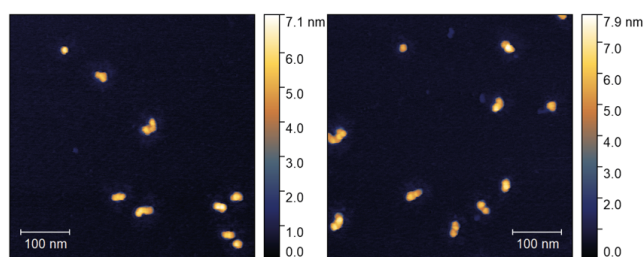**Figure S7**. CryoTEM images of CCPMs produced by micromixer (1-8-1; W3).

Figure S8. Additional AFM images of CCPMs produced by micromixer (1-8-1; W3).
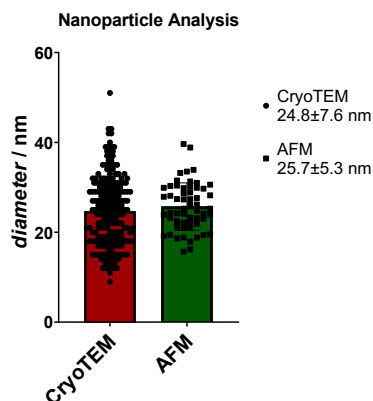

Figure S9. Particle size of micromixer-CCPMs (1-8-1; W3) as determined by CryoTEM and AFM image analysis.
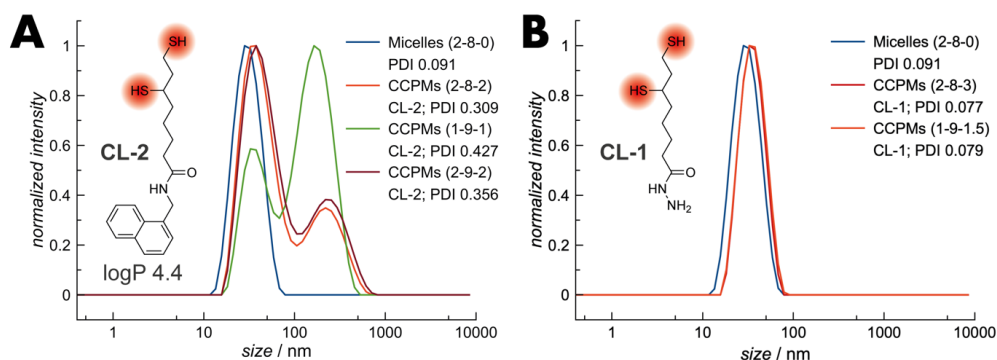
Figure S10. DLS analysis of CCPMs by micromixer: influence of the cross-linker. (**A**) Micelle cross-linking with the hydrophobic cross-linker (*R*)-5-(1,2-dithiolan-3-yl)-*N*-(naphthalen-1-ylmethyl)pentanamide (**6**) leads to aggregate formation (turbid solutions, multimodal size distribution in DLS) irrespective of the cross-linking flow rates. (**B**) Micelle cross-linking with the functional (*R*)-lipoic acid hydrazide (**3**) leads to CCPMs with

monomodal distribution and narrow PDI and is not affected by the applied volume flow ratios.

Cross-Linking by Pro-Drug Drug Cross-Linker (PTX-LEV-LA)

Applying the functional pro-drug cross-linker PTX-LEV-LA (**4**) leads to turbid particle solutions, whereby the particle structure cannot be preserved. Moreover, only low drug contents of 0.9 wt.% can be determined (encapsulation efficiency < 1%), which are not sufficient for stabilization by core cross-linking. Furthermore, low reaction yields do not justify the synthetic effort.
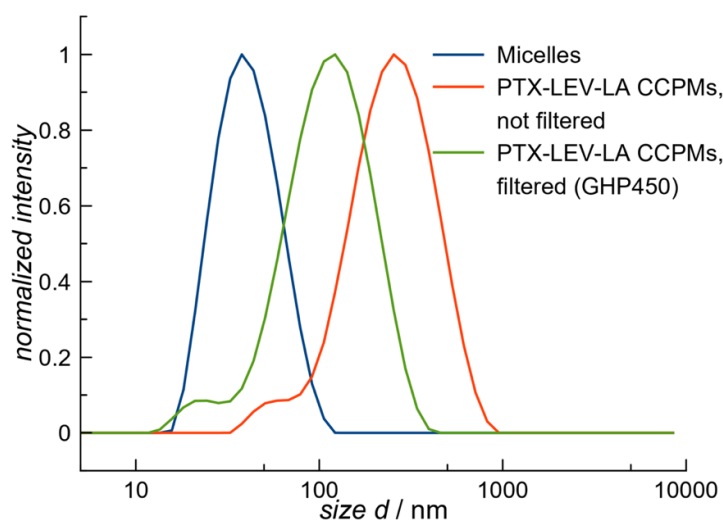

Figure S11. Dynamic light scattering of micelles before and after cross-linking with PTX-LEV-LA (**4**).

PTX-LEV Conjugation
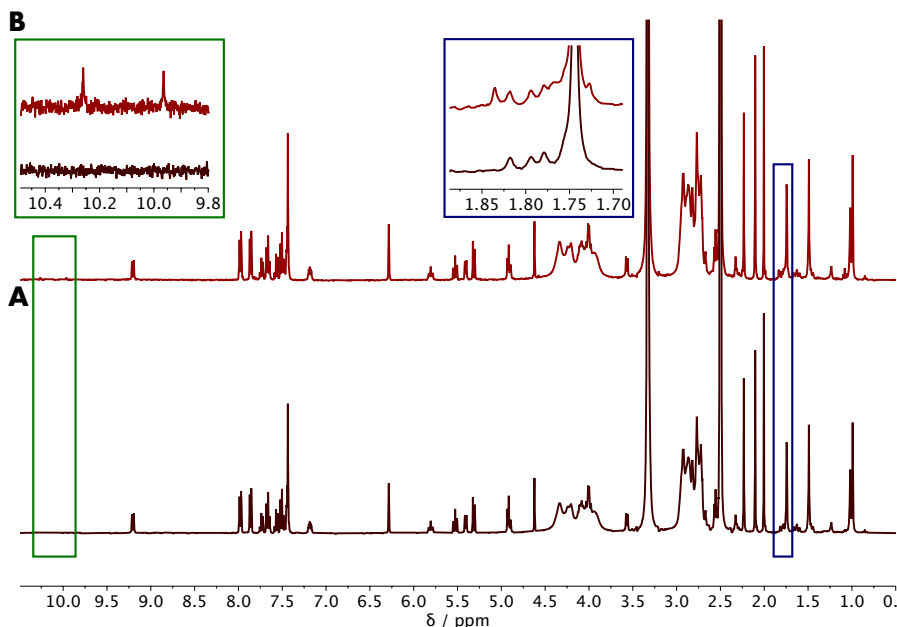
Figure S12. 1H NMR analysis of the PTX-LEV conjugation to lipoic acid hydrazide-functionalized CCPMs in DMSO-d_6. (**A**) CCPMs + PTX-LEV at t = 0 h. (**B**) CCPMs + PTX-LEV at t = 7 days. Significant peaks at 10.3/9.95ppm and 1.84 ppm account for hydrazone-bond formation: Green box: C=O-NH-N=CR'(CH$_3$); Blue box: -N=CR'(CH_3).
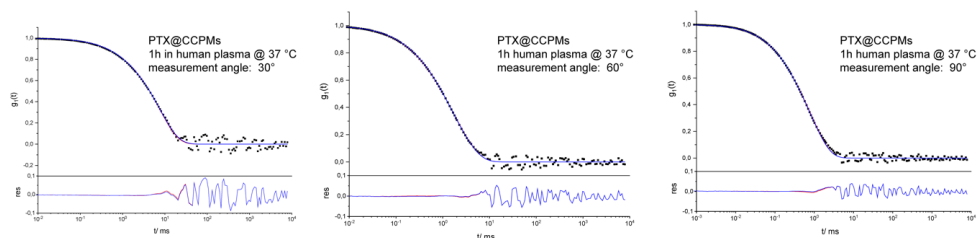
Figure S13. Multi angle DLS of PTX@CCPMs in undiluted human plasma: Autocorrelation function $g_1(t)$ given for the measurement angles of 30°, 60°, and 90°. The fits with (blue line) and without (red line) aggregation term (upper graph), and derived residuals for the fit w/o aggregate and correlation function indicate no significant aggregation (lower graph).

Cell Culture
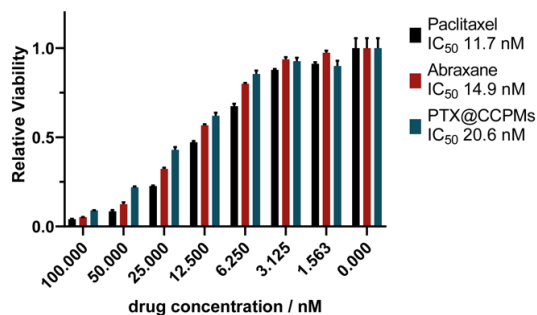
Figure S14. Analysis of PTX@CCPMs, Abraxane, and free PTX in HeLa cells. IC_{50} values were calculated for 100 μM as maximal inhibition show comparable performance of the three paclitaxel formulations.
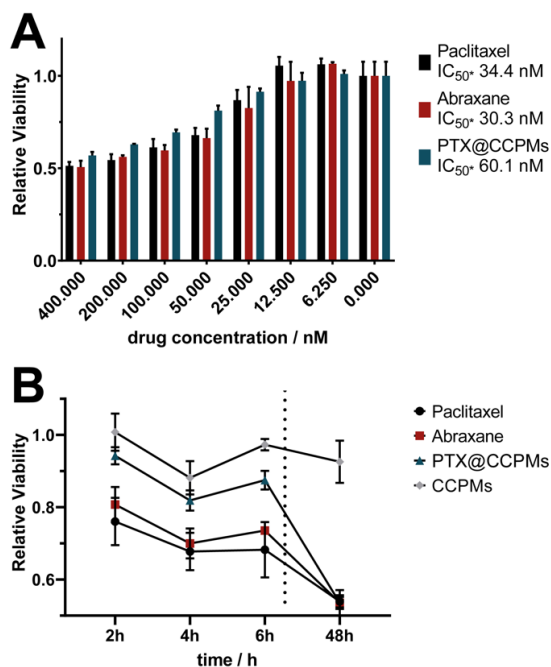
Figure S15. Analysis of PTX@CCPMs, Abraxane, and free PTX in B16F1 cells. (**A**) IC_{50} values were calculated for 400 μM as maximal inhibition. (**B**) Time-dependent toxicity of PTX formulations at 100 μM.

In vivo experiments
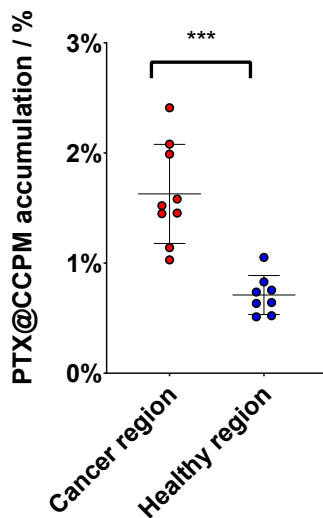
Figure S16. Tumor accumulation of PTX@CCPMs at 8 h post nanoparticle administration. Accumulation values based on nanoparticle fluorescence at t = 5 min (100% in circulation). According to Figure S17, more than 40% are expected to be still in circulation.
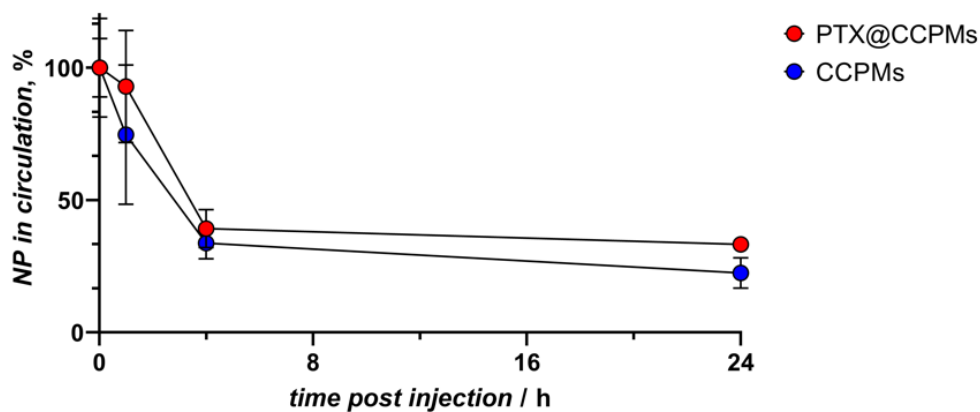
Figure S17. Circulation time analysis of PTX@CCPMs and CCPMs in zebrafish embryo.

References for Supporting Information

(1)   Weber, B.; Birke, A.; Fischer, K.; Schmidt, M.; Barz, M. Solution Properties of Polysarcosine: From Absolute and Relative Molar Mass Determinations to Complement Activation. *Macromolecules* **2018**, *51* (7), 2653–2661.

(2)   Rausch, K.; Reuter, A.; Fischer, K.; Schmidt, M. Evaluation of Nanoparticle Aggregation in Human Blood Serum. *Biomacromolecules* **2010**, *11* (11), 2836–2839.

(3)   Birke, A.; Huesmann, D.; Kelsch, A.; Weilbächer, M.; Xie, J.; Bros, M.; Bopp, T.; Becker, C.; Landfester, K.; Barz, M. Polypeptoid- Block -Polypeptide Copolymers: Synthesis, Characterization, and Application of Amphiphilic Block Copolypept(o)Ides in Drug Formulations and Miniemulsion Techniques. *Biomacromolecules* **2014**, *15* (2), 548–557.

(4)   Schäfer, O.; Huesmann, D.; Muhl, C.; Barz, M. Rethinking Cysteine Protective Groups: S -Alkylsulfonyl- l -Cysteines for Chemoselective Disulfide Formation. *Chem. - A Eur. J.* **2016**, *22* (50), 18085–18091.

(5)   Klinker, K.; Schäfer, O.; Huesmann, D.; Bauer, T.; Capelôa, L.; Braun, L.; Stergiou, N.; Schinnerer, M.; Dirisala, A.; Miyata, K.; Osada, K.; Cabral, H.; Kataoka, K.; Barz, M. Secondary-Structure-Driven Self-Assembly of Reactive Polypept(o)Ides: Controlling Size, Shape, and Function of Core Cross-Linked Nanostructures. *Angew. Chemie Int. Ed.* **2017**, *56* (32), 9608–9613.

(6)   Bauer, T. A.; Imschweiler, J.; Muhl, C.; Weber, B.; Barz, M. Secondary Structure-Driven Self-Assembly of Thiol-Reactive Polypept(o)Ides. *Biomacromolecules* **2021**, *22* (5), 2171–2180.

(7)   Hassan, H. M. A.; Maltman, B. A. Mixed SAMs and MALDI-ToF MS: Preparation of N-Glycosylamine Derivative and Thioctic Acid Methyl Ester Bearing 1,2-Dithiolane Groups and Detection of Enzymatic Reaction on Au. *Bioorg. Chem.* **2012**, *40* (1), 6–9.

(8)   Koufaki, M.; Kiziridi, C.; Alexi, X.; Alexis, M. N. Design and Synthesis of Novel Neuroprotective 1,2-Dithiolane/Chroman Hybrids. *Bioorg. Med. Chem.* **2009**, *17* (17), 6432–6441.

(9)   Dal, N. K.; Kocere, A.; Wohlmann, J.; Van Herck, S.; Bauer, T. A.; Resseguier, J.; Bagherifam, S.; Hyldmo, H.; Barz, M.; De Geest, B. G.; Fenaroli, F. Zebrafish Embryos Allow Prediction of Nanoparticle Circulation Times in Mice and Facilitate Quantification of Nanoparticle–Cell Interactions. *Small* **2020**, *16* (5), 1906719.

(10)   Bauer, T. A.; Muhl, C.; Schollmeyer, D.; Barz, M. Racemic S -(Ethylsulfonyl)- Dl -cysteine N -Carboxyanhydrides Improve Chain Lengths and Monomer Conversion for B-Sheet-Controlled Ring-Opening Polymerization. *Macromol. Rapid Commun.* **2021**, *42* (8), 2000470.

(11)   Bauer, T. A.; Horvat, N. K.; Marques, O.; Chocarro, S.; Mertens, C.; Colucci, S.; Schmitt, S.; Carrella, L. M.; Morsbach, S.; Koynov, K.; Fenaroli, F.; Blümler, P.; Jung, M.; Sotillo, R.; Hentze, M. W.; Muckenthaler, M. U.; Barz, M. Core Cross-Linked Polymeric Micelles for Specific Iron Delivery: Inducing Sterile Inflammation in Macrophages. *Adv. Healthc. Mater.* **2021**, *10* (19), 2100385.

Appendix

NMR Spectroscopy

Cross-Linker Syntheses
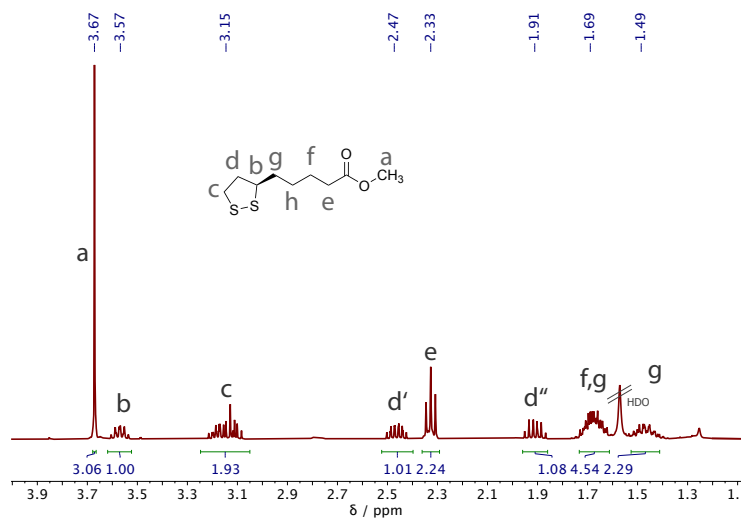
Figure S18. ^{1}H NMR Analysis of (*R*)-methyl liponamide (**2**) in CDCl$_3$.
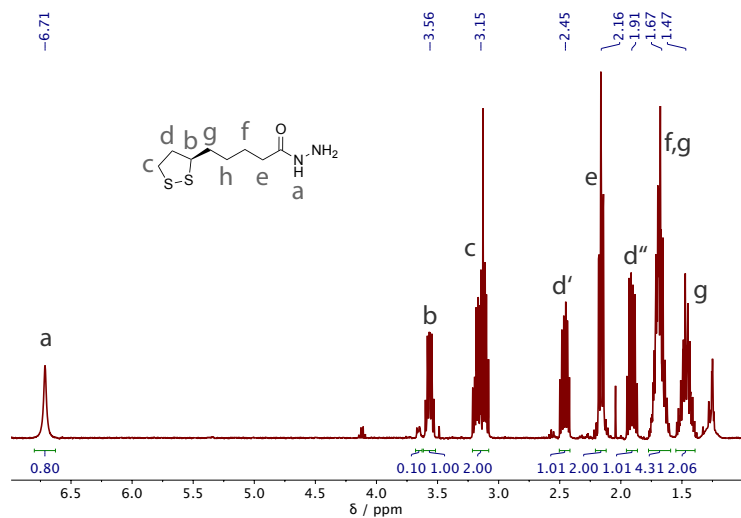
Figure S19. ^{1}H NMR Analysis of (*R*)-lipoic acid hydrazide (**3**) in CDCl$_3$.
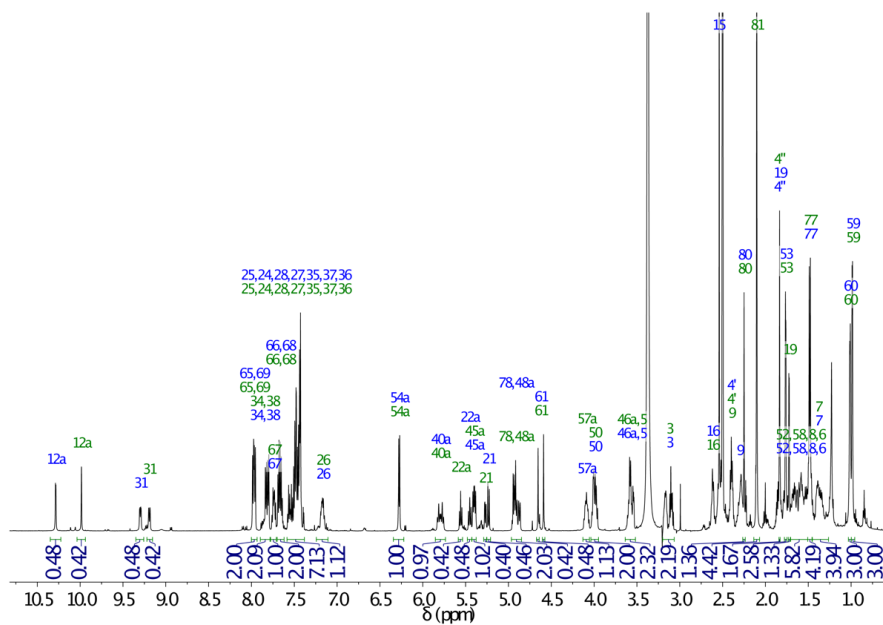
Figure S20. ^{1}H NMR analysis of PTX-LEV-LA (**4**) in DMSO-d_6.

Assignment for PTX-LEV-LA:
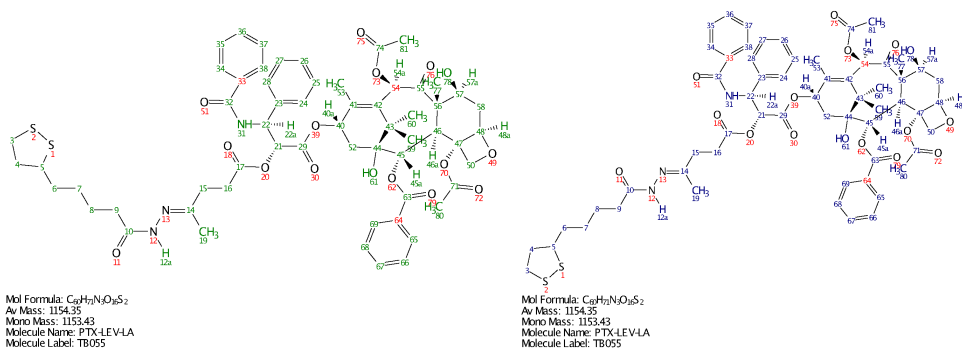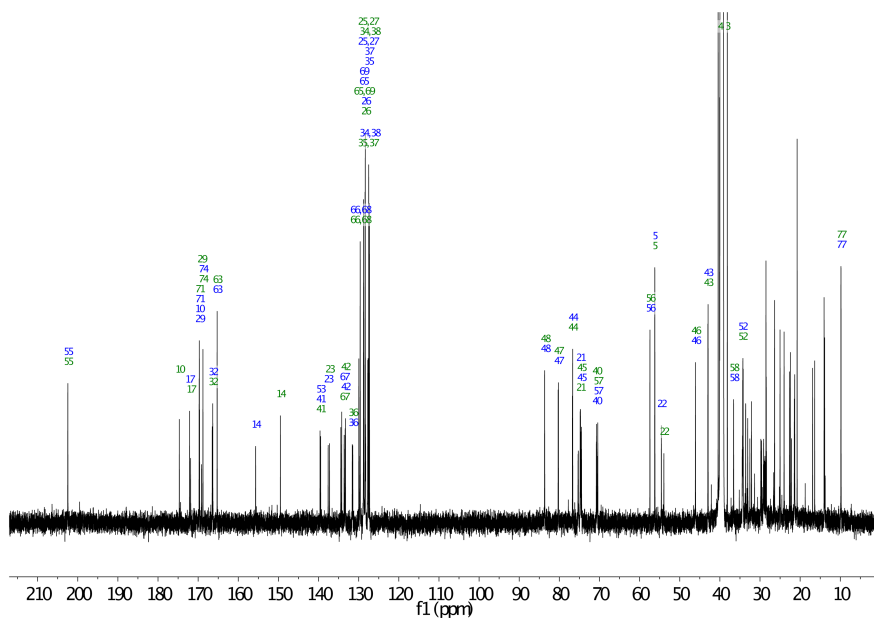
Figure S21. ^{13}C NMR analysis of PTX-LEV-LA (**4**) in DMSO-d$_6$.
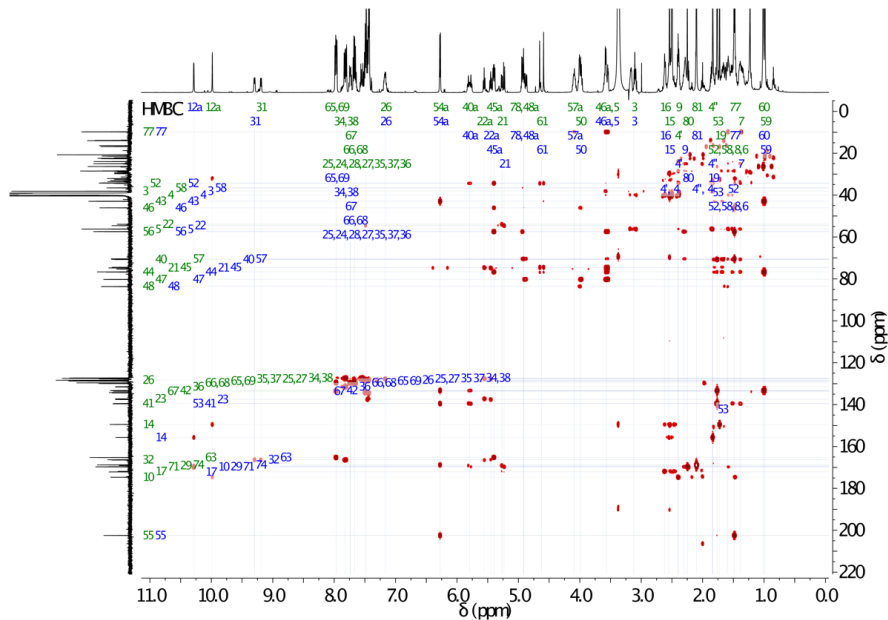
Figure S22. ^{1}H,^{13}C HMBC analysis of PTX-LEV-LA (**4**) in DMSO-*d$_6$*.
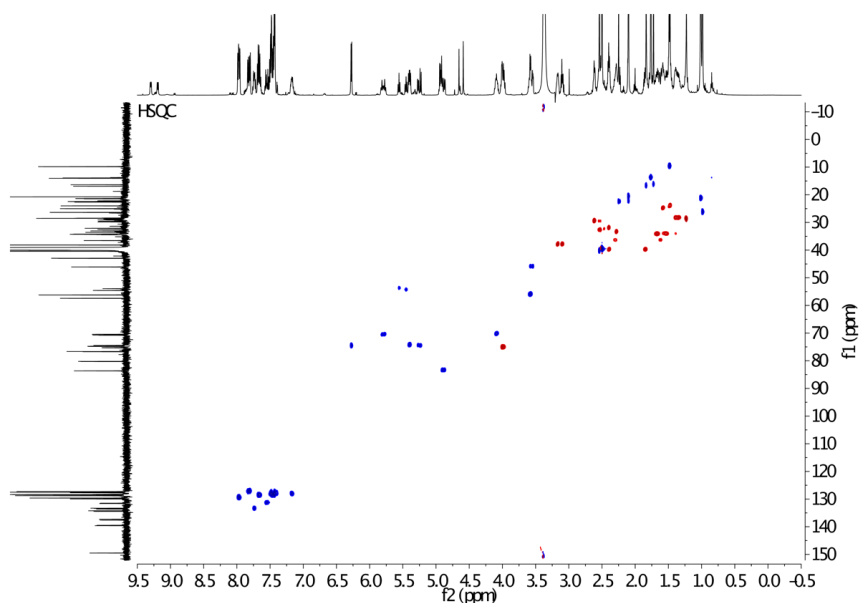
Figure S23. ¹H, ¹³C HSQC analysis of PTX-LEV-LA (**4**) in DMSO-*d₆*.
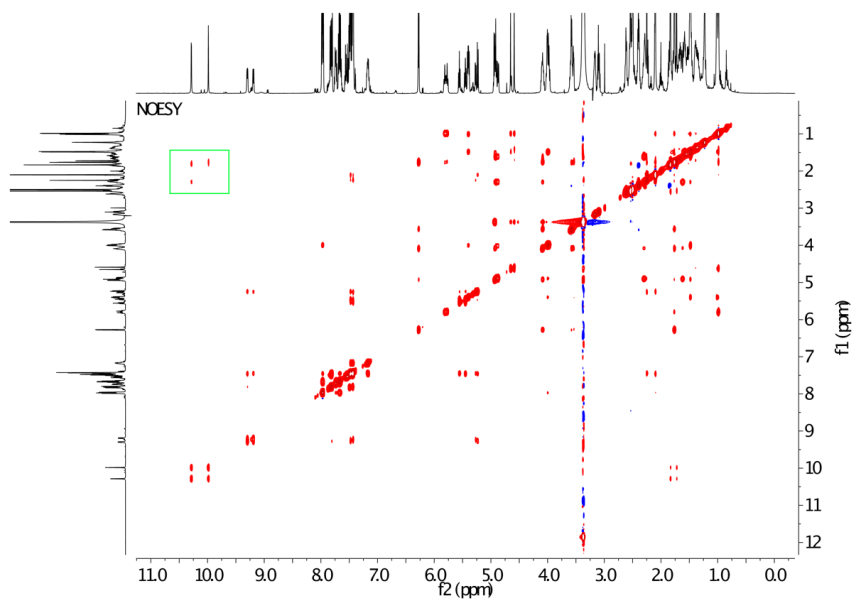
Figure S24. ¹H NOESY analysis of PTX-LEV-LA (**4**) DMSO-*d₆*. The green box indicates different coupling between *cis*- and *trans*-rotamers of PTX-LEV-LA (**4**).
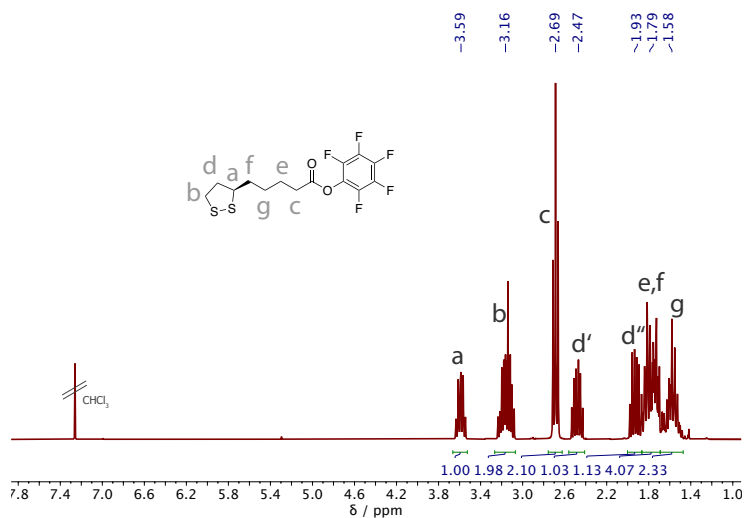
Figure S25. ^{1}H NMR Analysis of perfluorophenyl (*R*)-5-(1,2-dithiolan-3-yl)pentanoate (**5**) in CDCl3.
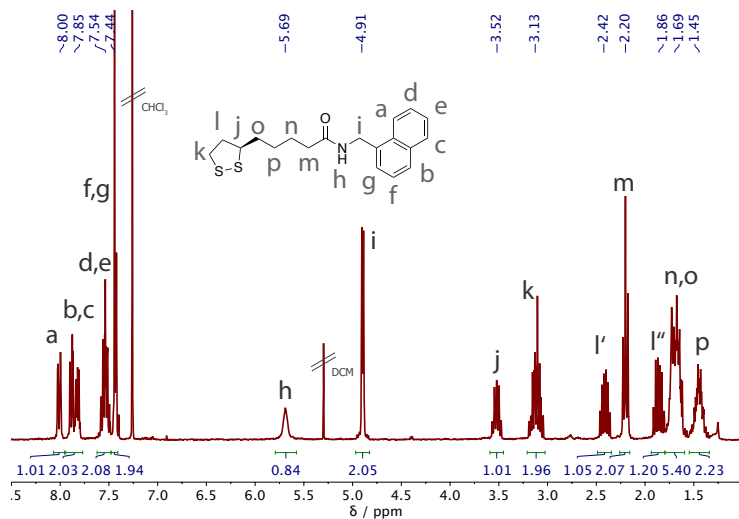
Figure S26. ^{1}H NMR Analysis of (*R*)-5-(1,2-dithiolan-3-yl)-*N*-(naphthalen-1-ylmethyl)pentanamide (**6**) in CDCl3.

Polypept(o)ides
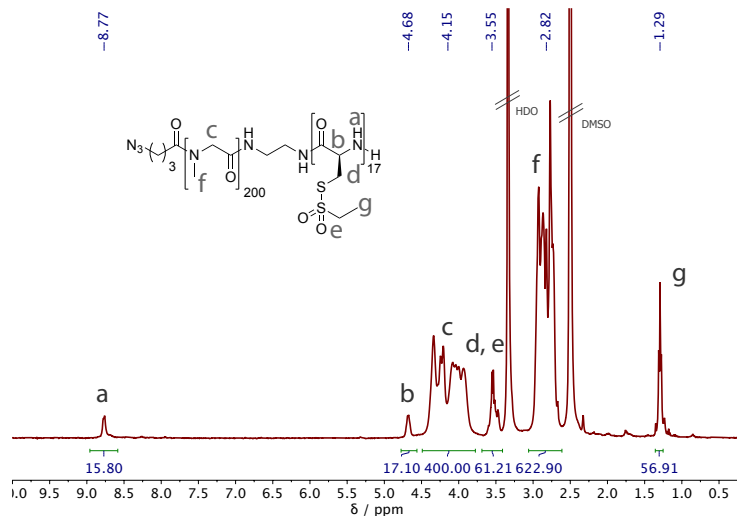
Figure S27. ¹H NMR Analysis of pSar₂₀₀-*b*-p(L)Cys(SO₂Et)₁₇ in DMSO-*d₆*.
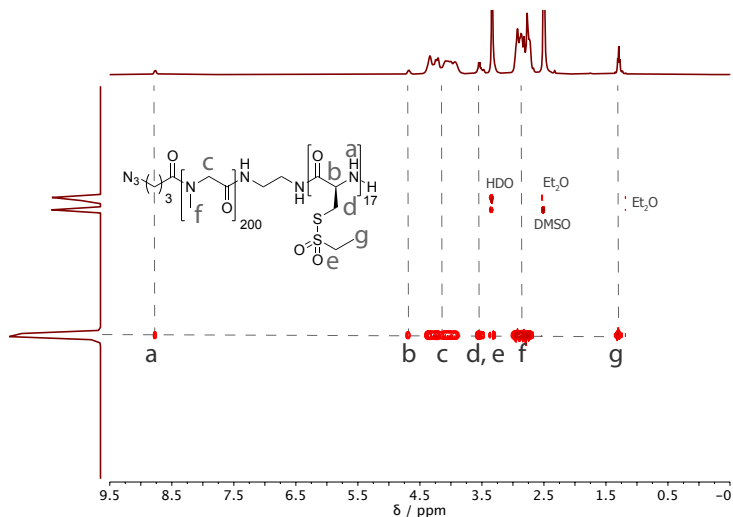
Figure S28. DOSY NMR Analysis of pSar₂₀₀-*b*-p(L)Cys(SO₂Et)₁₇ in DMSO-*d₆*.
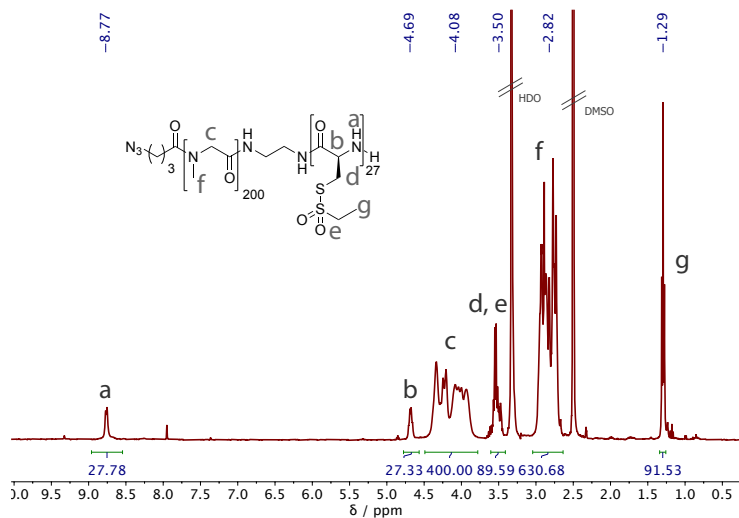
Figure S29. ^{1}H NMR Analysis of pSar$_{200}$-b-p(L)Cys(SO$_2$Et)$_{27}$ in DMSO-d_6.
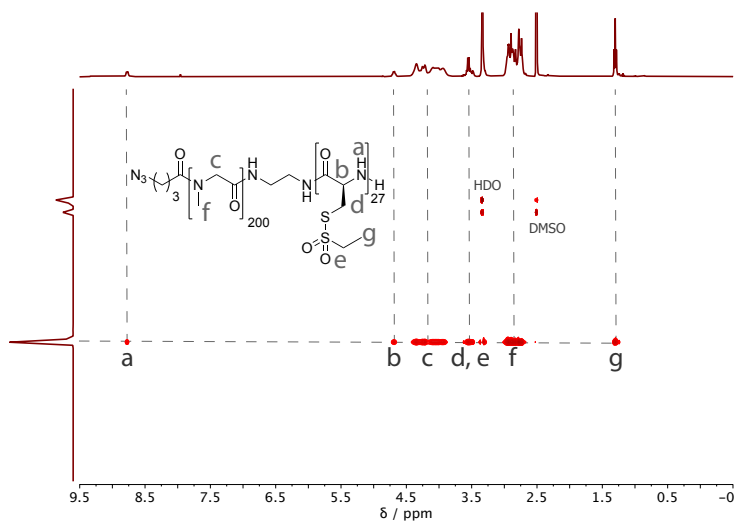
Figure S30. DOSY NMR Analysis of pSar$_{200}$-b-p(L)Cys(SO$_2$Et)$_{27}$ in DMSO-d_6.
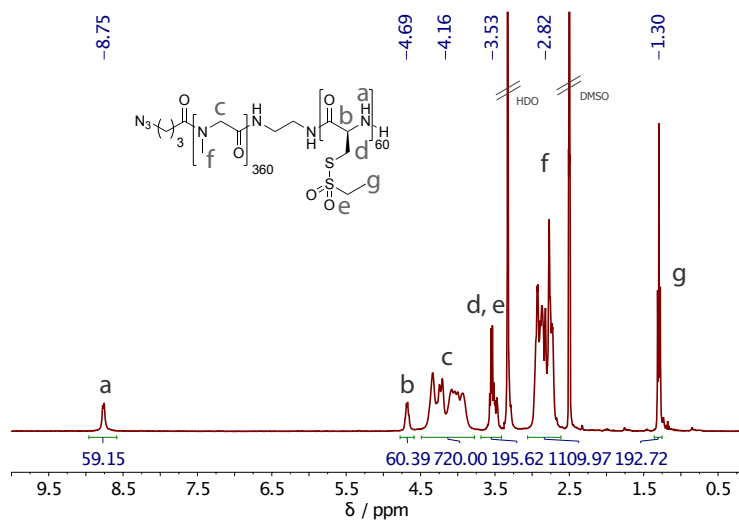
Figure S31. ^{1}H NMR Analysis of pSar$_{360}$-b-p(L)Cys(SO$_2$Et)$_{60}$ in DMSO-d_6.
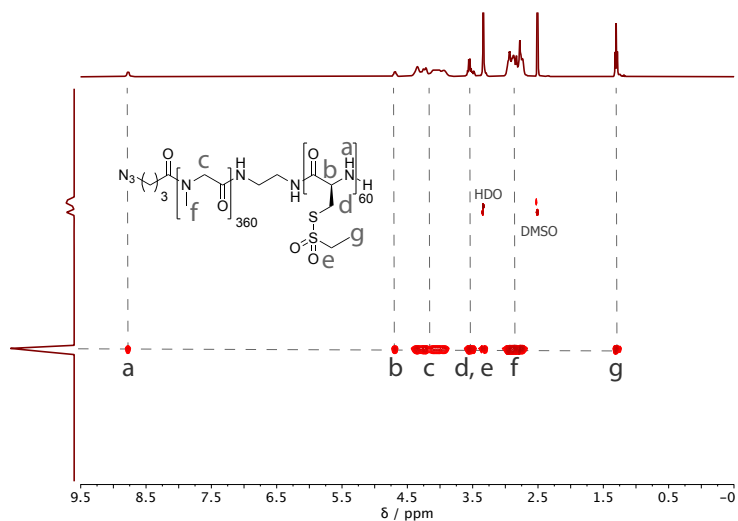
Figure S32. DOSY NMR Analysis of pSar$_{360}$-b-p(L)Cys(SO$_2$Et)$_{60}$ in DMSO-d

6

Photocleavable Core Cross-Linked Polymeric Micelles of Polypept(o)ides and Ruthenium(II) Complexes

amphiphilic
polypept(o)ide

cross-linked
core

released Ru(II)
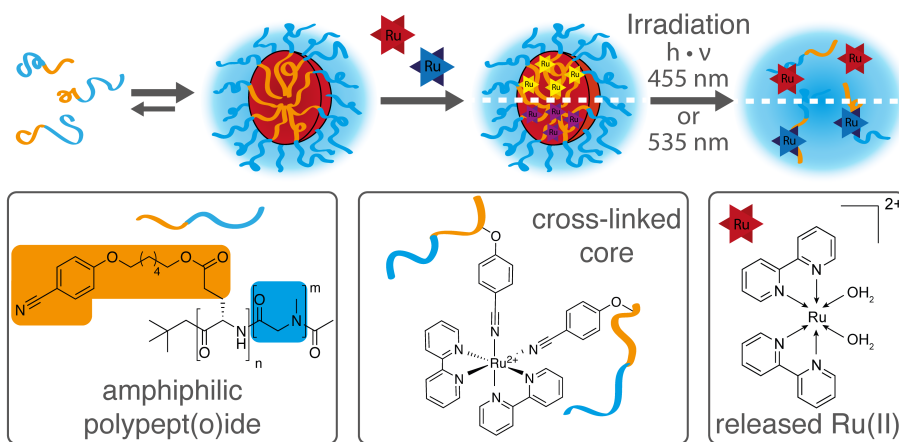
Photocleavable Core Cross-Linked Polymeric Micelles of Polypept(o)ides and Ruthenium(II) Complexes

Tobias Alexander Bauer,[a,b] Jonas Eckrich,[c,d] Nadine Wiesmann,[c] Felix Kuczelinis,[b] Wen Sun,[e] Xiaolong Zeng,[e] Benjamin Weber,[b] Si Wu,[e] Nicolas Hubert Bings,[b] Sebastian Strieth,[c,d] Matthias Barz *[a,b]

Leiden Academic Centre for Drug Research (LACDR), Leiden University, Einsteinweg 55, 2333CC Leiden, The Netherlands.

Department of Chemistry, Johannes Gutenberg University Mainz, Duesbergweg 10-14, 55128 Mainz, Germany.

Department of Otorhinolaryngology, Head and Neck Surgery, University Medical Center Mainz, Langenbeckstr. 1, 55131 Mainz, Germany.

Department of Otorhinolaryngology, University Medical Center Bonn (UKB), Venusberg-Campus 1, 53127 Bonn, Germany.

Max Planck Institute for Polymer Research, Ackermannweg 10, 55128 Mainz, Germany.

Abstract

Core cross-linking of polymeric micelles has been demonstrated to contribute to enhanced stability that can improve the therapeutic efficacy. Photochemistry has the potential to provide spatial resolution and on-demand drug release. In this study, light-sensitive polypyridyl-ruthenium(II) complexes were combined with polypept(o)ides for photocleavable core cross-linked polymeric micelles. Block copolymers of polysarcosine-*block*-poly(glutamic acid) were synthesized by ring-opening *N*-carboxyanydride polymerization and modified with aromatic nitrile-groups on the glutamic acid side chain. The modified copolymers self-assembled into micelles and were cross-linked by *cis*-diaquabis(2,2'-bipyridine)-ruthenium(II) ($[Ru(bpy)_2(H_2O)_2]^{2+}$) or *cis*-diaquabis(2,2'-bisquinoline)-ruthenium(II) ($[Ru(biq)_2(H_2O)_2]^{2+}$). Depending on the flexibility of the nitrile linker, either small spherical structures (D_h 45 nm, PDI 0.11) or worm-like micelles were obtained. The cross-linking reaction did not affect the overall size distribution but induced a change in the metal-to-ligand charge transfer peak from 482 to 420 nm and 592 to 548 nm. The cross-linked micelles displayed colloidal stability after incubation with human blood plasma and during gel permeation chromatography in hexafluoroisopropanol. Light-induced cleavage of $[Ru(bpy)_2(H_2O)_2]^{2+}$ was accomplished within 300s, while $[Ru(biq)_2(H_2O)_2]^{2+}$ could not be completely released. Analysis in HuH-7 cells revealed increased cytotoxicity via micellar delivery of $[Ru(bpy)_2(H_2O)_2]^{2+}$ but mostly irradiation damage for $[Ru(biq)_2(H_2O)_2]^{2+}$. Further evaluation *in ovo* confirmed stable circulation pointing towards the future development of quick-release complexes.

Cover page

Journal of
Materials Chemistry B

Materials for biology and medicine

rsc.li/materials-b
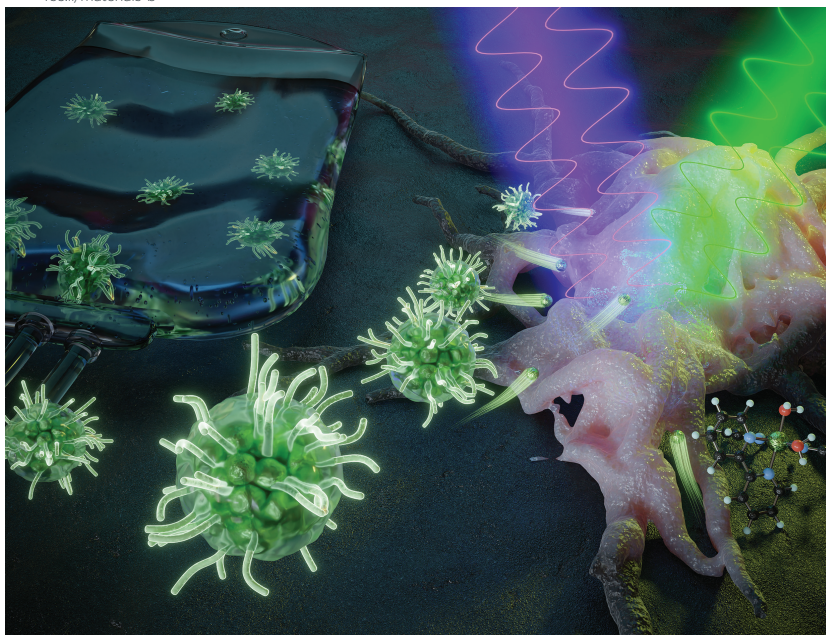
ROYAL SOCIETY
OF CHEMISTRY

PAPER
Matthias Barz *et al.*
Photocleavable core cross-linked polymeric micelles
of polypept(o)ides and ruthenium(II) complexes

Indexed in
Medline!

Polypept(o)ides and ruthenium(II) complexes feature photocleavable core cross-linked polymeric micelles with tuneable size and morphology. Irradiation induces ligand exchange and release of pro-drug ruthenium(II) complexes for photoactivated chemotherapy. The functional design provides spatial resolution to therapeutic intervention.

Introduction

Polymeric micelles have emerged to solubilize hydrophobic drugs and could already demonstrate to improve the off-target toxicity and biodistribution of pharmaceutical agents for applications ranging from cancer treatment to inflammatory diseases.[1–4] To prevent rapid carrier disintegration and premature drug release after intravenous administration, additional stabilization strategies are required. This calls for the next generation of polymeric micelles and for specific delivery beyond replacing low molecular weight surfactants in drug formulations.[5–8] Stabilization by non-covalent interaction, e.g., by π-π-stacking seems promising and simple yet is barely understood in its full depth for drug delivery systems with triggered release profiles.[9–13] Cross-linking by dynamic covalent bonds is thus a straightforward approach accounting for drug release by either disease-related or external stimuli.[5] Free radical cross-linking of thermosensitive poly(ethylene glycol)-*b*-poly(*N*-(2-hydroxypropyl) methacryl-amide)-based copolymers has been combined with a pH-sensitive docetaxel-pro drug cross-linker (CPC634) and is currently under clinical investigation in phase II studies for the treatment of ovarian cancer.[14,15] In clinical phase I studies, the delivery of docetaxel by CPC634 increased the total intratumoral drug concentration by 4-fold compared to Taxol.[16] Nevertheless, a close-up study revealed that the majority of docetaxel was still conjugated to the carrier, which underscores the importance of carrier stability but comprehensive and controlled drug release.[16,17] To reduce the dose-limiting nephrotoxicity of free cisplatin, Kataoka and co-workers introduced NC-6004, in which the platin(II) complex is covalently conjugated to block copolymers of poly(ethylene glycol)-*block*-poly(glutamic acid) (pGlu).[18,19] The exchange of cisplatin's chloride ligands by the carboxylate group of the pGlu side chain induces self-assembly into small spherical core cross-linked polymeric micelles ($D_h \approx 30$ nm). Under physiological conditions, cisplatin is released from the carrier by an erosion process leading to an 11-fold higher area under the curve for NC-6004 compared to conventional cisplatin.[20] The given examples demonstrate how the pharmacologic profile of a drug can be altered by nanomedicine. In combination with photoactivated chemotherapy, actual spatial control over drug release can be added, as cytotoxic agents are activated only at the location of interest by irradiation.[21,22] In reminiscence of cisplatin, ruthenium(II) complexes were found to bind to DNA leading to cytotoxicity but also exhibit rich photochemistry.[23–27] In particular, polypyridyl-ruthenium(II) complexes have been thoroughly investigated and

could be successfully integrated into amphiphilic metallopolymers that self-assembled to polymeric micelles.[28–30] Upon irradiation at the metal-to-ligand charge transfer (MLCT) peak, the ruthenium pro-drugs were cleaved from the polymer backbone, which inhibited tumor growth *in vitro* and *in vivo* by uncaging cytotoxic agents and additional production of singlet oxygen.[28–31]

We now propose to expand these features to core cross-linked polymeric micelles by combining ruthenium(II) complexes with polypept(o)ides. Polypept(o)ides comprise a novel material class of hybrid copolymers that connect the shielding properties of polysarcosine (pSar) with the functional diversity of polypeptides.[32–34] The polymeric architectures thereof can be easily synthesized by living ring-opening *N*-carboxyanhydride (NCA) polymerization.[32,35–37] For nanomedicine applications, pSar, poly(*N*-methyl glycine), provides water solubility and prevents unspecific interaction with proteins, whereas polypeptides allow for stimuli-responsiveness and drug conjugation at the functional amino acid side chain.[38–43] Due to its low immunogenic profile and the potential to evade the accelerated blood clearance phenomenon, pSar is considered a promising substitute for poly(ethylene glycol) but is based on an endogenous amino acid.[39,44–46]

Experimental

Materials and Methods. Unless stated otherwise, solvents were purchased from Sigma Aldrich and used as received. Tetrahydrofuran (THF) was dried over Na and freshly distilled prior to use. *N,N*-Dimethyl formamide (DMF) was bought from Acros (99.8%, extra dry over molecular sieve) and purified by repetitive freeze-thaw cycles to remove dimethylamine prior to use. Dry dimethyl sulfoxide (DMSO) (99.7%, extra dry, over molecular sieve) was obtained from Acros and used without further purification. MilliQ water was prepared using a MILLI-Q® Reference A+ System. Water was used at a resistivity of 18.2 MΩ·cm and total organic carbon of <5 ppm. Hexafluoroisopropanol (HFIP) was purchased from Fluorochem. Deuterated solvents were obtained from Deutero GmbH and were used as received. Nanoparticle purification was performed by Amicon Ultra spin filters (MWCO 3 kDa, 10 kDa or 100 kDa) with ethanol/water mixtures or MilliQ water. Centrifugation was carried out in a Thermo Scientific Heraeus Multifuge 1 or in a Thermo Scientific Heraeus MFresco centrifuge. Photos were recorded with a Nikon D90 digital single lens reflex camera.

NMR Spectroscopy. ^{1}H NMR spectra were recorded on a Bruker Avance II 400 (400 MHz) at room temperature at a frequency of 400 MHz. Diffusion ordered

spectroscopy (DOSY) data were recorded on a Bruker Avance III HD 400 (400 MHz). Calibration of the spectra was achieved using the solvent signals. NMR spectra were analyzed with MestReNova version 12.0.4 from Mestrelab Research S.L. Degrees of polymerization (X_n) by ^{1}H NMR were calculated comparing the integral of the initiator peak and the integrals of the α-protons for pSar and pGlu(OtBu), respectively.

Infrared Spectroscopy. Attenuated total reflectance Fourier transform infrared (ATR-FT-IR) spectroscopy was performed on a FT/IR-4100 (JASCO Corporation) with an ATR sampling accessory (MIRacle, Pike Technologies). IR spectra were analyzed using Spectra Manager 2.0 (JASCO Corporation). NCA polymerization was judged to be completed when NCA-associated carbonyl peaks at 1853 and 1786 cm^{-1} had vanished.

Gel Permeation Chromatography. Analytical gel permeation chromatography (GPC) was performed at 40 °C using HFIP as the eluent, which was equipped with 3 g·L^{-1} potassium trifluoroacetate. The column material was modified silica gel (PFG columns, particle size: 7 µm, porosity: 100 Å and 4000 Å), purchased from PSS Polymer Standards Service GmbH. For polymer detection a UV detector (JASCO UV-2075+) at a wavelength of $\lambda = 230$ nm (or $\lambda = 565$ nm, as indicated) was employed. Molecular weights were determined by using a calibration with poly(methyl methacrylate) (PMMA) (PSS Polymer Standards Services GmbH) and pSar standards with toluene as internal standard. The elution diagram was evaluated with PSS WinGPC (PSS Polymer Standard Service GmbH).

Single-Angle DLS and Zeta Potential. Single-angle dynamic light scattering (DLS) experiments and ξ-potential measurements were performed with a ZetaSizer Nano ZS instrument (Malvern Instruments Ltd., Worcestershire, UK) equipped with a He-Ne laser ($\lambda = 632.8$ nm) as the incident beam. All DLS measurements were performed at 25 °C and a detection angle of 173°. Zeta potential was determined in MilliQ water equipped with 3 mm sodium chloride. For aggregation experiments, polymers were dissolved in DMSO (5 g·L^{-1}), water was added, and the count rate was measured at equal time intervals.

UV-Vis Spectroscopy. UV-Vis spectra were recorded using a Jasco V-630 spectrophotometer (1 cm × 1 cm quartz cell). Visible light irradiation was performed with high brightness light emitting diodes (LEDs) and UV-Vis measurements were performed at the indicated time points.

Multi-Angle DLS. For multi-angle DLS, cylindrical quartz cuvettes (Hellma, Mühlheim, Germany) were cleaned by dust-free distilled acetone and transferred to a dust free flow box. Solutions were filtered into the cuvettes through Pall GHP filters, 0.45 µm pore size. DLS measurements were performed by the following instrument at 20 °C. The apparatus consists of a Uniphase He/Ne Laser (22.5 mW output power at $\lambda = 632.8$ nm) and an ALV/CGS-8F SLS/DLS 5022F goniometer with eight simultaneously working ALV 7004 correlators and eight ALV/High QEAPD avalanche photodiode detectors. The correlation functions of the particles were fitted using a sum of two exponentials. The z-average diffusion coefficient Dz was calculated by extrapolating D_{app} for q = 0. By formal application of Stokes law, the inverse z-average hydrodynamic radius is $R_h = \langle R_h^{-1} \rangle_z^{-1}$. To investigate the aggregation behavior of the particles in human plasma,[47] citrate plasma pooled from 6 probands was used. Plasma was obtained from the university medical center Mainz and filtered through a Millex GS 0.22 µm filter. The particle solutions were filtered through 0.45 µm pore size Pall GHP filters. The following mixtures have been prepared: plasma/PBS 9:1 and plasma/particle solution 9:1 ($\beta = 0.01$ g·L^{-1}). The cuvettes were incubated for 20 min at room temperature before measurement.

Atomic Force Microscopy. Atomic force microscopy (AFM) was measured on mica using a CypherTM AFM (Asylum Research) using tapping mode at a scan rate of 1 Hz. Samples were prepared by drop-casting of a particle solution ($\beta = 50$ mg·L^{-1} in MilliQ water) onto freshly cleaned mica. The sample was dried overnight at room temperature. Images were evaluated and apparent height profiles were extracted using Gwyddion 2.49.

Transmission Electron Microscopy. Transmission electron microscopy (TEM) was performed on a FEI Tecnai G2 Spirit microscope equipped with a Gatan US1000 2k x 2k CCD camera and LaB$_6$ cathode operated at 120 kV. Images were recorded using freshly glow discharged carbon coated copper grids (CF300-Cu, 300 mesh). For non-stained samples, 5 µL nanoparticle solution ($\beta = 50$ mg·L^{-1} in MilliQ water) was drop-coated on the TEM grid surface and removed with a filter paper after 1 min. For negatively stained samples, 5 µL nanoparticle solution ($\beta = 50$ mg·L^{-1} in MilliQ water) was drop-coated on the TEM grid, removed with a filter paper after 1 minute. Next, 5 µL uranyl acetate solution (2 wt.% in ethanol) were added and removed after 15 s incubation time. All sample-deposited grids were air-dried overnight before measurement. Software ImageJ 1.52h (National Institutes of Health, USA) was used for image evaluation.

Cryogenic Transmission Electron Microscopy. 5 µL of the nanoparticle solution (50 mg $\cdot L^{-1}$, in MilliQ water) were applied to freshly glow-discharged carbon grids with a copper 200 mesh (Quantifoil Micro Tools GmbH). Excess fluid was removed by direct blotting (2.5 s) and the grids were individually plunge-frozen in liquid ethane. Grids were cryo-transferred in liquid nitrogen using a Gatan cryoholder (model 626 DH) to a Tecnai T12 transmission electron microscope equipped with a field emission electron source and operating at 120 kV accelerating voltage. Images were recorded using a TemCam-F416 (TVIPS, Gauting, Germany). Software ImageJ 1.52h (National Institutes of Health, USA) was used for image evaluation.

Solution Nebulization-Inductively Coupled Plasma-Mass Spectrometry. The Ru-concentration in the nanoparticles was determined using solution nebulization inductively coupled plasma-mass spectrometry (SN-ICP-MS). Therefore, 100 µL of each nanoparticle solution was diluted to 100 mL with ultrapure water (Millipore, Milli-Q System, USA). For quantification *via* external calibration solutions containing Ru at concentrations of 1, 3, 5, 7, 10, 20, 30, 40, 50, and 60 µg $\cdot L^{-1}$ were used. All solutions were acidified with HNO_3 (65% p.a. grade, Fluka, Honeywell, USA) to 2% (v/v) and 25 µg $\cdot L^{-1}$ of Rh were added as internal standard prior to ICP-MS analysis. For ICP-MS measurements a sample introduction system consisting of a concentric MicroMist™ nebulizer and a double pass spray chamber (Agilent Technologies, Santa Clara, CA, USA) were coupled to a quadrupole ICP-MS instrument 7800 (Agilent Technologies, Santa Clara, CA, USA). The signal intensities of $^{101}Ru^+$, $^{99}Ru^+$, and $^{103}Rh^+$ were measured for data evaluation. The optimum instrumental parameters of the developed ICP-MS method are as follows: plasma power: 1550 W, plasma gas flow rate: 15 L $\cdot min^{-1}$, auxiliary gas flow rate: 0.9 L $\cdot min^{-1}$, nebulizer gas flow rate: 0.99–1.05 L $\cdot min^{-1}$, sampler and skimmer cone: Ni, data acquisition: 0.1 s integration time, 40 sweeps per replicate, 6 replicates.

Synthesis of Ruthenium (II) Complexes

cis-Diaquabis(2,2'-bipyridine)-ruthenium (II) bis(hexafluorophosphate) *([Ru(bpy)$_2$(H$_2$O)$_2$] (PF$_6$)$_2$).* The synthesis of [Ru(bpy)$_2$(H$_2$O)$_2$] (PF$_6$)$_2$ was adapted and modified from Theis *et al.*[48] Ru(bpy)$_2$Cl$_2$ (300 mg, 0.620 mmol) was suspended in 15 mL water. The suspension was stirred at 80 °C under N$_2$ and after dissolution. The reaction mixture was heated for 4 h. After cooling to room temperature, the compound was precipitated with a saturated aqueous solution

of KPF$_6$. The orange powder was washed with a small amount of water and dried overnight. ^{1}H NMR (250 MHz, CD$_2$Cl$_2$) δ [ppm] = 10.19 (d, J = 5.7 Hz, 2H), 8.21 (d, J = 8.1 Hz, 2H), 8.06 (d, J = 8.1 Hz, 2H), 7.96 (m, J = 7.6 Hz, 2H), 7.64 (m, 4H), 7.54 (t, J = 7.8 Hz, 2H), 6.94 (t, J = 6.7 Hz, 2H).

cis-Diaquabis(2,2′-biquinoline)-ruthenium (II) bis(hexafluorophosphate) *([Ru(biq)$_2$(H$_2$O)$_2$] (PF$_6$)$_2$).* The synthesis of [Ru(biq)$_2$(H$_2$O)$_2$] (PF$_6$)$_2$ was adapted and modified from Sun *et al.*[29] RuCl$_3$·H$_2$O (0.18 g, 0.67 mmol), 2,2′-biquinoline (0.37 g, 1.5 mmol), and LiCl (0.087 g, 2.1 mmol) were dissolved in 7 mL of DMF. The solution was stirred until all solids dissolved, was degassed with N$_2$ for 5 min, and was then refluxed for 24 h turning a dark green color. The reaction mixture was slowly cooled to room temperature and pipetted dropwise into 500 mL of stirring H$_2$O, forming a green precipitate that was collected by vacuum filtration. The solid was dissolved in CH$_2$Cl$_2$ forming a dark green solution, and then filtered to get rid of any remaining solid that did not dissolve. The green filtrate was washed 5 times with 20 mL of H$_2$O and then evaporated to a minimal amount of CH$_2$Cl$_2$. An excess of diethyl ether was added to the green CH$_2$Cl$_2$ solution, resulting in the formation of a green precipitate that was collected by vacuum filtration. The green solid (Ru(biq)$_2$Cl$_2$) was used for next step without any further purification (0.22 g, 48% yield). Ru(biq)$_2$Cl$_2$ (100 mg, 0.14 mmol) and AgPF$_6$ (46 mg, 0.29 mmol) were dissolved in 1:1 ethanol/H$_2$O mixture (10 mL). The solution was degassed and heated under reflux overnight in an argon atmosphere. The solution was cooled and filtered to remove AgCl. The solvent of the reaction was reduced to ~5 mL. Then, an aqueous solution of KPF$_6$ was added. The precipitate was filtered, washed with H$_2$O, and dried to obtain a blue solid ([Ru(biq)$_2$(H$_2$O)$_2$](PF$_6$)$_2$). ^{1}H NMR (250 MHz, acetone-d_6) δ [ppm] = 9.58 (d, J = 9.0 Hz, 1H), 8.88 (d, J = 8.8 Hz, 3H), 8.50 (m, 2H), 8.38 (m, 5H), 8.15 (m, 4H), 8.04 (d, J = 8.3 Hz, 2H), 7.59 (m, 3H), 6.97 (m, 4H).

Polymer Synthesis & Modification

All NCA monomers were prepared according to the Fuchs-Farthing method with purification by recrystallization (Glu(OtBu)-NCA) or sublimation (Sar-NCA), as reported previously.[34,49]

Synthesis of poly(γ-tert-butyl-L-glutamic acid) (pGlu(OtBu)) and poly(γ-tert-butyl-L-glutamic acid)-block-poly(sarcosine) (pGlu(OtBu)-b-pSar) Neopentylamine (NPA)-initiated poly(γ-*tert*-butyl-L-glutamic acid)-*block*-poly(sarcosine) (pGlu(OtBu)-*b*-pSar) was prepared *via* sequential NCA polymerization, as reported previously.[50]

Briefly, 394.5 mg (1.72 mmol; 30 eq.) of γ-*tert*-butyl-L-glutamic acid (Glu(O*t*Bu)) NCA were weighed into a pre-died Schlenk-flask, dissolved in anhydrous DMF (freshly amine-purified by freeze-thaw cycles) at a concentration of 200 g·L^{-1}, cooled to 0 °C, and NPA (5.0 mg; 57.4 µmol; 1.0 eq.) was added as a stock solution in THF (ß$_{NPA}$ = 10 g·L^{-1}). An amount of THF was added to ensure polymerization in a THF/DMF (1:1) mixture. After completed Glu(O*t*Bu)-NCA consumption, as monitored by FT-IR spectroscopy, a sample (P1) was taken for GPC-measurements and a solution of Sar-NCA (1.1 g; 9.18 mmol; 160 eq.) in dry DMF (ß = 200 g·L^{-1}) was added and the polymerization was continued at 10 °C. For end-group-modification, acetic anhydride (54 µL; 0.57 mmol; 10 eq.) and *N,N*-diisopropylethylamine (DIPEA) (195 µL; 1.11 mmol; 20 eq.) were added and the solution was stirred for 1 day at room temperature. The obtained block copolymer was purified by repetitive (3x) precipitation and centrifugation (4500 rpm, 15 min, 4 °C) into a mixture of n-hexane and diethyl ether (2:1). The product (NPA-pGlu(O*t*Bu)$_{36}$-*b*-pSar$_{171}$-Ac) was dried in vacuo and obtained as a white powder (846 mg, 86%). ^{1}H NMR. pGlu(O*t*Bu)$_{36}$-*b*-pSar$_{171}$ (P2) (400 MHz, CD$_2$Cl$_2$), δ [ppm] = 8.45−8.13 (b s, 23H (1n), CON*H*), 4.40−3.78 (m, 366H (1n + 2m), α-C*H*$_{(pGlu)}$, α-C*H*$_{2(pSar)}$), 3.14−2.80 (m, 513H (3m), -C*H*$_{3(pSar)}$), 2.66−1.95 (m, 149H, ß-C*H*$_{2(pGlu)}$, γ-C*H*$_{2(pGlu)}$), 1.53−1.35 (s, 324H (9n), -C*H*$_{3(pGlu)}$), 0.94−0.81 (b s, 9H, -C*H*$_{3(NPA)}$). HFIP-GPC, relative to PMMA standards. pGlu(O*t*Bu)$_{36}$ (P1): M_n = 19.7 kg/mol, M_w = 22.9 kg/mol; $Đ$ = 1.16. pGlu(O*t*Bu)$_{36}$-*b*-pSar$_{171}$ (P2): M_n = 44.0 kg/mol, M_w = 52.9 kg/mol; $Đ$ = 1.20.

Synthesis of poly(L-glutamic acid)-block-poly(sarcosine) (pGlu(OH)-b-pSar) PGlu(O*t*Bu)$_{36}$-*b*-pSar$_{171}$ (P2) was dissolved in a mixture of (45:45:5:5) DCM/trifluoroacetic acid (TFA)/triisopropylsilane (TIPS)/water and stirred for 3 h at 0 °C. Polymers were precipitated in ether, centrifuged (4000 rpm, 10 min, 4 °C) and the precipitate was dialyzed against aqueous NaHCO$_3$ solution and MilliQ water (MWCO 3.5 kDa), followed by lyophilization (yield 80%). ^{1}H NMR. pGlu(OH)$_{36}$-*b*-pSar$_{171}$ (P3) (400 MHz, D$_2$O), δ [ppm] = 4.55−4.02 (m, 373H (1n + 2m), α-C*H*$_{(pGlu)}$, α-C*H*$_{2(pSar)}$), 3.13−2.77 (m, 513H (3m), -C*H*$_{3(pSar)}$), 2.40−2.17 (m, 72H (2n), γ-C*H*$_{2(pGlu)}$), 2.10−1.79 (m, 74H (2n), ß-C*H*$_{2(pGlu)}$), 1.42−1.38 (m, 5H, residual PG), 0.86−0.80 (s, 7H, -C*H*$_{3(NPA)}$). HFIP-GPC, relative to PMMA standards. pGlu(OH)$_{36}$-*b*-pSar$_{171}$ (P3): M_n = 37.9 kg/mol, M_w = 59.1 kg/mol; $Đ$ = 1.56.

Synthesis of (pGlu(Mod)-b-pSar) PGlu(OH)$_{36}$-*b*-pSar$_{171}$ (P3) (100 mg; 5.95 µmol; 1.0 eq.) was dissolved in 2.0 mL of anhydrous DMSO and 0.5 mL DMF.

Subsequently, *N,N,N',N'*-tetramethyl-*O*-(1*H*-benzotriazol-1-yl)uronium hexafluorophosphate (HBTU) (135 mg, 357 µmol, 60 eq.), 1-hydroxy benzotriazole (HOBt) (48.2 mg; 357 µmol; 60 eq.), DIPEA (75.9 µL, 446 µmol, 75 eq.), 3-azidopropylamine (1.2 mg, 11.9 µmol, 2.0 eq.) and 4-((6-hydroxyhexyl)oxy)benzonitrile (156 mg, 714 µmol, 60 eq.) were added. The reaction mixture was stirred for 3 days at room temperature. For purification, the reaction mixture was diluted with DMSO and dialyzed (MWCO 3.5 kDa) against DMSO followed by MilliQ water. Upon lyophilization, cyano- and azide-modified NPA-pGlu(Mod)$_{36}$-*b*-pSar$_{171}$-Ac (P4) was obtained as a white solid (60 mg, 43%), with a cyano-grafting efficiency of 52%, as determined by ^{1}H NMR. ^{1}H NMR. pGlu(Mod)$_{36}$-*b*-pSar$_{171}$ (P4) (400 MHz, DMSO-*d$_6$*), δ [ppm] = 8.17−7.89 (b s, 11H (1u, 1v, 1w), CON*H*$_{(pGlu)}$), 7.83−7.60 (b s, 37H (2v), -CNCCC*H*$_{(arom.)}$), 7.17−6.91 (b s, 37H (2v), -OCC*H*$_{(arom.)}$), 4.53−3.71 (m, 436H (2m, 1u, 5v, 1w), α-C*H*$_{(pGlu)}$, α-C*H*$_{2(pSar)}$, -OC*H$_2$*, -COOC*H$_2$*), 3.05−2.64 (m, 513H (2m), -C*H*$_{3(pSar)}$), 2.04−1.09 (m, 246H (8u, 12v, 4w), β-C*H*$_{2(pGlu)}$, γ-C*H*$_{2(pGlu)}$, -C*H$_2$*-),. HFIP-GPC, relative to PMMA standards. pGlu(Mod)$_{36}$-*b*-pSar$_{171}$ (P4): M_n = 53.1 kg/mol, M_w = 74.8 kg/mol; *Đ* = 1.41. FT-IR. pGlu(Mod)$_{36}$-*b*-pSar$_{171}$ (P4) (ATR unit) ṽ [cm^{-1}] = 2936 (C-H), 2871 (C-H), 2223 (CN), 2100 (N$_3$), 1731 (CO, ester), 1646 (CO, amide).

Synthesis of poly(sarcosine) pSar macroinitiators were prepared as reported previously.[42] Sarcosine NCA (1.04g; 90.6 mmol; 200 eq.), was dissolved in 10 mL dry DMF and *N*-boc-1,2-diaminoethane (7.17 µL; 45.2 µmol; 1.0 eq.) was added *via* stock solution in DMF. The clear, colorless solution was stirred at room temperature and the reaction was completed after three days, as monitored by FT-IR-spectroscopy. The sarcosine amino terminus was quenched by addition of acetic anhydride (43 µL; 452 µmol; 10 eq.) and DIPEA (154 µL; 906 µmol; 20 eq.). The solution was allowed to stir for an additional day at room temperature. Precipitation in diethyl ether yielded *N*-boc-protected poly(sarcosine) (P5) as a colorless solid (610 mg, 95%). For removal of the Boc protection group, *N*-Boc-pSar (P5) was dissolved in a mixture of (1:1) TFA/H$_2$O and stirred at 0 °C for 3 h. The clear yellow solution was dialyzed against aqueous NaHCO$_3$ and MilliQ water (MWCO 3.5 kDa) for 2 days each. The polymer was lyophilized from water and obtained as a white powder (455 mg, 71%). The chain length of the pSar block was determined by HFIP-GPC with pSar standards (pSar$_{140}$).[39] ^{1}H NMR. *N*-Boc-pSar$_p$-Ac (P5) (400 MHz, DMSO-*d$_6$*), δ [ppm] = 4.56-3.78 (m, 381H (2p), α-C*H*$_{2(pSar)}$), 3.10−2.68 (m, 586H (3p), -C*H*$_{3(pSar)}$), 1.40−1.33 (s, 9H, -C*H*$_{3(Boc)}$). NH$_2$-pSar$_{140}$ (P6) (400 MHz, DMSO-*d$_6$*), δ [ppm] = 4.50−3.79 (m, 280H (2p), α-C*H*$_{2(pSar)}$), 3.10−2.60

(m, 420H (3p), -C$H_{3(pSar)}$). HFIP-GPC, relative to PMMA standards. NH$_2$-pSar$_{140}$ (P6): M_n = 28.7 kg/mol, M_w = 34.5 kg/mol; Đ = 1.20.

Synthesis of poly(sarcosine)-block-poly(γ-tert-butyl-L-glutamic acid) (pSar-b-pGlu(OtBu) The synthesis of pSar-*b*-pGlu(O*t*Bu) was adapted from literature and modified.[34,42] pSar (pSar$_{140}$, 110 mg; 10.9 µmol, 1.0 eq.) was weighed into a pre-dried Schlenk-flask and dried *via* azeotropic distillation with toluene. Next, the macroinitiator was dissolved in dry 1.0 mL DMF (freshly amine-purified by freeze-thaw cycles), cooled to 0 °C under N$_2$ atmosphere, and Glu(O*t*Bu) NCA (50 mg, 21.8 µmol, 20 eq.) was added *via* stock solution in DMF. Absolute THF was added to ensure polymerization in a THF/DMF (1:2) mixture. Upon completed monomer consumption, as monitored by FT-IR, pentafluorphenyl-4-azidobutanoate (6.44 mg; 21.8 µmol, 2.0 eq.) and DIPEA (7.4 µL; 43.6 µmol; 4.0 eq.) were added and the solution was stirred at room temperature for 18 h. To quench residual free end-groups, acetic anhydride (10.4 µL; 109 µmol; 10 eq.) and DIPEA (37.1 µL; 218 µmol; 20 eq.) were added and the solution was stirred for 1 day. Precipitation in diethyl ether yielded Ac-pSar$_{140}$-*b*-pGlu(O*t*Bu)$_{20}$-N$_3$ (P7) as a colorless solid (144 mg, 93%). ^{1}H NMR. pSar$_{140}$-*b*-pGlu(O*t*Bu)$_{20}$ (P7-A) (400 MHz, CD$_2$Cl$_2$), δ [ppm] = 8.61−8.03 (b s, 14H (1q), -CON*H*), 4.40−3.78 (m, 292H (1q, 2p), α-C*H*$_{(pGlu)}$, α-C*H*$_{2(pSar)}$), 3.14−2.80 (m, 420H (3p), -C*H*$_{3(pSar)}$), 2.66−1.95 (m, 72H, ß-C*H*$_{2(pGlu)}$, γ-C*H*$_{2(pGlu)}$), 1.53−1.35 (s, 172H, -C*H*$_{3(pGlu)}$). Ac-pSar$_{140}$-*b*-pGlu(O*t*Bu)$_{15}$-N$_3$ (P7-B) (400 MHz, CD$_2$Cl$_2$), δ [ppm] = 8.61−8.03 (b s, 8H (1q), -CON*H*), 4.40−3.78 (m, 284H (1q, 2p), α-C*H*$_{(pGlu)}$, α-C*H*$_{2(pSar)}$), 3.14−2.80 (m, 420H (3p), -C*H*$_{3(pSar)}$), 2.66−1.95 (m, 65H, ß-C*H*$_{2(pGlu)}$, γ-C*H*$_{2(pGlu)}$), 1.53−1.35 (s, 133 H, -C*H*$_{3(pGlu)}$). HFIP-GPC, relative to PMMA standards. pSar$_{140}$-*b*-pGlu(O*t*Bu)$_{20}$ (P7-A): M_n = 30.0 kg/mol, M_w = 39.3 kg/mol; Đ = 1.31. pSar$_{140}$-*b*-pGlu(O*t*Bu)$_{15}$ (P7-B): M_n = 30.3 kg/mol, M_w = 40.7 kg/mol; Đ = 1.34.

Synthesis of poly(sarcosine)-block-poly(L-glutamic acid) (pSar-b-pGlu(OH) For removal of the *tert*-butyl protecting group, pSar$_p$-*b*-pGlu(O*t*Bu)$_q$ (P7) was dissolved in a mixture of (45:45:5:5) DCM/TFA/TIPS/water and stirred for 3 h at 0 °C. Polymers were precipitated in ether, centrifuged (4000 rpm, 10 min, 4 °C) and the precipitate was dialyzed against aqueous NaHCO$_3$ solution and MilliQ water (MWCO 3.5 kDa), followed by lyophilization. The procedure was repeated until successful deprotection was verified by the absence (or presence of minor traces) of the *tert*-butyl group by ^{1}H NMR. ^{1}H NMR. pSar$_{140}$-*b*-pGlu(OH)$_{20}$ (P8-A) (400 MHz, D$_2$O), δ [ppm] = 4.55−4.02 (m, 295H (1q, 2p), α-C*H*$_{(pGlu)}$, α-C*H*$_{2(pSar)}$), 3.13−2.77 (m, 420H (3p), -C*H*$_{3(pSar)}$), 2.58−2.25 (m, 36H (2q), γ-C*H*$_{2(pGlu)}$), 2.20−1.85

(m, 38 H (2q), β-C$H_2$$_{(pGlu)}$). pSar$_{140}$-$b$-pGlu(OH)$_{15}$ (P8-B) (400 MHz, D$_2$O), δ [ppm] = 4.55−4.02 (m, 293H (1q, 2p), α-C$H_{(pGlu)}$, α-C$H_2$$_{(pSar)}$), 3.13−2.77 (m, 420H (3p), -C$H_3$$_{(pSar)}$), 2.48−2.22 (m, 29H (2q), γ-C$H_2$$_{(pGlu)}$), 2.12−1.83 (m, 30H (2q), β-C$H_2$$_{(pGlu)}$). HFIP-GPC, relative to PMMA standards. pSar$_{140}$-b-pGlu(OH)$_{20}$ (P8-A): M_n = 28.2 kg/mol, M_w = 35.6 kg/mol; $Đ$ = 1.26. pSar$_{140}$-b-pGlu(OH)$_{15}$ (P8-B): M_n = 30.9 kg/mol, M_w = 54.1 kg/mol; $Đ$ = 1.75.

Synthesis (pSar-b-pGlu(Mod) PSar$_{140}$-b-pGlu(OH)$_{20}$ (P8-A) (90 mg; 7.18 µmol; 1.0 eq.) was dissolved in 2.0 mL of anhydrous DMSO and HBTU (163 mg, 431 µmol, 60 eq.), HOBt (58.2 mg, 431 µmol, 60 eq.), DIPEA (85.5 µL, 503 µmol, 70 eq.) and 4-(2-aminoethoxy)benzonitrile (46.6 mg, 287 µmol, 40 eq.) were added subsequently. The reaction mixture was stirred for 3 days at room temperature. Repetitive precipitation in acetone (3800 rpm, 15 min, 4 °C) yielded statistically modified Ac-pSar$_{140}$-b-pGlu(Mod)$_{20}$-N$_3$ (P9-A) as a colorless solid (77.5 mg, 70%). Successful modification was verified by FT-IR spectroscopy and DOSY NMR. Grafting efficiencies of 65% and 100% were obtained for P9-A and P9-B, as determined by ^{1}H NMR. ^{1}H NMR. pSar$_{140}$-b-pGlu(Mod)$_{20}$ (P9-A) (400 MHz, DMSO-d_6), δ [ppm] = 8.28−7.90 (b s, 23H (2r, 1s), CON$H_{(pGlu)}$), 7.83−7.63 (b s, 26H (2r), -CNCCC$H_{(arom.)}$), 7.14−6.98 (b s, 26H (2r), -OCC$H_{(arom.)}$), 4.56−3.70 (m, 310H (3r, 1s, 2p), α-C$H_{(pGlu)}$, α-C$H_2$$_{(pSar)}$, -OC$H_2$), 3.47−3.37 (m, 21H (2r), -CONHC$H_2$$_{(pGlu)}$), 3.08−2.62 (m, 420H (2p), -C$H_3$$_{(pSar)}$), 2.29−1.53 (m, 117H (4r, 4s), β-C$H_2$$_{(pGlu)}$, γ-C$H_2$$_{(pGlu)}$). pSar$_{140}$-$b$-pGlu(Mod)$_{15}$ (P9-B) (400 MHz, DMSO d_6), δ [ppm] = 8.28−7.90 (b s, 26H (2r, 1s), CON$H_{(pGlu)}$), 7.83−7.63 (b s, 30H (2r), -CNCCC$H_{(arom.)}$), 7.14−6.98 (b s, 29H (2r), -OCC$H_{(arom.)}$), 4.56−3.70 (m, 318H (3r, 1s, 2p), α-C$H_{(pGlu)}$, α-C$H_2$$_{(pSar)}$, -OC$H_2$), 3.08−2.62 (m, 420H (2p), -C$H_3$$_{(pSar)}$), 2.29−1.53 (m, 76H (4r, 4s), β-C$H_2$$_{(pGlu)}$, γ-C$H_2$$_{(pGlu)}$). FT-IR. pSar$_{140}$-$b$-pGlu(Mod)$_{20}$ (P9-A) (ATR unit) $\tilde{v}$ [cm^{-1}] = 2936 (C-H), 2871 (C-H), 2223 (CN), 1640 (CO, amide). HFIP-GPC, relative to PMMA standards. pSar$_{140}$-b-pGlu(Mod)$_{20}$ (P9-A): M_n = 71.3 kg/mol, M_w = 113.2 kg/mol; $Đ$ = 1.58. pSar$_{140}$-b-pGlu(Mod)$_{15}$ (P9-B): M_n = 47.9 kg/mol, M_w = 61.5 kg/mol; $Đ$ = 1.28.

Preparation of Photocleavable Core Cross-Linked Polymeric Micelles

Cyano-group-modified pGlu(Mod)-b-pSar was dissolved in DMSO at a concentration of 5.0 g·L^{-1}. The clear solution was dialyzed against MilliQ water (MWCO 3.5 kDa), filtered (GHP 450) and concentrated to the 5.0 g·L^{-1} by spin filtration (Amicon Ultra, MWCO 3 kDa), yielding the micelle solution. For cross-linking, ruthenium complexes were dissolved in methanol (10 g·L^{-1}) and added at

equimolar concentration with respect to the number of nitrile groups. The reaction mixture was protected from light and kept at 50 °C until completed ligand exchange, as monitored optically (PCCPM-1: color change from red to yellow; PCCPM-2: dark blue to purple) and *via* UV-Vis spectroscopy (PCCPM-1: λ_{max} = 482 nm to 420 nm; PCCPM-2: λ_{max} = 590 nm to 550 nm). To remove residual cross-linker and not cross-linked polymer, the particle solution was diluted with a mixture of ethanol/water (1:1) and purified by repetitive spin filtration (Amicon Ultra, MWCO 100 kDa) and dilution steps with MilliQ water until no residual free polymer was detectable in HFIP-GPC. In cases where labelling was required for biological evaluation, sulforhodamine-B-PEG$_4$-dibenzocyclooctine (DBCO) (0.4 eq. per polymer) was added, and the solution stirred for 3 days before core cross-linking was performed. Labelled micelles were purified from free dye by repetitive spin filtration (Amicon Ultra, MWCO 10 kDa) and dilution steps. Successful removal of free dye was ensured by HFIP-GPC. Final particle solutions could be stored in the absence of light at 4 °C.

Photocleavage

Light-induced cleavage of PCCPMs was performed using high brightness LEDs with narrow emission spectra of blue (λ_{max} = 455 nm), green (λ_{max} = 535 nm), or red orange (λ_{max} = 620 nm) light. Particle solutions were transferred into sealed transparent vials, diluted with MilliQ water to a concentration of approx. 0.1 g·L^{-1} and irradiated with LED light. For time-dependent UV-Vis measurements, aliquots were taken and analyzed. For HFIP-GPC analysis, aliquots were taken, concentrated *in vacuo* and analyzed. The following LEDs were used: Blue LED: (λ_{max} = 455 nm), Osram, High-Brightness-LED, OSLON SSL 80 Series, Blue, 455 nm, 80°, 1A. Green LED: (λ_{max} = 535 nm), Cree, High-Brightness-LED, XLamp XP-E2, Green, 535 nm, 135°, 114 lm, 1A. Red orange LED: (λ_{max} = 620 nm), Cree, High Brightness SMD, Red Orange, 87.4 lm.

Biologic Evaluation

Cell Viability. To measure cellular viability, the AlamarBlue assay was performed according to manufacturer's specifications as recently described in detail by Ernst *et al.* with minor modifications.[51] Briefly, 40'000 HuH-7 tumor cells were seeded in 96-well-plates in 200 µl cell culture medium per well. After 24 h, cells were subjected to the indicated treatment. After incubation with PCCPMs or ruthenium(II) complex at 10 µM ruthenium(II) complex 1 or 2 for 24h, cells were either exposed to light (455 nm, 5 minutes; 535 nm, 15 minutes) or kept in the

dark to avoid light exposure. To measure cellular viability, medium was exchanged for medium with 10% AlamarBlue (Invitrogen, Life Technologies Corp., Eugene, OR, USA) and the cells were incubated for 4 h at 37°C before recording the fluorescence on a fluorescence microplate reader (Fluoroskan Ascent Microplate reader, Thermo Fisher Scientific GmbH, Rockford, USA). Results were given as relative values using a 538 nm excitation filter and a 600 nm emission filter, normalized to the respective control (100%).

Chicken Chorioallantoic Membrane Assay. White leghorn hens' eggs (Bio-Aufzucht LSL Rhein-Main GmbH, Dieburg, Germany) were placed horizontally in an incubator (Brutmaschinen-Janeschitz GmbH, Hammelburg, Deutschland) at 37.5 °C. After removal of 6 mL albumin by aspiration on day 3 of incubation the eggshell was opened and partly removed with sterilized scissors to expose the chorioallantoic membrane (CAM). Between further experiments the aperture was constantly covered with PARAFILM® (Bemis Company Inc., Neenah, Wisconsin, USA) to avoid evaporation. On day 13 of cultivation, 500 µL of PCCPM-nanoparticles were intravascularly injected using a sterile-single-use-syringe (B. Braun Melsungen AG, Meldungen, Germany) with a 30G x ½" needle (BD Microlance™ 3, Becton, Dickinson and Company United, Louth, Ireland). 19 eggs were investigated. Death of the embryo within the timeframe of observation as well as a lack of particle circulation due to paravasal injection were reasons for a dropout from further investigation. After intravascular application of the sulforhodamine-B-labeled nanoparticles, *in vivo* fluorescent microscopy (BXFM intravital microscope (Olympus BXFM, OLYMPUS DEUTSCHLAND GmbH, Hamburg, Germany) was performed and repeated after 3 h and 24 h after the application of the nanoparticles respectively. By using the Cy3 Filter (Ex: 545 nm; Em: 525 nm), video sequences of 20 s each were taken in a representative region of interest on the CAM using the microscope camera system (CAM-XM10, OLYMPUS DEUTSCHLAND GmbH, Hamburg, Germany). The video sequences were later analyzed offline. After blinding, video sequences were investigated repetitively three times. As the number of particles in the vascular system did not allow a sufficient quantitative analysis, we used the following numerical analogue scale: 5 = intravascular PCCPMs can be detected ubiquitously; 4 = intravascular PCCPMs can be detected predominantly; 3 = intravascular PCCPMs can be detected occasionally; 2 = PCCPMs can be detected; 1 = no PCCPMs can be detected.

Staining and Histological Analysis. Histology was performed 24 h after intravascular injection of sulforhodamine-B-labeled PCCPMs. Brain, heart, liver, and kidney were put in a formalin solution (VWR International bvba, Leuven, Belgium) 4% (v/v) in PBS and embedded in paraffin (Roti® Plast, Carl Roth GmbH + Co. KG, Karlsruhe, Germany) on the following day. After embedding the samples in paraffin, the fixed preparations were cut into slides with the microtome (Leica CM1900, Leica Biosystems Nussloch GmbH, Nußloch, Germany) and then transferred to the specific staining/immunohistochemical analysis, respectively. Samples were dewaxed by incubation in xylene solutions (AppliChem GmbH, Darmstadt, Germany) with descending concentrations (100%, 90%, 80%, 70%). Afterwards, the slides were transferred for 5 min in purified water. Subsequently, 25 µL of VECTASHIELD® HardSet™ Antifade Mounting with 4',6-diamidino-2-phenylindole (DAPI) (Vector Laboratories, Inc., Burlingame, CA, USA) was pipetted onto the histological specimen, which was subsequently covered with a cover slip. Hemalum-Eosin staining was also performed to allow light microscopical evaluation of the tissue samples. After dewaxing samples were put in in acidic hemalum solution acc. to Mayer (Carl Roth GmbH + Co. KG, Karlsruhe, Germany) for 5 min. Afterwards, blueing was performed for 10 min under running tap water. The sample was then transferred for 2 min in purified water again before being transferred to 0.5% eosin solution (Carl Roth GmbH + Co. KG, Karlsruhe, Germany) for 2-3 min. After re-rinsing under tap water specimens were transferred in isopropanol solution of ascending concentration (1-2 min in 80% isopropanol (Shell Chemicals Europe B.V., Rotterdam/Pernis, Netherlands) 1-2 min 90% isopropanol, 3 min 100% isopropanol) and for 2 x 5 min in 100% xylene. Finally, the specimen was covered with Eukitt® inclusion agent (Sigma-Aldrich, St. Louis, Missouri, USA). After preparation histological samples were analyzed using fluorescence microscopy (Nikon Eclipse TE2000, Nikon Corporation, Chiyoda, Japan). The inbuilt DAPI filter (Ex:340-380 nm, Em:435-485 nm) was used to identify stromal tissue after an image in DAPI staining was taken, the filter was subsequently switched to Cy3 (Ex:530-560, Em:573-648nm) and an image was taken in this staining respectively. Both images were merged using Nikon's imaging software NIS-Elements (Nikon Corporation, Chiyoda, Japan). The images were then blinded for analysis and the number of nanoparticles within the respective stromal tissue was qualitatively analyzed as follows. 5 = PCCPMs can be detected ubiquitously; 4 = PCCPMs can be detected predominantly; 3 = PCCPMs can be detected in

disseminated locations; 2 = PCCPMs can be detected occasionally; 1 = PCCPMs can be detected; 0 = no PCCPMs can be detected.

Data Management and Statistical Analysis. Data sets were managed using Microsoft Excel (Microsoft Corporation, Redmont, WA, USA) as well as Graph Pad Prism (GraphPad Software, La Jolla, CA, USA). Differences between individual groups in the AlamarBlue assay, the particle quantifications in both *in vivo* microscopy and the fluorescence microscopy were evaluated by two-way ANOVA. Differences p < 0,05 were considered significant.

Results and Discussion

The described photocleavable core cross-linked polymeric micelles are based on polypept(o)ides, which were synthesized by sequential nucleophilic ring-opening polymerization of the corresponding NCAs.[33,34] As shown in Scheme 1, the block copolymers of poly(*tert*-butyl-l-glutamic acid)-*block*-polysarcosine (pGlu(O*t*Bu)-*b*-pSar) were prepared starting from pGlu(O*t*Bu) (P1) followed by sequential monomer addition of sarcosine NCA. After end-capping with acetic anhydride, the *tert*-butyl protecting-group was removed from pGlu(O*t*Bu)-*b*-pSar (P2) yielding pGlu(OH)-*b*-pSar (P3). Upon purification by precipitation and dialysis, the pGlu(OH)-block was modified with aromatic cyano-groups that allow for coordination to the ruthenium complexes as well as with 3-azidopropylamine for optional dye conjugation *via* azide-alkyne click chemistry, which resulted in pGlu(Mod)-*b*-pSar (P4).[52,53]
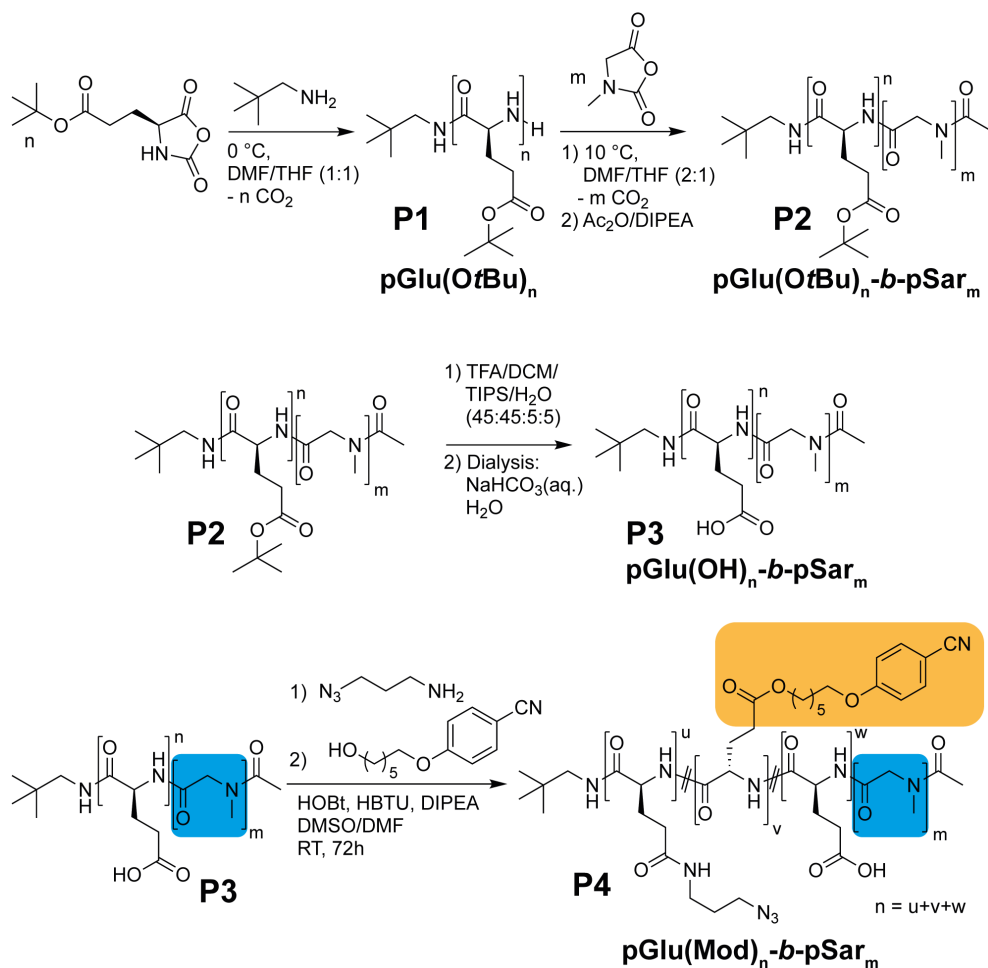
Scheme 1. Polymer synthesis and post polymerization modification reactions.

As shown in Figure 1A, symmetric and monomodal molecular weight distributions were obtained for pGlu(OtBu) (P1), pSar-b-pGlu(OtBu) (P2), and pGlu(Mod)-b-pSar (P4) by GPC in HFIP. A distinct shift in the elution volume maximum can be detected after the addition of the second block accounting for the living nature of the NCA polymerization, which is also reflected by the narrow dispersities of 1.16 and 1.20 for P1 and P2.[35,36,54] Moreover, the chain lengths of $X_n = 36$ for pGlu(OtBu) and $X_m = 171$ for pSar, which were determined by end-group analysis in ^{1}H NMR are in well agreement with the calculated monomer-to-initiator ratios as summarized in Table 1.
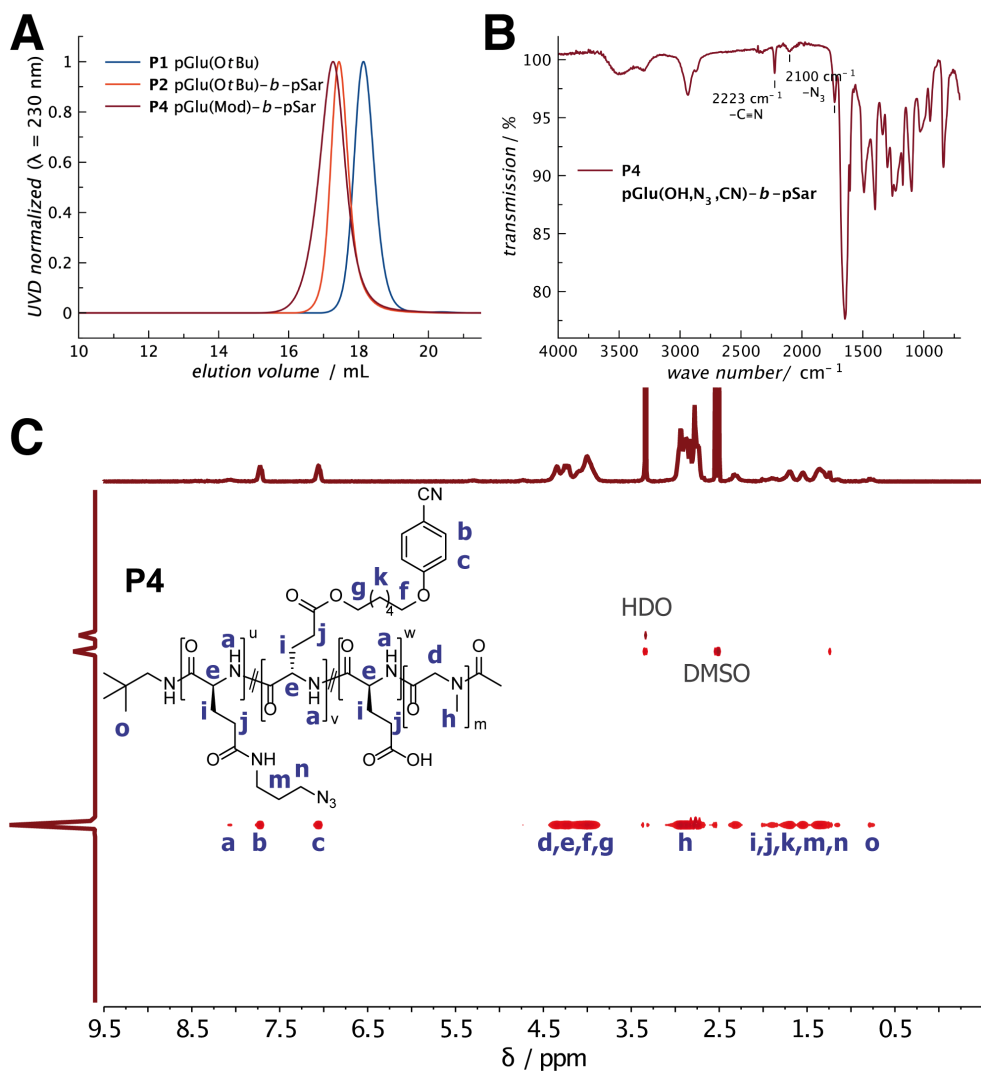
Figure 1. Polymer Analysis. (**A**) HFIP-GPC displays monomodal and symmetric molecular weight distributions for P1, P2, and P4; (**B**) FT-IR spectroscopy confirms successful polymer modification with azide and nitrile groups; (**C**) DOSY NMR spectroscopy in DMSO-d_6 shows only one diffusing polymer species with all signals aligned in one horizontal axis.

After modification with 4-(6-hydroxyhexyloxy)-benzonitrile and 3-azidopropylamine, a grafting density of 52% was determined by ^{1}H NMR analysis. Besides larger molecular weights only a slightly increased dispersity

was obtained by GPC. The successful backbone modification reaction was then verified by DOSY NMR spectroscopy. Here, only one diffusing polymer species was detected with all signals aligned in one horizontal axis (Figure 1C). The presence of the conjugated nitrile- and azide-groups was confirmed by FT-IR spectroscopy where distinct peaks at 2223 cm^{-1} (-C≡N) and 2100 cm^{-1} (-N$_3$), as well as peaks of the associated ester bond (1731 cm^{-1}) are visible (Figure 1B).

Table 1. Analytical results of the polymer synthesis and post-polymerization modification reactions.

polymer	X_n (pGlu)[a]	X_n (pSar)[a]	M_n[b] / kDa	M_w[b] / kDa	$Đ$[b] /kDa	CN-grafting
P1, pGlu(OtBu)	36	-	19.7	22.9	1.16	-
P2, pGlu(OtBu)-b-pSar	36	171	44.0	52.9	1.20	-
P3, pGlu(OH)-b-pSar	36	171	37.9	59.1	1.56	-
P4, pGlu(Mod)-b-pSar	36	171	53.1	74.8	1.41	52%

[a] ^{1}H NMR end-group analysis, [b] relative to PMMA standards.

Polymeric micelles were formed by self-assembly of the amphiphilic nitrile-modified polypept(o)ide pGlu(Mod)-b-pSar (P4) using the solvent switch-method from DMSO to water, as illustrated in Figure 2. After solvent exchange by dialysis was completed, the polymeric micelles were core cross-linked by the addition of the respective Ruthenium complex and purified by ultrafiltration. The progress of the ligand exchange reaction, and thus the proceeding of the cross-linking could easily be monitored by eye (Figure S3) and UV-Vis spectroscopy (Figure 2B).

For *cis*-diaquabis(2,2'-bipyridine)-ruthenium (II) bis(hexafluorophosphate) ([Ru(bpy)$_2$(H$_2$O)$_2$] (PF$_6$)$_2$; Ru-CPX-1), a color change from red to bright yellow was observed that corresponds to a blue-shift in the wavelength of the MLCT from 482 nm to 420 nm. Similarly, for *cis*-diaquabis(2,2'-biquinoline)-ruthenium (II) bis(hexafluorophosphate) ([Ru(biq)$_2$(H$_2$O)$_2$] (PF$_6$)$_2$; Ru-CPX-2), which has a larger π-system, a color change from dark blue to purple could be seen, which refers to a change in the wavelength of the MLCT from 592 nm to 548 nm upon ground state exchange of the two aqua-ligands by nitrile-ligands.[55,56] When analyzed by DLS, polymeric micelles showed a hydrodynamic diameter of 41 nm and a narrow PDI of 0.058. As shown in Figure 2C, this was neither affected by cross-linking with [Ru(bpy)$_2$(H$_2$O)$_2$] (PF$_6$)$_2$ (PCCPM-1) nor by [Ru(biq)$_2$(H$_2$O)$_2$] (PF$_6$)$_2$ (PCCPM-2).
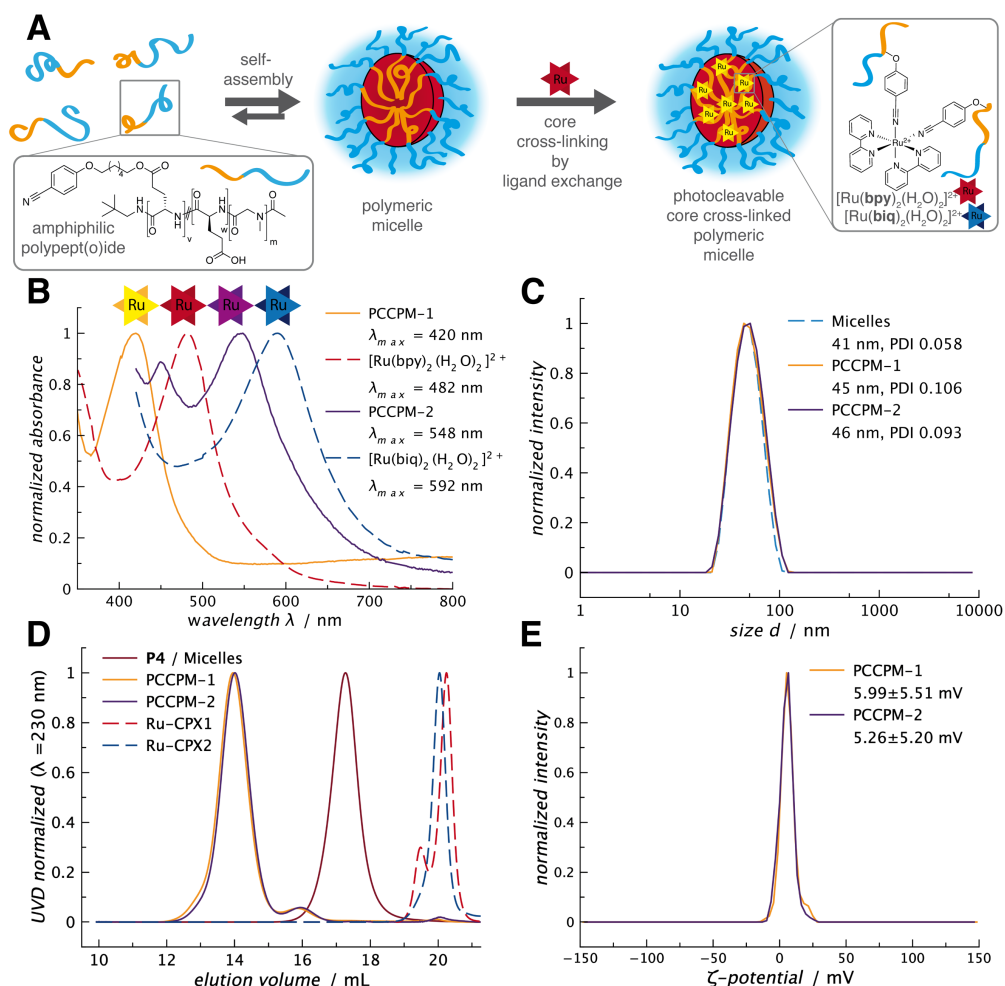
Figure 2. Nanoparticle characterization. (**A**) Schematic illustration of the self-assembly and core cross-linking process; (**B**) UV-Vis spectroscopy for ruthenium complexes and core cross-linked micelles with indicated λ_{MLCT} values; (**C**) DLS of micelles and PCCPMs; (**D**) HFIP-GPC demonstrates stable cross-linking after incubation for ≥ 1 h; (**E**) Neutral ξ-potentials account for efficient shielding by the pSar corona.

After purification by ultrafiltration the particle structure remained stable even in the GPC with HFIP, whereby no significant traces of free polymer or ruthenium complex could be detected after incubation for at least one hour (Figure 2D). The particle stability was further confirmed by DLS in human plasma, following the technique introduced by Rausch *et al.*, whereby no aggregation could be detected

(Figure S4).[47] These results confirm the integrity of the proposed core cross-linked micellar structure demonstrating the suitable basis for smart drug delivery in which carrier disintegration solely follows internal or external stimuli.[57–59] When analyzed by solution nebulization inductively coupled plasma mass spectrometry (SN-ICP-MS), drug loading contents of 4.37 ± 0.18 and 4.34 ± 0.17 weight% were determined for both, PCCPM-1 ($[Ru(bpy)_2(H_2O)_2]$ $(PF_6)_2$) and PCCPM-2 ($[Ru(biq)_2(H_2O)_2]$ $(PF_6)_2$). Furthermore, neutral ξ-potentials were detected accounting for sufficient shielding by the pSar corona (Figure 2E). The results of the particle preparation are summarized in Table 2.

For Ruthenium-cross-linked polymeric micelles of pGlu(Mod)-*b*-pSar (P4), spherical morphologies with sizes well below 50 nm were detected by TEM and AFM analysis for both, PCCPM-1 and PCCPM-2, which corresponds well with the DLS data (Figure 3, Figure S7). With more detail, for PCCPM-2, narrow dispersities and small particle diameters of 20.2 ± 4.5 nm (PDI 0.05, no staining) and 22.8 ± 4.3 nm (PDI 0.03, negative staining) were derived from TEM image analysis (Figure S5, S6).

Table 2. Analytical results of the PCCPM preparation

particle	Ru-CPX	D_h / nm[a]	PDI[a]	Ru-CPX wt.%[b]	ξ-potential / mV[a]
Micelles	-	41	0.058	-	-
PCCPM-1	$[Ru(bpy)_2]^{2+}$	45	0.106	4.37 ± 0.18	5.99 ± 5.51
PCCPM-2	$[Ru(biq)_2]^{2+}$	46	0.093	4.34 ± 0.17	5.26 ± 5.20

[a] single-angle DLS at 173°, [b] ICP-Ms.

Given the fact that DLS is used to calculate the intensity weighted size distribution and the hydrodynamic diameter of a given particle solution, the smaller sizes determined by TEM analysis refer to the particle analysis in the dry state.[60,61] Moreover, the slightly smaller diameters detected for non-stained compared to negatively stained samples indicate that the ruthenium complex which primarily accounts for the transmission contrast mainly concentrates in the core of the particle confirming the illustrated core-shell structure.[20,62]
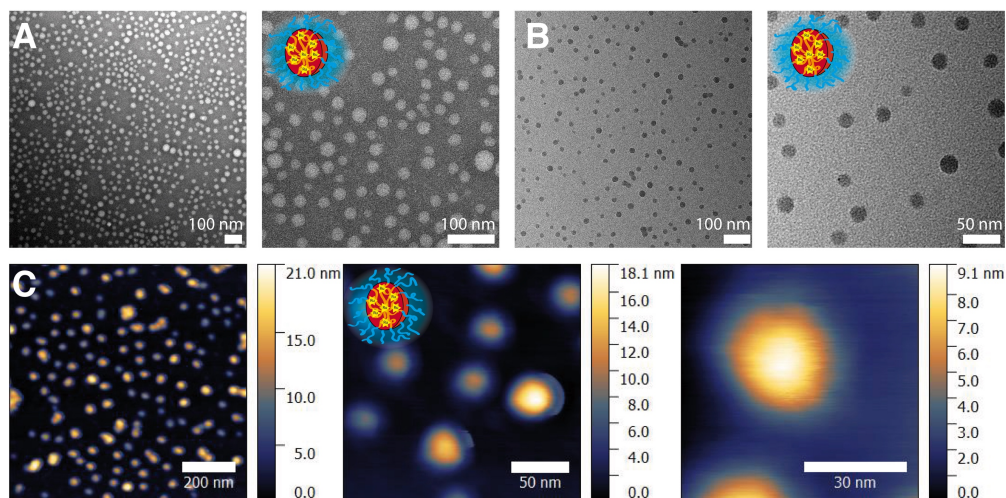
Figure 3. Particle analysis of PCCPMs by imaging techniques reveals small spherical structures. (**A**) TEM images (negatively stained with uranyl acetate); (**B**) TEM images of (non-stained); (**C**) AFM images with apparent height profiles.

Interestingly, when the aromatic nitrile-linker for the conjugation of the ruthenium complexes that was grafted to the polymer backbone was exchanged to a less flexible structure with only two instead of six methylene units, much larger micelles of 88 nm were detected by DLS (Figure 4, Table 3). Again, the overall size distribution was not changed after core cross-linking with $[Ru(bpy)_2(H_2O)_2]$ $(PF_6)_2$ or $[Ru(biq)_2(H_2O)_2]$ $(PF_6)_2$. However, further analysis by multi-angle DLS indicated an angle-dependency for these structures, pointing towards non-spherical morphologies (Figure S8). Finally, by imaging techniques, worm-like structures could be revealed for PCCPMs based on polymer P9-A. As shown in Figure 4D, the worm-like core cross-linked micelles displayed uniform widths of approx. 25 ± 3 nm (N = 27) with variable lengths (157 ± 83 nm; N = 90), accompanied by a fraction of small spherical structures (also see Figure S9, S10). The coexistence of worm-like and spherical structures was confirmed by cryo-TEM analysis (Figure 4B) and is further reflected in the GPC elugrams, whereby a fraction of very large species at or above the upper detection limit (12 mL) together with a smaller fraction (15 mL) have been detected for w-PCCPM-1 and w-PCCPM-2. Of note, no free polymer was detected accounting for core cross-linked micelles.

Table 3. Analytical results of the PCCPM preparation

particle	Ru-CPX	D_h / nm[a]	PDI[a]	Ru-CPX wt.%[b]
w-micelles	-	88	0.163	-
w-PCCPM-1	$[Ru(bpy)_2]^{2+}$	91	0.216	4.81 ± 0.11
w-PCCPM-2	$[Ru(biq)_2]^{2+}$	98	0.170	15.5 ± 0.34

[a] single-angle DLS at 173°, [b] ICP-MS.

Figure 4. Analysis of worm-like core cross-linked polymeric micelles (w-PCCPMs). (**A**) The less flexible linker (orange) for ruthenium complex conjugation directs self-assembly to

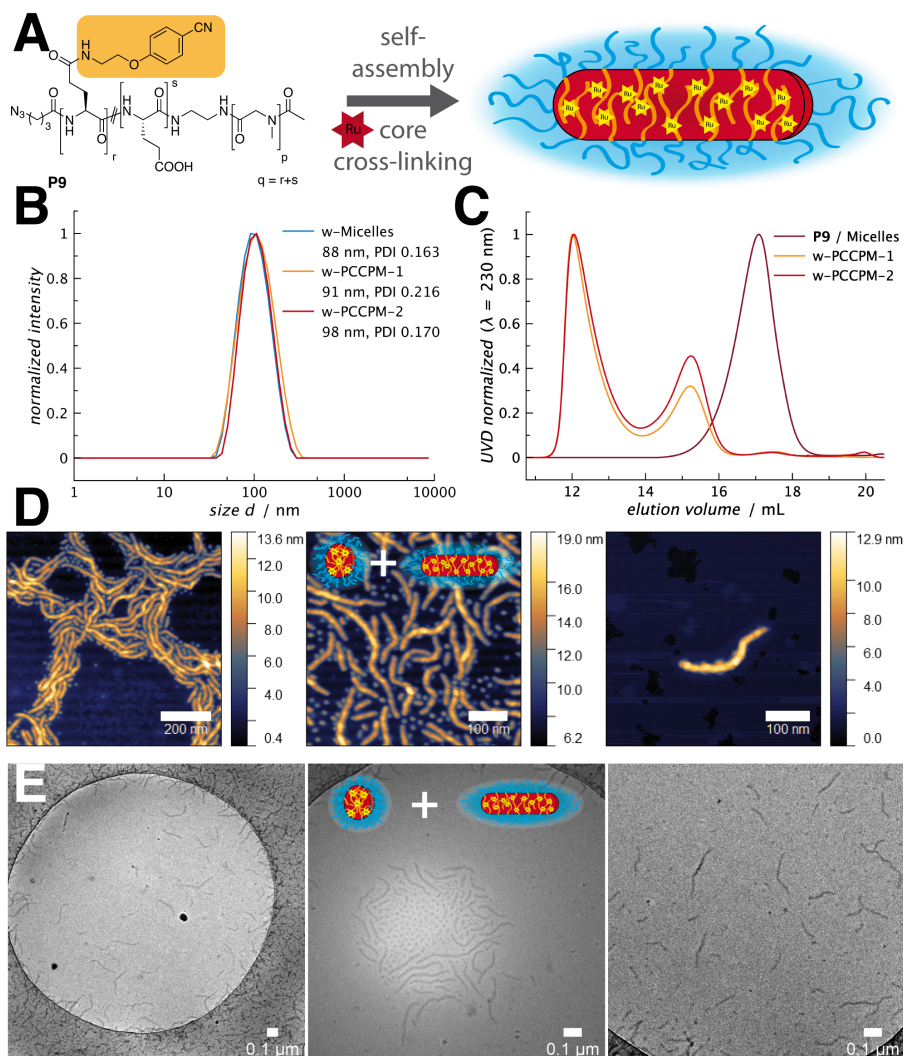worm-like micelles; (**B**) Cross-linking does not affect the size distribution in DLS analysis; (**C**) HFIP-GPC reveals the coexistence of small and large particles and absence of free polymer or leaking Ruthenium complex; (**D**) AFM images with apparent height profiles confirm the coexistence of spherical and worm-like particles; (**E**) Cryogenic TEM analysis confirms worm-like particles in solution.

Due to the strong absorbance of the aromatic rings, CD spectroscopy did not provide interpretable data on whether a change in the secondary structure is directing to the worm-like assemblies (data not shown). Nevertheless, reducing the chain lengths of the pGlu block while keeping the less flexible linker, again resulted in the formation of mainly small spherical core cross-linked polymeric micelles (Figure S11). In the uncharged state pGlu(OH) is known to adopt an α-helix secondary structure, which has been reported to facilitate the formation of spherical rather than worm-like structures.[63,64] A supramolecular stacking of the conjugated aromatic rings might thus account for the discovered 1-dimensional growth of the polymeric micelles derived from polymer P9-A.[65] Furthermore, the altered morphology could also be explained by differences in the hydrophobicity of the two linkers. Based on calculated *logP* values, the hexamethylene ester-linker is more hydrophobic than the ethylene amide-linker (*logP* = 2.84 and 1.04). This correlates well with pSar$_{140}$-*b*-pGlu$_{15}$ copolymers that have been modified with the two linkers, whereby aggregation starts earlier for the more hydrophobic copolymer when water is added to the polymer solution in DMSO (Figure S12).[66]

When exposed to light, the ruthenium(II) complexes have been reported to undergo photoinduced hydrolysis resulting in the cleavage of the nitrile-group coordination to the central metal-ion.[67,68] To verify this feature for ruthenium-based core cross-linked polymeric micelles, the nanoparticles were irradiated by narrow bandwidth high brightness LEDs, and the reaction was monitored by UV-Vis spectroscopy, as illustrated in Figure 5A. A blue LED ($\lambda \geq 455$ nm) was used to irradiate PCCPM-1 close to the local maximum of the nitrile-conjugated MLCT ($\lambda = 420$ nm). Within 60 s, a tremendous decrease of the local maximum could be observed, and the reaction was completed after irradiation for 5 minutes. The spectrum then matches the one of $[Ru(bpy)_2(H_2O)_2]^{2+}$, accounting for completed ligand exchange.
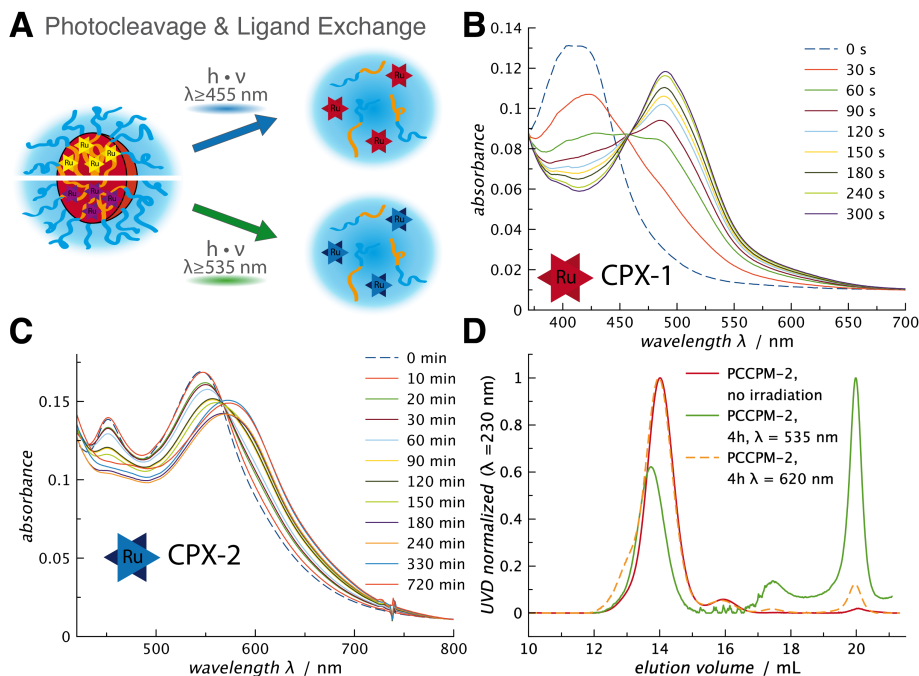
Figure 5. Analysis of the light-induced ligand exchange reaction. (**A**) Illustration of the performed irradiation experiments for PCCPM-1 and PCCPM-2; (**B**) UV-Vis spectroscopy of PCCPM-1 indicates completed cleavage within 300 s; (**C**) UV-Vis spectroscopy shows incomplete cleavage of PCCPM-2 after green-light irradiation for 12 h; (**D**) HFIP-GPC of PCCPM-2 before and after irradiation.

For PCCPM-2, a green LED ($\lambda \geq 535$ nm) was used to induce the cleavage reaction. As shown in Figure 5C, the wavelength of the local absorbance maximum shifts from 548 nm to 575 nm throughout the reaction, however, the MLCT peak does not recover the 590 nm of $[Ru(biq)_2(H_2O)_2]^{2+}$, which implies incomplete hydrolysis. Moreover, no significant change can be observed between 330 min and 720 min of irradiation. When analyzed by HFIP-GPC, released ruthenium complex (V = 20 mL) together with still intact particles (V = 14 mL) can be detected after 4 h of green light irradiation. When the photocleavage was performed with a red-orange LED ($\lambda = 620$ nm), progress was even slower (Figure S13) with hardly any cross-linker being released after 4 h. The distinctive kinetics of the photoinduced hydrolysis of PCCPM-1 and PCCPM-2 is also reflected by the reported quantum yields for the acetonitrile derivatives $[Ru(bpy)_2(CH_3CN)_2]^{2+}$ and $[Ru(biq)_2(CH_3CN)_2]^{2+}$. The light-induced exchange of the nitrile ligands by

irradiation at the MLCT follows a stepwise procedure involving intermediate monoaqua ruthenium(II) species.[69–71] For $[Ru(biq)_2(CH_3CN)_2]^{2+}$ quantum yields of $\varphi_{550\,nm}$ 0.15 and $\varphi_{550\,nm}$ 0.0014 indicate that the second ligand exchange is significantly slower which is in good agreement with our findings.[69] On the other hand, for $[Ru(bpy)_2(CH_3CN)_2]^{2+}$ high quantum yields of $\varphi_{450\,nm} = 0.22$ have been reported for the overall process yielding $[Ru(bpy)_2(H_2O)_2]^{2+}$, which is also reflected by the complete cleavage in less than 5 min for PCCPM-1.[70]

To investigate a potential application for photodynamic or photoactivated chemotherapy, PCCPMs were evaluated for their cytotoxicity *in vitro*, and the circulation behavior and organ distribution *in ovo* (Figure 6). When HuH-7 tumor cells were treated with photocleavable polymeric micelles containing 10 µM of $[Ru(bpy)_2(H_2O)_2]$ $(PF_6)_2$ (Ru-CPX-1) in the dark, a slight reduction in cell viability could be detected ($p < 0.01$), whereby the blue light irradiation ($\lambda \geq 455$ nm) did not induce significant cell death (Figure 6A). Moreover, the cell viability decreased only at very high concentrations above 200 µM for the micelle-free Ru-CPX-1 (Figure S14). These findings are congruent with the literature reporting $[Ru(bpy)_2(H_2O)_2]^{2+}$ as non-toxic, while it has been intensively studied as a model drug for binding of ruthenium(II) complexes to nucleosides or DNA.[72–75] Contrariwise, IC_{50} values of 25 µg·mL^{-1} and 2.5 µg·mL^{-1} have been reported for HeLa cells incubated with Ru-CPX-2 ($[Ru(biq)_2(H_2O)_2]$ $(PF_6)_2$) in the dark and with additional red light irradiation.[29] As shown in Figure 6B, however, HuH-7 cells did not respond to the treatment with $[Ru(biq)_2(H_2O)_2]$ $(PF_6)_2$ to the same extent. When treated with matching doses of 10 µM native Ru-CPX-2, no significant toxicity could be detected without irradiation, while the green light itself ($\lambda = 535$ nm) is the major cause of cell death for the irradiated samples (two-way ANOVA, $p < 0.0001$).
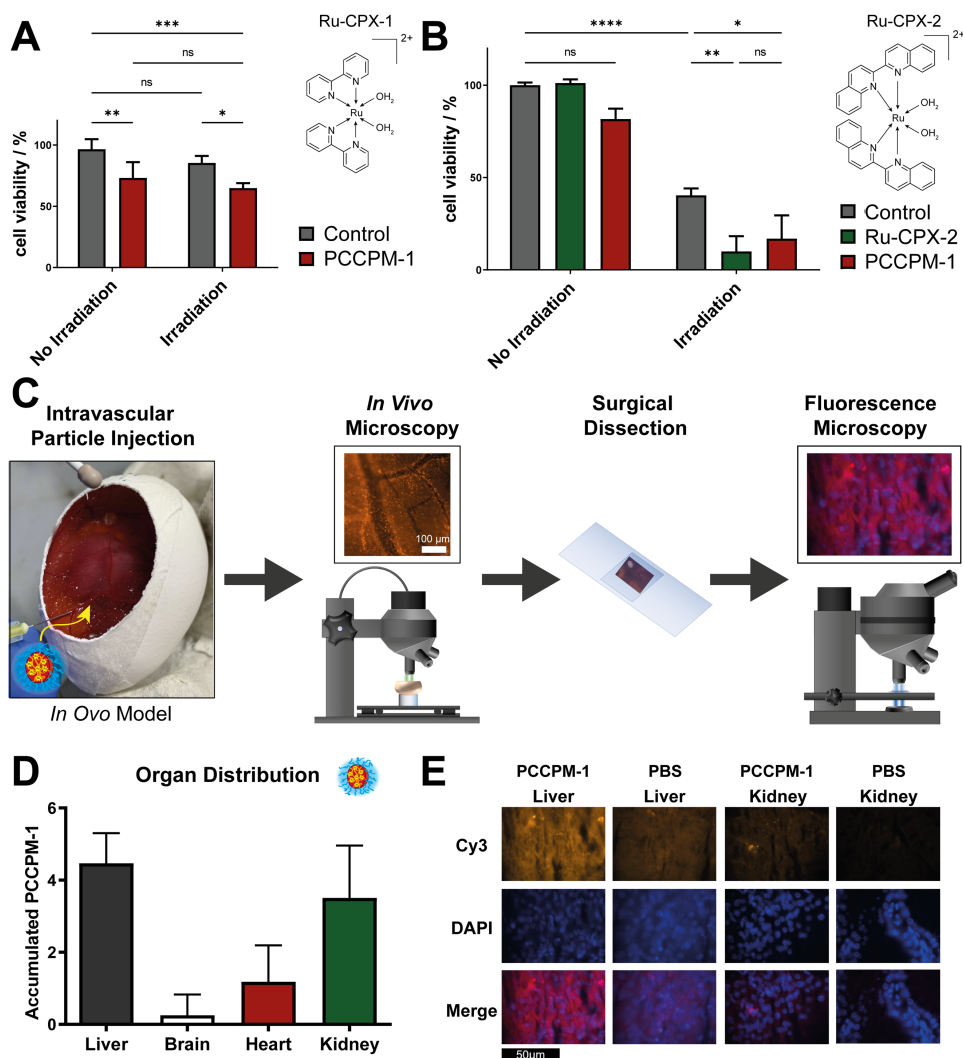
Figure 6. Biologic evaluation of PCCPMs. (**A**) Cell viability of HuH-7 tumor cells after incubation with NaCl (control) or PCCPM-1 at equivalent concentrations of 10 μM [Ru(bpy)$_2$(H$_2$O)$_2$] (PF$_6$)$_2$, with and without irradiation (λ ≥ 455 nm) for 5 minutes; (**B**) Cell viability of HuH-7 cells after incubation with NaCl (control), [Ru(biq)$_2$(H$_2$O)$_2$] (PF$_6$)$_2$, and PCCPM-2 at equivalent concentrations of 10 μM [Ru(biq)$_2$(H$_2$O)$_2$] (PF$_6$)$_2$,with and without irradiation (λ ≥ 535 nm) for 15 minutes; (**C**) Schematic illustration of the particle analysis in ovo; (**D**) Organ distribution *in ovo* (n = 14), at 24 h post injection, determined by image analysis of fluorescence microscopy; (**E**) Representative fluorescence microscopy images for liver and kidney after injection of PCCPM-1 or PBS. In vitro data reported as mean ±

Standard Error of the Mean (SEM) and representative of 3 independent experiments. Two-way ANOVA(*): * $p < 0.05$, ** $p < 0.01$, *** $p < 0.001$, **** $p < 0.0001$.

Furthermore, free Ru-CPX-2 and PCCPM-2 only slightly induced additional toxicity that is significant relative to the irradiated control (Ru-CPX-2, $p < 0,01$; PCCPM-2, $p < 0,05$), whereby no more difference was observed among the free complex or the micellar formulation.

For further biologic evaluation, PCCPMs were covalently labeled with DBCO-sulforhodamine B by alkyne-azide click chemistry and investigated in the *in ovo* in the chorioallantoic membrane assay (CAM assay).[76] The CAM assay has been previously described as well suited model for the evaluation of nanoparticle toxicity and the study of circulation times, as well as clearance of nanoparticles from the organism.[77] As illustrated in Figure 6C, following intravascular administration of the particles, the circulation time was qualitatively analyzed by *in vivo* microscopy followed by surgical dissection and fluorescence microscopy of the fixated organ slices after the sacrifice of the embryo. Of the 19 eggs included in the study, 14 eggs finished the study according to protocol. Death of the embryo within the timeframe of observation as well as a lack of particle circulation due to paravasal injection were reasons for a dropout. Spherical photocleavable micelles showed a stable but decreasing circulation and were still detectable in circulation even 24 h post-injection (Figure S15). According to the histological analysis, the particles mainly sequestered in the tissue of liver and kidney (Figure 6D, E), and only minor accumulation was found in the heart, while hardly any particle-related fluorescence could be detected in the brain tissue slices (Figure S16). Of note, within the heart tissue the accumulation pattern was mostly disseminated and showed agglomerates predominantly in the vessels within the tissue, while in the brain tissue the fluorescent signal is mostly located within the vascular network. Since liver and kidney are the organs responsible for the excretion these are the typical sites where nanoparticles are deposited.[78,79]

Taken together, polypept(o)ides and ruthenium(II) complexes were successfully combined in photocleavable core cross-linked polymeric micelles. The cross-linking by the ruthenium(II) complexes provided colloidal stability, whereby the choice of the nitrile linker for complex conjugation showed a critical influence on the particle morphology. Light-induced cleavage and cytotoxicity was governed by the dense micellar core and the incorporated ruthenium(II) complex.

Conclusions

We demonstrate how polypept(o)ides and ruthenium(II) complexes can be combined for light-sensitive core cross-linked polymeric micelles. Block copolymers of pSar-*b*-pGlu that have been modified with flexible linkers containing aromatic nitrile moieties were self-assembled into spherical nanostructures and cross-linked by $[Ru(bpy)_2(H_2O)_2]$ $(PF_6)_2$ or $[Ru(biq)_2(H_2O)_2]$ $(PF_6)_2$ without affecting the overall size distribution (45 nm, PDI 0.11). The morphology was further tuned by changing to a shorter, less flexible, and less hydrophobic nitrile linker, whereby worm-like particles are observed in AFM and cryo-EM depending on the chain length of the modified pGlu block. According to the analysis by GPC in HFIP, the photocleavable core cross-linked polymeric micelles display colloidal stability and do not cause aggregation in human plasma as detected by DLS. Of note, after completed purification, rather low ruthenium complex contents of 4.3 to 4.8 wt.% have been determined by SN-ICP-MS yet seem sufficient for stabilization. By irradiation at the MLCT peak $[Ru(bpy)_2]^{2+}$ is completely cleaved within 5 minutes, whereas only insufficient light-induced solvolysis is observed for $[Ru(biq)_2]^{2+}$, which may be attributed to the low quantum yield and dense micellar core. Finally, the biologic evaluation underlines the potential of these functional metal- and polypept(o)ide-based nanomedicines, while future investigation for the application in photodynamic or photoactivated chemotherapy will focus on improving the cytotoxicity of the pro-drug complexes.

Author Contributions

All polymers and nanoparticles were synthesized, characterized, and evaluated by T.A.B., B.W. contributed multi-angle DLS and cryo-EM, F.K. and N.B. contributed SN-ICP-MS measurements. The ruthenium complexes were contributed by W.S. and X.Z. supervised by S.W. J.E. and N.W. performed *in vitro* and *in ovo* experiments guided by S.S. The manuscript was written by T.A.B., J.E., N.W., and M.B., the overall project was supervised by M.B.

Conflicts of interest

There are no conflicts to declare.

Acknowledgements

Notes and References

(1)   Cabral, H.; Miyata, K.; Osada, K.; Kataoka, K. Block Copolymer Micelles in Nanomedicine Applications. *Chem. Rev.* **2018**, *118* (14), 6844–6892.

(2)   Mi, P.; Miyata, K.; Kataoka, K.; Cabral, H. Clinical Translation of Self-Assembled Cancer Nanomedicines. *Adv. Ther.* **2021**, *4* (1), 2000159.

(3)   Zhou, Q.; Zhang, L.; Yang, T. H.; Wu, H. Stimuli-Responsive Polymeric Micelles for Drug Delivery and Cancer Therapy. *Int. J. Nanomedicine* **2018**, *13*, 2921–2942.

(4)   Rösler, A.; Vandermeulen, G. W. M.; Klok, H.-A. Advanced Drug Delivery Devices via Self-Assembly of Amphiphilic Block Copolymers. *Adv. Drug Deliv. Rev.* **2012**, *64*, 270–279.

(5)   Talelli, M.; Barz, M.; Rijcken, C. J. F. F.; Kiessling, F.; Hennink, W. E.; Lammers, T. Core-Crosslinked Polymeric Micelles: Principles, Preparation, Biomedical Applications and Clinical Translation. *Nano Today* **2015**, *10* (1), 93–117.

(6)   Owen, S. C.; Chan, D. P. Y.; Shoichet, M. S. Polymeric Micelle Stability. *Nano Today* **2012**, *7* (1), 53–65.

(7)   Talelli, M.; Rijcken, C. J. F.; Hennink, W. E.; Lammers, T. Polymeric Micelles for Cancer Therapy: 3 C's to Enhance Efficacy. *Curr. Opin. Solid State Mater. Sci.* **2012**, *16* (6), 302–309.

(8)   Barenholz, Y. Doxil® - The First FDA-Approved Nano-Drug: Lessons Learned. *J. Control. Release* **2012**, *160* (2), 117–134.

(9)   Martinez, C. R.; Iverson, B. L. Rethinking the Term "Pi-Stacking." *Chem. Sci.* **2012**, *3* (7), 2191–2201.

(10)   Liang, C.; Bai, X.; Qi, C.; Sun, Q.; Han, X.; Lan, T.; Zhang, H.; Zheng, X.; Liang, R.;

Jiao, J.; Zheng, Z.; Fang, J.; Lei, P.; Wang, Y.; Möckel, D.; Metselaar, J. M.; Storm, G.; Hennink, W. E.; Kiessling, F.; Wei, H.; Lammers, T.; Shi, Y.; Wei, B. Π Electron-Stabilized Polymeric Micelles Potentiate Docetaxel Therapy in Advanced-Stage Gastrointestinal Cancer. *Biomaterials* **2021**, *266* (September 2020), 10.

(11) Shi, Y.; Van Steenbergen, M. J.; Teunissen, E. A.; Novo, L.; Gradmann, S.; Baldus, M.; Van Nostrum, C. F.; Hennink, W. E. Π-Π Stacking Increases the Stability and Loading Capacity of Thermosensitive Polymeric Micelles for Chemotherapeutic Drugs. *Biomacromolecules* **2013**, *14* (6), 1826–1837.

(12) Lin, M.; Dai, Y.; Xia, F.; Zhang, X. Advances in Non-Covalent Crosslinked Polymer Micelles for Biomedical Applications. *Mater. Sci. Eng. C* **2021**, *119* (September 2020), 111626.

(13) Deng, C.; Zhang, Q.; Guo, J.; Zhao, X.; Zhong, Z. Robust and Smart Polypeptide-Based Nanomedicines for Targeted Tumor Therapy. *Adv. Drug Deliv. Rev.* **2020**, *160*, 199–211.

(14) Atrafi, F.; Dumez, H.; Mathijssen, R. H. J.; Menke van der Houven van Oordt, C. W.; Rijcken, C. J. F.; Hanssen, R.; Eskens, F. A. L. M.; Schöffski, P. A Phase I Dose-Escalation and Pharmacokinetic Study of a Micellar Nanoparticle with Entrapped Docetaxel (CPC634) in Patients with Advanced Solid Tumours. *J. Control. Release* **2020**, *325* (March), 191–197.

(15) Rijcken, C. J.; Snel, C. J.; Schiffelers, R. M.; van Nostrum, C. F.; Hennink, W. E. Hydrolysable Core-Crosslinked Thermosensitive Polymeric Micelles: Synthesis, Characterisation and in Vivo Studies. *Biomaterials* **2007**, *28* (36), 5581–5593.

(16) Atrafi, F.; van Eerden, R. A. G.; van Hylckama Vlieg, M. A. M.; Oomen-de Hoop, E.; de Bruijn, P.; Lolkema, M. P.; Moelker, A.; Rijcken, C. J.; Hanssen, R.; Sparreboom, A.; Eskens, F. A. L. M.; Mathijssen, R. H. J.; Koolen, S. L. W. Intratumoral Comparison of Nanoparticle Entrapped Docetaxel (CPC634) with Conventional Docetaxel in Patients with Solid Tumors. *Clin. Cancer Res.* **2020**, *26* (14), 3537–3545.

(17) Van Eerden, R. A. G.; Mathijssen, R. H. J.; Koolen, S. L. W. Recent Clinical Developments of Nanomediated Drug Delivery Systems of Taxanes for the Treatment of Cancer. *Int. J. Nanomedicine* **2020**, *15*, 8151–8166.

(18) Nishiyama, N.; Okazaki, S.; Cabral, H.; Miyamoto, M.; Kato, Y.; Sugiyama, Y.; Nishio, K.; Matsumura, Y.; Kataoka, K. Novel Cisplatin-Incorporated Polymeric Micelles Can Eradicate Solid Tumors in Mice. *Cancer Res.* **2003**, *63* (24), 8977–8983.

(19) Plummer, R.; Wilson, R. H.; Calvert, H.; Boddy, A. V.; Griffin, M.; Sludden, J.; Tilby, M. J.; Eatock, M.; Pearson, D. G.; Ottley, C. J.; Matsumura, Y.; Kataoka, K.; Nishiya, T. A Phase i Clinical Study of Cisplatin-Incorporated Polymeric Micelles (NC-6004) in Patients with Solid Tumours. *Br. J. Cancer* **2011**, *104* (4), 593–598.

(20) Mochida, Y.; Cabral, H.; Miura, Y.; Albertini, F.; Fukushima, S.; Osada, K.; Nishiyama, N.; Kataoka, K. Bundled Assembly of Helical Nanostructures in Polymeric Micelles Loaded with Platinum Drugs Enhancing Therapeutic Efficiency against Pancreatic Tumor. *ACS Nano* **2014**, *8* (7), 6724–6738.

(21) Bonnet, S. Why Develop Photoactivated Chemotherapy? *Dalt. Trans.* **2018**, *47* (31), 10330–10343.

(22) Farrer, N. J.; Salassa, L.; Sadler, P. J. Photoactivated Chemotherapy (PACT): The Potential of Excited-State d-Block Metals in Medicine. *Dalt. Trans.* **2009**, No. 48,

10690.

(23) Williams, R. L.; Toft, H. N.; Winkel, B.; Brewer, K. J. Synthesis, Characterization, and DNA Binding Properties of a Series of Ru, Pt Mixed-Metal Complexes. *Inorg. Chem.* **2003**, *42* (14), 4394–4400.

(24) Li, W.; Jiang, G. Bin; Yao, J. H.; Wang, X. Z.; Wang, J.; Han, B. J.; Xie, Y. Y.; Lin, G. J.; Huang, H. L.; Liu, Y. J. Ruthenium(II) Complexes: DNA-Binding, Cytotoxicity, Apoptosis, Cellular Localization, Cell Cycle Arrest, Reactive Oxygen Species, Mitochondrial Membrane Potential and Western Blot Analysis. *J. Photochem. Photobiol. B Biol.* **2014**, *140*, 94–104.

(25) Villemin, E.; Ong, Y. C.; Thomas, C. M.; Gasser, G. Polymer Encapsulation of Ruthenium Complexes for Biological and Medicinal Applications. *Nat. Rev. Chem.* **2019**, *3* (4), 261–282.

(26) Singh, T. N.; Turro, C. Photoinitiated DNA Binding by Cis-[Ru(Bpy)2(NH3)2]2+. *Inorg. Chem.* **2004**, *43* (23), 7260–7262.

(27) Knoll, J. D.; Albani, B. A.; Turro, C. New Ru(II) Complexes for Dual Photoreactivity: Ligand Exchange and 1 O 2 Generation. *Acc. Chem. Res.* **2015**, *48* (8), 2280–2287.

(28) Sun, W.; Wen, Y.; Thiramanas, R.; Chen, M.; Han, J.; Gong, N.; Wagner, M.; Jiang, S.; Meijer, M. S.; Bonnet, S.; Butt, H.; Mailänder, V.; Liang, X.; Wu, S. Red-Light-Controlled Release of Drug-Ru Complex Conjugates from Metallopolymer Micelles for Phototherapy in Hypoxic Tumor Environments. *Adv. Funct. Mater.* **2018**, *28* (39), 1804227.

(29) Sun, W.; Li, S.; Häupler, B.; Liu, J.; Jin, S.; Steffen, W.; Schubert, U. S.; Butt, H.-J. J.; Liang, X.-J. J.; Wu, S. An Amphiphilic Ruthenium Polymetallodrug for Combined Photodynamic Therapy and Photochemotherapy In Vivo. *Adv. Mater.* **2017**, *29* (6), 1603702.

(30) Sun, W.; Parowatkin, M.; Steffen, W.; Butt, H. J.; Mailänder, V.; Wu, S. Ruthenium-Containing Block Copolymer Assemblies: Red-Light-Responsive Metallopolymers with Tunable Nanostructures for Enhanced Cellular Uptake and Anticancer Phototherapy. *Adv. Healthc. Mater.* **2016**, *5* (4), 467–473.

(31) Zeng, X.; Wang, Y.; Han, J.; Sun, W.; Butt, H. J.; Liang, X. J.; Wu, S. Fighting against Drug-Resistant Tumors Using a Dual-Responsive Pt(IV)/Ru(II) Bimetallic Polymer. *Adv. Mater.* **2020**, *32* (43), 1–9.

(32) Birke, A.; Ling, J.; Barz, M. Polysarcosine-Containing Copolymers: Synthesis, Characterization, Self-Assembly, and Applications. *Prog. Polym. Sci.* **2018**, *81*, 163–208.

(33) Klinker, K.; Barz, M. Polypept(o)Ides: Hybrid Systems Based on Polypeptides and Polypeptoids. *Macromol. Rapid Commun.* **2015**, *36* (22), 1943–1957.

(34) Birke, A.; Huesmann, D.; Kelsch, A.; Weilbächer, M.; Xie, J.; Bros, M.; Bopp, T.; Becker, C.; Landfester, K.; Barz, M. Polypeptoid- Block -Polypeptide Copolymers: Synthesis, Characterization, and Application of Amphiphilic Block Copolypept(o)ides in Drug Formulations and Miniemulsion Techniques. *Biomacromolecules* **2014**, *15* (2), 548–557.

(35) Vayaboury, W.; Giani, O.; Cottet, H.; Deratani, A.; Schué, F. Living Polymerization of α-Amino Acid N-Carboxyanhydrides (NCA) upon Decreasing the Reaction Temperature. *Macromol. Rapid Commun.* **2004**, *25* (13), 1221–1224.

(36)   Aliferis, T.; Iatrou, H.; Hadjichristidis, N. Living Polypeptides. *Biomacromolecules* **2004**, *5* (5), 1653–1656.

(37)   Fetsch, C.; Grossmann, A.; Holz, L.; Nawroth, J. F.; Luxenhofer, R. Polypeptoids from N -Substituted Glycine N -Carboxyanhydrides: Hydrophilic, Hydrophobic, and Amphiphilic Polymers with Poisson Distribution. *Macromolecules* **2011**, *44* (17), 6746–6758.

(38)   Alberg, I.; Kramer, S.; Schinnerer, M.; Hu, Q.; Seidl, C.; Leps, C.; Drude, N.; Möckel, D.; Rijcken, C.; Lammers, T.; Diken, M.; Maskos, M.; Morsbach, S.; Landfester, K.; Tenzer, S.; Barz, M.; Zentel, R. Polymeric Nanoparticles with Neglectable Protein Corona. *Small* **2020**, *16* (18), 1907574.

(39)   Weber, B.; Birke, A.; Fischer, K.; Schmidt, M.; Barz, M. Solution Properties of Polysarcosine: From Absolute and Relative Molar Mass Determinations to Complement Activation. *Macromolecules* **2018**, *51* (7), 2653–2661.

(40)   Lau, K. H. A.; Ren, C.; Sileika, T. S.; Park, S. H.; Szleifer, I.; Messersmith, P. B. Surface-Grafted Polysarcosine as a Peptoid Antifouling Polymer Brush. *Langmuir* **2012**, *28* (46), 16099–16107.

(41)   Deming, T. J. Synthesis of Side-Chain Modified Polypeptides. *Chem. Rev.* **2016**, *116* (3), 786–808.

(42)   Klinker, K.; Schäfer, O.; Huesmann, D.; Bauer, T.; Capelôa, L.; Braun, L.; Stergiou, N.; Schinnerer, M.; Dirisala, A.; Miyata, K.; Osada, K.; Cabral, H.; Kataoka, K.; Barz, M. Secondary-Structure-Driven Self-Assembly of Reactive Polypept(o)Ides: Controlling Size, Shape, and Function of Core Cross-Linked Nanostructures. *Angew. Chemie Int. Ed.* **2017**, *56* (32), 9608–9613.

(43)   Heller, P.; Zhou, J.; Weber, B.; Hobernik, D.; Bros, M.; Schmid, F.; Barz, M. The Influence of Block Ionomer Microstructure on Polyplex Properties: Can Simulations Help to Understand Differences in Transfection Efficiency? *Small* **2017**, *13* (17), 1603694.

(44)   Nogueira, S. S.; Schlegel, A.; Maxeiner, K.; Weber, B.; Barz, M.; Schroer, M. A.; Blanchet, C. E.; Svergun, D. I.; Ramishetti, S.; Peer, D.; Langguth, P.; Sahin, U.; Haas, H. Polysarcosine-Functionalized Lipid Nanoparticles for Therapeutic MRNA Delivery. *ACS Appl. Nano Mater.* **2020**, *3* (11), 10634–10645.

(45)   Son, K.; Ueda, M.; Taguchi, K.; Maruyama, T.; Takeoka, S.; Ito, Y. Evasion of the Accelerated Blood Clearance Phenomenon by Polysarcosine Coating of Liposomes. *J. Control. Release* **2020**, *322* (March), 209–216.

(46)   Barz, M.; Luxenhofer, R.; Zentel, R.; Vicent, M. J. Overcoming the PEG-Addiction: Well-Defined Alternatives to PEG, from Structure–Property Relationships to Better Defined Therapeutics. *Polym. Chem.* **2011**, *2* (9), 1900–1918.

(47)   Rausch, K.; Reuter, A.; Fischer, K.; Schmidt, M. Evaluation of Nanoparticle Aggregation in Human Blood Serum. *Biomacromolecules* **2010**, *11* (11), 2836–2839.

(48)   Theis, S.; Iturmendi, A.; Gorsche, C.; Orthofer, M.; Lunzer, M.; Baudis, S.; Ovsianikov, A.; Liska, R.; Monkowius, U.; Teasdale, I. Metallo-Supramolecular Gels That Are Photocleavable with Visible and Near-Infrared Irradiation. *Angew. Chemie - Int. Ed.* **2017**, *56* (50), 15857–15860.

(49)   Holm, R.; Klinker, K.; Weber, B.; Barz, M. Synthesis of Amphiphilic Block Copolypept(o)Ides by Bifunctional Initiators: Making PeptoMicelles Redox

Sensitive. *Macromol. Rapid Commun.* **2015**, *36* (23), 2083–2091.

(50)   Steinborn, B.; Hirschle, P.; Höhn, M.; Bauer, T.; Barz, M.; Wuttke, S.; Wagner, E.; Lächelt, U. Core-Shell Functionalized Zirconium-Pemetrexed Coordination Nanoparticles as Carriers with a High Drug Content. *Adv. Ther.* **2019**, *2* (11), 1900120.

(51)   Ernst, B. P.; Wiesmann, N.; Gieringer, R.; Eckrich, J.; Brieger, J. HSP27 Regulates Viability and Migration of Cancer Cell Lines Following Irradiation. *J. Proteomics* **2020**, *226* (March), 103886.

(52)   Schäfer, O.; Klinker, K.; Braun, L.; Huesmann, D.; Schultze, J.; Koynov, K.; Barz, M. Combining Orthogonal Reactive Groups in Block Copolymers for Functional Nanoparticle Synthesis in a Single Step. *ACS Macro Lett.* **2017**, *6* (10), 1140–1145.

(53)   Conejos-Sánchez, I.; Duro-Castano, A.; Birke, A.; Barz, M.; Vicent, M. J. A Controlled and Versatile NCA Polymerization Method for the Synthesis of Polypeptides. *Polym. Chem.* **2013**, *4* (11), 3182.

(54)   Gangloff, N.; Fetsch, C.; Luxenhofer, R. Polypeptoids by Living Ring-Opening Polymerization of N-Substituted N-Carboxyanhydrides from Solid Supports. *Macromol. Rapid Commun.* **2013**, *34* (12), 997–1001.

(55)   Durham, B.; Wilson, S. R.; Hodgson, D. J.; Meyer, T. J. Cis-Trans Photoisomerization in Ru(Bpy)2(OH2)22+. Crystal Structure of Trans-[Ru(Bpy)2(OH2)(OH)](ClO4)2. *J. Am. Chem. Soc.* **1980**, *102* (2), 600–607.

(56)   Kobayashi, K.; Ohtsu, H.; Nozaki, K.; Kitagawa, S.; Tanaka, K. Photochemical Properties and Reactivity of a Ru Compound Containing an NAD/NADH-Functionalized 1,10-Phenanthroline Ligand. *Inorg. Chem.* **2016**, *55* (5), 2076–2084.

(57)   Lammers, T. SMART Drug Delivery Systems: Back to the Future vs. Clinical Reality. *Int. J. Pharm.* **2013**, *454* (1), 527–529.

(58)   Mitragotri, S.; Lammers, T.; Bae, Y. H.; Schwendeman, S.; De Smedt, S.; Leroux, J. C.; Peer, D.; Kwon, I. C.; Harashima, H.; Kikuchi, A.; Oh, Y. K.; Torchilin, V.; Hennink, W.; Hanes, J.; Park, K. Drug Delivery Research for the Future: Expanding the Nano Horizons and Beyond. *J. Control. Release* **2017**, *246*, 183–184.

(59)   Soetaert, F.; Korangath, P.; Serantes, D.; Fiering, S.; Ivkov, R. Cancer Therapy with Iron Oxide Nanoparticles: Agents of Thermal and Immune Therapies. *Adv. Drug Deliv. Rev.* **2020**, *163–164*, 65–83.

(60)   Bhattacharjee, S. DLS and Zeta Potential - What They Are and What They Are Not? *J. Control. Release* **2016**, *235*, 337–351.

(61)   Fischer, K.; Schmidt, M. Pitfalls and Novel Applications of Particle Sizing by Dynamic Light Scattering. *Biomaterials* **2016**, *98*, 79–91.

(62)   Franken, L. E.; Boekema, E. J.; Stuart, M. C. A. Transmission Electron Microscopy as a Tool for the Characterization of Soft Materials: Application and Interpretation. *Adv. Sci.* **2017**, *4* (5), 1–9.

(63)   Lecommandoux, S.; Achard, M. F.; Langenwalter, J. F.; Klok, H. A. Self-Assembly of Rod-Coil Diblock Oligomers Based on α-Helical Peptides. *Macromolecules* **2001**, *34* (26), 9100–9111.

(64)   Bonduelle, C. Secondary Structures of Synthetic Polypeptide Polymers. *Polym. Chem.* **2018**, *9* (13), 1517–1529.

(65)   Palmer, L. C.; Stupp, S. I. Molecular Self-Assembly into One-Dimensional

Nanostructures. *Acc. Chem. Res.* **2008**, *41* (12), 1674–1684.

(66)   Bauer, T. A.; Imschweiler, J.; Muhl, C.; Weber, B.; Barz, M. Secondary Structure-Driven Self-Assembly of Thiol-Reactive Polypept(o)Ides. *Biomacromolecules* **2021**, *22* (5), 2171–2180.

(67)   Garner, R. N.; Gallucci, J. C.; Dunbar, K. R.; Turro, C. [Ru(Bpy) 2 (5-Cyanouracil) 2] 2+ as a Potential Light-Activated Dual-Action Therapeutic Agent. *Inorg. Chem.* **2011**, *50* (19), 9213–9215.

(68)   Garner, R. N.; Joyce, L. E.; Turro, C. Effect of Electronic Structure on the Photoinduced Ligand Exchange of Ru(II) Polypyridine Complexes. *Inorg. Chem.* **2011**, *50* (10), 4384–4391.

(69)   Albani, B. A.; Durr, C. B.; Turro, C. Selective Photoinduced Ligand Exchange in a New Tris-Heteroleptic Ru (II) Complex Selective Photoinduced Ligand Exchange in a New Tris-Heteroleptic Ru (II) Complex. *J. Phys. Chem. A* **2013**, *117* (Ii), 13885–13892.

(70)   Liu, Y.; Turner, D. B.; Singh, T. N.; Angeles-Boza, A. M.; Chouai, A.; Dunbar, K. R.; Turro, C. Ultrafast Ligand Exchange: Detection of a Pentacoordinate Ru(II) Intermediate and Product Formation. *J. Am. Chem. Soc.* **2009**, *131* (1), 26–27.

(71)   Zeng, L.; Gupta, P.; Chen, Y.; Wang, E.; Ji, L.; Chao, H.; Chen, Z. S. The Development of Anticancer Ruthenium(II) Complexes: From Single Molecule Compounds to Nanomaterials. *Chem. Soc. Rev.* **2017**, *46* (19), 5771–5804.

(72)   Nováková, O.; Kašpárková, J.; Vrána, O.; van Vliet, P. M.; Reedijk, J.; Brabec, V. Correlation between Cytotoxicity and DNA Binding of Polypyridyl Ruthenium Complexes. *Biochemistry* **1995**, *34* (38), 12369–12378.

(73)   Vázquez, M.; Martínez, M. Kinetico-Mechanistic Studies on the Substitution Reactivity on the {Ru II (Bpy) 2 } Core with Nucleosides and Nucleotides at Physiological PH. *Inorg. Chem.* **2016**, *55* (13), 6731–6738.

(74)   Cuello-Garibo, J.-A.; Meijer, M. S.; Bonnet, S. To Cage or to Be Caged? The Cytotoxic Species in Ruthenium-Based Photoactivated Chemotherapy Is Not Always the Metal. *Chem. Commun.* **2017**, *53* (50), 6768–6771.

(75)   Azar, D.; Audi, H.; Farhat, S.; El Sibai, M.; Abi-Habib, R.; Khnayzer, R. S. Phototoxicity of Strained Ru(II) Complexes: Is It the Metal Complex or the Dissociating Ligand? *Dalt. Trans.* **2017**, *46* (35), 11529–11532.

(76)   Buhr, C. R.; Wiesmann, N.; Tanner, R. C.; Brieger, J.; Eckrich, J. The Chorioallantoic Membrane Assay in Nanotoxicological Research—an Alternative for in Vivo Experimentation. *Nanomaterials* **2020**, *10* (12), 1–16.

(77)   Ribatti, D. The Chick Embryo Chorioallantoic Membrane (CAM). A Multifaceted Experimental Model. *Mech. Dev.* **2016**, *141*, 70–77.

(78)   Poon, W.; Heinmiller, A.; Zhang, X.; Nadeau, J. L. Determination of Biodistribution of Ultrasmall, near-Infrared Emitting Gold Nanoparticles by Photoacoustic and Fluorescence Imaging. *J. Biomed. Opt.* **2015**, *20* (6), 066007.

(79)   Buhr, C. R.; Eckrich, J.; Kluenker, M.; Bruns, K.; Wiesmann, N.; Tremel, W.; Brieger, J. Determination of the LD 50 with the Chick Embryo Chorioallantoic Membrane (CAM) Assay as a Promising Alternative in Nanotoxicological Evaluation. *Nanotoxicology* **2021**, 1–16.

Supporting Information

Results and Discussion

Polymer Synthesis

Table S1. Analytical results of the polymer synthesis of **P1** to **P9**.

polymer	M/I (calc.)	X_n (pGlu)[a]	X_n (pSar)[a]	M_n[b] / kDa	M_w[b] / kDa	$Đ$[b]	CN-grafting
P1, pGlu(OtBu)$_{36}$	30	36	-	19.7	22.9	1.16	-
P2, pGlu(OtBu)$_{36}$-b-Sar$_{171}$	160	36	171	44.0	52.9	1.20	-
P3, pGlu(OH)$_{36}$-b-Sar$_{171}$	-	36	171	37.9	59.1	1.56	-
P4, pGlu(Mod)$_{36}$-b-Sar$_{171}$	-	36	171	53.1	74.8	1.41	52%
P5, N-Boc-pSar$_{140}$	200	-	140	-	-	-	-
P6, pSar$_{140}$	-	-	140	28.7	34.5	1.20	-
P7A, pSar$_{140}$-b-pGlu(OtBu)$_{20}$	20	19	140	30.0	39.3	1.31	-
P7B, pSar$_{140}$-b-pGlu(OtBu)$_{15}$	15	14	140	30.3	40.7	1.34	-
P8A, pSar$_{140}$-b-pGlu(OH)$_{20}$	-	19	140	28.2	35.6	1.26	-
P8B, pSar$_{140}$-b-pGlu(OH)$_{15}$	-	14	140	30.9	54.1	1.75	-
P9A, pSar$_{140}$-b-pGlu(Mod)$_{20}$	-	19	140	71.3	113.2	1.58	65%
P9B, pSar$_{140}$-b-pGlu(Mod)$_{15}$	-	14	140	47.9	61.5	1.28	100%

[a] determined by ^{1}H NMR, [b] determined by HFIP-GPC with pSar standards, [c] determined by HFIP-GPC with PMMA standards.

HFIP-GPC Analysis
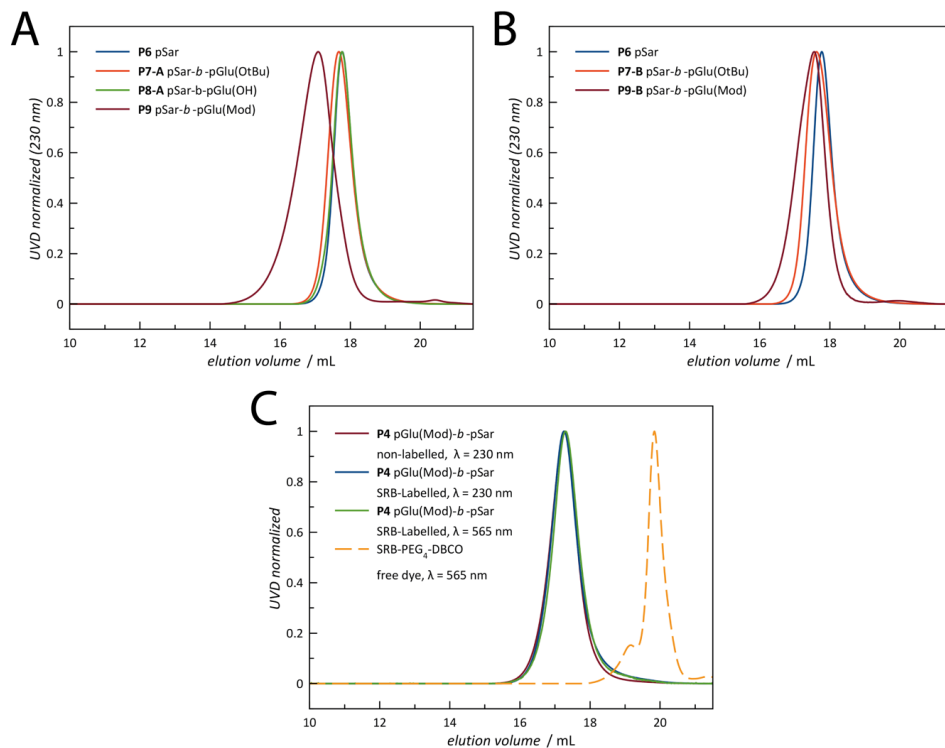
Figure S1. Analytical HFIP-GPC. (**A**) Polymers P6 to P9-A, (**B**) Polymers P6 to P9-B, (**C**) Labelling of P4 with Sulforhodamine-B, whereby no free unconjugated dye is detectable.

FT-IR Spectroscopy
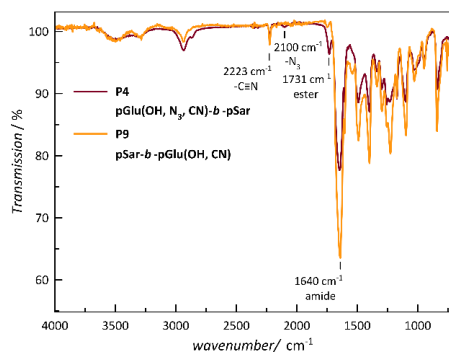
Figure S2. Comparison of cyano-modified polymers P4 (dark red) and P9-A (orange) by FT-IR spectroscopy. As expected, the ester bond is not visible in P9-A, but only in P4.

Photocleavable Core Cross-Linked Polymeric Micelles (PCCPMs)

Images
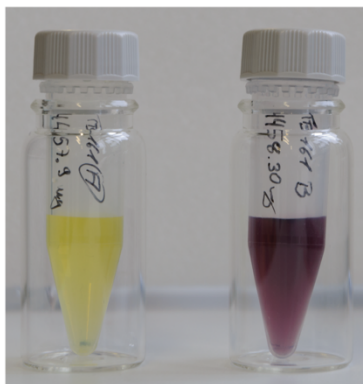
Figure S3. Images of PCCPMs after completed purification by spin-filtration. PCCPM-1 (left) and PCCPM-2 (right).

Multi-Angle Dynamic Light Scattering in Human Plasma
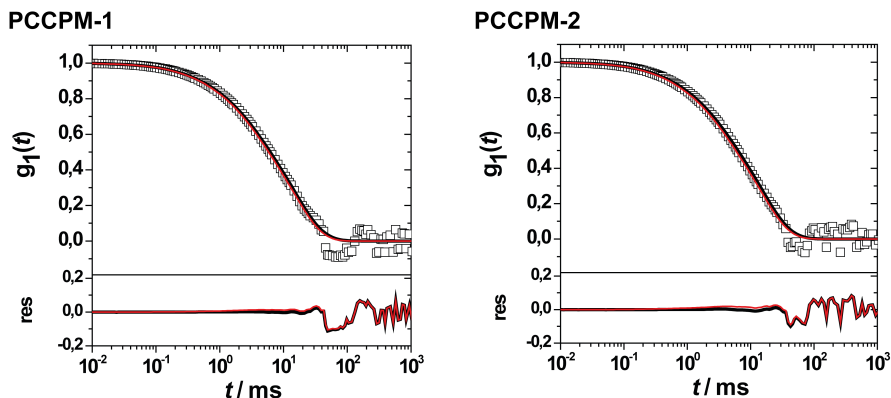
PCCPM-1

PCCPM-2

Figure S4. Multi-Angle Dynamic Light Scattering of PCCPM-1 (left) and PCCPM-2 (right) in human plasma.[1] Autocorrelation function $g_1(t)$ for an exemplary scattering angle of 30° for fits with (red) and without (black line) aggregate term (upper graph), and the residuals of fits w/o aggregate and correlation function (lower graph).

Extended TEM Analysis

TEM-Analysis

□ no staining
▨ negative staining
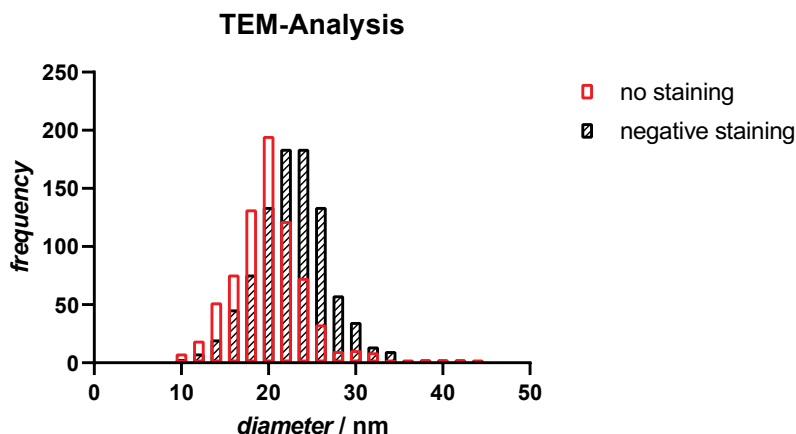
Figure S5. Particle analysis by TEM for PCCPM-2. (red) without staining; average particle diameter of 20.2 ± 4.5 nm, PDI 0.050. (black) negatively stained with uranyl acetate; average particle diameter of 22.8 ± 4.3 nm, PDI 0.034. Objects smaller than 10 nm diameter were excluded for statistics.

PCCPM-2, stained   PCCPM-2, NON-stained
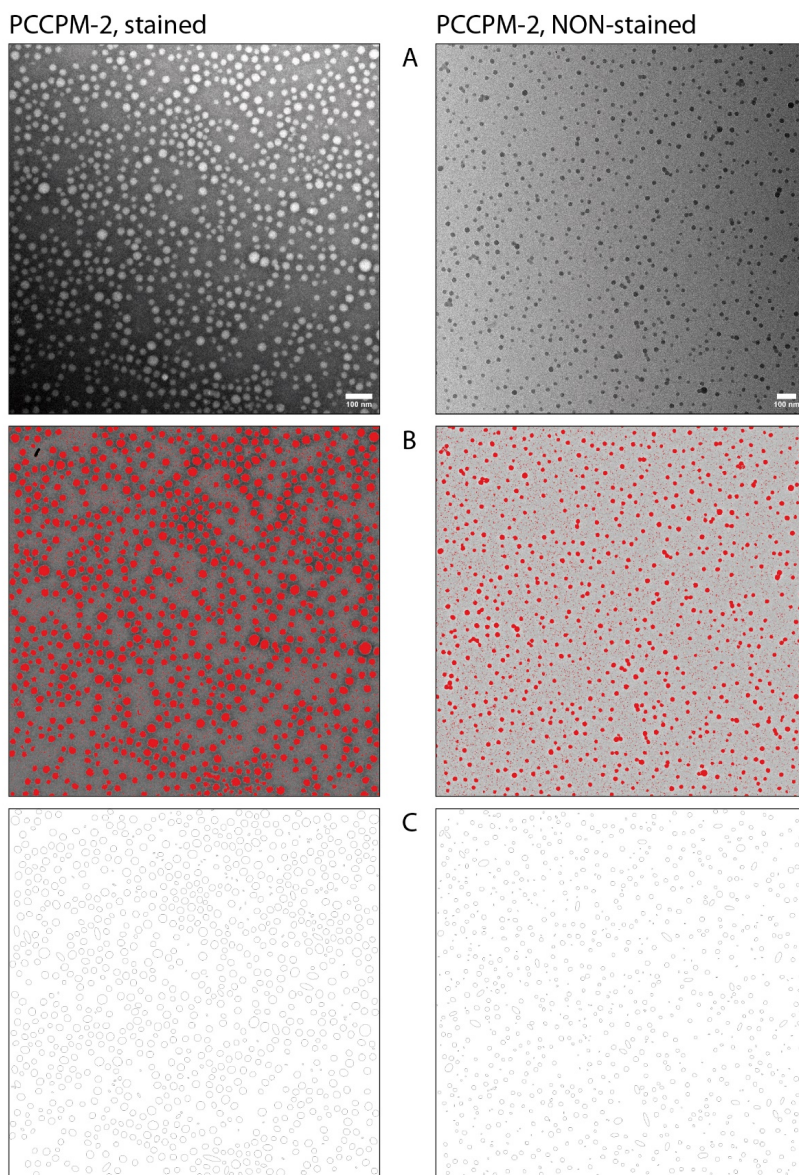
Figure S6. Exemplified particle counting for non-stained (left) and negatively stained samples (right) using ImageJ 1.52h.(**A**) parent TEM image, (**B**) derived threshold image, (**C**) area analysis for given threshold objects. Assuming spherical shape, diameters were calculated for each object.
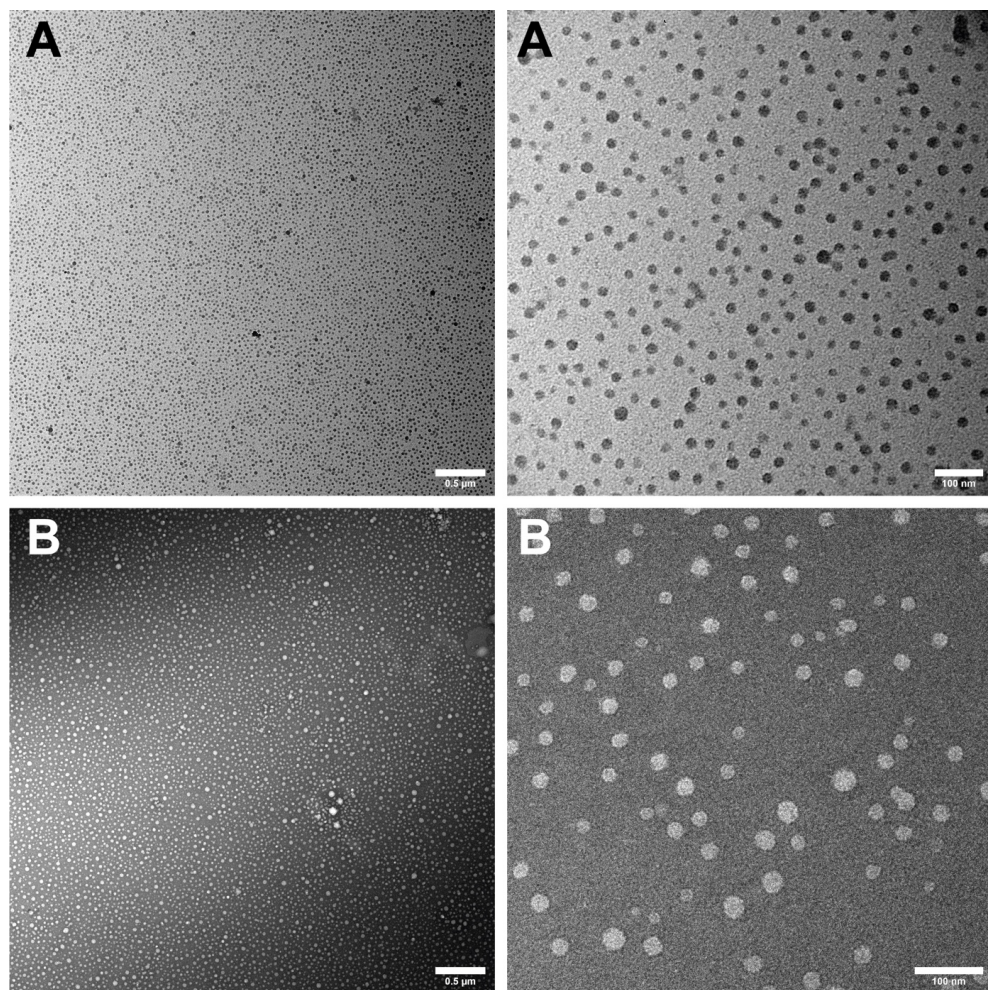
Figure S7. TEM Analysis of PCCPM-1. (**A**) without staining, (**B**) negative staining.

Worm-like Photocleavable Core Cross-Linked Polymeric Micelles (w-PCCPM)

Multi-Angle Dynamic Light Scattering of Worm-Like PCCPMs
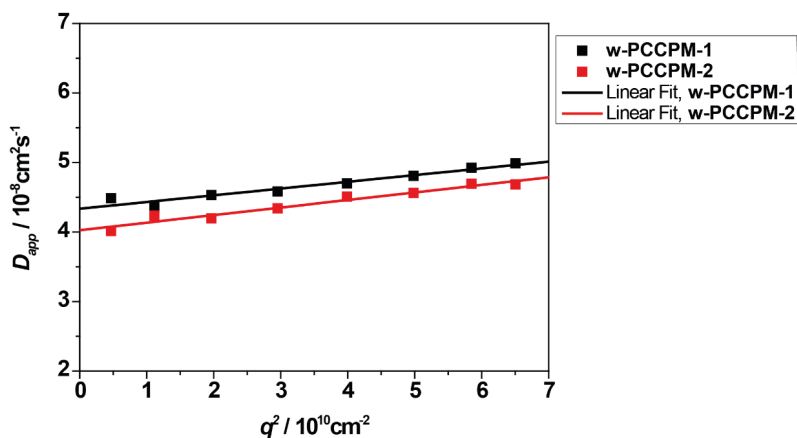
Figure S8. Multi-angle dynamic light scattering of worm-like PCCPMs in PBS prepared from **P9-A**.

AFM Analysis of Worm-Like PCCPMs
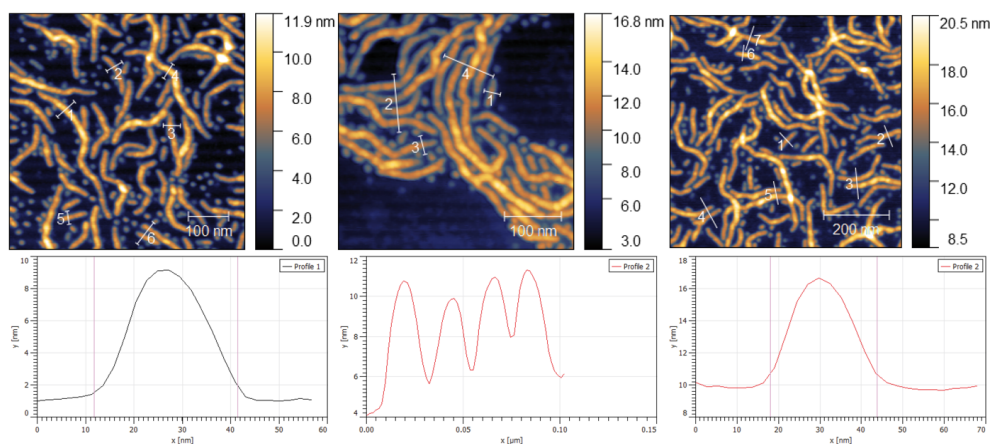
Figure S9. AFM image analysis of w-PCCPM-1. AFM images with indicated profiles (lower) and exemplary apparent height profiles.
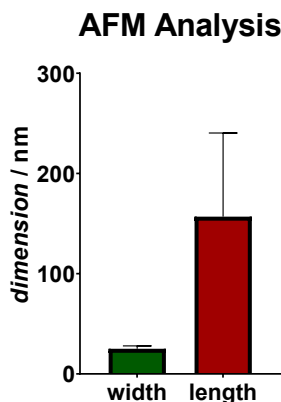
AFM Analysis

Figure S10. AFM image analysis of w-PCCPM-1. Average rod width 25 ± 3 nm (N = 27); Average rod length 157 ± 83 nm (N = 90).

Block Length Variations for Spherical PCCPMs
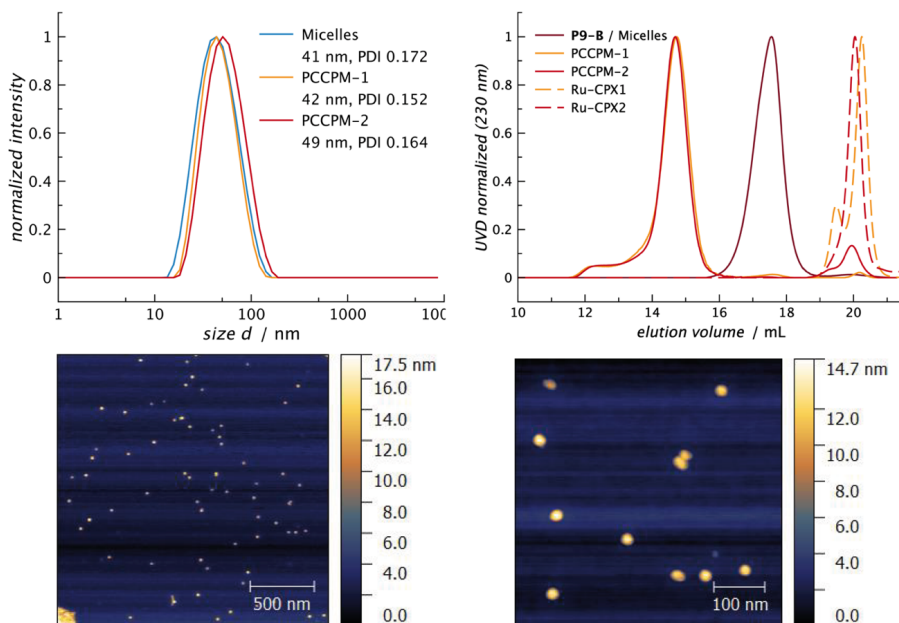
Figure S11. Spherical PCCPMs from amide-modified pSar$_{140}$-b-pGlu$_{15}$ block copolymer. Only slight bimodal GPC-trace. PCCPM-2 shows large amounts of non-covalent Ru-CPX-encapsulation, well corresponding with higher drug contents (11.84 wt.%).

Table S2. Characterization of spherical PCCPMs from pSar$_{140}$-b-pGlu(Mod)$_{15}$ (**P9-B**).

particle	Ru-CPX	D_h / nm^a	PDI^a	D_h / nm^b	Ru-CPX-content / wt.%
Micelles/P9-B	-	41	0.172	-	-
PCCPM-1/P9-B	[Ru(bpy)$_2$]$^{2+}$	42	0.152	63	3.19 ± 0.25
PCCPM-2/P9-B	[Ru(biq)$_2$]$^{2+}$	49	0.164	71	11.84 ± 0.93

^{a} determined by single-angle dynamic light scattering at an angle of 173°, ^{b} determined by multi-angle light scattering, ^{c} determined by ICP-MS.
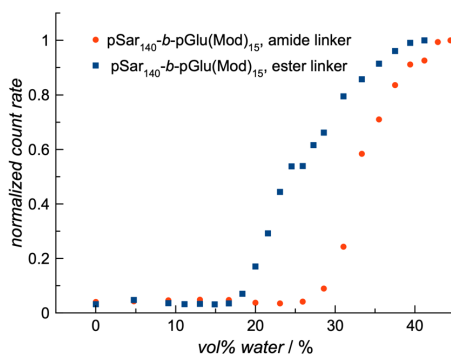
Figure S12. DLS count rate analysis accounts for aggregation of modified pSar$_{140}$-b-pGlu(Mod)$_{15}$ copolymers. Copolymers were dissolved in DMSO (5 g·L^{-1}) and water was added sequentially.

Photocleavage

UV-Vis Spectroscopy
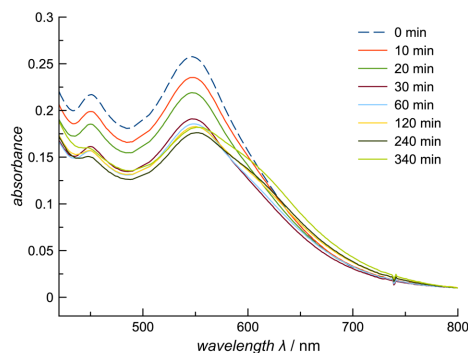
Figure S13. Photocleavage of PCCPM-2 with a red-orange LED (620 nm).

Biological Evaluation

In vitro Studies
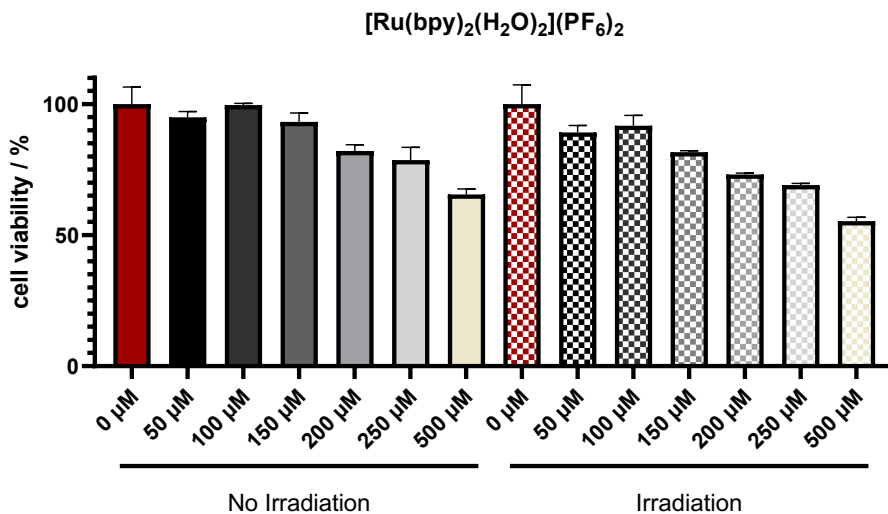
Figure S14. Viability of HuH-7 cells after incubation with Ru-CPX-1 for 24 h with or without irradiation relative to untreated control (0 µM), as analyzed by Alamar Blue Assay.

In ovo Studies
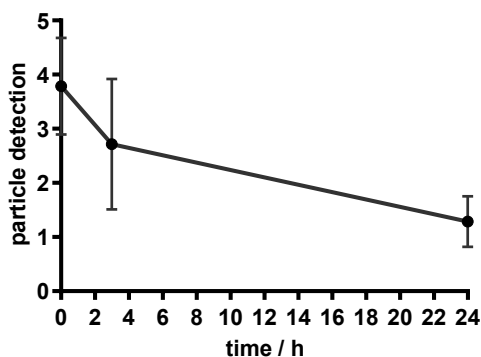
Figure S15. Analysis of intravascular circulation. After intravascular application of the sulforhodamine B labeled nanoparticles, in vivo fluorescent microscopy was performed. After blinding, video sequences were investigated repetitively three times. As the intensity of particles in the vascular system did not allow a sufficient quantitative analysis the following numerical analogue scale was applied: 5 = intravascular nanoparticles can be detected ubiquitously; 4 = intravascular nanoparticles can be detected predominantly; 3 = intravascular nanoparticles can be detected occasionally; 2 = nanoparticles can be detected; 1 = no nanoparticles can be detected. Data shown as Mean + Error.
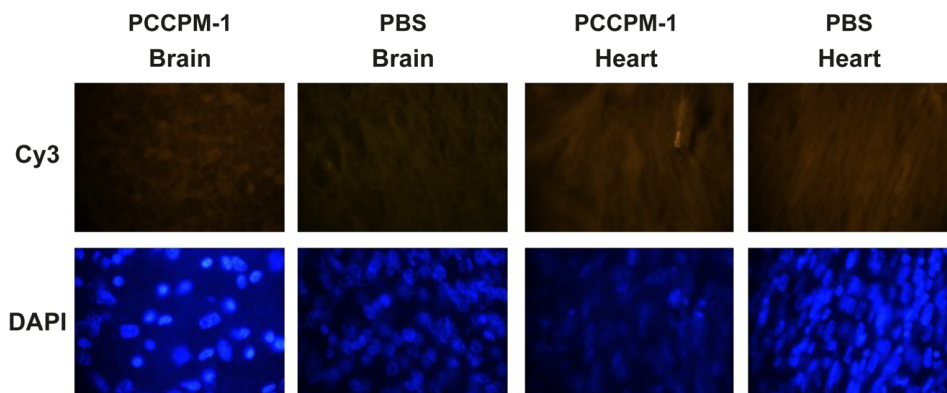
Figure S16. Representative fluorescence microscopy images of brain and heart tissue taken with the Cy3 and DAPI filter after application of sulforhodamine B labeled PCCPM or control (PBS).

References for Supporting Information

(1)   Rausch, K.; Reuter, A.; Fischer, K.; Schmidt, M. Evaluation of Nanoparticle Aggregation in Human Blood Serum. *Biomacromolecules* **2010**, *11* (11), 2836–2839.

Appendix

¹H NMR Spectroscopy
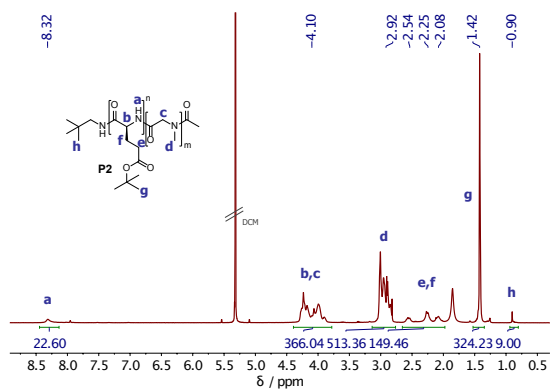
Figure S17. ¹H NMR spectrum of **P2** (pGlu(OtBu)$_{36}$-*b*-pSar$_{171}$) in CD$_2$Cl$_2$.
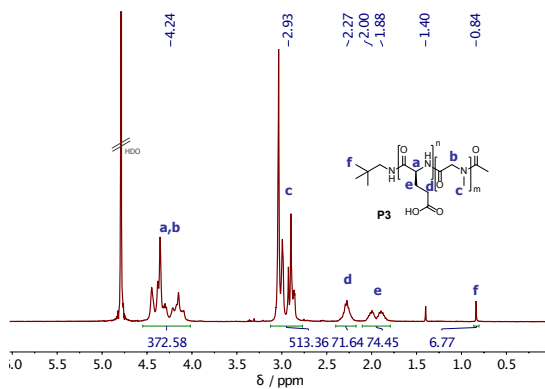
Figure S18. ¹H NMR spectrum of **P3** (pGlu(OH)$_{36}$-*b*-pSar$_{171}$) in D$_2$O.
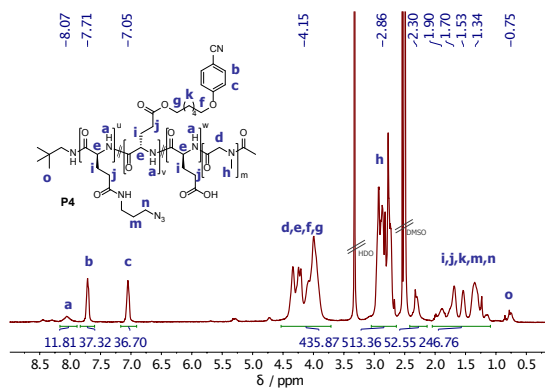
Figure S19. ^{1}H NMR spectrum of **P4** (pGlu(Mod)$_{36}$-b-pSar$_{171}$) in DMSO-d_6.
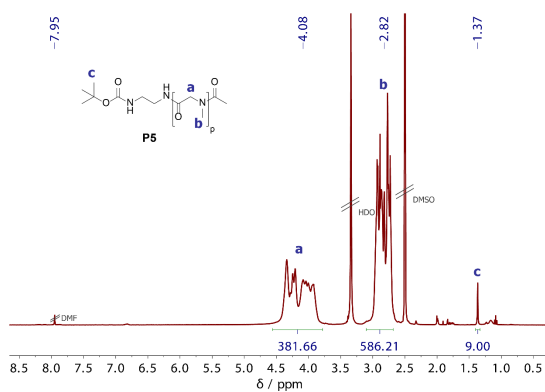
Figure S20. ^{1}H NMR spectrum of **P5** (N-Boc-pSar$_{140}$) in DMSO-d_6.
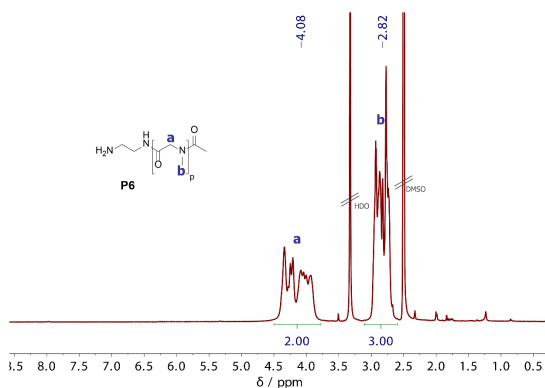
Figure S21. ^{1}H NMR spectrum of **P6** (pSar$_{140}$) in DMSO-d_6.
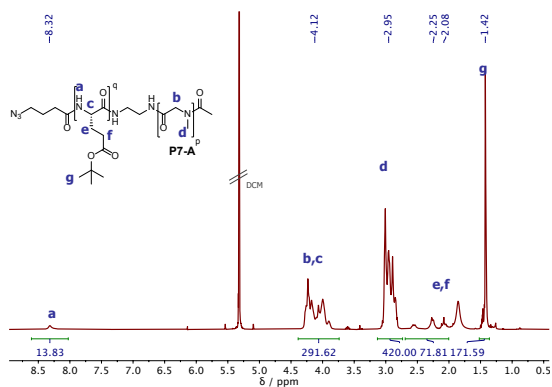
Figure S22. ^{1}H NMR spectrum of **P7-A** (pSar$_{140}$-b-pGlu(OtBu)$_{20}$) in CD$_2$Cl$_2$.
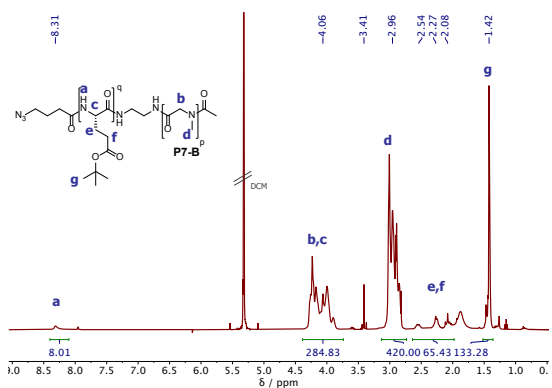
Figure S23. ^{1}H NMR spectrum of **P7-B** (pSar$_{140}$-b-pGlu(OtBu)$_{15}$) in CD$_2$Cl$_2$.
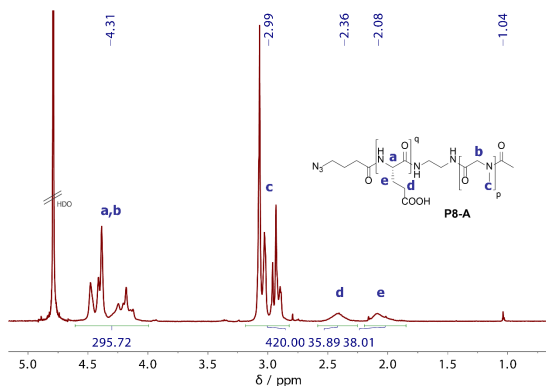
Figure S24. ^{1}H NMR spectrum of **P8-A** (pSar$_{140}$-b-pGlu(OH)$_{20}$) in D$_2$O.
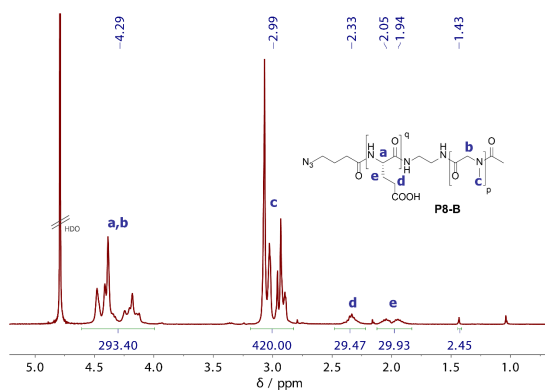
Figure S25. ^{1}H NMR spectrum of **P8-B** (pSar$_{140}$-b-pGlu(OH)$_{15}$) in D$_2$O.
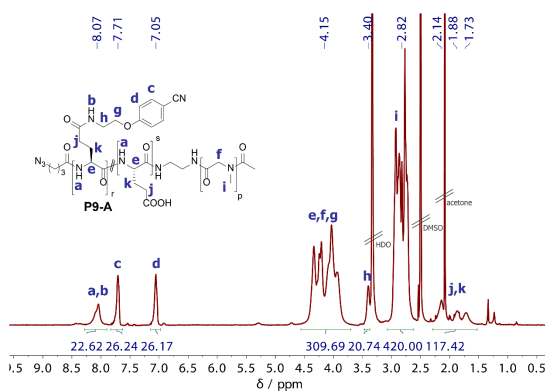
Figure S26. ^{1}H NMR spectrum of **P9-A** (pSar$_{140}$-b-pGlu(Mod)$_{20}$) in DMSO-d_6.
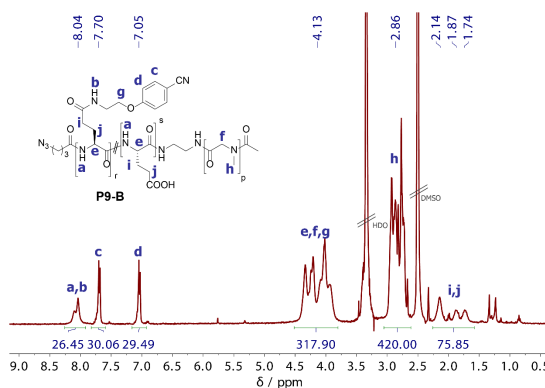
Figure S27. ^{1}H NMR spectrum of **P9-B** (pSar$_{140}$-b-pGlu(Mod)$_{15}$) in DMSO-d_6.

DOSY NMR Spectra
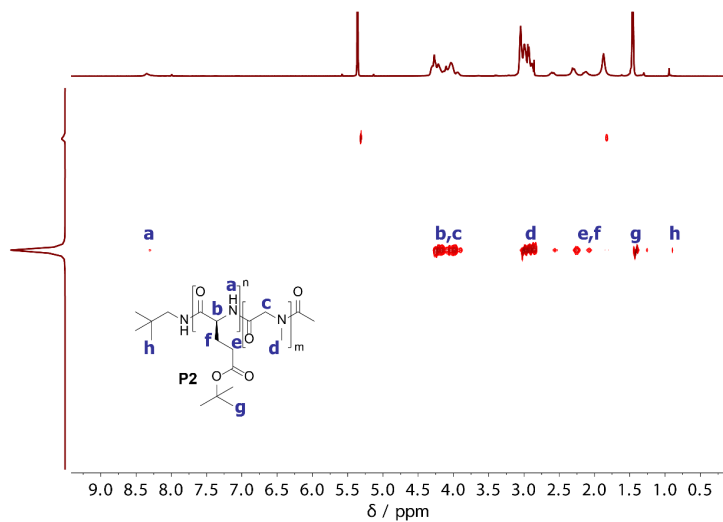
Figure S28. DOSY NMR spectrum of **P2** (pGlu(O*t*Bu)$_{36}$-*b*-pSar$_{171}$) in CD$_2$Cl$_2$.
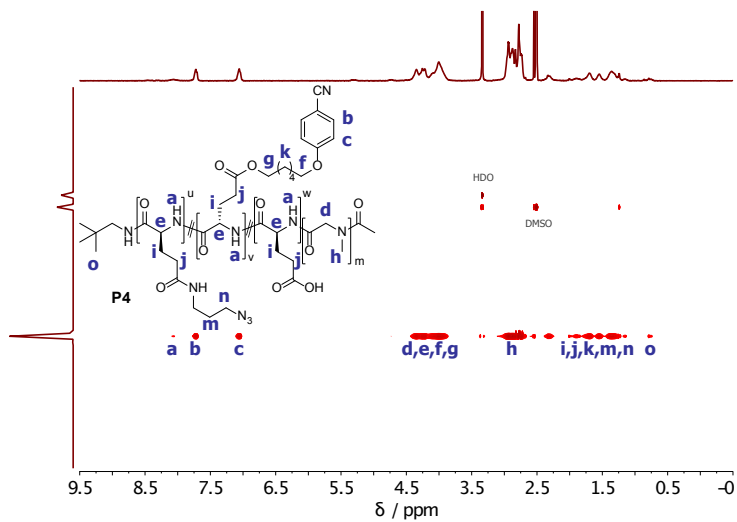
Figure S29. DOSY NMR spectrum of **P4** (pGlu(Mod)$_{36}$-*b*-pSar$_{171}$) in DMSO-*d$_6$*.
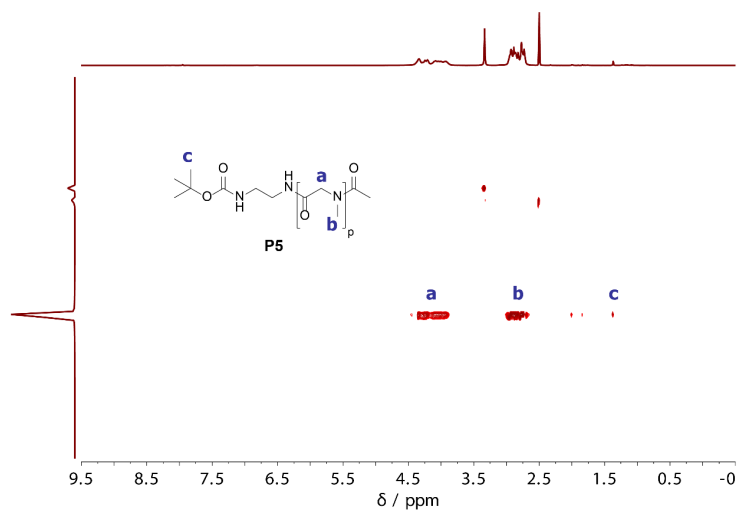
Figure S30. DOSY NMR spectrum of **P5** (*N*-Boc-pSar$_{140}$) in DMSO-*d$_6$*.
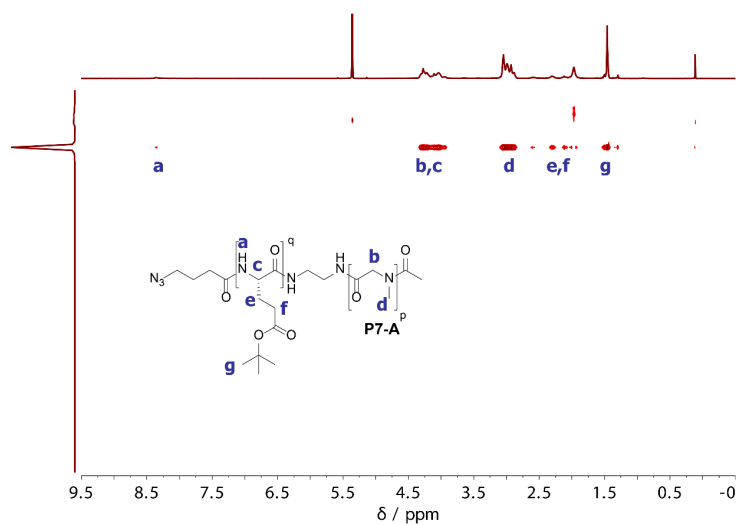
Figure S31. DOSY NMR spectrum of **P7-A** (pSar$_{140}$-*b*-pGlu(O*t*Bu)$_{20}$) in CD$_2$Cl$_2$.
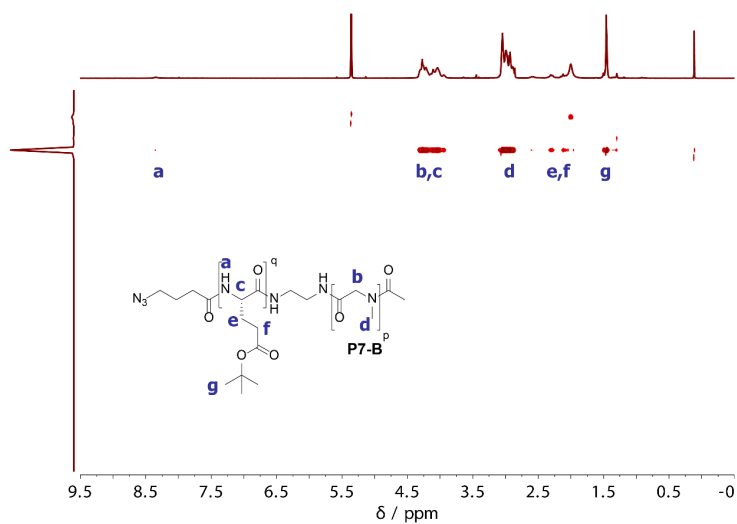
Figure S32. DOSY NMR spectrum of **P7-B** (pSar$_{140}$-b-pGlu(OtBu)$_{15}$) in CD$_2$Cl$_2$.
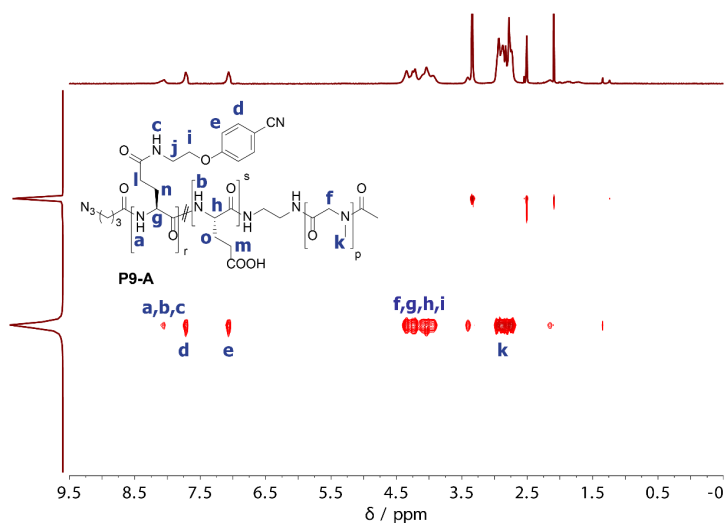
Figure S33. DOSY NMR spectrum of **P9-A** (pSar$_{140}$-b-pGlu(Mod)$_{20}$) in DMSO-d_6.

7

Targeting Cancer Chemotherapy Resistance by Precision Medicine Driven Nanoparticle-Formulated Cisplatin
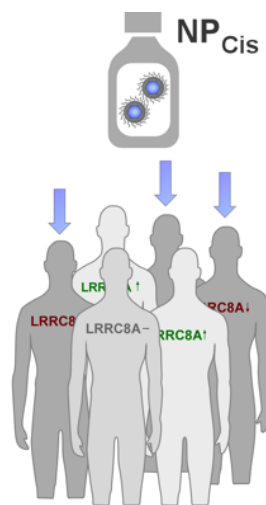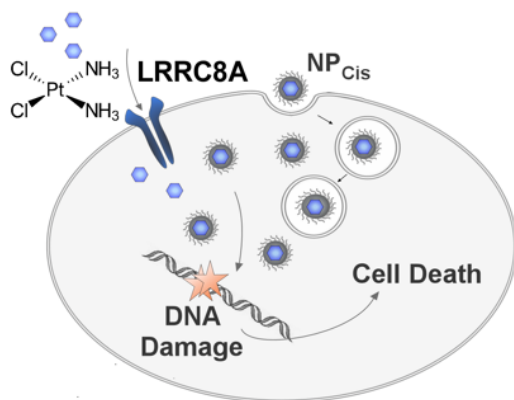
Targeting Cancer Chemotherapy Resistance by Precision Medicine Driven Nanoparticle-Formulated Cisplatin

Svenja Siemer[a], Tobias A. Bauer[b,c], Paul Scholz[d], Christina Breder[a], Federico Fenaroli[e], Gregory Harms[f], Dimo Dietrich[g], Jörn Dietrich[g], Christine Rosenauer[h], Matthias Barz[b,c], Sven Becker[i], Sebastian Strieth[g], Christoph Reinhardt[j], Torsten Fauth[d], Jan Hagemann[a], Roland H. Stauber*[,a]

[a] *Nanobiomedicine/ENT Department, University Medical Center Mainz, Langenbeckstr. 1, 55131 Mainz, Germany.*

[b] *Leiden Academic Centre for Drug Research (LACDR), Leiden University, Einsteinweg 55, 2333CC Leiden, The Netherlands.*

[c] *Department of Chemistry, Johannes Gutenberg University Mainz, Duesbergweg 10-14, 55128 Mainz, Germany.*

[d] *Department of Dermatology, University Medical Center Mainz, Langenbeckstr. 1, 55131 Mainz, Germany.*

[e] *BRAIN AG, Darmstaedter Straße 34, 64673 Zwingenberg, Germany.*

[f] *Department of Biosciences, University of Oslo, Blindernveien 31, 0371 Oslo, Norway.*

[g] *Department of Otorhinolaryngology, University Medical Center Bonn, 53127 Bonn, Germany.*

[h] *Max Planck Institute for Polymer Research, Ackermannweg 10, 55128 Mainz, Germany.*

[i] *Department of Otorhinolaryngology, University Medical Center Tuebingen, Elfriede-Aulhorn-Str. 5, 72076 Tuebingen, Germany.*

[j] *Center for Thrombosis and Hemostasis (CTH), University Medical Center Mainz, Langenbeckstr. 1, 55131 Mainz, Germany.*

Abstract

Therapy resistance is the major cause of cancer death. As patients respond heterogeneously, precision/personalized medicine needs to be considered, including the application of nanoparticles (NPs). Success of therapeutic NPs requires to first identify clinically relevant resistance mechanisms and to define key players, followed by a rational design of biocompatible NPs capable to target resistance.

Consequently, we employed a tiered experimental pipeline from *in silico* to analytical and *in vitro* to overcome cisplatin resistance. First, we generated cisplatin-resistant cancer cells and used next-generation sequencing together with CRISPR/Cas9 knock-out technology to identify the ion channel LRRC8A as a critical component for cisplatin resistance. LRRC8A's cisplatin-specificity was verified by testing free as well as nanoformulated paclitaxel or doxorubicin. The clinical relevance of LRRC8A was demonstrated by its differential expression in a cohort of 500 head and neck cancer patients, correlating with patient survival under cisplatin therapy. To overcome LRRC8A-mediated cisplatin resistance, we constructed cisplatin-loaded, polysarcosine-based core cross-linked polymeric NPs (NP$_{Cis}$, Ø~28 nm) with good colloidal stability, biocompatibility (low immunogenicity, low toxicity, prolonged *in vivo* circulation, no complement activation, no plasma protein aggregation), and low corona formation properties. 2D/3D-spheroid cell models were employed to demonstrate that in contrast to standard of care cisplatin, NP$_{Cis}$ significantly ($p<0.001$) eradicated all cisplatin-resistant cells by circumventing the LRRC8A-transport pathway *via* the endocytic delivery route.

We here identified LRRC8A as critical for cisplatin resistance and suggest LRRC8A-guided patient stratification for ongoing or prospective clinical studies assessing therapy resistance to nanoscale platinum drug nanoformulations *versus* current standard of care formulations.

Keywords

nanomedicine · cisplatin resistance · rational design · personalized medicine · polypept(o)ides

Introduction

Cancer is one of the main causes for human hospitalizations and deaths globally.[1,2] Classical cancer treatments include surgical removal, radiotherapy, and (immuno-)chemotherapy. Despite the initial treatment success of chemotherapeutics, the development of therapy-resistance over time is the main cause for deaths for all types of cancer, urging for improved strategies to overcome resistances.

The rapid progress in nanotechnology combined with our increased knowledge of the complex cross-talk at nano-bio interfaces has raised high expectations in nanomedicine to also combat cancer, including therapy resistances.[3-5] Numerous delivery and theranostic nanotools have been developed to date, often claiming to be superior to small molecule chemotherapeutics due to sustained drug release, better cancer cell uptake, enhanced permeation and retention (EPR) effect in tumors, prolonged bioavailability, and less side-effects.[6-10] Impressive developments also include the design of multifunctional nano-tools, allowing co-deliveries of drugs with siRNAs or peptides as well as the addition of active tumor cell targeting decoys, such as antibodies, aptamers or peptides onto the NPs' surfaces.[11-15] Moreover, NPs have been reported to better kill resistant cancer cells through enhanced cell internalization, stimuli-responsive drug release, inhibition of drug efflux, and more. However, postulated effects have not always been investigated sufficiently or understood mechanistically and multifunctional nano-tools have not reached the clinic yet.[16]

Though, the use of nanoscale platinum drug delivery devices (soft or hard nanoparticles, such as Lipoplatin, SPI-077 or NC-6004) as potential alternatives have entered (pre)clinical studies.[6,17-19] Among these, the small-sized polymeric micelles of NC-6004 currently exhibit the greatest potential for clinical translation (phase III). The evolution of NC-6004 from poly(asparagine) to poly(L-glutamic acid) as the functional polymer block provided stable yet reversible conjugation of cisplatin.[6,20-22] Despite these advances, the successful clinical translation of such nanomedicals, particularly of 'hard' NPs, is still limited. Notably, besides safety/toxicity considerations for the active drug, it is expected and desired that nanoencapsulation is changing the pharmacokinetics of a drug, which needs to be taken into consideration for the application.[23] Moreover, the biocompatibility of the used nanocarriers needs, including biomolecule corona formation, need to be examined as well. It is accepted that when NPs enter

(patho)physiological environments, proteins and other biomolecules rapidly bind to the nanomaterial surface, leading to the rapid formation of a biomolecule corona. The corona may be critically co-defining the biological, medical, biotechnological and pathophysiological identity of NPs, although the mechanistic details have not been resolved in detail.[24-30] As the impact of the corona can still not be predicted reliably, the design of NPs with low biomolecule adsorption properties is desirable and can be achieved by several chemical functionalization strategies.[31,32] Here, the use of polypept(o)ide-based formulations promise good colloidal stability, biocompatibility (low immunogenicity, low toxicity, prolonged *in vivo* circulation, no complement activation, no plasma protein aggregation), and low corona formation properties. Polypept(o)ides are hybrid copolymers combining polypeptides with the polypeptoid polysarcosine (pSar, poly(*N*-methyl glycine)), which is biologically well tolerated.[33,34] pSar is considered a promising alternative to poly(ethylene glycol), showing advantages of reduced proinflammatory cytokine secretion, reduced complement activation, and evasion of the accelerated blood clearance (ABC) phenomenon.[35-38]

However, despite the impressive progress on potential nanomedicals, their clinical applicability and superiority compared to drug formulations used in the clinical routine for decades needs to be based on a mechanistic understanding of their advantages.[3,5,39]

First-line chemotherapy head and neck cancers (HNSCC) is predominantly platinum-based with cisplatin being the primary option despite its drawbacks like severe nausea, dose-limiting nephrotoxicity, myelosuppressive effects, ototoxicity or peripheral neuropathy.[40-42] Differences in the toxic effects of platinum compounds are mainly due to their chemical reactivity but seems also to be influenced by the expression of organ/cell-specific drug transporter/detoxification machineries.[6,43-48]

Resistance to chemotherapeutics, such as platinum-based drugs, on the individual, organismal as well as on the cancer cell level are manifold, complex, and not yet fully understood.[6,43-45] Especially in head and neck cancers (HNSCCs) as well as in other malignancies, therapy resistant relapses are common due to molecularly highly heterogeneous cell populations[40] and associated with high patient morbidity.[49,50] Main clinically relevant effects impact the drug's intracellular concentration and induced DNA damage, ultimately triggering cancer cell death (Figure 1a).[46-48] Cisplatin-resistant cancer cells may show a wide range of responses, including decreased cellular drug uptake, increased drug

efflux, enhanced DNA repair, improved drug detoxification as well as additional prosurvival signaling pathways.[46]
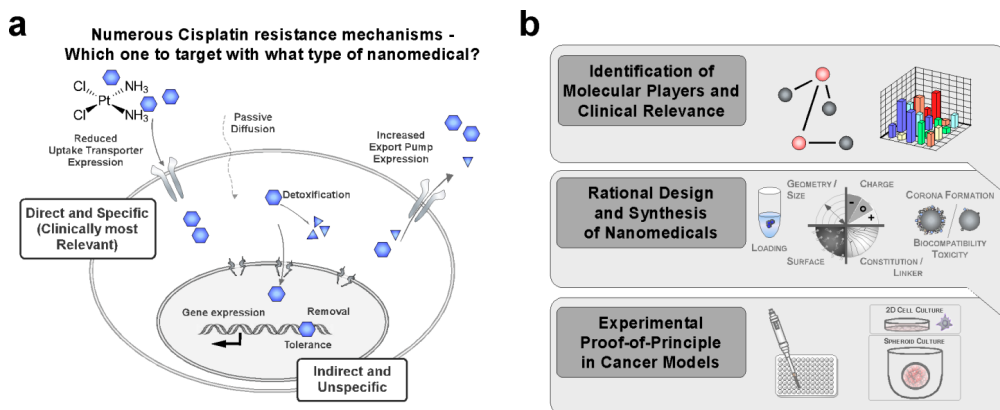
Figure 1: Summary of suggested potentially cisplatin resistance mechanisms and experimental pipeline to overcome chemoresistance. a) Illustration summarizing suggested main cellular cisplatin resistance mechanisms. Reducing the drug's intracellular concentration may result from reduced expression of drug uptake transporters, increased expression of drug efflux pumps, enhanced drug detoxification, improved DNA repair as well as additional prosurvival signaling pathways. Cisplatin and cell compartments are indicated. Not drawn to scale. **b**) Illustration summarizing the study's tiered experimental targeting strategy**.**

Adding even another level of complexity, it is accepted that depending on the type of resistance mechanism combined with their (epi)genetic fingerprints, patients may respond differently to (nano)therapeutics, necessitating precision/personalized treatments.[18,51] The field, including the FDA, thus started to move away from block-buster treatments for all patients who may not profit but rather suffer from often expensive therapeutics. Examples for such precision/personalized treatments from the current clinical routine are therapeutic antibodies for the treatment of EGFR-expressing head and neck and colorectal tumors or Her2-positive breast cancers, as well as the application of kinase inhibitors/therapeutic antibodies for *Ras*-mutated lung cancers.[52-55]

The aim of the study was to develop a nanomedical-based strategy to overcome therapy resistance as part of a potential personalized medicine approach. It is evident that the clinical need as well as success of therapeutic NPs to break chemoresistances requires to first identify clinically relevant (personalized) cancer resistance mechanisms and key players followed by a rational design and

application of targeting NPs to overcome the identified resistances (overview and experimental strategy see: Figure 1; Supplementary Figure S1).

Consequently, we here employed a tiered experimental pipeline from *in silico* to analytical and *in vitro* to overcome cisplatin resistance in head and neck cancer as a clinically relevant model. Collectively, we identified the ion channel LRRC8A as a critical component for cisplatin-specific uptake and resistance, confirmed its potential clinical relevance, and applied cisplatin-loaded NPs to kill cisplatin-resistant cells by bypassing the LRRC8A-transport pathway. The strategy and results of our study may aid the personalized application of nanomedicals to overcome chemotherapy resistance in general.

Results and Discussion

Identification of Molecular Pathways and Key Players of Cisplatin Resistance

Focusing on head and neck cancer (HNSCC) as a clinically highly relevant disease entity, we first generated cell culture models to identify molecular cisplatin resistance mechanisms, which is not trivial for an effective anticancer drug. Whereas tumors in patients contain $>10^9$ cells as a starting population to select cisplatin-resistant (stem)cell clones over months or years, *in vitro* cell cultures start with much lower cell numbers and a less heterogeneous phenotypic population. However, a homogeneous cisplatin-resistant cell line favors the identification of resistance pathways by molecular 'omics' methods. By selecting HNSCC Fadu cells with subtoxic concentrations of cisplatin (3-5 μM) for six months, we successfully established a cisplatin-resistant cell line, Fadu$_C$ (Figure 2a). Compared to the parental Fadu$_{WT}$ cells, Fadu$_C$ cells were highly resistant to cisplatin (~2 μM *versus* ≤ 20 μM) used to treat HNSCC patients in the clinical routine. Macroscopically, Fadu$_C$ did not show differences to the initial cell population (Figure 2b). Of note, the cisplatin-resistant phenotype was maintained even when Fadu$_C$ cells were cultured in the absence of cisplatin for up to one month, indicating that stable genetic alterations have occurred. This marked Fadu$_C$ cells as an ideal tool to identify HNSCC resistance mechanisms. Thus, we next performed next-generation RNA sequencing as a powerful tool to obtain genome-wide transcriptomics profiles. Although current bioinformatic algorithms seem to facilitate the comparison and (meta-)analysis of gene expression data generated by different profiling platforms from data bases, it is accepted that optimal results are obtained by using the same platform. To reduce intrinsic technical variations, generating 'data noise' and potentially occluding data

reliability, we analyzed the samples in three independent replicates in a single experiment.
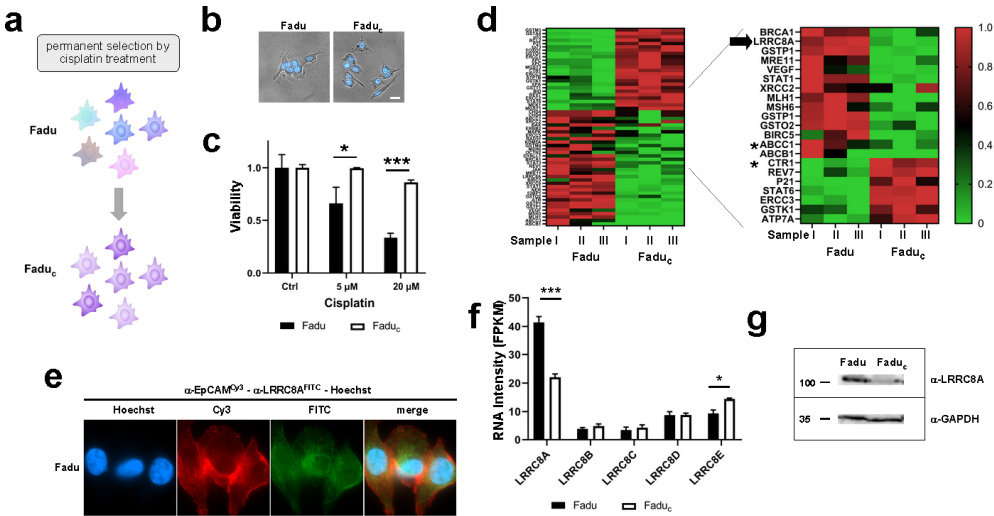
Figure 2: Identification of molecular players most relevant for cisplatin resistance. a) Illustration of selection process to establish cisplatin-resistant Faduc cells. **b**) Similar cell morphology visualized by microscopy. Nuclei stained with Hoechst dye (blue). Scale bar, 20 µm **c**) Faduc are highly cisplatin-resistant. Cells treated for 48h and viability normalized to untreated controls. **d**) RNASeq-transcriptomics to identify cisplatin resistance candidates. Heatmap analysis of FPKM values visualizing genes differentially expressed in cisplatin sensitive (Fadu) *versus* resistant (Faduc) cells (green: down-regulated, red: up-regulated; full list of genes and raw expression data: Supplementary Table S5 and S6). Potentially most relevant transporter genes LRRC8A, CTR1, and ABCC1 are marked. **e**) Immunofluorescence detection of EpCAM and LRRC8A. Cells were stained with indicated antibodies. Scale bar, 5 µm. **f**) Differential expression of LRRC8 components. LRRC8A expression was significantly reduced in cisplatin-resistant (Faduc) cells, LRRC8E slightly upregulated. RNA intensities (FPKM) in n = 3 samples shown. Statistical analysis by unpaired Student's t-test. *, p<0.05; ***, p<0.005. **g**) Immunoblot analysis confirming decreased protein levels of LRRC8A in Faduc cells. GAPDH served as loading control. Cells were stained with indicated antibodies. MW (kD) is indicated.

The comprehensive data sets were subsequently bioinformatically analyzed to identify genes differentially expressed between cisplatin sensitive and resistant cells (see Supplementary Figure S1, Supplementary Table S6). Here, genes significantly differentially expressed (p<0.05 as the cut-off) in our cisplatin resistant cell model were selected by strictly following established protocols. As

the data volume and complexity from RNA-seq experiments necessitate fast, scalable, and mathematically principled analysis, we used the approaches described in detail in the excellent works of Love *et al.* and Trapnell *et al.*, mainly using *TopHat*, *Cufflinks*, and negative binomial distribution assisted by *DESeq2* to perform such analyses.[56,57] Our protocol begins with raw sequencing reads and produces a transcriptome assembly, lists of differentially expressed and regulated genes and transcripts (see Supplementary Table S5, S7 and heatmap Fig. 2d, left). As indicated also in Supplementary Table S5, it is not uncommon to find genes with relatively small fold changes (*e.g.*, less than twofold) in expression marked as significant. This reflects the high overall sensitivity of RNA-seq compared with other whole-transcriptome expression quantification platforms. We identified potential factors involved in cisplatin resistance by transcriptomics relying on significantly differentially transcribed genes in our cell model (Fig.2; Supplementary Table S8; summarized in Supplementary Table S6-S7). Supplementary Table S7 lists the most significant genes that were up- or downregulated with their respective gene IDs and locus, absolute values, and ratios ranked by significance. Notably, the data set showed good correlation of the three independent replicates confirming the experimental quality and reliability of the data, prerequisite for their subsequent bioinformatic exploitation.

As several proteins have already been suggested to be directly or indirectly involved in influencing cisplatin resistance,[48,58,59] we additionally performed supervised analyses of such factors, supported by *Ingenuity/Reactome* pathway tools,[60] and further meta-analyses including overall survival Kaplan Meier curves of *The Cancer Genome Atlas* collective (Supplementary Figure S2-S3). Hierarchical clustering was performed on a selected subset of 58 of these candidates (Figure 2d left; Supplementary Table S5). The candidates were further condensed, based on their highest potential as relevant cisplatin resistance factors (Figure 2d, right) (Supplementary Figure S1). Besides indirect contributors such as cell signaling and/or cell cycle regulators (*e.g.*, STATs, p21) or proteins known to be involved in detoxifications processes of metal ions, such as glutathione conjugation enzymes (*e.g.,* GSTK1), also (metal) ion/small molecule uptake and export transporter (*e.g.*, CTR1, ABC/MDR, LRRC8A, MRP1)[16,61-63] were significantly differentially expressed. Notably, in contrast to other studies reporting for example enhanced expression of the (metal) ion/small molecule export transporter MRP1,[16] we found its reduced expression in the cisplatin-resistant cells. Likewise, the drug uptake transporter CTR1 was up-regulated in

the cisplatin-resistant cells, in contrast to other reports.[62] Of note, none of these studies did perform a direct genome-wide comparison of relevant resistance factors employing sensitive *vs* resistant models.

The Drug Uptake Transporter Component LRRC8A is a Critical Determinant for Cisplatin Resistance

As a strong candidate for cisplatin uptake and resistance in our data set, we further investigated LRRC8A, significantly down-regulated in all of the cisplatin-resistant cell samples. LRRC8A is the constituting member of the volume-regulated anion channel (VRAC), a heteromer constituted of six subunits, composed of LRRC8A/B/C/D and E (Figure 3a).[64,65] Its differential expression has been suggested to additionally affect various tumor cell survival pathways, including (selective) drug uptake and resistance.[61,64,65] For our HNSCC models, we confirmed LRRC8A's membranous expression and down-regulation in the resistant cell line not only at the RNA but importantly also on the protein level by immunoblot analyses (Figure 2e-g). In contrast to reduced LRRC8A levels, the other subunits were equally expressed, and we found a slight upregulation of LRRC8E (Figure 2f). Although LRRC8A is the major constituting subunit, and thus, mainly responsible for cisplatin uptake, also LRRC8D was suggested to further contribute to efficacy and specificity of drug uptake.[64-67] However, the molecular details are not fully understood and we did not detect relevant differences in LRRC8D transcription in our KO or cisplatin resistant cell lines (Supplementary Figure S6). Hence, we subsequently focused on LRRC8A.
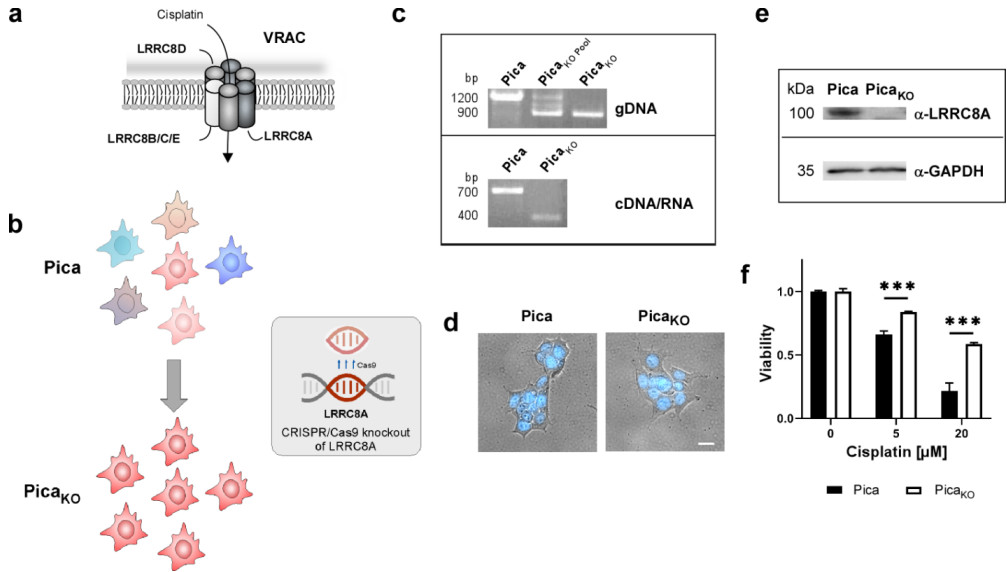
Figure 3: LRRC8A is critical for cisplatin response. a) Scheme of the VRAC channel, consisting of six heteromeric subunits. LRRC8A is critical for function, subunits LRRC8B/C/D/E suggested to further contribute to substrate specificity. **b**) Generation of LRRC8A-deficient knockout cells (Pica$_{KO}$) by CRISPR/Cas9 technology. **c**) Knockout was confirmed on the genomic DNA and RNA/cDNA level. For primer design and location see Supplementary Figure S4. **d**) Similar cell morphology of Pica and Pica$_{KO}$ visualized by microscopy. Nuclei were stained with Hoechst dye (blue). Scale bar, 20 µm. **e**) Immunoblot analysis confirming absence of LRRC8A protein in Pica$_{KO}$ cells. GAPDH served as loading control. Blots were stained with indicated antibodies. MW (kD) is indicated. **f**) LRRC8A-deficient Pica$_{KO}$ cells are highly cisplatin-resistant. Cells were treated for 48h and viability normalized to untreated controls.

To unambiguously verify LRRC8A's role in cisplatin resistance, we performed its CRISPR/Cas9 knockout (KO) in the HNSCC cell line Pica as an additional independent cell model. Underlined by the Nobel prize award to the CRISPR/Cas9 technology, this method allows to exclusively eliminate the LRRC8A protein without inducing other genetic alterations (Figure 3). For maximal comparability and genetic homogeneity, different single cell KO clones were generated and thoroughly characterized (Figure 3c-e, Supplementary Figure S4, Supplementary Table S3). Analytical PCRs on the genomic gDNA and cDNA level verified LRRC8A depletion, which was further confirmed by immunoblot analysis in the resulting cell line Pica$_{KO}$ (Figure 3c, e, Supplementary Figure S5). Importantly, LRRC8A depletion alone was sufficient to confer cisplatin resistance, underlining

its relevance as a key cisplatin resistance factor (Figure 3f). Hence, other factors suspected by previous studies do not seem to contribute significantly to resistance of our cancer models, although LRRC8A expression was not examined in these studies.[16,59,62] Also, the reported specific reduction of MRP1 expression by cisplatin-resistance-braking NPs cannot be explained mechanistically and certainly requires further detailed analysis.[16,62]

Again, the cisplatin-resistant cell line Pica$_{KO}$ was morphologically similar to the sensitive parental cell line (Figure 3c). As an additional control, we verified that the identified mechanism is specific for cisplatin. None of the cell lines showed cross-resistance to clinically employed chemotherapeutics, such as paclitaxel or doxorubicin, either when employed as a free drug or as nano-formulations, *e.g.*, Abraxane[R]/Caelyx[R] (Supplementary Figure S8, S9).

Notably, cisplatin resistance through LRRC8A depletion was confirmed not only in 2D conventional cell cultures, but also in 3D tumor spheroids, mimicking more closely the tumor micro-architecture in patients without having to rely on LRRC8A knockout animal models which show multiple physiological impacts and defects.[67] Pica$_{KO}$-derived tumor spheroids remained intact and viable even after prolonged treatment with high concentrations of cisplatin, while LRRC8A expressing wildtype cells were efficiently killed (Figure 4b, d).

The main direct cisplatin toxicity mechanism is the induction of DNA breaks, triggering apoptosis. If cisplatin uptake is reduced by low LRRC8A levels, reduced cisplatin induced DNA-damage should occur in the resistant cell lines. We therefore applied automated high content quantification as well as conventional microscopy to probe γH2AX DNA-damage foci (Figure 4a, c, Supplementary Figure S7). Indeed, reduced DNA-damage was detected, confirming our hypothesis (Figure 4a, c, Supplementary Figure S7).
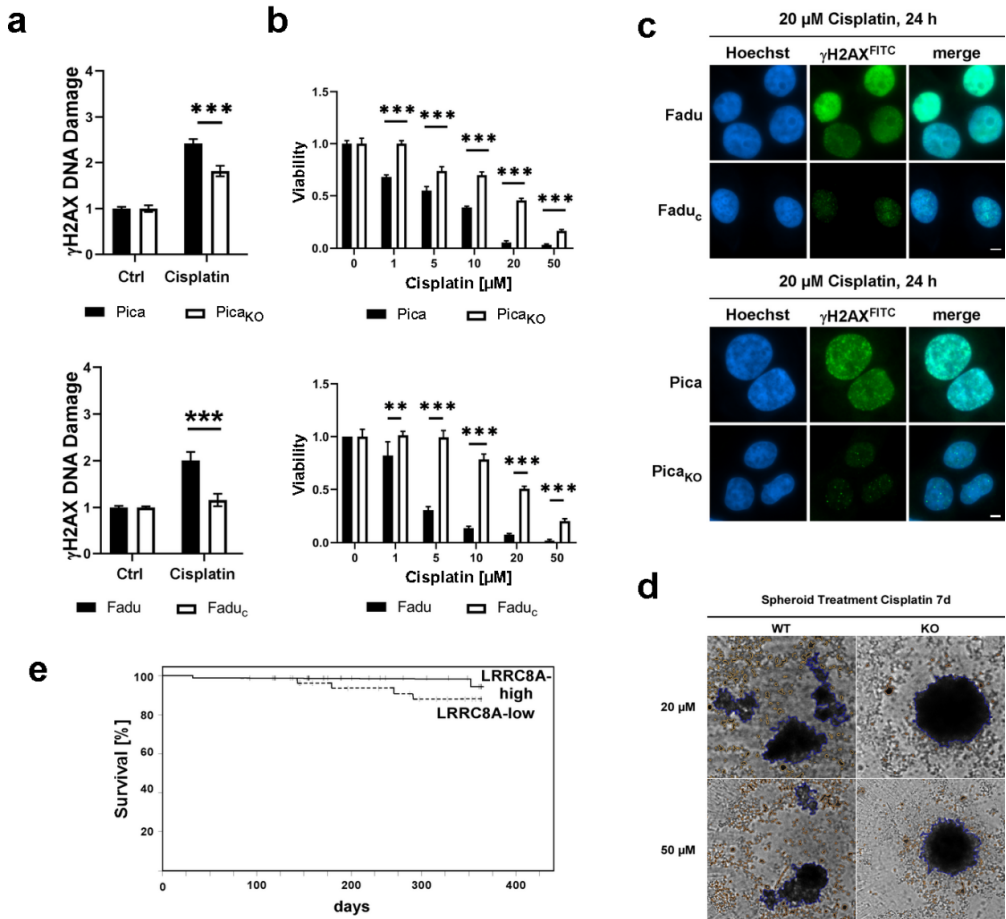
Figure 4: Low LRRC8A levels protect against cisplatin-induced DNA damage, cancer cell death, and correlate with patients' chemoresistance and survival. a-c) Reduced number of cisplatin DNA damage events (γH2AX foci) in resistant, LRRC8A low/deficient, cells. **a)** Automatic quantification of γH2AX foci *via* high-throughput automated microscopy. Cells were treated for 24h and DNA damage events normalized to untreated controls. **b)** Induction of cancer cell deaths correlates with cisplatin-induced DNA damage. Cells treated for 48 h and viability normalized to untreated controls. **c)** Detection of cisplatin-induced DNA damage events (γH2AX foci) by immunofluorescence-microscopy, 24h post-treatment. γH2AX foci were detected by specific antibodies. Scale bars, 5 μm. **d)** LRRC8A-mediated resistance is relevant also for 3D tumor-spheroids. In contrast to killed Pica$_{WT}$ spheroids, Pica$_{KO}$ spheroids stay viable even after prolonged treatment with high cisplatin concentrations. Microscopy images after treatment for 7d. **e)** Low LRRC8A expression levels, favoring resistance of tumor cells, indicate reduce survival of cisplatin treated HNSCC patients (n=78) shown by Kaplan Meier plots. p=0.26.

Collectively, we here established LRRC8A-low HNSCC cisplatin-resistant cell lines by cisplatin selection as well as by CRISPR/Cas9 knockout of LRRC8A, clearly demonstrating its key relevance for cellular cisplatin transport, cancer cell death, and thus, drug resistance.

Clinical Relevance of LRRC8A Expression Levels in HNSCC Patients

Key for the success of precision/personalized (nano)medicine is the identification of biomarkers to stratify patients who will most likely profit from treatments. For example, assessing Her2 expression in breast cancers prior to immunotherapy increased therapy success from 25 % to 70 %.[52,53] Thus, to further validate our pre-clinical findings, we examined the transcriptomics data set of HNSCC patients from The Cancer Genome Atlas (TCGA) (n=473). Interestingly, LRRC8A expression levels varied widely in tumors in contrast to healthy adjacent tissue (Supplementary Figure S10a). As LRRC8A is suspected to also support tumor cell survival pathways in addition to drug uptake,[64,65] such heterogeneity can be expected. To investigate cisplatin therapy-specific effects for patient survival, we analyzed overall survival for patients that received cisplatin (n=73). The expression data from the TCGA cohort were used to select HNSCC patients with high and low LRCC8A gene expression (Supplementary Figure S10). As cisplatin therapy acts rather rapidly, we restricted our analysis to one year. Based on our data, we hypothesized that low LRCC8A expression, *i.e.*, reduced uptake of cisplatin, favors cancer cell survival, which may lead to tumor recurrences ultimately causing patient death. Indeed, a trend in the Kaplan-Meier curve of overall survival indicates that patients with low LRCC8A expression displayed a reduced survival (p=0.26) (Figure 4e). This trend was lost when all patients were analyzed (p=0.46), suggesting that cisplatin treatment might act as selection pressure *in vivo* (Supplementary Figure S10b). Further comprehensive prospective clinical studies in various malignancies are clearly required to fully validate the prognostic value of LRCC8A expression for cisplatin therapy and the application of potentially therapeutic nanomedicals to overcome resistances in general.

Currently, there is ongoing (pre)clinical research to decide if and what types of nanoscale platinum drug delivery devices are indeed superior compared to current standard of care formulations for certain tumor types and cancer patients, including HNSCC.[6,17,18] Particularly, it would be important to guide clinical studies of therapeutic nanomedicals, such as NC-6004 (NCT: NCT00910741),[6] by

LRCC8A-based patient stratification in order to better reveal their therapeutic benefits.

Rational Design and Synthesis of NP Formulations to Overcome LRRC8A-mediated Cisplatin Resistance

Having confirmed LRRC8A-mediated resistance as well as its clinical relevance, we investigated chemical strategies to overcome cisplatin resistances. As reconstitution of the cisplatin uptake channel by small molecules or NPs is quite unlikely, we subsequently aimed at increasing intracellular cisplatin concentrations by nanoformulation-mediated endocytic uptake, thereby circumventing LRRC8A-mediated drug resistance. Consequently, cisplatin-loaded, poly-sarcosine based core cross-linked polymeric NPs (NP$_{Cis}$) were designed for cancer-targeted drug delivery. NP$_{Cis}$ were synthesized from polypept(o)ides of polysarcosine-*block*-poly(glutamic acid) (pSar-*b*-pGlu) and cisplatin was conjugated to the pGlu-block *via* ligand exchange (Figure 5a).
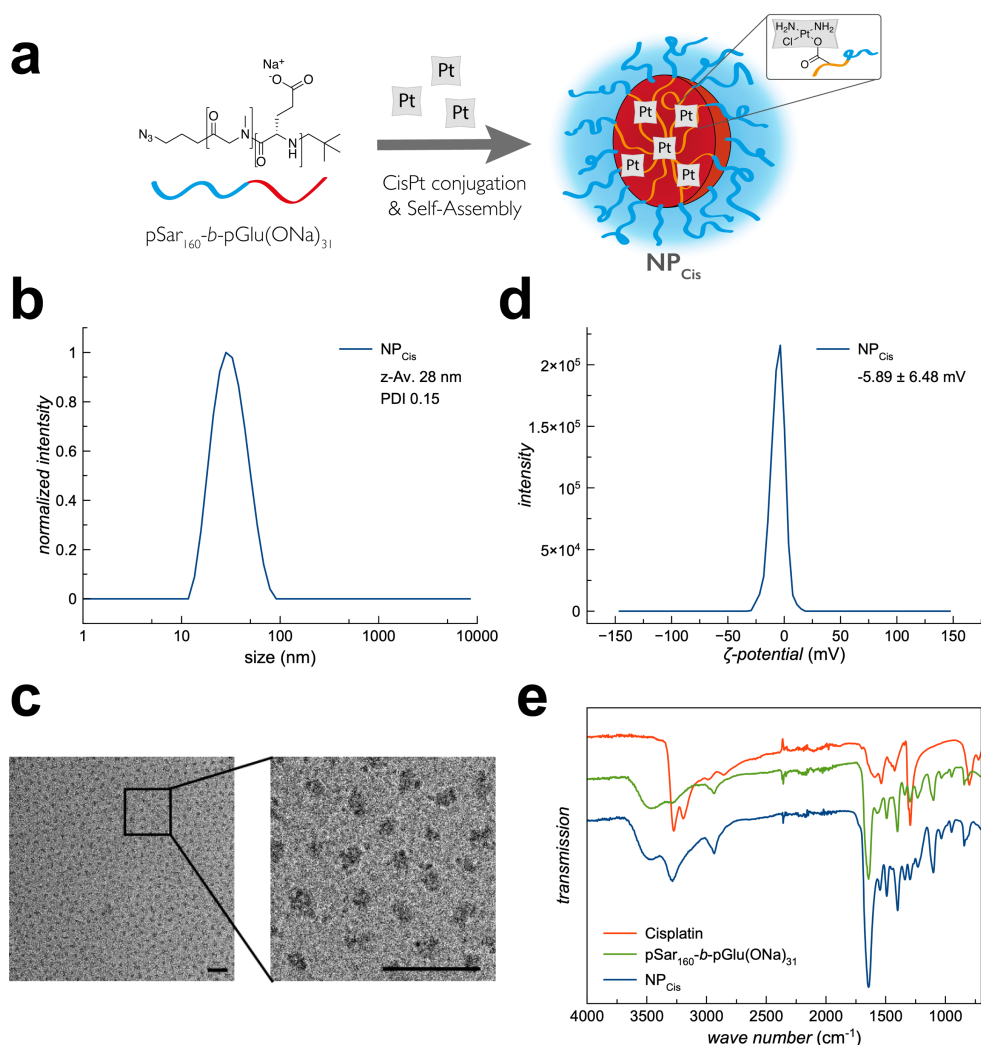
Figure 5: Design and characterization of cisplatin loaded polymeric micelles (NP_Cis). a) Illustration of polysarcosine-*block*-poly(glutamic acid) (pSar$_{160}$-*b*-pGlu(ONa)$_{31}$) building blocks, cisplatin conjugation, and expected NP$_{Cis}$ structure **b)** DLS analysis shows z-average size of Ø ~28 nm and a narrow PDI of 0.15. **c)** Cryo-EM analysis confirms shape, size, and homogeneity of NP$_{Cis}$. Scale bars, 50 nm. **d)** NP$_{Cis}$ show neutral zeta potential. **e)** FT-IR spectroscopy confirms successful coupling of cisplatin and pSar$_{160}$-*b*-pGlu(ONa)$_{31}$.

Polypept(o)ides are hybrid copolymers combining polypeptides with the polypeptoid polysarcosine (pSar, poly(N-methyl glycine)), which is biologically well tolerated.[33,34] Polysarcosine is a weak hydrogen bond acceptor and highly soluble in aqueous solution adopting a random coil conformation. As such, pSar is considered a promising alternative to poly(ethylene glycol), showing advantages of reduced proinflammatory cytokine secretion, reduced complement activation, and evasion of the accelerated blood clearance (ABC) phenomenon.[35-38] The biocompatibility and absence of detectable toxicity of pSar-b-pGlu was verified for our cell models by exposing cells for 48 h (Supplementary Figure S11). In combination with pSar, the functionality of polypeptides was further exploited for the design of core-shell architectures. The use of building blocks based on natural amino acids like glutamic acid is a promising strategy to facilitate biodegradability, which is a critical *in vivo* safety factor.[68,69] For pSar-b-pGlu(ONa), block copolymers were prepared from ɣ-*tert* butyl-L-glutamate NCA, followed by polymerization of sarcosine NCA. For the preparation of NP$_{Cis}$, block lengths of 160 for pSar and 31 for pGlu were used, accounting for steric shielding and assembly to small spherical structures (Figure 5a, c). Conjugation of cisplatin induced self-assembly of the hydrophilic pSar$_{160}$-b-pGlu(ONa)$_{31}$, yielding polymeric micelles with a diameter of Ø ~28 nm and a narrow PDI of 0.15 (Figure 5b). Our NP size was reported to be small enough to ensure bloodstream circulation while still allowing passive EPR targeting even of poorly permeable tumors, and seems optimal for endocytosis-mediated transport.[70-72] To avoid artifacts caused by the fixation procedures of conventional TEM, we used cryo-EM to confirm shape, size, and homogeneity of our NP$_{Cis}$ (Figure 5c). The neutral ξ-potential of -5.89 ± 6.48 mV accounts for the steric shielding by the pSar layer (Figure 5d). To allow dose matched treatments, cisplatin concentrations were calculated from platinum quantifications, performed by atomic absorption spectroscopy (AAS) using external platinum calibration standards. NP$_{Cis}$ showed a cisplatin concentration of 0.936 g $\cdot$L^{-1} (3.12 mM), corresponding to a drug loading of 6.8 % (w/w) at an overall yield of 47% (Supplementary Table S4). Successful coupling of cisplatin to pSar$_{160}$-b-pGlu(ONa)$_{31}$ was further verified by FT-IR spectroscopy (Figure 5e).
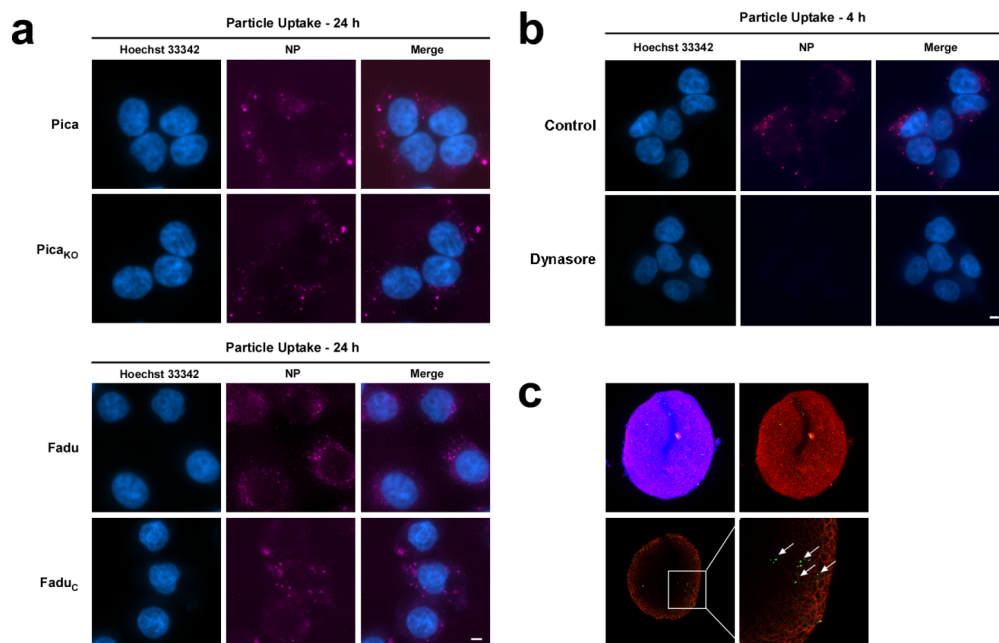
Figure 6: NP uptake does not require the LRRC8A ion channel but is mediated by endocytosis. a) Uptake of polymeric NPs (Atto647N) occurs in LRRC8A-deficient knockout (Pica$_{KO}$)/low (Fadu$_C$) and LRRC8A high WT cells (Pica)/(Fadu). Cells were treated for 24 h. Nuclei marked in blue. Scale bars, 5 µm. **b**) Uptake is prevented by treatment (10 min) with endocytosis inhibitor dynasore (40 µM). Excitation time fixed at 5000 ms for image acquisition. Scale bar, 5 µm. **c**) Two-photon microscopy shows NPs penetrating 3D tumor spheroids. Spheroids (3D) were treated with NP^{green} (6 µg·mL^{-1}, green) for 48h. Spheroids were stained for cell surface EpCAM expression (red) and nuclei (blue). Lower panel: Representative image of single z-plane. White arrows mark intraspheroid NPs.

To next investigate that our nanoformulations are capable of also entering LRRC8A-low, cisplatin-resistant cells, we additionally synthesized Atto647N fluorescently-labelled NPs (Ø ~50 nm, PDI 0.15) (Supplementary Figure S12), allowing to visualize NP trafficking by live cell microscopy (Figure 6). NP uptake in cisplatin sensitive as well as in resistant cells could be confirmed (Figure 6a, Supplementary Figure S13) and automated quantification by high content microscopy demonstrated its concentration-dependency (Supplementary Figure S14). These data indicate that resistant cells seems to be more active in endocytosis. Although our RNASeq data indicate differences in metabolic pathways, the mechanistic details need to be investigated in comprehensive

follow-up studies. Such aspects might be relevant for drug resistances in general and NP-based targeting of resistant cells. NP uptake was further blocked by the dynamin-dependent endocytosis inhibitor dynasore, confirming NPs' targeting to the endocytic, LRRC8A-independent uptake pathway (Figure 6b (Figure 6b). To verify endocytic uptake, which is expected not to be restricted to NP$_{Cis}$, we also studied fluorescent silica NPs (NP$_{Si}$, 30 nm). Here, endocytic uptake of NP$_{Si}$ was confirmed not only in 2D cell cultures (Supplementary Figure S13), but importantly also in 3D tumor spheroids, mimicking more closely the tumor micro-architecture in patients. Notably, NPs were not only observed in the spheroids' outer cell layers, but deep two-photon microscopy demonstrated that NPs could also penetrate into deeper cell layers (Figure 6c).

NP$_{Cis}$ Show Good Biocompatibility, Enhanced Blood Circulation, Low Toxicity, and Low Corona Formation

Having successfully shown the potential of NP$_{Cis}$ to enter resistant cells independent of the LRRC8A-uptake pathway, we next tested our particles for their general safety profile and biocompatibility (Figure 7). Cells treated with NP$_{Cis}$ or the parent pSar$_{160}$-b-pGlu(ONa)$_{31}$ polypept(o)ide did not show any signs of short-term toxicity triggered by the material composition (Figure 7c). In contrast, exposure to silica NPs with high corona formation properties rapidly triggered cell death at higher concentrations (Figure 7c). Moreover, NP$_{Cis}$ did not trigger human macrophage activation, as shown by assessing the induction of IL-1ß production (Figure 7a). Again, high corona formation silica NPs strongly induced IL-1ß (Figure 7a).
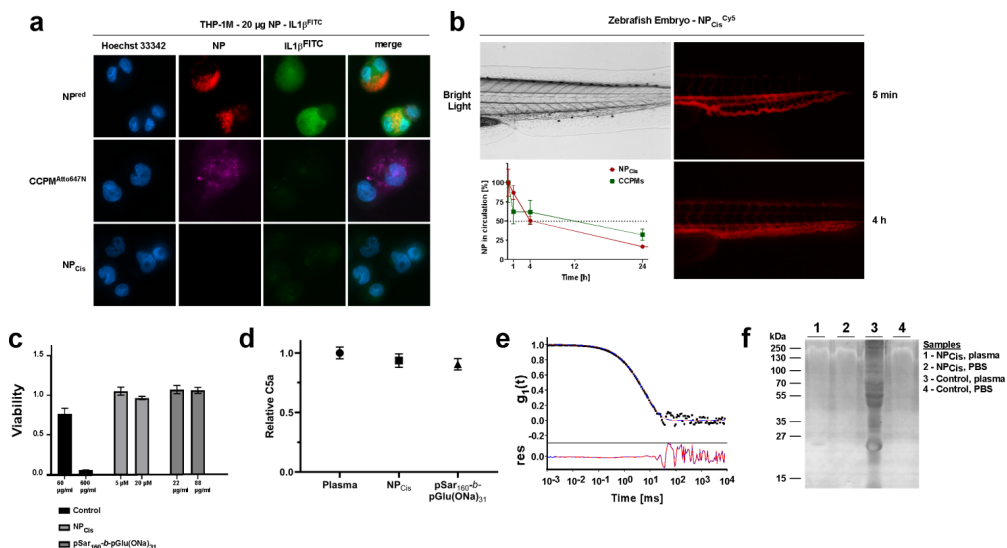
Figure 7: Cisplatin loaded polymeric micelles (NP$_{Cis}$) show good *in vitro* and *in vivo* biocompatibility and low corona formation properties. a) NP$_{Cis}$ do not trigger macrophage activation. Differentiated THP-1M macrophages do not produce IL-1ß when treated with NP$_{Cis}$ (lower panel) or unloaded fluorescent polysarcosine control particles (CCPMs; middle panel). In contrast, exposure to fluorescent silica NPs (NP^{red}) with high corona formation properties strongly induced IL-1ß production (upper panel). Cells were treated with indicated NPs (20 µg each) for 24 h before cells were fixed and immunofluorescent stained for IL-1ß (green). Cell nuclei, blue. Fluorescently labelled NPs, red. Scale bar, 5 µm. **b**) pSar NPs display reduced recognition by the reticuloendothelial system resulting in prolonged blood circulation. Fluorescently labelled NP$_{Cis}$ (NP$_{Cis}$^{Cy5}) or covalently linked polysarcosine control particles (CCPMs) were injected into zebrafish embryos and circulation analyzed by *in vivo* imaging microscopy for up to 24 h. Bright light image of a zebrafish tail containing circulating fluorescent NPs (upper left panel). Fluorescence microscopy images of a zebrafish tail containing circulating NP$_{Cis}$^{Cy5} at indicated time points (left, lower panel). Quantification of the circulation half-life for indicated NPs based on the average fluorescence intensity of the artery region normalized by the average total fluorescence of the zebrafish. Circulation half-life: NP$_{Cis}$^{Cy5} ≈ 4 h; CCPMs ≈ 12 h (lower left panel). **c**) NP$_{Cis}$ or the polysarcosine polymer show no short-term toxicity. Cells were treated for 4 h and viability normalized to untreated cells. In contrast, exposure to silica NPs (control) with high corona formation properties rapidly triggered cell death at higher concentrations. **d**) NP$_{Cis}$ do not trigger complement activation. Human plasma was untreated or exposed to NP$_{Cis}$ or the respective polysarcosine-*block*-poly(glutamic acid) polymer (37 °C, 1 h) and levels of C5a as an indicator for complement activation quantified by ELISA. **e**) NP$_{Cis}$ display good colloidal stability and do not induce

human plasma protein aggregation. Multiangle DLS measurements were performed in plasma in the presence of NP$_{Cis}$. Temperature 37 °C, t =1 h. Upper graph: Autocorrelation function $g_1(t)$ for the exemplary scattering angle of 30° together with fits without (red) and with (blue) additional aggregate term. Lower graph: Calculated residuals between the respective fit and the correlation function. **f)** Low corona formation on NP$_{Cis}$ after incubation in human plasma. NP$_{Cis}$ were incubated in indicated media for 30 min at room temperature, washed, and collected by centrifugation. Corona proteins were resolved on a 12 % SDS Page. Silica NPs (control) with high corona formation properties served as positive control.

Importantly, exposure of human blood plasma to NP$_{Cis}$ did not lead to activation of the complement system as shown by analyzing complement C5a levels (Figure 7d). In addition, we did not detect aggregation of plasma proteins demonstrated by multi-angle DLS analysis (Figure 7e). Consequently, the low toxicity profile paired with no non-specific activation of macrophages or the complement cascade confirmed the biocompatibility of NP$_{Cis}$, suggesting their potential therapeutic safety also in human settings. These findings are in line with previous reports on the biocompatibility of pSar, whereby complement activation and cytokine induction were not observed.[34,37,73]

To also investigate the NP$_{Cis}$'s potential suitability for intravenous administration, we performed biocompatibility *in vivo* studies employing the ethically less questionable zebrafish embryo model.[35,73-75] *In vivo* imaging microscopy demonstrated that pSar NPs display reduced recognition by the reticuloendothelial system (RES) allowing prolonged blood circulation (Figure 7b). Here, quantitative fluorescence analysis in zebrafish embryos revealed a circulation half-life of approx. 4 h for fluorescently labeled NP$_{Cis}$ (Figure 7b). The half-life values for NP$_{Cis}$ are lower compared to disulfide cross-linked CCPMs ($\approx$ 12 h), yet comparable to PEGylated liposomes while exceeding non-PEGylated liposomes, as reported previously.[75] Taken together, NP$_{Cis}$ seem suitable for intravenous administration, and the pSar shielding together with the stabilized core architecture provide the basis for passive tumor targeting.

When NPs enter physiological environments, proteins and other biomolecules rapidly bind to the NP surface, leading to the rapid formation of a biomolecule corona. The corona may critically codefine the biological, medical, and pathophysiological identity of NPs, although the mechanistic details have not been resolved in detail.[25-27,30,76] Hence, the design of NPs with low biomolecule adsorption properties seems to be desirable in general, unless a specific 'corona-

driven' application is envisaged. Several chemical strategies haven been reported, including our polysarcosine based approaches with the potential to prevent aggregation, protein corona formation as well as stable blood circulation after intravenous administration.[31,75] Indeed, low corona formation could be verified for NP$_{Cis}$ using human plasma as a relevant model (Figure 7e,f). Collectively, NP$_{Cis}$ are thus based on polypept(o)ides but resemble NC-6004, which is based on copolymers of PEG-*b*-pGlu(OH) and under clinical evaluation for several malignancies (NC-6004/NCT00910741).[6,48,77,78] Therefore, our approach takes profit of a clinically relevant cisplatin formulation, translates it to polypeptide(o)ides avoiding the use of PEG and combines it with aspects of personalized medicine. In addition to the improved therapeutic profile of pSar[35-38], from a synthetic perspective, the polypept(o)ide-based design offers the potential to synthesize the polymeric material by sequential monomer addition using living ring-opening *N*-carboxyanhydride (NCA) polymerization.[33,69,79] This technique may facilitate the industrial scale-up of the block copolymer synthesis. Moreover, NCA polymerization provides easy access to functional end-groups that could be used to introduce targeting moieties, such as antibodies, Fab-fragments, or peptides to enhance or specify the cellular uptake.[21,33,79,80]

Although our findings are most likely of general relevance for other platinum drug nanoformulations, we though wish to emphasize that that we do not claim that our nanoscale cisplatin drug delivery devices are superior to other nanoformulations already in clinical trials, such as NC-6004/NCT00910741. Here, additional (pre)clinical evaluation studies are required.

Application of NP$_{Cis}$ to Break Cisplatin Resistance

Next, we evaluated the potential of our NP$_{Cis}$ to overcome cisplatin resistance. A key issue, which has been neglected in most studies, is the problem of comparing 'free' drug *versus* NP-based delivered drug concentrations, particularly if these agents enter cells *via* completely different pathways. Here, not only uptake kinetics but also drug-release from NPs and organelles will significantly affect the relevant intracellular biologically active dose (BAD), ultimately triggering effects, such as tumor cell death. Hence, BAD for 1 μM of a free *versus* 1 μM of a NP-complexed drug will most certainly never be the same.

Consequently, we developed an assay allowing to determine BAD for our agents, by analyzing the levels of DNA-damage induced by free cisplatin *versus* NP$_{Cis}$. As shown in Figure 8a, about three-fold more NP$_{Cis}$ induced the same levels of DNA-

damage compared to free cisplatin in wildtype cells (BAD: free cisplatin=1/3 NP$_{Cis}$). Taking into account the different entry pathways together with the drug-release from NPs and endosomes, such values are expected and relevant for subsequent biological testing, though not reported so far. Thus, we strongly suggest to employ our strategy for studies of other nanoformulated DNA-damaging chemotherapeutics in general.

Importantly, in contrast to free cisplatin as the current standard of care, NP$_{Cis}$ were able to significantly ($p<0.005$) kill all cisplatin-resistant cells (Figure 8b) by circumventing the LRRC8A-transport pathway and instead exploiting the endocytic delivery route. Again, cytotoxicity correlated well with the induction of DNA-damage, revealed by our objective, automated γH2AX assay (Supplementary Figure S15). As expected from NP$_{Cis}$'s low corona formation properties (7f), cancer cell killing was similar in the absence or presence of biomolecules. In contrast, the cytotoxicity of silica NPs, showing high protein adsorption, was strongly affected by corona formation (Supplementary Figures S16 and S17).
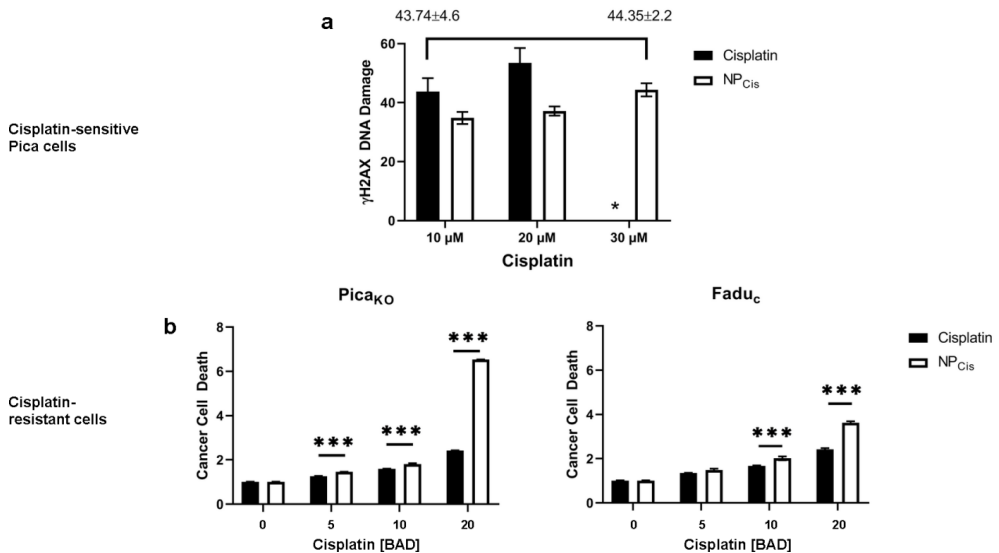
Figure 8: NP$_{Cis}$-treatment can overcome cisplatin resistance. **a**) Quantifying cisplatin-induced DNA-damage to determine the biologically active dose (BAD) of NP$_{Cis}$ *versus* free cisplatin in sensitive Pica cells. Cells were treated for 24 h and DNA damage events (γH2AX foci) quantified *via* high-throughput automated microscopy. Similar DNA-damage was induced by standard of care cisplatin (10 μM) or NP$_{Cis}$ (30 μM). *****, cells were killed prior to analysis. **b**) NP$_{Cis}$ significantly kill cisplatin-resistant HNSCC cells

(Pica$_{KO}$/Fadu$_C$). Cells were treated for 48h and death normalized to untreated controls. BAD values (μM; free cisplatin=1/3 NP$_{Cis}$). Statistical analysis: ***, p<0.005.

Of note, a variety of other (multifunctional) nanoscale platinum drug delivery devices have been developed.[6,17,18] Although we did not test other nanoformulations experimentally, it is expected that they may also be useful to eradicate LRRC8A-based cisplatin-resistant cells, although their cellular uptake and biocompatibility need to be examined. Likewise, multifunctional nano-tools, allowing co-deliveries of drugs with siRNAs for specific gene silencing, have been designed in the past, as an approach to increase the power of nanoformulations by targeting proteins which contribute to cisplatin resistance due to their overexpression.[11-15] We though demonstrated that low LRRC8A levels are key for cisplatin resistance and thus, codelivery of LRRC8A gene silencing siRNA would rather increase instead of breaking resistance, and thus, seems not applicable for our target.

Conclusion

Despite the current enthusiasm on multi-functional or theranostic nanomedicals, their clinical applicability and superiority compared to drug formulations used in the clinical routine for decades needs to be based on a mechanistic understanding of their advantages. As the field moves away from block-buster treatments of all patients, the need for precision medicine is now accepted and must also to be considered in nanomedicine. We here employed a comprehensive *in silico*, analytical, and *in vitro* experimental pipeline to identify down-regulation of LRRC8A-driven cisplatin uptake as key for cisplatin resistance of HNSCC tumor cells. Likewise, reduced LRRC8A levels seem to be relevant for therapy resistance and survival of HNSCC cancer patients. [6] To overcome cisplatin resistance, highly biocompatible cisplatin-loaded NPs were constructed, allowing drug delivery *via* the endocytic, LRRC8A-independent, uptake pathway. In direct comparison to cisplatin as the current standard of care, our strategy finally succeeded in killing all cisplatin-resistant cells.

There is ongoing (pre)clinical research to determine if nanoscale platinum drug delivery devices are indeed superior compared to current standard of care formulations in general. Here, an important criteria is the definition and comparison of a biologically active dose (BAD) for nanoparticles *versus* free drugs that enter cells by different mechanisms, as shown here. Our findings strongly suggest that LRRC8A-low expressing patients should profit most from such

platinum nanomedicals. Our findings are most likely of general relevance for other platinum drug nanoformulations. Here, LRRC8A-guided patient stratification is expected to facilitate the evaluation of such clinical trials (such as NC-6004/NCT00910741, driven by the Kataoka group), and thus, may promote the clinical translation of nanomedicals to overcome chemotherapy resistance (TOC figure).

Experimental

Chemicals and Reagents. If not stated otherwise, chemicals were sourced from Sigma Aldrich/Merck. Cell culture reagents were sourced from Gibco/Thermo Fisher Scientifc. Cell Viability Kits (Cell Titer Glo and Cell Titer Glo 3D) were purchased from Promega. Fluorescent silica NPs were obtained from Kisker Biotech or MSC UG&CoKG. Antibodies were sourced as indicated in Supplementary Table S1. Clinical cisplatin formulations were sourced from Accord Healthcare GmbH.

Nanoparticle Synthesis and Characterization. The preparation of cisplatin NPs (NP$_{Cis}$) was adapted from literature and modified by the use of polypept(o)ides of polysacrosine-*block*-poly(L-glutamic acid) (pSar-*b*-pGlu).[69,78,79] For dye-labeled NP$_{Cis}$ cyanine5-amine (1.36 mg, 2.1 µmol, 0.3 eq.) was coupled to pSar-*b*-pGlu (110 mg, 6.9 µmol, 1.0 eq.) *via* 4-(4,6-dimethoxy-1,3,5-triazin-2-yl)-4-methylmorpholinium chloride (DMTMM·Cl) (1.91 mg, 6.9 µmol, 1.0 eq.). All reagents were dissolved in water and stirred at room temperature for 72 h. Purification was performed by dialysis (MWCO 3.5 kDa) with water (+ 1% NaHCO$_3$) and pure water, followed by precipitation in acetone (4500 rpm, 5 min, 4 °C). The product was dried *in vacuo* (91.1 mg, 82%), and the absence of unconjugated dye was verified by HFIP-GPC. The synthesis of pSar-*b*-pGlu was performed as described previously in Steinborn *et al.*[70] Similarly, block lengths of 160 for pSar and 31 for pGlu were used for NP$_{Cis}$ formation. For preparation of NP$_{Cis}$, 64.5 mg (4.06 µmol, 1.0 eq.) of pSar$_{160}$-*b*-pGlu$_{31}$ were dissolved in MilliQ water at a concentration of 2.65 g·L^{-1}, corresponding to a pGlu concentration of 5 mmol L^{-1}. After 1 h, a solution of cisplatin (36.5 mg, 121 µmol, 1.0 eq. per Glu) in MilliQ water was added, and the reaction mixture was placed in a benchtop shaker at 25°C. After 7 days, the solution was purified from not conjugated cisplatin by spin-filtration (Amicon Ultra 15, MWCO 100 kDa, 3000 rpm) followed by sterile filtration (Millex GPX 220 nm). The total mass concentration was determined by lyophilization, and platinum quantification was performed by

atomic absorption spectroscopy (AAS) using external platinum calibration standards.

To serve as control nanoparticles, core cross-linked polymeric micelles (CCPMs) were prepared from polypept(o)ides of polysarcosine-*block*-poly(*S*-ethylsulfonyl-L-cysteine) (pSar-*b*-pCys(SO$_2$Et)) according to previous reports.[20,21,75] These NPs are covalently labelled with Atto647N and stabilized by disulfide bonds formed from the reactive pCys(SO$_2$Et) block and a lipoic acid-based cross-linker. Here, pSar$_{225}$-*b*-pCys(SO$_2$Et)$_{31}$ was dissolved in dimethyl sulfoxide (DMSO) equipped with 1 M thiourea at a concentration of 7.5 gL^{-1} for 1 h. Next, 20 vol.% of 1 mM acetate buffer (pH 4.75) with 10 mM thiourea were added to adjust the concentration to 6.6 g·L^{-1}. The solution was left to equilibrate at room temperature for 5 h, followed by dialysis (MWCO 3.5 kDa) against 1 mM acetate buffer (pH 4.75) with 10 mM thiourea. The solution was filtered (GHP 450) and concentrated to 6.6 gL^{-1} by spin filtration (Amicon Ultra, MWCO 3 kDa). For cross-linking, in a separate flask, the liponamide cross-linker was dissolved in ethanol at a concentration of ß = 10 g·L^{-1} and one equivalent of an aqueous solution of tris(2-carboxyethyl)phosphine hydrochloride (TCEP·HCl) (50 g·L^{-1}) was added. After 18 h, the cross-linker solution was added to the micelle solution at equimolar amounts of thiols per cysteines. After reaction for 48 h at room temperature, unreacted polymer and cross-linker were removed by dialysis against DMSO and MilliQ water (MWCO 6-8 kDa). For labelling, 0.3 equivalents of Atto647 NHS-ester were added per polymer end-group at pH 7.4 (adjusted with 1 M NaHCO$_3$ solution). After 72 h, excess dye was removed by repetitive spin filtration (Amicon Ultra, 100 kDa) using ethanol/water mixtures. The final particle solution (in MilliQ water) was stored at 4°C in the dark. The absence of free polymer and free dye was verified by gel permeation chromatography in hexafluoro isopropanol.

Atom Absorption Spectroscopy Measurements. The atom absorption spectroscopy (AAS) measurements were conducted using a Perkin Elmer 5100 ZL AA spectrometer with a Zeeman Furnace Module and a Pt hollow cathode lamp at 265.9 nm and air/acetylene mixture.

Dynamic Light Scattering and Zeta Potential Measurements. Single-angle dynamic light scattering (DLS) measurements were performed with a ZetaSizer Nano ZS instrument (Malvern Instruments Ltd., Worcestershire, UK) equipped with a He-Ne laser (λ = 632.8 nm) as the incident beam. All measurements were performed at 25 °C and a detection angle of 173° unless stated otherwise. Disposable

polystyrene or PMMA cuvettes (VWR, Darmstadt, Germany) were used for single-angle DLS measurements. Cumulant size, polydispersity index (PDI), and size distribution (intensity weighted) histograms were calculated based on the autocorrelation function of the samples, with automated position and attenuator adjustment at multiple scans. Zeta potential measurements were performed with folded capillary cells (DTS 1061) in aqueous solution containing 3 mM sodium chloride.

Multi-Angle Dynamic Light Scattering. For multi-angle DLS cylindrical quartz cuvettes (Hellma, Mühlheim, Germany) were cleaned with dust-free distilled acetone and handled in a dust-free flow box. Dynamic light scattering measurements were performed on an ALV spectrometer (ALV-5004, multiple-τ full digital correlator, He-Ne laser (632.8 nm)). To investigate the aggregation behavior of the particles in human plasma, undiluted citrate plasma and the particle solutions were filtered by syringe filters (Millex GS 0.2 µm). The following mixtures were prepared from the particle solutions in water (ß = 5.0 g·L^{-1}): PBS/particle solution 4:1 (ß = 1.0 g·L^{-1}), and plasma/particle solution 4:1 (ß = 1.0 g·L^{-1}). The cuvettes were incubated for 60 min at 37 °C before measurement at T = 37 °C. The data were analyzed according to the procedure reported by Rausch *et al.*[81] The correlation functions of the plasma measurements were fitted with a triexponential decay function, and the particles were fitted using a sum of two exponentials. The mixtures were fitted by using a sum of both exponential decay functions with or without additional aggregate term.

Infrared Spectroscopy. Attenuated total reflection (ATR) Fourier-transformed infrared (FT-IR) spectroscopy was performed on a Jasco FT-IR 4600 spectrometer with a Jasco ATR Pro ONE unit. Lyophilized solids were measured, and spectra were analyzed by Spectra Manager 2.15.18 (Jasco).

Cryo EM. NP$_{Cis}$ (3.5 µL, 150 mg·L^{-1} total solid concentration) were applied to freshly glow discharged Quantifoil® holey carbon films (R2/1 Cu 200, Quantifoil Micro Tools GmbH) and the grids were blotted for 2.5 s at 100% humidity in a Vitrobot plunge-freezer (FEI Vitrobot Mark III, Thermo Fisher Scientific). Cryo-EM images were recorded on a Talos L120C transmission electron microscope (Thermo Fisher Scientific) operating at 120 kV. The images were recorded at 13'500, 36'000, and 73'000-fold magnification.

Cell Culture. Pica cell line was established as is described in Mack *et al.*[82] Fadu and THP-1 cell lines were purchased form ATCC (ATCC®-HTB43, ATCC®-TIB-

202). Cell lines were cultured under standard cell culture conditions in their respective media (37 °C, 5 % CO_2) and subcultured every 3-5 d. Cells were checked for absence of mycoplasmas using the commercial Venor GeM Advance detection kit (Minerva biolabs) according to manufacturer's instructions. Cells were counted using a Casy Cell Counter and Analyzer TT (Innovatis). For spheroid culture, cells were seeded at a density of 1,000 cells per well in round-bottom ultra low-attachment cell culture plates (96-well, Corning) and used 3 d after seeding. THP-1 cells were differentiated into THP-1M cells at a concentration of $0.5x10^6$ cells/mL and 50 ng $\cdot$mL^{-1} PMA overnight, then washed with medium twice and used for experiments 48 h post-differentiation.

Generation of the Conditioned Sub-Cell Lines. For the generation of conditioned sub-cell line Fadu$_C$, cells were first selected by treatment with high doses of cisplatin corresponding to roughly IC90 (5 µM). After the cell line showed constant proliferation under this selection, cells were routinely kept in medium containing cisplatin (3 µM). First experiments were started 6 months after constant conditioning in cisplatin-containing medium.

CRISPR/Cas9 Knockout. PiCa-LRRC8A-/- knockout cells were generated by using the recently described CRISPR/Cas9 tools[83] with the exception that plasmids instead of adenoviruses were used for the delivery of Cas9/sgRNA gene expression cassettes. Plasmids pBbsI-Cas9-OFP-sgLRRC8#1 and pBbsI-Cas9-OFP-sgLRRC8#2 contain the CMV promoter driven gene expression cassette encoding for *Streptococcus pyogenes* Cas9 nuclease, fused to nuclear-localization sequences, followed by a T2A-linker and orange fluorescent protein OFP. In addition, *LRRC8A*-targeting single-guide RNAs (guide sequences sgRNA-LRRC8A_fw and sgRNA-LRRC8A_rev see Supplementary Table S2) are under the control of the human U6 promoter. PiCa cells were transfected with total 2 µg plasmid DNA and 5 µl Lipofectamine 2000 reagent using OptiMEM cell culture medium (Gibco) according to manufacturer's instructions (Invitrogen/ThermoFisher). To eliminate non-transfected and non-edited wildtype cells, the transfected cell pool was transferred from 6-well plates to 10 cm dishes 96 h after transfection and 24 h later treated with 2 µg/ml Blasticidin S Hydrochlorid (Fisher Bioreagent) for 9 d. Since LRRC8 ion channel is responsible for Blasticidin uptake,[84] wildtype cells and non-edited cells (which express functional LRRC8) will not survive Blasticidin treatment whereas successfully edited *LRRC8*$^{-/-}$ cells do not express functional LRRC8 ion channels and will therefore survive Blasticidin treatment. From the surviving cell pool clonal single cell-derived cell lines were generated

and successful *LRRC8* gene disruption was confirmed by PCR and subsequent Sanger sequencing. Absence of LRRC8A protein was determined by Western blot analysis.

Single Cell Clone Generation and Characterization. For the generation of single cell-derived cell lines, cells were seeded in round cell culture dishes (≙ 10 cm) at serial dilutions. Dishes were checked for absence of cell clusters and incubated for 7-10 d. Sterile filter papers were soaked in Trypsin/EDTA before being placed on resulting cell clusters with a minimum distance of about 2 cm. After incubation (5 min, 37 °C) filter papers and any attached cells were transferred to a 24-well cell culture plate with fresh medium and the plate incubated for another 7-10 days. Samples which showed successful proliferation after this period were used to isolate gDNA (DNeasy Blood & Tissue Kit, Qiagen) and checked by PCR for the correct band lengths. Further analysis was performed after isolation of RNA (RNeasy Mini Kit, Qiagen) and subsequent transcription to cDNA (Transcriptor First Strand cDNA Synthesis Kit, Roche). All isolation and transcription steps were performed according to manufacturer's instructions. DNA and RNA concentrations were measured on a Nanodrop. PCR analysis was performed on a thermocycler with Taq Polymerase according to manufacturer's instructions. For primer design see Supplementary Figure S4.[28,85]

Cell Viability Measurement. Cell Viability measurements were performed on a Tecan Spark® (Tecan) using the kits CellTiter-Glo® 2.0 Viability Assay and CellTiter-Glo® 3D Viability Assay according to the manufacturer's instructions. Viability was normalized to control samples incubated under the same conditions. For two-dimensional assays, cells were treated 24 h after seeding in fresh medium containing the respective substances. Viability was assessed 48 h after treatment. For three-dimensional assays, cells were treated 3 d after seeding, after spheroid formation. Half of the culture medium was replaced with fresh medium containing 2x of the target concentration of each substance. After 48 h, another medium change of half the samples volume was performed. The fresh medium contained 1 x of the target concentration of each substance. Viability assessment was performed 96 h after initial treatment.

γH2AX-Assay. Cells were counted and seeded in controlled densities (10,000 cells/well) in clear-bottom 96well plates (Greiner). Immunofluorescence staining of γH2AX was performed after treatment with cisplatin in the given concentrations for 24 h. The cells were then fixed with 4 % PFA (20 min, RT) and

permeabilized with 0.1 % Triton-X 100/PBS (10 min, RT). The primary antibody α-γH2AX (rabbit, A300-081A, bethyl) was diluted 2000-fold in 10 % FCS/PBS and the cells stained for 1 h at room temperature. After extensive washing with PBS, Cy3-labelled α-rabbit-antibody was diluted 300-fold in 10% FCS/PBS and incubated with the samples for 1 h at room temperature. The nuclei were stained by addition of Hoechst 33342 (50 ng $\cdot$mL^{-1}) in PBS for 30 min at room temperature after another washing step. The fluorescence signal was quantified on the automated high-content microscopy platform ArrayScan VTI (Thermo Fisher), using the TargetActivation assay at fixed excitation times. The region of interest was defined by the nucleus stain. Each sample was measured in triplicates with at least 5,000 cell nuclei analyzed per well. For further information on antibodies and dilutions, see Supplementary Table S1.

Fluorescence Microscopy. Fluorescence microscopy was performed on a Axiovert 200 M fluorescence microscope (Zeiss) on cells seeded in 35 mm microscopy dishes (MatTek). Depending on further use, cells were either imaged live or fixed with PFA (4 %, 20 min room temperature (RT)). Before immunofluorescence staining, cells were permeabilized with Triton X-100 (0.1 %, 10 min RT). Antibody staining was performed as described for γH2AX-staining. Hoechst 33342 (50 ng $\cdot$mL^{-1}) was used for the staining of nuclei (30 min RT). For further information on antibodies and dilutions, see Supplementary Table S1.

Two-photon Excitation Microscopy. Two-photon excitation (2PE) microscopy was performed to visualize intact spheroids on a Leica TCS SP8 DIVE System (Leica). Image analysis was performed with Leica image suite and imageJ. To this means, spheroids were collected 3 d after seeding by gentle centrifugation (100 g, 3 min) and fixed by incubation with 4 % PFA at RT (20 min). Cells were then blocked and permeabilized in BSA/PBSTD (PBS, 0.3% Triton X-100, 1 % DMSO, 1 % BSA). Incubation with the primary antibody, diluted in 5 % FCS/PBSTD (PBS, 0.3% Triton X-100, 1 % DMSO) was performed over night at 4 °C. The secondary antibody, diluted in 5 % FCS/PBSTD, was incubated with the sample for 3 h at room temperature. Nuclei were stained by addition of Hoechst 33342 (50 ng $\cdot$mL^{-1}) for 15 min at room temperature. For further information on antibodies and dilutions, see Supplementary Table S1.

Zebrafish Circulation Studies. The zebrafish embryos were kept in petri dishes containing zebrafish egg water supplemented with 0.003% phenythiourea (PTU). The petri dishes were maintained in an incubator at a stable temperature of

28.5 °C. All experiments were performed in accordance with the ethical standards and legislation for animal research in Norway (License FOTS-ID: 13563).

To evaluate the blood circulation of nanoparticles in zebrafish embryos the protocol described in Dal *et al.* was applied.[75] In short, borosilicate needles for injections were produced using a pipette puller (P-97, Sutter Instrument) and mounted on a micromanipulator (Narishige MN-153) connected to an Eppendorf FemtoJet express pump. Before the injections, the zebrafish embryos were sedated in a tricaine bath (Finquel; 0.02% in zebrafish egg water) and placed on a plate containing hardened agarose gel (2% in water). Two-day old zebrafish embryos were injected in the posterior cardinal vein with 5 nL of the nanoparticle solution. At defined time points (5 min, 1 h, 4 h, 24 h, and 72 h) images were recorded for the whole zebrafish (30X magnification) and the caudal region (120X magnification) using a Leica DFC365FX stereo microscope with a 1.0X plan apo lens. The average fluorescence intensity of the artery region (AF, 30X), normalized by the average total fluorescence of the zebrafish (TF, 120X), was used to determine the nanoparticle circulation in the blood flow. The average artery fluorescence at 5 minutes (AF-5min) was considered as 100% meaning that all nanoparticles were considered to be in circulation at this time point. The obtained values were subtracted by the background fluorescence analyzed in zebrafish injected with PBS.

Antibodies and Western Blot Analysis. For Western Blot analysis, whole cell lysates were prepared in RIPA buffer and samples were separated on a 12 % SDS gel. Blotting on to a PVDF membrane was performed with a Trans-Blot Turbo (bio-rad). After blocking with milk for 1 h at RT, incubation with the primary antibody diluted in milk was performed at 4 °C overnight. Horse-radish-peroxidase (HRP)-coupled secondary antibodies were incubated with the blot for 1 h at RT. Detection of luminescence signal after addition of Clarity Western ECL Substrate (bio-rad) was performed on a ChemiDocTM (bio-rad). For antibodies and respective dilutions see Supplementary Table S1.

Quantification of complement component C5a. Complement activation was determined after incubation of 2 μg NP in 20 μL human plasma (37 °C, 300 rpm, 1 h) with the help of abcam's Human Complement C5a ELISA Kit according to manufacturer's instructions as has been described in detail.[61]

Clinical Gene Expression and Survival Analysis. Publicly available gene expression data was obtained from The Cancer Genome Atlas (TCGA) Research Network

(http://cancergenome.nih.gov/) and assessed *via* the USCS Xena browser.[86] The TCGA Research Network included patients in accordance with the guidelines of the Declaration of Helsinki of 1975 and all patients provided signed informed consent. Data of n=50 normal adjacent tissue (NAT) and n=528 HNSCC tissue samples were included. Patients were grouped based on their expression level of LRRC8A, treatment, observation time as indicated, and survival analysis performed as described.[87] Data was visualized with the help of GraphPad PRISM.

Differential Gene Expression Analysis. Cell lysis and RNA isolation was performed using the RNeasy Mini kit (Qiagen, Hilden) according to manufacturer's instructions. RNA samples (2 μg) were checked for DNA contamination by performing cDNA transcription with and without addition of reverse transcriptase and then checking for amplification of housekeeping gene actin in a PCR reaction. For primer sequences see Supplementary Table S2. RNA sequencing was performed as described in.[83] FPKM values to quantify the expression of the RNA sequencing data were calculated using cufflinks,[56] differential gene expression was performed using deseq2[57] and the results were visualized by DEBrowser.[88] Further analysis and heatmap plotting of data was performed on GraphPad Prism.

References

1. Wild, C. P.; Weiderpass, E.; Stewart, B. W. *World Cancer Report: Cancer Research for Cancer Prevention.*; International Agency for Research on Cancer: Lyon, France, **2020**.

2. Bray, F.; Ferlay, J.; Soerjomataram, I.; Siegel, R. L.; Torre, L. A.; Jemal, A., Global Cancer Statistics 2018: GLOBOCAN Estimates of Incidence and Mortality Worldwide for 36 Cancers in 185 Countries. *CA Cancer J Clin* **2018,** *68* (6), 394-424.

3. Niazi, M.; Zakeri-Milani, P.; Najafi Hajivar, S.; Soleymani Goloujeh, M.; Ghobakhlou, N.; Shahbazi Mojarrad, J.; Valizadeh, H., Nano-Based Strategies to Overcome P-Glycoprotein-Mediated Drug Resistance. *Expert opinion on drug metabolism & toxicology* **2016,** *12* (9), 1021-33.

4. Perez-Herrero, E.; Fernandez-Medarde, A., Advanced Targeted Therapies in Cancer: Drug Nanocarriers, the Future of Chemotherapy. *Eur J Pharm Biopharm* **2015,** *93*, 52-79.

5. Bar-Zeev, M.; Livney, Y. D.; Assaraf, Y. G., Targeted Nanomedicine for Cancer Therapeutics: Towards Precision Medicine Overcoming Drug Resistance. *Drug Resist Updat* **2017,** *31*, 15-30.

6. Uchino, H.; Matsumura, Y.; Negishi, T.; Koizumi, F.; Hayashi, T.; Honda, T.; Nishiyama, N.; Kataoka, K.; Naito, S.; Kakizoe, T., Cisplatin-Incorporating Polymeric Micelles (NC-6004) Can Reduce Nephrotoxicity and Neurotoxicity of Cisplatin in Rats. *Br J Cancer* **2005,** *93* (6), 678-87.

7. Lammers, T.; Kiessling, F.; Hennink, W. E.; Storm, G., Drug Targeting to Tumors: Principles, Pitfalls and (Pre-)Clinical Progress. J Control Release **2012**, 161 (2), 175-87.

8. Dhar, S.; Kolishetti, N.; Lippard, S. J.; Farokhzad, O. C., Targeted Delivery of a Cisplatin Prodrug for Safer and More Effective Prostate Cancer Therapy in Vivo. Proc Natl Acad Sci U S A **2011**, 108 (5), 1850-5.

9. Yang, X. Z.; Du, X. J.; Liu, Y.; Zhu, Y. H.; Liu, Y. Z.; Li, Y. P.; Wang, J., Rational Design of Polyion Complex Nanoparticles to Overcome Cisplatin Resistance in Cancer Therapy. *Adv Mater* **2014,** *26* (6), 931-6.

10. Mi, P.; Miyata, K.; Kataoka, K.; Cabral, H., Clinical Translation of Self-Assembled Cancer Nanomedicines. *Adv Ther-Germany* **2021,** *4* (1).

11. Lin, Y. X.; Wang, Y.; An, H. W.; Qi, B.; Wang, J.; Wang, L.; Shi, J.; Mei, L.; Wang, H., Peptide-Based Autophagic Gene and Cisplatin Co-Delivery Systems Enable Improved Chemotherapy Resistance. *Nano Lett* **2019,** *19* (5), 2968-2978.

12. Xu, X.; Xie, K.; Zhang, X. Q.; Pridgen, E. M.; Park, G. Y.; Cui, D. S.; Shi, J.; Wu, J.; Kantoff, P. W.; Lippard, S. J.; Langer, R.; Walker, G. C.; Farokhzad, O. C., Enhancing Tumor Cell Response to Chemotherapy through Nanoparticle-Mediated Codelivery of siRNA and Cisplatin Prodrug. *Proc Natl Acad Sci U S A* **2013,** *110* (46), 18638-43.

13. Dhar, S.; Gu, F. X.; Langer, R.; Farokhzad, O. C.; Lippard, S. J., Targeted Delivery of Cisplatin to Prostate Cancer Cells by Aptamer Functionalized Pt(IV) Prodrug-PLGA-PEG Nanoparticles. *Proc Natl Acad Sci U S A* **2008,** *105* (45), 17356-61.

14. Blanco, M. D.; Teijon, C.; Olmo, R. M.; Teijon, J. M., Targeted Nanoparticles for

Cancer Therapy. In *Recent Advantages in Novel Drug Carrier Systems*, Sezer, A. D., Ed. BoD - Books on Demand: Rijeka, Croatia, **2012**; 241-280.

15. Martinez, A.; Muniz, E.; Teijon, C.; Iglesias, I.; Teijon, J. M.; Blanco, M. D., Targeting Tamoxifen to Breast Cancer Xenograft Tumours: Preclinical Efficacy of Folate-Attached Nanoparticles Based on Alginate-Cysteine/Disulphide-Bond-Reduced Albumin. *Pharmaceutical Research* **2014,** *31* (5), 1264-1274.

16. Li, Y.; Deng, Y.; Tian, X.; Ke, H.; Guo, M.; Zhu, A.; Yang, T.; Guo, Z.; Ge, Z.; Yang, X.; Chen, H., Multipronged Design of Light-Triggered Nanoparticles to Overcome Cisplatin Resistance for Efficient Ablation of Resistant Tumor. *ACS Nano* **2015,** *9* (10), 9626-37.

17. Johnstone, T. C.; Suntharalingam, K.; Lippard, S. J., The Next Generation of Platinum Drugs: Targeted Pt(II) Agents, Nanoparticle Delivery, and Pt(IV) Prodrugs. *Chem Rev* **2016,** *116* (5), 3436-86.

18. van der Meel, R.; Sulheim, E.; Shi, Y.; Kiessling, F.; Mulder, W. J. M.; Lammers, T., Smart Cancer Nanomedicine. *Nature Nanotechnology* **2019,** *14* (11), 1007-1017.

19. Mochida, Y.; Cabral, H.; Kataoka, K., Polymeric Micelles for Targeted Tumor Therapy of Platinum Anticancer Drugs. *Expert Opin Drug Deliv* **2017,** *14* (12), 1423-1438.

20. Klinker, K.; Schafer, O.; Huesmann, D.; Bauer, T.; Capeloa, L.; Braun, L.; Stergiou, N.; Schinnerer, M.; Dirisala, A.; Miyata, K.; Osada, K.; Cabral, H.; Kataoka, K.; Barz, M., Secondary-Structure-Driven Self-Assembly of Reactive Polypept(o)ides: Controlling Size, Shape, and Function of Core Cross-Linked Nanostructures. *Angew Chem Int Ed Engl* **2017,** *56* (32), 9608-9613.

21. Schafer, O.; Klinker, K.; Braun, L.; Huesmann, D.; Schultze, J.; Koynov, K.; Barz, M., Combining Orthogonal Reactive Groups in Block Copolymers for Functional Nanoparticle Synthesis in a Single Step. *Acs Macro Letters* **2017,** *6* (10), 1140-1145.

22. Nishiyama, N.; Kato, Y.; Sugiyama, Y.; Kataoka, K., Cisplatin-Loaded Polymer-Metal Complex Micelle with Time-Modulated Decaying Property as a Novel Drug Delivery System. *Pharm Res* **2001,** *18* (7), 1035-41.

23. Atrafi, F.; van Eerden, R. A. G.; Koolen, S. L. W.; de Bruijn, P.; Rijcken, C. J. F.; Hanssen, R.; Eskens, F.; Lolkema, M. P.; Oomen-de Hoop, E.; Damman, J.; Mathijssen, R. H. J., Docetaxel Skin Exposure and Micronucleation Contributes to Skin Toxicity Caused by CPC634. *Cancers (Basel)* **2021,** *13* (15).

24. Stauber, R. H.; Westmeier, D.; Wandrey, M.; Becker, S.; Docter, D.; Ding, G. B.; Thines, E.; Knauer, S. K.; Siemer, S., Mechanisms of Nanotoxicity - Biomolecule Coronas Protect Pathological Fungi against Nanoparticle-Based Eradication. *Nanotoxicology* **2020**, 1-18.

25. Gianneli, M.; Polo, E.; Lopez, H.; Castagnola, V.; Aastrup, T.; Dawson, K. A., Label-Free In-Flow Detection of Receptor Recognition Motifs on the Biomolecular Corona of Nanoparticles. *Nanoscale* **2018,** *10* (12), 5474-5481.

26. Walkey, C. D.; Olsen, J. B.; Song, F.; Liu, R.; Guo, H.; Olsen, D. W.; Cohen, Y.; Emili, A.; Chan, W. C., Protein Corona Fingerprinting Predicts the Cellular Interaction of Gold and Silver Nanoparticles. *ACS Nano* **2014,** *8* (3), 2439-55.

27. Hadjidemetriou, M.; Al-Ahmady, Z.; Kostarelos, K., Time-Evolution of *in Vivo* Protein Corona onto Blood-Circulating PEGylated Liposomal Doxorubicin (DOXIL)

Nanoparticles. *Nanoscale* **2016,** *8* (13), 6948-57.

28. Westmeier, D.; Posselt, G.; Hahlbrock, A.; Bartfeld, S.; Vallet, C.; Abfalter, C.; Docter, D.; Knauer, S. K.; Wessler, S.; Stauber, R. H., Nanoparticle Binding Attenuates the Pathobiology of Gastric Cancer-Associated *Helicobacter pylori*. *Nanoscale* **2018,** *10* (3), 1453-1463.

29. Docter, D.; Strieth, S.; Westmeier, D.; Hayden, O.; Gao, M.; Knauer, S. K.; Stauber, R. H., No King without a Crown--Impact of the Nanomaterial-Protein Corona on Nanobiomedicine. *Nanomedicine (Lond)* **2015,** *10* (3), 503-19.

30. Kreyling, W. G.; Abdelmonem, A. M.; Ali, Z.; Alves, F.; Geiser, M.; Haberl, N.; Hartmann, R.; Hirn, S.; de Aberasturi, D. J.; Kantner, K.; Khadem-Saba, G.; Montenegro, J. M.; Rejman, J.; Rojo, T.; de Larramendi, I. R.; Ufartes, R.; Wenk, A.; Parak, W. J., *In Vivo* Integrity of Polymer-Coated Gold Nanoparticles. *Nat Nanotechnol* **2015,** *10* (7), 619-23.

31. Alberg, I.; Kramer, S.; Schinnerer, M.; Hu, Q.; Seidl, C.; Leps, C.; Drude, N.; Mockel, D.; Rijcken, C.; Lammers, T.; Diken, M.; Maskos, M.; Morsbach, S.; Landfester, K.; Tenzer, S.; Barz, M.; Zentel, R., Polymeric Nanoparticles with Neglectable Protein Corona. *Small* **2020,** *16* (18), e1907574.

32. Alberg, I.; Kramer, S.; Leps, C.; Tenzer, S.; Zentel, R., Effect of Core-Crosslinking on Protein Corona Formation on Polymeric Micelles. *Macromol Biosci* **2021,** *21* (4), e2000414.

33. Birke, A.; Ling, J.; Barz, M., Polysarcosine-Containing Copolymers: Synthesis, Characterization, Self-Assembly, and Applications. *Progress in Polymer Science* **2018,** *81*, 163-208.

34. Weber, B.; Birke, A.; Fischer, K.; Schmidt, M.; Barz, M., Solution Properties of Polysarcosine: From Absolute and Relative Molar Mass Determinations to Complement Activation. *Macromolecules* **2018,** *51* (7), 2653-2661.

35. Son, K.; Ueda, M.; Taguchi, K.; Maruyama, T.; Takeoka, S.; Ito, Y., Evasion of the Accelerated Blood Clearance Phenomenon by Polysarcosine Coating of Liposomes. *Journal of Controlled Release* **2020,** *322*, 209-216.

36. Shiraishi, K.; Kawano, K.; Maitani, Y.; Aoshi, T.; Ishii, K. J.; Sanada, Y.; Mochizuki, S.; Sakurai, K.; Yokoyama, M., Exploring the Relationship between Anti-PEG IgM Behaviors and PEGylated Nanoparticles and Its Significance for Accelerated Blood Clearance. *Journal of Controlled Release* **2016,** *234*, 59-67.

37. Nogueira, S. S.; Schlegel, A.; Maxeiner, K.; Weber, B.; Barz, M.; Schroer, M. A.; Blanchet, C. E.; Svergun, D. I.; Ramishetti, S.; Peer, D.; Langguth, P.; Sahin, U.; Haas, H., Polysarcosine-Functionalized Lipid Nanoparticles for Therapeutic mRNA Delivery. *Acs Appl Nano Mater* **2020,** *3* (11), 10634-10645.

38. Barz, M.; Luxenhofer, R.; Zentel, R.; Vicent, M. J., Overcoming the PEG-Addiction: Well-Defined Alternatives to PEG, from Structure-Property Relationships to Better Defined Therapeutics. *Polym Chem-Uk* **2011,** *2* (9), 1900-1918.

39. Vinogradov, S.; Wei, X., Cancer Stem Cells and Drug Resistance: The Potential of Nanomedicine. *Nanomedicine (Lond)* **2012,** *7* (4), 597-615.

40. Alsahafi, E.; Begg, K.; Amelio, I.; Raulf, N.; Lucarelli, P.; Sauter, T.; Tavassoli, M., Clinical Update on Head and Neck Cancer: Molecular Biology and Ongoing Challenges. *Cell Death Dis* **2019,** *10* (8), 540.

41.   Price, K. A.; Cohen, E. E., Current Treatment Options for Metastatic Head and Neck Cancer. *Curr Treat Options Oncol* **2012,** *13* (1), 35-46.

42.   Oosting, S. F.; Haddad, R. I., Best Practice in Systemic Therapy for Head and Neck Squamous Cell Carcinoma. *Front Oncol* **2019,** *9*, 815.

43.   Galluzzi, L.; Senovilla, L.; Vitale, I.; Michels, J.; Martins, I.; Kepp, O.; Castedo, M.; Kroemer, G., Molecular Mechanisms of Cisplatin Resistance. *Oncogene* **2012,** *31* (15), 1869-83.

44.   Bagrodia, A.; Lee, B. H.; Lee, W.; Cha, E. K.; Sfakianos, J. P.; Iyer, G.; Pietzak, E. J.; Gao, S. P.; Zabor, E. C.; Ostrovnaya, I.; Kaffenberger, S. D.; Syed, A.; Arcila, M. E.; Chaganti, R. S.; Kundra, R.; Eng, J.; Hreiki, J.; Vacic, V.; Arora, K.; Oschwald, D. M. *et al.*, Genetic Determinants of Cisplatin Resistance in Patients with Advanced Germ Cell Tumors. *J Clin Oncol* **2016,** *34* (33), 4000-4007.

45.   Zhu, S.; Shanbhag, V.; Wang, Y.; Lee, J.; Petris, M., A Role for the ATP7A Copper Transporter in Tumorigenesis and Cisplatin Resistance. *J Cancer* **2017,** *8* (11), 1952-1958.

46.   Siddik, Z. H., Cisplatin: Mode of Cytotoxic Action and Molecular Basis of Resistance. *Oncogene* **2003,** *22* (47), 7265-79.

47.   Holohan, C.; Van Schaeybroeck, S.; Longley, D. B.; Johnston, P. G., Cancer Drug Resistance: An Evolving Paradigm. *Nat Rev Cancer* **2013,** *13* (10), 714-26.

48.   Rottenberg, S.; Disler, C.; Perego, P., The Rediscovery of Platinum-Based Cancer Therapy. *Nat Rev Cancer* **2021,** *21* (1), 37-50.

49.   Jou, A.; Hess, J., Epidemiology and Molecular Biology of Head and Neck Cancer. *Oncol Res Treat* **2017,** *40* (6), 328-332.

50.   Sacco, A. G.; Cohen, E. E., Current Treatment Options for Recurrent or Metastatic Head and Neck Squamous Cell Carcinoma. *J Clin Oncol* **2015,** *33* (29), 3305-13.

51.   Lammers, T.; Kiessling, F.; Ashford, M.; Hennink, W.; Crommelin, D.; Storm, G., Cancer Nanomedicine: Is Targeting Our Target? *Nat Rev Mater* **2016,** *1* (9).

52.   Cameron, D.; Piccart-Gebhart, M. J.; Gelber, R. D.; Procter, M.; Goldhirsch, A.; de Azambuja, E.; Castro, G.; Untch, M.; Smith, I.; Gianni, L.; Baselga, J.; Al-Sakaff, N.; Lauer, S.; McFadden, E.; Leyland-Jones, B.; Bell, R.; Dowsett, M.; Jackisch, C.; Trial, H. A. H., 11 Years' Follow-Up of Trastuzumab after Adjuvant Chemotherapy in HER2-Positive Early Breast Cancer: Final Analysis of the HERceptin Adjuvant (HERA) Trial. *Lancet* **2017,** *389* (10075), 1195-1205.

53.   Swain, S. M.; Baselga, J.; Kim, S. B.; Ro, J.; Semiglazov, V.; Campone, M.; Ciruelos, E.; Ferrero, J. M.; Schneeweiss, A.; Heeson, S.; Clark, E.; Ross, G.; Benyunes, M. C.; Cortes, J.; Group, C. S., Pertuzumab, Trastuzumab, and Docetaxel in HER2-Positive Metastatic Breast Cancer. *The New England journal of medicine* **2015,** *372* (8), 724-34.

54.   Humblet, Y., Cetuximab: An IgG(1) Monoclonal Antibody for the Treatment of Epidermal Growth Factor Receptor-Expressing Tumours. *Expert Opin Pharmacother* **2004,** *5* (7), 1621-33.

55.   Ferrer, I.; Zugazagoitia, J.; Herbertz, S.; John, W.; Paz-Ares, L.; Schmid-Bindert, G., KRAS-Mutant Non-Small Cell Lung Cancer: From Biology to Therapy. *Lung Cancer* **2018,** *124*, 53-64.

56.   Trapnell, C.; Roberts, A.; Goff, L.; Pertea, G.; Kim, D.; Kelley, D. R.; Pimentel, H.;

Salzberg, S. L.; Rinn, J. L.; Pachter, L., Differential Gene and Transcript Expression Analysis of RNA-Seq Experiments with TopHat and Cufflinks. *Nat Protoc* **2012,** *7* (3), 562-78.

57.   Love, M. I.; Huber, W.; Anders, S., Moderated Estimation of Fold Change and Dispersion for RNA-Seq Data with DESeq2. *Genome Biol* **2014,** *15* (12), 550.

58.   Kelland, L., The Resurgence of Platinum-Based Cancer Chemotherapy. *Nat Rev Cancer* **2007,** *7* (8), 573-84.

59.   Heijink, A. M.; Everts, M.; Honeywell, M. E.; Richards, R.; Kok, Y. P.; de Vries, E. G. E.; Lee, M. J.; van Vugt, M., Modeling of Cisplatin-Induced Signaling Dynamics in Triple-Negative Breast Cancer Cells Reveals Mediators of Sensitivity. *Cell Rep* **2019,** *28* (9), 2345-2357 e5.

60.   Wu, G.; Haw, R., Functional Interaction Network Construction and Analysis for Disease Discovery. *Methods Mol Biol* **2017,** *1558*, 235-253.

61.   Sorensen, B. H.; Dam, C. S.; Sturup, S.; Lambert, I. H., Dual Role of LRRC8A-Containing Transporters on Cisplatin Resistance in Human Ovarian Cancer Cells. *J Inorg Biochem* **2016,** *160*, 287-95.

62.   Sonego, M.; Pellizzari, I.; Dall'Acqua, A.; Pivetta, E.; Lorenzon, I.; Benevol, S.; Bomben, R.; Spessotto, P.; Sorio, R.; Gattei, V.; Belletti, B.; Schiappacassi, M.; Baldassarre, G., Common Biological Phenotypes Characterize the Acquisition of Platinum-Resistance in Epithelial Ovarian Cancer Cells. *Sci Rep* **2017,** *7* (1), 7104.

63.   Sorensen, B. H.; Nielsen, D.; Thorsteinsdottir, U. A.; Hoffmann, E. K.; Lambert, I. H., Downregulation of LRRC8A Protects Human Ovarian and Alveolar Carcinoma Cells against Cisplatin-Induced Expression of p53, MDM2, p21Waf1/Cip1, and Caspase-9/-3 Activation. *Am J Physiol Cell Physiol* **2016,** *310* (11), C857-73.

64.   Voss, F. K.; Ullrich, F.; Munch, J.; Lazarow, K.; Lutter, D.; Mah, N.; Andrade-Navarro, M. A.; von Kries, J. P.; Stauber, T.; Jentsch, T. J., Identification of LRRC8 Heteromers as an Essential Component of the Volume-Regulated Anion Channel VRAC. *Science* **2014,** *344* (6184), 634-8.

65.   Jentsch, T. J.; Lutter, D.; Planells-Cases, R.; Ullrich, F.; Voss, F. K., VRAC: Molecular Identification as LRRC8 Heteromers with Differential Functions. *Pflugers Arch* **2016,** *468* (3), 385-93.

66.   Planells-Cases, R.; Lutter, D.; Guyader, C.; Gerhards, N. M.; Ullrich, F.; Elger, D. A.; Kucukosmanoglu, A.; Xu, G.; Voss, F. K.; Reincke, S. M.; Stauber, T.; Blomen, V. A.; Vis, D. J.; Wessels, L. F.; Brummelkamp, T. R.; Borst, P.; Rottenberg, S.; Jentsch, T. J., Subunit Composition of VRAC Channels Determines Substrate Specificity and Cellular Resistance to Pt-Cased Anti-Cancer Drugs. *EMBO J* **2015,** *34* (24), 2993-3008.

67.   Bao, J.; Perez, C. J.; Kim, J.; Zhang, H.; Murphy, C. J.; Hamidi, T.; Jaubert, J.; Platt, C. D.; Chou, J.; Deng, M.; Zhou, M. H.; Huang, Y.; Gaitan-Penas, H.; Guenet, J. L.; Lin, K.; Lu, Y.; Chen, T.; Bedford, M. T.; Dent, S. Y.; Richburg, J. H. *et al.*, Deficient LRRC8A-Dependent Volume-Regulated Anion Channel Activity Is Associated with Male Infertility in Mice. *JCI Insight* **2018,** *3* (16).

68.   Li, A.; Zhang, D., Synthesis and Characterization of Cleavable Core-Cross-Linked Micelles Based on Amphiphilic Block Copolypeptoids as Smart Drug Carriers. *Biomacromolecules* **2016,** *17* (3), 852-61.

69.   Birke, A.; Huesmann, D.; Kelsch, A.; Weilbacher, M.; Xie, J.; Bros, M.; Bopp, T.; Becker, C.; Landfester, K.; Barz, M., Polypeptoid-Block-Polypeptide Copolymers: Synthesis, Characterization, and Application of Amphiphilic Block Copolypept(o)ides in Drug Formulations and Miniemulsion Techniques. *Biomacromolecules* **2014,** *15* (2), 548-57.

70.   Steinborn, B.; Hirschle, P.; Hohn, M.; Bauer, T.; Barz, M.; Wuttke, S.; Wagner, E.; Lachelt, U., Core-Shell Functionalized Zirconium-Pemetrexed Coordination Nanoparticles as Carriers with a High Drug Content. *Adv Ther-Germany* **2019,** *2* (11).

71.   Cabral, H.; Matsumoto, Y.; Mizuno, K.; Chen, Q.; Murakami, M.; Kimura, M.; Terada, Y.; Kano, M. R.; Miyazono, K.; Uesaka, M.; Nishiyama, N.; Kataoka, K., Accumulation of Sub-100 nm Polymeric Micelles in Poorly Permeable Tumours Depends on Size. *Nat Nanotechnol* **2011,** *6* (12), 815-23.

72.   Ye, H.; Shen, Z.; Yu, L.; Wei, M.; Li, Y., Manipulating Nanoparticle Transport within Blood Flow through External Forces: An Exemplar of Mechanics in Nanomedicine. *Proc Math Phys Eng Sci* **2018,** *474* (2211), 20170845.

73.   Bleher, S.; Buck, J.; Muhl, C.; Sieber, S.; Barnert, S.; Witzigmann, D.; Huwyler, J.; Barz, M.; Suss, R., Poly(sarcosine) Surface Modification Imparts Stealth-Like Properties to Liposomes. *Small* **2019,** *15* (50), e1904716.

74.   Kurihara, K.; Ueda, M.; Hara, I.; Ozeki, E.; Togashi, K.; Kimura, S., Control of *in Vivo* Disposition and Immunogenicity of Polymeric Micelles by Adjusting Poly(sarcosine) Chain Lenghts on Surface. *J Nanoparticle Res* **2017,** *19*, 242.

75.   Dal, N. J. K.; Kocere, A.; Wohlmann, J.; Van Herck, S.; Bauer, T. A.; Resseguier, J.; Bagherifam, S.; Hyldmo, H.; Barz, M.; De Geest, B. G.; Fenaroli, F., Zebrafish Embryos Allow Prediction of Nanoparticle Circulation Times in Mice and Facilitate Quantification of Nanoparticle-Cell Interactions. *Small* **2020,** *16* (5).

76.   Tenzer, S.; Docter, D.; Kuharev, J.; Musyanovych, A.; Fetz, V.; Hecht, R.; Schlenk, F.; Fischer, D.; Kiouptsi, K.; Reinhardt, C.; Landfester, K.; Schild, H.; Maskos, M.; Knauer, S. K.; Stauber, R. H., Rapid Formation of Plasma Protein Corona Critically Affects Nanoparticle Pathophysiology. *Nat Nanotechnol* **2013,** *8* (10), 772-81.

77.   Mochida, Y.; Cabral, H.; Miura, Y.; Albertini, F.; Fukushima, S.; Osada, K.; Nishiyama, N.; Kataoka, K., Bundled Assembly of Helical Nanostructures in Polymeric Micelles Loaded with Platinum Drugs Enhancing Therapeutic Efficiency against Pancreatic Tumor. *ACS Nano* **2014,** *8* (7), 6724-38.

78.   Nishiyama, N.; Okazaki, S.; Cabral, H.; Miyamoto, M.; Kato, Y.; Sugiyama, Y.; Nishio, K.; Matsumura, Y.; Kataoka, K., Novel Cisplatin-Incorporated Polymeric Micelles Can Eradicate Solid Tumors in Mice. *Cancer Res* **2003,** *63* (24), 8977-83.

79.   Klinker, K.; Barz, M., Polypept(o)ides: Hybrid Systems Based on Polypeptides and Polypeptoids. *Macromol Rapid Commun* **2015,** *36* (22), 1943-57.

80.   Kappel, C.; Seidl, C.; Medina-Montano, C.; Schinnerer, M.; Alberg, I.; Leps, C.; Sohl, J.; Hartmann, A. K.; Fichter, M.; Kuske, M.; Schunke, J.; Kuhn, G.; Tubbe, I.; Passlick, D.; Hobernik, D.; Bent, R.; Haas, K.; Montermann, E.; Walzer, K.; Diken, M. *et al.*, Density of Conjugated Antibody Determines the Extent of Fc Receptor Dependent Capture of Nanoparticles by Liver Sinusoidal Endothelial Cells. *ACS Nano* **2021**.

81.   Rausch, K.; Reuter, A.; Fischer, K.; Schmidt, M., Evaluation of Nanoparticle

Aggregation in Human Blood Serum. *Biomacromolecules* **2010,** *11* (11), 2836-9.

82. Mack, B.; Eggert, C.; Eder, K.; Imrich, S.; Baumeister, P.; Harreus, U.; Gires, O., Rapid and Non-Enzymatic *in Vitro* retrieval of Tumour Cells from Surgical Specimens. *PLoS One* **2013,** *8* (1), e55540.

83. Trothe, J.; Ritzmann, D.; Lang, V.; Scholz, P.; Pul, U.; Kaufmann, R.; Buerger, C.; Ertongur-Fauth, T., Hypotonic Stress Response of Human Keratinocytes Involves LRRC8A as Component of Volume-Regulated Anion Channels. *Exp Dermatol* **2018,** *27* (12), 1352-1360.

84. Lee, C. C.; Freinkman, E.; Sabatini, D. M.; Ploegh, H. L., The Protein Synthesis Inhibitor Blasticidin S Enters Mammalian Cells *via* Leucine-Rich Repeat-Containing Protein 8D. *J Biol Chem* **2014,** *289* (24), 17124-31.

85. Stauber, R. H.; Knauer, S. K.; Habtemichael, N.; Bier, C.; Unruhe, B.; Weisheit, S.; Spange, S.; Nonnenmacher, F.; Fetz, V.; Ginter, T.; Reichardt, S.; Liebmann, C.; Schneider, G.; Kramer, O. H., A Combination of a Ribonucleotide Reductase Inhibitor and Histone Deacetylase Inhibitors Downregulates EGFR and Triggers BIM-Dependent Apoptosis in Head and Neck Cancer. *Oncotarget* **2012,** *3* (1), 31-43.

86. Goldman, M. J.; Craft, B.; Hastie, M.; Repecka, K.; McDade, F.; Kamath, A.; Banerjee, A.; Luo, Y.; Rogers, D.; Brooks, A. N.; Zhu, J.; Haussler, D., Visualizing and Interpreting Cancer Genomics Data *via* the Xena Platform. *Nature biotechnology* **2020,** *38* (6), 675-678.

87. Bockhorst, C.; Dietrich, J.; Vogt, T. J.; Stauber, R. H.; Strieth, S.; Bootz, F.; Dietrich, D.; Vos, L., The DNA Methylation Landscape of PD-1 (PDCD1) and Adjacent lncRNA AC131097.3 in Head and Neck Squamous Cell Carcinoma. *Epigenomics* **2021,** *13* (2), 113-127.

88. Kucukural, A.; Yukselen, O.; Ozata, D. M.; Moore, M. J.; Garber, M., DEBrowser: Interactive Differential Expression Analysis and Visualization Tool for Count Data. *BMC Genomics* **2019,** *20* (1), 6.

Supporting Information

Supplementary Methods

NP corona analysis. NPs were incubated in human plasma (100 μL) from healthy volunteers for 30 min at room temperature (300 rpm). Particles were then extensively washed with a 10-fold excess of PBS for three times (13,000 rpm; 20 min; 4 °C). Corona proteins were eluted by incubation with SDS sample buffer (62.5 mM Tris HCl, 2 % SDS, 10 % glycerol, 50 mM DTT, 0.01 % bromphenol blue) at 95 °C for 5 min. Eluted samples were then applied to precast SDS gels (12 % Mini-PROTEAN, bio-rad) and proteins evolved at 100 V for 2 h. Staining was performed by incubation with Instant Blue (VWR) and gels imaged on a ChemiDoc (bio-rad).

Supplementary Figures

RNA Sequencing and Analysis

Literature and Pathway Review

**Supervised Heatmap Analysis
of Possible Candidates**
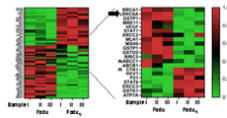
**Further Analysis of
58 'Candidate Hits'**

**Analysis of Clinical Data
for Import Transporters**
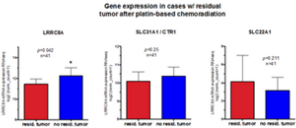
Focus on LRRC8A
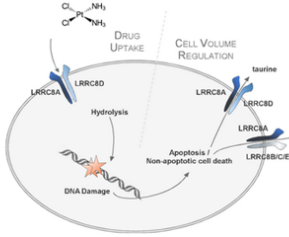
Figure S1: Flow chart illustrating the consecutive decision making process to identify relevant targets critical for cisplatin resistance and targetable by nanomedicals. RNA sequencing revealed genes significantly differentially expressed in cisplatin resistant cell models, which were further refined by meta-analysis (literature research and *Ingenuity Pathway Analyses* to identify genes previously described to be relevant for cisplatin resistance). Results of these supervised analyses are visualized in heatmaps and summarized in tables, listing relevant information for the candidates. Focusing on transporters facilitating active influx or efflux of platinum drugs as the most relevant candidates, a subsequent screening of gene expression and clinical data of the cancer genome atlas collective (*TCGA* HNSCC patient cohort) allowed to identify genes correlating with reduced response to cisplatin chemotherapy. In our study, these *in vitro* and bioinformatic findings strongly suggested to focus on the LRRC8A cisplatin import pathway as the most relevant protein for cisplatin resistance, which could potentially be overcome by rational nanomedicals.
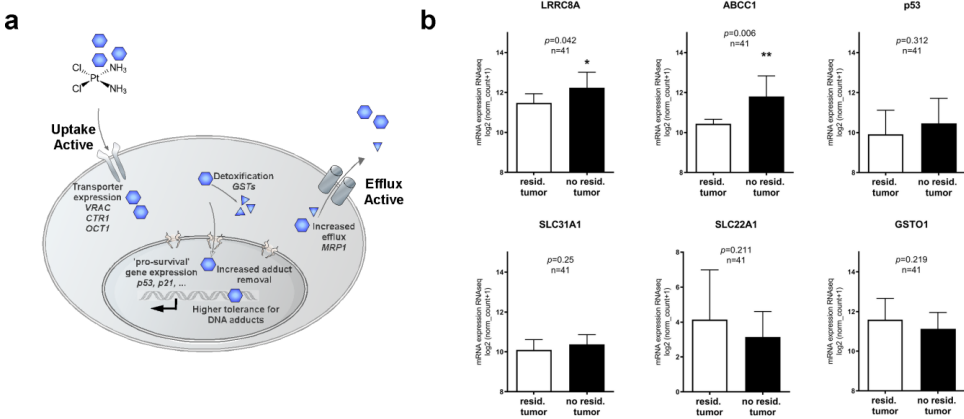
Figure S2: Potential candidates contributing to cisplatin resistance in HNSCC. a) Illustration of mechanisms potentially involved in cisplatin resistance. Reduced intracellular drug concentrations can be a consequence of reduced uptake, accelerated efflux or intracellular detoxification. Additionally, improved DNA repair and various (indirect) pro-survival pathways may improve cancer cells' ability to cope with cisplatin toxicity. **b)** Bioinformatic identification of potentially relevant candidates in the transcriptomics data set of HNSCC patients from *The Cancer Genome Atlas* (TCGA) (n=565). Correlation of transcription levels with residual tumors after first-line chemoradiotherapy and full clinical documentation (n=41) were assessed.
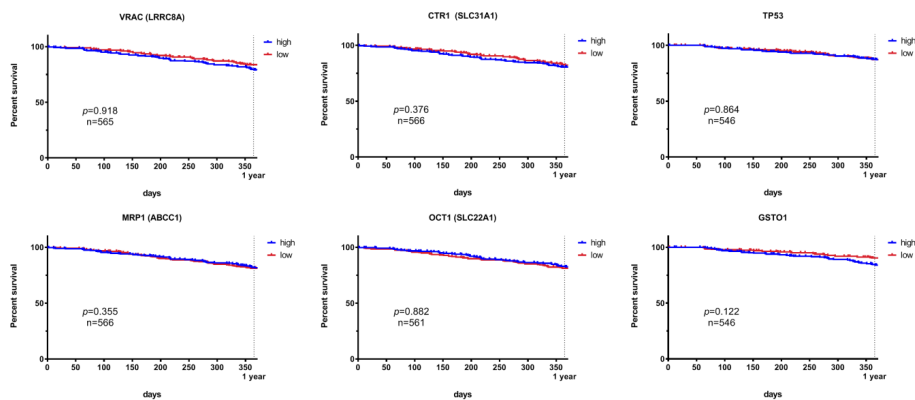
Figure S3: Overall survival of HNSCC patients correlating with potential cisplatin resistance candidates. Overall survival of HNSCC patients depending on VRAC (LRRC8A), MRP1 (ABCC1), CTR1 (SLC31A1), OCT1 (SLC22A1), TP53 (p53), and GSTO1 expression levels shown by Kaplan Meier plots.
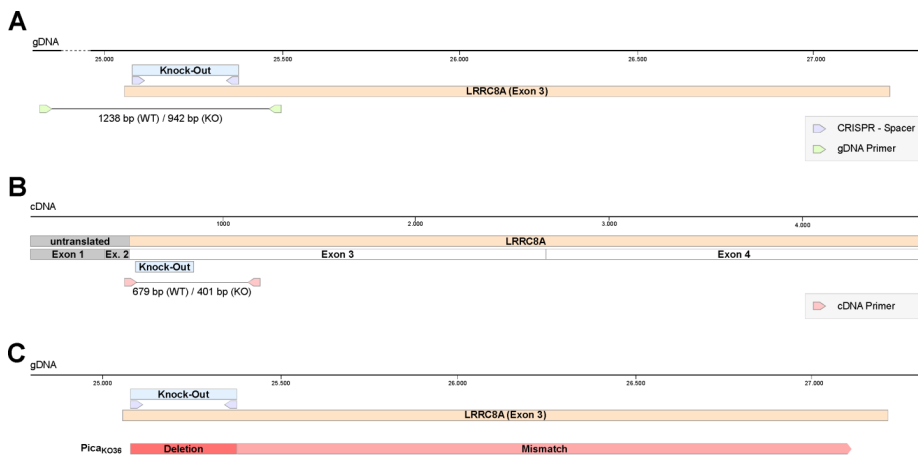
Figure S4: Verification of LRRC8A-deficient knockout cells (Pica$_{KO}$) on the genomic gDNA and RNA/cDNA level by PCR and sequencing. A, Position of CRISPR spacers and primers used to characterize knockout clone gDNA. **B**, Position of primers used to characterize knockout clone cDNA. **C**, Visualization of the gDNA sequencing result of the knockout clone Pica$_{KO}$. For primer sequences refer to Supplementary Table S2.
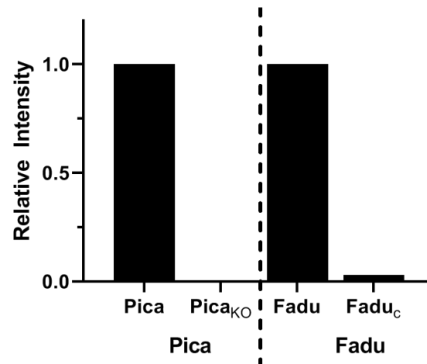
Figure S5: Verification of LRRC8A-deficiency of cell lines $Pica_{KO}$ and $Fadu_C$ on protein level by immunoblot analysis. Immunoblot analysis confirms LRRC8A-deficiency in established cell lines $Pica_{KO}$ and $Fadu_C$. Quantification of immunoblot band intensities normalized to respective wildtype cell lines.
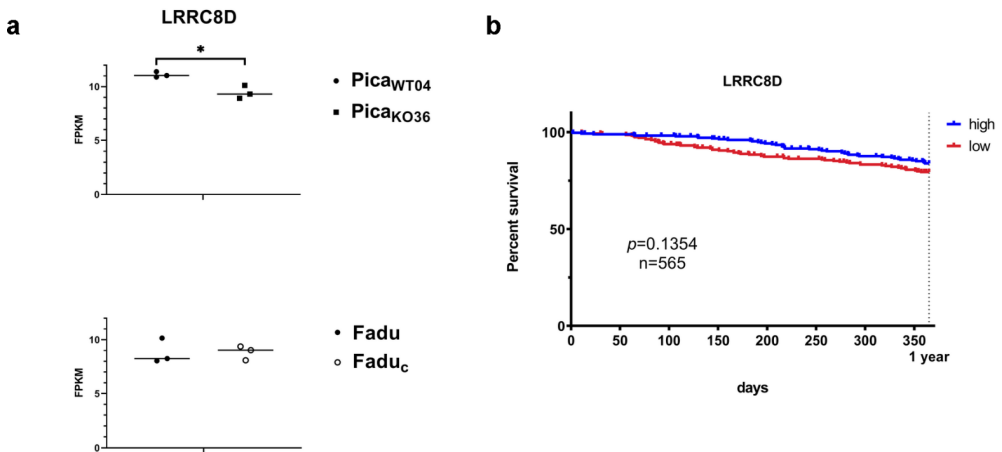
Figure S6: Interdependence of cisplatin resistance and LRRC8D expression. a) RNA sequencing reveals no relevant change in LRRC8D transcription in cisplatin resistant cells. RNASeq-transcriptomics to identify interdependence of LRRC8A and LRRC8D transcription in cisplatin resistant cells. *, $p < 0.05$. **b)** Overall survival of HNSCC patients depending on LRRC8D expression levels shown by Kaplan Meier plots.
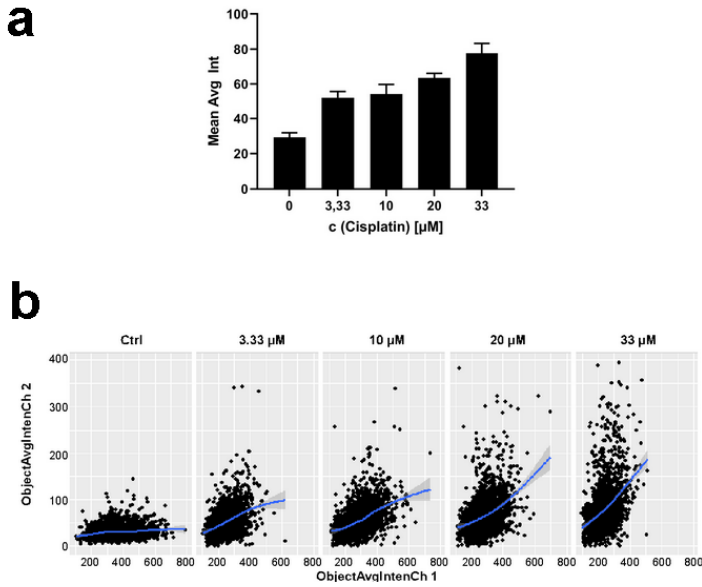
Figure S7: Automated high-content quantification of cisplatin-induced DNA damage. a) Quantification of double-strand breaks induced by cisplatin in Pica$_{WT}$ cells. Cells were treated for 24 h and then fixed and permeabilized. Double-strand break-induced expression of γH2AX was detected by immunofluorescence staining and nuclei stained with Hoechst 33342. The mean average intensity (Mean Avg Int) per cell was determined with Array Scan VTI. **b)** Cy3-signal intensities in the defined target ROIs were plotted against Hoechst staining intensities per single cell as dot plots *via* ggplot/R.
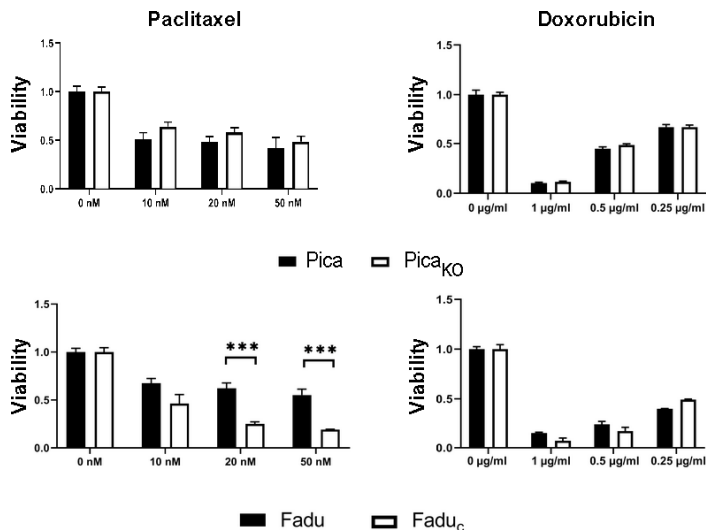
Figure S8: LRRC8A-deficient cell lines Pica_KO and Fadu_C show no resistance for paclitaxel or doxorubicin. Pica and Fadu cells were treated with the indicated drugs for 48 h. Viability was normalized to untreated controls. Statistical analysis was performed according to the unpaired Student's t-test. ***, $p < 0.005$.
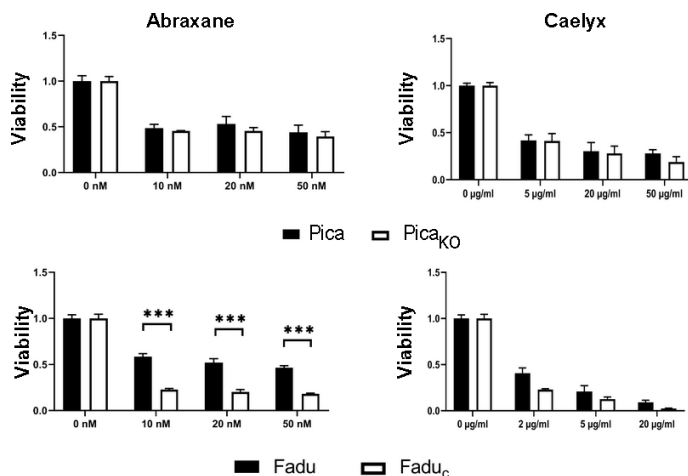
Figure S9. LRRC8A-deficient cell lines Pica_KO and Fadu_C show no resistance for Abraxane or Caelyx. Pica and Fadu cells were treated with the indicated drugs for 48h. Viability was normalized to untreated controls. Statistical analysis was performed according to the unpaired Student's t-test. ***, $p < 0.005$.

324
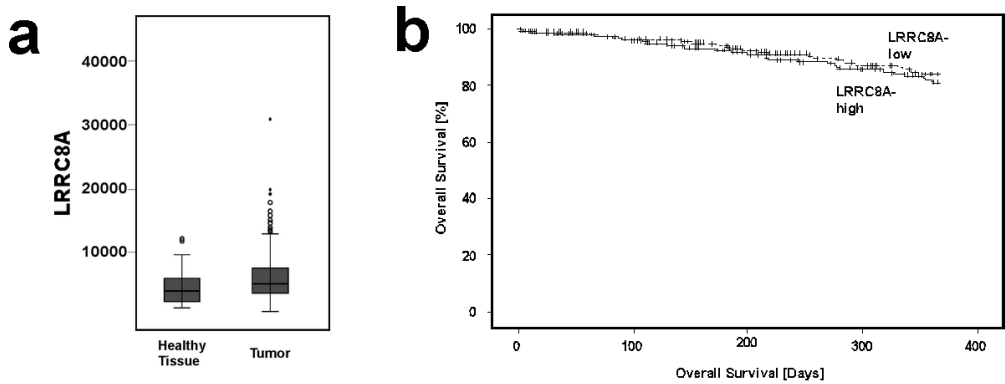
Figure S10: LRRC8A expression in HNSCC tumors. a) LRRC8A expression levels in a cohort of HNSCC patients (n=473) demonstrates heterogeneous expression in tumors compared to healthy tissues. **b)** LRRC8A-low *versus* LRRC8A-high expression levels in unstratified HNSCC patients (n=473) shown by Kaplan-Meier plot.
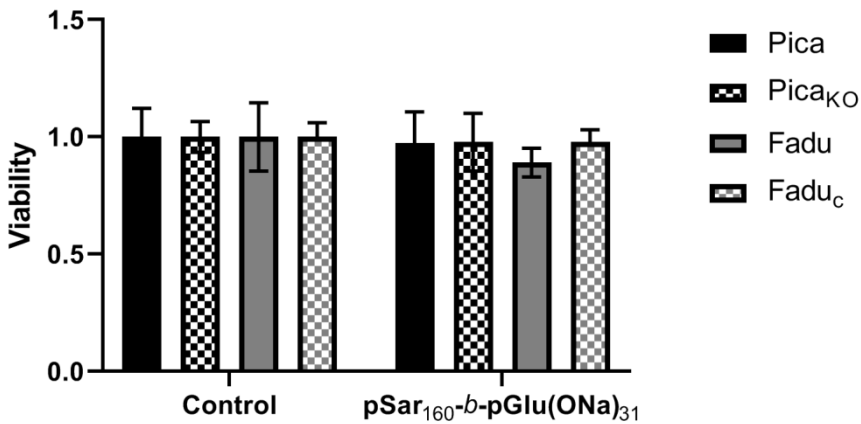
Figure S11: Polysarcosine building blocks forming NP$_{Cis}$ do not show cytotoxicity. Indicated cell lines were treated with pSar$_{160}$-b-pGlu(ONa)$_{31}$ (16.75 µg/µl) for 48 h and viability normalized to untreated controls.
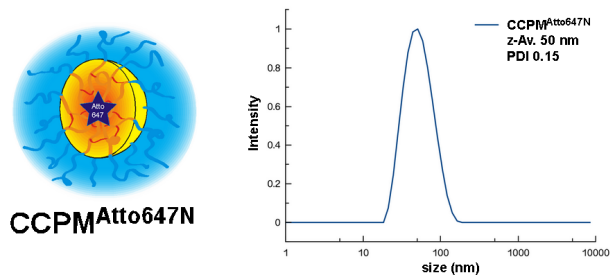
Figure S12: CCPM^{Atto647N} design and characterization. Illustration of expected CCPM^{Atto647N} structure. Particles show a z-average size of 50 nm and a narrow PDI of 0.15.
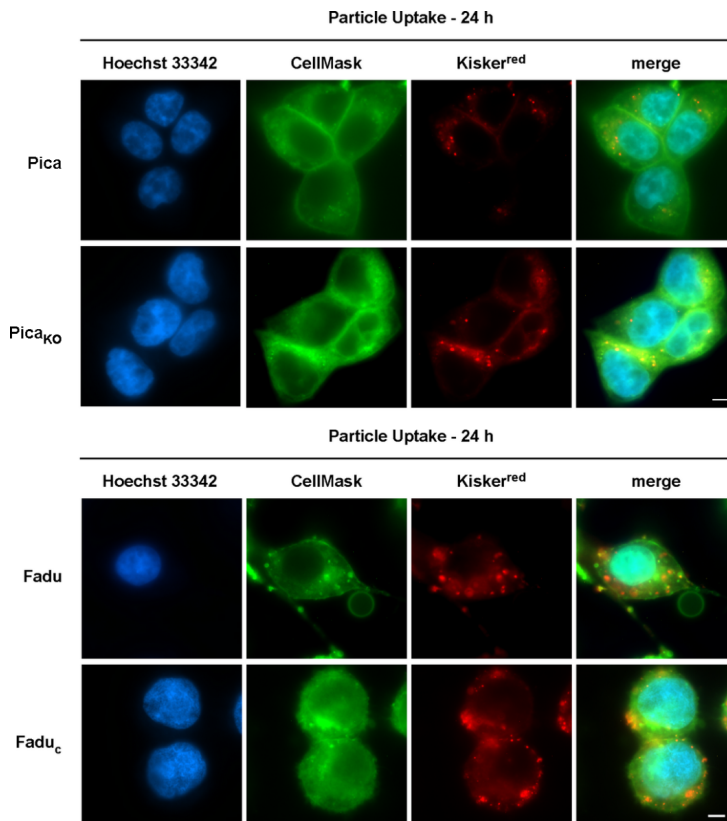
Figure S13: Uptake of silica nanoparticles by LRRC8A-deficient cell lines Pica$_{KO}$ and Fadu$_C$. Cells were treated with Kisker^{red} (50 µg/ml, red) for 24 h. Cell membranes were stained with CellMask (green) prior to fixation and staining of nuclei with Hoechst 33342 (blue). Scale bars, 5 µm.
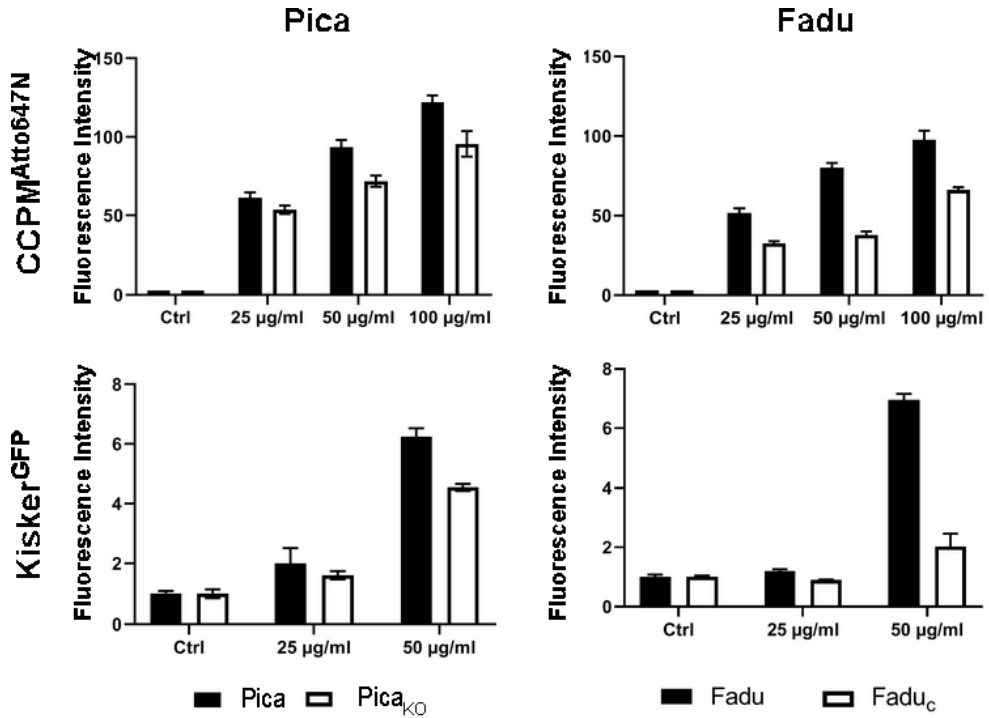
Figure S14: LRRC8A-deficient cell lines Pica$_{KO}$ and Fadu$_C$ internalize fluorescent NPs concentration-dependently. Cells were treated with indicated fluorescent NPs for 24 h prior to fixation and staining of nuclei with Hoechst 33342. Mean average fluorescence intensities were determined with the Array Scan VTI in a radius of 10 pixels around the nucleus.
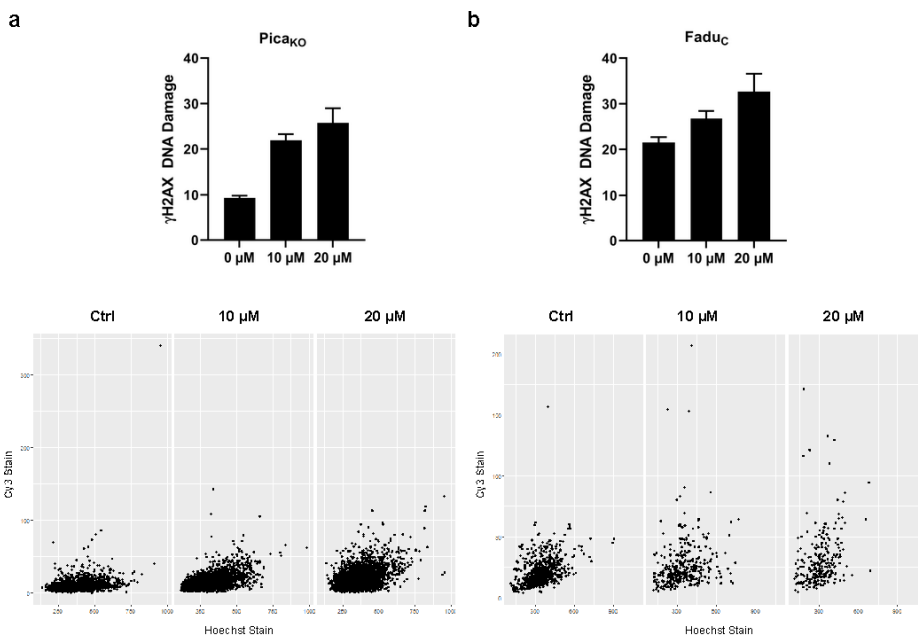
Figure S15: NP$_{Cis}$ induce DNA damage in LRRC8A-deficient cell lines Pica$_{KO}$ and Fadu$_C$. Quantification of double-strand breaks induced by NP$_{Cis}$. Cells were treated for 24 h and then fixed and permeabilized. Cisplatin-induced expression of γH2AX was detected by immunofluorescence staining and nuclei stained with Hoechst 33342. Signal quantification *via* Array Scan VTI. Cy3-signal intensities in the defined target ROIs were plotted against Hoechst staining intensities per single cell as dot plots *via* ggplot/R.
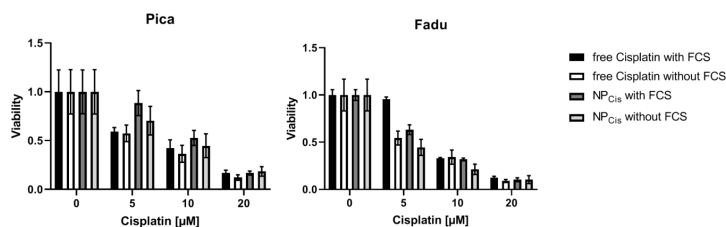
Figure S16: NP$_{Cis}$ toxicity is independent of corona forming conditions. NP$_{Cis}$ does not show corona-dependence of toxicity. Pica and Fadu cells were treated with the respective particles for 48 h in the absence or presence of corona-inducing FCS during the first 4 h or treatment. Viability was normalized to untreated controls. Free cisplatin for comparability.
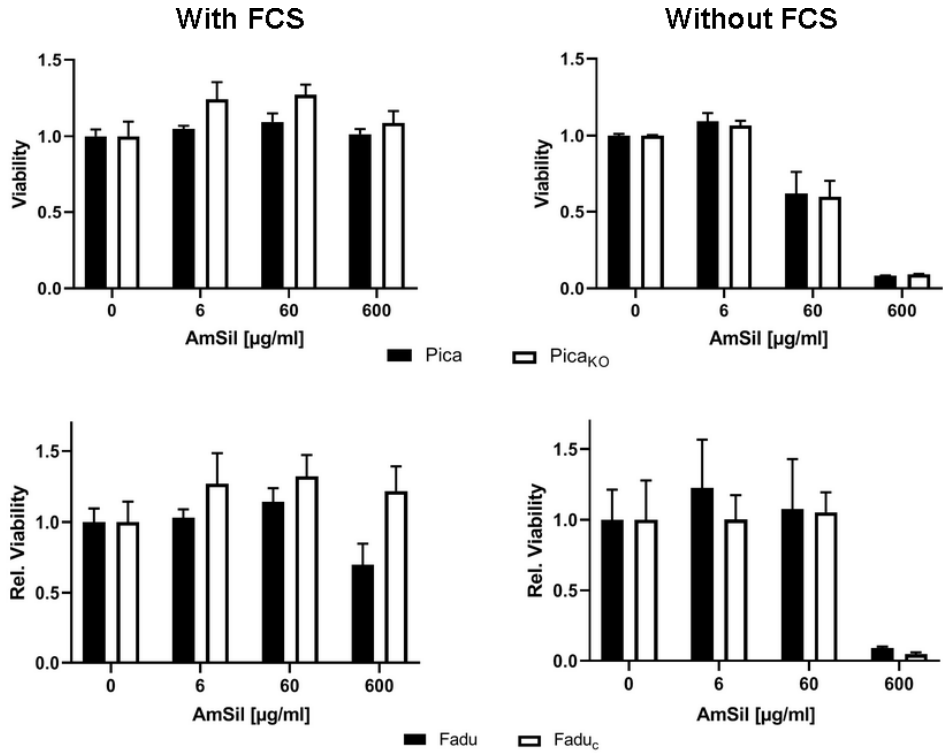
Figure S17: Silica NP toxicity is dependent on corona forming conditions. Cells were treated for 4 h with indicated concentrations of AmSil NPs in medium with or without FCS. Viability was normalized to untreated controls.

Supplementary Tables

Table S1. Antibodies and dilutions.

Antigen	Host	Manufacturer and Article Number	Dilution (x-fold) for Western Blots	Dilution (x-fold) for Immuno-fluorescence
Epcam/CD326	mouse	eBioscience; 13-9326	1000	200
LRRC8A	rabbit	Novusbio; NBP2-32082	500	200
γH2AX	rabbit	Bethyl; A300-081A	n.a.	2000
IL1β	goat	Bio-techne; AF-401-NA	n.a.	25
Rabbit (Cy3 coupled)	goat	Dianova; 111-165-003	n.a.	300
Rabbit (HRP coupled)	goat	Cell Signaling; 7074	5000	n.a.
Mouse (HRP coupled)	mouse	Cell Signaling; 7076	5000	n.a.
Goat (FITC-coupled)	donkey	Santa Cruz; sc-2024	n.a.	300

Table S2. Primer Sequences.

Name	Sequence (5' → 3')	Application
β-Actin_for	GTGGGGCGCCCCAGGCACCA	RNA/cDNA analysis housekeeping control
β-Actin_rev	CTCCTTAATGTCACGCACGATTTC	RNA/cDNA analysis housekeeping control
LRRC8A_for	TGGTTTCCCAGCCAAGTG	RNA/cDNA analysis
LRRC8A_rev	GCGGGAATTTGAACCAGAAG	RNA/cDNA analysis
P_CC1_fw	CTGGGATTACAGACGTGAAC	Characterization knockout clone
Seq_SwellSelect_rev	TGCTCGATCCGTGACTTG	Characterization knockout clone
LRRC8A-rtPCR_Ex2Ex3_forw	ATCCTTGGGGTTGAACCATGAT	Characterization knockout clone
LRRC8A_rtPCR_Ex3Ex4_forw	TCTACCTGAACCGCAACAAGAT	Characterization knockout clone
LRRC8A_rtPCR_Ex3Ex4_rev	GCGCTCTTGAGACTTGCTCT	Characterization knockout clone
sgRNA-LRRC8A_fw	GCTGCGTGTCCGCAAAGTAG	Guide sequence CRISPR/Cas9 LRRC8A knockout forward
sgRNA-LRRC8A_rev	CCGGCACCAGTACAACTACG	Guide sequence CRISPR/Cas9 LRRC8A knockout reverse

Table S3. Genetic characterization of LRRC8A Knockout Clone.

Cell line	Genetic modification	Protein modification
PicaKO: Pica-LRRC8A$^{-/-}$	Δ294 nt (c27-c321)	F10T and additional frameshift after aa10; stop codon at aa66
PicaKO38: Pica-LRRC8A(short)	Δ314 nt (t20-g334)	Δ104 aa (R8-V112)

Table S4. Quantification of NP$_{Cis}$.

Results - Quantification	
total volume	3.19 mL
solid concentration	13.8 g·L^{-1}
total amount	44.1 mg
Calculations based on AAS	
Pt concentration	20.3 mg·L^{-1}
c (CisPt)	936 mg·L^{-1}

Table S5. RNA Sequencing Results to Identify Molecular Cisplatin Resistance Candidates. Genes included in heatmap analysis. All values given in FPKM.

Name	Fadu			Fadu$_c$			Significant
	1	2	3	1	2	3	
GSTM3	0.00	0.00	0.00	6.53	9.46	8.44	x
GSTA4	0.47	0.22	0.00	10.14	9.56	8.14	x
p53	1.71	1.31	1.50	21.88	23.05	25.59	x
BCL2	0.88	0.61	0.32	5.45	3.34	4.74	x
P21	24.02	21.63	21.83	155.85	211.00	128.05	x
tp73	1.45	1.46	0.53	6.52	5.00	6.87	x
FOXO1	0.82	0.68	0.54	2.43	2.38	2.80	x
GSTO1	69.30	93.77	88.04	284.20	339.98	263.67	x
ERCC1	36.83	42.66	55.16	146.85	178.23	119.63	x
XPC	9.13	8.94	6.07	23.59	27.08	20.35	x
Name	**Fadu**			**Fadu$_c$**			**Significant**
	1	2	3	1	2	3	
XPC	9.13	8.94	6.07	23.59	27.08	20.35	x

Name	Fadu			Fadu$_C$			Significant
	1	2	3	1	2	3	
MGST3	18.71	23.74	16.96	53.44	58.83	51.50	x
CTR1	11.57	13.41	11.85	30.92	27.23	28.60	x
ERCC3	19.05	21.43	18.62	46.02	46.14	46.87	x
ATP7B	1.43	1.02	0.54	2.27	2.39	2.14	x
GSTK1	49.07	43.37	22.64	80.33	97.94	73.01	x
XPA	6.21	8.37	6.50	12.67	15.67	15.01	x
GSTT1	16.88	17.39	13.99	35.01	33.49	27.62	x
BID	14.48	16.59	14.37	29.16	33.14	28.10	x
REV7	50.26	69.23	54.51	104.77	100.74	105.63	x
ERCC2	9.13	12.97	13.04	20.35	18.46	22.69	x
STAT6	18.75	17.62	17.46	31.12	30.78	31.71	x
MEK1	29.00	35.20	36.84	55.56	52.53	52.04	x
MGST1	86.73	99.18	104.16	127.69	161.87	161.63	x
CHD4	49.90	49.84	51.71	46.88	41.12	47.54	x
CHD4	49.90	49.84	51.71	46.88	41.12	47.54	x
ABCC1	16.16	15.27	14.30	13.86	12.97	13.60	x
XRCC2	9.64	7.89	7.44	7.51	5.19	9.15	x
BAX	126.86	159.62	162.08	122.34	147.87	101.63	x
ERBB2	21.53	18.32	16.68	15.52	15.21	15.83	x
MAPK	32.65	30.46	38.04	29.44	21.28	30.30	x
ERCC5	15.34	10.58	12.95	11.83	10.24	8.46	x
RAD51	16.84	21.66	21.59	15.60	15.44	14.49	x
KDM5A	11.41	8.80	9.00	7.58	7.07	7.08	x
GSTM4	14.12	18.36	12.56	9.98	12.59	10.15	x
MSH6	26.25	27.56	21.19	18.21	15.73	19.98	x
OCTN2	4.94	3.52	2.45	3.23	2.19	2.33	x
DYNLL1	351.11	450.80	476.91	296.51	331.86	273.57	x
BRCA1	10.01	8.96	9.07	6.03	5.82	7.24	x
STAT3	31.81	31.46	32.91	21.93	22.37	19.05	x
REV1	5.94	5.15	5.70	3.65	2.98	3.66	x

JAK	29.33	23.75	19.42	14.31	13.38	16.07	**x**
MRE11	6.17	4.45	5.14	2.53	2.52	3.35	**x**
LRRC8A	**39.15**	**42.19**	**42.93**	**23.42**	**21.16**	**21.72**	**x**
BIRC5	76.18	122.87	153.17	56.24	56.36	68.47	**x**
XRCC6	555.64	704.37	647.97	308.69	313.60	344.84	**x**
STAT1	68.54	61.73	61.53	27.45	29.73	27.48	**x**
NER	64.47	67.72	62.36	23.20	26.33	22.82	**x**
53BP1	17.08	14.18	12.51	5.54	4.99	5.67	**x**
GSTO2	23.61	25.10	24.10	8.00	12.55	5.75	**x**
ATR	6.07	7.08	8.25	2.42	2.25	2.73	**x**
GSTP1	2014.92	2196.2	2143.7	429.52	492.76	423.75	**x**
GSTP1	2014.92	2196.2	2143.7	429.52	492.76	423.75	**x**
VEGF	68.85	35.47	25.60	9.20	7.89	9.22	**x**
MSH3	5.65	4.79	6.17	0.58	0.51	0.28	**x**
MLH1	14.97	18.93	15.63	0.00	0.00	0.00	**x**
ABCC3	5.13	2.28	2.00	0.00	0.00	0.00	**x**
ABCB1	0.06	0.03	0.00	0.00	0.00	0.00	**x**

Table S6. Candidates relevant for cisplatin resistance identified by RNA sequencing analysis. Potentially relevant transporter genes marked in grey.

Target	Suggested main pathobiological function	Mechanistic contribution specific for cisplatin resistance reported	Clinical Relevance Specific for Cisplatin Resistance (type of malignancy)	Studies targeting cisplatin resistance by nanomedicals reported
Cell Signalling Mediators				
TP73	Transcription factor, stress response	no (indirect/multifold for various physico/chemical stressors)	no	no
FOXO1	Transcription factor, glucose metabolism	no (indirect/multifold for various physico/chemical stressors)	no	no
STAT1	Transcription activator	no (indirect/multifold for various physico/chemical stressors)	no	no
STAT3	Transcription activator	no (indirect/multifold for various physico/chemical stressors)	no	no
STAT6	Transcription activator	no (indirect/multifold for various physico/chemical stressors)	no	no
KDM5A	Histone demethylase, gene regulation	no (indirect/multifold for various physico/chemical stressors)	no	no
CHD4	Helicase, nucleosome remodeling	no (indirect/multifold for various physico/chemical stressors)		no
TP53	Cellular homeostasis regulator against various physico/chemical stressors; tumor suppressor protein; apoptosis regulation	no (indirect/multifold for various physico/chemical stressors)	no	no
BCL2	Cellular homeostasis regulator against various physico/chemical stressors; mitochondrial membrane protein; apoptosis regulation	no (indirect/multifold for various physico/chemical stressors)	no	no
Target	Suggested main pathobiological function	Mechanistic contribution specific	Clinical Relevance Specific for	Studies targeting cisplatin

		for cisplatin resistance reported	Cisplatin Resistance (type of malignancy)	resistance by nanomedicals reported
Cell Signalling Mediators				
P21	Cyclin-dependent kinase inhibitor, regulates cell cycle progression	no (indirect/multifold for various physico/chemical stressors)	no	no
General Detoxification				
MGST1	Gluthathione S-transferase; general detoxification	no (indirect/multifold for various chemicals)	no	no
GSTO2	Gluthathione S-transferase; general detoxification	no (indirect/multifold for various chemicals))	no	no
GSTM4	Gluthathione S-transferase; general detoxification	no (indirect/multifold for various chemicals))	no	no
GSTT1	Gluthathione S-transferase; general detoxification	no (indirect/multifold for various chemicals)	no	no
GSTK1	Gluthathione S-transferase; general detoxification	no (indirect/multifold for various chemicals)	no	no
GSTM3	Gluthathione S-transferase; general detoxification	no (indirect/multifold for various chemicals))	no	no
GSTA4	Gluthathione S-transferase; general detoxification	no (indirect/multifold for various chemicals))	no	no
GSTO1	Gluthathione S-transferase; general detoxification	no (indirect/multifold for various chemicals)	no	no
GSTP1	Gluthathione S-transferase; general detoxification	no (indirect/multifold for various chemicals)	no	no
DNA Repair				
REV1	DNA repair, translesion synthesis	no (indirect; DNA repair and/or mutagenesis)	no	no
Target	**Suggested main pathobiological function**	**Mechanistic contribution specific for cisplatin resistance reported**	**Clinical Relevance Specific for Cisplatin Resistance**	**Studies targeting cisplatin resistance by nanomedicals reported**

		(type of malignancy)		
DNA Repair				
REV7	DNA repair, mitochondrial DNA repair, translesion synthesis	no (indirect; DNA repair and/or mutagenesis)	no	no
BRCA1	Genomic stability mediator, tumor suppressor	no (DNA repair and/or mutagenesis)	no	no
ERCC1	DNA helicase, nucleotide excision repair	no (indirect; DNA repair and/or mutagenesis)	no	no
ERCC2	DNA helicase, nucleotide excision repair	no (indirect; DNA repair and/or mutagenesis)	no	no
ERCC3	DNA helicase, nucleotide excision repair	no (indirect; DNA repair and/or mutagenesis)	no	no
ERCC5	DNA helicase, nucleotide excision repair	no (indirect; DNA repair and/or mutagenesis)	no	no
MLH1	Part of mismatch repair system, allows exonuclease degradation	yes (indirect; DNA repair and/or mutagenesis)	no	no
XPC	DNA damage recognition and repair	no (indirect; DNA repair and/or mutagenesis)	no	no
XPA	DNA damage recognition and repair	no (indirect; DNA repair and/or mutagenesis)	no	no
RAD51	DNA damage repair by homologous recombination	no (indirect; DNA repair and/or mutagenesis)	no	no
MRE11	DNA double strand repair protein	no (indirect; DNA repair and/or mutagenesis)	no	no
XRCC2	DNA double strand repair protein, homologeous recombination	no (indirect; DNA repair and/or mutagenesis)	no	no
XRCC6	Helicase, nonhomologous DNA repair	no (indirect; DNA repair and/or mutagenesis)	no	no
Target	**Suggested main pathobiological function**	**Mechanistic contribution specific for cisplatin resistance reported**	**Clinical Relevance Specific for Cisplatin Resistance (type of malignancy)**	**Studies targeting cisplatin resistance by nanomedicals reported**

DNA Repair

Target	Suggested main pathobiological function	Mechanistic contribution specific for cisplatin resistance reported	Clinical Relevance Specific for Cisplatin Resistance (type of malignancy)	Studies targeting cisplatin resistance by nanomedicals reported
MSH3	Member of the DNA mismatch repair MutS family	no (indirect; DNA repair and/or mutagenesis)	no	no
MSH6	Member of the DNA mismatch repair MutS family	no (indirect; DNA repair and/or mutagenesis)	no	no
53BP1	Promotion of non-homologeous end joining DNA repair pathways	no (indirect; DNA repair and/or mutagenesis)	no	no

Cellular Membrane Transporter

Target	Suggested main pathobiological function	Mechanistic contribution specific for cisplatin resistance reported	Clinical Relevance Specific for Cisplatin Resistance (type of malignancy)	Studies targeting cisplatin resistance by nanomedicals reported
OCTN2	Organic cation transporter	(yes) (suggested to be also involved in cisplatin transport)	no	no
CTR1	Copper transporter	(yes) (suggested to be also involved in cisplatin transport)	(ovarian)	no
ATP7B	(Copper) efflux transporter, detoxification	(yes) (potentially involved in cisplatin export)	no	no
LRRC8A	Volume regulation, anion channel, small molecule transport	yes (suggested to be involved in cisplatin transport)	ovarian	no
ABCB1	ABC-transporter, drug export/general detoxification	(yes) (suggested to be also involved in cisplatin transport)	no	no
ABCC1	ABC-transporter, drug export/general detoxification	(yes) (suggested to be also involved in cisplatin transport)	(yes) (osteosarcoma, neuroblastoma, non-small lung cancer)	no
ABCC3	ABC transporter, drug export/general detoxification	(yes) (suggested to be also involved in cisplatin transport)	no	no

Target	Suggested main pathobiological function	Mechanistic contribution specific for cisplatin resistance reported	Clinical Relevance Specific for Cisplatin Resistance (type of malignancy)	Studies targeting cisplatin resistance by nanomedicals reported

Regulator of Cell Death

BAX	Apoptosis regulation	no (indirect, induction of apoptosis mandatory for cisplatin efficiency)	no	no
BID	Apoptosis regulation	no (indirect, induction of apoptosis mandatory for cisplatin efficiency)	no	no
BIRC5	negative regulatory protein, regulation of apoptotic cell death	no (indirect, induction of apoptosis mandatory for cisplatin efficiency)	no	no
Transcription Regulator				
MEK1	Mitogen-activated protein kinase	no (indirect/multifold for various physico/chemical stressors)	no	no
ERBB2	Tyrosine kinase, epidermal growth factor	no (indirect/multifold for various physico/chemical stressors)	no	no
MAPK1	Signal-regulated kinase: proliferation, differentiation, transcription regulation	no (indirect/multifold for various physico/chemical stressors)	no	no
VEGF	Growth factor, induces proliferation and migration of vascular endothelial cells, angiogenesis	no (indirect/multifold for various physico/chemical stressors)	no	no
DYNLL1	Intracellular transport and mobility	no (indirect/multifold for various physico/chemical stressors)	no	no
MGST3	Inflammation mediation	no (indirect/multifold for various physico/chemical stressors)	no	no
JAK1	Immune and inflammation response	no (indirect/multifold for various physico/chemical stressors)	no	no
ATR	Serine/Threonine kinase, DNA damage sensing	no (indirect/multifold for various physico/chemical stressors)	no	no

8

Core Cross-Linked Polymeric Micelles for Specific Iron Delivery: Inducing Sterile Inflammation in Macrophages

SPION-Loaded Core Cross-Linked Polymeric Micelles
Induce Sterile Inflammation
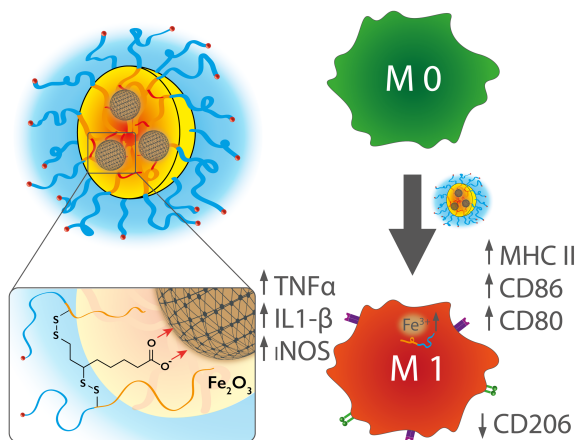
Core Cross-Linked Polymeric Micelles for Specific Iron Delivery: Inducing Sterile Inflammation in Macrophages

Tobias A. Bauer[‡,a,b], Natalie K. Horvat[‡,c,d,e], Oriana Marques[d,f], Sara Chocarro[g], Christina Mertens[f], Silvia Colucci[d,f], Sascha Schmitt[h], Luca M. Carrella[b], Svenja Morsbach[h], Kaloian Koynov[h], Federico Fenaroli[i], Peter Blümler[j], Michaela Jung[k], Rocio Sotillo[g,e], Matthias W. Hentze[*,c], Martina U. Muckenthaler[*,d,e,f], Matthias Barz[*,a,b]

[‡] These authors contributed equally to this work.

[a] Leiden Academic Centre for Drug Research (LACDR), Leiden University, Einsteinweg 55, 2333CC Leiden, The Netherlands

[b] Department of Chemistry, Johannes Gutenberg University Mainz, Duesbergweg 10-14, 55128 Mainz, Germany

[c] European Molecular Biology Laboratory (EMBL), ◊Collaboration for joint PhD degree between EMBL and the Faculty of Biosciences, University of Heidelberg, Meyerhofstr.1, 69117 Heidelberg, Germany.

[d] Molecular Medicine Partnership Unit (MMPU), Otto-Meyerhof-Zentrum, Im Neuenheimer Feld 350, 69120 Heidelberg, Germany.

[e] Translational Lung Research Center Heidelberg (TLRC), German Center for Lung Research (DZL), University of Heidelberg, Im Neuenheimer Feld 350, 69120 Heidelberg, Germany.

[f] Department of Pediatric Oncology, Hematology, Immunology, and Pulmonology, Heidelberg University Hospital, Im Neuenheimer Feld 350, 69120 Heidelberg, Germany.

[g] Department of Molecular Thoracic Oncology, German Cancer Research Center (DKFZ), Im Neuenheimer Feld 280, 69120 Heidelberg, Germany.

[h] Max Planck Institute for Polymer Research, Ackermannweg 10, 55128 Mainz, Germany.

[i] Department for Biosciences, University of Oslo, Blindernveien 31, 0371 Oslo, Norway.

[j] Institute of Physics, Johannes Gutenberg University Mainz, Staudingerweg 9, 55128 Mainz, Germany.

[k] Institute of Biochemistry I, Faculty of Medicine, Goethe-University Frankfurt, Theodor-Stern-Kai 7, 60590 Frankfurt am Main, Germany.

Abstract

Iron is an essential co-factor for cellular processes. In the immune system, it can activate macrophages and represents a potential therapeutic for various diseases. To specifically deliver iron to macrophages, iron oxide nanoparticles were embedded in polymeric micelles of reactive polysarcosine-*block*-poly(S-ethylsulfonyl-L-cysteine). Upon surface functionalization *via* dihydrolipoic acid, iron oxide cores act as crosslinker themselves and undergo chemoselective disulfide bond formation with the surrounding poly(S-ethylsulfonyl-L-cysteine) block, yielding glutathione-responsive core cross-linked polymeric micelles (CCPMs). When applied to primary murine and human macrophages, these nanoparticles displayed preferential uptake, sustained intracellular iron release, and induced a strong inflammatory response. This response was also demonstrated *in vivo* when nanoparticles were intratracheally administered to wild-type C57Bl/6N mice. Most importantly, the controlled release concept to deliver iron oxide in redox-responsive CCPMs induces significantly stronger macrophage activation than any other iron source at identical iron levels (e.g., Feraheme), directing to a new class of immune therapeutics.

Keywords

macrophage polarization · iron metabolism · polypept(o)ide · polymeric micelle · cross-linking · immunomodulation

Cover page

Designed to release: Core Cross-linked micelles based on polypept(o)ides have been designed for specific delivery of iron to macrophages and trigger sterile inflammation. Iron recognition leads to feedback mechanisms for preferred cell uptake, inducing macrophage activation. The approach abolishes undesired immune tolerance unleashing the potential of iron as therapeutic agent.

Introduction

Diseases, such as cancer, atherosclerosis, traumatic nerve injury, and autoimmune disorders are hallmarked by inflammation, whereby infiltration of innate immune cells can exacerbate the disease condition.[1–5] Phagocytic cells, such as monocytes and monocyte-derived macrophages comprise a significant proportion of these infiltrating cells, and a growing number of macrophage subtypes were identified, which are characterized by different functional capabilities, depending on niche-derived stimuli, such as cytokines, chemokines, and metabolites.[6–10] Recruited monocyte-derived macrophages residing in the periphery of solid tumors can mediate adaptive immunity, promote angiogenesis, tissue remodeling and repair, and often contribute to the aggressiveness of a cancer's invasive front.[11–13] Apart from immune functions, macrophages play a pivotal role in maintaining iron homeostasis, as they recycle hemoglobin-derived iron from senescent red blood cells.[14–17] The intricate connection between the immune function of macrophages and their role in iron metabolism was demonstrated by the exposure to metabolites, such as free heme or iron, that directly affect the macrophage activation state, leading to not only changes in the expression of iron-regulatory genes but also in innate immune effector functions.[1,18] By locally applying iron in the form of superparamagnetic iron oxide nanoparticles (SPIONs) within the tumor microenvironment (TME), macrophages become activated, a process that can correlate with inhibition of tumor growth.[1,19] In previous studies, Ferumoxytol (Feraheme, Rienso), a formulation of an iron oxide nanoparticle in a matrix of covalently cross-linked carbohydrates (polyglucose sorbitol carboxymethylether), was used as iron source.[19–23] Despite its approval for the treatment of iron deficiency anemia in patients with chronic kidney disease, the original intention of Ferumoxytol was as a contrast agent for magnetic resonance imaging designed for minimal iron release.[24–30] We now propose that delivery systems which allow for controlled iron release in the TME can serve as immunotherapeutic agent.

SPION-loaded core cross-linked polymeric micelles (SPION-CCPMs) were developed based on polysarcosine-*block*-poly(*S*-ethylsulfonyl-L-cysteine) copolypept(o)ides.[31,32] In these systems, cross-linking by chemoselective disulfide formation features glutathione (GSH)-dependent particle degradation inside the endo- or phagosomal pathway of macrophages.[33]

Results and Discussion

The polymer synthesis was performed by nucleophilic ring-opening polymerization of a-amino acid *N*-carboxyanhydrides (NCAs), yielding polypept(o)ides of polysarcosine-*block*-poly(*S*-ethylsulfonyl-L-cysteine) (pSar-*b*-pCys(SO$_2$Et)).[31,32,34] As shown in Figure 1, block copolymers were obtained using a bifunctional initiator approach, leading to polymers P1 - P3 with chain lengths of 170 to 225 for polysarcosine and 17 to 31 for poly(*S*-ethylsulfonyl-L-cysteine), well suited for steric shielding and cross-linking.[35,36] The syntheses were accomplished on a gram-scale, yielding 2.9 g of P2 and 2.3 g of P3 (Scheme S1, Table S1, and Figure S1 - S5) demonstrating the scalability of the presented approach. For nanoparticle preparation, oleic acid-coated SPIONs (γ-maghemite, Fe$_2$O$_3$, D = 6 nm) were solubilized with the amphiphilic pSar-*b*-pCys(SO$_2$Et) block copolymers, cross-linked with dihydrolipoic acid, and labeled on the amine end-group with Cy5-NHS ester (Figure 1). During co-self-assembly, initial solvent mixtures of chloroform and dimethyl sulfoxide (DMSO) were exchanged stepwise to pure DMSO and water, resulting in SPION-CCPMs as an aqueous dispersion. In addition to disulfide bond formation, dihydrolipoic acid enables direct grafting onto the iron oxide nanoparticle surface by substituting oleic acid, connecting the respective building blocks and stabilizing SPION encapsulation (Figure 1D). Unconjugated dye, residual oleic acid, and free polymer were removed by extraction and repetitive ultra-filtration (MWCO 100 kDa) yielding SPION-CCPM^{Cy5} as a dark green aqueous dispersion (Figure 1E, S9).

To serve as control nanoparticles, empty core cross-linked polymeric micelles (CCPMs) were prepared from pSar-*b*-pCys(SO$_2$Et), according to previous reports (Table S2, Figure S6 and S7).[35,37]

The illustration of SPION-CCPMs as spherical structures containing multiple SPION cores was derived from nanoparticle characterization, which is summarized in Figure 1 and Table 1. According to single-angle dynamic light scattering (DLS), co-self-assembly of oleic acid-coated SPIONs and P3 (mass ratio 1:1) yielded micelles with a hydrodynamic diameter (D_h) of 71 nm (Figure 1A), whereby the size slightly increased to D_h = 82 nm upon cross-linking, dye conjugation, and particle purification. Importantly, the narrow size distribution (PDI ≤ 0.16) of SPION-CCPMs^{Cy5} remained identical when particles were lyophilized and re-constituted in water (SPION-CCPM^{Cy5}-Lyo), which facilitates their scalability and pharmaceutical use.[38]
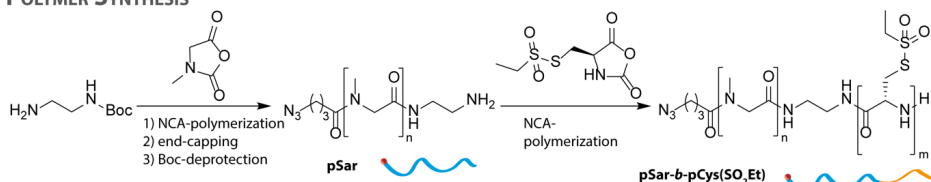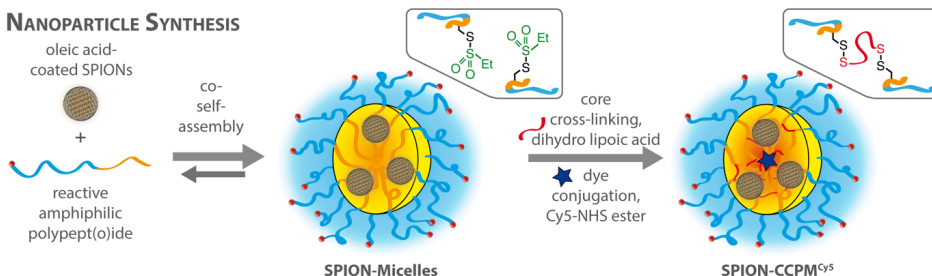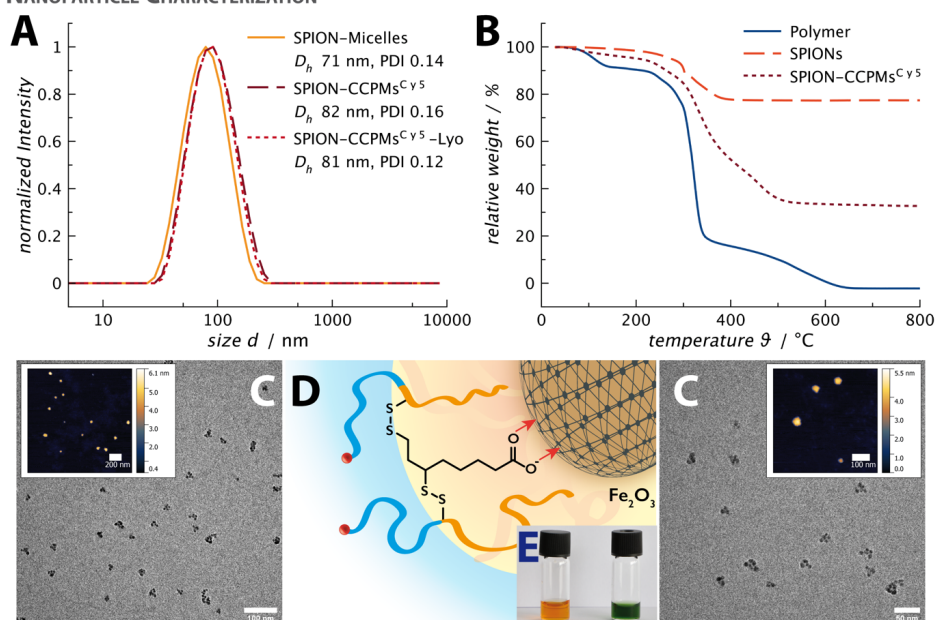
Figure 1. Polymer and nanoparticle synthesis, and characterization of SPION-CCPMs. (**A**) Single-angle DLS of SPION-Micelles and SPION-CCPM^{Cy5} before and after lyophilization and redispersion in water (lyo). (**B**) Iron oxide quantification by TGA in pure O_2 atmosphere. (**C**) Analysis of SPION-CCPM^{Cy5} by AFM and TEM. (**D**) Illustrated surface grafting by the carboxyl group of the lipoic acid cross-linker in the micellar core. (**E**) Image of SPION-CCPM dispersions in MilliQ water before (left) and after dye-labeling (right).

Table 1. Analytical results of the polymer synthesis.

particle	polymer[a]	wt% Fe_2O_3[b] / %	D_h[c] / nm	D_h[d] / nm	ξ-potential[c] / mV
SPION-CCPM[Cy5]	P3, pSar$_{170}$-*b*-pCys(SO$_2$Et)$_{27}$	33.0	-	37.7	45.7
CCPM[Cy5]	P1, pSar$_{225}$-*b*-pCys(SO$_2$Et)$_{31}$	-	44	39.2	54.0

[a] pSar chain lengths relative to pSar standards, pCys(SO$_2$Et) chain lengths derived from ^{1}H NMR, [b] TGA in pure O$_2$ atmosphere, [c] single-angle DLS at a scattering angle of 173°, [d] fluorescence correlation spectroscopy.

Morphological analysis of SPION-CCPMs by atomic force microscopy (AFM) revealed spherical structures with sizes below 100 nm (Figure 1C), congruent with DLS and fluorescence correlation spectroscopy (FCS) (Table 1, Figure S10). Transmission electron microscopy (TEM) was used to elucidate the encapsulated SPION cores. SPIONs were organized in patterns of local clusters with total dimensions below 50 nm containing multiple cores each (Figure 1C, S11). The individual SPION cores showed diameters of 6 to 10 nm. In contrast, oleic acid-coated SPIONs were randomly arranged (Figure S12). Since the polymer shell could not be visualized due to large contrast discrepancies, the observed local clustering emphasizes successful encapsulation of iron oxide nanoparticles into core cross-linked polymeric micelles.[39–41] Taken together, AFM and TEM analysis affirm the structure of SPION-CCPMs as spherical nano-sized containers with multiple iron oxide nanoparticles embedded. The quantification of iron in lyophilized SPION-CCPMs was performed by thermogravimetric analysis (TGA) in a pure O$_2$ atmosphere. At these conditions, the polymeric matrix is entirely oxidized, and the remnant corresponds to iron oxide (Fe$_2$O$_3$) (Figure 1B).[42] For SPION-CCPMs, an iron oxide content of 33 weight% was determined (Table 1). Moreover, SPION-CCPMs were analyzed by Fourier transform infrared (FT-IR) spectroscopy. Characteristic peaks at 2853, 1738, and 1709 cm^{-1} corresponding to oleic acid dissipated upon encapsulation, and peaks of the polymer backbone (3470 cm^{-1}, 3275 cm^{-1} (amide N-H), 1633 cm^{-1} (amide C=O)) were detected (Figure S8), indicating complete replacement of the oleic acid-coating and successful surface functionalization by lipoic acid.[43]

The superparamagnetic nature of SPION-CCPMs was confirmed by magnetization hysteresis loops recorded at temperatures of 300 K and 5 K. No significant remanence magnetization could be detected and a blocking

temperature of 42 K was obtained corresponding to iron oxide nanoparticles with a diameter of approximately 10 nm (Figure S13).[44] Accordingly, the SPION-CCPM[Cy5] dispersion showed response to magnetic fields (Figure S14) without aggregation. In an *in vitro* setting, particles could be guided by a combined dipolar/quadrupolar magnetic field (supplementary video).[45,46] However, no signs of magnetic guidance were distinguishable in zebrafish larvae (see SI for further details).
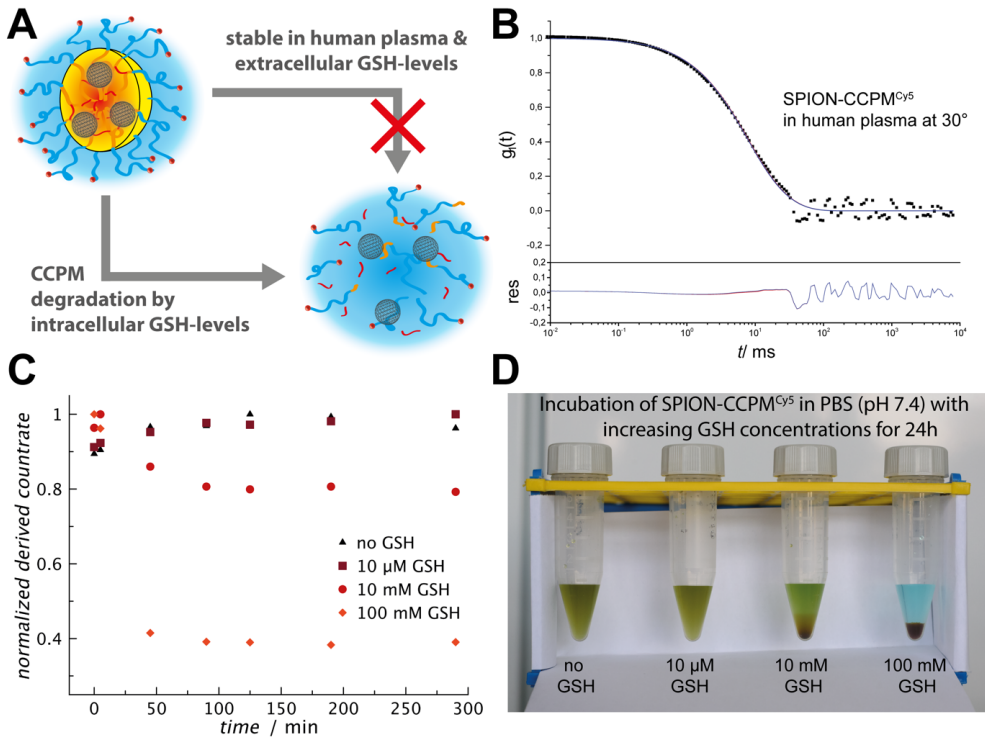
Figure 2. SPION-CCPMs display colloidal stability and stimuli-responsive degradation. (**A**) Concept of intracellular iron release inside macrophages (**B**) Multi-angle DLS of SPION-CCPM[Cy5] in undiluted human plasma: autocorrelation function $g_1(t)$ for an exemplary scattering angle of 30° together with fits with (blue line) and without (red line) additional aggregate term (upper graph), and the corresponding residuals between fit w/o aggregate and correlation function. (**C**) Glutathione (GSH)- induced particle degradation after incubation in carbonate buffer (pH 7.4) at 37 °C detected by single-angle DLS. (**D**) GSH-induced degradation performed in phosphate buffer (pH 7.4, 37 °C) after 24 h.

To account for colloidal stability, SPION-CCPMs were analyzed by multi-angle DLS in human blood plasma, following the procedure by Rausch *et al.*[47] Here, no aggregation was detected after incubation of SPION-CCPM[Cy5] in human blood plasma at a nanoparticle concentration of 0.1 g·L^{-1} (Figure 2B). Moreover, SPION-CCPM[Cy5] remained intact even during analysis by gel permeation chromatography (GPC) in hexafluoroisopropanol (Figure S8), a good solvent for pSar-*b*-pCys(SO$_2$Et) copolymers. The absence of unconjugated dye was further verified by FCS (Figure S10).[48] SPION-CCPMs[Cy5] exhibit a slightly negative ζ-potential of -5.1 mV, comparable to empty CCPMs, accounting for efficient compensation of the iron oxide surface charge by lipoic acid as well as sufficient shielding by the polysarcosine corona (Figure S8).[49] The stimuli-responsive behavior of disulfide cross-linked SPION-CCPMs was evaluated by DLS in carbonate buffer (pH 7.4) at GSH concentrations present in the endo-phagosomal compartments of macrophages.[50] At extracellular GSH levels (10 μM) the derived count rate remains constant, while a decrease was observed at intracellular GSH levels (10 mM) indicating particle degradation (Figure 2C).[35] Interestingly, when conducted in phosphate buffer (pH 7.4), precipitation of iron oxide/phosphate is observed for SPION-CCPMs treated with GSH concentrations above 10 μM (Figure 2D), exemplifying the combination of stability in blood-like conditions with triggered (redox-dependent) release of the encapsulated iron.

When tested in cell lines or primary murine and human cells, the internalization of nanoparticles was measured by intracellular fluorescent intensity using fluorescence-activated cell sorting (FACS) and fluorescence microscopy. In a co-culture of Lewis lung carcinoma cells (LLCs) and primary murine bone marrow-derived macrophages (BMDMs), SPION-CCPMs appear to sequester mainly in macrophages. *Vice versa,* LLCs accumulate more CCPMs than SPION-CCPMs (Figure 3A), suggesting that iron released from SPION-CCPMs may further reduce SPION-CCPM uptake in LLCs, in a negative feedback manner. The iron released from SPION-CCPMs likely stimulates BMDMs' uptake rate. This leads to a remarkable ~100-fold difference in relative nanoparticle uptake between the epithelial and myeloid cell type. These results indicate that SPION-CCPMs are preferably taken up by macrophages and not by other cell types (primary hepatocytes, LLCs; Figure S17). To further explore whether SPION-CCPMs release iron inside macrophages and if it is metabolically active, we analyzed the expression of iron regulatory genes in BMDMs. After 1 hour incubation, SPION-CCPMs was detected in BMDMs (Figure S18) but iron was not detected to the

same extent as BMDMs treated with a dose-matched iron source ferric ammonium citrate (FAC) (Figure 3B). After 24 hours, BMDMs treated SPION-CCPMs show iron accumulation to a similar extent as FAC treated BMDMs (Figure 3B), indicating a sustained release profile.

At the molecular level, iron accumulation decreased *transferrin receptor 1* mRNA (Tfrc) and protein expression (TFR1) (Figure 3C) also seen in BMDMs treated with FAC (20 µM) or lipopolysaccharide (LPS), which can trigger iron sequestration in pro-inflammatory macrophages.[7,11,15]

Iron accumulation in cells triggers oxidative stress and target gene expression of the oxidative stress responsive transcription factor nuclear factor E2-related factor-2(Nrf2)/BTB and CNC homolog 1 basic leucine zipper (bZIP) transcription factor 1 (Bach1) signaling pathway.[51] Expression of two Nrf2 target genes, *HO-1* (Figure 3C) and *Fpn1* (Figure 3D), are strongly induced in macrophages treated with SPION-CCPMs. At an early time point (4 hours), ROS levels induced by SPION-CCPM treatment were high in the cytoplasm and low in nuclear and mitochondrial regions (Figure 3E), suggesting that iron is released into the cytoplasm soon after nanoparticle internalization. Of note, 18 hours after SPION-CCPM treatment, ROS detection shifted to nuclear and mitochondrial compartments (Figure 3F), similar to FAC treated cells. Importantly, CCPMs did not increase ROS levels in BMDMs, suggesting that iron released from the SPION-CCPMs specifically triggers ROS production. Taken together, these data support the concept of SPION-CCPMs, which degrade slowly so that BMDMs safely handle internalized particles without detectable cellular toxicity (Figure S19). Most importantly, the released iron is metabolically active and able to alter iron metabolism and oxidative defense.

A Nanoparticle (red) Iba1(green) Merge

NT

SPION-CCPM^cy5 Mouse1

Mouse2

CCPM^cy5 Mouse1

Mouse2

20 μm

Nanoparticle intensity in co-cultured cells

Fold-change signal intensity relative to background

SPIONs-CCPMs
CCPMs

BMDM   LLC

****   ****

Ratio of SPION-CCPM to CCPM uptake

SPION-CCPMs/CCPMs

BMDMs   LLCs

****

B **Prussian Blue Iron Staining**

6 hrs

15 hrs

24 hrs

NT   FAC   SPION-CCPMs   CCPMs

20 μM

C ***Tfrc* mRNA expression**

Fold-change vs. NT

NT LPS FAC SPION-CCPMs CCPMs

****

TFR1 protein expression

NT FAC SPION-CCPMs CCPMs

TFR1 — 100 kDA
β−actin — 42 kDA
HO-1 — 33 kDA

TFR1 quantification

F.C. over β-actin

PBS FAC SPIONs-CCPMs CCPMs

*   #   *

HO-1 quantification

F.C. over β-actin

PBS FAC SPIONs-CCPMs CCPMs

***   #   *

D ***Fpn1* mRNA expression**

Fold-change vs. NT

NT LPS SPION-CCPMs CCPMs

*   #

E **Cytoplasmic ROS detection**

Fold-change signal intensity relative to NT

4 hours   18 hours

0.0754
**
*

F **Nuclear and Mitochondrial ROS detection**

Fold-change signal intensity relative to NT

NT
LPS
FAC
SPION-CCPMs
CCPMs

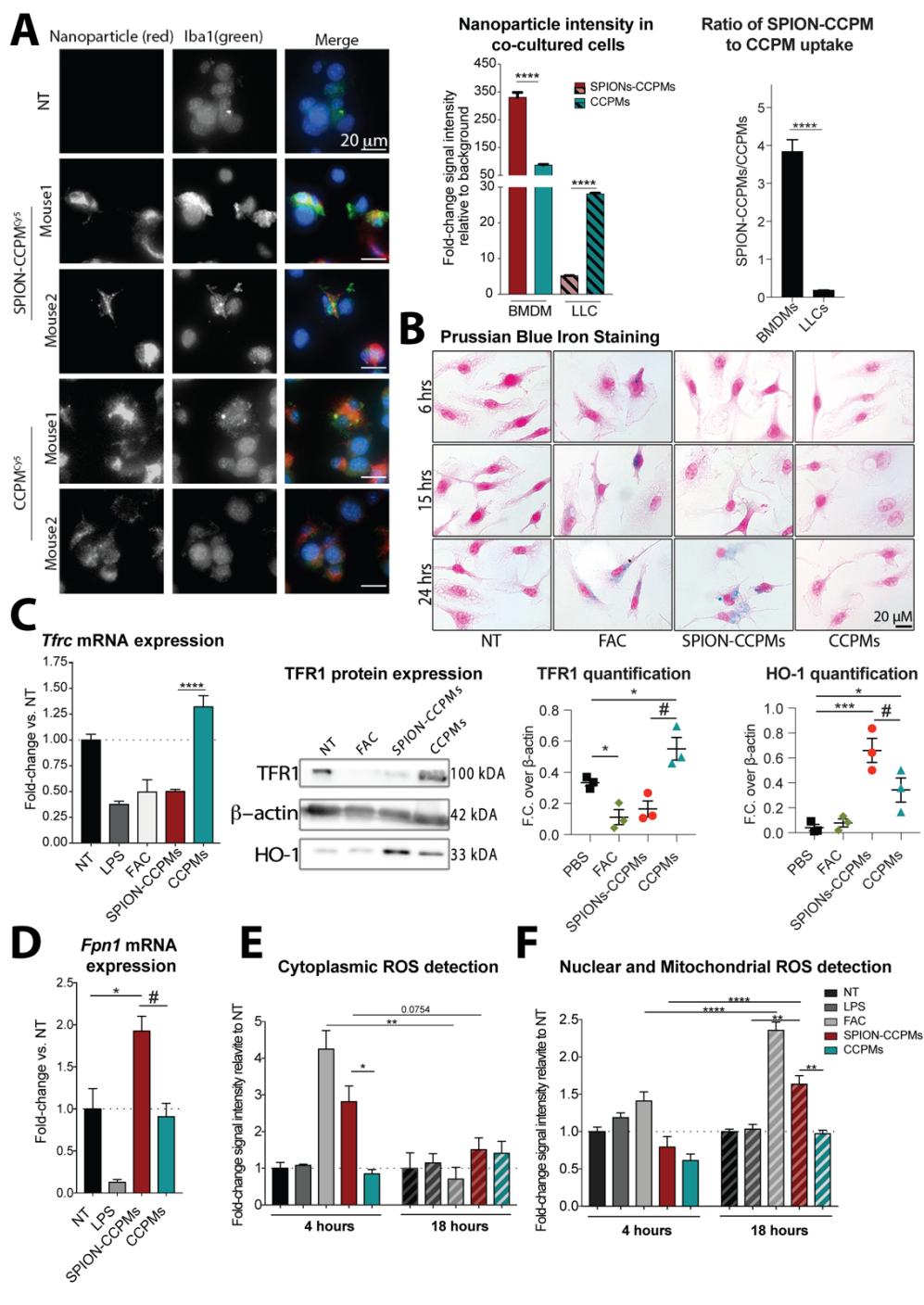4 hours   18 hours

****   ****
**
**

352

Figure 3. *In vitro* analysis of SPION-CCPMs. (**A**) Co-culture of LLCs and BMDMs incubated with SPION-CCPMs[Cy5] and CCPMs[Cy5] or not treated (NT). Representative fluorescence microscopy images and Cy5 fluorescence detection by FACS after 24 hours. (**B**) Detection of released iron by Perls' Prussian blue staining. Cells were counterstained with nuclear fast red (pink). (**C**) Detection of transferrin receptor (*Tfrc*) mRNA as well as TFR1 and heme oxygenase 1 (HO-1) protein by qPCR and western blot. mRNA expression was corrected to *Rpl19* expression. (**D**) Ferroportin (*Fpn1*) mRNA expression after 6 hours. (**E**) Cytoplasmic or nuclear and (**F**) mitochondrial ROS detection using CELLROX Orange and CELLROX Green probes in BMDMs after 4- and 18-hours. Fluorescent intensities produced by ROS probes were measured by FACS and represented as fold-change compared to non-treated (NT) condition. Data reported as n ± Standard Error of the Mean (SEM) and representative of 3 independent experiments. One-way ANOVA(*) or students t-test(#): * $p < 0.01$, ** $p < 0.001$, *** $p < 0.0001$.

The exposure of macrophages to heme or non-transferrin bound iron has been reported to activate an inflammatory state, hallmarked by increased expression of inflammatory cytokines, such as interleukin (IL)-1a/b, IL-6, and tumor necrosis factor (TNF)a, as well as elevated surface proteins, such as Cluster of Differentiation (CD) 86, CD80, and Class II major histocompatibility complex molecules (MHC II).[1,19,52] We analyzed these important markers of inflammation in BMDMs exposed to LPS or IL4, serving as positive and negative controls, respectively, and 20 μM of FAC, SPION-CCPMs, as well as the non-loaded CCPMs. BMDMs treated with SPION-CCPMs remarkably increase the expression of MHC II, CD80, CD301 and CD86, similar to LPS stimulated cells (Figure 4A). Similarly, inflammatory cytokines and enzymes, such as *Tnfa, Il6, Il1b, Nos2,* and *Cxcl10* were significantly upregulated (Figure 4B). In contrast, expression of the mannose receptor, CD206, an indicator of anti-inflammatory activation, was reduced in BMDMs exposed to SPION-CCPMs compared to those with CCPMs (Figure 4A). Notably, the specific inflammatory response to SPION-CCPMs was also reflected in human macrophages (Figure 4D, Figure S20).

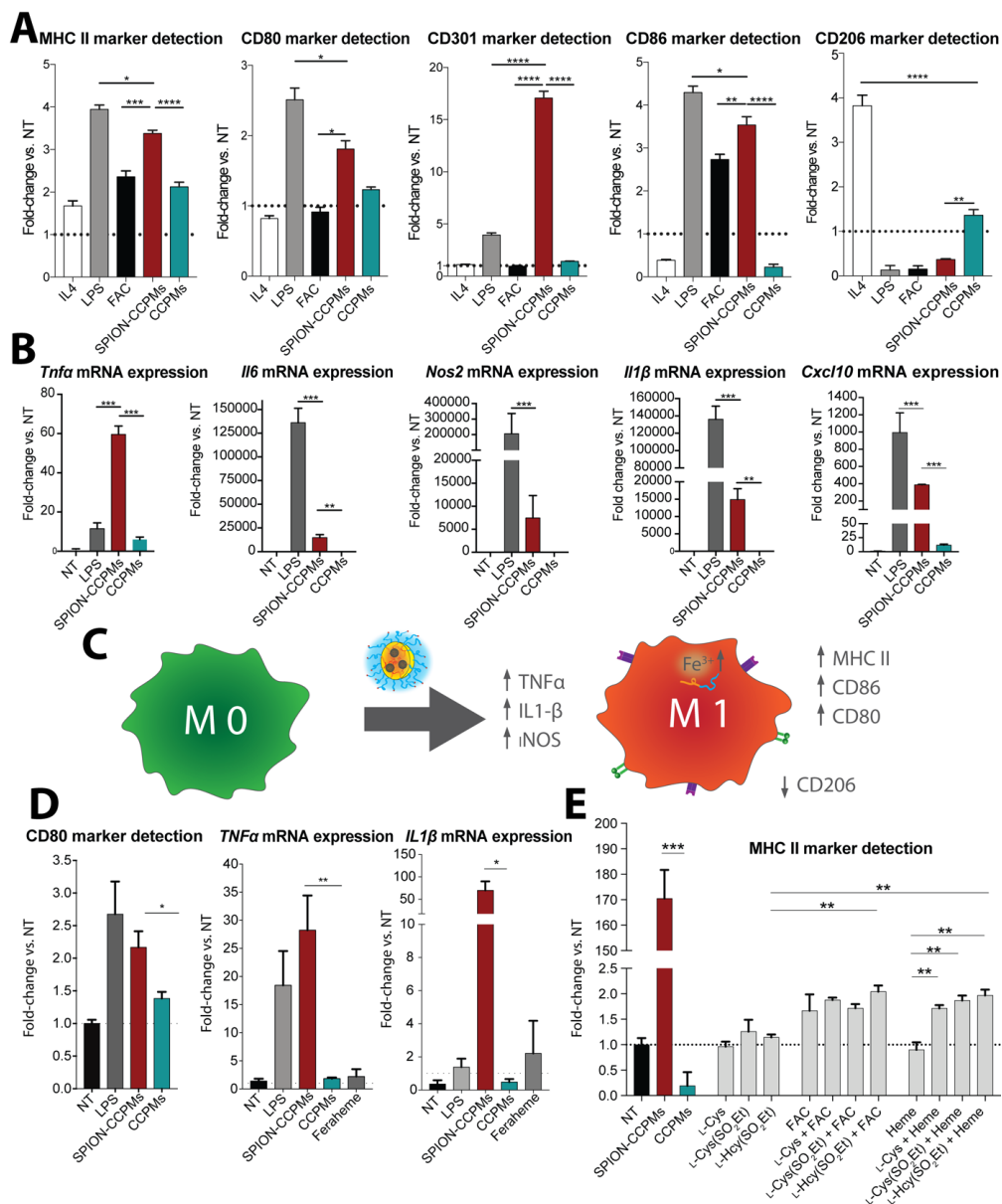**Figure 4.** SPION-CCPMs induce sterile inflammation in macrophages. (**A**) Cell surface protein expression and (**B**) mRNA expression levels of inflammatory cytokines and chemokines in primary murine BMDM after 24 or 6 hours, respectively. (**C**) Illustration of the inflammatory response. (**D**) Upregulation of inflammatory mRNA and protein expression in human macrophages. (**E**) Cell surface marker MHC II expression for

individual CCPM components. (**A-E**) All graphs represent data as fold change compared to the non-treated condition (NT) and mRNA expression were corrected to *Rpl19*. Data reported as n ± SEM and representative of 3 independent experiments. One-way ANOVA: * $p < 0.05$, ** $p < 0.01$, *** $p < 0.001$, **** $p < 0.0001$.

Iron delivery by SPION-CCPMs induces a remarkably robust pro-inflammatory response in human and murine macrophages (Figure 4), an effect that is significantly more pronounced than for feraheme (ferumoxytol) at identical iron levels. To understand the basis of this effect, we tested individual components of the polypept(o)ide-based delivery system, such as L-cysteine, *S*-ethylsulfonyl-L-cysteine (L-Cys(SO$_2$Et)) or analogous *S*-ethylsulfonyl-L-homocysteine (L-Hcy(SO$_2$Et), either alone or in combination with heme and FAC. When added with iron, L-Cys(SO$_2$Et) and L-Hcy(SO$_2$Et) induced expression of MHC II and CD86, albeit to a much lower extent than intact SPION-CCPMs (Figure 4E and S21). We thus propose that the chemical nature of the nanoparticles together with the intracellular iron release are responsible for the observed strong inflammatory responses. Examination of the gene expression changes (Figure 4) indicate sterile inflammation is triggered by SPION-CCPMs, resembling LPS-like inflammation in macrophages. Differences were observed for mRNA expression of arginase-1, Nrf2 target genes, NAD(P)H dehydrogenase (quinone) 1, and Glutathione *S*-Transferase Mu 1 (Figure S22). We thus speculate that SPION-CCPM treatment induces a combination of signaling pathways through both iron and inflammatory patterns.[22]

To verify that SPION-CCPMs can also induce inflammation *in vivo*, the nanoparticles were applied to wild-type C57Bl/6N mice (Figure 5A). Female mice, aged 6-8 weeks, were intratracheally instilled with PBS or SPION-CCPMs. At 4 h and 24 h post-treatment, mice were sacrificed and evaluated for immune cell recruitment and iron content in the lungs. Among other indications, we expect the developed SPION-CCPMs to be highly beneficial for the application as an adjuvant in cancer therapy.[1,53] Since the lungs are densely populated with macrophages and offer the advantage to apply SPION-CCPMs non-invasively to macrophages reducing off-target immune activation in other organs, intratracheal administration is a preferable application route.[12,54–57]
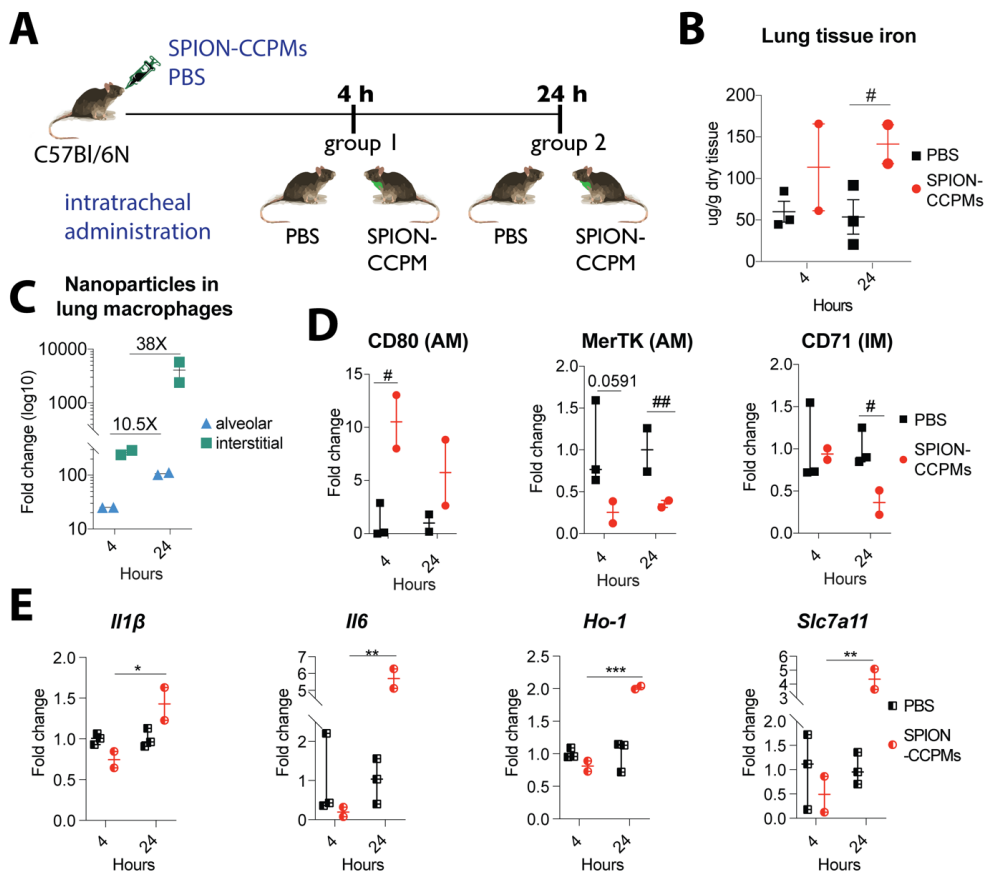
Figure 5. SPION-CCPMs induce inflammation in vivo. (**A**) C57Bl/6 mice were analyzed 4 h and 24 h after intratracheal administration of SPION-CCPMs or PBS as control. (**B**) non-heme iron levels in lung tissue. (**C**) Nanoparticle uptake in interstitial (IM) and alveolar (AM) macrophages. (**D**) Cell surface protein expression on AM and IM. (**E**) Analysis of mRNA expression of inflammatory cytokines and enzymes in total lung tissue. One-way ANOVA(*) or students' t-test (#): * $p < 0.05$, ** $p < 0.01$, *** $p < 0.001$, **** $p < 0.0001$.

We found that at 24 h after instillation, non-heme iron content increased ~3-fold in the lungs of SPION-CCPMs administered mice compared to PBS administered mice (Figure 5B). Furthermore, FACS analysis demonstrated that SPION-CCPMs could be detected in both, alveolar (AM) and interstitial (IM) macrophages as early as 4 h following application. The intensity of SPION-CCPMs increased significantly in both cell types at the 24 h time point (Figure 5C), indicating that

IM and AM are rapidly taking up SPION-CCPMs. We speculate that the difference in uptake between these two populations may be explained by their residing location within the lungs. The intratracheal instillation applied here delivers SPION-CCPMs to the bronchus of the lungs where IMs are mainly localized. This may explain the brighter SPION signal in IMs 4h after SPION-CCPMs application compared to AM that are located in the alveolar space and thus take longer time to reach.[58,59] We next evaluated the inflammatory response in the lungs of mice upon administration of either PBS or SPION-CCPMs. Cell surface marker expression in AM and IM were quantified by FACS, and mRNA expression of pro-inflammatory cytokines and enzymes were analyzed in total lung tissue. At both time points analyzed, AM showed increased expression of CD80 (a known inflammatory protein) and lacked expression of C-Mer proto-oncogene tyrosine kinase (MerTK, a protein expressed under conditions when inflammation resolves), demonstrating macrophage inflammatory activation by SPION-CCPM administration.[13,60] IM were also responsive to SPION-CCPMs, showing reduced CD71 levels at the 24 h time point indicating a time-dependent intracellular degradation of SPION-CCPMs triggering a well-known response to iron accumulation (Figure 5D). This observation parallels our findings of SPION-CCPM treatment of BMDMs in cell culture (Figure 3B,C). The inflammatory response in lung tissue was further substantiated by showing time-dependent expression of the pro-inflammatory cytokines *Il1b* and *Il6*, as well as of oxidative stress response enzymes *Ho-1* and *Slc7a11* (Figure 5E). Notably, the delayed inflammatory response program at the 24 h time point substantiates findings in cultured cells (Figure 4) that suggest that SPION-CCPMs induce inflammation distinctly from LPS.[61] Taken together, we show that SPION-CCPMs induce sterile activation of macrophages in cell-based assays and in the mouse lung, illustrating the significant potential for the activation of macrophages as an adjuvant therapy.

Conclusion

Our study demonstrates that specific delivery of an iron source to macrophages can trigger pronounced pro-inflammatory responses, both *in vitro* (primary murine and human cells) and *in vivo* (C57Bl/6N mouse model). The design concept of polypept(o)ide-based SPION-CCPMs combines steric shielding and surface functionalization of SPIONs featuring colloidal stability and stimuli-responsive degradation, whereby the iron becomes available to macrophages upon internalization within 24 hours by cleavage of the disulfide cross-links in the nanoparticle core. In primary murine and human macrophages, the sustained release of iron induces sterile inflammation as indicated by pro-inflammatory surface marker expression and cytokine secretion, resembling a shift towards an M1-like phenotype. This effect was confirmed *in vivo* following intratracheal administration of SPION-CCPMs to wild-type C57Bl/6N mice. Due to the immunomodulatory properties, SPION-CCPMs outcompete established iron oxide nanoparticles like Feraheme, making them a promising adjuvant therapy for the treatment of diseases, such as in autoimmune disorders, traumatic nerve injury, or interventions of the tumor microenvironment of solid cancers.

Experimental Section

Materials and Instrumentation: Unless stated otherwise, solvents were purchased from Sigma Aldrich. THF and n-hexane were dried over Na and freshly distilled prior to use. DMF was bought from Acros (99.8 %, Extra Dry over Molecular Sieve), freshly freeze-pumped prior to use to remove residual dimethyl amine, and handled in the absence of light. HFIP was purchased from Fluorochem, deuterated solvents from Deutero and were used as received. MilliQ water was prepared using a MILLI-Q® Reference A+ System. Water was used at a resistivity of 18.2 MΩ·cm^{-1} and total organic carbon of <5 ppm. Diphosgene was purchased from Alfa Aesar. Sarcosine was bought from Sigma Aldrich and dried in vacuum before NCA synthesis. N-tert-butoxycarbonyl (Boc)-1,2-diaminoethane and N,N-diisopropyl ethylamine (DIPEA) were purchased from Sigma Aldrich, fractionally distilled and stored at -78°C and -20°C, respectively. Oleic acid coated iron oxide nanoparticles were obtained from Sanofi-Aventis Deutschland GmbH, as well as obtained from Ocean Nanotech. D,L-Lipoic and was bought from TCI Europe. Pentafluorophenyl trifluoroacetate, tris(2-carboxyethyl)phosphine (TCEP·HCl) and acetic acid anhydride were obtained from Sigma Aldrich and used without further purification. Cyanine 5 NHS Ester was obtained from Lumiprobe GmbH.

Human blood plasma for DLS measurements was collected at the Transfusion Center of the University Clinic of Mainz (Germany) from ten healthy donors after physical examination and after obtaining informed consent in accordance with the Declaration of Helsinki. The study was approved by the local ethics committee "Landesärztekammer Rheinland-Pfalz" (837.439.12 (8540-F)). All plasma batches were stored at -20 °C.

Nuclear Magnetic Resonance: ^1H, ^{19}F and ^{13}C NMR spectra were recorded on a Bruker Avance II 400 at room temperature at a frequency of 400, 376 and 101 MHz and on a Bruker Avance III HD 300 at room temperature at a frequency of 300, 282 and 75 MHz. DOSY spectra were recorded on a Bruker Avance III HD 400 (400 MHz). Calibration of the spectra was achieved using the solvent signals. NMR spectra were analyzed with MestReNova version 12.0.4 from Mestrelab Research S.L. Degrees of polymerization (X_n) were calculated by comparing the integral of the initiator peak and the integrals of the protons for pSar and pCys(SO_2Et).

Infrared and UV-Vis Spectroscopy: Attenuated total reflectance Fourier transform infrared (ATR-FT-IR) spectroscopy was performed on a FT/IR-4100 (Jasco) with an ATR sampling accessory (MIRacle, Pike Technologies). IR spectra were analyzed using Spectra Manager 2.0 (Jasco) for integration. NCA polymerization was monitored by FT-IR spectroscopy. UV-Vis spectra were recorded using a Jasco V-630 spectrophotometer (1 cm × 1 cm quartz cell).

Gel Permeation Chromatography: Analytical GPC was performed using HFIP as eluent, which contained 3 g·L^{-1} of potassium trifluoroacetate (KOTFA) at a flow rate of 0.8 mL min^{-1} at 40°C. GPC columns were packed with modified silica (PFG-columns, particle size 7 µm, porosity 100 Å and 1000Å) purchased from Polymer Standards Service GmbH. Poly(methyl methacrylate) standards (Polymer Standards Service GmbH) and pSar standards were used for calibration and toluene was used as the internal standard.[62] A refractive index detector (G1362A RID, JASCO) and a UV detector (λ = 230nm, UV-2075+, JASCO) were used for polymer detection and analysis was performed using PSS WinGPC from PSS Polymer Standards Service GmbH.

Dynamic Light Scattering: Single-angle DLS measurements were performed with a ZetaSizer Nano ZS instrument (Malvern Instruments Ltd., Worcestershire, UK) equipped with a He-Ne laser (λ = 632.8 nm) as the incident beam. All measurements were performed at 25 °C and a detection angle of 173° unless

stated otherwise. Disposable polystyrene cuvettes (VWR, Darmstadt, Germany) were used for single-angle DLS measurements. Disposable folded capillary cells (Malvern Instruments Ltd., Worcestershire, UK) were employed for zeta potential measurements. Zeta potential measurements were conducted in solutions containing 3 mM sodium chloride. Cumulant size, polydispersity index (PDI), and size distribution (intensity weighted) histograms were calculated based on the autocorrelation function of the samples, with automated position and attenuator adjustment at multiple scans. The derived count rate was used for aggregation and dissociation experiments.

Thermogravimetric Analysis: TGA was performed on a Pyris 6 thermogravimetric analyzer (Perkin Elmer Inc.) using Pyris software. Analysis of lyophilized particle samples was performed in pure oxygen atmosphere at a heating rate of 10°C/minute from 50 to 800 °C. The mass concentration of iron was calculated from the residual iron oxide.

Atomic Force Microscopy: AFM was measured on mica using a Cypher AFM (Asylum Research) using tapping mode at a scan rate of 1 Hz. Samples were prepared by drop-casting of a particle solution ($\beta = 50$ mg $\cdot L^{-1}$ in MilliQ water) onto freshly cleaned mica. The sample was dried overnight at room temperature. The AFM images were evaluated using Gwyddion 2.49.

Transmission Electron Microscopy: TEM was performed on a FEI Tecnai G2 Spirit microscope equipped with a Gatan US1000 2k x 2k CCD camera and LaB_6 cathode operated at 120 kV. Images were recorded using freshly glow discharged carbon coated copper grids (CF300-Cu, 300 mesh). For non-stained samples, 5 µL nanoparticle solution ($\beta = 50$ mg $\cdot L^{-1}$ in MilliQ water) was drop-coated on the TEM grid surface and removed with a filter paper after 1 min. For negatively stained samples, 5 µL nanoparticle solution (b = 50 mg $\cdot L^{-1}$ in MilliQ water) was drop-coated on the TEM grid, removed with a filter paper after 1 minute. Next, 5 µL uranyl acetate solution (2 wt.% in ethanol) were added and removed after 15 s incubation time. All sample-deposited grids were air-dried overnight before measurement. Software ImageJ 1.52h (National Institutes of Health, USA) was used for image evaluation.

For cryogenic TEM (CryoTEM), 5 µL of the nanoparticle solution (50 g L^{-1}, in MilliQ water) were applied to freshly glow-discharged carbon grids with a copper 200 mesh (Quantifoil Micro Tools GmbH). Excess fluid was removed by direct blotting (2.5 s) and the grids were individually plunge-frozen in liquid ethane.

Grids were cryotransferred in liquid nitrogen using a Gatan cryoholder (model 626 DH) to a Tecnai T12 transmission electron microscope equipped with a field emission electron source and operating at 120 kV accelerating voltage. Images were recorded using a TemCam-F416 (TVIPS, Gauting, Germany). Software ImageJ 1.52h (National Institutes of Health, USA) was used for image evaluation.

Magnetic Response: Images and videos of the magnetic response and particle guidance were recorded using digital single lens reflex cameras Nikon D90 and Nikon D750.

Magnetic data of SPION-CCPMs were collected with the help of a Quantum Design MPMS-XL-7 SQUID magnetometer on powdered sample. ZFC/FC experiment were recorded in a temperature range 4 to 300 K. The sample was cooled to 4 K before applying a field of 100 Oe. The sample was heated to 300 K and subsequent cooled to 4 K with a heating/cooling rate of 1 K /min. The maximum of the ZFC magnetization curve is at ca. 42 K. Below 44 K a splitting of the ZFC/FC magnetization curve can be observed. Magnetization data were collected at 5 and 300 K with magnetic fields up to 50000 Oe.

Fluorescence Correlation Spectroscopy: FCS measurements were performed using a commercial setup, a LSM 880 microscope (Carl Zeiss, Jena, Germany). For excitation of Cy5 an He/Ne-laser (633 nm) was used. The excitation light was focused into the sample by a C-Apochromat 40x/1.2 W (Carl, Zeiss, Jena, Germany) water immersion objective. The fluorescence light was collected with the same objective and after passing through a confocal pinhole, directed to a spectral detection unit (Quasar, Carl Zeiss). The detected emission range was in the spectral range of 642-696 nm. For calibration of the detection volume Atto Fluor643® was used, as a reference dye with known diffusion coefficient.

The measurements were performed in an eight-well polystyrene-chambered coverglass (Laboratory-Tek, Nalge Nunc Internation, Penfield, NY, USA). All samples were measured twenty times with a total duration of 3 minutes. The diffusion of the fluorescent particle through the confocal observation volume caused a time-dependent intensity fluctuation, which can be analysed by an autocorrelation function:

$$G(\tau) = 1 + \frac{\langle \delta I(t) \cdot \delta I(t+\tau) \rangle}{\langle I(t) \rangle^2} \tag{1}$$

For an ensemble of *m* different types of freely diffusion fluorescent species, $G(\tau)$ has the following form:[63]

$$G(\tau) = 1 + \frac{1}{N} \sum_{i=1}^{m} \frac{f_i}{\left(1 + \frac{\tau}{\tau_{D,i}}\right) \cdot \sqrt{1 + \frac{\tau}{S^2 \cdot \tau_{D,i}}}} \tag{2}$$

N represents the average number of fluorescent species in the observation volume, $\tau_{D,i}$ is the diffusion time of the i-th species, f_i is the fraction of the i-th component and S is the so-called structure factor $S = \frac{z_0}{r_0}$, where z_0 and r_0 represent the axial and radial dimension of the confocal volume, respectively. The diffusion time $\tau_{D,i}$ relates to the diffusion coefficient D_i, through $D_i = \frac{r_0^2}{4 \cdot \tau_{D,i}}$. The hydrodynamic radii R_h can be calculated using the Stokes-Einstein relation as $R_h = \frac{k_B \cdot T}{6 \cdot \pi \cdot \eta \cdot D}$, where T is the absolute temperature, k_B the Boltzmann constant and η the viscosity of the solvent.

By fitting the experimental autocorrelation curves with Equation 2, we determined the hydrodynamic radii of the studied nanoparticles. Furthermore, their fluorescence brightness was also determined as $\langle I(t) \rangle / N$. To estimate the average number of Cy5 molecules per particle, the fluorescence brightness of the particles was divided by the fluorescence brightness of the Cy5 molecules.

Multi-Angle Dynamic Light Scattering: For multi-angle DLS cylindrical quartz cuvettes (Hellma, Mühlheim, Germany) were cleaned by dust-free distilled acetone and transferred to a dust free flow box. Light scattering measurements were performed on an ALV spectrometer consisting of a goniometer and an ALV-5004 multiple-tau full-digital correlator (320 channels) which allows measurements over an angular range from 30° to 150°. A He-Ne Laser (λ=632.8 nm) was used as light source. The correlation functions of the particles were fitted using a sum of two exponentials. The z-average diffusion coefficient D_z was calculated by extrapolating D_{app} for q = 0. By formal application of Stokes law, the inverse z-average hydrodynamic radius is $R_h = \langle R_h^{-1} \rangle_z^{-1}$ was determined. To investigate the aggregation behavior of the particles in human plasma, undiluted citrate plasma was filtered through a Millex GS 0.2 µm filter. The particle solutions were filtered through 0.45 µm pore size Millex LCR filters. The following mixtures were prepared from initial particle solutions in PBS (ß = 1 g·L⁻¹): PBS/particle solution 9:1 (ß = 0.1 g·L⁻¹), plasma/PBS 9:1 and plasma/particle solution 9:1 (ß = 0.1 g·L⁻¹). The cuvettes were incubated for 30 min at room temperature before measurement at T = 20°C. Data analysis was performed according to a procedure reported by Rausch *et al.*[47] The correlation functions of plasma were fitted with a triexponential decay function, while the particles were

fitted using a sum of two exponentials. Mixtures were fitted using a sum of both exponential decay functions with or without an additional aggregate term.

Polymer and Cross-Linker Synthesis: Polysarcosine-*block*-poly(*S*-ethylsulfonyl-L-cysteine) block copolymers were prepared by ring-opening *N*-carboxyanhydride (NCA) polymerization via bifunctional initiator approach, according to Scheme S1.[35] Results are summarized in Table S1. The synthesis of sarcosine NCA and *S*-ethylsulfonyl-L-cysteine NCA was performed as reported previously.[34,64]

Synthesis of Poly(sarcosine): Sarcosine NCA (3.00 g, 26.1 mmol, 200 eq.) was transferred into a pre-dried Schlenk-tube, dissolved in dry DMF (10 mL) and *N*-(*tert*-butoxycarbonyl)-1,2-diaminoethane (20.9 mg, 0.13 mmol, 1.0 eq.) was added *via* a stock solution in dry DMF. The clear, colorless solution was stirred at 10 °C in the absence of light until the reaction was completed after six days (as monitored by IR spectroscopy). The sarcosine amino terminus was quenched by addition perfluorophenyl 4-azidobutanoate (115 mg, 0.39 mmol, 3.0 eq) and *N,N*-diisopropylethylamine (133 µL, 0.78 mmol, 6.0 eq.). The reaction mixture was stirred overnight, followed by addition of acetic anhydride (134 µL, 1.30 mmol, 10 eq) and *N,N*-diisopropylethylamine (443 µL, 2.61 mmol, 20 eq.) to react residual end groups. The slightly yellow solution was stirred for an additional day at room temperature. Precipitation in diethyl ether yielded 1.82 g (97%) of a colorless solid. ^{1}H NMR (400 MHz, DMSO-d_6) δ [ppm] = 4.50-3.76 (m, 2nH, -CH_2-), 3.06-2.76 (m, 3nH, -CH_3), 1.37 (m, 9H, -OC(CH_3)$_3$). The chain length was determined by HFIP GPC relative to polysarcosine standards.[62]

The Boc protection group was removed in a mixture of water/trifluoro acetic acid (TFA) (1:1). The polymer (1.82g) was dissolved in water (32 mL), cooled with an ice bath, followed by addition of TFA (32 mL). After 4 h, the solution was transferred into a dialysis bag (MWCO 3.5 kDa) and dialyzed against MilliQ water, saturated sodium hydrogen carbonate solution, and MilliQ water. The aqueous solution was lyophilized, and the polymer was obtained as a colorless powder (1.65 g, 88%). ^{1}H NMR (400 MHz, DMSO-d_6) δ [ppm] = 4.50-3.76 (m, 2nH, -CH_2-), 3.06-2.76 (m, 3nH, -CH_3).

Synthesis of Poly(sarcosine)ₙ-block-poly(S-ethylsulfonyl-L-cysteine)ₘ: The poly-(sarcosine) macroinitiator (1.58 g, 0.138 mmol, 1.0 eq.) was weighed into a pre-dried Schlenk-tube and dried by azeotropic distillation with toluene in vacuo. The macroinitiator was dissolved in dry DMF (8.0 mL), cooled to -10 °C, and *S*-ethylsulfonyl-L-cysteine NCA (1.65 g, 6.90 mmol, 50 eq.) was added as a stock

solution in dry DMF. The polymerization was performed at a monomer concentration of β_{NCA} = 110 g·L^{-1} and monitored by IR spectroscopy. After 2 days, the conversion was 63 % and the reaction was stopped by precipitation in THF. The suspension was centrifuged (4500 rpm, 15 min, 4°C) and decanted. This procedure was repeated twice concluding with pure diethyl ether. The product was dried in vacuo yielding poly(sarcosine)-*block*-poly(*S*-ethylsulfonyl-L-cysteine) (2.30 g, 79%) as a colorless solid. ^{1}H NMR (400 MHz, DMSO-d_6) δ [ppm] = 8.75 (b s, 1mH, N*H*CO), 4.69 (m, 1mH, α-*H*$_{(Cys)}$), 4.49 - 3.78 (m, 2nH, -C*H*$_2$-$_{(Sar)}$), 3.69 - 3.41 (m, 4mH, -C*H*$_2$S-, -SO$_2$C*H*$_2$-), 3.06 - 2.61 (m, 3nH, -C*H*$_{3(Sar)}$), 1.30 (t, 3mH, -C*H*$_{3(Cys)}$).

Synthesis of N-(3-azidopropyl)liponamide: The synthesis of *N*-(3-azidopropyl)-liponamide was performed similar to previous reports.[35]

Pentafluorophenol lipoate (260 mg, 698 µmol, 1.0 eq.) was weight into a pre-dried Schlenk flask and dissolved in absolute DMF (5.0 mL), before *N*,*N*-diisopropylethylamine (0.712 mL, 4.19 mmol, 6.0 eq.) and 3-azido-1-propanamine (76.8 mg, 768 µmol, 1.1 eq.) were added under nitrogen flow. The solution was stirred at room temperature for 16 h. The solvent was removed in vacuo and the reaction mixture was dissolved in dichloromethane (50 mL), washed with water (2 x 50 mL) and saturated NaHCO$_3$ solution (2 x 50 mL). The organic phase was dried over MgSO$_4$, filtered and concentrated under reduced pressure. The product purified by column chromatography using dichloromethane/methanol (2%) as eluent and obtained as a yellow liquid (180 mg, 0.625 mmol, 89 %). ^{1}H NMR (400 MHz, CDCl$_3$) δ [ppm] = 5.63 (s, 1H, -CON*H*-), 3.57 (dq, ^3J = 8.5 Hz, ^3J = 6.4 Hz, 1H, dq, -SC*H*-), 3.36 (m, 4H, -NHC*H*$_2$-,-C*H*$_2$N$_3$), 3.14 (m, 2H, -SC*H*$_2$-), 2.46 (m, 1H, -SCH$_2$C*H*$_2$-), 2.18 (td, ^3J = 7.4 Hz, ^3J = 1.2 Hz, 2H, α-C*H*$_2$), 1.91 (m, 1H, -SCH$_2$C*H*$_2$-), 1.80 (p, ^3J = 6.6 Hz, 2H, -C*H*$_2$CH$_2$N$_3$), 1.67 (m, 4H, ß-C*H*$_2$, δ-C*H*$_2$), 1.46 (m, 2H, γ-C*H*$_2$). ESI-MS m/z = 289.1 [M+H]$^+$, ([M+H]$^+$, (calc.) 289.1 g·mol^{-1}).

Synthesis of SPION-Loaded Core Cross-Linked Polymeric Micelles: Oleic acid-coated superparamagnetic iron oxide nanoparticles (SPIONs) (ß = 5.8 g L^{-1}, 9.0 mL) dispersed in hexanes were precipitated into 40 mL of ethanol, sonicated for 15 minutes and sedimented (4500 rpm, 15 min, 20°C). The pellet was resuspended in 5.0 mL of chloroform, sonicated for 30 minutes, precipitated in 45 mL of ethanol, and sedimented (4500 rpm, 15 min, 20°C) to remove excess oleic acid. SPIONs were resuspended in 20 mL of chloroform and a polymer solution in DMSO/CHCl$_3$ (1:2) (ß = 5.0 g L^{-1}, 10 mL) was added dropwise. The resulting clear

brown solution was placed in a dialysis bag (MWCO 3.5 kDa) and dialyzed against CHCl$_3$, followed by dialysis against DMSO. The solution was diluted with DMSO by factor 2 and dialyzed against MilliQ water to obtain SPION-loaded polymeric micelles. The obtained micelles were filtered through a PVDF 0.45 µm filter and concentrated to a total volume of 8.0 mL by spin filtration (Amicon Ultra-15, MWCO 3.0 kDa, 4500 rpm, 20°C). For core cross-linking, D,L-lipoic acid (8.0 mg, 39.1 mmol, 0.5 eq. per pCys(SO$_2$Et) repeating unit) was dissolved in ethanol (5.0 g L^{-1}) and treated with tris(2-carboxyethyl)phosphine hydrochloride (11.2 mg, 39.1 mmol, 50 g L^{-1} in MilliQ water) for 18 h yielding dihydro lipoic acid. The cross-linker solution was added to the micelle solution and the reaction mixture was placed on a benchtop shaker for 24 h. Subsequently, excess cross-linker and residual oleic acid were removed by dialysis (MWCO 3.5 kDa) against DMSO/MilliQ water mixtures (1:1) followed by dialysis against MilliQ water yielding a clear light brown solution. For dye conjugation, the SPION-CCPM solution was adjusted to pH 7.4 using 1 M sodium hydrogen carbonate solution, Cy5-NHS ester (540 µg, 0.3 eq. per polymer, 25 g L^{-1} in DMSO) was added, and the solution was stirred at room temperature for 72 h. Upon addition of the blue dye solution, the particle solution turned dark green immediately. The excess dye was removed by repetitive extraction with dichloromethane, followed by dialysis against ethanol/MilliQ water mixtures (1:1) and MilliQ water (MWCO 6-8 kDa). To remove the free polymer, Cy5-labelled SPION-loaded core cross-linked polymeric micelles (SPION-CCPM^{Cy5}) were purified by repetitive spin filtration (Amicon Ultra-15, MWCO 100 kDa, 3000 rpm, 20°C), and finally concentrated to a total volume of 8.5 mL, yielding 23 mg of SPION-CCPM^{Cy5} (overall yield 23%).

Synthesis of Core Cross-Linked Polymeric Micelles (Control-Particles): The preparation of core cross-linked polymeric micelles was performed as described previously.[35,37]

Poly(sarcosine)-*block*-poly(*S*-ethylsulfonyl-L-cysteine) (pSar$_{225}$-*b*-pCys(SO$_2$Et)$_{31}$) was dissolved in dimethyl sulfoxide (DMSO) equipped with 1 M thiourea at a concentration of 7.5 g·L^{-1} for 1 h. Next, 20 vol.% of 1 mM acetate buffer (pH 4.75) with 10 mM thiourea were added to adjust the concentration to 6.6 g·L^{-1}. The solution was left to equilibrate at room temperature for 5 h, followed by dialysis against 1 mM acetate buffer (pH 4.75) with 10 mm thiourea. The solution was filtered (GHP 450) and concentrated to 6.6 g·L^{-1} by spin filtration (Amicon Ultra, MWCO 3 kDa), yielding the micelle solution. For cross-linking, in a separate flask, *N*-3-azidopropyl liponamide was dissolved in ethanol at a concentration of ß =

$10 \text{ g} \cdot \text{L}^{-1}$ and one equivalent of an aqueous solution of tris(2-carboxyethyl)phosphine hydrochloride (TCEP·HCl) ($50 \text{ g} \cdot \text{L}^{-1}$) was added per disulfide. After 18 h, the cross-linker solution was added to the micelle solution at equimolar amounts of thiols per cysteines. The reaction mixture was allowed to stand at room temperature for 48 h. To remove residual cross-linker and free polymer, the solution was dialyzed against DMSO and MilliQ water (MWCO 6-8 kDa), followed by repetitive spin filtration (Amicon Ultra, MWCO 100 kDa). For labelling, the pH was adjusted to 7.4 (1 m NaHCO₃ solution) and 0.3 equivalents of Cyanine 5-NHS-ester stock solution in DMSO ($25 \text{ g} \cdot \text{L}^{-1}$) were added per polymer end-group. After 72 h, excess dye was removed by repetitive spin filtration (Amicon Ultra, 100 kDa) using ethanol/water mixtures and the final particle solution (in MilliQ water) was stored at 4°C. The absence of free polymer and free dye was verified by gel permeation chromatography in hexafluoro isopropanol.

Isolation of Bone Marrow-Derived Macrophages: The procedure conducted follows previously established protocol.[65] Briefly, bone marrow cells were flushed from the tibia and femurs of C57BL/6N wild-type mice (8-10 weeks of age) using ice cold HBSS, filtered through a 70 µm filter cell strainer and plated at a density of 3.5×10^5 cells/ml. Cells were differentiated for one-week using RPMI medium supplemented with 10 ng/mL M-CSF (M9170, Sigma-Aldrich), 10 % fetal bovine serum (FBS) and 1 % penicillin/streptomycin (Gibco). For each independent experiment, BMDMs were prepared from three different mice.

Cell Lines: LLC cells were regularly tested for mycoplasma contamination and authenticated by visual observations of cell morphology. Cells were cultured in Roswell Park Memorial Institute Medium (RPMI, Life Technologies) containing 10 % FBS and 1 % penicillin/streptomycin.

Hepatocyte Isolation: Hepatocytes from C57BL/6N wild-type mice (8-10 weeks of age) were prepared following a standard two-step perfusion method.[66–68] Briefly, liver perfusion (Life Technologies #17701038) and liver digest medium (Life Technologies #17703-034) were pumped into the liver through the cava vein with a $5 \text{ mL} \cdot \text{min}^{-1}$ flux rate. The liver capsule was mechanically disrupted in hepatocyte wash medium (Life Technologies #17704-024). The cell suspension obtained was passed through 100 µm filter and centrifuged for 5 minutes at 50 G and 4°C. The pellet of hepatocytes was resuspended in William's E medium (Life Technologies #32551-020) supplemented with 4% FBS and 2.50×10^5 cells $\cdot \text{mL}^{-1}$

were plated on 13 mm collagen-coated (Life Technologies #A1048301) glass cover slips.

Mice: 10 female C57Bl/6 mice, aged 6-8 weeks, were housed in specific pathogen-free conditions under constant light-dark cycle and maintained on a standard mouse diet. Experimentation was performed at the DKFZ animal facilities, in accordance with institutional guidelines, and were approved by the Regierungspräsidium Karlsruhe, Germany, under permit number G214/19. Mice were anaesthetized by intraperitoneal injection of 100 µg·g^{-1} ketamine and 14 µg·g^{-1} xylazine and intratracheally instilled with SPION-CCPM (10 mg·kg^{-1} of iron to body weight) or PBS in a final volume of 50 µL.

Immunofluorescence: BMDMs were plated on 13 mm collagen-coated (Life Technologies #A1048301) glass cover slips in a density of 1.0 x 10^5 cells/slip. After treatment, cells were washed three times with phosphate-buffered saline (PBS) and fixed with 4% paraformaldehyde for 15 minutes at room temperature. Cells were then washed three times with PBS and blocked with 2.5% milk in PBS-T (0.1% Tween) solution for 30 minutes on an orbital shaker. Slips were then washed three times with 0.1% PBS-T and incubated with primary antibody Iba1 (NB100-1028SS, Bio Techne) overnight at 4°C or 1 hour at room temperature. After washing with PBS-T, samples were incubated with secondary antibody (A-11057, Donkey anti-Goat IgG (H+L) Cross-adsorbed Secondary Antibody Alexa Fluor 568, Life Technologies) for 1 hour at room temperature. Slips were then washed with PBS and mounted using Prolong Gold Antifade Mountant with DAPI (P36931, Life Technologies). Samples were acquired at the University of Heidelberg Nikon Imaging Centre using a Ni-E confocal microscope. Images were analysed using Fiji (National Institute for Health) using a written macro for intracellular quantification of the Cy5+ signal. Images were compiled into figures using Adobe Photoshop and Illustrator.

Flow Cytometry: Mouse lungs were resected and washed in PBS. Single cell suspensions (200 µL) were generated by applying chemical and mechanical digestion using the Miltenyi Lung Dissociation Kit and pelleted by centrifugation for 5 mins at 300G. Cells were then washed with FACS Buffer (1% fetal bovine serum, 2.5 mM 1M HEPES, 1 mM EDTA) prior to antibody staining. Cells were stained with anti-mouse CD45-PERCPCy5.5 (BD Biosciences), LY6G-FITC (BioLegend, California, USA), LY6C-PEDAZZLE (BD Biosciences), F4/80-BV605 (BioLegend, California, USA), CD11C-PE (BioLegend, California, USA),

SIGLECF-APCCY7 (BD Biosciences), CD11B-PERCP (BD Biosciences), CD64-BV711 (BioLegend, California, USA), CD80-BV650 (BioLegend, California, USA), CD71-BV510 (BioLegend, California, USA), MERTK-BV421 (BD Biosciences) and the viability stain DAPI (BioLegend, California, USA). Samples were acquired using Cytotek Aurora flow cytometer at the EMBL Flow Cytometry Core Facility and analysis was performed using the FlowJo Software (Tree Star Inc).

BMDMs were incubated with Fc-γ receptor blocking solution and stained with anti-mouse CD206-FITC, CD86-PE, MHC II-PeCy5 (BioLegend, California, USA), CD301-PerCPCy5.5, CD38-FITC (BD Biosciences) and the viability staining solution 7AAD (420404, Biozol) (see Table S3). Data were acquired using a FACS Fortessa (BD, Biosciences) or Cytotek Aurora flow cytometer at the EMBL Flow Cytometry Core Facility and analysis was performed using the FlowJo Software (Tree Star Inc). The expression of surface markers in mouse lung cells and BMDM was calculated by subtracting the geometric median fluorescence intensity (MFI) of cells stained with the isotype-matched antibody from the MFI of those stained with the specific antibody and is shown as fold-change compared to the non-treated (NT) control.

Tissue Non-Heme Iron Measurement: Lungs of mice were measured for non-heme iron content using the bathophenantroline method and calculated against dry weight of tissue.[69]

Cytotoxicity: BMDM viability was quantified using CytoTox96 kit from Promega. Cells were plated in a black side/black bottom 96 well plate at a concentration of 10,000 cells in 100 µL/well 24 hours before start of the experiment. To measure LDH release into the supernatant, plate was centrifuged at 500 G for 10 mins to sediment cells and 100 µL was transferred to a new 96 well plate. 50 µL of substrate was added to 50 µL of supernatant and incubated for 30 minutes at room temperature in the dark. After 30 minutes, 20 µL stop solution was added to each well and the 490 nm signal was measured in a spectrofluorimeter (SpectraMax, Molecular Devices). Viability was calculated by subtracting the media blank from experimental values and normalized to the non-treated condition (NT). To measure redox capacity, after incubation times with conditions, 10 µL of Celltiter Blue was added to each well and plate was incubated at 37°C for 4 hours. Absorbance was then measured at 520 nm and all values were subtracted from the media blank control and normalized to the non-treated condition (NT).

RNA extraction, Reverse Transcription, and Quantitative Real-Time Polymerase Chain Reaction Analysis: RNA was extracted from lung tissue using Trizol (Life Technologies). RNA was extracted from BMDMS using the RNeasy Mini Kit (74134, Qiagen). 0.5 to 1 µg of total RNA was reverse transcribed by using RevertAid H Minus Reverse Transcriptase (FERMEP0452, Thermo Scientific), random primers (48190-011, Invitrogen) and dNTPs (R0193, ThermoScientific). SYBR green qRT-PCR was performed on a Step One Plus Real Time PCR System (Applied Biosystems, California, USA). Primers and probes were designed using the ProbeFinder software (www.roche-applied-science.com) (See Table S4). Differences in Relative Quantity (RQ) are shown as fold-change compared to the control condition (untreated cells, NT).

Measurement of Intracellular ROS Accumulation: Accumulation of ROS in BMDM cells was assessed by using the oxidant-sensitive fluorescent dye CELLROX™ Green and CELLROX™ Orange (Life Technologies). Upon cellular uptake, the non-fluorescent CELLROX™ probe undergoes deacetylation by intracellular esterases producing a highly green fluorescent signal following oxidation by intracellular ROS. BMDMs were maintained untreated or were treated for 4 or 18 hours with 20 µM SPION-CCPMs, CCPMs, 100 ng·mL^{-1} lipopolysaccharide (LPS) or interferon-γ, 20 µM ferric ammonium citrate (FAC), or 20 µM heme. The amount of SPION-CCPMs added to cells was calculated to 20 µM iron from within the core. Then the amount of CCPMs added to cells was calculated to match the mass of CCPMs contained within added SPION-CCPMs. 2.5 mM of CELLROX™ Green or Orange was added to cells and incubated for 30 minutes at 37 °C under 5% CO_2 atmosphere. Cells were washed twice with Hanks' Balanced Salt Solution (HBSS) and fluorescence intensity was measured using FACS. Fluorescence intensity is represented as fold change compared to the non-treated condition (NT).

Protein Extraction and Western Blotting: Protein lysates were obtained by homogenizing cells in RIPA buffer supplemented with protease inhibitors (Roche Diagnostics). Protein concentration was determined using the DC™ Protein Assay Kit II system (5000112, Bio-Rad, München, Germany). 50 µg of total protein extracts were separated by 12% SDS-PAGE and analyzed by Western blotting using antibodies against HO-1 (Stressgen, Victoria, Canada) or TfR1 (136800, Invitrogen/Life Tech). ß-actin (A1978-200UL, Sigma-Aldrich) was used as a loading control. Densitometric analysis is reported in Arbitrary Unit (AU), as ratio to the untreated (NT) sample (AU=1). Western blot images were

quantitatively acquired with the Vilber Lourmat Fusion-FX Chemiluminescence system (Eberhardzell).

Pearls' Prussian Blue Staining: 3.5×10^5 BMDMs were plated on a 13 mm (Life Technologies #A1048301) glass slips. After incubation or treatment, cells were washed three times with PBS and fixed with 4% paraformaldehyde at room temperature for ten minutes. Cells were then washed three times with PBS and stained with Accustain Iron Stain No. HT20 (Sigma-Aldrich) following manufacturer's instructions and counterstained with Fast Red (Sigma Aldrich). Samples were mounted using the water-soluble mounting agent VectaMount (H5501, Biozol). Images were digitally acquired with a Nikon Ni-E microscope, using the Nikon NIS-Elements Viewer software and assembled into figures using Adobe Photoshop and Illustrator software packages.

Buffy Coat Preparation: Human monocytes were isolated from commercially available buffy coats (DRK-Blutspendedienst Baden-Württemberg-Hessen, Frankfurt, Germany) using Ficoll-Hypaque gradients (LSM-1077; PAA Laboratories). Monocytes were differentiated into primary human macrophages with RPMI 1640 containing 5% AB-positive human serum (DRK-Blutspendedienst) for 7 days and achieved approximately 80% confluence. 24 hours prior to stimulation, cells were serum starved. Cells were then prepared to analyze cell surface expression of proteins by FACS measurement (antibodies in Table S3) or differential mRNA expression by qPCR (primers in Table S5).

Statistical Analysis: Data are shown as mean ± SEM. Statistical analyses were performed using Prims v10 (GraphPad Software, La Jolla, CA). One-way ANOVA was used and p-values < 0.05 (*), < 0.01 (**), < 0.001 (***) and < 0.0001 (****) are indicated.

Acknowledgement

Conflict of Interest

T.A.B., N.K.H., M.U.M., M.W.H., and M.B. have submitted the patent application "SPION-CCPM; Nanoparticles Comprising Iron Oxide Particles Embedded in Polymeric Micelles" EP20210176.2.

References

(1)   Costa da Silva, M.; Breckwoldt, M. O.; Vinchi, F.; Correia, M. P.; Stojanovic, A.; Thielmann, C. M.; Meister, M.; Muley, T.; Warth, A.; Platten, M.; Hentze, M. W.; Cerwenka, A.; Muckenthaler, M. U. Iron Induces Anti-Tumor Activity in Tumor-Associated Macrophages. *Front. Immunol.* **2017**, *8* (November).

(2)   Ardura, J. A.; Rackov, G.; Izquierdo, E.; Alonso, V.; Gortazar, A. R.; Escribese, M. M. Targeting Macrophages: Friends or Foes in Disease? *Front. Pharmacol.* **2019**, *10* (October), 1–8.

(3)   Chinetti-Gbaguidi, G.; Staels, B. Macrophage Polarization in Metabolic Disorders. *Curr. Opin. Lipidol.* **2011**, *22* (5), 365–372.

(4)   Tangudu, N. K.; Alan, B.; Vinchi, F.; Wörle, K.; Lai, D.; Vettorazzi, S.; Leopold, K.; Vujić Spasić, M. Scavenging Reactive Oxygen Species Production Normalizes Ferroportin Expression and Ameliorates Cellular and Systemic Iron Disbalances in Hemolytic Mouse Model. *Antioxid. Redox Signal.* **2018**, *29* (5), 484–499.

(5)   Ruffell, B.; Coussens, L. M. Macrophages and Therapeutic Resistance in Cancer. *Cancer Cell* **2015**, *27* (4), 462–472.

(6)   Murray, P. J. Macrophage Polarization. *Annu. Rev. Physiol.* **2017**, *79*, 541–566.

(7)   Cairo, G.; Recalcati, S.; Mantovani, A.; Locati, M. Iron Trafficking and Metabolism in Macrophages: Contribution to the Polarized Phenotype. *Trends Immunol.* **2011**, *32* (6), 241–247.

(8)   Bao, Y.; Sherwood, J. A.; Sun, Z. Magnetic Iron Oxide Nanoparticles as: T 1 Contrast Agents for Magnetic Resonance Imaging. *J. Mater. Chem. C* **2018**, *6* (6), 1280–1290.

(9)   Mebius, R. E.; Kraal, G. Structure and Function of the Spleen. *Nat. Rev. Immunol.* **2005**, *5* (8), 606–616.

(10)   Sica, A.; Mantovani, A. Macrophage Plasticity and Polarization: In Vivo Veritas. *J. Clin. Invest.* **2012**, *122* (3), 787–795.

(11)   Lewis, C. E.; Pollard, J. W. Distinct Role of Macrophages in Different Tumor

Microenvironments. *Cancer Res.* **2006**, *66* (2), 605–612.

(12)   Guerriero, J. L. Macrophages: The Road Less Traveled, Changing Anticancer Therapy. *Trends Mol. Med.* **2018**, *24* (5), 472–489.

(13)   Davra, V.; Kimani, S.; Calianese, D.; Birge, R. Ligand Activation of TAM Family Receptors-Implications for Tumor Biology and Therapeutic Response. *Cancers (Basel).* **2016**, *8* (12), 107.

(14)   Recalcati, S.; Locati, M.; Marini, A.; Santambrogio, P.; Zaninotto, F.; De Pizzol, M.; Zammataro, L.; Girelli, D.; Cairo, G. Differential Regulation of Iron Homeostasis during Human Macrophage Polarized Activation. *Eur. J. Immunol.* **2010**, *40* (3), 824–835.

(15)   Sukhbaatar, N.; Weichhart, T. Iron Regulation: Macrophages in Control. *Pharmaceuticals* **2018**, *11* (4), 137.

(16)   Hentze, M. W.; Muckenthaler, M. U.; Galy, B.; Camaschella, C. Two to Tango: Regulation of Mammalian Iron Metabolism. *Cell* **2010**, *142* (1), 24–38.

(17)   Muckenthaler, M. U.; Rivella, S.; Hentze, M. W.; Galy, B. A Red Carpet for Iron Metabolism. *Cell* **2017**, *168* (3), 344–361.

(18)   Vinchi, F.; Costa da Silva, M.; Ingoglia, G.; Petrillo, S.; Brinkman, N.; Zuercher, A.; Cerwenka, A.; Tolosano, E.; Muckenthaler, M. U. Hemopexin Therapy Reverts Heme-Induced Proinflammatory Phenotypic Switching of Macrophages in a Mouse Model of Sickle Cell Disease. *Blood* **2016**, *127* (4), 473–486.

(19)   Zanganeh, S.; Hutter, G.; Spitler, R.; Lenkov, O.; Mahmoudi, M.; Shaw, A.; Pajarinen, J. S.; Nejadnik, H.; Goodman, S.; Moseley, M.; Coussens, L. M.; Daldrup-Link, H. E. Iron Oxide Nanoparticles Inhibit Tumour Growth by Inducing Pro-Inflammatory Macrophage Polarization in Tumour Tissues. *Nat. Nanotechnol.* **2016**, *11* (11), 986–994.

(20)   Wang, G.; Zhao, J.; Zhang, M.; Wang, Q.; Chen, B.; Hou, Y.; Lu, K. Ferumoxytol and CpG Oligodeoxynucleotide 2395 Synergistically Enhance Antitumor Activity of Macrophages against NSCLC with EGFRL858R/T790M Mutation. *Int. J. Nanomedicine* **2019**, *14*, 4503–4515.

(21)   Zhao, J.; Zhang, Z.; Xue, Y.; Wang, G.; Cheng, Y.; Pan, Y.; Zhao, S.; Hou, Y. Anti-Tumor Macrophages Activated by Ferumoxytol Combined or Surface-Functionalized with the TLR3 Agonist Poly (I : C) Promote Melanoma Regression. *Theranostics* **2018**, *8* (22), 6307–6321.

(22)   Jin, R.; Liu, L.; Zhu, W.; Li, D.; Yang, L.; Duan, J.; Cai, Z.; Nie, Y.; Zhang, Y.; Gong, Q.; Song, B.; Wen, L.; Anderson, J. M.; Ai, H. Iron Oxide Nanoparticles Promote Macrophage Autophagy and Inflammatory Response through Activation of Toll-like Receptor-4 Signaling. *Biomaterials* **2019**, *203*, 23–30.

(23)   Trujillo-Alonso, V.; Pratt, E. C.; Zong, H.; Lara-Martinez, A.; Kaittanis, C.; Rabie, M. O.; Longo, V.; Becker, M. W.; Roboz, G. J.; Grimm, J.; Guzman, M. L. FDA-Approved Ferumoxytol Displays Anti-Leukaemia Efficacy against Cells with Low Ferroportin Levels. *Nat. Nanotechnol.* **2019**, *14* (6), 616–622.

(24)   El-Boubbou, K. Magnetic Iron Oxide Nanoparticles as Drug Carriers: Clinical Relevance. *Nanomedicine* **2018**, *13* (8), 953–971.

(25)   Balakrishnan, V. S.; Rao, M.; Kausz, A. T.; Brenner, L.; Pereira, B. J. G.; Frigo, T. B.; Lewis, J. M. Physicochemical Properties of Ferumoxytol, a New Intravenous Iron

Preparation. *Eur. J. Clin. Invest.* **2009**, *39* (6), 489–496.

(26)   EMA. *Rienso Withdrawal of the Marketing Authorization in the European Union*; EMA/43791/2015; 2015.

(27)   Dadfar, S. M.; Roemhild, K.; Drude, N. I.; von Stillfried, S.; Knüchel, R.; Kiessling, F.; Lammers, T. Iron Oxide Nanoparticles: Diagnostic, Therapeutic and Theranostic Applications. *Adv. Drug Deliv. Rev.* **2019**, *138*, 302–325.

(28)   Weissleder, R.; Stark, D.; Engelstad, B.; Bacon, B.; Compton, C.; White, D.; Jacobs, P.; Lewis, J. Superparamagnetic Iron Oxide: Pharmacokinetics and Toxicity. *Am. J. Roentgenol.* **1989**, *152* (1), 167–173.

(29)   Lu, M.; Cohen, M. H.; Rieves, D.; Pazdur, R. FDA Report: Ferumoxytol for Intravenous Iron Therapy in Adult Patients with Chronic Kidney Disease. *Am. J. Hematol.* **2010**, *85* (5), NA-NA.

(30)   Toth, G. B.; Varallyay, C. G.; Horvath, A.; Bashir, M. R.; Choyke, P. L.; Daldrup-Link, H. E.; Dosa, E.; Finn, J. P.; Gahramanov, S.; Harisinghani, M.; Macdougall, I.; Neuwelt, A.; Vasanawala, S. S.; Ambady, P.; Barajas, R.; Cetas, J. S.; Ciporen, J.; DeLoughery, T. J.; Doolittle, N. D.; Fu, R.; Grinstead, J.; Guimaraes, A. R.; Hamilton, B. E.; Li, X.; McConnell, H. L.; Muldoon, L. L.; Nesbit, G.; Netto, J. P.; Petterson, D.; Rooney, W. D.; Schwartz, D.; Szidonya, L.; Neuwelt, E. A. Current and Potential Imaging Applications of Ferumoxytol for Magnetic Resonance Imaging. *Kidney Int.* **2017**, *92* (1), 47–66.

(31)   Birke, A.; Ling, J.; Barz, M. Polysarcosine-Containing Copolymers: Synthesis, Characterization, Self-Assembly, and Applications. *Prog. Polym. Sci.* **2018**, *81*, 163–208.

(32)   Klinker, K.; Barz, M. Polypept(o)Ides: Hybrid Systems Based on Polypeptides and Polypeptoids. *Macromol. Rapid Commun.* **2015**, *36* (22), 1943–1957.

(33)   Sevier, C. S.; Kaiser, C. A. Formation and Transfer of Disulphide Bonds in Living Cells. *Nat. Rev. Mol. Cell Biol.* **2002**, *3* (11), 836–847.

(34)   Birke, A.; Huesmann, D.; Kelsch, A.; Weilbächer, M.; Xie, J.; Bros, M.; Bopp, T.; Becker, C.; Landfester, K.; Barz, M. Polypeptoid- Block -Polypeptide Copolymers: Synthesis, Characterization, and Application of Amphiphilic Block Copolypept(o)ides in Drug Formulations and Miniemulsion Techniques. *Biomacromolecules* **2014**, *15* (2), 548–557.

(35)   Klinker, K.; Schäfer, O.; Huesmann, D.; Bauer, T.; Capelôa, L.; Braun, L.; Stergiou, N.; Schinnerer, M.; Dirisala, A.; Miyata, K.; Osada, K.; Cabral, H.; Kataoka, K.; Barz, M. Secondary-Structure-Driven Self-Assembly of Reactive Polypept(o)Ides: Controlling Size, Shape, and Function of Core Cross-Linked Nanostructures. *Angew. Chemie Int. Ed.* **2017**, *56* (32), 9608–9613.

(36)   Talelli, M.; Barz, M.; Rijcken, C. J. F. F.; Kiessling, F.; Hennink, W. E.; Lammers, T. Core-Crosslinked Polymeric Micelles: Principles, Preparation, Biomedical Applications and Clinical Translation. *Nano Today* **2015**, *10* (1), 93–117.

(37)   Dal, N. K.; Kocere, A.; Wohlmann, J.; Van Herck, S.; Bauer, T. A.; Resseguier, J.; Bagherifam, S.; Hyldmo, H.; Barz, M.; De Geest, B. G.; Fenaroli, F. Zebrafish Embryos Allow Prediction of Nanoparticle Circulation Times in Mice and Facilitate Quantification of Nanoparticle–Cell Interactions. *Small* **2020**, *16* (5), 1906719.

(38)   Ojha, T.; Hu, Q.; Colombo, C.; Wit, J.; Geijn, M.; Steenbergen, M. J.; Bagheri, M.;

König-Werner, H.; Buhl, E. M.; Bansal, R.; Shi, Y.; Hennink, W. E.; Storm, G.; Rijcken, C. J. F.; Lammers, T. Lyophilization Stabilizes Clinical-stage Core-crosslinked Polymeric Micelles to Overcome Cold Chain Supply Challenges. *Biotechnol. J.* **2021**, *16* (6), 2000212.

(39) Kim, B.-S.; Qiu, J.-M.; Wang, J.-P.; Taton, T. A. Magnetomicelles: Composite Nanostructures from Magnetic Nanoparticles and Cross-Linked Amphiphilic Block Copolymers. *Nano Lett.* **2005**, *5* (10), 1987–1991.

(40) Talelli, M.; Rijcken, C. J. F.; Lammers, T.; Seevinck, P. R.; Storm, G.; van Nostrum, C. F.; Hennink, W. E. Superparamagnetic Iron Oxide Nanoparticles Encapsulated in Biodegradable Thermosensitive Polymeric Micelles: Toward a Targeted Nanomedicine Suitable for Image-Guided Drug Delivery. *Langmuir* **2009**, *25* (4), 2060–2067.

(41) Schmidtke, C.; Eggers, R.; Zierold, R.; Feld, A.; Kloust, H.; Wolter, C.; Ostermann, J.; Merkl, J. P.; Schotten, T.; Nielsch, K.; Weller, H. Polymer-Assisted Self-Assembly of Superparamagnetic Iron Oxide Nanoparticles into Well-Defined Clusters: Controlling the Collective Magnetic Properties. *Langmuir* **2014**, *30* (37), 11190–11196.

(42) Amstad, E.; Zurcher, S.; Mashaghi, A.; Wong, J. Y.; Textor, M.; Reimhult, E. Surface Functionalization of Single Superparamagnetic Iron Oxide Nanoparticles for Targeted Magnetic Resonance Imaging. *Small* **2009**, *5* (11), 1334–1342.

(43) Karaoğlu, E.; Baykal, A.; Erdemi, H.; Alpsoy, L.; Sozeri, H. Synthesis and Characterization of Dl-Thioctic Acid (DLTA)–Fe3O4 Nanocomposite. *J. Alloys Compd.* **2011**, *509* (37), 9218–9225.

(44) Demortière, A.; Panissod, P.; Pichon, B. P.; Pourroy, G.; Guillon, D.; Donnio, B.; Bégin-Colin, S. Size-Dependent Properties of Magnetic Iron Oxidenanocrystals. *Nanoscale* **2011**, *3* (1), 225–232.

(45) Baun, O.; Blümler, P. Permanent Magnet System to Guide Superparamagnetic Particles. *J. Magn. Magn. Mater.* **2017**, *439*, 294–304.

(46) Kawasaki, R.; Sasaki, Y.; Katagiri, K.; Mukai, S.; Sawada, S.; Akiyoshi, K. Magnetically Guided Protein Transduction by Hybrid Nanogel Chaperones with Iron Oxide Nanoparticles. *Angew. Chemie* **2016**, *128* (38), 11549–11553.

(47) Rausch, K.; Reuter, A.; Fischer, K.; Schmidt, M. Evaluation of Nanoparticle Aggregation in Human Blood Serum. *Biomacromolecules* **2010**, *11* (11), 2836–2839.

(48) Koynov, K.; Butt, H. J. Fluorescence Correlation Spectroscopy in Colloid and Interface Science. *Curr. Opin. Colloid Interface Sci.* **2012**, *17* (6), 377–387.

(49) Mahmoudi, M.; Sant, S.; Wang, B.; Laurent, S.; Sen, T. Superparamagnetic Iron Oxide Nanoparticles (SPIONs): Development, Surface Modification and Applications in Chemotherapy. *Adv. Drug Deliv. Rev.* **2011**, *63* (1–2), 24–46.

(50) Michelet, F.; Gueguen, R.; Leroy, P.; Wellman, M.; Nicolas, A.; Siest, G. Blood and Plasma Glutathione Measured in Healthy Subjects by HPLC: Relation to Sex, Aging, Biological Variables, and Life Habits. *Clin. Chem.* **1995**, *41* (10), 1509–1517.

(51) Ahmed, S. M. U.; Luo, L.; Namani, A.; Wang, X. J.; Tang, X. Nrf2 Signaling Pathway: Pivotal Roles in Inflammation. *Biochim. Biophys. Acta - Mol. Basis Dis.* **2017**, *1863* (2), 585–597.

(52) Shenoy, N.; Stenson, M.; Lawson, J.; Abeykoon, J.; Patnaik, M.; Wu, X.; Witzig, T.

Drugs with Anti-Oxidant Properties Can Interfere with Cell Viability Measurements by Assays That Rely on the Reducing Property of Viable Cells. *Lab. Investig.* **2017**, *97* (5), 494–497.

(53)   Thielmann, C. M.; Costa da Silva, M.; Muley, T.; Meister, M.; Herpel, E.; Muckenthaler, M. U. Iron Accumulation in Tumor-Associated Macrophages Marks an Improved Overall Survival in Patients with Lung Adenocarcinoma. *Sci. Rep.* **2019**, *9* (1), 11326.

(54)   Ponzoni, M.; Pastorino, F.; Di Paolo, D.; Perri, P.; Brignole, C. Targeting Macrophages as a Potential Therapeutic Intervention: Impact on Inflammatory Diseases and Cancer. *Int. J. Mol. Sci.* **2018**, *19* (7), 1953.

(55)   Lee, W.-H.; Loo, C.-Y.; Traini, D.; Young, P. M. Nano- and Micro-Based Inhaled Drug Delivery Systems for Targeting Alveolar Macrophages. *Expert Opin. Drug Deliv.* **2015**, *12* (6), 1009–1026.

(56)   Shah, D. P. Fundamentals of Nanocarriers and Drug Targeting. In *Nanocarriers: Drug Delivery System*; Springer Singapore: Singapore, 2021; pp 3–42.

(57)   Chakraborty, A.; Royce, S.; Selomulya, C.; Plebanski, M. A Novel Approach for Non-Invasive Lung Imaging and Targeting Lung Immune Cells. *Int. J. Mol. Sci.* **2020**, *21* (5), 1613.

(58)   Shi, T.; Denney, L.; An, H.; Ho, L.; Zheng, Y. Alveolar and Lung Interstitial Macrophages: Definitions, Functions, and Roles in Lung Fibrosis. *J. Leukoc. Biol.* **2020**, JLB.3RU0720-418R.

(59)   Bedoret, D.; Wallemacq, H.; Marichal, T.; Desmet, C.; Quesada Calvo, F.; Henry, E.; Closset, R.; Dewals, B.; Thielen, C.; Gustin, P.; de Leval, L.; Van Rooijen, N.; Le Moine, A.; Vanderplasschen, A.; Cataldo, D.; Drion, P.-V.; Moser, M.; Lekeux, P.; Bureau, F. Lung Interstitial Macrophages Alter Dendritic Cell Functions to Prevent Airway Allergy in Mice. *J. Clin. Invest.* **2009**, *119* (12), 3723–3738.

(60)   Cai, B.; Kasikara, C.; Doran, A. C.; Ramakrishnan, R.; Birge, R. B.; Tabas, I. MerTK Signaling in Macrophages Promotes the Synthesis of Inflammation Resolution Mediators by Suppressing CaMKII Activity. *Sci. Signal.* **2018**, *11* (549), eaar3721.

(61)   Ulich, T. R.; Watson, L. R.; Yin, S.; Guo, K.; Wang, P.; Thang, H.; Del Castillo, J. The Intratracheal Administration of Endotoxin and Cytokines: I. Characterization of LPS-Induced IL-1 and TNF MRNA Expression and the LPS-, IL-1-, and TNF-Induced Inflammatory Infiltrate. *Am. J. Pathol.* **1991**, *138* (6), 1485–1496.

(62)   Weber, B.; Birke, A.; Fischer, K.; Schmidt, M.; Barz, M. Solution Properties of Polysarcosine: From Absolute and Relative Molar Mass Determinations to Complement Activation. *Macromolecules* **2018**, *51* (7), 2653–2661.

(63)   Rigler, R.; Elson, E. S. *Fluorescence Correlation Spectroscopy: Theory and Applications*; Springer Series in Chemical Physics; Springer Berlin, 2012.

(64)   Schäfer, O.; Huesmann, D.; Muhl, C.; Barz, M. Rethinking Cysteine Protective Groups: S -Alkylsulfonyl- l -Cysteines for Chemoselective Disulfide Formation. *Chem. - A Eur. J.* **2016**, *22* (50), 18085–18091.

(65)   Guida, C.; Altamura, S.; Klein, F. A.; Galy, B.; Boutros, M.; Ulmer, A. J.; Hentze, M. W.; Muckenthaler, M. U. A Novel Inflammatory Pathway Mediating Rapid Hepcidin-Independent Hypoferremia. *Blood* **2015**, *125* (14), 2265–2275.

(66)   Klaunig, J. E.; Goldblatt, P. J.; Hinton, D. E.; Lipsky, M. M.; Trump, B. F. Mouse

Liver Cell Culture. I. Hepatocyte Isolation. *In Vitro* **1981**, *17* (10), 913–925.

(67) Klaunig, J. E.; Goldblatt, P. J.; Hinton, D. E.; Lipsky, M. M.; Trump, B. F. Mouse Liver Cell Culture. II. Primary Culture. *In Vitro* **1981**, *17* (10), 926–934.

(68) Severgnini, M.; Sherman, J.; Sehgal, A.; Jayaprakash, N. K.; Aubin, J.; Wang, G.; Zhang, L.; Peng, C. G.; Yucius, K.; Butler, J.; Fitzgerald, K. A Rapid Two-Step Method for Isolation of Functional Primary Mouse Hepatocytes: Cell Characterization and Asialoglycoprotein Receptor Based Assay Development. *Cytotechnology* **2012**, *64* (2), 187–195.

(69) Torrance, J. D.; Bothwell, T. H. A Simple Technique for Measuring Storage Iron Concentrations in Formalinised Liver Samples. *S Afr J Med Sci.* **1968**, *33* (1), 9–11.

Supporting Information

Results and Discussion

Polymer Synthesis and Characterization
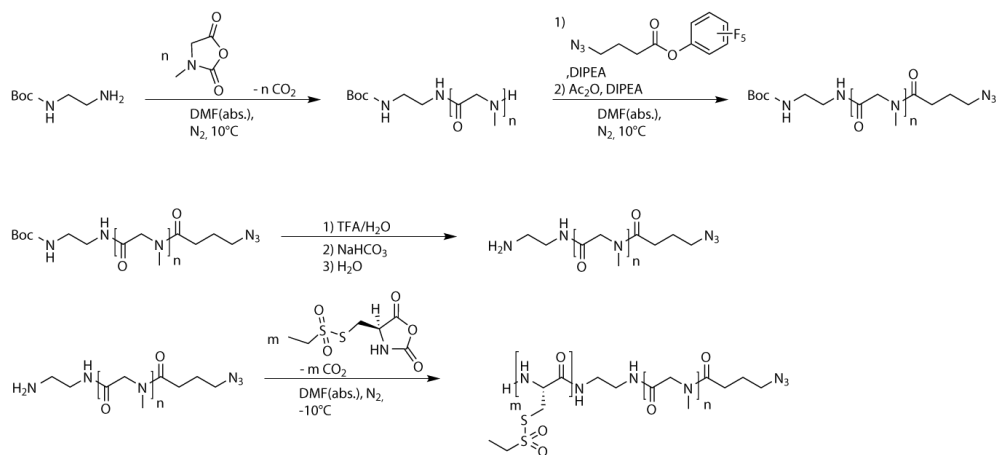
Scheme S1. Polymerization scheme for azide-functionalized pSar$_n$-*block*-pCys(SO$_2$Et)$_m$ (**P1** to **P3**) copolypepti(o)ides.

Table S1. Characterization of pSar$_n$-*block*-pCys(SO$_2$Et)$_m$ (**P1** to **P3**) copolymers.

polymer	end-group	X_n (pSar)[a]	X_n (pCys(SO$_2$Et))[b]	wt.% Cys(SO$_2$Et)	M_n[c] / kDa	$Đ$[b]
P1	Ac	225	31	27.5	31.2	2.64
P2	N$_3$	200	17	18.9	31.7	1.25
P3	N$_3$	170	27	30.4	35.1	7.06

[a] HFIP-GPC, relative to pSar standards. [b] as determined by ^{1}H-NMR. [c] HFIP-GPC, relative to PMMA standards.
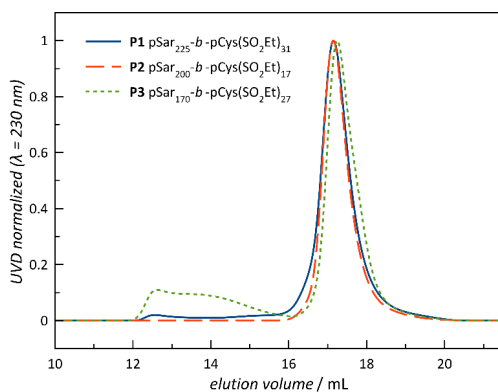
Figure S1. HFIP-GPC traces of **P1-P3** (see Table 1). Note that secondary structures are not suppressed in the eluent (HFIP containing 3 g·L⁻¹ of CF₃COOK), and elution volumes may be influenced by the degree of secondary structure formation of the pCys(SO₂Et)ₘ block, as reported by previously.[1-3]
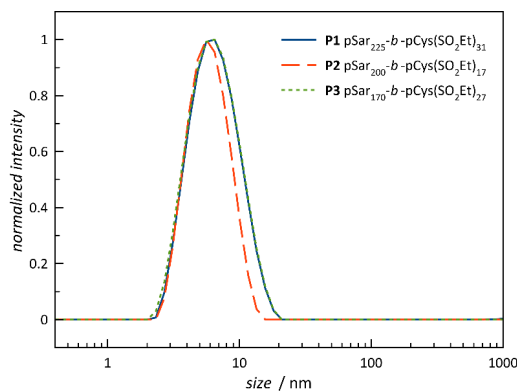
Figure S2. Single-angle DLS of pSar-*b*-pCys(SO₂Et) block copolymers (**P1** - **P3**) in DMSO (β = 18 g·L⁻¹) confirms the absence of larger structures but polymer species only.
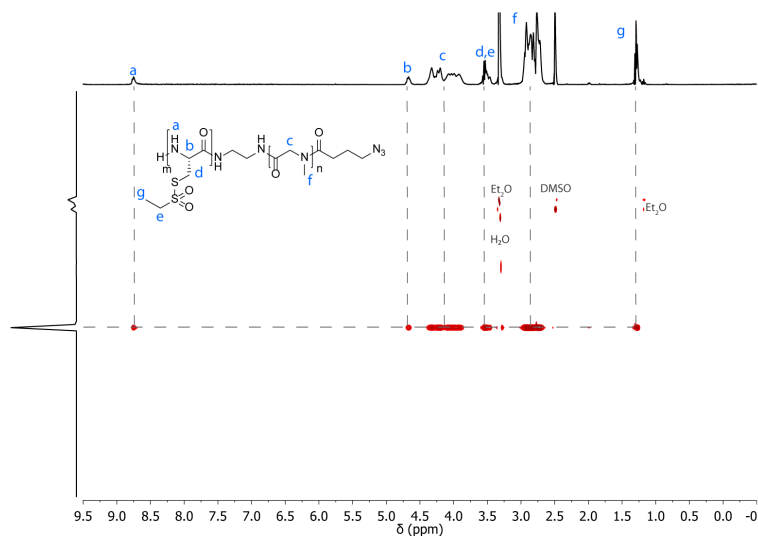
Figure S3. ^{1}H DOSY NMR spectrum of **P1** (pSar$_{225}$-*block*-pCys(SO$_2$Et)$_{31}$) in DMSO-d_6.
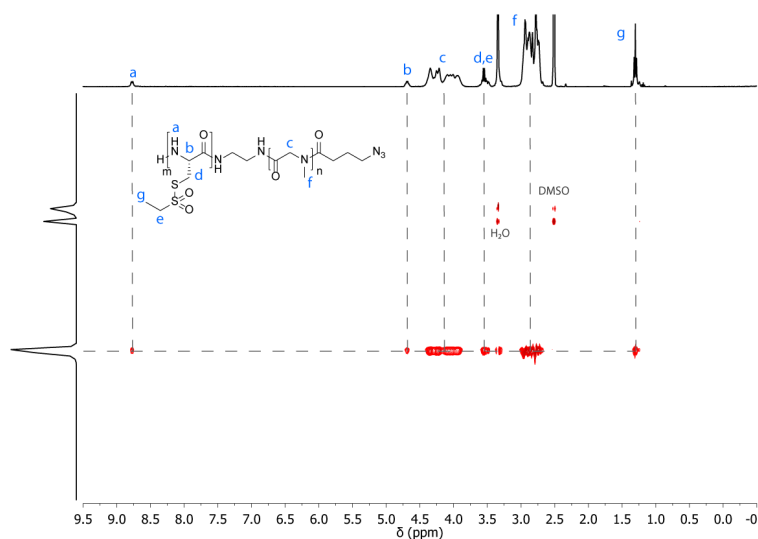
Figure S4. ^{1}H DOSY NMR spectrum of **P2** (pSar$_{200}$-*block*-pCys(SO$_2$Et)$_{17}$) in DMSO-d_6.
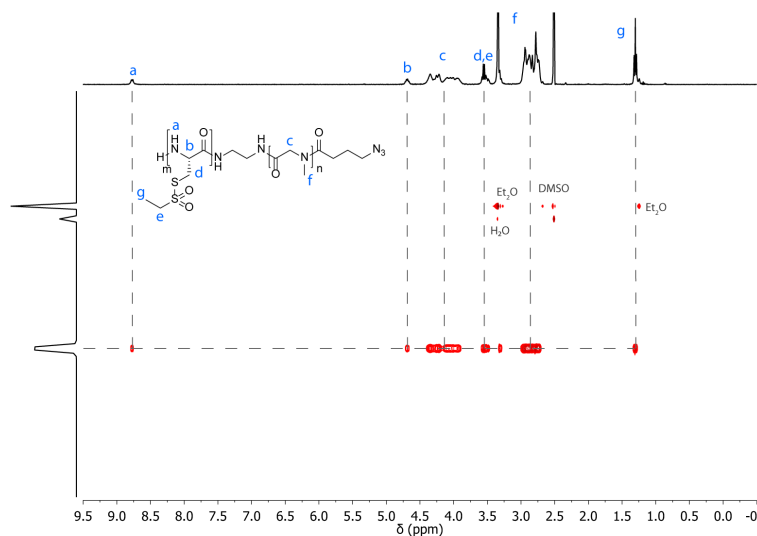
Figure S5. ^{1}H DOSY NMR spectrum of **P3** (pSar$_{170}$-*block*-pCys(SO$_2$Et)$_{27}$) in DMSO-d_6.

Nanoparticle Characterization

Table S2. Characterization of core cross-linked polymeric micelles with and without embedded iron oxide nanoparticles.

particle	polymer	cross-linker	yield	D_h / nm[a]	PDI[a]	wt.% Fe_2O_3[b]	N_{Dye}[c]
SPION-CCPM^{Cy5}	P3	Lipoic acid	22%	82	0.163	33	16.5
SPION-CCPM^{Cy5}#2	P2	Lipoic acid	36%	63	0.122	42	4.1
CCPMs^{Cy5}	P1	*N*-3-Azidopropyl-liponamide	46%	49	0.131	-	2.5

[a] determined by single-angle DLS. [b] determined by TGA in O$_2$ atmosphere. [c] determined by FCS.
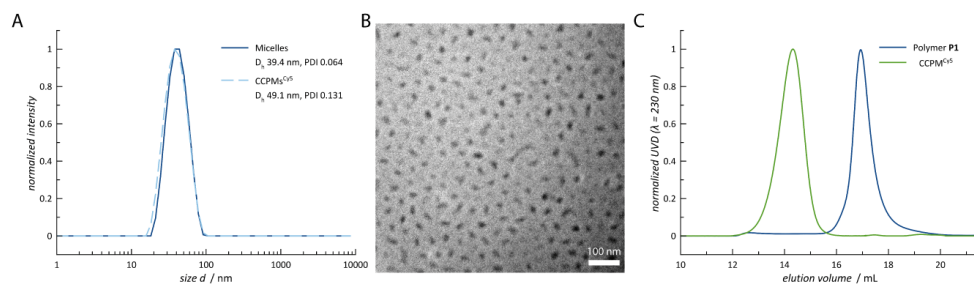
Figure S6. Characterization of CCPM control particles. (**A**) DLS analysis shows core cross-linked polymeric micelles (CCPMS) with narrow dispersity. (**B**) CryoTEM confirmed the presence of nanoparticles with sizes well below 100 nm with spherical morphology. (**C**) HFIP GPC analysis confirmed successful cross-linking.
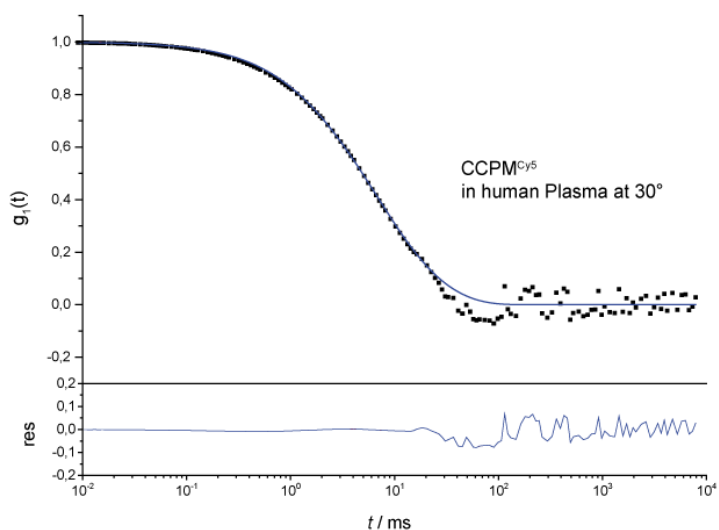
Figure S7. Multi-angle DLS shows no aggregation or increasing sizes for CCPM[Cy5] after incubation in human plasma.
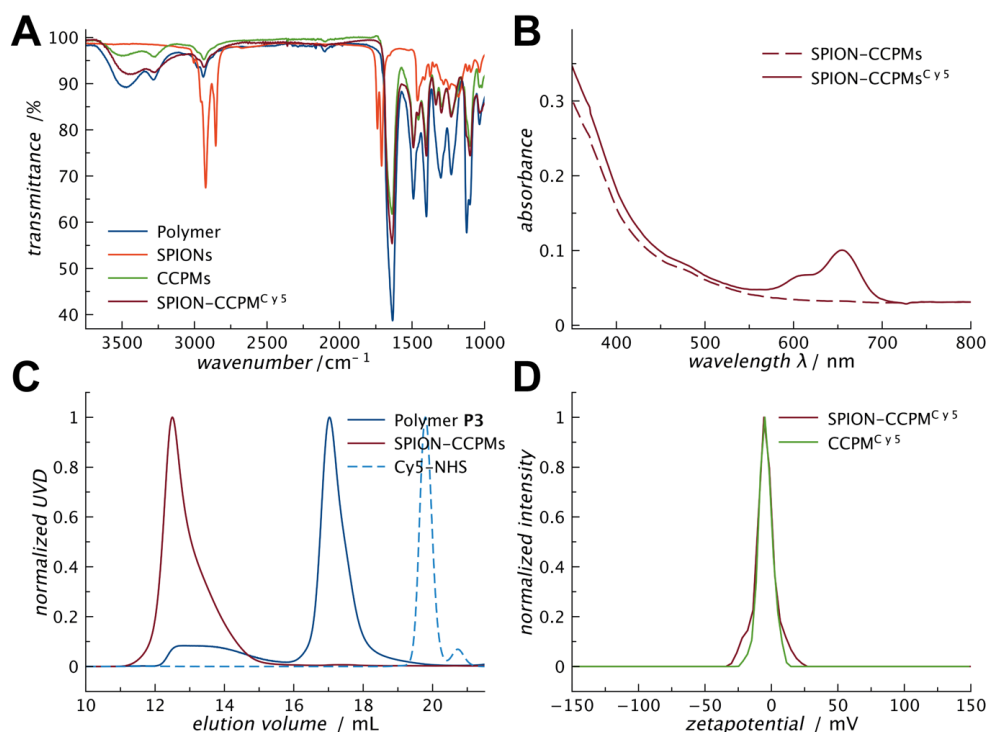
Figure S8. Characterization of SPION-CCPMs (**A**) ATR-FT-IR Spectroscopy of SPION-CCPMs, CCPMs, SPIONs and block copolymer pSar-*b*-pCys(SO₂Et). (**B**) UV-Vis spectroscopy of SPION-CCPM dispersions in water. Strong absorbance below $\lambda = 500$ nm refers to embedded iron oxide nanoparticles. Distinct absorbance of Cy5 can be detected for SPION-CCPM[Cy5] after dye conjugation and purification. (**C**) GPC-analysis in HFIP implies stable cross-linking and absence of residual unconjugated dye or polymer for SPION-CCPM[Cy5]. The multimodal GPC-trace for polymer P3 is attributed to ß-sheet induced aggregation (see Figure S1). (**D**) Zeta potential distribution. Slightly negative zeta-potentials were determined for both, SPION-CCPM[Cy5] and CCPM[Cy5], in 3 mM sodium chloride solution.
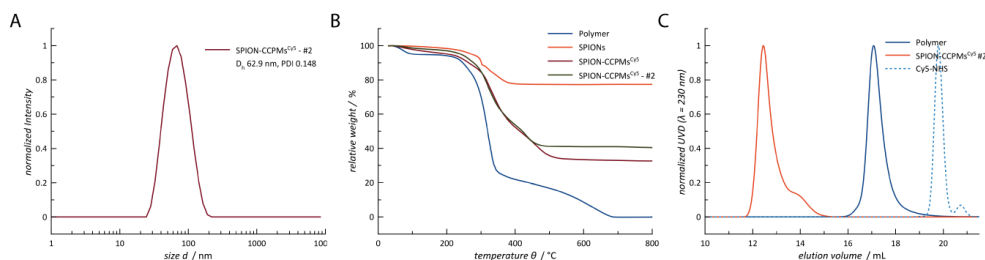
Figure S9. Characterization of SPION-CCPM[Cy5] #2 particles. (**A**) DLS analysis reveals SPION-CCPM[Cy5] #2 particles with narrow dispersity. (**B**) TGA analysis confirms higher iron oxide contents for SPION-CCPM[Cy5] #2 (42 wt.%) compared to SPION-CCPM[Cy5] (33 wt.%). (**C**) HFIP GPC analysis confirmed successful cross-linking and removal of unconjugated dye or polymer.
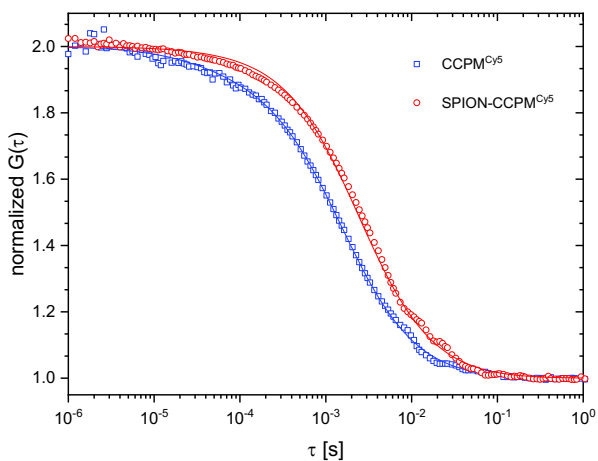
Figure S10. Fluorescence correlation spectroscopy. Normalized autocorrelation curves of Cy5-labelled SPION-CCPMs[Cy5] (red circles) and CCPMs[Cy5] (blue squares) measured in PBS buffer. The solid lines represent the corresponding fits with eq. 2 (main text). The fitting was done using single component ($m = 1$ in eq. 2) that confirms the absence of unconjugated dye.
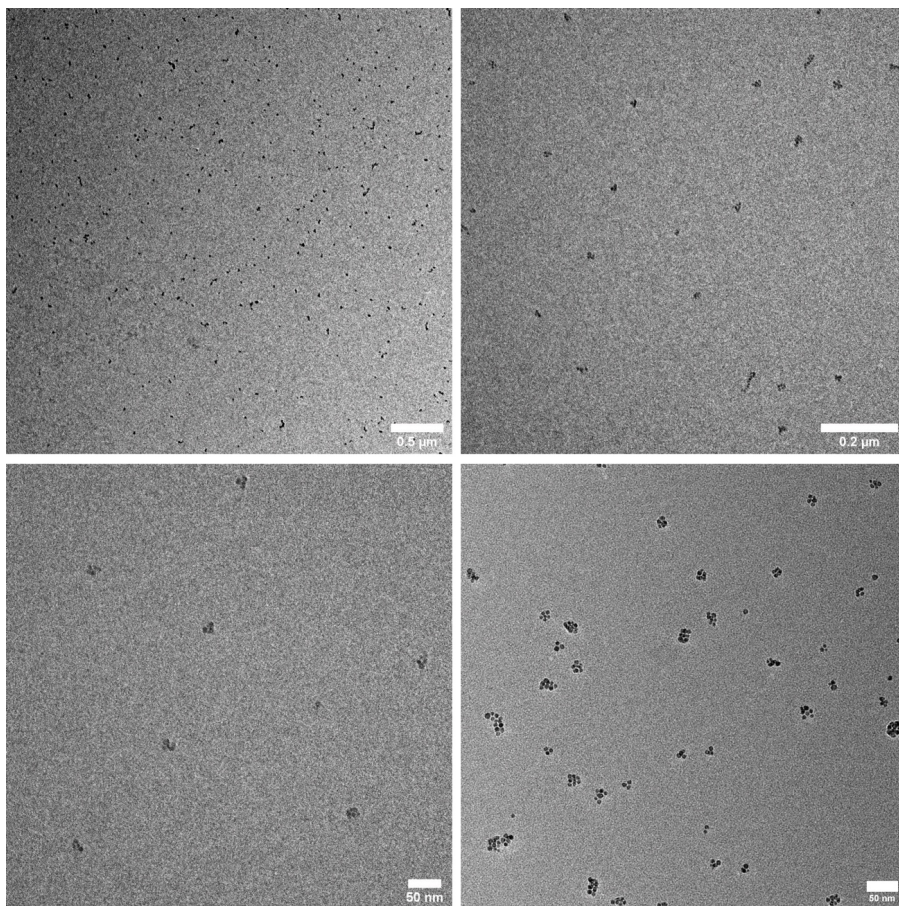
Figure S11. Additional TEM images of SPION-CCPMs[Cy5].
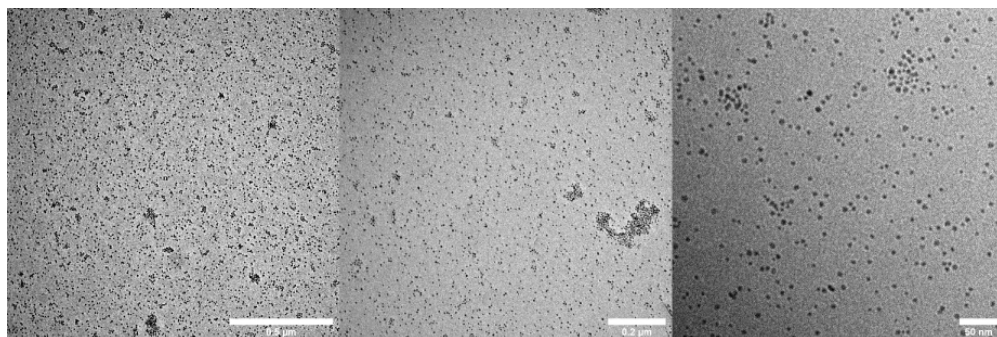
Figure S12. TEM images of oleic acid coated SPIONs. No organized clusters of nanoparticles can be detected.

Magnetic Response & Guidance
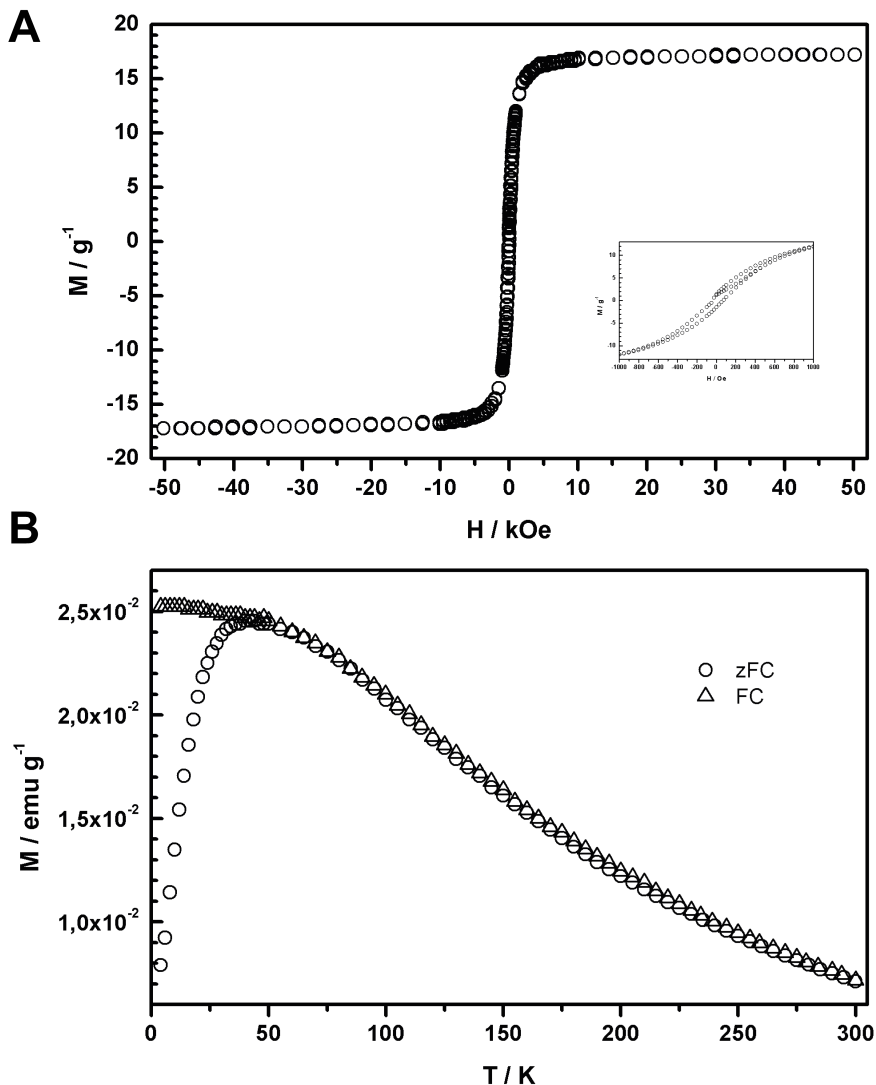
Figure S13. (**A**) Magnetization hysteresis loop recorded for SPION-CCPMs at 5 K conforms superparamagnetic behavior. (**B**) Zero field cooling/field cooling curves revealed a blocking temperature of 42 K, confirming the presence of superparamagnetic iron oxide nanoparticles.[4]
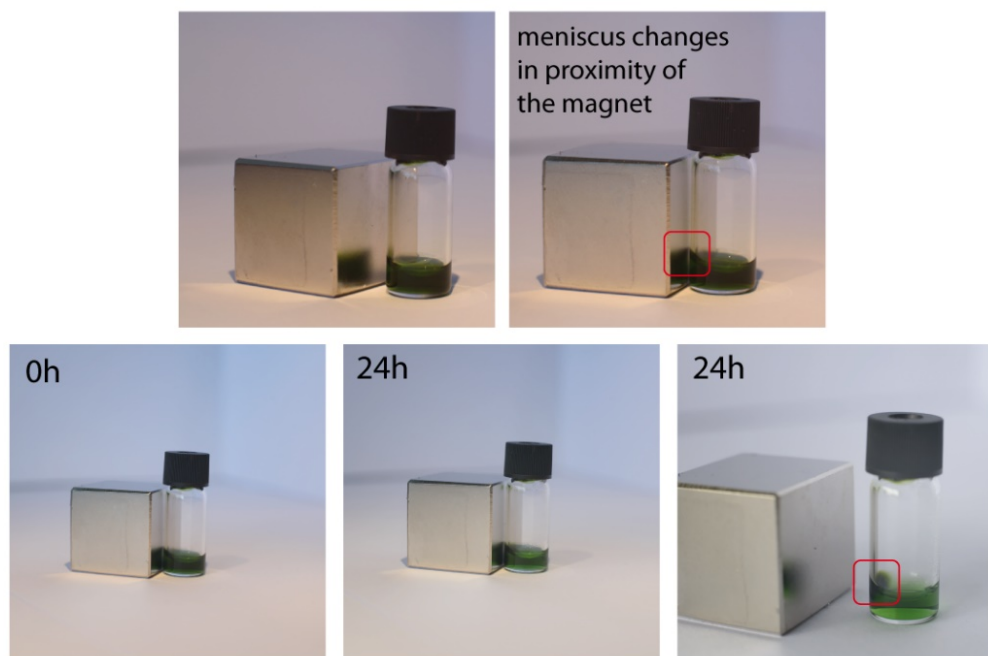
Figure S14. Images of the magnetic response of SPION-CCPM[Cy5] dispersions in water. (upper images) In proximity of a permanent magnet, the meniscus of the dispersion changes immediately. (lower images) Slow accumulation of SPION-CCPM[Cy5] by magnetic force.
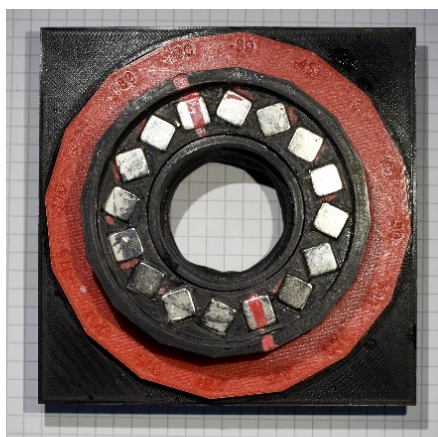
Figure S15. Image of the quadrupolar/dipolar ring-type magnet used for magnetic guidance experiments.[5]

Magnetic Guidance in vivo

If a magnetic particle should be moved against a blood stream, the magnetic force, F_{mag}, must overcome the hydrodynamic (Stokes) friction, F_{fric}. A straight-forward calculation then gives

$$F_{mag} > F_{\text{fric}} \tag{S1}$$

$$mG = \varrho VMG > 6\pi\eta R_h v \tag{S2}$$

Where m [Am^2] is the magnetic moment of the particle and G [T·m^{-1}] the magnetic field gradient. It is more useful to express m by a magnetization per mass M [Am^2·kg^{-1}] times its mass or density (ρ [kg·m^{-3}]) times particle volume (V [m^3]). On the other side of the equation, the dynamic viscosity, η [Pa·s], of the surrounding liquid, its velocity, v [m·s^{-1}], relative to a sphere with hydrodynamic radius, R_h [m], is determining the friction. If, like in our case, a larger particle contains N spherical SPION centers of radius R, this can be rearranged to find the necessary field gradient to counter the blood flow:

$$G > \frac{9 \cdot v \cdot \eta \cdot R_h}{2 \cdot \rho \cdot N \cdot R^3 \cdot M} \tag{S3}$$

Equation S3. Approximation of the magnetic gradient required to direct magnetic particles in dispersion of a fluid in motion.

with v as the velocity of the blood flow ($2 \cdot 10^{-3}$ m·s^{-1} (zebrafish embryo)[6], 0.15 m·s^{-1} (human)[7]), η as the dynamic viscosity of the blood ($5 \cdot 10^{-3}$ Pa·s (zebrafish embryo)[6], $3.5 \cdot 10^{-3}$ Pa·s (human)[8]), R_h as the hydrodynamic radius of the SPION-CCPM nanoparticle, ρ as the density of the nanoparticle (approx. 1500 kg·m^{-3} for SPION-CCPMs), R as the radius magnetic SPION core, and M as the saturation magnetization of the SPION nanoparticle (50 Am^2·kg^{-1} for 10 nm iron oxide nanoparticles, 74 Am^2·kg^{-1} for magnetite nanoparticles > 20 nm).[4]

For SPION-CCPMs with R_h = 40 nm, each containing 5 SPIONs cores of R = 5 nm, the magnetic gradient needs to be larger than $3.84 \cdot 10^7$ T·m^{-1} or $2.02 \cdot 10^9$ T·m^{-1} to overcome the velocity of the blood flow and guide those nanoparticles in the vasculature of zebrafish embryos or humans. For SPION-CCPMs with increased dimension of the magnetic cores (R_h = 20 nm, R_{SPION} = 10 nm, N = 3) values slightly decrease to $2.70 \cdot 10^6$ T·m^{-1} or $1.42 \cdot 10^8$ T·m^{-1} for zebrafish embryos or humans, still by far extending the capabilities of the displayed magnet guidance system (G = 2.5 T·m^{-1}).[5]

Macrophage Uptake & Stimulation
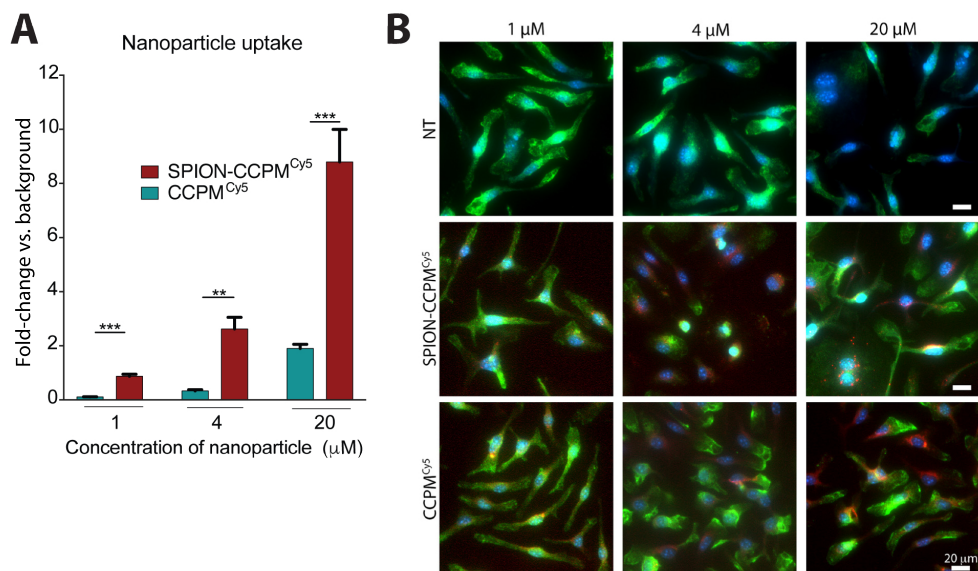
Figure S16. Concentration dependent uptake of SPION-CCPMs[Cy5] and CCPMs[Cy5] in BMDMs. (**A** and **B**) Non-treated (NT) BMDMs, or BMDMs treated with increasing concentrations of SPION-CCPMs[Cy5] or CCPMs[Cy5] (red) for 24 hrs. (**A**) Internalization of nanoparticles was measured by FACS fluorescence detection (intensity of Cy5). (**B**) Representative images of BMDMs with and without nanoparticle treatment. Cells were stained with Iba1 (green), a cell surface marker for macrophages, and DAPI. Data reported as mean ± SEM, n = 3 independent experiments. One-way ANOVA (black): * $p < 0.01$, ** $p < 0.001$, *** $p < 0.0001$.
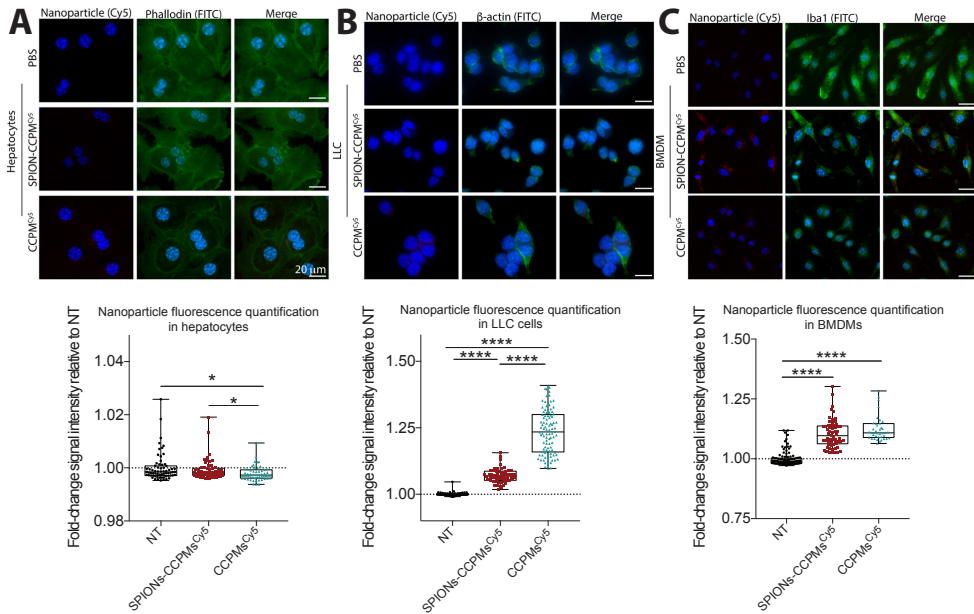
Figure S17. Uptake of SPION-CCPMs and CCPMs in primary murine Hepatocytes, LLCs and BMDMs. Cells were incubated with SPION-CCPMs or CCPMs. Amount of SPION-CCPMs added to cells was calculated based on iron concentration from the core and the amount of CCPMs was calculated to match the mass of CCPMs contained within SPION-CCPMs. (**A**) Representative images of primary hepatocytes, (**B**) Lewis Lung Cancer Cells (LLCs), and (**C**) BMDMs treated with SPION-CCPMsCy5 or CCPMsCy5 (red) for 24 hours. Quantification of nanoparticle signal within cells is below each respective cell type, whereby at least n = 30 cells was analyzed. Primary hepatocytes and LLCs were stained with Phallodin or ß-actin (green) and DAPI (blue). BMDMs were stained with Iba1 antibody (green). Data reported as n ± Standard Error of the Mean (SEM). One-way ANOVA: * $p < 0.01$, ** $p < 0.001$, *** $p < 0.0001$.
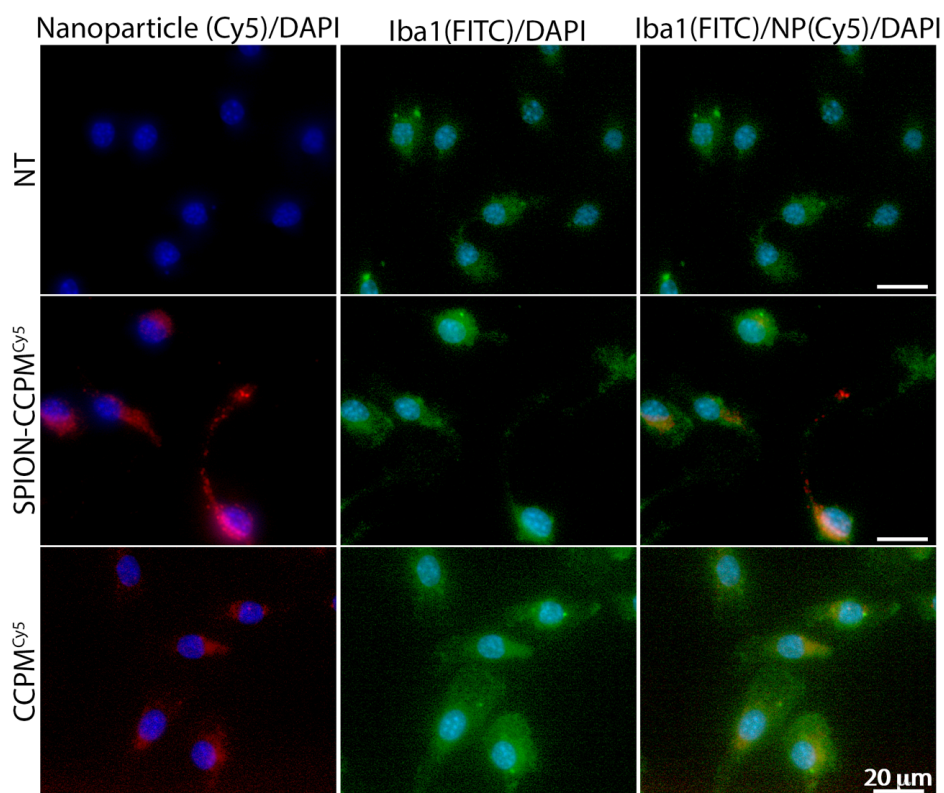
Figure S18. SPION-CCPMs and CCPMs are taken up by BMDMs after a 1-hour incubation. BMDMs were incubated with 20 µM SPION-CCPMs or CCPMs and fixed with 4 % paraformaldehyde after one hour. Cells were stained with a macrophage marker, Iba1 (green), and DAPI (blue).
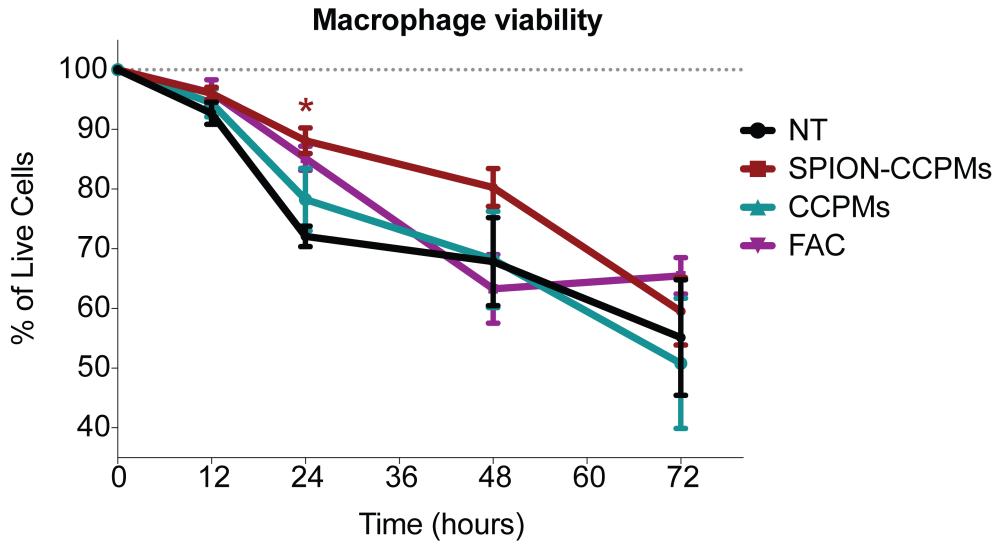
Figure S19. SPION-CCPMs do not cause cytotoxicity in BMDMs. Cells were incubated with 20 mM SPION-CCPMs, dose matched CCPMs, or 20 µM ferric ammonium citrate (FAC). Lactate dehydrogenase (LDH) quantities were measured in the supernatant of cell cultures at 490 nm wavelength after adding CytoTox 96© substrate (Promega). Values are represented as a percentage of the 0 hour condition at each time point. Data reported as n ± SEM. n = 3 independent experiments. One-way ANOVA: * $p < 0.05$, ** $p < 0.01$, *** $p < 0.001$.
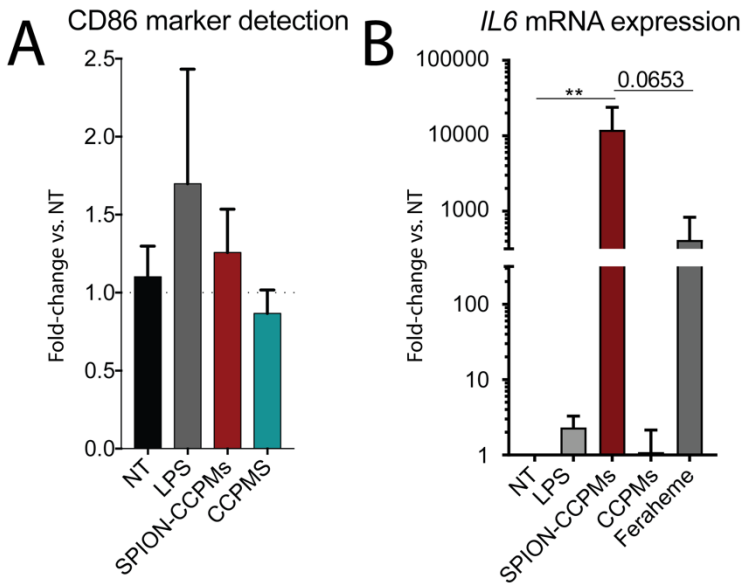
Figure S20. SPION-CCPMs and not CCPMs activate an inflammatory response in human macrophages. (**A** and **B**) Human peripheral monocytes were differentiated for 10 days using M-CSF to produce macrophages. Macrophages were incubated with 20 µM SPION-CCPMs, Feraheme, CCPMs, or 100 ng/mL lipopolysaccharide (LPS). After 24 hours, cells were harvested for FACS analysis to detect the cell surface markers CD80 and CD86 (**A**) or differential cytokine mRNA expression using qPCR (**B**). (**B**) Data show mean and SEM of mRNA expression compared to the non-treated (NT) condition and all samples were corrected for *RPL19* mRNA expression. One-way ANOVA (black): * $p < 0.05$, ** $p < 0.01$, *** $p < 0.001$, **** $p < 0.0001$.

CD86 marker detection
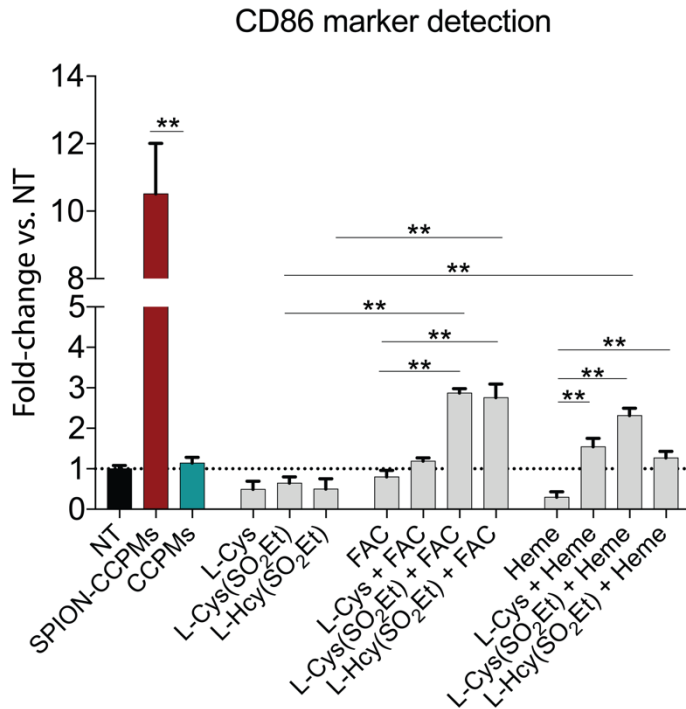
Figure S21. CD86 protein expression in macrophages following treatment with various cysteine dimers. Cells were incubated for 24 hours with 20 µM iron (SPION-CCPMs, heme or ferric ammonium citrate (FAC)), CCPMs, L-cysteine (L-Cys), S-ethylsulfonyl-L-cysteine (L-Cys(SO$_2$Et)), S-ethylsulfonyl-L-homocysteine (L-Hcy(SO$_2$Et)), and cell surface marker CD86 was measured using fluorescence detection by FACS. Values are represented as fold-change compared to non-treated (NT) condition. Data show mean and SEM, n = 2 independent experiments. One-way ANOVA (black): * $p < 0.05$, ** $p < 0.01$, *** $p < 0.001$, **** $p < 0.0001$.
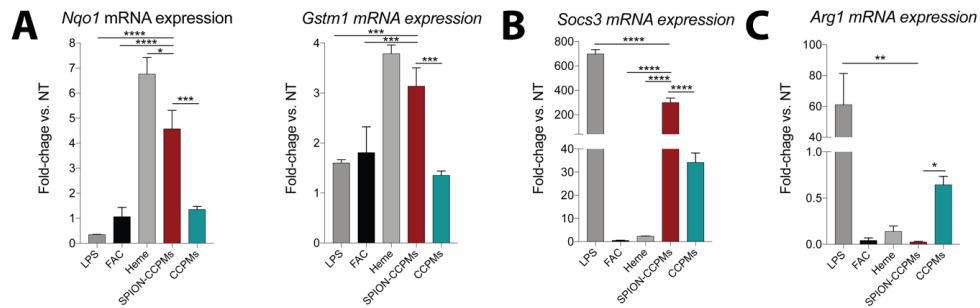
Figure S22. SPION-CCPMs induce sterile inflammation in macrophages. (A-C) BMDMs were incubated with 100 ng/mL LPS, 20 µM FAC, 20 µM Heme, 20 µM SPION-CCPMs or CCPMs for 18 hours. Amount of SPION-CCPMs added to cells was calculated to 20 µM iron from the core and the amount of CCPMs added to cells was calculated to match the mass of CCPMs contained within SPION-CCPMs. The graphs show mean and SEM of mRNA expression compared to the non-treated (NT) condition and all samples were corrected for *Rpl19* mRNA expression. One-way ANOVA (black): * $p < 0.05$, ** $p < 0.01$, *** $p < 0.001$, **** $p < 0.0001$.

Table S3. Antibodies used for Flow Cytometry.

antibody	fluorophore	clone	isotype	manufacturer
Anti-mouse cell culture experimentation				
CD206	Alexa Fluor 700	MR6F3	Rat IgG2b, κ	ThermoFisher
CD38	FITC	90	Rat IgG2a, κ	BioLegend
CD86	Brilliant Violet 421	GL-1	Rat IgG2a, κ	BioLegend
CD80	Brilliant Violet 650	16-10A1	Armenian Hamster IgG	BioLegend
MHC II	PE-Cy7	M5/114.15.2	Rat IgG2b, κ	BioLegend
Anti-mouse in vivo experimentation				
CD45	PerCP-Cy5.5	104	N/A	ThermoFisher
Ly6G	FITC	1A8	N/A	BioLegend
Ly6C	PE-Dazzle	HK1.4	N/A	BioLegend
F4/80	BV605	T45-2342	N/A	ThermoFisher
CD11c	PE	N418	N/A	BioLegend
Siglec-F	APC-Cy7	E50-2440	N/A	ThermoFisher
CD11b	PerCP	ICRF44	N/A	ThermoFisher
CD64	BV711	X54-5/7.1	N/A	BioLegend
CD80	BV650	16-10A1	Armenian Hamster IgG	BioLegend
CD71	BV510	RI7217	Rat IgG2a, κ	BioLegend
MerTK	BV421	108928	Rat IgG2a	ThermoFisher
Anti-human				
CD80	PE	2D10	Mouse IgG1, κ	BioLegend
CD86	Alexa Fluor 488	IT2.2	Mouse IgG2b, κ	BioLegend

Table S4. Primers for quantitative RT-PCR (*mus musculus*).

gene	sequence
Arg1	Forward 5' AATCTGCATGGGCAACCTGT 3' Reverse 5' GTCTACGTCTCGCAAGCCAA 3'
Cxcl10	Forward 5' ACGTGTTGAGATCATTGCCAC 3' Reverse 5' GTCGCACCTCCACATAGCTT 3'
Fpn1	Forward 5' TGTCAGCCTGCTGTTTGCAGGA 3' Reverse 5' TCTTGCAGCAACTGTGTCACCG 3'
Gstm1	Forward 5' TCCGTGCAGACATTGTGGAG 3' Reverse 5' CTGCTTCTCAAAGTCAGGGTTG 3'
Ho-1	Forward 5' AGGCTAAGACCGCCTTCCT 3' Reverse 5' TGTGTTCCTCTGTCAGCATCA 3'
Il6	Forward 5' GCTACCAAACTGGATATAATCAGGA 3' Reverse 5' CCAGGTAGCTATGGTACTCCAGAA 3'
Il1β	Forward 5' GCAACTGTTCCTGAACTCAACT 3' Reverse 5' ATCTTTTGGGGTCCGTCAACT 3'
Nos2	Forward 5' TGGAGACTGTCCCAGCAATG 3' Reverse 5' CAAGGCCAAACACAGCATACC 3'
Nqo1	Forward 5' AGCGTTCGGTATTACGATCC 3' Reverse 5' AGTACAATCAGGGCTCTTCTCG 3'
Rpl19	Forward 5' AGGCATATGGGCATAGGGAAGAG 3' Reverse 5' TTGACCTTCAGGTACAGGCTGTG 3'
Slc7a11	Forward 5' TCCACAAGCACACTCCTCTG 3' Reverse 5' CGTCAGAGGATGCAAAACAA 3'
Socs3	Forward 5' CCTTTGACAAGCGGACTCTC 3' Reverse 5' GCCAGCATAAAAACCCTTCA 3'
Tfr1	Forward 5' CCCATGACGTTGAATTGAACCT 3' Reverse 5' GTAGTCTCCACGAGCGGAATA 3'
Tnfa	Forward 5' TGCCTATGTCTCAGCCTCTTC 3' Reverse 5' GAGGCCATTTGGGAACTTCT 3'

Table S5. Primers for quantitative RT-PCR (*homo sapiens*).

gene	sequence
IL6	Forward 5' AAATTCGGTACATCCTCGACGGA 3'
	Reverse 5' GGAAGGTTCAGGTTGTTTTCTGC 3'
IL1β	Forward 5' CTCGCCAGTGAAATGATGGCT 3'
	Reverse 5' GTCGGAGATTCGTAGCTGGAT 3'
RPL19	Forward 5' TCGCCTCTAGTGTGTCCTCCG 3'
	Reverse 5' GCGGCCCAAGGTGTTTTTC 3'
TNFα	Forward 5' ATGAGCACTGAAAGCATGATCC 3'
	Reverse 5' GAGGGCTGATTAGAGAGAGGTC 3'

References for Supporting Information

(1) Schäfer, O.; Huesmann, D.; Barz, M. Poly(S -Ethylsulfonyl- l -Cysteines) for Chemoselective Disulfide Formation. *Macromolecules* **2016**, *49* (21), 8146–8153.

(2) Huesmann, D.; Birke, A.; Klinker, K.; Türk, S.; Räder, H. J.; Barz, M. Revisiting Secondary Structures in NCA Polymerization: Influences on the Analysis of Protected Polylysines. *Macromolecules* **2014**, *47* (3), 928–936.

(3) Bauer, T. A.; Muhl, C.; Schollmeyer, D.; Barz, M. Racemic S -(Ethylsulfonyl)- Dl - cysteine N -Carboxyanhydrides Improve Chain Lengths and Monomer Conversion for B-Sheet-Controlled Ring-Opening Polymerization. *Macromol. Rapid Commun.* **2021**, *42* (8), 2000470.

(4) Demortière, A.; Panissod, P.; Pichon, B. P.; Pourroy, G.; Guillon, D.; Donnio, B.; Bégin-Colin, S. Size-Dependent Properties of Magnetic Iron Oxidenanocrystals. *Nanoscale* **2011**, *3* (1), 225–232.

(5) Baun, O.; Blümler, P. Permanent Magnet System to Guide Superparamagnetic Particles. *J. Magn. Magn. Mater.* **2017**, *439*, 294–304.

(6) Chen, C. Y.; Patrick, M. J.; Corti, P.; Kowalski, W.; Roman, B. L.; Pekkan, K. Analysis of Early Embryonic Great-Vessel Microcirculation in Zebrafish Using High-Speed Confocal MPIV. *Biorheology* **2011**, *48* (5–6), 305–321.

(7) Schmidt, R. F.; Lang, F.; Heckmann, M. *Physiologie Des Menschen*; **2010**.

(8) Brandes, R.; Busse, R. *Kreislauf. Physiologie des Menschen*; **2010**; p 576f.

Appendix

¹H NMR Spectra
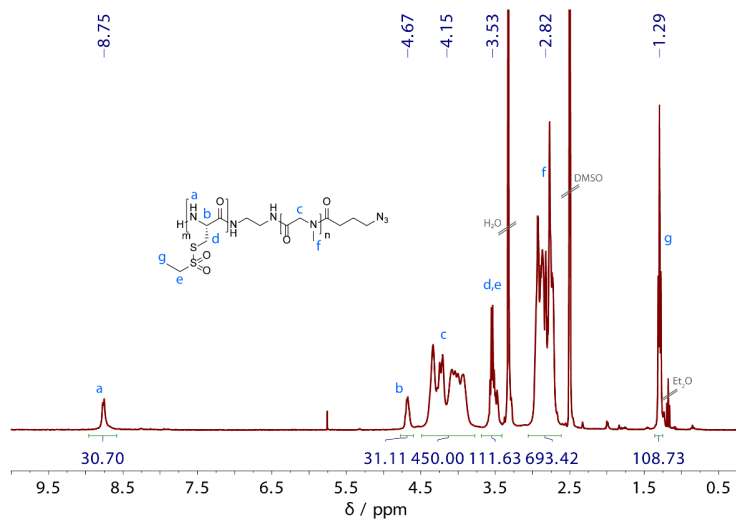
Figure S23. ¹H NMR spectrum of **P1** (pSar$_{225}$-*block*-pCys(SO$_2$Et)$_{31}$) in DMSO-d_6.
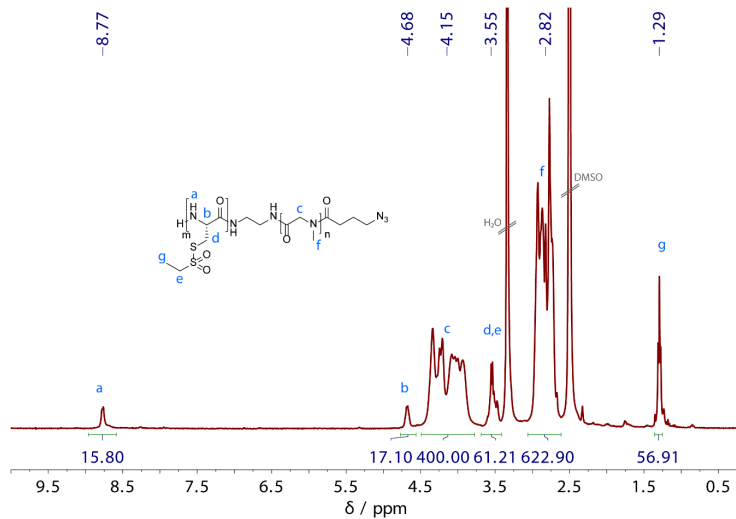
Figure S24. ¹H NMR spectrum of **P2** (pSar$_{200}$-*block*-pCys(SO$_2$Et)$_{17}$) in DMSO-d_6.
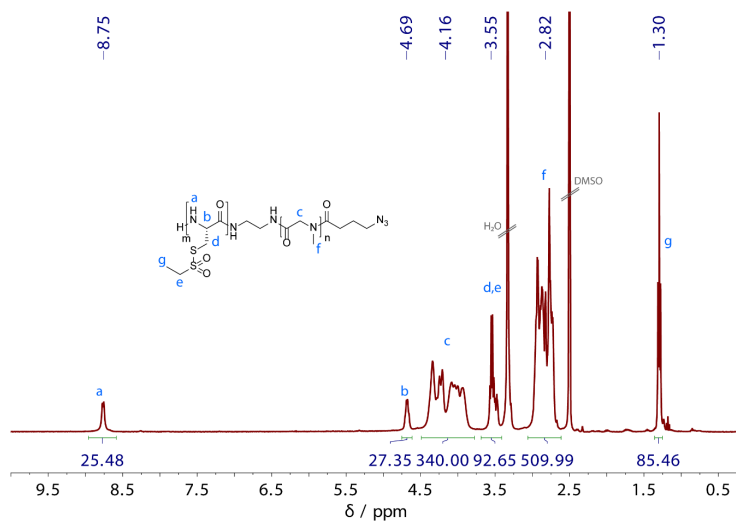
Figure S25. ^{1}H NMR spectrum of **P3** (pSar$_{170}$-*block*-pCys(SO$_2$Et)$_{27}$) in DMSO-d_6.
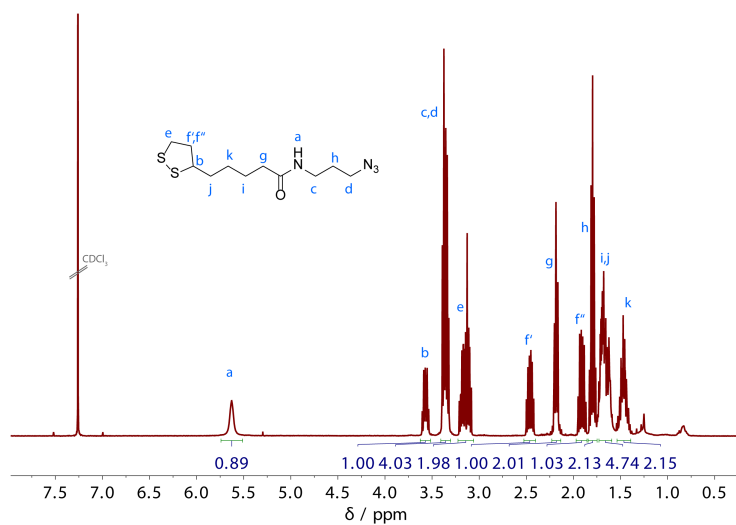
Figure S26. ^{1}H NMR spectrum *N*-3-azidopropyl liponamide in CDCl$_3$.

9

General Discussion

Summary

This thesis aimed to investigate core cross-linked polymeric micelles (CCPMs) and expand their potential for the delivery of hydrophobic drugs and co-factors. Applying polypept(o)ides as the polymeric platform technology, the fundamental implications of secondary structure formation on ring-opening *N*-carboxyanhydride (NCA) polymerization and self-assembly were examined and optimized. CCPMs with functional core architectures serving external or disease-related stimuli were developed. To establish robust CCPM production, overcome drug resistance mechanisms, and explore therapeutic agents for immunomodulation, polymer science was combined with organic and inorganic chemistry.

A general introduction about nanomedicine and polypept(o)ides was given in **chapter 1**. Herein, the rationale for the use of nanocarriers to tune the pharmacokinetic profile of active pharmaceutical ingredients (API) was explained. Relevant carrier systems were presented, and the significance of surface shielding to prevent non-specific uptake by the mononuclear phagocyte system (MPS) was outlined. The enhanced permeability and retention (EPR) effect was introduced and critically discussed as a mechanism for passive drug targeting, and future directives were disclosed. Current developments on polymeric micelles and CCPMs were reviewed. In addition, polypept(o)ides were explored as a novel class of functional polymers entirely based on endogenous amino acids. The mechanism of the ring-opening NCA polymerization was explained, and current trends in NCA polymerization were identified. Ultimately, the early and most recent developments on the biomedical application of polypept(o)ides were outlined.

In **chapter 2**, racemic *S*-ethylsulfonyl-DL-cysteine was investigated to improve the ring-opening polymerization of polypeptides such as polycysteine that form strong anti-parallel ß-sheets during polymerization. The thiol-reactive *S*-ethylsulfonyl-DL-cysteine NCA was synthesized and polymerized in analogy to enantiopure *S*-ethylsulfonyl-L-cysteine. For the racemic NCA, complete monomer conversion and increased chain lengths up to $X_n = 102$ corresponding to molecular weights of 20.0 kDa could be obtained. Moreover, kinetic investigations revealed higher rate constants (40% on average) even though the reaction kinetics still followed the Avrami model indicating low solubility. Indeed, only a reduced tendency but not entirely resolved ß-sheets were detected by infrared (IR)

spectroscopy. Nevertheless, the full monomer conversion of *S*-ethylsulfonyl-DL-cysteine NCA granted the synthesis of a triblock copolymer by sequential monomer addition otherwise inaccessible to the enantiopure amino acid unless purification steps were introduced.

The influence of the secondary structure on the self-assembly of thiol-reactive copolymers was examined in **chapter 3**. Therefore, a library of copolymers of enantiopure polysarcosine-*block*-poly(*S*-ethylsulfonyl-L-cysteine) (pSar-*b*-p(L)Cys(SO$_2$Et)), racemic pSar-*b*-p(DL)Cys(SO$_2$Et), and pSar-*b*-poly(*S*-ethylsulfonyl-L-homocysteine) (pSar-*b*-p(L)Hcy(SO$_2$Et)) was synthesized. The secondary structure formation of the polypeptides was analyzed by IR and circular dichroism spectroscopy, whereby an α-helix was detected for pSar-*b*-pHcy(SO$_2$Et), anti-parallel ß-sheets for pSar-*b*-p(L)Cys(SO$_2$Et), and disrupted ß-sheets for racemic pSar-*b*-p(DL)Cys(SO$_2$Et). During self-assembly induced by solvent switch, anti-parallel ß-sheets showed the strongest tendency for self-assembly followed by the α-helical copolymer and ultimately the disrupted ß-sheets, as quantified by analysis *via* dynamic light scattering (DLS). These findings translated to the morphology of the assemblies, leading to worm-like, entirely spherical, or slightly elongated structures, as analyzed by atomic force microscopy (AFM) or transmission electron microscopy (TEM). Secondary structure formation of thiol-reactive copolymers was demonstrated to be an elegant tool for adjusting the features of nanomedicines.

In **chapter 4**, the cross-linking density was assessed as a parameter to fine-tune the stability of CCPMs based on pSar-*b*-pCys(SO$_2$Et)$_n$. To define structure-activity relationships, the length of the cross-linkable p(L)Cys(SO$_2$Et)$_n$ block was selected as X_n = 17 or 30, and mono-, bi-, or trifunctional thiol-reagents were synthesized and applied to address the *S*-ethylsulfonyl group for quenching or cross-linking reactions. Asymmetrical flow field-flow fractionation (AF4) and fluorescence correlation spectroscopy (FCS) were applied as the screening techniques. Analysis by AF4 in human blood plasma revealed a clear connection between the cross-linking density and the particle stability. Large fractions of aggregates were found for non-cross-linked particles and still for CCPMs from bifunctional cross-linkers and X_n = 17, yet not when the trifunctional peptide cross-linker was applied. Nevertheless, no significant differences for the circulation half-life or biodistribution could be detected after intravenous administration to mice, whereby the circulation half-lives of 11.3 - 19.1 h indicated sufficient stability for drug delivery *via* passive targeting mechanisms.

Envisioning large-scale production of CCPMs, a continuous flow process, and a strategy for decoupled drug conjugation was presented in **chapter 5**. Self-assembly and core cross-linking of pSar-*b*-p(L)Cys(SO$_2$Et) with dihydrolipoic acid hydrazide were adjusted and transferred to the production *via* slit-interdigital micromixers. The process parameters were optimized, yielding a robust procedure for up to 650 mg CCPMs/h without numbering up. CCPMs were further purified by online tangential flow filtration reducing the concentration of unconjugated polymer to below the limit of detection ($\leq 0.5\%$). The CCPMs could then be loaded with paclitaxel-levulinic acid in a separate step (PTX@CCPMs), allowing for stimuli-responsive drug release at endo-lysosomal pH values. When tested in cell culture and xenograft B16F1 zebrafish larvae models, PTX@CCPMs showed comparable performance yet reduced toxicity compared to state-of-the-art treatment with nanoparticle albumin-bound paclitaxel. The disclosed strategy may ease CCPM production, allowing to screen for combination therapies.

In **chapter 6**, polypept(o)ides were combined with photo-responsive ruthenium(II) complexes as metal-based APIs offering to use light as an external trigger for drug release from CCPMs. Polypept(o)ides based on pSar-*b*-poly(glutamic acid) (pSar-*b*-pGlu) were synthesized and modified with aromatic nitrile moieties for coordination of bis(bipyridine)ruthenium(II) ([Ru(bpy)$_2$]$^{2+}$) or bis(biquinoline)ruthenium(II) ([Ru(biq)$_2$]$^{2+}$) complexes. Depending on the flexibility or hydrophobicity of the linker, either spherical or worm-like micelles were obtained. The progress of the cross-linking reaction could be monitored *via* the color change originating from the ligand exchange reaction. Cross-linking did not affect the size distribution yet resulted in stable CCPMs according to GPC in hexafluoroisopropanol (HFIP) and DLS in human blood plasma. For drug release, CCPMs containing [Ru(bpy)$_2$]$^{2+}$ could be cleaved within 300 s, whereas only insufficient light-induced solvolysis was observed for [Ru(biq)$_2$]$^{2+}$ referring to low quantum yields and the dense micellar core. The photocleavable CCPMs were assessed in cell culture and the *in ovo* model confirming high biocompatibility and prolonged vascular circulation providing the basis for future investigations incorporating metal-based APIs with high cytotoxicity and fast-cleavage profiles.

Chapter 7 was focused on assessing precision medicine to account for the heterogeneous response of head and neck cancer patients to therapeutic regimens. Therefore, a cisplatin-resistant head and neck cancer cell line was established and sequenced. Drug uptake *via* the ion channel LRRC8A was identified as the molecular pathway for cisplatin resistance. The clinical significance of LRRC8A

as a biomarker was examined among a cohort of 500 head and neck cancer patients with data from The Cancer Genome Atlas. For patients under cisplatin treatment, low levels of LRRC8A correlated with lower overall survival. To bypass drug uptake by LRRC8A, cisplatin was conjugated to polypept(o)ides of pSar-*b*-pGlu(ONa). The chloride ligands of cisplatin were exchanged by the carboxylate groups in the side chain of glutamic acid, leading to small spherical polymeric micelles (NP$_{Cis}$, $D_h \approx 28$ nm) with high biocompatibility. NP$_{Cis}$ did not induce complement activation, colloidal stability was confirmed by DLS in human blood plasma, and the circulation half-life of approx. 4 h in zebrafish larvae indicated effective stabilization providing the basis for passive tumor targeting. In cell culture, NP$_{Cis}$ successfully reversed cisplatin resistance by circumventing the LRRC8A channel, which confirmed the significance of combining nanomedicine and molecular pathways for patient stratification.

The therapeutic potential of the co-factor iron upon specific delivery to macrophages was investigated in **chapter 8**. Iron oxide nanoparticles (SPIONs) were embedded in CCPMs based on pSar-*b*-p(L)Cys(SO$_2$Et). The building blocks were combined by cross-linking with dihydrolipoic acid aimed at chemoselective disulfide bond formation and coordination to the SPION surface *via* the carboxylate group. The resulting SPION-CCPMs showed colloidal stability in human blood plasma, and glutathione-responsive particle degradation. In co-cultures of primary murine macrophages and Lewis lung carcinoma cells SPION-CCPMs specifically sequestered in macrophages in an iron-related feedback-loop manner. The sustained iron release of SPION-CCPMs induced a strong inflammatory phenotype in both murine and human macrophages. Significantly elevated levels of inflammatory surface markers, e.g., cluster of differentiation 86 (CD86), and cytokines such as tumor necrosis factor α (TNFα) and interleukin 1ß (IL1ß) were thus detected. The observed sterile inflammation of macrophages was further confirmed *in vivo* after intratracheal administration of SPION-CCPMs to mice. Based on the design-to-release concept, SPION-CCPMs could be introduced as a promising adjuvant to overcome pathological immune tolerance and activate macrophages in the tumor microenvironment.

Discussion and Outlook

Throughout this thesis, CCPMs have been investigated as drug delivery systems, and tailored strategies have been applied to combine external or disease-related stimuli for controlled drug release. Established APIs such as paclitaxel and cisplatin, as well as novel therapeutics and co-factors, e.g., ruthenium(II) complexes and iron, were successfully implemented to CCPMs. The toolbox of polypept(o)ides as functional copolymers for straightforward synthesis of complex polymeric architectures was therefore explored and expanded.[1–3]

Considering the influence of the secondary structure formation on the synthesis of polypeptides *via* NCA polymerization, the focus of **chapter 2** was to improve the synthesis of thiol-reactive polypeptides.[4] The *S*-ethylsulfonyl-protecting group was introduced by Huesmann *et al.* in 2016 and remains intact during NCA polymerization with hard amine nucleophiles but can be addressed by soft nucleophile thiols in post-polymerization modification reactions for chemo-selective disulfide bond formation.[5] Despite this outstanding feature, the polymerization of cysteine NCA is severely hampered by the formation of strong anti-parallel ß-sheets during the polymerization.[6–8] Consequently, only low monomer conversion can be achieved albeit with long reaction times. Moreover, for chain lengths above $X_n = 20$, multimodal molecular weight distributions are obtained by HFIP-GPC, complicating reliable analysis.[8–10] On the other hand, the polymerization of *S*-ethylsulfonyl-L-homocysteine NCA leads to a favorable α-helix promoting the polymerization, but the synthesis of the protected amino acid requires laborious and time-consuming purification by preparative high-performance liquid chromatography compromising larger-scale production.[11–14] To disrupt the interfering hydrogen bonds, the addition of chaotropic thiourea was suggested, however did not contribute to improving the polymerization of *S*-ethylsulfonyl cysteine NCA.[15,16] As outlined, the use of racemic *S*-ethylsulfonyl-DL-cysteine successfully improved the polymerization. Full monomer conversion and polymers with molecular weights up to 20 kDa and well-defined dispersity could be achieved. Even though the reaction kinetics still followed the Avrami model of a physically hindered polymerization, the rate constant was on average 40 % faster compared to the enantiopure L-cysteine analog.[8,17–19] Nevertheless, the polymerization of α-helical *S*-ethylsulfonyl-L-homocysteine NCA was 5-fold faster, which underlines the critical influence of the secondary structure on the polymerization. For these reasons, mostly α-helical polypeptides have been

investigated throughout the literature, and recent developments on accelerated NCA polymerization using organocatalysts do not cover ß-sheet forming polypeptides.[7,12,14,20–23] Since more complex polymeric architectures, such as triblock copolymers, could be conveniently realized with racemic *S*-ethylsulfonyl-DL-cysteine, this chapter provides a valuable contribution to the field of NCA polymerization. Future applications of the thiol-reactive protecting group may thus be facilitated by the easier synthesis and handling of p(DL)Cys(SO$_2$Et), supporting the design of cross-linkable materials and drug delivery systems.

Building up on the results of chapter 2, the influence of secondary structure formation on self-assembly of thiol-reactive block copolymers was investigated in **chapter 3**.[16] As reported by Klinker *et al.*, anti-parallel ß-sheet formation can be used to direct self-assembly of pSar-*b*-p(L)Cys(SO$_2$Et), leading to worm-like micelles unless the secondary structure was suppressed by the addition of chaotropic thiourea during self-assembly.[9] In a similar manner, ß-sheets have been exploited previously as a driving force for hydrogelation.[24] To expand the application of thiol-reactive copolymers, the influence of the three secondary structure motifs was elucidated by direct comparison of enantiopure pSar-*b*-p(L)Cys(SO$_2$Et), racemic pSar-*b*-p(DL)Cys(SO$_2$Et), and α-helical pSar-*b*-p(L)Hcy(SO$_2$Et). Indeed, albeit similar primary structure and thus similar hydrophobicity of the polypeptide block, secondary structure formation was confirmed as the major driving force for self-assembly. In particular the comparison of racemic pSar-*b*-p(DL)Cys(SO$_2$Et) and enantiopure pSar-*b*-p(L)Cys(SO$_2$Et) revealed that aggregation during the solvent switch starts at significantly lower water content for intact anti-parallel ß-sheets. Regarding the nanoparticle morphology, interestingly the racemic pSar-*b*-p(DL)Cys(SO$_2$Et) induced the formation of less uniform spherical to slightly elongated structures indicating a residual directing character of the racemic ß-sheets.[25,26] In contrast, solely spherical morphologies were detected for CCPMs based on α-helical pSar-*b*-p(L)Hcy(SO$_2$Et) for copolymers containing up to 27 wt.% of pHcy(SO$_2$Et). These findings relate to reports by the Kataoka group for the bundled assembly of poly(ethylene glycol)-*b*-pGlu helices for NC-6004 containing cisplatin conjugated to the pGlu block.[27,28] The detailed understanding of the relation between secondary structure, self-assembly and particle morphology of the thiol-reactive copolypept(o)ides may support future studies elucidating the effect of the shape on the performance of the core cross-linked drug delivery system with a soft nanoparticle surface.[29–32]

To further develop CCPMs from the established copolypept(o)ides of enantiopure pSar-*b*-p(L)Cys(SO$_2$Et), the influence of the core cross-linking itself on nanoparticle stability was analyzed in **chapter 4**. The detailed study was motivated by initial findings that CCPMs cross-linked with lipoic acid derivatives induced aggregation during analysis by AF4 in human blood plasma, despite being considered stable according to analysis by HFIP-GPC, DLS in human blood plasma, and circulation half-life in zebrafish larvae.[33–35] The analysis of nanoparticles by AF4 in human blood plasma was previously realized by Alberg *et al.* to investigate the protein corona formation for soft nanoparticles of low density.[36] In fact, a negligible protein corona was found for CCPMs (CPC634) and pSar-shielded peptobrushes, which was attributed to the steric shielding by the dense hydrophilic polymer shell. These results are of significance for the clinical investigation of CPC634 (CCPMs containing covalently encapsulated docetaxel) since otherwise patient-specific protein corona formation could impact the performance of the nanomedicine.[36–40] For non-cross-linked PMs, however, clear signs of interaction with plasma proteins were observed.[41] Since pSar was confirmed as protein resistant material, the results described in chapter 4 thus indicated that the core cross-linking for $X_{n,\,pCys(SO2Et)}$ = 17 and bifunctional cross-linkers did not sufficiently stabilize the micellar structure to prevent interaction with blood plasma components.[36,42–44] By increasing the number of cross-linking net points, the particle stability could be precisely tuned. In particular, the designed trifunctional peptide cross-linker yielded a lower tendency for aggregate formation. Besides more efficient cross-linking referring to the Carothers equation, the peptide containing cysteine mimics symmetrical disulfide bonds, and self-immolative cleavage by shuffling of disulfide bonds is unlikely since only 11-membered rings can be formed.[45,46] Conversely, 5-membered dithiolane rings can be released in the case of lipoic acid.[45] Surprisingly, the results of the AF4 analysis were not reflected by FCS analysis in human blood plasma, despite being a sensitive tool to elucidate nanoparticle stability in complex media.[47,48] Moreover, intravenous administration to mice did not reveal statistically significant differences for the circulation half-life and biodistribution among the different particle groups. Variations in the sensitivity of the detection modes may account for the observed disparities. As such, light scattering is highly sensitive to larger structures (I ~r^6) overinterpreting aggregates.[49,50] A deeper understanding of the core architecture using NMR spectroscopy or neutron scattering may thus be required to assess the microstructural differences in the micellar core.[51] *Vice*

versa, the non-significant differences observed in the *in vivo* experiment advocate for reducing complexity when designing functional cross-linkers.[52]

Envisioning the larger-scale production of drug-loaded CCPMs, a continuous flow process for self-assembly, cross-linking, and purification, as well as a strategy for decoupled drug conjugation was presented in **chapter 5**. Bottlenecks for CCPM production were identified as the cross-linking and, more severely, the nanoparticle purification. Microfluidics are considered the state-of-the-art technique for liposome and lipid nanoparticle production.[53–56] Micro-structured mixers allowing for precise control of solvent mixing were thus adapted and applied as the central device defining self-assembly and core cross-linking.[57,58] Furthermore, the tedious manual spin-filtration process was substituted by the online tangential flow filtration. In combination, the designed continuous flow process enabled the robust production of purified CCPMs with significantly higher throughput compared to the laboratory procedure. Additional scale-up can be readily performed by numbering-up circumventing classical scale-up tasks of re-defining the optimum parameters. Polypept(o)ides of pSar-*b*-p(L)Cys(SO$_2$Et) were selected as the functional material accounting for their fast and chemoselective disulfide bond formation.[5,9,59–61] The starting material was complemented by dihydrolipoic acid hydrazide and paclitaxel-levulinic acid, enabling hydrazone bond formation, adding the pH-value as an additional trigger for drug release.[16,62–64] The dual stimuli-responsive system was designed aiming for complete drug release, since slow and deficient clearance was observed during the clinical investigation of NK105 (PMs containing paclitaxel stabilized by π-π interactions) and CPC634 (CCPMs with conjugated docetaxel for gradual release at pH 7.4).[38,39,65–67] In the presented concept, CCPM synthesis and purification were first completed before drug conjugation was performed in a second step. Despite mediocre conjugation efficiency for the relatively large molecule paclitaxel, this approach can be expanded to other APIs allowing for rapid screening of combination therapies featured by nanomedicine.[68–70]

Implementing light as an external trigger for drug release, polypept(o)ides were synthesized and modified for stimuli-responsive conjugation of ruthenium(II) complexes in **chapter 6**.[71] Besides monoclonal antibodies and classical taxane or anthracycline small-molecule drugs, metal-based chemotherapeutics are frequently used in the first-line treatment for many types of cancer.[72–78] Ruthenium complexes have been investigated as an alternative to conventional cisplatin, combining the ability to induce cytotoxicity by DNA cross-links with a

rich photochemistry prone to light-induced ligand exchange reactions and singlet oxygen production.[79–82] In combination with nanomedicine, the hydrophobic ruthenium complexes can be encapsulated in carrier systems providing passive tumor targeting while being activated only after irradiation which provides additional spatial resolution for drug release.[83,84] To serve as the functional material, polypept(o)ides of pSar-*b*-pGlu were synthesized, and the carboxyl side chain of pGlu was modified with linkers containing aromatic nitrile moieties.[71] The coordination of the nitrile-nitrogen atom to the central ruthenium ion was previously investigated and established as a light-responsive dynamic covalent bond for polypyridyl ruthenium(II) complexes.[84–87] Aiming to improve the grafting efficiency of the post-polymerization modification reaction, two linkers were applied to differentiate the connection to pGlu *via* amide or ester bond. Interestingly, the variations induced alterations in the morphology of the PMs. Modification with the shorter and more hydrophobic amine resulted in worm-like PMs, whereas solely spherical morphologies were obtained for the ester linkage with a longer and more flexible alkyl chain. Despite flexibility and hydrophobicity, also differences in hydrogen bond and secondary structure formation could account for the structural transitions.[7,88,89] Cross-linking with the ruthenium(II) complexes did not influence the morphologies, and similar conjugation efficiencies were obtained. Referring to the biological application, high biocompatibility and particle stability were found for the photocleavable CCPMs. Nevertheless, in cell culture and the *in ovo* model, the intended cytotoxicity upon photoactivation was mainly attributed to the irradiation itself. In particular, for $[Ru(biq)_2]^{2+}$, the low quantum yield of the ligand exchange reaction combined with the dense micellar core reduced the toxicity of the conjugated complex.[87,90] Since combining nanomedicine and photoactivated chemotherapy represents a promising concept for therapy of certain types of cancer, e.g., head and neck cancer, future studies will be focused on the design of metal complexes with high cytotoxicity and fast release profile.[91]

In **chapter 7**, the mechanisms for resistance to cisplatin therapy were analyzed and correlated to the survival of head and neck cancer patients. Nanomedicine featured by polypept(o)ides was then applied to provide an additional drug uptake pathway *via* endocytosis and overcome drug resistance. Cisplatin resistant head and neck cancer cells (Fadu) were established by prolonged treatment with sub-toxic drug concentrations mimicking the induced selection process upon chemotherapy.[92,93] By RNA sequencing transcriptomics, among other transporter

genes, genetic alterations in the expression of the ion channel LRRC8A were identified as the most prominent variation between resistant and wild-type Fadu cells. Low expression levels of LRRC8A impaired cisplatin uptake and were even maintained when cells were cultured in the absence of cisplatin, accounting for stable genetic modification. Besides reduced expression of VRAC channels required for cisplatin uptake, other mechanisms for drug resistance have been described in the literature.[76,93–95] In particular, elevated levels of glutathione, methionine, and other cysteine-rich proteins were identified to detoxify cisplatin, rescuing cancer cells from chemotherapy.[94,96,97] Nevertheless, for head and neck cancer patients under cisplatin therapy, decreased levels of LRRC8A could be correlated with reduced overall survival, giving a rationale and a biomarker for personalized nanomedicine.[98,99] Polypept(o)ides of pSar-*b*-pGlu(ONa) were thus synthesized, and cisplatin was conjugated to the carboxyl side chain of pGlu(ONa) yielding NP$_{Cis}$. During nanoparticle synthesis, the exchange of the chloride ligands by the carboxyl groups converted the hydrophilic charged pGlu(ONa) block to an uncharged and hydrophobic polymer, inducing self-assembly. Hence, NP$_{Cis}$ resemble NC-6004 based on PEG-*b*-pGlu(ONa), which is currently under clinical investigation (phase III) for the treatment of pancreatic cancer.[28,100,101] Of note, the preparation NP$_{Cis}$ based on polypept(o)ides by the mild NCA polymerization offers block copolymer synthesis by sequential polymerization, and access to functional end-groups for further modification with targeting moieties to enhance or specify cellular uptake.[3,102,103] Concerning the core structure, for NC-6004, predominantly bundled assembly of cisplatin-containing α-helices was reported from small-angle X-ray scattering, however, a certain degree of cross-linking cannot generally be excluded.[27,101,104] Compared to the free cisplatin, nanoparticles allow for uptake *via* endocytic pathways bypassing LRRC8A. In cell culture, NP$_{Cis}$ thus significantly reduced the viability of cisplatin-resistant Fadu cells. The presented approach demonstrates the potential of nanomedicine when combined with genomic analysis of drug resistance mechanisms. Future studies will continue elucidating relevant resistance pathways to target therapeutic failures and relapse. In addition, the obtained results will be further validated in cell culture and in *in vivo* disease models.

Empowering the co-factor iron as a therapeutic for immunomodulation, SPION-CCPMs were designed for sustained release and specific delivery of iron to macrophages, as introduced in **chapter 8**.[34] The essential co-factor iron is involved in numerous cellular processes in the human body, and impaired iron

homeostasis is linked to multiple pathologies and diseases.[105–107] Despite that potential, iron oxide nanoparticles were initially intended as contrast agents for magnetic resonance imaging, and drug delivery systems were designed for effective shielding of the delicate cargo.[108–110] In spite, the majority of the administered iron was metabolized, and Ferumoxytol (SPIONs encapsulated in a matrix of cross-linked carboxymethyl dextran) was instead approved for the treatment of iron deficiency anemia.[110–112] Referring to the therapeutic potential of iron, Zanganeh *et al.* reported on reduced tumor growth upon local administration of Ferumoxytol in 2016.[113] Moreover, Thielmann *et al.* correlated increased iron levels in tumor-associated macrophages with higher overall survival of patients with lung adenocarcinoma.[114] The therapeutic effects were attributed to the activation of tumor-associated macrophages leading to a stimulated anti-tumor immune response.[113–116] To specifically enable sustained and stimuli-responsive release and exploit the potential of iron as a stimulating agent for immunotherapy, SPION-CCPMs were designed based on polypept(o)ides of pSar-*b*-p(L)Cys(SO$_2$Et). Herein, SPIONs were encapsulated in a matrix of polycysteine that was cross-linked with dihydrolipoic acid. Since lipoic acid can anchor to the iron oxide nanoparticle surface *via* the carboxyl group, all building blocks were connected while being sensitive to redox-responsive release.[117–119] In the co-culture of macrophages and cancer cells, interestingly, a feedback mechanism leads to enhanced uptake of SPION-CCPMs in macrophages, whereas non-iron-loaded CCPMs were predominantly accumulated in the cancer cells. The selective distribution may thus direct to cell-specific therapies applying stimulating agents to macrophages and cytotoxic APIs to cancer cells. In addition, the detailed mechanisms of the sterile inflammation induced by SPION-CCPMs remain to be elucidated. The described activation of primary murine and human macrophages by SPION-CCPMs extended the effects induced by other iron sources, suggesting an influence of the factual co-delivery of cysteine and iron. Replacing SPIONs with iron sulfide nanoparticles or iron-containing metal-organic frameworks may thus direct to novel classes of therapeutics to defeat pathologic immune tolerance mechanisms.

Taken together, polypept(o)ides and CCPMs were explored as functional materials to improve the therapeutic potential of APIs. The developed understanding of the relationship between secondary structure formation on polymerization and self-assembly will support exploring thiol-reactive polypept(o)ides in nanomedicine and for the design of advanced materials. Next-

generation nanomedicines that aim to refine the potential of novel APIs and drug combinations embrace a complex subset of tasks. The presented design concepts of stimuli-responsive CCPMs may thus add to produce adaptive drug carriers by scalable and reproducible techniques.

References

(1)   Birke, A.; Huesmann, D.; Kelsch, A.; Weilbächer, M.; Xie, J.; Bros, M.; Bopp, T.; Becker, C.; Landfester, K.; Barz, M. Polypeptoid- Block -Polypeptide Copolymers: Synthesis, Characterization, and Application of Amphiphilic Block Copolypept(o)ides in Drug Formulations and Miniemulsion Techniques. *Biomacromolecules* **2014**, *15* (2), 548–557.

(2)   Birke, A.; Ling, J.; Barz, M. Polysarcosine-Containing Copolymers: Synthesis, Characterization, Self-Assembly, and Applications. *Prog. Polym. Sci.* **2018**, *81*, 163–208.

(3)   Klinker, K.; Barz, M. Polypept(o)Ides: Hybrid Systems Based on Polypeptides and Polypeptoids. *Macromol. Rapid Commun.* **2015**, *36* (22), 1943–1957.

(4)   Bauer, T. A.; Muhl, C.; Schollmeyer, D.; Barz, M. Racemic S -(Ethylsulfonyl)- Dl - cysteine N -Carboxyanhydrides Improve Chain Lengths and Monomer Conversion for B-Sheet-Controlled Ring-Opening Polymerization. *Macromol. Rapid Commun.* **2021**, *42* (8), 2000470.

(5)   Schäfer, O.; Huesmann, D.; Muhl, C.; Barz, M. Rethinking Cysteine Protective Groups: S -Alkylsulfonyl- l -Cysteines for Chemoselective Disulfide Formation. *Chem. - A Eur. J.* **2016**, *22* (50), 18085–18091.

(6)   Berger, A.; Noguchi, J.; Katchalski, E. Poly-L-Cysteine. *J. Am. Chem. Soc.* **1956**, *78* (17), 4483–4488.

(7)   Bonduelle, C. Secondary Structures of Synthetic Polypeptide Polymers. *Polym. Chem.* **2018**, *9* (13), 1517–1529.

(8)   Schäfer, O.; Huesmann, D.; Barz, M. Poly(S -Ethylsulfonyl- l -Cysteines) for Chemoselective Disulfide Formation. *Macromolecules* **2016**, *49* (21), 8146–8153.

(9)   Klinker, K.; Schäfer, O.; Huesmann, D.; Bauer, T.; Capelôa, L.; Braun, L.; Stergiou, N.; Schinnerer, M.; Dirisala, A.; Miyata, K.; Osada, K.; Cabral, H.; Kataoka, K.; Barz, M. Secondary-Structure-Driven Self-Assembly of Reactive Polypept(o)Ides: Controlling Size, Shape, and Function of Core Cross-Linked Nanostructures. *Angew. Chemie Int. Ed.* **2017**, *56* (32), 9608–9613.

(10)   Huesmann, D.; Birke, A.; Klinker, K.; Türk, S.; Räder, H. J.; Barz, M. Revisiting Secondary Structures in NCA Polymerization: Influences on the Analysis of Protected Polylysines. *Macromolecules* **2014**, *47* (3), 928–936.

(11)   Muhl, C.; Schäfer, O.; Bauer, T.; Räder, H.-J.; Barz, M. Poly(S -Ethylsulfonyl- l - Homocysteine): An α-Helical Polypeptide for Chemoselective Disulfide Formation. *Macromolecules* **2018**, *51* (20), 8188–8196.

(12)   Baumgartner, R.; Fu, H.; Song, Z.; Lin, Y.; Cheng, J. Cooperative Polymerization of α-Helices Induced by Macromolecular Architecture. *Nat. Chem.* **2017**, *9* (7), 614–622.

(13)   Chen, C.; Fu, H.; Baumgartner, R.; Song, Z.; Lin, Y.; Cheng, J. Proximity-Induced

Cooperative Polymerization in "Hinged" Helical Polypeptides. *J. Am. Chem. Soc.* **2019**, *141* (22), 8680–8683.

(14) Kricheldorf, H. R. Polypeptides and 100 Years of Chemistry of α-Amino Acid N-Carboxyanhydrides. *Angew. Chemie - Int. Ed.* **2006**, *45* (35), 5752–5784.

(15) Ulkoski, D.; Scholz, C. Synthesis and Application of Aurophilic Poly(Cysteine) and Poly(Cysteine)-Containing Copolymers. *Polymers (Basel).* **2017**, *9* (12), 500.

(16) Bauer, T. A.; Imschweiler, J.; Muhl, C.; Weber, B.; Barz, M. Secondary Structure-Driven Self-Assembly of Thiol-Reactive Polypept(o)Ides. *Biomacromolecules* **2021**, *22* (5), 2171–2180.

(17) Iguchi, M. A Comment on the Kinetics in a Heterogeneous Polymerization System. *J. Polym. Sci. Part A-1 Polym. Chem.* **1970**, *8* (4), 1013–1021.

(18) Kawai, T.; Komoto, T. Crystallization of Polypeptides during Polymerization. *J. Cryst. Growth* **1980**, *48* (2), 259–282.

(19) Komoto, T.; Oya, M.; Kawai, T. Crystallization of Polypeptides in the Course of Polymerization. *Macromol. Chem.* **1974**, *175* (1), 301–310.

(20) Zhao, W.; Lv, Y.; Li, J.; Feng, Z.; Ni, Y.; Hadjichristidis, N. Fast and Selective Organocatalytic Ring-Opening Polymerization by Fluorinated Alcohol without a Cocatalyst. *Nat. Commun.* **2019**, *10* (1), 3590.

(21) Lv, S.; Kim, H.; Song, Z.; Feng, L.; Yang, Y.; Baumgartner, R.; Tseng, K. Y.; Dillon, S. J.; Leal, C.; Yin, L.; Cheng, J. Unimolecular Polypeptide Micelles via Ultrafast Polymerization of N-Carboxyanhydrides. *J. Am. Chem. Soc.* **2020**, *142* (19), 8570–8574.

(22) Xia, Y.; Song, Z.; Tan, Z.; Xue, T.; Wei, S.; Zhu, L.; Yang, Y.; Fu, H.; Jiang, Y.; Lin, Y.; Lu, Y.; Ferguson, A. L.; Cheng, J. Accelerated Polymerization of N-Carboxyanhydrides Catalyzed by Crown Ether. *Nat. Commun.* **2021**, *12* (1).

(23) Lundberg, R. D.; Doty, P. Polypeptides. XVII. A Study of the Kinetics of the Primary Amine-Initiated Polymerization of N-Carboxy-Anhydrides with Special Reference to Configurational and Stereochemical Effects. *J. Am. Chem. Soc.* **1957**, *79* (15), 3961–3972.

(24) Otter, R.; Henke, N. A.; Berac, C.; Bauer, T.; Barz, M.; Seiffert, S.; Besenius, P. Secondary Structure-Driven Hydrogelation Using Foldable Telechelic Polymer–Peptide Conjugates. *Macromol. Rapid Commun.* **2018**, *39* (17).

(25) Rubinstein, I.; Eliash, R.; Bolbach, G.; Weissbuch, I.; Lahav, M. Racemic β Sheets in Biochirogenesis. *Angew. Chemie* **2007**, *119* (20), 3784–3787.

(26) Pauling, L.; Corey, R. B. Two Rippled-Sheet Configurations of Polypeptide Chains, and a Note about the Pleated Sheets. *Proc. Natl. Acad. Sci.* **1953**, *39* (4), 253–256.

(27) Mochida, Y.; Cabral, H.; Miura, Y.; Albertini, F.; Fukushima, S.; Osada, K.; Nishiyama, N.; Kataoka, K. Bundled Assembly of Helical Nanostructures in Polymeric Micelles Loaded with Platinum Drugs Enhancing Therapeutic Efficiency against Pancreatic Tumor. *ACS Nano* **2014**, *8* (7), 6724–6738.

(28) Mochida, Y.; Cabral, H.; Kataoka, K. Polymeric Micelles for Targeted Tumor Therapy of Platinum Anticancer Drugs. *Expert Opin. Drug Deliv.* **2017**, *14* (12), 1423–1438.

(29) Toy, R.; Peiris, P. M.; Ghaghada, K. B.; Karathanasis, E. Shaping Cancer Nanomedicine: The Effect of Particle Shape on the in Vivo Journey of Nanoparticles.

Nanomedicine **2014**, *9* (1), 121–134.

(30) Venkataraman, S.; Hedrick, J. L.; Ong, Z. Y.; Yang, C.; Ee, P. L. R.; Hammond, P. T.; Yang, Y. Y. The Effects of Polymeric Nanostructure Shape on Drug Delivery. *Adv. Drug Deliv. Rev.* **2011**, *63* (14–15), 1228–1246.

(31) Kinnear, C.; Moore, T. L.; Rodriguez-Lorenzo, L.; Rothen-Rutishauser, B.; Petri-Fink, A. Form Follows Function: Nanoparticle Shape and Its Implications for Nanomedicine. *Chem. Rev.* **2017**, *117* (17), 11476–11521.

(32) Richtering, W.; Alberg, I.; Zentel, R. Nanoparticles in the Biological Context: Surface Morphology and Protein Corona Formation. *Small* **2020**, *16* (39), 1–8.

(33) Dal, N. K.; Kocere, A.; Wohlmann, J.; Van Herck, S.; Bauer, T. A.; Resseguier, J.; Bagherifam, S.; Hyldmo, H.; Barz, M.; De Geest, B. G.; Fenaroli, F. Zebrafish Embryos Allow Prediction of Nanoparticle Circulation Times in Mice and Facilitate Quantification of Nanoparticle–Cell Interactions. *Small* **2020**, *16* (5), 1906719.

(34) Bauer, T. A.; Horvat, N. K.; Marques, O.; Chocarro, S.; Mertens, C.; Colucci, S.; Schmitt, S.; Carrella, L. M.; Morsbach, S.; Koynov, K.; Fenaroli, F.; Blümler, P.; Jung, M.; Sotillo, R.; Hentze, M. W.; Muckenthaler, M. U.; Barz, M. Core Cross-Linked Polymeric Micelles for Specific Iron Delivery: Inducing Sterile Inflammation in Macrophages. *Adv. Healthc. Mater.* **2021**, *10* (19), 2100385.

(35) Rausch, K.; Reuter, A.; Fischer, K.; Schmidt, M. Evaluation of Nanoparticle Aggregation in Human Blood Serum. *Biomacromolecules* **2010**, *11* (11), 2836–2839.

(36) Alberg, I.; Kramer, S.; Schinnerer, M.; Hu, Q.; Seidl, C.; Leps, C.; Drude, N.; Möckel, D.; Rijcken, C.; Lammers, T.; Diken, M.; Maskos, M.; Morsbach, S.; Landfester, K.; Tenzer, S.; Barz, M.; Zentel, R. Polymeric Nanoparticles with Neglectable Protein Corona. *Small* **2020**, *16* (18), 1907574.

(37) Docter, D.; Distler, U.; Storck, W.; Kuharev, J.; Wünsch, D.; Hahlbrock, A.; Knauer, S. K.; Tenzer, S.; Stauber, R. H. Quantitative Profiling of the Protein Coronas That Form around Nanoparticles. *Nat. Protoc.* **2014**, *9* (9), 2030–2044.

(38) Atrafi, F.; Dumez, H.; Mathijssen, R. H. J.; Menke van der Houven van Oordt, C. W.; Rijcken, C. J. F.; Hanssen, R.; Eskens, F. A. L. M.; Schöffski, P. A Phase I Dose-Escalation and Pharmacokinetic Study of a Micellar Nanoparticle with Entrapped Docetaxel (CPC634) in Patients with Advanced Solid Tumours. *J. Control. Release* **2020**, *325* (March), 191–197.

(39) Atrafi, F.; van Eerden, R. A. G.; van Hylckama Vlieg, M. A. M.; Oomen-de Hoop, E.; de Bruijn, P.; Lolkema, M. P.; Moelker, A.; Rijcken, C. J.; Hanssen, R.; Sparreboom, A.; Eskens, F. A. L. M.; Mathijssen, R. H. J.; Koolen, S. L. W. Intratumoral Comparison of Nanoparticle Entrapped Docetaxel (CPC634) with Conventional Docetaxel in Patients with Solid Tumors. *Clin. Cancer Res.* **2020**, *26* (14), 3537–3545.

(40) Mahmoudi, M.; Bertrand, N.; Zope, H.; Farokhzad, O. C. Emerging Understanding of the Protein Corona at the Nano-Bio Interfaces. *Nano Today* **2016**, *11* (6), 817–832.

(41) Alberg, I.; Kramer, S.; Leps, C.; Tenzer, S.; Zentel, R. Effect of Core-Crosslinking on Protein Corona Formation on Polymeric Micelles. *Macromol. Biosci.* **2021**, *2000414*.

(42) Ostuni, E.; Chapman, R. G.; Liang, M. N.; Meluleni, G.; Pier, G.; Ingber, D. E.; Whitesides, G. M. Self-Assembled Monolayers That Resist the Adsorption of

Proteins and the Adhesion of Bacterial and Mammalian Cells. *Langmuir* **2001**, *17* (20), 6336–6343.

(43)   Ostuni, E.; Chapman, R. G.; Holmlin, R. E.; Takayama, S.; Whitesides, G. M. A Survey of Structure-Property Relationships of Surfaces That Resist the Adsorption of Protein. *Langmuir* **2001**, *17* (18), 5605–5620.

(44)   Lau, K. H. A.; Ren, C.; Sileika, T. S.; Park, S. H.; Szleifer, I.; Messersmith, P. B. Surface-Grafted Polysarcosine as a Peptoid Antifouling Polymer Brush. *Langmuir* **2012**, *28* (46), 16099–16107.

(45)   Zhang, X.; Waymouth, R. M. 1,2-Dithiolane-Derived Dynamic, Covalent Materials: Cooperative Self-Assembly and Reversible Cross-Linking. *J. Am. Chem. Soc.* **2017**, *139* (10), 3822–3833.

(46)   Poole, L. B. The Basics of Thiols and Cysteines in Redox Biology and Chemistry. *Free Radic. Biol. Med.* **2015**, *80*, 148–157.

(47)   Negwer, I.; Best, A.; Schinnerer, M.; Schäfer, O.; Capeloa, L.; Wagner, M.; Schmidt, M.; Mailänder, V.; Helm, M.; Barz, M.; Butt, H. J.; Koynov, K. Monitoring Drug Nanocarriers in Human Blood by Near-Infrared Fluorescence Correlation Spectroscopy. *Nat. Commun.* **2018**, *9* (1).

(48)   Holm, R.; Douverne, M.; Weber, B.; Bauer, T.; Best, A.; Ahlers, P.; Koynov, K.; Besenius, P.; Barz, M. Impact of Branching on the Solution Behavior and Serum Stability of Starlike Block Copolymers. *Biomacromolecules* **2019**, *20* (1), 375–388.

(49)   Bhattacharjee, S. DLS and Zeta Potential - What They Are and What They Are Not? *J. Control. Release* **2016**, *235*, 337–351.

(50)   Fischer, K.; Schmidt, M. Pitfalls and Novel Applications of Particle Sizing by Dynamic Light Scattering. *Biomaterials* **2016**, *98*, 79–91.

(51)   Grüne, M.; Luxenhofer, R.; Iuga, D.; Brown, S. P.; Pöppler, A. C. 14N-1H HMQC Solid-State NMR as a Powerful Tool to Study Amorphous Formulations-an Exemplary Study of Paclitaxel Loaded Polymer Micelles. *J. Mater. Chem. B* **2020**, *8* (31), 6827–6836.

(52)   Leroux, J. C. Drug Delivery: Too Much Complexity, Not Enough Reproducibility? *Angew. Chemie - Int. Ed.* **2017**, 2–4.

(53)   Belliveau, N. M.; Huft, J.; Lin, P. J.; Chen, S.; Leung, A. K.; Leaver, T. J.; Wild, A. W.; Lee, J. B.; Taylor, R. J.; Tam, Y. K.; Hansen, C. L.; Cullis, P. R. Microfluidic Synthesis of Highly Potent Limit-Size Lipid Nanoparticles for in Vivo Delivery of SiRNA. *Mol. Ther. - Nucleic Acids* **2012**, *1* (8), e37.

(54)   Evers, M. J. W.; Kulkarni, J. A.; van der Meel, R.; Cullis, P. R.; Vader, P.; Schiffelers, R. M. State-of-the-Art Design and Rapid-Mixing Production Techniques of Lipid Nanoparticles for Nucleic Acid Delivery. *Small Methods* **2018**, *2* (9), 1700375.

(55)   Allen, T. M.; Cullis, P. R. Liposomal Drug Delivery Systems: From Concept to Clinical Applications. *Adv. Drug Deliv. Rev.* **2013**, *65* (1), 36–48.

(56)   Marre, S.; Jensen, K. F. Synthesis of Micro and Nanostructures in Microfluidic Systems. *Chem. Soc. Rev.* **2010**, *39* (3), 1183–1202.

(57)   Keßler, S.; Drese, K.; Schmid, F. Simulating Copolymeric Nanoparticle Assembly in the Co-Solvent Method: How Mixing Rates Control Final Particle Sizes and Morphologies. *Polymer (Guildf).* **2017**, *126*, 9–18.

(58)   Thiermann, R.; Bleul, R.; Maskos, M. Kinetic Control of Block Copolymer Self-

Assembly in a Micromixing Device – Mechanistical Insight into Vesicle Formation Process. *Macromol. Chem. Phys.* **2017**, *218* (2), 1–9.

(59)   Huesmann, D.; Schäfer, O.; Braun, L.; Klinker, K.; Reuter, T.; Barz, M. Exploring New Activating Groups for Reactive Cysteine NCAs. *Tetrahedron Lett.* **2016**, *57* (10), 1138–1142.

(60)   Schäfer, O.; Klinker, K.; Braun, L.; Huesmann, D.; Schultze, J.; Koynov, K.; Barz, M. Combining Orthogonal Reactive Groups in Block Copolymers for Functional Nanoparticle Synthesis in a Single Step. *ACS Macro Lett.* **2017**, *6* (10), 1140–1145.

(61)   Schäfer, O.; Barz, M. Of Thiols and Disulfides: Methods for Chemoselective Formation of Asymmetric Disulfides in Synthetic Peptides and Polymers. *Chem. - A Eur. J.* **2018**, *24* (47), 12131–12142.

(62)   Kölmel, D. K.; Kool, E. T. Oximes and Hydrazones in Bioconjugation: Mechanism and Catalysis. *Chem. Rev.* **2017**, *117* (15), 10358–10376.

(63)   Quader, S.; Liu, X.; Toh, K.; Su, Y. L.; Maity, A. R.; Tao, A.; Paraiso, W. K. D.; Mochida, Y.; Kinoh, H.; Cabral, H.; Kataoka, K. Supramolecularly Enabled PH-Triggered Drug Action at Tumor Microenvironment Potentiates Nanomedicine Efficacy against Glioblastoma. *Biomaterials* **2021**, *267*, 120463.

(64)   Shi, Y.; Van Nostrum, C. F.; Hennink, W. E. Interfacially Hydrazone Cross-Linked Thermosensitive Polymeric Micelles for Acid-Triggered Release of Paclitaxel. *ACS Biomater. Sci. Eng.* **2015**, *1* (6), 393–404.

(65)   Mukai, H.; Kato, K.; Esaki, T.; Ohsumi, S.; Hozomi, Y.; Matsubara, N.; Hamaguchi, T.; Matsumura, Y.; Goda, R.; Hirai, T.; Nambu, Y. Phase I Study of NK105, a Nanomicellar Paclitaxel Formulation, Administered on a Weekly Schedule in Patients with Solid Tumors. *Invest. New Drugs* **2016**, *34* (6), 750–759.

(66)   Kato, K.; Chin, K.; Yoshikawa, T.; Yamaguchi, K.; Tsuji, Y.; Esaki, T.; Sakai, K.; Kimura, M.; Hamaguchi, T.; Shimada, Y.; Matsumura, Y.; Ikeda, R. Phase II Study of NK105, a Paclitaxel-Incorporating Micellar Nanoparticle, for Previously Treated Advanced or Recurrent Gastric Cancer. *Invest. New Drugs* **2012**, *30* (4), 1621–1627.

(67)   Fujiwara, Y.; Mukai, H.; Saeki, T.; Ro, J.; Lin, Y. C.; Nagai, S. E.; Lee, K. S.; Watanabe, J.; Ohtani, S.; Kim, S. B.; Kuroi, K.; Tsugawa, K.; Tokuda, Y.; Iwata, H.; Park, Y. H.; Yang, Y.; Nambu, Y. A Multi-National, Randomised, Open-Label, Parallel, Phase III Non-Inferiority Study Comparing NK105 and Paclitaxel in Metastatic or Recurrent Breast Cancer Patients. *Br. J. Cancer* **2019**, *120* (5), 475–480.

(68)   Komarova, N. L.; Boland, R. Calculated Treatment. *Nature* **2013**, *499*, 291–292.

(69)   Mokhtari, R. B.; Homayouni, T. S.; Baluch, N.; Morgatskaya, E.; Kumar, S.; Das, B.; Yeger, H. Combination Therapy in Combating Cancer. *Oncotarget* **2017**, *8* (23), 38022-38043.

(70)   Greco, F.; Vicent, M. J. Combination Therapy: Opportunities and Challenges for Polymer–Drug Conjugates as Anticancer Nanomedicines. *Adv. Drug Deliv. Rev.* **2009**, *61* (13), 1203–1213.

(71)   Bauer, T. A.; Eckrich, J.; Wiesmann, N.; Kuczelinis, F.; Sun, W.; Zeng, X.; Weber, B.; Wu, S.; Bings, N. H.; Strieth, S.; Barz, M. Photocleavable Core Cross-Linked Polymeric Micelles of Polypept(o)ides and Ruthenium(II) Complexes. *J. Mater. Chem. B* **2021**, *9* (39), 8211–8223.

(72)   Weaver, B. A. How Taxol/Paclitaxel Kills Cancer Cells. *Mol. Biol. Cell* **2014**, *25* (18), 2677–2681.

(73)   Stage, T. B.; Bergmann, T. K.; Kroetz, D. L. Clinical Pharmacokinetics of Paclitaxel Monotherapy: An Updated Literature Review. *Clin. Pharmacokinet.* **2018**, *57* (1), 7–19.

(74)   Goffin, J.; Lacchetti, C.; Ellis, P. M.; Ung, Y. C.; Evans, W. K. First-Line Systemic Chemotherapy in the Treatment of Advanced Non-Small Cell Lung Cancer: A Systematic Review. *J. Thorac. Oncol.* **2010**, *5* (2), 260–274.

(75)   Muhammad, N.; Guo, Z. Metal-Based Anticancer Chemotherapeutic Agents. *Curr. Opin. Chem. Biol.* **2014**, *19* (1), 144–153.

(76)   Shaloam, D.; Tchounwou, P. B. Cisplatin in Cancer Therapy: Molecular Mechanisms of Action. *Eur. J. Pharmacol.* **2014**, *740*, 364–378.

(77)   Costa, R. L. B.; Czerniecki, B. J. Clinical Development of Immunotherapies for HER2+ Breast Cancer: A Review of HER2-Directed Monoclonal Antibodies and Beyond. *npj Breast Cancer* **2020**, *6* (1), 10.

(78)   Rottenberg, S.; Disler, C.; Perego, P. The Rediscovery of Platinum-Based Cancer Therapy. *Nat. Rev. Cancer* **2020**, *21* (January), 37–50.

(79)   Mari, C.; Pierroz, V.; Ferrari, S.; Gasser, G. Combination of Ru(II) Complexes and Light: New Frontiers in Cancer Therapy. *Chem. Sci.* **2015**, *6* (5), 2660–2686.

(80)   Thota, S.; Rodrigues, D. A.; Crans, D. C.; Barreiro, E. J. Ru(II) Compounds: Next-Generation Anticancer Metallotherapeutics? *J. Med. Chem.* **2018**, *61* (14), 5805–5821.

(81)   Wielopolski, L.; Zhang, R.; Clarke, M. J.; Cohn, S. H. Determination of Ruthenium on DNA by XRF. *Biol. Trace Elem. Res.* **1987**, *13* (1), 283–290.

(82)   Zeng, L.; Gupta, P.; Chen, Y.; Wang, E.; Ji, L.; Chao, H.; Chen, Z. S. The Development of Anticancer Ruthenium(II) Complexes: From Single Molecule Compounds to Nanomaterials. *Chem. Soc. Rev.* **2017**, *46* (19), 5771–5804.

(83)   Villemin, E.; Ong, Y. C.; Thomas, C. M.; Gasser, G. Polymer Encapsulation of Ruthenium Complexes for Biological and Medicinal Applications. *Nat. Rev. Chem.* **2019**, *3* (4), 261–282.

(84)   Sun, W.; Li, S.; Häupler, B.; Liu, J.; Jin, S.; Steffen, W.; Schubert, U. S.; Butt, H.-J. J.; Liang, X.-J. J.; Wu, S. An Amphiphilic Ruthenium Polymetallodrug for Combined Photodynamic Therapy and Photochemotherapy In Vivo. *Adv. Mater.* **2017**, *29* (6), 1603702.

(85)   Liu, Y.; Turner, D. B.; Singh, T. N.; Angeles-Boza, A. M.; Chouai, A.; Dunbar, K. R.; Turro, C. Ultrafast Ligand Exchange: Detection of a Pentacoordinate Ru(II) Intermediate and Product Formation. *J. Am. Chem. Soc.* **2009**, *131* (1), 26–27.

(86)   Garner, R. N.; Gallucci, J. C.; Dunbar, K. R.; Turro, C. [Ru(Bpy) 2 (5-Cyanouracil) 2] 2+ as a Potential Light-Activated Dual-Action Therapeutic Agent. *Inorg. Chem.* **2011**, *50* (19), 9213–9215.

(87)   Sun, W.; Thiramanas, R.; Slep, L. D.; Zeng, X.; Mailänder, V.; Wu, S. Photoactivation of Anticancer Ru Complexes in Deep Tissue: How Deep Can We Go? *Chem. - A Eur. J.* **2017**, *23* (45), 10832–10837.

(88)   Palmer, L. C.; Stupp, S. I. Molecular Self-Assembly into One-Dimensional Nanostructures. *Acc. Chem. Res.* **2008**, *41* (12), 1674–1684.

(89) Lecommandoux, S.; Achard, M. F.; Langenwalter, J. F.; Klok, H. A. Self-Assembly of Rod-Coil Diblock Oligomers Based on α-Helical Peptides. *Macromolecules* **2001**, *34* (26), 9100–9111.

(90) Albani, B. A.; Durr, C. B.; Turro, C. Selective Photoinduced Ligand Exchange in a New Tris-Heteroleptic Ru (II) Complex Selective Photoinduced Ligand Exchange in a New Tris-Heteroleptic Ru (II) Complex. *J. Phys. Chem. A* **2013**, *117* (Ii), 13885–13892.

(91) Bonnet, S. Why Develop Photoactivated Chemotherapy? *Dalt. Trans.* **2018**, *47* (31), 10330–10343.

(92) Ughachukwu, P.; Unekwe, P. Efflux Pump-Mediated Resistance in Chemotherapy. *Ann. Med. Health Sci. Res.* **2012**, *2* (2), 191.

(93) Makovec, T. Cisplatin and beyond: Molecular Mechanisms of Action and Drug Resistance Development in Cancer Chemotherapy. *Radiol. Oncol.* **2019**, *53* (2), 148–158.

(94) Galluzzi, L.; Senovilla, L.; Vitale, I.; Michels, J.; Martins, I.; Kepp, O.; Castedo, M.; Kroemer, G. Molecular Mechanisms of Cisplatin Resistance. *Oncogene* **2012**, *31* (15), 1869–1883.

(95) Planells-Cases, R.; Lutter, D.; Guyader, C.; Gerhards, N. M.; Ullrich, F.; Elger, D. A.; Kucukosmanoglu, A.; Xu, G.; Voss, F. K.; Reincke, S. M.; Stauber, T.; Blomen, V. A.; Vis, D. J.; Wessels, L. F.; Brummelkamp, T. R.; Borst, P.; Rottenberg, S.; Jentsch, T. J. Subunit Composition of <scp>VRAC</Scp> Channels Determines Substrate Specificity and Cellular Resistance to <scp>P</Scp> T-based Anti-cancer Drugs. *EMBO J.* **2015**, *34* (24), 2993–3008.

(96) Chen, H. H. W.; Kuo, M. T. Role of Glutathione in the Regulation of Cisplatin Resistance in Cancer Chemotherapy. *Met. Based. Drugs* **2010**, *2010*, 1–7.

(97) Kasahara, K.; Fujiwara, Y.; Nishio, K.; Ohmori, T.; Sugimoto, Y.; Komiya, K.; Matsuda, T.; Saijo, N. Metallothionein Content Correlates with the Sensitivity of Human Small Cell Lung Cancer Cell Lines to Cisplatin. *Cancer Res.* **1991**, *51* (12), 3237–3242.

(98) Lammers, T.; Rizzo, L. Y.; Storm, G.; Kiessling, F. Personalized Nanomedicine. *Clin. Cancer Res.* **2012**, *18* (18), 4889–4894.

(99) Bar-Zeev, M.; Livney, Y. D.; Assaraf, Y. G. Targeted Nanomedicine for Cancer Therapeutics: Towards Precision Medicine Overcoming Drug Resistance. *Drug Resist. Updat.* **2017**, *31*, 15–30.

(100) Uchino, H.; Matsumura, Y.; Negishi, T.; Koizumi, F.; Hayashi, T.; Honda, T.; Nishiyama, N.; Kataoka, K.; Naito, S.; Kakizoe, T. Cisplatin-Incorporating Polymeric Micelles (NC-6004) Can Reduce Nephrotoxicity and Neurotoxicity of Cisplatin in Rats. *Br. J. Cancer* **2005**, *93* (6), 678–687.

(101) Nishiyama, N.; Okazaki, S.; Cabral, H.; Miyamoto, M.; Kato, Y.; Sugiyama, Y.; Nishio, K.; Matsumura, Y.; Kataoka, K. Novel Cisplatin-Incorporated Polymeric Micelles Can Eradicate Solid Tumors in Mice. *Cancer Res.* **2003**, *63* (24), 8977–8983.

(102) Kappel, C.; Seidl, C.; Medina-Montano, C.; Schinnerer, M.; Alberg, I.; Leps, C.; Sohl, J.; Hartmann, A.-K.; Fichter, M.; Kuske, M.; Schunke, J.; Kuhn, G.; Tubbe, I.; Paßlick, D.; Hobernik, D.; Bent, R.; Haas, K.; Montermann, E.; Walzer, K.; Diken, M.; Schmidt, M.; Zentel, R.; Nuhn, L.; Schild, H.; Tenzer, S.; Mailänder, V.; Barz,

M.; Bros, M.; Grabbe, S. Density of Conjugated Antibody Determines the Extent of Fc Receptor Dependent Capture of Nanoparticles by Liver Sinusoidal Endothelial Cells. *ACS Nano* **2021**.

(103) Alkilany, A. M.; Zhu, L.; Weller, H.; Mews, A.; Parak, W. J.; Barz, M.; Feliu, N. Ligand Density on Nanoparticles: A Parameter with Critical Impact on Nanomedicine. *Adv. Drug Deliv. Rev.* **2019**, *143*, 22–36.

(104) Gao, X.; Lu, Y.; Wu, B.; Miao, J.; Chen, P.; Yang, B.; Qian, J.; Si, J.; Cao, M.; Xia, R. Interface Cisplatin-Crosslinked Doxorubicin-Loaded Triblock Copolymer Micelles for Synergistic Cancer Therapy. *Colloids Surfaces B Biointerfaces* **2020**, *196* (June), 111334.

(105) Hentze, M. W.; Muckenthaler, M. U.; Galy, B.; Camaschella, C. Two to Tango: Regulation of Mammalian Iron Metabolism. *Cell* **2010**, *142* (1), 24–38.

(106) Ganz, T. Macrophages and Systemic Iron Homeostasis. *J. Innate Immun.* **2012**, *4* (5–6), 446–453.

(107) Muckenthaler, M. U.; Rivella, S.; Hentze, M. W.; Galy, B. A Red Carpet for Iron Metabolism. *Cell* **2017**, *168* (3), 344–361.

(108) Weissleder, R.; Stark, D.; Engelstad, B.; Bacon, B.; Compton, C.; White, D.; Jacobs, P.; Lewis, J. Superparamagnetic Iron Oxide: Pharmacokinetics and Toxicity. *Am. J. Roentgenol.* **1989**, *152* (1), 167–173.

(109) Dadfar, S. M.; Roemhild, K.; Drude, N. I.; von Stillfried, S.; Knüchel, R.; Kiessling, F.; Lammers, T. Iron Oxide Nanoparticles: Diagnostic, Therapeutic and Theranostic Applications. *Adv. Drug Deliv. Rev.* **2019**, *138*, 302–325.

(110) Toth, G. B.; Varallyay, C. G.; Horvath, A.; Bashir, M. R.; Choyke, P. L.; Daldrup-Link, H. E.; Dosa, E.; Finn, J. P.; Gahramanov, S.; Harisinghani, M.; Macdougall, I.; Neuwelt, A.; Vasanawala, S. S.; Ambady, P.; Barajas, R.; Cetas, J. S.; Ciporen, J.; DeLoughery, T. J.; Doolittle, N. D.; Fu, R.; Grinstead, J.; Guimaraes, A. R.; Hamilton, B. E.; Li, X.; McConnell, H. L.; Muldoon, L. L.; Nesbit, G.; Netto, J. P.; Petterson, D.; Rooney, W. D.; Schwartz, D.; Szidonya, L.; Neuwelt, E. A. Current and Potential Imaging Applications of Ferumoxytol for Magnetic Resonance Imaging. *Kidney Int.* **2017**, *92* (1), 47–66.

(111) Kowalczyk, M.; Banach, M.; Rysz, J. Ferumoxytol: A New Era of Iron Deficiency Anemia Treatment for Patients with Chronic Kidney Disease. *J. Nephrol.* **2011**, *24* (6), 717–722.

(112) EMA. *Rienso Withdrawal of the Marketing Authorization in the European Union*; EMA/43791/2015; 2015.

(113) Zanganeh, S.; Hutter, G.; Spitler, R.; Lenkov, O.; Mahmoudi, M.; Shaw, A.; Pajarinen, J. S.; Nejadnik, H.; Goodman, S.; Moseley, M.; Coussens, L. M.; Daldrup-Link, H. E. Iron Oxide Nanoparticles Inhibit Tumour Growth by Inducing Pro-Inflammatory Macrophage Polarization in Tumour Tissues. *Nat. Nanotechnol.* **2016**, *11* (11), 986–994.

(114) Thielmann, C. M.; Costa da Silva, M.; Muley, T.; Meister, M.; Herpel, E.; Muckenthaler, M. U. Iron Accumulation in Tumor-Associated Macrophages Marks an Improved Overall Survival in Patients with Lung Adenocarcinoma. *Sci. Rep.* **2019**, *9* (1), 11326.

(115) Costa da Silva, M.; Breckwoldt, M. O.; Vinchi, F.; Correia, M. P.; Stojanovic, A.;

Thielmann, C. M.; Meister, M.; Muley, T.; Warth, A.; Platten, M.; Hentze, M. W.; Cerwenka, A.; Muckenthaler, M. U. Iron Induces Anti-Tumor Activity in Tumor-Associated Macrophages. *Front. Immunol.* **2017**, *8* (November).

(116) Trujillo-Alonso, V.; Pratt, E. C.; Zong, H.; Lara-Martinez, A.; Kaittanis, C.; Rabie, M. O.; Longo, V.; Becker, M. W.; Roboz, G. J.; Grimm, J.; Guzman, M. L. FDA-Approved Ferumoxytol Displays Anti-Leukaemia Efficacy against Cells with Low Ferroportin Levels. *Nat. Nanotechnol.* **2019**, *14* (6), 616–622.

(117) Menk, F.; Fokina, A.; Oschmann, B.; Bauer, T. A.; Nyquist, Y.; Braun, L.; Kiehl, J.; Zentel, R. Functionalization of P3HT with Various Mono- and Multidentate Anchor Groups. *J. Braz. Chem. Soc.* **2018**, *29* (5).

(118) Amstad, E.; Gillich, T.; Bilecka, I.; Textor, M.; Reimhult, E. Ultrastable Iron Oxide Nanoparticle Colloidal Suspensions Using Dispersants with Catechol-Derived Anchor Groups. *Nano Lett.* **2009**, *9* (12), 4042–4048.

(119) Sevier, C. S.; Kaiser, C. A. Formation and Transfer of Disulphide Bonds in Living Cells. *Nat. Rev. Mol. Cell Biol.* **2002**, *3* (11), 836–847.
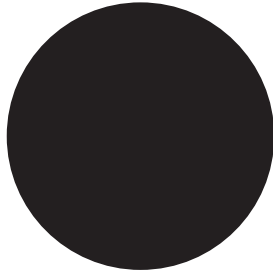
Nederlandse Samenvatting

Nederlandse Samenvatting

In dit proefschrift worden gecross-linkte polymere micellen (core cross-linked polymeric micelles, CCPMs) onderzocht en hun potentieel vergroot voor het transport van hydrofobe actieve farmaceutische ingrediënten. Met polypept(o)iden als de polymeerplatformtechnologie werden de fundamentele implicaties van secundaire structuurvorming op de ringopening polymerisatie van *N*-carboxyanhydriden (NCAs) en de zelf-assemblage van reactieve amfifiele polymeren onderzocht en geoptimaliseerd. CCPMs met functionele kernarchitecturen die externe of ziekte-gerelateerde stimuli bedienen, werden ontwikkeld. Om een robuuste CCPM-productie tot stand te brengen, mechanismen van geneesmiddelenresistentie te overwinnen en therapeutische middelen voor immunomodulatie te onderzoeken, werd polymeerwetenschap gecombineerd met organische en anorganische chemie.

Hoofdstuk 1 geeft een algemene inleiding over nanogeneeskunde en polypept(o)iden. Hier werd de reden verklaart voor het gebruik van nanocarriers om het farmacokinetisch profiel van actieve farmaceutische ingrediënten (APIs) te veranderen. Relevante dragersystemen werden gepresenteerd, en het belang van afscherming van het oppervlak om niet-specifieke opname door het mononucleaire fagocyten-systeem (MPS) te voorkomen werd geschetst. Het versterkte permeabiliteits- en retentie-effect (EPR) als een mechanisme voor de passieve aanrijking van geneesmiddelen in tumoren werd geïntroduceerd, kritisch besproken, en toekomstige trends werden bekendgemaakt. De actuele ontwikkelingen op het gebied van polymere micellen en CCPMs werden besproken. Verder werden polypept(o)iden onderzocht als een nieuwe klasse van functionele polymeren die volledig gebaseerd zijn op endogene aminozuren. Het mechanisme van de ringopening polymerisatie van NCAs werd uitgelegd, en huidige trends in NCA polymerisatie werden geïdentificeerd. Tenslotte werden de vroege en meest recente ontwikkelingen op het gebied van de biomedische toepassing van polypept(o)iden aangegeven.

In **hoofdstuk 2** werd de invloed van racemisch *S*-ethylsulfonyl-DL-cysteïne onderzocht om de ringopening polymerisatie te verbeteren voor polypeptiden die zoals polycysteine tijdens de polymerisatie antiparallele ß-platen ontwikkelen. De thiol-reactive *S*-ethylsulfonyl-DL-cysteïne NCA werd gesynthetiseerd en gepolymeriseerd volgens analogie met de enantiomerisch zuivere *S*-ethylsulfonyl-L-cysteïne. Met de racemische NCA was het mogelijk om volledige monomeer

transformatie te bereiken en dus ketenlengtes tot $X_n = 102$ te synthetiseren, corresponderend met een moleculairgewicht van 20.0 kDa. Bovendien toonde onderzoek van de reactiesnelheid hogere reactiesnelheidsconstantes (gemiddeld 40% sneller), terwijl de reactie nog steeds door het Avrami-model kon worden beschreven, wijzend op een lage oplosbaarheid. Vervolgens was alleen een lagere tendens, maar geen volledige scheiding van de ß-platen met infraroodspectroscopie (IR) herkenbaar. Echter, de volledige omzetting van momomeer S-ethylsulfonyl-DL-cysteïne NCA maakte de polymerisatie van een triblokcopolymeer mogelijk door het stapgewijs toevoegen van monomeer, die anders ontoegankelijk zou zijn voor het enantiopure aminozuur, tenzij extra opzuivering zou worden geïntroduceerd.

De invloed van de secundaire structuur op de zelf-assemblage van thiol-reactive copolymeren werd in **hoofdstuk 3** onderzocht. Daarom werd een bibliotheek van copolymeren van enantiomerisch zuivere polysarcosine-*blok*-poly(S-ethylsulfonyl-L-cysteïne) (pSar-*b*-p(L)Cys(SO$_2$Et)), racemisch pSar-*b*-p(DL)Cys(SO$_2$Et), en pSar-*b*-poly(S-ethylsulfonyl-L-homocysteïne) (pSar-*b*-p(L)Hcy(SO$_2$Et)) gesynthetiseerd. De secundaire structuurvorming van de polypeptiden werd geanalyseerd door IR en circulaire dichroïsmespectroscopie, waarbij een α-helix werd gedetecteerd voor pSar-*b*-p(L)Hcy(SO$_2$Et), antiparallele ß-platen voor pSar-*b*-p(L)Cys(SO$_2$Et), en verstoorde ß-platen voor racemisch pSar-*b*-p(DL)Cys(SO$_2$Et). Gedurende zelfassemblage geïnduceerd door oplosmiddel wisseling, toonden de antiparallele ß-platen de sterkste neiging tot zelfassemblage, gevolgd door het α-helix copolymeer en als laatste de verstoorde ß-platen, zoals gekwantificeerd werd door dynamic light scattering (DLS). Deze resultaten werden verder zichtbaar toen de structuren werden geanalyseerd via atoomkrachtmicroscopie (AFM) of transmissie-elektronenmicroscopie (TEM), waarbij wormachtige, volledig ronde of enigszins langwerpige vormen zichtbaar waren. Secundaire structuurvorming van thiol-reactieve copolymeren is dus een elegant instrument om de kenmerken van nano-geneesmiddelen aan te passen.

In **hoofdstuk 4** werd de cross-linkingsdichtheid als parameter beoordeeld om de stabiliteit van CCPMs gebaseerd op pSar-*b*-p(L)Cys(SO$_2$Et)$_n$ te verfijnen. Om structuur-activiteit relaties te definiëren werden de lengtes van het te cross-linken p(L)Cys(SO$_2$Et)$_n$ blok geselecteerd op $X_n = 17$ of 30, en mono-, bi-, of tri-functionele thiol-reagentia werden gesynthetiseerd en toegepast om de S-ethylsulfonyl groep aan te pakken voor uitdovings of cross-linkingsreacties. Als screeningstechnieken werden asymmetrische flowveld-flow fractionering (AF4)

en fluorescentie correlatiespectroscopie (FCS) toegepast. Hierbij toonde de AF4 analyse in menselijk bloedplasma en eenduidige connectie tussen de cross-linkingsdichtheid en de stabiliteit van de polymere micellen. Grote fracties van aggregaten werden gevonden voor niet-gecrosslinkte micellen en nog steeds voor CCPMs van de bi-functionele cross-linkers en $X_n = 17$, maar niet wanneer de tri-functionele peptide cross-linker werd toegepast. Evenwel, volgens de analyse van de bloed circulatiehalfwaardetijd of biodistributie na intraveneuze toediening aan muizen was geen onderscheid tussen de verschillende nanodeeltjes mogelijk, waarbij een halfwaardetijd van 11.3 - 19-1 h voldoende stabiliteit aangaf voor medicijnafgifte via passieve targeting mechanismen.

Om een grootschalige productie van CCPMs mogelijk te maken werd in **hoofdstuk 5** een continu productieproces ontwikkeld en een strategie gepresenteerd om deze CCPMs onafhankelijk van de synthese stimuli-responsief met APIs te beladen. De zelf-assemblage en de cross-linking van micellen gebaseerd op pSar-*b*-p(L)Cys(SO$_2$Et) met dihydrolipoïnezuurhydrazide werd aangepast voor de productie middels spleet-interdigitale micromixers. Met geoptimaliseerde proces parameters was het mogelijk om tot 650 mg CCPMs/h met een enkel instrument te produceren. Verder werden deze CCPMs gezuiverd door online tangentiële flowfiltratie, waarbij het aandeel van ongeconjugeerd polymer onder de detectie limit blijft ($\leq 0.5\%$). In een volgende stap werden deze CCPMs met paclitaxel-levulinezuur geladen (PTX@CCPMs), waardoor stimuli-responsieve afgifte van de API bij endo-lysosomale pH-waarden mogelijk was. Wanneer getest in celweek- en xenograft B16F1 zebravislarvenmodellen, vertoonden PTX@CCPMs vergelijkbare prestaties maar verminderde toxiciteit in vergelijking met state-of-the-art behandeling met paclitaxel, geformuleerd als albumine-gebonden nanodeeltjes (nab-paclitaxel). In conclusie kan de gepresenteerde strategie de CCPM-productie eenvoudiger en robuuster maken, waardoor gescreend kan worden op combinatietherapiën.

In **hoofdstuk 6** werden polypept(o)ides gecombineerd met fotoresponsieve ruthenium(II)-complexen als op metaal gebaseerde APIs om licht als externe stimulans voor medicijnafgifte uit CCPMs te gebruiken. Polypept(o)ides op basis van pSar-*b*-poly(glutaminezuur) (pSar-*b*-pGlu) werden gesynthetiseerd en gemodificeerd met aromatische nitrilgroepen voor de coördinatie van bis(bipyridine)ruthenium(II) ([Ru(bpy)$_2$]$^{2+}$) of bis(biquinoline)ruthenium(II) ([Ru(biq)$_2$]$^{2+}$) complexen. Afhankelijk van de flexibiliteit of hydrofobiciteit van de linker werden bolvormige of wormachtige micellen verkregen. De voortgang van

de cross-linkingsreactie kon worden gevolgd via de kleurverandering die voortkomt uit de liganduitwisselingsreactie. De cross-linking had geen invloed op de grootteverdeling, maar resulteerde in stabiele CCPMs volgens GPC in hexafluoroisopropanol (HFIP) en DLS in menselijk bloedplasma. Voor medicijnafgifte konden CCPMs die [Ru(bpy)$_2$]$^{2+}$ bevatten binnen 300 s worden gesplitst, terwijl slechts onvoldoende lichtgeïnduceerde solvolyse werd waargenomen voor [Ru(biq)$_2$]$^{2+}$, verwijzend naar lage kwantumopbrengsten en de dichte micellaire kern. De fotoresponsieve CCPMs werden beoordeeld in celweek en het *in ovo*-model bevestigde een hoge biocompatibiliteit en langdurige vasculaire circulatie die samen de basis vormen voor toekomstig onderzoek voor op metaal gebaseerde APIs met hoge cytotoxiciteit en snelle splitsingsprofielen.

Hoofdstuk 7 was gericht op het beoordelen van precisiegeneeskunde om de heterogene respons te verklaren van hoofd-halskankerpatiënten op therapeutische behandelingen. Daarom werd een cisplatine-resistente hoofd-halskankercellijn bewerkstelligd en gesequenced. Medicijnopname via het ionkanaal LRRC8A werd geïdentificeerd als de moleculaire route voor cisplatineresistentie. De klinische betekenis van LRRC8A als biomarker werd onderzocht onder een cohort van 500 hoofd-halskankerpatiënten met gegevens uit The Cancer Genome Atlas. Voor patiënten die behandeling met cisplatine kregen, correleerden lage niveaus van LRRC8A met een lagere totale overleving. Om de opname van geneesmiddelen onafhankelijk te maken van LRRC8A, werd cisplatine geconjugeerd aan polypept(o)ides van pSar-*b*-pGlu(ONa). De chlorideliganden van cisplatine werden uitgewisseld door de carboxylaatgroepen in de zijketen van glutaminezuur, wat leidde tot kleine bolvormige polymere micellen (NP$_{Cis}$, $D_h \approx 28$ nm) met een hoge biocompatibiliteit. NP$_{Cis}$ induceerde geen activering van het complementsysteem, colloïdale stabiliteit werd bevestigd door DLS in menselijk bloedplasma en de circulatiehalfwaardetijd van ca. 4 uur in zebravislarven wees op effectieve stabilisatie die de basis vormde voor passieve tumortargeting. In celweek keerde NP$_{Cis}$ met succes cisplatineresistentie om door het LRRC8A-kanaal te omzeilen, wat het belang bevestigde van het combineren van nanogeneeskunde en moleculaire routes voor selectie van patiënten.

Het therapeutisch potentieel van de cofactor ijzer bij specifieke toediening aan macrofagen werd onderzocht in **hoofdstuk 8**. Ijzeroxide nanodeeltjes (SPIONs) werden ingebed in CCPMs op basis van pSar-*b*-p(L)Cys(SO$_2$Et). De genoemde bouwstenen werden gecombineerd door cross-linking met dihydrolipoïnezuur

gericht op chemoselectieve disulfidebindingsvorming en coördinatie naar het SPION-oppervlak middels de carboxylaatgroep. De resulterende SPION-CCPMs toonden colloïdale stabiliteit in menselijk bloedplasma en glutathion-responsieve degradatie. In co-culturen van primaire muriene macrofagen en Lewis longcarcinoomcellen werden de SPION-CCPMs specifiek door macrofagen opgenomen in een op ijzer gerelateerde feedback-loop manier. De langzame ijzerafgifte van SPION-CCOMs veroorzaakte een sterk ontsteking gerelateerd fenotype in zowel muizen- als menselijke macrofagen. Vervolgens werden significant verhoogde niveaus gedetecteerd van ontstekingachtige oppervlaktemarkers, bijvoorbeeld cluster van differentiatie 86 (CD86) en cytokines zoals tumornecrosefactor α (TNFα) en interleukine 1ß (IL-1ß). De steriele ontsteking van macrofagen werd verder bevestigd *in vivo*, waarbij SPION-CCPMs intratracheal aan muizen toegediend werden. Op basis van het concept van ontwerp-voor-vrijgave kunnen SPION-CCPMs worden geïntroduceerd als een kansrijk adjuvans om pathologische immuuntolerantie te overwinnen en macrofagen in de tumormicro-omgeving te activeren.
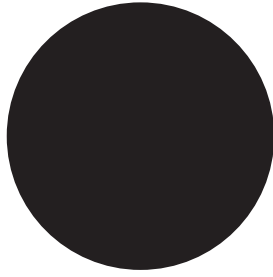
Curriculum Vitae

Scientific Publications

Ph.D. Portfolio

Curriculum Vitae

Tobias Alexander Bauer was born on May 10th, 1989, in Mainz, Germany. In 2008, he obtained his high school degree from the Bischöfliches Willigis-Gymnasium in Mainz, Germany. In the same year, he started a vocational training as a chemical laboratory technician at Sanofi-Aventis Deutschland GmbH in Frankfurt a. M., Germany, and graduated in 2011. After six months of working as a technician, he started studying chemistry at Johannes Gutenberg University (JGU) in Mainz, Germany. In 2015, he obtained the degree Bachelor of Science in chemistry, followed by the degree Master of Science in chemistry in 2017. For his bachelor's thesis, he focused on the synthesis of polythiophenes for applications in hybrid solar cells under the supervision of Prof. Dr. R. Zentel. During his master's studies, he joined the University of Toronto, Canada, for six months. Supported by Prof. Dr. M. Shoichet, he encountered the medical application of polymers for tissue engineering and drug delivery. Back at JGU, he started research for his master's thesis on polymeric micelles for drug delivery with Dr. M. Barz. His master's thesis was awarded by the Fritz-Henkel-Stiftung. After his studies, he returned to Sanofi-Aventis Deutschland GmbH for an internship opportunity in project management. In 2017, he started his Ph.D. research at the Department of Chemistry at the JGU in Mainz under the supervision of Dr. M. Barz in close collaboration with the collaborative research center CRC1066 for nanodimensional polymer therapeutics for tumor therapy. He successfully applied for funding from the HaVo Stiftung and the Graduate School of Excellence Materials Science in Mainz. In his Ph.D. research, he investigated polypept(o)ides as a novel material for drug delivery, focusing on the synthesis and application of core cross-linked polymeric micelles, as described in this thesis. Together with Prof. Dr. M. Barz, he transferred to Leiden Academic Centre for Drug Research at Leiden University, Leiden, the Netherlands, in 2020. Here, he was further supervised by Prof. Dr. A. Kros from the Leiden Institute of Chemistry. Until December 2021, he finalized his research projects leading to several publications. He presented his research at numerous summer schools and national and international conferences and received two presentation awards. During his Ph.D. research, he was involved in lecturing and teaching practical academic courses. Further, he trained and supervised a laboratory technician trainee and Bachelor and Master students. Since February 2022, he has been working as a project manager for polymer development at the department of Research, Development & Innovation at Evonik Operations GmbH in Darmstadt, Germany.

Scientific Publications / Manuscripts of This Thesis

Bauer, T. A.; Muhl, C.; Schollmeyer, D.; Barz, M. Racemic S-(Ethlylsulfonyl)-DL-cysteine N-Carboxyanhydrides Improve Chain Lengths and Monomer Conversion for B-Sheet-Controlled Ring-Opening Polymerization. *Macromol. Rapid Commun.* **2021**, *42* (8), 2000470.

Bauer, T. A.; Imschweiler, J.; Muhl, C.; Weber, B.; Barz, M. Secondary Structure-Driven Self-Assembly of Thiol-Reactive Polypept(o)ides. *Biomacromolecules* **2021**, *22* (5), 2171–2180.

Bauer, T.A.; Alberg, I.; Zengerling, L.A.; Zhang, H.; Besenius, P.; Koynov, K.; Slütter, B.; Zentel, R.; Barz, M. Tuning the Cross-Linking Density of Polymeric Micelles and its Implications on Particle Stability in Human Blood Plasma. *to be submitted to Biomacromolecules*.

Bauer, T.A.; Schramm, J.; Fenaroli, F.; Siemer, S.; Seidl, C.I.; Morsbach, S.; Bleul, R.; Stauber, R.; Maskos, M.; Barz, M Complex Structures Made Simple - Continuous Flow Production of Core Cross-Linked Polymeric Micelles for Paclitaxel Pro-Drug-Delivery. *to be submitted to Advanced Materials*.

Bauer, T. A.; Eckrich, J.; Wiesmann, N.; Kuczelinis, F.; Sun, W.; Zeng, X.; Weber, B.; Wu, S.; Bings, N. H.; Strieth, S.; Barz, M. Photocleavable Core Cross-Linked Polymeric Micelles of Polypept(o)ides and Ruthenium(II) Complexes. *J. Mater. Chem. B* **2021**, *9* (39), 8211–8223.

Siemer, S.; **Bauer, T.A.**; Scholz, P.; Breder, C.; Fenaroli, F.; Harms, G.; Dietrich, D.; Dietrich, J.; Rosenauer, C.; Barz, M.; Becker, S.; Strieth, S.; Reinhardt, C.; Fauth, T.; Hagemann, J.; Stauber, R.H. Targeting Cancer Chemotherapy Resistance by Precision Medicine Driven Nanoparticle-Formulated Cisplatin. *ACS Nano* **2021**, *15*, 18541–18556.

Bauer, T. A.*; Horvat, N. K.*; Marques, O.; Chocarro, S.; Mertens, C.; Colucci, S.; Schmitt, S.; Carrella, L. M.; Morsbach, S.; Koynov, K.; Fenaroli, F.; Blümler, P.; Jung, M.; Sotillo, R.; Hentze, M. W.; Muckenthaler, M. U.; Barz, M. Core Cross-Linked Polymeric Micelles for Specific Iron Delivery: Inducing Sterile Inflammation in Macrophages. *Adv. Healthc. Mater.* **2021**, *10* (19), 2100385.

* both authors contributed equally

Other Scientific Publications

Dal, N.-J. K.; Kocere, A.; Wohlmann, J.; Van Herck, S.; **Bauer, T. A.**; Resseguier, J.; Bagherifam, S.; Hyldmo, H.; Barz, M.; De Geest, B. G.; Fenaroli, F. Zebrafish Embryos Allow Prediction of Nanoparticle Circulation Times in Mice and Facilitate Quantification of Nanoparticle–Cell Interactions. *Small* **2020**, *16*, 1906719.

Johann, K.; Svatunek, D.; Seidl, C.; Rizzelli, S.; **Bauer, T. A.**; Braun, L.; Koynov, K.; Mikula, H.; Barz, M. Tetrazine- and: Trans -Cyclooctene-Functionalised Polypept(o)ides for Fast Bioorthogonal Tetrazine Ligation. *Polym. Chem.* **2020**, *11*, 4396–4407.

Holm, R.; Douverne, M.; Weber, B.; **Bauer, T.**; Best, A.; Ahlers, P.; Koynov, K.; Besenius, P.; Barz, M. Impact of Branching on the Solution Behavior and Serum Stability of Starlike Block Copolymers. *Biomacromolecules* **2019**, *20*, 375–388.

Steinborn, B.; Hirschle, P.; Höhn, M.; **Bauer, T.**; Barz, M.; Wuttke, S.; Wagner, E.; Lächelt, U. Core-Shell Functionalized Zirconium-Pemetrexed Coordination Nanoparticles as Carriers with a High Drug Content. *Adv. Ther.* **2019**, *2*, 1900120.

Zimpel, A.; Al Danaf, N.; Steinborn, B.; Kuhn, J.; Höhn, M.; **Bauer, T.**; Hirschle, P.; Schrimpf, W.; Engelke, H.; Wagner, E.; Barz, M.; Lamb, D. C.; Lächelt, U.; Wuttke, S. Coordinative Binding of Polymers to Metal-Organic Framework Nanoparticles for Control of Interactions at the Biointerface. *ACS Nano* **2019**, *13*, 3884–3895.

Menk, F.*; Fokina, A.*; Oschmann, B.*; **Bauer, T. A.***; Nyquist, Y.; Braun, L.; Kiehl, J.; Zentel, R. Functionalization of P3HT with Various Mono- and Multidentate Anchor Groups. *J. Braz. Chem. Soc.* **2018**, *29*, 1076–1085.

* these authors contributed equally

Otter, R.; Henke, N. A.; Berac, C.; **Bauer, T.**; Barz, M.; Seiffert, S.; Besenius, P. Secondary Structure-Driven Hydrogelation Using Foldable Telechelic Polymer–Peptide Conjugates. *Macromol. Rapid Commun.* **2018**, *39*, 1800459.

Muhl, C.; Schäfer, O.; **Bauer, T.**; Räder, H.-J.; Barz, M. Poly(*S*-Ethylsulfonyl-L-Homocysteine): An α-Helical Polypeptide for Chemoselective Disulfide Formation. *Macromolecules* **2018**, *51*, 8188–8196.

Kemper, B.; Zengerling, L.; Spitzer, D.; Otter, R.; **Bauer, T.**; Besenius, P. Kinetically Controlled Stepwise Self-Assembly of Au$^{\mathrm{I}}$-Metallopeptides in Water. *J. Am. Chem. Soc.* **2018**, *140*, 534–537.

Klinker, K.; Schäfer, O.; Huesmann, D.; **Bauer, T.**; Capelôa, L.; Braun, L.; Stergiou, N.; Schinnerer, M.; Dirisala, A.; Miyata, K.; Osada, K.; Cabral, H.; Kataoka, K.; Barz, M. Secondary-Structure-Driven Self-Assembly of Reactive Polypept(o)ides: Controlling Size, Shape, and Function of Core Cross-Linked Nanostructures. *Angew. Chemie Int. Ed.* **2017**, *56*, 9608–9613.

Patent Application

Bauer, T.A.; Barz, M.; Horvat, N.; Muckenthaler, M.U.; Hentze, M.W.;

Nanoparticles Comprising Iron Oxide Particles Embedded in Polymeric Micelles,

Patent Application Nr. PCT/EP2021/083200; filed together with the European Molecular Biology Laboratory and the Heidelberg University.

Ph.D. Portfolio

Conference Attendencies

2021   LACDR Spring Symposium (online/Leiden, The Netherlands), oral presentation.

Controlled Release Society, BeNeLux Local Chapter Meeting (online/Aachen, Germany), oral flash-presentation.

2019   Debugging the NanoBio-Interfaces to Promote Clinical Translation (Mainz, Germany), oral presentation.

8th BioIron Symposium (Heidelberg, Germany).

2018   12th International Symposium on Polymer Therapeutics (Valencia, Spain), poster presentation.

256th Annual Meeting of the American Chemical Society (Boston, USA), oral presentations.

Gordon Research Conference: Drug Carriers in Medicine and Biology (Mt. Snow, USA), poster presentation.

12th CLINAM Summit (Basel, Switzerland).

2017   Annual Meeting SF Nano (France).

Summer Schools

2021   Leibniz Young Polymer Scientist Forum (online/Aachen, Germany)

2019   Nanomedicine - Formulation, Characterization, Translation (SFB 1066 and SFB1278, Fulda, Germany).

Student Seminar of the Graduate School of Excellence MAINZ (Strasbourg, France)

2018   Nanodimensionale polymere Therapeutika für die Tumortherapie (SFB1066, Bad Münster am Stein, Germany).

Student Seminar of the Graduate School of Excellence MAINZ (Budapest, Hungary).

2017   Summer School macro2fun (Mainz, Germany).

Compulsory Courses

2021   Scientific Conduct

2020   Basic Certificate in Project Management (IPMA Guideline)

2019   Young Entrepreneurs in Science

2018   Business Studies for Chemists

2017   Presentation in English

Industrial Process Engineering and Development